ABSTRACT

Title of Dissertation:	METHANE SOURCE APPORTIONMENT USING CLUMPED ISOTOPOLOGUES
	Jiayang Sun, Doctor of Philosophy, 2025
Dissertation directed by:	Professor James Farquhar, Department of Geology

The global atmospheric methane concentration continues to rise, exacerbating the greenhouse effect. This increase results from the rapid growth of methane source emissions that reflects an imbalance between sources and sinks. The development of methane clumped isotopologue (doubly-substituted methane molecules, $^{13}CH_3D$ and $^{12}CH_2D_2$) measurements provides new opportunities for methane emission source apportionment and for distinguishing methane sink intensities and pathways. However, significant uncertainties remain regarding the intensity and isotopic characteristics of various methane sources and sinks.

This dissertation provides a detailed introduction to various methane sources—categorized either by activity (fossil fuel-related, agriculture, waste, biomass burning, and wetlands) or by formation mechanisms (thermogenic, pyrogenic, and

microbial)—and methane sinks (including OH, Cl, $O(^1D)$, and soil), along with their subcategories and spatial and temporal flux variations. It further discusses the bulk carbon and hydrogen isotope characteristics of these sources and the isotope effects associated with different methane formation and oxidation pathways. The discussion then extends from bulk isotopes to clumped isotopologues. My research aims to enhance our understanding of clumped isotopologue signatures for specific methane sources and sinks and to develop a global atmospheric methane budget model incorporating clumped isotopologues.

Chapter 2 introduces this novel measurement technique. Chapter 3 presents vehicle exhaust methane clumped isotopologue measurements, and provides representative signatures for abiotic and biomass burning methane. The isotope effects of abiotic catalyzed methane oxidation are also discussed. Chapter 4 presents the first clumped isotopologue measurements of atmospheric methane and demonstrates how these data refine previous estimates of the global total methane source compositions. Chapter 5 explores an attempt to use air measurements to infer methane sources and track source variations. Chapter 6 reports measurements from Arctic firn-trapped air samples, allowing the reconstruction of an atmospheric methane clumped isotopologue signal profile for the past 30 years. These time-resolved clumped isotopologue data are incorporated into a global model, providing strong constraints on the source-sink imbalance. Finally, Chapter 7 summarizes the findings and discusses future research directions.

METHANE SOURCE APPORTIONMENT USING CLUMPED ISOTOPOLOGUES

by

Jiayang Sun

Dissertation submitted to the Faculty of the Graduate School of the
University of Maryland, College Park, in partial fulfillment
of the requirements for the degree of
Doctor of Philosophy
2025

Advisory Committee:
Professor James Farquhar, Chair
Professor Karen L. Prestegaard
Professor Alan Jay Kaufman
Professor Laura Lapham
Professor Stephanie Yarwood

Preface

This doctoral dissertation was written during a period of great chaos and upheaval. In February-April 2025, there has been a drastic cut in funding for research, education, environment, and climate-related initiatives, accompanied by the indiscriminate layoff of a large number of government employees. I had originally planned to join the National Oceanic and Atmospheric Administration (NOAA) after completing my Ph.D. to continue my academic research in top-down Greenhouse Gas emissions survey. However, with NOAA facing significant budget cuts and layoffs, this job disappeared. Forced to hastily search for new opportunities in an already turbulent academic and industrial landscape as a foreigner, while writing this dissertation, I found myself grappling with the anxiety of suddenly losing control over my future—I no longer know where I will be six months from now.

This reminded me of the beginning of my Ph.D. journey, which was also an unprecedented time. In 2020, the COVID-19 pandemic erupted globally, making international travel extremely difficult. I was stranded in China, completing the first year of my Ph.D. remotely with 12-hour time difference while waiting for my visa. For an entire year, I was unable to meet my lab colleagues or advisor in person or conduct any experiments. When I finally managed to travel to the U.S. in the summer of 2021, I faced skyrocketing airfare, surging COVID-19 cases, and the looming possibility of not being able to return to China for years.

I had visited the U.S. in 2019, when a round-trip flight from Beijing to Boston took just 13 hours one way and cost only $900 for the round-trip. In 2021, one-way ticket exceeded $1,000, and the journey required flying in the opposite direction—crossing Eurasia, transiting through Qatar or Saudi Arabia, and then crossing the Atlantic to reach the U.S., with the entire trip taking over 30 hours. This situation had not improved by 2025. That summer, the U.S. was recording over 130,000 daily COVID-19 infections and approximately 2,000 daily deaths directly caused by the virus. My suitcase was filled with masks, disinfectant wipes, and even a hazmat suit. The pandemic changed the way everyone worked, with many stores and government offices closed, and people shifting to online learning and remote work.

In addition to the chaotic beginning and end, the middle of my Ph.D. journey was also far from smooth. I have faced most of the challenges a Ph.D. student can encounter, but I have chosen not to list them—because they are all behind me now. I had to admit that a speck of dust from the era can feel like a mountain on the head of an ordinary individual.

Looking back, I don't think I solved all these problems, but I did manage to endure them and achieved some results. This was similar to what happened during my undergraduate. I believe the best thing I did was I did not stop—I didn't stop doing experiments, didn't stop thinking, didn't stop writing, and didn't stop solving problems. As long as I kept moving forward, I was not defeated. Additionally, I protected myself mentally, or rather, I made peace with myself—adjusting my expectations, changing my career goals, smoothly transitioning my research direction, and accepting everything with a calmer mindset.

While writing this dissertation, I realized that I am still well-suited for academia and that I genuinely love it. This dissertation aims to systematically summarize and present my knowledge and explorations related to methane and methane clumped isotopologues. I found myself unable to control the growing length of the dissertation—I was excited to compile and share what I had learned and discovered. I hope this dissertation will be helpful to researchers in the same field, and I hope that whoever reads it will enjoy it.

Jiayang Sun

Mar 8, 2025

Acknowledgements

In the first year of my Ph.D. (late 2020), I attended a friend's dissertation defense. After her academic presentation, she spent 20 minutes delivering a detailed acknowledgment. Seeing her display photos one by one, expressing gratitude to her family, teachers, colleagues, and friends at such a significant moment in her life, I found it deeply meaningful. Her photo with me also appeared on the screen, and though I expected it, I was still thrilled. From then on, I had this impression: a Ph.D. defense is a place where one can freely spend time expressing gratitude (though in the following five years, I realized that acknowledgments during defenses are usually brief). Over the course of my Ph.D., I frequently updated a document listing people who had significantly helped me in various aspects of life and research, just so I could mention their names here (though the list is inevitably incomplete). I am grateful to everyone who has helped me, and I will do my best to help those who seek my assistance—this is one of my life principles. I believe kindness must be passed on. Here, I sincerely express my gratitude to them.

I would like to especially thank my Ph.D. advisor, Prof. James Farquhar, and his wife, Lisa Tuit. James's passion for academia, his care for students, and the couple's love for life have deeply inspired me. Without his support, I could not have had such a rich and diverse Ph.D. experience. I am particularly grateful to my manager at the National Oceanic and Atmospheric Administration (NOAA) Air Resources Laboratory (ARL), Dr. Xinrong Ren. You are a diligent and dedicated academic and government employee, someone I aspire to emulate. Your support and assistance have not gone unnoticed, and I am fortunate to have you as my mentor. 我要尤其感谢我的父母 (I am especially thankful to my parents), 孙路明 (Luming Sun) and 张红亚

(Hongya Zhang), for 25 years of nurturing. You are my solid foundation, giving me the confidence to explore the world. I am deeply grateful to my girlfriend, 刘梓峤 (Ziqiao Liu). I never imagined someone could so seamlessly integrate into my world, becoming a part of my life and my emotional pillar. I hope to overcome all challenges with you and spend the rest of our life together.

I am grateful to Prof. 黄方 (Fang Huang) from my undergraduate alma mater, the University of Science and Technology of China (USTC), for guiding me onto the academic path. I thank Prof. 沈延安 (Yan'an Shen) and Prof. 郭卫福 (Weifu Guo) for their guidance and for keeping up with my progress during my Ph.D.. My summer research internship at Massachusetts Institute of Technology (MIT) in 2019 was a pivotal moment. I thank my advisor at the time, Prof. Shuhei Ono, a brilliant scientist and engineer. I also thank Dr. Jeemin Rhim, Dr. Ellen Lalk, Dr. Kelsey Moore, Prof. 崔行骞 (Xingqian Cui), Dr. Gareth Izon, and others for their constant kindness and encouragement. You solidified my decision to pursue a Ph.D.—being among such brilliant people, where everyone can be the "stupid" one receiving help or the "smart" one offering assistance. Special thanks to Dr. Jeemin Rhim—you are truly an exceptional mentor. I am grateful to my colleagues in the University of Maryland (UMD) Panorama research group: Prof. James Farquhar, Dr. Mojhgan A. Haghnegahdar, Dr. Cédric Magen, Dr. Julianne M. Fernandez, Prof. James W. Dottin III, Dr. Amaury Bouyon, Dr. Danielle Jing-Yi Niu, Juliana Guerra, Julia Elizabeth Famiglietti, Austin Turner, and Mikayla Mary Williams. Your steady approach to research has been a great help to me. Special thanks to postdoc Mojhgan Haghnegahdar—your guidance over the past five years, from teaching me experiments to collaborating on research, has been irreplaceable. I still remember you taking me grocery shopping for affordable food and

inviting us “homeless” international students to your home for Thanksgiving. I also thank postdoc Julianne M. Fernandez—your arrival helped me find a new academic direction. I am grateful to my colleagues at NOAA ARL and UMD’s Department of Atmospheric and Oceanic Science: Dr. Xinrong Ren, Prof. Russ Dickerson, Phillip Stratton (and his puppies Taco and Milo), Hannah Marie Daley, Paul Kelly, Dr. 何昊 (Hao He), and Tiberias Nyapanga Okanga.

I thank the UMD Geology community. I am grateful to my dissertation committee members—Prof. James Farquhar, Prof. Karen L. Prestegaard, Prof. Alan Jay Kaufman, Prof. Laura Lapham, and Prof. Stephanie Yarwood—for their guidance. I thank Prof. Michael N. Evans, Prof. Megan E. Newcombe, Prof. Richard J. Walker, Prof. Mengqiang Zhu (Mike Zhu), and Prof. Sarah Penniston-Dorland for their support and care. I thank Michelle Montero, Todd M. Karwoski, and other administrative staff for their dedicated assistance. I thank my UMD Geology colleagues and classmates: Dr. Ziqin Ni (Grace Ni), Dr. 黄泉城 (Quancheng Huang), Dr. 王静川 (Jingchuan Wang), Dr. 甘甜 (Tian Gan), Kyle Kim, Silvia Camila Castilla Montagut, Dr. Lori Willhite, Lucas Andrews, Kathy Stepien, Karla Núñez, Zachary Vig, Sydney Shelton, Jacob Giles, and Ashley Hanna. Though we worked on entirely different research topics, we always had common topics to discuss and shared hobbies like group sports. Special thanks to Dr. Grace Ni—your comprehensive help during my first three years of the Ph.D. was invaluable. I always hoped to pass on this help, but by the time I graduated, no new Chinese Ph.D. students had joined UMD’s geology program.

I thank researchers outside my lab in the similar research field: Prof. William Leavitt, Prof. Shuhei Ono, Dr. Jeemin Rhim, Dr. Ellen Lalk, Dr. 刘佳睿 (Jiarui Liu), Dr. 董冠男 (Guannan

Dong), 李嘉文 (Jiawen Li), 王欣楚 (Xinchu Wang), 徐漫琳 (Manlin Xu), Prof. 李蒋翰炀 (Ben Li). Thank you for your guidance and for learning alongside me. Special thanks to Dr. 刘佳睿 (Jiarui Liu)—your timely and professional guidance makes you like a half-mentor to me. I also thank Prof. 彭永波 (Yongbo Peng), Prof. 林莽 (Mang Lin), Dr. 解东来 (Donglai Xie), Prof. 谢豪 (Hao Xie), Prof. Amy Townsend-Small, Dr. Cynthia A. Randles, Dr. David T. Wang, Dr. Carrie Tuit, Dr. Felipe Javier Cardoso Saldana, Dr. Johan Weijers, Dr. 严董纾 (Jinshu Yan), Dr. Ziqin Ni (Grace Ni), Dr. 黄泉城 (Quancheng Huang), Dr. 刘璐 (Lu Liu) for their guidance in my academic and career development. I thank SLB for my internship opportunity and my co-workers in the SLB End-to-end Methane Emissions Consultant Team and other teams: Tim Okabayashi, Dr. Kanan Patel, Dr. Adolfo Contreras Ruiz Esparza, Glen Hay, Maurane Gelb, and Jeanne BIU. You are all professional and helpful.

I thank my USTC classmates and friends: Dr. 董冠男 (Guannan Dong), Prof. 谢豪 (Hao Xie), Dr. 苏雪 (Xue Su), 孙郁东 (Yudong Sun), 秦子洋 (Ziyang Qin), 陈曦 (Xi Chen), and others, many of whom, like me, continue to explore academia in the U.S. We have maintained communication. I also thank all the USTC alumni I met in Houston during my internship and the USTC Alumni Association for making me feel the power of alumni connections. Special thanks to Dr. 董冠男 (Guannan Dong)—our strikingly similar academic and career paths, as well as our shared personal perspectives, have made your presence at multiple critical moments in my life profoundly meaningful. I thank the Chinese friends I met at UMD—some were my roommates, some my badminton partners, and others I met in various settings: 王佳琦 (Jiaqi Wang), 王紫轩 (Zixuan Wang), 董许亮 (Xuliang Dong, and his puppy Dongdong), Dr. 张化雨 (Huayu Zhang),

司千垚 (Qianyao Si), Dr. Ziqin Ni (Grace Ni), Dr. 黄泉城 (Quancheng Huang), Dr. 刘璐 (Lu Liu), Dr. 王静川 (Jingchuan Wang), Dr. 甘甜 (Tian Gan), Dr. 刘伟哲 (Weizhe Liu), 徐源诚 (Yuancheng Xu), 章维益 (Weiyi Zhang), 沙蕴 (Sasha Sha), 沈子杨 (Ziyang Shen), Siyuan Shen (Sydnie Shen), 王静川 (Jingchuan Wang), 向世元 (Shiyuan Xiang), 李天奕 (Eddie Li), 徐维佳 (Weijia Xu), 叶其然 (Qiran Ye), 殷纬地 (Weidi Yin), 张佩祺 (Peiqi Zhang), 张祎铭 (Yiming Zhang), 李陶然 (Taoran Li), 王清泽 (Qingze Wang) and 顾昊喆 (Alex Gu). Special thanks to 王佳琦 (Jiaqi Wang) and 王紫轩 (Zixuan Wang)—you are exceptionally great roommates. As wanderers far from home, only by supporting each other can we avoid feeling rootless. I thank my middle school 宁波外国语学校 (Ningbo Foreign Language School) and high school 宁波效实中学 (Ningbo Xiaoshi High School) classmates and friends in my hometown of 宁波 (Ningbo, Zhejiang, China): 邱天 (Yumi Qiu) and 郑智镭 (Zhilei Zheng), 马霄羽 (Xiaoyu Ma), 王之艺 (Zhiyi Wang), 蒋楚沁 (Chuqin Jiang), 石子康 (Zikang Shi), 邓宇 (Yu Deng), 叶啸雷 (Xiaolei Ye), 苏起冬 (Qidong Su), 袁昊琦 (Haoqi Yuan), 王超 (Chao Wang), 徐健哲 (Jianzhe Xu), 蔡烨怡 (Yeyi Cai), 王宇歆 (Yuxin Wang), and many others for their help and emotional support during my Ph.D.

我想要再次感谢我的父母，以及我的外公外婆，和已故的爷爷奶奶 (I thank my parents again, as well as my maternal grandparents and my late paternal grandparents). 在外求学这么多年，没有机会好好陪伴你们，我感到非常愧疚 (I feel deeply guilty for not being able to spend more time with you during my years of study abroad). 我的舅舅，阿姨，表弟，堂妹也对我有很多帮助 (My uncles, aunts, cousins, and other relatives have also been a great help). 我

有一个血缘上的大家庭，随着年龄增长，我越来越深刻地感受到了血浓于水的亲情 (I have a large extended family, and as I grow older, I increasingly feel the profound bond of blood ties). 还要感谢在中国许许多多曾对我的学业和家庭有过帮助的人，许多我称你们为“叔叔”，“阿姨”，“伯伯”，“嬸嬸”，其中的许多人我也把你们当作亲人看待 (I also thank the many people in China who have supported my education and family over the years—many of whom I call “Uncle,” “Aunt,” “Elder Uncle,” or “Elder Aunt.” Many of you are like family to me).

Finally, I thank myself for overcoming all the challenges I faced, maintaining high academic ethics and standards, preserving my physical and mental health, and having a rich and fulfilling five years.

My research was financially supported by NASA 80NSSC20K0611, NSF MRI 1725766, NOAA grant NA19NES4320002 (Cooperative Institute for Satellite Earth System Studies - CISESS), Ann G. Wylie Dissertation Fellowship, ESSIC Travel Grant, Green Fellowship in Global Climate Change, Dean’s Fellowship, and James Farquhar’s lab account.

Table of Contents

List of Figures

List of Tables

Chapter 1: Introduction

1.1. Methane and Global Warming

Methane (CH_4) is an important greenhouse gas (GHG). It can efficiently absorb ~7.6 μm infrared radiation. The global warming potential of methane is 81.2 times that of carbon dioxide (CO_2) on a 20-year time scale and 27.9 times on a 100-year time scale (IPCC AR6 WGI SM7, Szopa et al. (2021)). Although atmospheric methane concentration is about 200 times lower than atmospheric CO_2 concentration, the contribution of methane to global radiative forcing is equivalent to about one-third that of carbon dioxide due to its high warming potential (National Academies of Sciences Engineering and Medicine, 2018).

The atmospheric concentration of methane has increased dramatically since the industrial revolution (Figure 1.1). The current global-averaged atmospheric methane concentration (~1936.64 ppb, NOAA GML, Sept. 2024) has almost tripled compared to what it was in 1750 (around 700 ppm, MacFarling Meure et al. (2006)). Methane concentration stopped increasing between 2000 and 2007, but the rise has resumed since 2008 and shows an accelerating trend after 2015. The methane concentration surged in 2020 and 2021, despite pandemic shutdowns (Figure 1.2). The increase rate set a new record in 2020 (14.81 ppb/year) and was outpaced by the rate in 2021 (17.63 ppb/year). The growth rate remains high in recent years (Lan et al. ,2025).

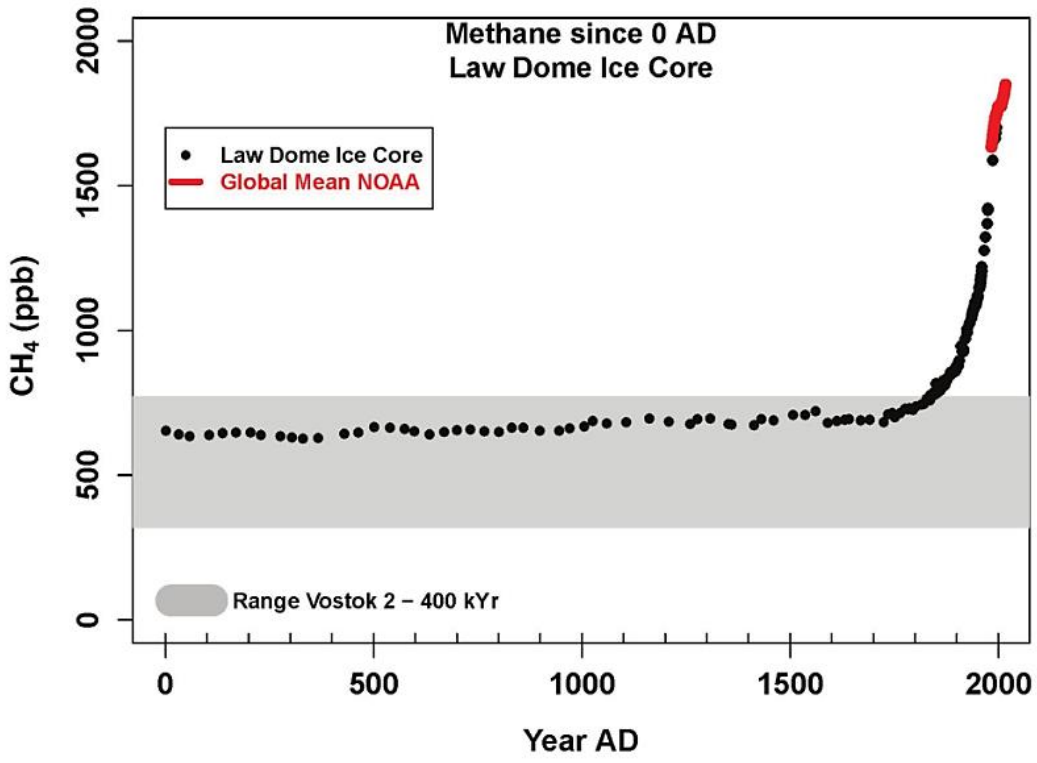

Figure 1.1. **Historical atmospheric methane concentration trend.** The grey shaded area shows the range of methane concentrations from the Vostok, Antarctica ice core, 2000 to 400,000 years before present (Petit et al., 1999). The black points are for methane concentrations in the recent 2000 years obtained from the Law Dome Ice Core (MacFarling Meure et al., 2006). NOAA observations of global mean methane concentrations from 1983 to 2017 are shown in red. (Figure taken from National Academies of Sciences Engineering and Medicine (2018), with permission)

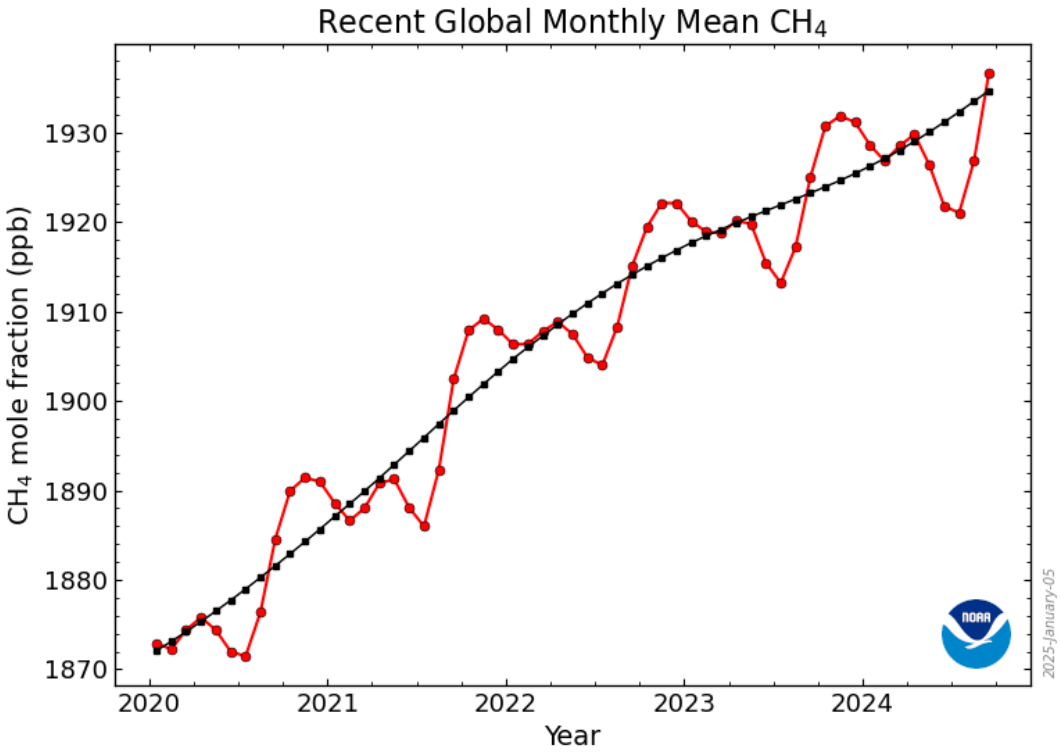

Figure 1.2. **Globally-averaged, monthly mean atmospheric methane concentration in ppb**. Time ranged from Jan. 2020 to July 2024. The red circles are global mean values centered on the middle of each month. The black line is a smoothed trend by calculating 12-month running means. (Figure taken from NOAA GML website, updated on Jan. 05, 2025, Lan et al.)

Climate change driven by global warming in turn has the potential to accelerate methane emissions (Nisbet, 2023a). More frequent extreme weather events and rising temperatures may lead to increased anthropogenic energy consumption, driving greater demand for methane and fossil fuels, thereby increase anthropogenic methane emissions (Nisbet, Jones, et al., 2021). Additionally, increased precipitation and flooding in some area, together with increased temperature, may create more favorable conditions for methanogens and/or trigger large methane emission events. Emissions from wetlands, the largest natural source of methane, are likely to increase (Nisbet, 2023a; Zhang et al., 2017). Increased emissions from tropical and subtropical wetlands haven been observed (Feng et al., 2022; France et al., 2022; Gloor et al., 2021; Peng et

al., 2022; Qu et al., 2022; Shaw et al., 2022) and might be a major reason for atmospheric methane concentrations increasing since 2007 (Feng et al., 2022; Nisbet et al., 2019; Oh et al., 2022; Zhang et al., 2023). Permafrost (Sayedi et al., 2020) and seafloor methane hydrates (Chong et al., 2016) store large amounts of methane and stand to increase their emissions with rising temperatures. Some studies reported methane emissions in subarctic regions that were higher than expected (e.g., Łakomiec et al. (2021)). Thawing permafrost might release huge amounts of methane that has been trapped for a long time, as well as turn permafrost into a suitable environment for methanogen metabolism. Evidence shows that submarine and terrestrial permafrost along the East Siberian Arctic Shelf is becoming unstable and releasing methane into the ocean (Shakhova et al., 2013). The consequence of catastrophic methane release from extensive destabilization of methane hydrates is unpredictable. While some studies suggested that methane released from the seafloor is depleted by the water column before reaching the atmosphere (Berchet et al., 2016; Pisso et al., 2016; Ruppel & Kessler, 2017), the possibility of methane released into the atmosphere from methane hydrates has not been ruled out (Biastoch et al., 2011). The mass extinction events (possibly) caused by methane hydrate release at the end of the Permian should sound an alarm for humans (Brand et al., 2016).

The short atmospheric lifetime of methane makes the reduction of methane emissions a feasible option for mitigating global warming in the short term. Due to the long lifetime of CO_2 at the level of hundreds to thousands of years, the long-term greenhouse effect and climate inertia are irreversible for centuries to millennia (IPCC, 2021). The steady-state lifetime for troposphere atmospheric methane is 9.1±0.9 years according to IPCC AR6 WGI SM7 (IPCC, 2021), or between 9 and 10 years according to Nisbet et al. (2023). The perturbation lifetime is about 12

years, which reflects atmospheric chemistry relaxation times (IPCC, 2013). The ~10-year lifetime means that about 95% of methane currently present in the atmosphere would be scavenged within 20 years if all methane emissions ceased. This short lifetime implies that increasing methane emissions is directly contributing to rising atmospheric methane concentrations. However, it also means that rapid reductions in methane emissions could effectively slow and even reverse the current upward trend, helping to slow global warming in the near term. This could provide humanity with crucial additional time to address broader climate challenges.

Most policymakers have recognized the need and urgency to reduce methane emissions. Climate policies at all levels impose direct and indirect requirements on reducing methane emissions. On the state level, the Greenhouse Gas Reduction Act (GGRA) Plan developed by the Maryland Department of Environment (MDE) set the goal to reduce statewide GHG emissions by 40% from 2006 levels by 2030. On the federal level, the Biden administration committed to cutting total GHG emissions by 50-52% from 2005 levels by 2030. On the global level, more than 110 countries have signed the Global Methane Pledge, which committed to collectively reduce methane emissions by 30% from 2020 levels by 2030. The IPCC report (IPCC, 2021) pointed out that without a substantial reduction in methane emissions in the short term, it will be very difficult to achieve the goal of the Paris Agreement, which is to limit global warming to below 2 degrees Celsius compared to pre-industrial levels. Nevertheless, efforts to reduce methane emissions face significant challenges. Developing countries struggle with limited financial resources and the necessity of economic development, making it difficult for them to play a key role in reducing greenhouse gas emissions. Meanwhile, developed countries face obstacles such

as policy discontinuity and a lack of mutual trust in international cooperation. Although the prevailing global sentiment leans towards collaborating to reduce greenhouse gas emissions in response to global warming, dissenting voices have never vanished. The Trump administration's announcements in 2017 and 2025 of the U.S. withdrawal from the Paris Agreement (The White House, Jan. 20, 2025, https://www.whitehouse.gov/presidential-actions/2025/01/putting-america-first-in-international-environmental-agreements/) cast a shadow over global efforts to reduce greenhouse gas emissions. Some major oil-producing countries strongly lobbied at the 28th United Nations Climate Change Conference (COP28) climate summit, striving to exclude the phrasing of "phasing out fossil fuels" from the agreement (Reuters, Dec. 13, 2023, https://www.reuters.com/business/environment/countries-push-cop28-deal-fossil-fuels-talks-spill-into-overtime-2023-12-12/).

1.2. Methane Budget

To reduce methane emissions, we need to understand the methane budget, i.e., what are the sources of methane (methane release) and sinks of methane (methane consumption), and how much methane each source/sink emits. The methane budget can also be characterized by temporal and spatial attributes, i.e., how emissions and sinks vary across different regions, and how they change over time.

There are two approaches to estimate methane emissions. One is bottom-up method, which estimates source emissions by aggregating and scaling up source-specific measurements, activity data, and emission factors, often derived from ground-based field studies, inventories, or

process-based models. Another one is top-down method, which estimates and apportions methane emissions using satellite remote sensing, aircraft and tower in situ measurements, and atmospheric transport models of the atmosphere. A combination of two methods is often used to construct a methane budget (Figure 1.3). Readers are referred to National Academies of Sciences Engineering and Medicine (2018) and references therein for details on the two methods. There have already been many efforts at global, national, and sectoral levels to create methane inventories at different scales. Some commonly used inventories include the Global Carbon Project (https://www.globalcarbonproject.org/) (Saunois et al., 2024) (Figure 1.4); the Emissions Database for Global Atmospheric Research (EDGAR) (https://edgar.jrc.ec.europa.eu/) (Crippa et al., 2024), developed by the European Union; the GHG Inventory of the United States (US GHGI) (USEPA) (https://www.epa.gov/ghgemissions/inventory-us-greenhouse-gas-emissions-and-sinks-1990-2021), compiled by the U.S. Environmental Protection Agency (EPA); the Oil & Gas Methane Partnership 2.0 (OGMP 2.0) (OGMP, 2023) (https://ogmpartnership.com/), initiated by the United Nations Environment Programme (UNEP); and the Global 0.5-degree Wetland Methane Emissions and Uncertainty (WetCHARTs v1.3.3) (https://daac.ornl.gov/cgi-bin/dsviewer.pl?ds_id=2346) (Bloom et al., 2024), maintained by Oak Ridge National Laboratory (ORNL). Most of these inventories follow the IPCC Guidelines for National Greenhouse Gas Inventories (IPCC, 2006, 2019) and are integrated into the United Nations Framework Convention on Climate Change (UNFCCC) annual GHG emissions reporting framework (https://unfccc.int/topics/mitigation/resources/registry-and-data/ghg-data-from-unfccc).

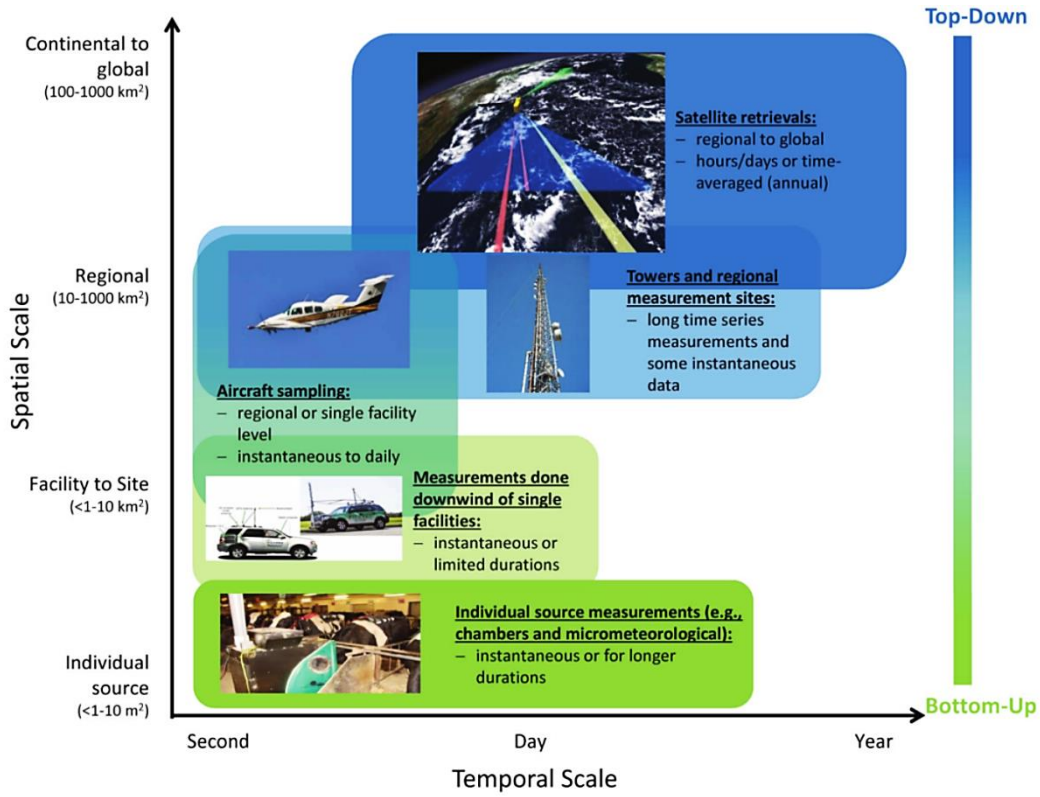

Figure 1.3. **Examples of top-down methods and bottom-up methods.** (Figure taken from National Academies of Sciences Engineering and Medicine (2018), with permission)

Due to the uncertainty in methane emission fluxes from various sources and the strength of methane sinks over the years, the driving factors behind atmospheric methane concentration trends since 2000 remain debated, particularly the causes of the stagnation in methane growth from 2000 to 2007. Some studies suggest that fossil fuel-related methane emissions have increased rapidly since 2000 (e.g., (Franco et al., 2016; Hausmann et al., 2016; Helmig et al., 2016)), implying that the stagnation in methane growth from 2000 to 2007 was due to a significant reduction in microbial emissions counteracting the rise in fossil fuel-related methane emissions, such as reduced methane emissions from rice agriculture in Asia (Kai et al., 2011). On the other hand, other studies have reached the opposite conclusion, arguing that fossil fuel emissions either decreased (e.g., (Nisbet et al., 2016; Schaefer et al., 2016)) or did not increase

(Milkov & Etiope, 2018; Schwietzke et al., 2016), while microbial emissions rose instead. Worden et al. (2017) further pointed out that the role of reduced biomass burning emissions had been underestimated. Looking at the issue of rising methane concentrations from another perspective, McNorton et al. (2016); McNorton et al. (2018) and Rigby et al. (2017); Rigby et al. (2013) argued that variations in atmospheric OH concentrations could significantly influence the strength of methane sink reactions (i.e., its lifetime), providing an alternative explanation to the source-flux-based hypotheses. However, recent modeling studies suggest that OH variations are negligible (Basu et al., 2022; Oh et al., 2022). An increasing number of observational and modeling studies now suggest that the rapid rise in atmospheric methane concentrations since 2007 is primarily driven by large-scale microbial methane emissions from tropical and subtropical regions (Feng et al., 2022; Nisbet, 2023a, 2023b; Nisbet, Jones, et al., 2021; Nisbet et al., 2019; Zhang et al., 2023).

Local and regional budgets are usually even rougher, if not unavailable, because top-down methods often lack the spatial resolution needed to accurately capture such fine-scale emissions and variations, while bottom-up estimations may solely be based on a few field studies. This issue is particularly pronounced in underdeveloped regions.

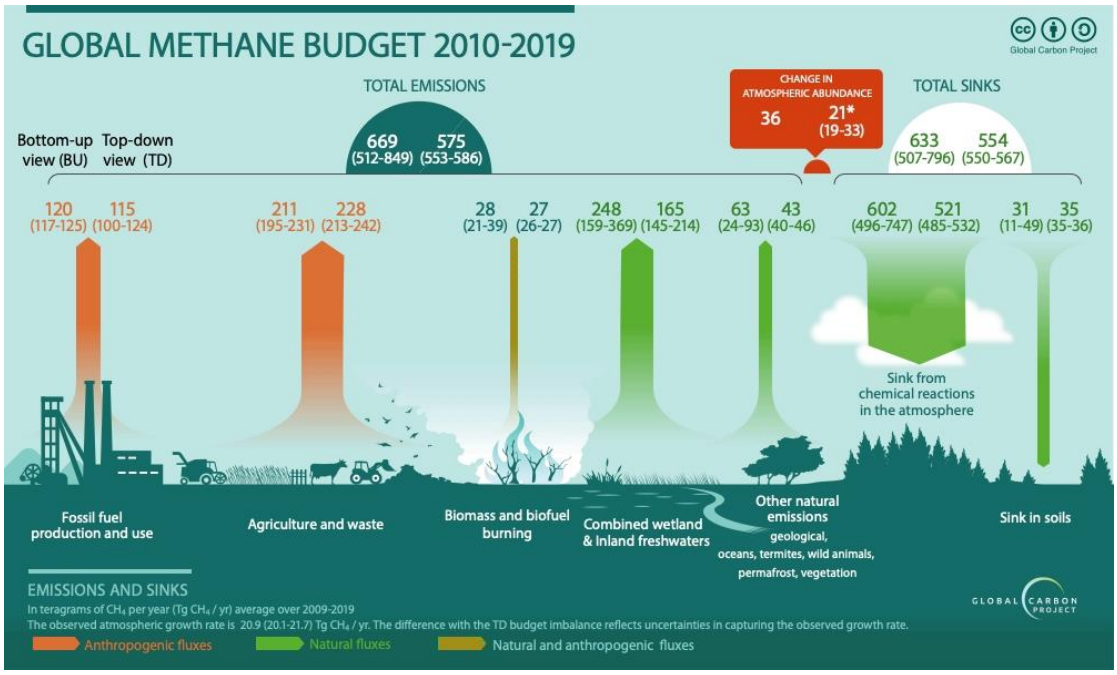

Figure 1.4. **Global methane budget (fluxes for each source and sink category in Tg CH_4 yr^{-1}) for 2010-2019.** The numbers on the left are bottom-up estimations. The numbers on the right are top-down estimations. Natural sources/sinks are in green color and anthropogenic sources are in orange color. (Figure taken from Saunois et al. (2024), under CC BY 4.0)

1.2.1. Methane Sources

For the decade 2010-2019, global methane emissions were estimated to be 575 (553-586) Tg CH_4 yr^{-1} (top-down method) or 669 (512-849) Tg CH_4 yr^{-1} (bottom-up method) (Saunois et al., 2024). About 60% of emissions were attributed to anthropogenic sources, including fossil fuel-related emissions, agriculture, waste treatment, and part of biomass burning. The rest were from natural sources, mainly from wetlands, while inland waters, geological activities, oceans, termites, wild animals, permafrost, and vegetation were thought to contribute less to global methane emissions (Figure 1.4) (Saunois et al., 2024). Compare to the report published four years ago (Saunois et al., 2020), the values estimated using the top-down method remain nearly unchanged, while the bottom-up estimate has been significantly revised downward from 737 Tg

CH_4 yr^{-1} to 669 Tg CH_4 yr^{-1}. This change is primarily due to more precise estimations of methane emissions from wetlands and other natural sources. With significant advancements in satellite measurements (Jacob et al., 2016; Jacob et al., 2022), top-down methane emission inventories have become increasingly accurate, with improved temporal and spatial resolution. This progress has also driven improvements in bottom-up inventories.

However, there is still a mismatch between the top-down and bottom-up estimations, especially when divided into individual sources. Bottom-up methods are challenged by limited spatial coverage and uneven distribution of scientific resources around the world. Further, the temporal variability of methane emissions for sources, such as wetlands, can be substantial. Seasonal fluxes differing by a factor of two to three is common in wetlands (Morin et al., 2014). This makes it challenging to account for fluctuating emission patterns across different seasons or specific time periods. Top-down emission estimation has advanced rapidly over the past decade; however, significant challenges remain. These include limitations in data availability and coverage due to the number and orbital constraints of satellites, restrictions in instrument spatial resolution and flux detection thresholds, and uncertainties associated with the inversion algorithms used to infer emissions (Jacob et al., 2022). The top-down method is still incapable of detecting low-concentration methane enhancements (about 10 ppb level) caused by diffuse regional methane emissions, which are common in wetland areas (Gålfalk et al., 2016). What's more, attributing the fluxes observed through top-down approaches to specific sources still requires accurate and comprehensive ground-based information (Chen et al., 2024; Sherwin et al., 2024). The combination of these factors has led to a mismatch between top-down and bottom-up estimations of emissions.

The following few sections (Sections 1.2.1.1 to 1.2.1.4) will give further introductions on some major methane emission sources.

1.2.1.1. Fossil Fuel-related Emissions

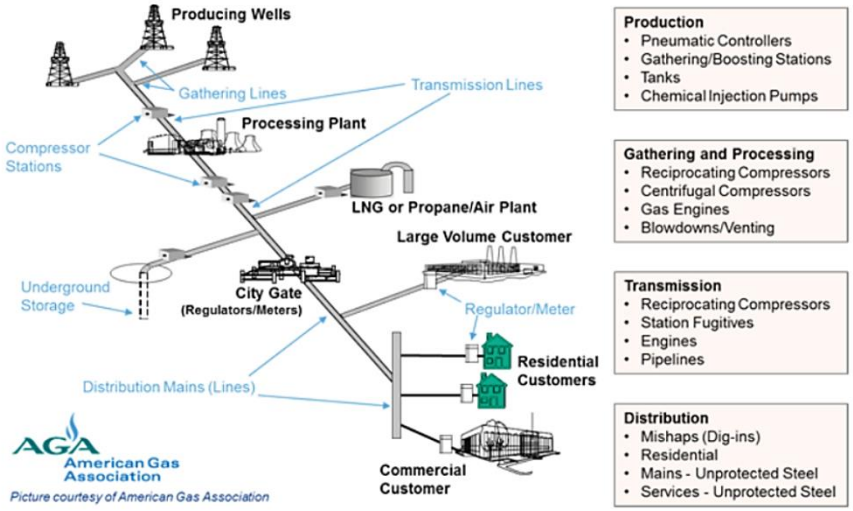

Figure 1.5. **Segments of the natural gas industry**. It includes production, gathering and processing, transmission, and distribution. The top methane emission sources for each category are listed on the right. (Figure taken from National Academies of Sciences Engineering and Medicine (2018), with permission. Originally from American Gas Association.)

The majority of emissions in the "fossil fuel-related emissions" category originate from the exploitation, production, gathering, storage, transportation, processing, and use of oil, natural gas (Figure 1.5), and coal. Among these, exploitation and production are generally referred to as upstream, while gathering, storage, transportation, and processing are classified as midstream, and refining, manufacturing, and distribution fall under downstream. Approximately 80% of emissions come from the upstream sector, particularly from the production phase (IEA, 2024). Within the upstream category, emissions are further classified into stationary combustion,

flaring, fugitives, and venting. For comprehensive definitions of each category, please refer to the OGMP Technical Guidance Document ((OGMP, 2023), https://ogmpartnership.com/guidance-documents-and-templates/) and the American Petroleum Institute Compendium (American Petroleum Institute, 2021).

For example, flaring refers to the incomplete combustion of waste gases that are intentionally directed to a flare system. During various upstream operations, such as drilling, well testing, and oil-gas separation, some gases cannot be fully captured into the production line or are economically unfeasible to recover. These gases are required to be sent to a flaring system, where they are combusted and converted into CO_2 to reduce overall greenhouse gas emissions. When a flaring system operates in compliance with U.S. EPA regulations, U.S. law assumes that at least 98% of CH_4 is destroyed ("40 CFR 60.18,"). However, a field study by Plant, Kort, Brandt, et al. (2022) found that the average Destruction and Removal Efficiency (DRE) in the U.S. is 91.1%, mainly due to increased emissions from unlit and inefficiently combusted flares. Continuous monitoring of the flaring system to ensure that the flame remains in an optimal combustion state can significantly improve the overall DRE. According to World Bank (2023), flaring burns approximately 139 billion cubic meters (~3% of global gas production) annually, accounting for 5-10% of the global GHG emissions from the oil and gas industry.

Another example is venting, which refers to the intentional release of methane. In some coal mines, air must be pumped into ventilation shafts to dilute the associated gas for safety reasons. This diluted gas is then exchanged with the surface air, and most of it is directly released into the atmosphere, leading to methane emissions.

On the other hand, fugitive emissions, also known as leakage, refer to unintentional methane emissions. For instance, pneumatic valves powered by compressed methane, despite not being designed to emit methane, have been identified as one of the most significant leakage sources (Brandt et al., 2016; Frankenberg et al., 2016). Additionally, liquid storage tank hatches and vents may also represent a major source of fugitive emissions (Alvarez et al., 2018). Persistent fugitive emissions generally emit methane slowly, while intermittent or accidental fugitive emissions typically release large amounts of methane over a short period. For example, the Nord Stream natural gas pipeline sabotage possibly released as much as half a million metric tons of methane according to NPR news ("The Nord Stream pipelines have stopped leaking. But the methane emitted broke records," 2022), which might be the largest single methane release event ever recorded, roughly equivalent to 1-2 days of daily methane emissions from the fossil fuel industry. The fugitive leakage percentage during conventional and unconventional oil and gas exploitation is estimated to be 1-3% of production or 13 (+2.1/-1.6) Tg CH_4 yr^{-1} (Alvarez et al., 2018), but some studies suggested that it could be as high as 17% (e.g. (Caulton et al., 2014; Karion et al., 2013; Peischl et al., 2013; Sargent et al., 2021; Schneising et al., 2014)).

More and more research has revealed that, fossil-fuel related methane emissions from the end user side might have been underestimated. Methane mappings in multiple cities (e.g., Boston, MA; Washington D.C.; Indianapolis, IN; London, UK; Paris, France) have detected considerable leakage from underground natural gas pipelines (e.g., (Defratyka et al., 2021; Jackson et al., 2014; Lamb et al., 2016; Lowry et al., 2020; Lu et al., 2025; Phillips et al., 2013; Vogel et al., 2024; von Fischer et al., 2017)). Urban areas with aging cast iron pipelines (e.g., Boston, MA)

have approximately 25 times the methane leakage than cities with more modern piping materials (e.g., Indianapolis, IN) (von Fischer et al., 2017). Replacement of aging pipelines with modern materials has been undertaken to mitigate natural gas leaks; however, Sargent et al. (2021) found that although many leaking natural gas pipelines have been fixed or replaced in Boston since 2013, the city's natural gas leak rate has not decreased significantly. They suggested that the end-use losses might be a large component of emissions that was missing in the inventories. For example, the gas stove and gas fireplace might not quantitatively burn natural gas. Unburned methane from U.S. gas stoves is estimated to be about 0.8–1.3% of their natural gas use (Lebel et al., 2022). The emission factors for these sources have high uncertainties.

The methane emissions from fossil-fuel industry follows a fat-tail distribution, that is, a small proportion of units or incidents contributes a large proportion of the emissions. The fat-tail distribution increases the difficulty of determining fossil fuel-related emissions (Zavala-Araiza et al., 2015). The sampling time interval is not able to capture all the super-emitters, and methane emissions from the fossil fuel category may be underestimated. The fat-tail distribution also provides a strategy for reducing fossil fuel-related emissions, which is that we need to better identify emission sources and prioritize fixing the parts with the highest emissions.

1.2.1.2. Agriculture and Waste

Agriculture and waste, both being anthropogenic emission sources, in total release about the same amount of methane as the fossil fuel industry. In agriculture, rice cultivation and livestock enteric fermentation are the primary contributors to methane emissions.

Rice cultivation, especially the continuous flooding method, requires large amounts of water to keep rice fields submerged under a shallow layer of water (Chen et al., 2013). This creates an ideal metabolic environment for methanogens. Under first-order approximation, methane emissions from rice cultivation are proportional to cultivated area (IPCC, 2006). However, they are also significantly influenced by factors such as plant productivity, soil temperature, soil type, fertilization methods, and whether routine drainage and aeration are applied. When the soil is flooded, it prevents the replenishment of oxygen from the air, thereby entering an anaerobic state that favors methanogenesis. When the soil is moist but not flooded, the presence of some oxygen inhibits the activity of methanogens. When the soil is dry, the activity of methanogen is further suppressed. Thus, continuous flooding generally results in the highest methane emissions, followed by intermittent flooding. In contrast, alternate wetting and drying (AWD) and upland rice farming can effectively reduce methane emissions. However, these methods may come at the cost of increased N_2O emissions (another greenhouse gas) and lower rice yields (IPCC, 2006).

According to the Food and Agriculture Organization of the United Nations (FAO), the global rice cultivation area and yield have been slowly increasing over the past 30 years, with an average annual growth rate of approximately 0.43% (FAO) (https://www.fao.org/faostat/en/#data/QCL/visualize). In China, the world's largest rice producer, rice production has remained relatively stable with fluctuations and has shown signs of gradual decline since 2020. Methane emissions from rice fields are not expected to change significantly, as the slow expansion of cultivated areas globally may be offset by the increasing

adoption of more environmentally friendly agricultural practices (Chen et al., 2013; Shen et al., 2024).

Domestic ruminants, mainly cattle, sheep, and goats, provide stable temperatures, pH, and sufficient carbon supplies in their stomachs, creating ideal conditions for methanogen growth. The IPCC Tier 1 approach assumes a linear relationship between the number of livestock and methane emissions (IPCC, 2006). According to data from (FAO) (https://www.fao.org/faostat/en/#data/QCL/visualize), the global ruminant stock has been steadily increasing over the past 60 years. Taking cattle as an example, the average annual growth rate on cattle number has been 0.86%, with an apparent acceleration in growth since 2003. The production of beef and dairy has increased at an even faster rate than the growth in livestock numbers, which may suggest that the average weight per animal has also increased. Consequently, methane emissions from domestic ruminants have risen accordingly, from approximately 60 Tg CH_4 yr^{-1} in 1960 to around 130 Tg CH_4 yr^{-1} in 2020 (Zhang, Tian, et al., 2022). There are significant differences in methane emission intensity (methane emitted per kilogram of protein produced) across countries, largely due to variations in farming efficiency. In low-income countries, emission intensities can be as high as 4 kg CH_4 per kg of protein, whereas in high-income countries, they can be as low as 0.5 kg CH_4 per kg of protein (Chang et al., 2021). Generally, more efficient livestock systems have lower methane emission intensities. High-income countries tend to have dairy and beef cattle with higher productivity, faster weight gain, younger slaughter ages, and more centralized manure management. This suggests that improving the efficiency of livestock systems could significantly reduce methane emissions from the domestic ruminant industry (Chang et al., 2021). Studies have also indicated that methane

emissions from livestock can be mitigated by modifying feed composition. For example, Roque et al. (2021) found that adding less than 0.5% red seaweed to cattle feed resulted in over an 80% reduction in methane emissions. This is because certain types of red seaweed can produce halogenated methane analogs, which competitively inhibit the methyl transfer reactions essential for methanogenesis. However, feeding practices and climatic conditions vary across countries, leading to differences in emission factors (Chang et al., 2019).

Waste management includes agricultural waste (manure management), landfill (solid waste treatment), and wastewater treatment. The United States is one of the world's largest waste-producing and landfilling countries. According to data from the Organization for Economic Cooperation and Development (OECD), the U.S. has one of the highest per capita waste generation rates, reaching 811 kg per year. Additionally, the recycling rate in the U.S. is relatively low among developed countries, at only 23.4% (OECD, 2018). A large amount of waste is sent to landfills, making them a major source of methane emissions (USEPA) (USEPA GHGI, 2022). Although the U.S. Environmental Protection Agency (EPA) enforces stringent design, operation, and closure requirements for modern landfills under the Resource Conservation and Recovery Act (RCRA) ("40 CFR Part 258,"), it remains uncertain whether landfills strictly comply with these regulations. Reports have indicated that high methane concentrations were detected at the Brown Station Landfill near Washington, D.C., with estimated annual methane emissions several times higher than those reported to the Maryland Department of the Environment (MDE) (Environmental Integrity Project, 2021). A recent nationwide study also suggests that landfill emissions may be higher than reported values

(Cusworth et al., 2024). There is a general lack of third-party oversight of landfill emissions, as accessing landfills for independent verification is challenging.

Landfill gas is produced by the degradation of organic waste. Without effective landfill gas collection systems, these gases can escape from uncovered operational areas and leak through the cover soil. A detailed study of landfills in California, using the California Landfill Methane Inventory Model (CALMIM) (Spokas et al., 2021), found that landfill size was not the determining factor for methane emissions—contrary to the assumption adopted by the IPCC guidance (IPCC, 2006). Instead, the study revealed that cover soil can significantly reduce methane emissions through aerobic methane oxidation. Operational factors such as the thickness and composition of the cover soil, as well as soil moisture and temperature profiles, play a crucial role in determining methane emissions (Spokas et al., 2021). The use of biologically active cover materials can significantly reduce landfill methane emissions (Stern et al., 2007), but the extent of their adoption remains unclear.

1.2.1.3. Biomass Burning

Although biomass burning and combustion-related methane emissions are relatively small compared to major sources, they remain important. These emissions release methane along with co-emitted hydrocarbons and exhibit distinct isotopic signatures (described in Section 1.3.2.2), making them crucial to account for when developing methane budget models. Biomass burning can be either anthropogenic or naturally occurring.

Different models have slightly different estimation on the global methane emissions from wildfires. For example, Zhao et al. (2025) estimated a global average annual methane emission of 24.0 (17.7–30.4) Tg yr^{-1} from 2003 to 2020, while the Global Fire Emissions Database (GFED) estimated an average of 21 ± 2 Tg yr^{-1} from 2002 to 2020 (van Wees et al., 2022). The discrepancy is mainly due to the challenges in quantifying methane emissions from small wildfires, which remain technically difficult to assess. However, both models and observations agree that global methane emissions from wildfires have shown a slight decline over the years, with an annual decrease of approximately 1.1% to 1.6% (van Wees et al., 2022; Worden et al., 2017; Zhao et al., 2025). This reduction is primarily attributed to a significant decline in emissions from the latitudinal band of 30°S–15°N, likely driven by population growth and agricultural expansion, particularly in Africa (Andela et al., 2017; Worden et al., 2017). Biomass burning emissions were likely higher in the 1990s (Hao & Ward, 1993; Simpson et al., 2006), with a peak in 1997. The 1997 forest fires in Indonesia caused a detectable spike in atmospheric methane concentrations (Dlugokencky et al., 2001).

The overall decline in emissions from wildfire does not contradict the statement that climate change has led to more frequent and intense wildfires in some regions (Goss et al., 2020). This is because biomass burning emissions exhibit strong seasonal and regional variations, with hotspots concentrated in tropical and boreal regions, and summer emissions being 2–4 times higher than those in other seasons (Zhao et al., 2025). It remains unclear whether the intensified wildfires since 2019 (e.g., 2019 Siberia, 2023 Canada) have led to an overall increase in emissions or whether they are responsible for the accelerated rise in atmospheric methane concentrations.

Biofuel burning is a type of controlled biomass combustion used for energy generation. Biofuels are widely utilized worldwide, primarily in households. Their incomplete combustion can produce some methane emissions (Vicente et al., 2015). However, the sporadic distribution of biofuel burning makes it challenging to estimate emissions. One available reference point is the global production of conventional biofuels, which increased from 92 billion liters in 2009 to 164.9 billion liters in 2023, with an average annual growth rate of 4.3% (IEA). Although household biofuel burning is more prone to incomplete combustion compared to centralized fuel burning due to limited ventilation (Vicente et al., 2015), the overall scale of biofuel combustion remains relatively small, making it unlikely to be a major source of methane emissions. Methane emissions from the incomplete combustion of household natural gas are generally classified as fossil fuel-related emissions instead of biofuel burning, as these emissions result from the leakage of unburned methane rather than being a byproduct of incomplete combustion.

1.2.1.4. Wetlands

Wetlands are the largest natural source of methane, accounting for about 20% to 30% of global methane emissions. Wetland methane emissions were estimated to be 149 (102-182) Tg CH_4 yr^{-1} (bottom-up) or 181 (159-200) Tg CH_4 yr^{-1} (top-down) for the period 2008-2017 (Saunois et al., 2020). These emissions are expected to increase with ongoing global warming (Zhang et al., 2017). A more recent inventory (Saunois et al., 2024) groups wetlands and inland freshwater sources together, estimating their combined methane emissions at 248 (159–369) Tg CH_4 yr^{-1} based on bottom-up approaches or 165 (145–214) Tg CH_4 yr^{-1} based on top-down methods for the period 2010–2019. The uncertainty in wetland methane emission estimates remains high, which could exceed 30%, largely due to ambiguities in the definition of wetlands and the highly

variable nature of wetland emissions. These emissions are influenced by multiple environmental factors and can vary significantly within individual wetlands, across different regions, and on diel and seasonal scales.

Methane in wetlands is almost entirely of microbial origin. Microbial methane production occurs through various methanogenesis pathways (see Section 1.3.3). Once methane is produced, it undergoes different degrees of oxidation. A portion of the methane reaches the soil surface or water surface and is ultimately released into the atmosphere. Compared to other land and water systems (e.g., dry grassland, ocean), wetlands are particularly favorable for methane production and emission. This is due to several factors. First, wetlands are typically covered by a shallow water layer, which prevents atmospheric oxygen from directly penetrating the soil through pore spaces, thereby maintaining an oxygen-depleted environment in the sediment. Second, the surface layer of wetlands is rich in organic matter. During organic matter decomposition, electron acceptors such as oxygen, sulfate, and nitrate are rapidly consumed, further reinforcing anaerobic conditions below the surface aerobic layer of the wetland soil where electron acceptors are still available. Third, many wetlands are freshwater systems with low sulfate concentrations. Sulfate-reducing bacteria generally outcompete methanogens for electron donors when sulfate is present (Whiticar, 2020), and sulfate can also be used for anaerobic oxidation of methane. The low sulfate levels in freshwater wetlands minimize these competitive and oxidative effects, favoring methanogenesis. Fourth, the methanogenic zone in wetlands is closer to the surface, and the anaerobic environment facilitates the formation of methane bubbles. This allows methane to ascend rapidly, reducing the extent of oxidation before reaching the atmosphere. Fifth, the roots and stems of certain plants like Typha and rice can serve as conduits for both substrate delivery

and methane transport. This mechanism facilitates the supply of necessary substrates for methanogens and provides a fast pathway for methane to be directly released into the atmosphere. Collectively, these factors make wetlands a primary source of natural methane emissions (Whiticar, 2020). Rice fields share many of these characteristics with wetlands. Section 1.3.3 will introduce the detailed definitions and controlling factors of these microbial processes.

Wetland emissions exhibit significant spatial and temporal variability. WetCHARTs is a parametric and process-based model capable of estimating global wetland emissions on a 0.5-degree spatial resolution and monthly time resolution (Bloom et al., 2024). There are also more and more work on evaluating wetland emissions based on satellite observations (e.g., (Jacob et al., 2016; Parker et al., 2018; Yu et al., 2023). On a global scale, tropical regions are methane emission hotspots, particularly the Amazon wetlands, the Indonesian archipelago, and Central Africa, which are estimated to contribute 29%, 13%, and 12% of total global wetland emissions, respectively (Bloom et al., 2021). Another high-emission region is around 50°N in the Northern Hemisphere, mainly the Hudson Bay lowlands. In the Northern Hemisphere's temperate and boreal regions, methane emissions peak between July and September, whereas the peak emission timing in tropical regions remains highly debated (Bloom et al., 2021). However, these findings are primarily based on model simulations or satellite observations (Parker et al., 2018), while field measurements remain sparse, especially in tropical, Southern Hemisphere, and Arctic regions (Dlugokencky et al., 2011; France et al., 2022; Song et al., 2020; Xiao et al., 2024), limiting the accuracy of global wetland emission estimates.

On a smaller scale, methane fluxes can also vary significantly, making it challenging to identify consistent patterns. Even within the same wetland or lake, methane fluxes can differ dramatically due to differences in vegetation patch types (e.g., ~15 mg CH_4 Carbon m^{-2} h^{-1} in sedges/rushes vs. ~8 mg CH_4 Carbon m^{-2} h^{-1} in submerged aquatic vegetation) (Kim et al., 1998; Stewart et al., 2024), time of the day (e.g., ~60 nmol CH_4 m^{-2} s^{-1} at noon vs. ~40 nmol CH_4 m^{-2} s^{-1} at night during summer) (Baldocchi et al., 2012; Kim et al., 1999; Morin et al., 2014), or just site-specific microenvironmental conditions (e.g., 4.9 mg CH_4 m^{-2} day^{-1} from a drier site vs. 100.0 mg CH_4 m^{-2} day^{-1} from a wetter site) (Sachs et al., 2010). These variations do not necessarily follow uniform diurnal or seasonal patterns. Overall, methane emissions from wetlands are strongly influenced by environmental conditions. Figure 1.6 provides a schematic demonstration that connect the wetland methane emissions with microbial activity, environmental factors, and measured parameters, which will be discussed in Section 1.3.3 and Section 1.4.3.5.

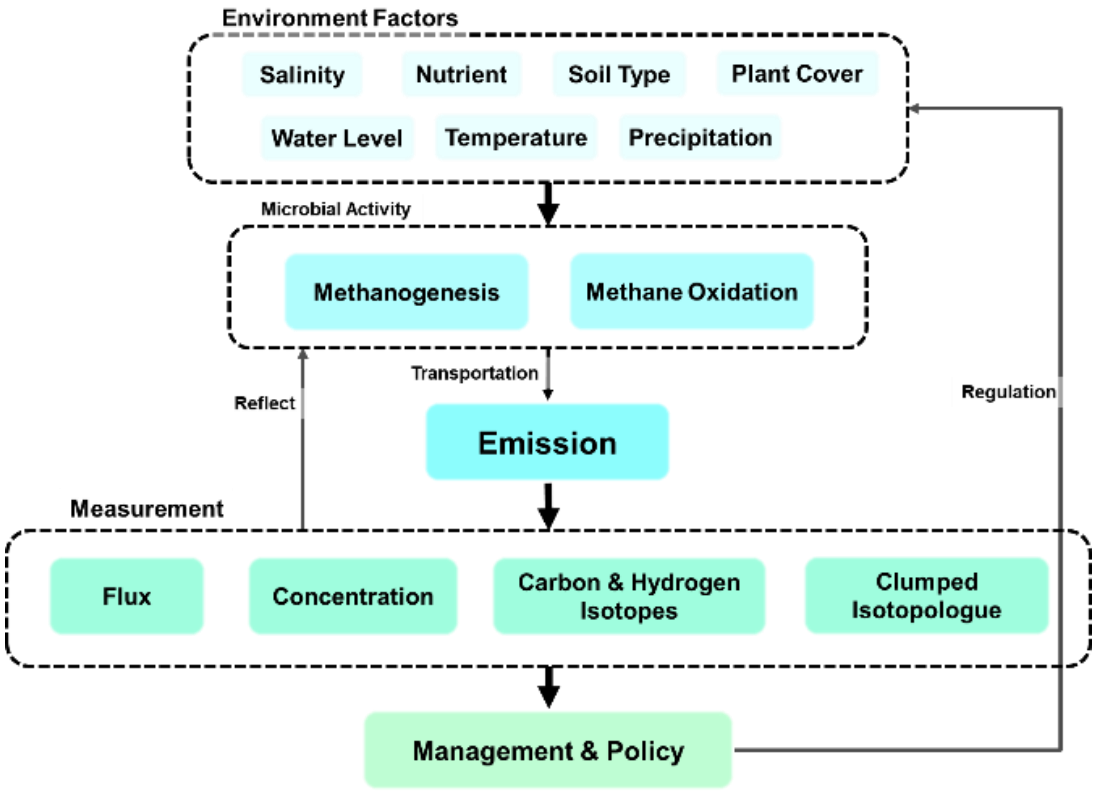

Figure 1.6. **A schematic diagram connecting wetland methane emissions with microbial activity, environmental factors, and measured parameters.**

1.2.2. Methane Sinks

The estimation and uncertainty of the total methane sink flux are dependent on the total source flux, which is 663 (507–796) Tg CH_4 yr^{-1} based on the bottom-up approach and 553 (550–567) Tg CH_4 yr^{-1} from top-down approach (Saunois et al., 2024). This dependency arises because the total sink strength is strongly constrained by global methane concentrations, meaning it must satisfy the sink-source mass balance. The global methane concentration is relatively well recorded (Lan et al.). However, this does not necessarily imply that our understanding of methane sinks is highly refined. Without constraints from methane sources, the sink reaction speed, from an atmospheric chemistry perspective, is a function of methane concentration, the

concentration of methane-oxidizing radicals, and temperature. The primary uncertainty in sink flux estimates stems from the poorly constrained concentrations of the various oxidants (reactive species capable of oxidizing methane) involved in different sink pathways. Overall, the uncertainty in methane sink flux is on the order of 10–40% (Saunois et al., 2024).

The methane sink categories are much simpler than the source. The vast majority of methane sink reactions occur in the troposphere, while only about 5–7% take place in the stratosphere. Approximately 90% of atmospheric methane is consumed by hydroxyl radicals (OH):

$$CH_4 + OH\cdot \rightarrow CH_3\cdot + H_2O \qquad (1.1)$$

The remaining sinks include the chlorine radicals (Cl) at oceanic boundary layer, atomic Cl in stratosphere, excited state oxygen atoms O(^{1}D) in troposphere, and soil oxidation by methanotrophs (IPCC, 2021; Saunois et al., 2024).

1.2.2.1. Troposphere OH

The reaction between methane and OH occurs primarily in the troposphere and depends on OH concentration, which carries significant uncertainty. In the presence of water vapor, ozone photolysis produces OH radicals ($O_3 + H_2O \xrightarrow{\text{UV light 290–320 nm}} 2\,OH\cdot + O_2$). These OH radicals react with carbon monoxide (CO), methane (CH_4), and non-methane volatile organic compounds (NMVOCs). Bottom-up estimates of CH_4+OH flux are mainly derived from modeling, such as the Coupled-Model Intercomparison Project 6 (CMIP6) simulations (Collins et al., 2017). The global mass-weighted mean OH concentration is estimated to be at the level of 13.3 [11.7–18.2] × 10^5 molecules/cm^3 or 11.5 [7.9–13.5] × 10^5 molecules/cm^3 (Collins et al., 2017; Naik et al., 2013; Plummer et al., 2021; Saunois et al., 2024). Model simulations suggest that OH

concentrations in the Northern Hemisphere may be higher than in the Southern Hemisphere, or the difference may be minimal (Naik et al., 2013; Zhao et al., 2019). The average OH concentration is believed to vary only slightly over a century or remain almost unchanged, with fluctuations within approximately 1% (Turner et al., 2019; Zhao et al., 2019), except for a temporary decrease in 1991–1992 caused by the eruption of Mt. Pinatubo (Dlugokencky et al., 1996). However, model results are highly dependent on chemical mechanisms, prior parameters, and atmospheric transport models, particularly the 3D distribution of OH (Zhao et al., 2023). Therefore, further improvements are still needed.

From a top-down perspective, atmospheric OH concentration has been derived from measured changes in methyl chloroform (CH_3CCl_3) concentrations (Montzka et al., 2011). The use of a proxy rather than direct measurements is necessary because direct measurement of OH concentration in ambient air is extremely difficult and has only been implemented under laboratory conditions (Siese et al., 2001; Winiberg et al., 2016). CH_3CCl_3 was primarily used as a solvent but was banned under the Montreal Protocol (1987) ("Montreal protocol on substances that deplete the ozone layer," 1987) due to its destructive effects on the ozone layer (Rowland, 1989). Since OH is the main sink of CH_3CCl_3, the rate of decline in atmospheric CH_3CCl_3 concentration has been used to estimate the OH concentrations. The lifetime of CH_3CCl_3 is about 5.04 years (Rigby et al., 2013), and its atmospheric concentration has dropped rapidly from about 130 ppt in 1990 to 1.2 ppt in 2022 (NOAA GML) due to the stringent restriction of its emission. However, today's low CH_3CCl_3 concentrations and uncertainties in annual CH_3CCl_3 emission fluxes add to the uncertainty in estimating OH concentrations using the proxy method. Additionally, the reaction rate between CH_4 and OH is also influenced by temperature (with

higher temperatures corresponding to higher rate constants), the vertical distribution of methane and OH (Zhao et al., 2019), and the presence of other atmospheric reactive species such as O_3 (Wang, Huang, et al., 2004) and NO_x (Fiore et al., 2006). However, this top-down proxy method can only provide an integrated OH concentration, rather than detailed spatial or temporal variations.

1.2.2.2. Stratosphere OH

In the stratosphere, the reaction between CH_4 and OH is a major source of stratospheric water vapor, which has significant implications for stratospheric chemistry and climate (le Texier et al., 1988). Additionally, excited oxygen atoms $O(^1D)$ produced through the photolysis of ozone under UV radiation ($O_3 \xrightarrow{\text{UV light 290–320 nm}} O(^1D) + O_2$) (DeMore & Raper, 1967), as well as chlorine and fluorine atoms, can also react with CH_4. However, our understanding of these sink reactions remains limited, and the estimated flux carries considerable uncertainty. Model estimates suggest a flux of 34 [10-51] Tg CH_4 yr^{-1} (Saunois et al., 2024).

1.2.2.3. Ocean-Atmosphere Boundary Layer Cl

Cl radicals can also oxidize methane. This mechanism was identified through carbon isotopic observations (Allan, Lowe, et al., 2001; Allan, Manning, et al., 2001; Allan et al., 2007). It is believed to occur mainly in the marine boundary layer, where Cl radicals can be formed through the photolysis of sea-salt-derived compounds, such as Cl_2 and $ClNO_2$. A study also suggests that in highly polluted terrestrial environments, $ClNO_2$ may be produced through reaction $N_2O_5 + Cl^- \rightarrow ClNO_2 + NO_3^-$ (Riedel et al., 2013), which releases Cl radicals upon photolysis.

Nevertheless, recent modeling studies increasingly suggest that the overall contribution of Cl oxidation to methane removal is low, and that Allan et al. (2007) likely overestimated the Cl sink flux. Estimates from different studies include 12-13 Tg CH_4 yr^{-1} (Hossaini et al., 2016), 5-6 Tg CH_4 yr^{-1} (Gromov et al., 2018), and 3.6 Tg CH_4 yr^{-1} (Wang et al., 2021).

1.2.2.4. Soil Sink

The soil surface is usually methane-unsaturated because methane consumption in surface soil by methanotrophic bacteria occurs faster than methane production in deeper soil layers by methanogens. As a result, soil acts as a sink for atmospheric methane, estimated to contribute approximately 5% of the total sink, with a flux of 32 [18-40] Tg CH_4 yr-1 (Saunois et al., 2024). This estimation is derived from a series of parameterization models based on methane diffusion and biological oxidation (Curry, 2007; Ito & Inatomi, 2012; Ridgwell et al., 1999; Tian et al., 2016). Overall, these models have progressively incorporated more factors and mechanisms while utilizing higher-resolution and more accurate parameters. However, despite these improvements, the simulated flux results have remained relatively stable, with large uncertainties and a strong dependence on assumptions and parameterizations related to various mechanisms.

Since non-OH sink fluxes account for less than 10% of the total methane sink, the uncertainty in total methane sinks is primarily driven by the OH sink. Only when considering methane isotopic composition (e.g., (Allan et al., 2007; Röckmann et al., 2011)) and stratosphere-troposphere interactions do other sink processes become more significant as they have larger kinetic isotope effects compared to OH sink (see Section 1.4.3.4).

1.3. Methane Carbon and Hydrogen Isotopes

Isotopes of a given element have the same number of protons but different numbers of neutrons in each atom. For chemical substances, the substitution of one isotope for another results in a small change in the mass and energy. As a result, small differences in the proportions of isotopes are produced by chemical and physical processes. For carbon, we are generally concerned about stable ^{12}C and ^{13}C atoms. For hydrogen, they are ^{1}H and ^{2}H (or D, deuterium) atoms. Isotopes are reported as the relative deviation of an isotope ratio in a sample compared to a standard reference material:

$$\delta^{13}C_{sample-standard} = \left(\frac{(^{13}C/_{12}C)_{sample}}{(^{13}C/_{12}C)_{standard}} - 1 \right) * 1000‰ \quad (1.2)$$

$$\delta D_{sample-standard} = \left(\frac{(D/H)_{sample}}{(D/H)_{standard}} - 1 \right) * 1000‰ \quad (1.3)$$

Where the standard is usually Vienna Pee Dee Belemnite (V-PDB) for carbon isotope, which has $^{13}C/^{12}C = 0.0112372$, and Vienna Standard Mean Ocean Water (V-SMOW) for hydrogen isotope, which has D/H = 0.00015576 (Coplen, 1994, 1995). The equation includes a final term multiplied by one thousand per mil, which does not change the numerical value but makes comparisons more intuitive, as the δ ratio difference is usually very small, typically on the order of per mil to percent. In isotope geochemistry, there are also some other commonly used notations. Among them, the isotope ratio (R) represents the ratio of a minor isotope to a major isotope in a given substance, for carbon and hydrogen isotope:

$$^{13C}R_{substance} = \left(\frac{^{13}C}{^{12}C}\right)_{substance} \quad (1.4)$$

$$^{D}R_{substance} = (\frac{D}{H})_{substance} \quad (1.5)$$

The fraction of an isotope is represented by X, where the denominator should include all isotopes of that element:

$$^{13C}X_{substance} \approx (\frac{^{13}C}{^{12}C+^{13}C})_{substance} \quad (1.6)$$

$$^{D}X_{substance} \approx (\frac{D}{H+D})_{substance} \quad (1.7)$$

The fractionation factor (α) is the degree of isotopic fractionation between two substances:

$$^{13C}\alpha_{substance\ A-substance\ B} = \frac{^{13C}R_{substance\ A}}{^{13C}R_{substance\ B}} = \frac{\delta^{13}C_{substance\ A-standard}+1}{\delta^{13}C_{substance\ B-standard}+1} \quad (1.8)$$

$$^{D}\alpha_{substance\ A-substance\ B} = \frac{^{D}R_{substance\ A}}{^{D}R_{substance\ B}} = \frac{\delta D_{substance\ A-standard}+1}{\delta D_{substance\ B-standard}+1} \quad (1.9)$$

The enrichment factor (ε) has been used to numerically simplify α:

$$^{13C}\varepsilon_{A-B} \approx 10^3 \ln(^{13C}\alpha_{A-B}) \approx 10^3(^{13C}\alpha_{A-B} - 1) \sim \delta^{13}C_A - \delta^{13}C_B \quad (1.10)$$

Bulk carbon and hydrogen isotopes of methane have long been used to differentiate methane sources. This is because methane from different sources or subjected to different processes may exhibit distinct isotopic signatures (i.e., $\delta^{13}C$ and δD). By directly sampling and measuring the sources introduced in Section 1.2.1, the isotopic composition of various methane sources can be determined. Large methane isotopic databases, such as the one shown in Figure 1.7 and Figure 1.8 (Menoud et al., 2022; Sherwood et al., 2017; Sherwood et al., 2021), have been established through this approach. The summarized isotopic compositions of each source are presented in Table 1.1. However, certain source categories have considerable overlap in isotopic signatures. For instance, methane from agriculture, waste, and wetlands predominantly exhibits similar methane isotopic characteristics, making them difficult to distinguish isotopically (Figure 1.8).

Therefore, when prior knowledge of methane sources is unavailable and only a set of isotopic data is available, instead of classifying methane sources based on their origin or emission activity—such as fossil fuel-related, agriculture, waste, biomass burning, and wetland methane (see Section 1.2.1)—isotopic signatures are generally only capable of categorizing methane into thermogenic, pyrogenic/abiotic, and microbial categories. This classification is based on the fact that these three types of methane typically exhibit distinct isotopic signatures and are generally distributed in three separate regions on the δD-$\delta^{13}C$ plot (Figure 1.7) (Sherwood et al., 2017; Whiticar, 2020).

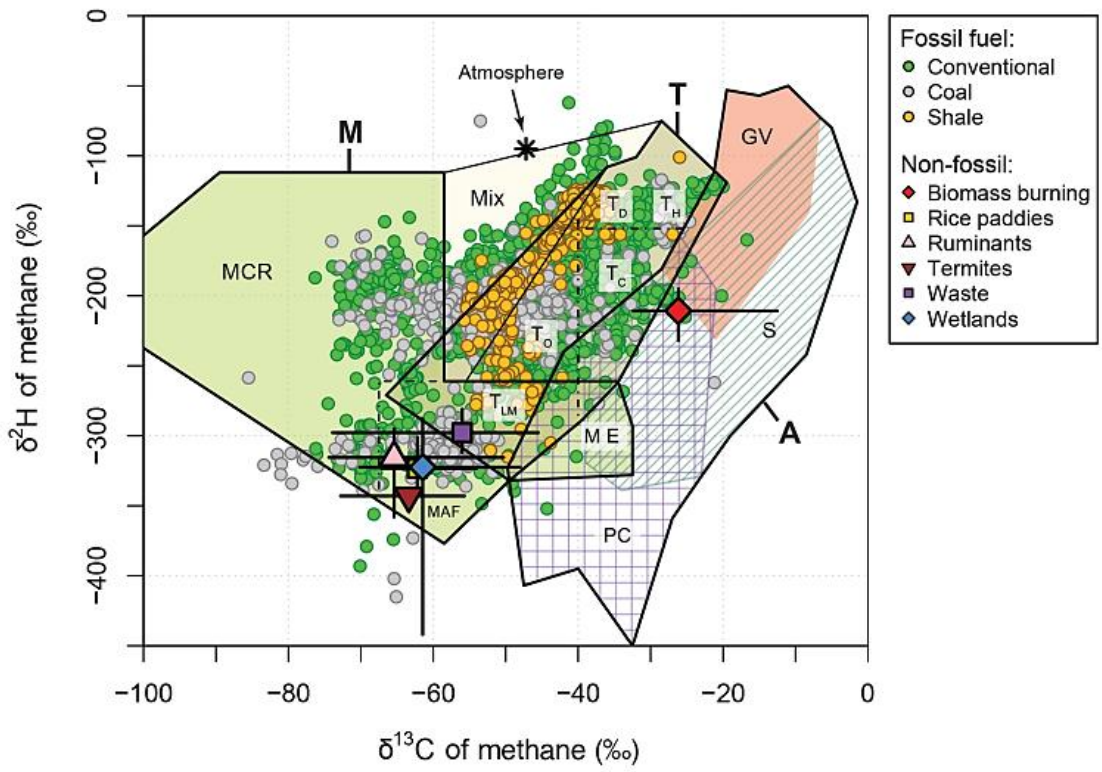

Figure 1.7. **A global compilation of δD and $\delta^{13}C$ values for fossil fuel-related methane samples.** These methane samples may originate from microbial (M), thermogenic (T), or abiotic (A) sources, or be a mixture of multiple origins. Conventional: oil and natural gas that have been extracted using simple technologies like drilling instead of hydraulic fracturing. MCR: microbial CO2 reduction; MAF: microbial acetate fermentation; ME: microbial in evaporitic environment; TO: thermogenic with oil; TC: thermogenic with condensate; TD: dry thermogenic; TH: thermogenic with high-temperature CO2-CH4 equilibration; TLM: thermogenic low maturity; GV: geothermal-volcanic systems; S: serpentinized ultramafic rocks; PC: Precambrian crystalline shields. (Figure taken from Sherwood et al. (2017), under CC BY 3.0)

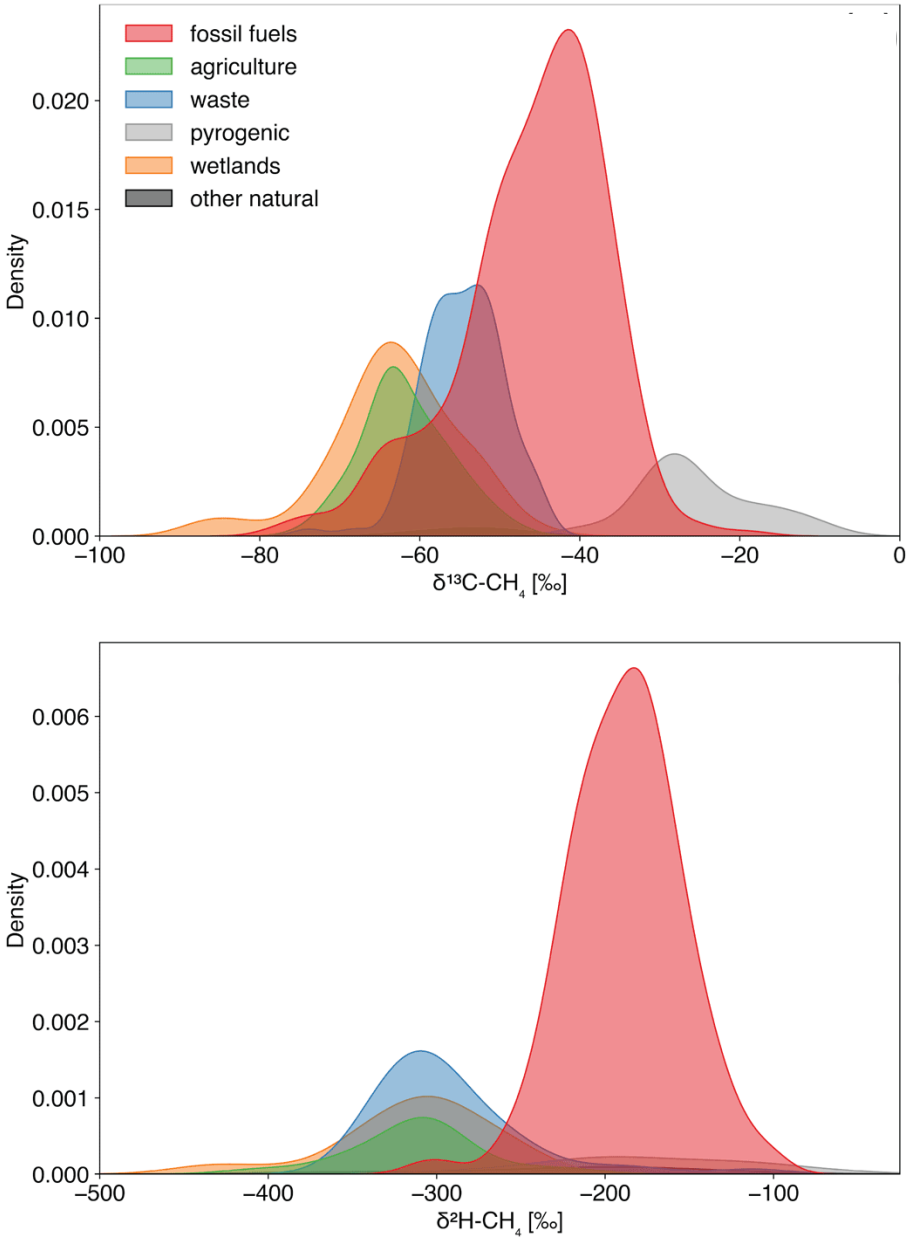

Figure 1.8. **Normalized probability density distribution of $\delta^{13}C$ and δD in CH_4 for different source categories.** Note that although the peak positions may differ among methane sources, there is significant overlap between them. (Figure adapted from Menoud et al. (2022), under CC BY 4.0)

Table 1.1. **Summary of methane source isotopic compositions.** Values presented are calculated using data from the Menoud et al. (2022) database. Notably, there are significant differences between the statistical results of the Menoud et al. (2022) and Sherwood et al. (2021) databases, particularly in the δD isotopic composition of methane from rice, ruminants, and waste sources. Due to ambiguities in the definition of uncertainty across different datasets within the databases, the mean values and uncertainties reported here are derived as weighted averages based on the number of measurements. The current understanding of the temporal and spatial distribution of isotopic compositions for each methane source is indicated in separate columns. YES: Sufficient information is available and corresponding work is published to determine the global distribution or interannual variations of the isotope composition for this source. SOME: Some geographic or temporal (e.g., interannual or seasonal) variation data exist for this isotope in the given source, but not enough to make a validated global/annual model. POSSIBLE: There may be some information available, or models exist that theoretically can simulate the distribution with limited data, but no established model is currently available. NO: There is essentially no available information on the temporal and spatial distribution of the isotope composition for this source.

	Mean $\delta^{13}C$ (‰)	Uncertainty (‰)	Spatial?	Temporal?	Mean δD (‰)	Uncertainty (‰)	Spatial?	Temporal?
Fossil-fuel	-45.86	0.53	YES	YES	-188.61	1.63	YES	SOME
Wetland	-63.07	3.22	YES	SOME	-319.66	29.3	YES	NO
Rice	-59.88	3.03	POSSBILE	NO	-323.25	9.75	NO	NO
Ruminants	-63.11	1.69	SOME	NO	-311.3	17.2	SOME	NO
Termites	-65.2	3.2	NO	NO	-343	4	NO	NO
Waste	-54.91	1.71	NO	NO	-293.51	10.12	NO	NO
Biomass Burning	-26.52	1.84	YES	SOME	-220	3.8	NO	POSSIBLE

If source information is unavailable, the origin of methane may be inferred solely from its isotopic values (Table 1.2). The most negative $\delta^{13}C$ and δD (usually $\delta^{13}C$ <-60‰, δD<-250‰) likely indicate microbial methane. If a set of samples shows $\delta^{13}C$ varying linearly with δD in a narrower range (usually $\delta^{13}C$ from -60‰ to -30‰ and δD from -250‰ to -150‰), thermogenic methane should be considered. If the $\delta^{13}C$ values are significantly less negative (usually $\delta^{13}C$ >-30‰), pyrogenic methane is a likely source, while its δD values may span the ranges of microbial and thermogenic or even extend beyond them (Etiope & Whiticar, 2019). This classification of methane origins based on carbon and hydrogen isotope compositions was first proposed by (Schöll, 1980), and the corresponding diagram is therefore commonly referred to as the Schöll plot. This plot has been widely adopted and continuously refined over the years (e.g., (Etiope et al., 2019; Etiope & Sherwood Lollar, 2013; Ganesan et al., 2018; Menoud et al., 2022; Milkov, Faiz, et al., 2020; Sherwood et al., 2017; Whiticar, 1999)). As more data have been incorporated into the plot, the isotopic boundaries of different methane sources have expanded, leading to increasing overlap between categories (Figure 1.8) (Menoud et al., 2022). For example, microbial methane produced under extreme laboratory conditions like very limited hydrogen supply (Valentine et al., 2004) and abiotic methane synthesized in the lab (McCollom et al., 2010) have been shown to extend into regions traditionally associated with thermogenic methane. As a result, relying solely on the Schöll plot to distinguish methane origins has become increasingly challenging. To improve source identification, additional geochemical diagnostic indicators are now used alongside methane's bulk carbon and hydrogen isotopes, such as methane-to-ethane-and-propane ratios $C_1/(C_2+C_3)$, hydrogen and carbon isotope compositions of ethane to butane ($\delta^{13}C_{C2H6}$, $\delta^{13}C_{C3H8}$, $\delta^{13}C_{C4H10}$), and the abundance and isotopic signatures of

noble gases (e.g., $^{3}He/^{4}He$). The following sub-sections (Sections 1.3.1 to 1.3.3) will provide a more detailed discussion of these three types of methane.

Table 1.2. **Summary of the characteristic isotopic compositions of thermogenic, pyrogenic, and microbial methane.** There is insufficient information to estimate statistical measures such as mean and median because the databases are based on bottom-up, activity-based classifications of methane sources (i.e., fossil-fuel, wetland, and etc.), lacking a database that categorizes methane sources based on formation pathways (i.e., thermogenic, pyrogenic, and microbial). Data from Table 1.1 can be referenced to estimate average values and uncertainties. Microbial methane is likely an average of wetland, rice cultivation, ruminants, and waste sources. Pyrogenic methane is roughly equivalent to biomass burning. Thermogenic methane tends to be slightly less negative than fossil-fuel methane because a portion of fossil-fuel methane is of microbial origin. ((Menoud et al., 2022; Sherwood et al., 2017; Sherwood et al., 2021; Whiticar, 2020) and references therein)

	δ13C (‰)	δD (‰)
Thermogenic	-60 to -30	-250 to -150
Pyrogenic	-30 to -10	-400 to -100
Microbial	-70 to -50	-400 to -200

1.3.1. Thermogenic Methane

Thermogenic methane is formed by the cleavage of carbon-carbon bonds (a process known as thermal cracking) of high-carbon-number hydrocarbons (mainly kerogen and subsequent products) under thermal activation (Hunt, 1995). This process primarily occurs under elevated temperature and pressure conditions over geological timescales. It mainly takes place in organic-rich source rock within sedimentary basins, which are also the primary locations for oil and natural gas formation. Thermogenic methane is sometimes confused with fossil-fuel-related

methane, which is not accurate. This is because fossil-fuel-related methane (methane collected from oil, natural gas, and coal wells) could contain both thermogenic- and microbial-origin methane. The proportion of microbial methane in these reservoirs varies significantly, ranging from nearly 0% to almost 100%, depending on the specific gas wells. It is estimated that more than 20% of the world's discovered gas reserves are of microbial origin (Rice & Claypool, 1981), with shallow coalbed methane serving as a representative example (Strąpoć et al., 2011).

The thermal cracking reaction occurs throughout all stages of petroleum formation. As temperature increases and maturity progresses (more degradation and gas formation), a sequence of products is generated, including bitumen, oil, char (carbon-rich solid residue structurally similar to graphite), and natural gas (pentane, butane, propane, ethane, and methane), at different stages (Figure 1.9):

$$C_n(\text{kerogen}) \xrightarrow{\text{heat}} \text{Bitumen} + \text{Oil} + \text{Char} + C_{2-5} + C_1 \qquad (1.11)$$

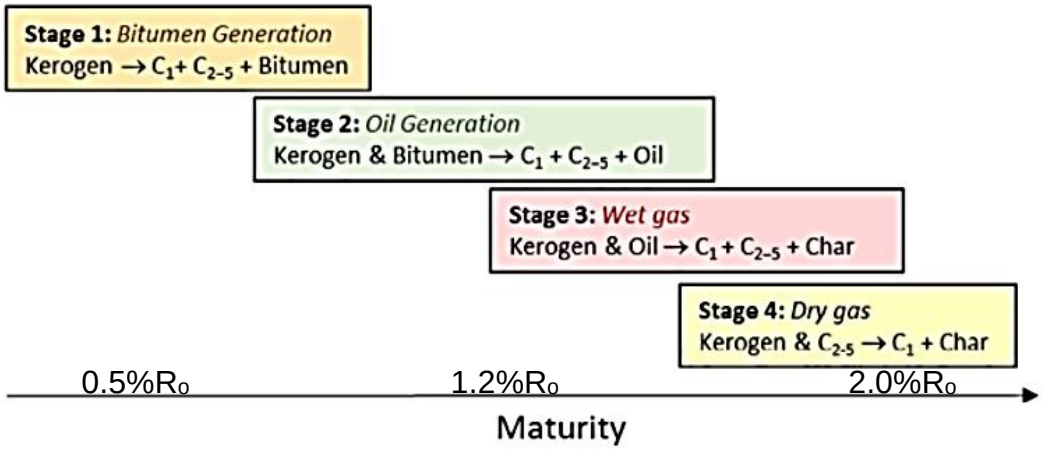

Figure 1.9. **A conceptual scheme for four stages of thermal degradation of kerogen to form natural gas.** The methane proportion increases as maturity increases. (Figure adapted from Shuai, Douglas, et al. (2018), with permission)

The maturity refers to the extent of thermal evolution of organic matter in the source rock. It is usually quantified by the percentage of incident light reflected from vitrinite particles of sedimentary rock, or, %-vitrinite reflectance (%R_0) (Mukhopadhyay, 1994). At the stage where %R_0 is less than 0.6%, the burial depth is shallow, and the temperature generally does not exceed 50°C. If methane is generated at this stage, it is typically microbial methane. As burial depth increases and temperature reaches 50–200°C, catagenesis occurs. The stage where %R_0 ranges from 0.6% to 1.2% is referred to as the "oil window," during which oil and minor wet gas are generated. When %R_0 is between 1.2% and 2.0%, it is known as the "wet gas window," where a mixture of C_4 to C_1 gases is predominantly formed. With further burial and increasing temperature above 200°C, %R_0 rises above 2.0%, marking the "dry gas window." At this stage, wet gas undergoes further thermal cracking, converting into predominantly methane-rich gas. Therefore, the mole ratio of methane to heavier light hydrocarbons, often represented and calculated as methane/(ethane + propane) or $C_1/(C_2+C_3)$, serves as an indicator of maturity. However, this ratio is often influenced by the presence of microbial methane. Generally speaking, the higher the reservoir temperature, the higher the maturity and the greater the proportion of methane (Dow, 1977).

Although bond cleavage can cause large isotopic fractionation, thermogenic gas usually reaches thermal equilibrium after being stored under high temperatures (e.g., >100°C) for millions of years. $\delta^{13}C$ and δD of thermogenic methane usually show a positive trend, with a large portion being approximately linear (e.g., shale gases in Figure 1.7). $\delta^{13}C$ and δD generally both become less negative with increasing maturity ($\delta^{13}C_{methane}$ from -45‰ to -35‰ with maturity R_0 from 0.5% to 2.0%), and may even overlap with the $\delta^{13}C$-δD field of pyrogenic methane ($\delta^{13}C_{methane}$ >

-30‰) (Liu et al., 2019; Shuai, Douglas, et al., 2018). In addition, it is generally considered that thermogenic methane has more enriched ^{13}C with increasing carbon numbers for the C_1-C_4 alkanes (Sherwood Lollar et al., 2002) (Figure 1.10):

$$\delta^{13}C_1 < \delta^{13}C_2 < \delta^{13}C_3 < \delta^{13}C_4 \quad (1.12)$$

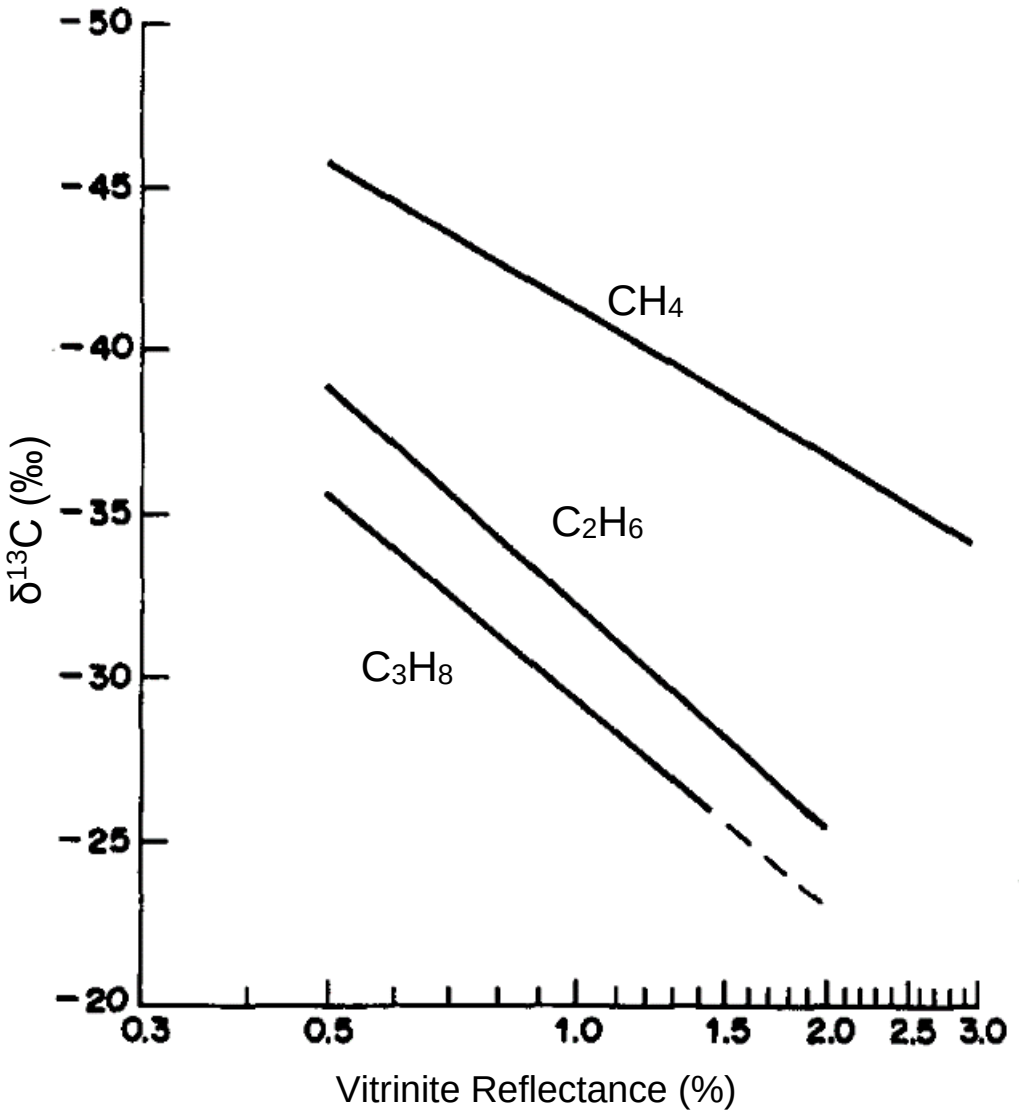

Figure 1.10. **Typical trends of carbon isotope signals of thermogenic methane, ethane, and propane changing with the maturity expressed as %R_0.** (Figure adapted from Berner and Faber (1988), with permission)

In addition to maturity, the composition of the source material influences the carbon and hydrogen isotopes of oil and gas, which heavily depends on the sedimentary environment (i.e., marine vs. terrigenous freshwater) (Liu et al., 2019). Secondary processes can also alter the isotopic signatures of thermogenic methane, such as thermochemical sulfate reduction (Machel, 2001) and diffusion (Zhang & Krooss, 2001). These processes may produce methane with isotopic values that exceed the previously defined ranges or even completely reverse the typical carbon and hydrogen isotopic trends of thermogenic methane. For example, a reversed trend in the carbon isotopes of C_1 to C_4 alkanes has been observed, where lighter hydrocarbons are more enriched in ^{13}C compared to heavier ones (Burruss & Laughrey, 2010).

1.3.2. Pyrogenic Methane

Pyrogenic methane refers to methane produced through high-temperature chemical processes that do not directly involve microbial activity. A more precise definition is needed to clarify which methane sources should fall under this category. Geologists, when referring to abiotic methane, typically focus on geological-origin methane and certain abiotically synthesized methane in laboratory settings. However, atmospheric scientists, when dealing with the global methane isotopic budget, often prefer a three-endmember classification—thermogenic, microbial, and all other sources—ensuring that all methane emissions are accounted for. As a result, the term "pyrogenic" is used instead of "abiotic" (e.g., (Basu et al., 2022)). Using "pyrogenic" is a reasonable approach because methane from geological sources, biomass burning, and even vehicle exhaust is all generated at relatively high temperatures without direct microbial involvement and shares similar isotopic compositions.

1.3.2.1. Abiotic/Geological methane

Etiope and Sherwood Lollar (2013) compiled nine mechanisms proposed in the literature for the formation of geological methane (Figure 1.11). These mechanisms operate across a wide range of temperatures, from very high temperatures (>500°C) in the mantle to low-temperature (<120°C) gas-water-rock reactions. Several important and representative mechanisms are commonly observed:

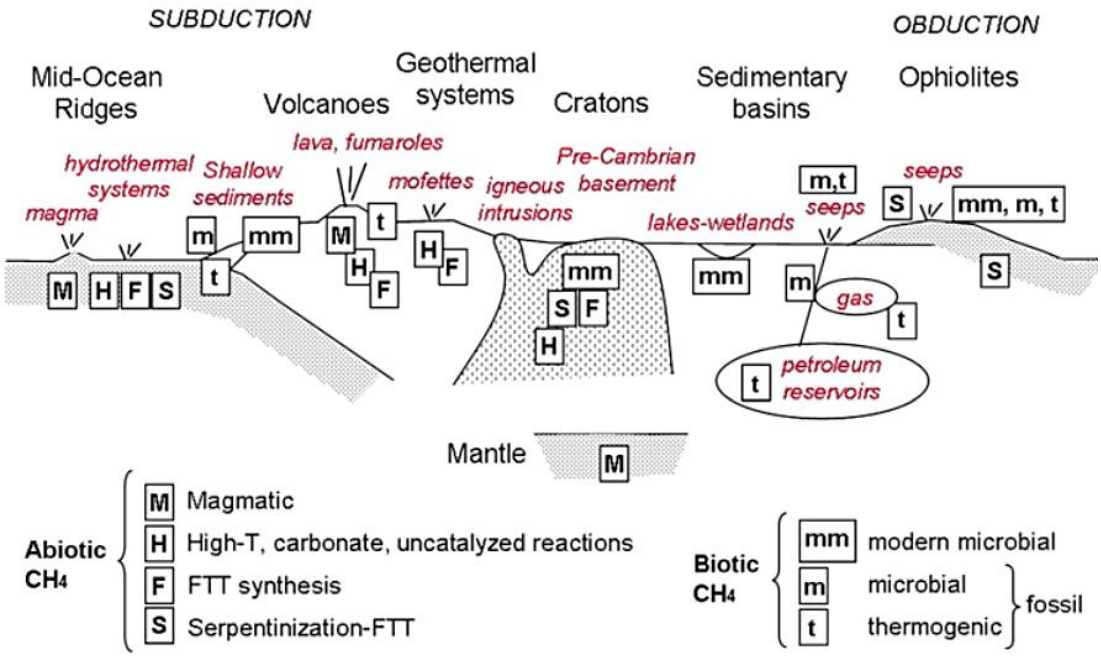

Figure 1.11. **Sketch of methane occurrences and mechanisms on Earth, with a specific focus on geological methane.** (Figure taken from Etiope and Sherwood Lollar (2013), with permission)

The first is methane formation in mantle or extraterrestrial environments under ultra-high temperature (>500°C) and high-pressure conditions (Gold, 1979; Scott et al., 2004). In this

process, methane is typically generated through the reaction of metal carbides or metal oxides with water, such as:

$$Al_4C_3 + 12\ H_2O \rightarrow 3\ CH_4 + 4\ Al(OH)_3 \quad (1.13)$$

$$8\ FeO + CaCO_3 + 2\ H_2O \rightarrow 4\ Fe_2O_3 + CH_4 + CaO \quad (1.14)$$

The second is equilibration of the C-H-O system in fluid-water-rock reactions at high temperature (400-600°C) (Kelley & Früh-Green, 1999; Kiyosu et al., 1992):

$$CO_2 + 2\ H_2O \rightarrow CH_4 + 2\ O_2 \quad (1.15)$$

$$8\ FeO + CO_2 + 2\ H_2O \rightarrow 4\ Fe_2O_3 + CH_4 \quad (1.16)$$

This mechanism often occurs in cooling magmatic or hydrothermal systems when fluids interact with rocks. Under low oxygen fugacity (fO_2) conditions, CO_2 tends to be reduced to methane while releasing oxygen (Frost, 1979). However, in geological systems, molecular O_2 is not a stable end-product, so mineral equilibria are required to regulate oxygen activity. Iron-bearing minerals, for instance, can act as oxygen carriers and become oxidized. A well-established reference for determining oxygen fugacity conditions in geochemistry is the Quartz (SiO_2)-Fayalite (Fe_2SiO_4)-Magnetite (Fe_3O_4) (QFM) buffer (O'Neill, 1987).

The third mechanism is Fischer-Tropsch Type (FTT) reactions, which refer to the catalytic hydrogenation of CO or CO_2 in the gas or aqueous phase. The most representative reaction in this category is the Sabatier reaction, a special case of one-step gas-phase FTT:

$$CO_2 + 4\ H_2 \xrightarrow{catalyst} CH_4 + 2\ H_2O \quad (1.17)$$

In geological settings, H_2 is primarily derived from serpentinization, and the catalysts are typically transition metals (Ni, Fe, Co, Cr, Ru), which are abundant in ultramafic rocks. This

reaction can occur at relatively low temperatures (<120°C) while still proceeding at a significant rate, making it one of the most important natural sources of geological methane. The Lost City hydrothermal field near the Mid-Atlantic Ridge (Kelley et al., 2005) and the Chimaera seep within the Tekirova ophiolites in Turkey (Etiope et al., 2011) are example methane emission regions where serpentinization-driven methane production has been extensively studied.

Abiotic/Geological methane generally has the least negative $\delta^{13}C$, typically greater than -30‰. However, its δD values are highly variable, spanning the widest range among methane types, from -450‰ to -50‰ (Figure 1.12). There is no clear systematic isotopic distinction between different types of abiotic/geological methane; instead, each location tends to have its own unique isotopic signature. Mantle-derived methane may exhibit isotopic compositions that fall on the high-maturity side of thermogenic methane (Taran et al., 2010; Tassi et al., 2012). Methane released from serpentinization of ultramafic rocks can have the most enriched $\delta^{13}C$ values, as observed at Lost City (Kelley et al., 2005), Chimaera (Etiope et al., 2011), and Genova (Boschetti et al., 2013). However, it can also exhibit more depleted $\delta^{13}C$ values (which means <-30‰) and highly negative δD signals, as seen in Poison Bay (Lyon & Giggenbach, 1994) and Happo (Suda et al., 2014). Given this variability, detailed investigations of the geological background are still necessary to accurately determine the origin of geological methane.

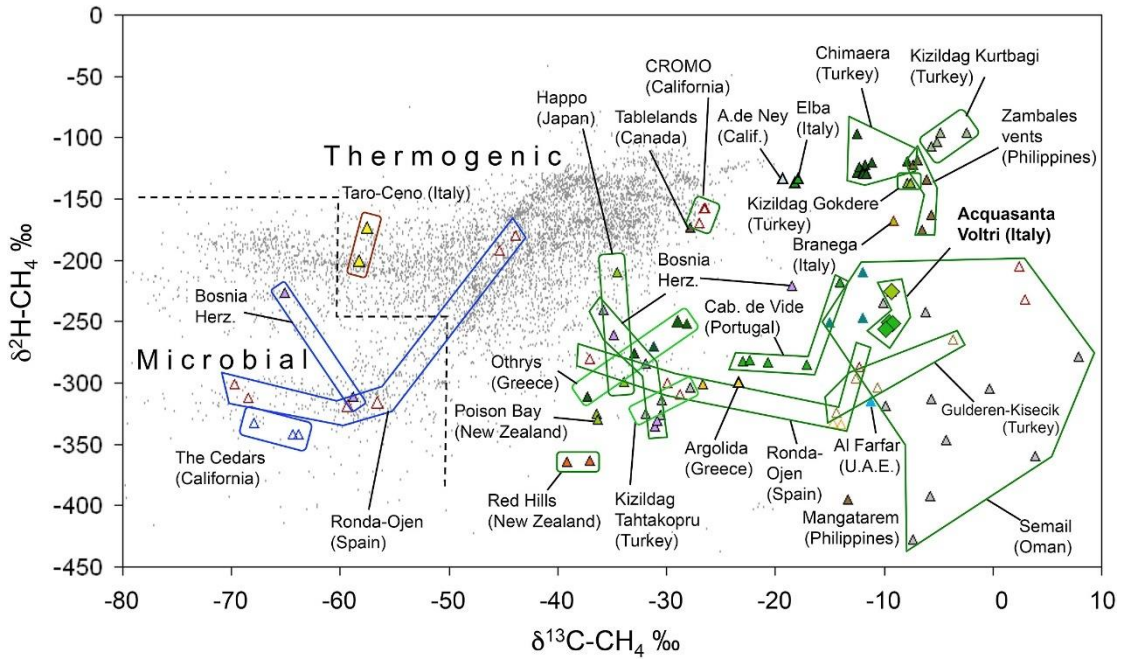

Figure 1.12. **A compilation of δD and $\delta^{13}C$ values for geological methane samples.** Please refer to Etiope and Whiticar (2019) for the geological background of each location. (Figure taken from Etiope and Whiticar (2019), with permission).

Other indicators can help identify geological methane. A decreasing trend of $\delta^{13}C$ with increasing carbon number (as opposed to thermogenic methane) is a diagnostic tool (Des Marais et al., 1981; Sherwood Lollar et al., 2002). However, as previously mentioned, thermogenic methane can sometimes exhibit a reversed trend due to secondary effects (Burruss & Laughrey, 2010). The $^{3}He/^{4}He$ ratio can indicate whether methane has a mantle origin, as mantle-derived helium has a high $^{3}He/^{4}He$ ratio (Craig & Lupton, 1976). The $C_1/(C_2+C_3)$ ratio can be used to diagnose mixing between different methane sources. Additionally, the carbon isotopes of associated CO_2 and the hydrogen isotopes of associated water can, when combined with isotopic fractionation models, provide further insights—especially in distinguishing microbial methane contributions when mixing with geological methane (Douglas et al., 2021; Whiticar, 1999).

1.3.2.2. Biomass Burning Methane

Biomass Burning has already been introduced in Section 1.2.1.3. This methane source is particularly important in the global isotopic budget because it typically exhibits the least negative $\delta^{13}C$ and δD values among all methane sources.

Available measurements are limited, but in general, $\delta^{13}C$ of biomass burning methane ranges from -35‰ to -9‰ (Chanton et al., 2000; Nisbet, Allen, et al., 2021). The global average is estimated to be $\delta^{13}C = -22.3 \pm 1.9$‰ (Schwietzke et al., 2016). The isotopic signature of biomass burning methane is primarily influenced by fuel type (e.g., C_3 plant, C_4 plants, gasoline, and diesel) and combustion efficiency (Chanton et al., 2000). The $\delta^{13}C$ of methane produced by combustion is generally similar to that of the fuel or slightly depleted by ~1‰ to 6‰ (Vernooij et al., 2022). A key distinction arises between the combustion of C_3 plants (e.g., trees and shrubs) and C_4 plants (e.g., prairie grasses and corn). C_3 plants typically have $\delta^{13}C$ around -27‰, whereas C_4 plants exhibit a less negative value, around -13‰ (Kohn, 2010). At the global scale, the relative proportions of C_3 vs. C_4 plant combustion determine the overall $\delta^{13}C$ signature of biomass burning emissions. This C_3/C_4 combustion ratio is often estimated using the Global Fire Emissions Database (Chen et al., 2023; van der Werf et al., 2017; van Wees et al., 2022). Additionally, as combustion temperature increases, leading to higher combustion efficiency, methane concentrations tend to decrease, while $\delta^{13}C$ becomes more enriched relative to the original fuel (Chanton et al., 2000; Vernooij et al., 2022).

Hydrogen isotope data for biomass burning methane are even more limited, with reported values ranging from -262‰ to -196‰ (Snover et al., 2000; Yamada et al., 2006). The global average

has been estimated at δD = -210 ± 16‰ (Snover et al., 2000). The D/H fractionation during combustion is substantial, but research on this topic remains scarce (Snover et al., 2000; Yamada et al., 2006). The δD of vegetation varies significantly, primarily due to differences in the hydrogen isotopic composition of water sources. C_3 plants typically have δD values between -130‰ and -50‰, while C_4 plants exhibit a range of -45‰ to -5‰ (Leaney et al., 1985; Schuler et al., 2024).

1.3.3. Microbial Methane

Microbial methane refers to methane formed through direct microbial involvement, encompassing categories such as agriculture, waste, and wetlands, as introduced in Section 1.2.1.2 and Section 1.2.1.4. Given its widespread distribution and diverse sources, microbial methane exhibits significant variability. The term microbial methane is often used interchangeably with biogenic methane (e.g., (Schaefer et al., 2016; Stolper, Lawson, et al., 2014)). However, when applying a three-end member classification, it is advisable to avoid the abiotic vs. biotic dichotomy, thus using microbial is preferred. Additionally, some researchers tend to use microbial methane strictly for methane freshly produced by methanogenic archaea via methanogenesis, while referring to methane that has undergone subsequent processes such as microbial oxidation as biogenic methane. In Chapter 1 of this dissertation, only the term microbial methane is used. In Chapters 3 and Chapter 4, the term biogenic appears once each, equivalent to microbial, but I have not modified it out of respect for the original published text.

When discussing the isotopic characteristics of thermogenic, microbial, and pyrogenic methane, microbial methane typically exhibits the most negative $\delta^{13}C$ values and usually falls within the most negative range of δD as well, due to the preferential use of lighter isotopes during methanogenesis. For the purpose of refining the atmospheric methane budget, the primary concern is net emissions—that is, the fraction of microbial methane that ultimately reaches the atmosphere. After microbial methane formation through methanogenesis, microbial methane must be transported to the surface before being released into the atmosphere. During this process, a portion of the methane may be consumed by microbial oxidation, which must be accounted for along with its isotopic effects. Oxidation generally alters the $\delta^{13}C$ and δD values of microbial methane, making them less negative and potentially causing the isotopic signature of microbial methane to become more similar to that of thermogenic methane, thereby increasing the challenge of distinguishing between the two sources.

1.3.3.1. Methanogenesis

Microbial methane production (i.e., methanogenesis) is conducted by methanogenic archaea mainly through hydrogenotrophic and acetotrophic pathways (Conrad, 2009; Whiticar, 1999). The hydrogenotrophic pathway (also called carbon reducing pathway or carbon dioxide reducing pathway) synthesizes methane with hydrogen and carbon dioxide:

$$CO_2 + 4\,H_2 \xrightarrow{H_2O} CH_4 + 2\,H_2O \qquad (1.18)$$

while the acetotrophic pathway (also called acetate fermentation pathway, methyl-type fermentation, or acetoclastic methanogenesis) decomposes acetate into carbon dioxide and methane through anaerobic fermentation:

$$^{*}CH_3COO^- + H^+ \xrightarrow{H_2O} {}^{*}CH_4 + CO_2 \qquad (1.19)$$

The carbon in methane is from the methyl group of acetate. Acetotrophic pathway comprises about 2/3 of microbial methane (Whiticar, 2020), while hydrogenotrophic takes the rest. There are also some less common methanogenesis pathways, such as the methylotrophic pathway, which utilizes methylated compounds such as methanol, methylamines, and methyl sulfides as substrates for methane production (Conrad, 2009). The importance of this pathway increases in saline environments (Conrad, 2020) and may also be significant in environments with abundant methylated compounds, such as peatlands, rumens, and wastewater treatment plants. Another example of less common methanogenesis pathway is the methoxylated pathway, which uses methoxylated aromatic compounds—such as those found in lignin-derived organic matter—as substrates. This pathway was first discovered and isolated in coal by Mayumi et al. (2016).

The availability of oxidants (e.g., oxygen, nitrate, ferric iron, or sulfate), substrate composition and availability, as well as microbial species, population size, and activity, are all key factors controlling microbial methanogenesis. From a thermodynamic perspective, methanogenesis becomes energetically favorable only when oxidant concentrations are sufficiently low and substrate concentrations are high enough. Under these conditions, the Gibbs free energy change of oxidation reactions becomes less negative than that of methanogenesis. This explains why methanogenesis strictly requires anaerobic conditions and generally occurs in sediment layers below the surface (ranging from a few centimeters to a few hundred meters). In these zones, conditions are strictly anoxic, and the concentrations of competing electron acceptors (e.g., O_2, SO_4^{2-}) are significantly reduced. Some methanogenic archaea may survive in oxic environments (Conrad, 2020; Fetzer et al., 1993), but they do not exhibit methanogenic activity under such conditions. From a kinetic perspective, the Michaelis-Menten equation for enzyme-catalyzed

reaction rates and the Monod equation for microbial population growth suggest that methanogenesis rates increase when both substrate availability and microbial population size are sufficiently high (Conrad, 2020). Competition exists among different methanogenic microbial communities, each occupying distinct micro-niches. While the discussion above focuses on a microbial-scale, microscopic perspective, environmental variables at a broader, macroscopic level, such as temperature, water table level, soil composition, and soil structure, can influence microbial activity and substrate availability. These environmental factors ultimately shape methanogenesis rates and the isotopic signature of the produced methane.

Methane hydrogen and carbon isotope signals were proven to have the ability to distinguish between microbial methane produced via the two major methanogenesis pathways (Figure 1.13) (Hornibrook et al., 1997; Schöll, 1988; Whiticar et al., 1986). Whiticar et al. (1986) and Whiticar (1999) plotted methane $\delta^{13}C$ and δD values on a single diagram. However, instead of following the plotting method of his advisor (Schöll, 1980), Whiticar et al. (1986) and Whiticar (1999) reversed the y-axis, placing $\delta^{13}C$ values with more negative numbers toward the top, while the x-axis represents δD values increasing from left to right. Whiticar (2020) explained his reasoning for this plotting style, stating, and I quote: "*My historical rationale for plotting $\delta^{13}C$-CH_4 on the ordinate axis and increasing upward with ^{12}C-enriched values is to help illustrate the typical, vertically downward depth trend of diagenesis to catagenesis observed in nature, e.g., normally encountered during drilling of a well.*" Within this plot, a triangular-like area is constrained, with the three corners defining methane of hydrogenotrophic, acetotrophic, and thermogenic origin. There have been several attempts to improve this diagram, primarily by increasing data points, refining classifications, and incorporating spatial and temporal distribution information (e.g.,

(Ganesan et al., 2018; Oh et al., 2022)). However, when databases include thermogenic and pyrogenic methane, the traditional Schöll plot is generally preferred (Etiope et al., 2019; Menoud et al., 2022; Milkov & Etiope, 2018; Sherwood et al., 2017). Overall, methane produced via the hydrogenotrophic pathway tends to be more depleted in ^{13}C ($\delta^{13}C$ ranging from -110‰ to -60‰) and less depleted in D (δD ranging from -250‰ to -170‰) compared to methane produced via the acetotrophic pathway ($\delta^{13}C$ ranging from -70‰ to -50‰ and δD ranging from -400‰ to -250‰). Methane with intermediate $\delta^{13}C$ and δD values was generally interpreted as a mixture derived from both pathways (Burke et al., 1988).

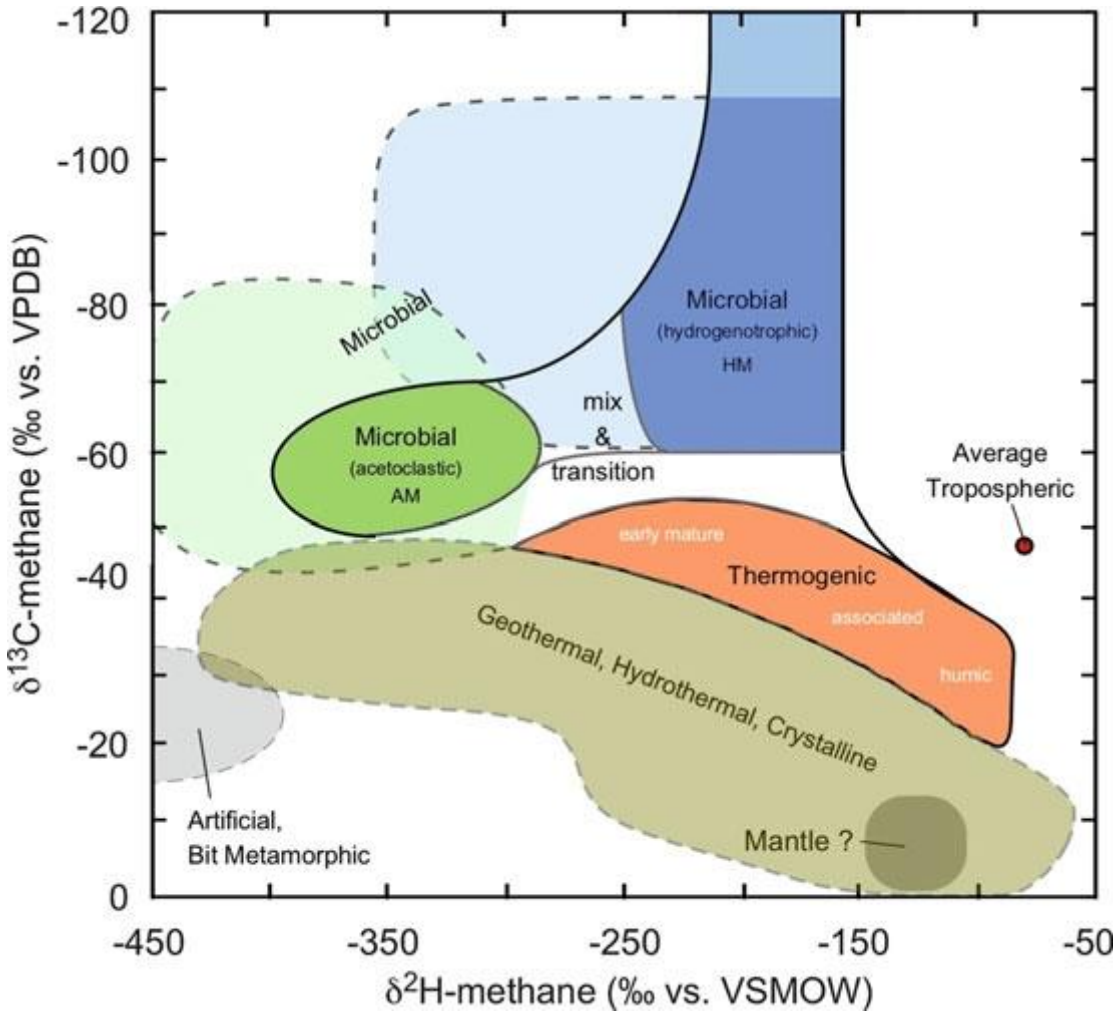

Figure 1.13. **$\delta^{13}C$-δD plot for distinguishing thermogenic methane from microbial methane, as well as distinguishing two methanogenesis pathways.** Please note that Figure 1.13 has switched x and y axes compared to Figure 1.7. (Figure taken from Whiticar (2020), with permission)

However, distinguishing methanogenesis pathways solely based on the carbon and hydrogen isotope values is challenging because these isotope signatures are integrated manifestations of underlying biogeochemical processes, which are modulated by environmental and physiological factors. Many lab incubation/pure culture studies have been conducted to investigate isotopic fractionation during methanogenesis under controlled environments, aiming to isolate one or more specific factors contributing to isotopic effects in methane production (e.g., (Botz et al., 1996; Kawagucci et al., 2014; Krzycki et al., 1987; Okumura et al., 2016; Penning et al., 2005;

Valentine et al., 2004; Yoshioka et al., 2008)). One observation is that isotopic fractionation occurs during the conversion of substrates into methane, meaning that the isotopic composition of the product is influenced by both the composition of the substrate and the extent of isotope fractionation (Figure 1.14).

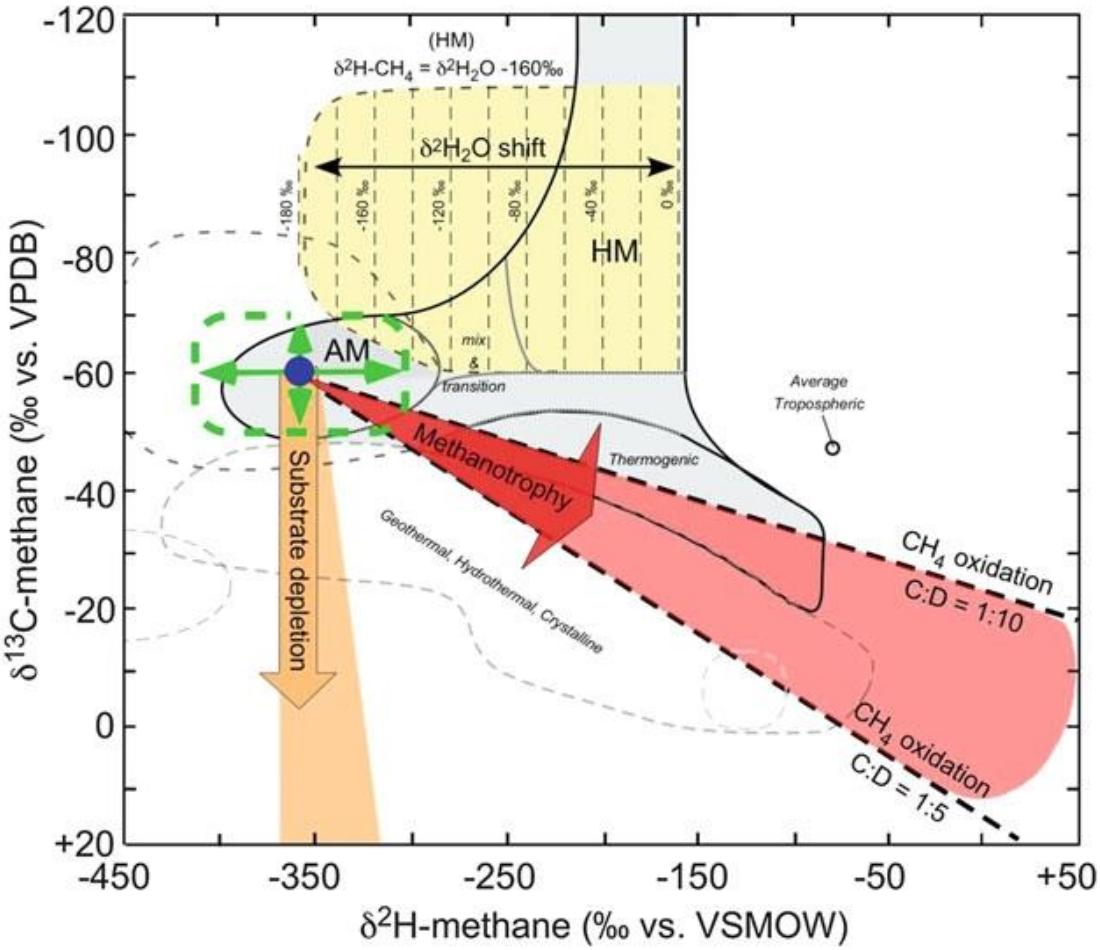

Figure 1.14. **$\delta^{13}C$-δD plot for demonstrating factors affecting microbial methane isotopic signatures.** The background of this figure is Figure 1.13. The effect from substrate carbon source composition on acetotrophic pathway is shown in green box. The effect from substrate water source composition on hydrogenotrophic pathway is shown in light yellow. The effect of substrate depletion is shown in orange. The effect of microbial methane oxidation is shown in red. (Figure taken from Whiticar (2020), with permission)

The influence of substrate composition is most evident in hydrogen isotopes because the δD of hydrogen sources can vary significantly. The hydrogen source for methanogenesis (H^+ and H_2) are generally in isotopic equilibrium with the surrounding environmental water, which its δD have a large variability. The methane produced inherits the hydrogen isotope composition from surrounding water to a certain extent, resulting in a wide range of variability (Figure 1.14, yellow area with annotation "δ^2H_2O shift"). For the hydrogenotrophic pathway, all four hydrogen atoms in the produced methane are either directly derived from or equilibrated with environmental water. As a result, the δD of methane is strongly influenced by the δD of surrounding water. We can say that the water's hydrogen isotope signature is fully inherited (i.e., a proportionality factor close to 1). In contrast, in the acetotrophic pathway, only one of the four hydrogen atoms in methane comes from water, while the other three originate from the methyl group pf acetate. Consequently , the influence of water's δD on the resulting methane is limited, with an effective inheritance factor of approximately 1/4 (Whiticar, 2020). By examining this relationship, we can compare the slopes of hydrogen isotope changes in H_2O and CH_4 to identify methane production processes (Figure 1.15).

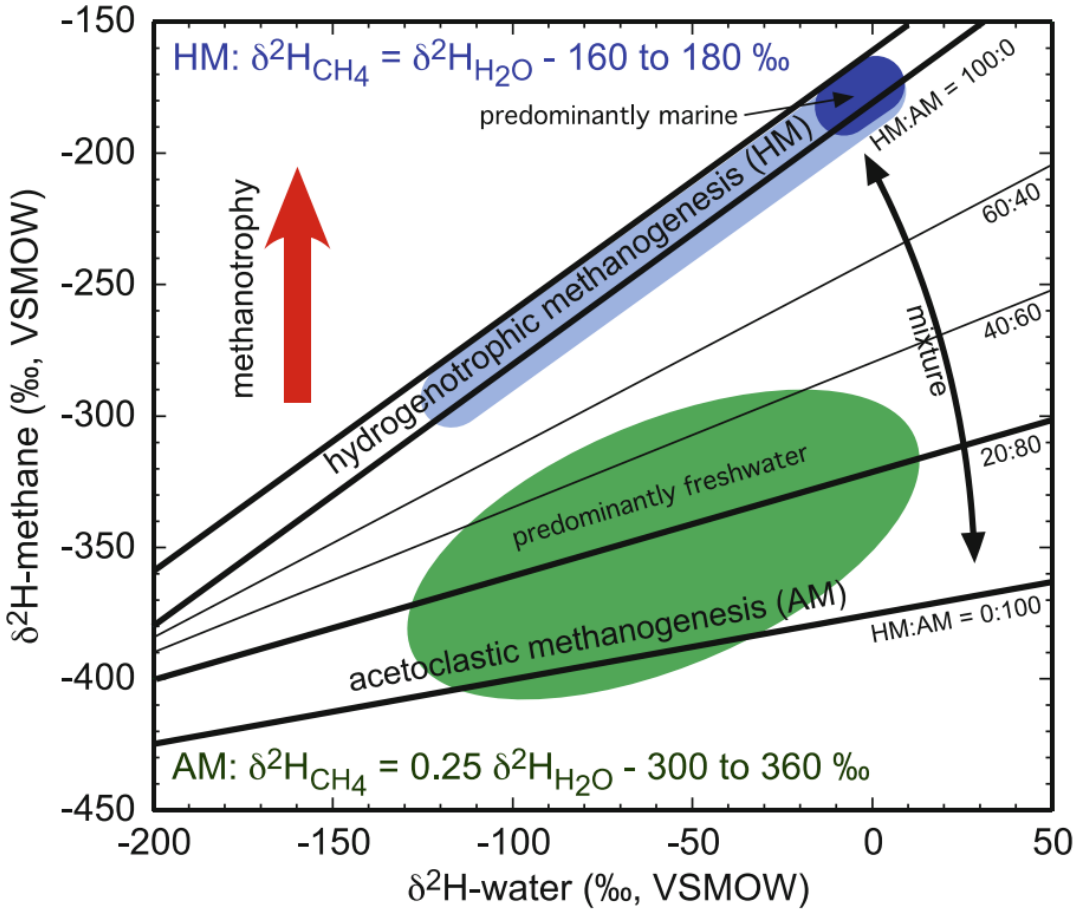

Figure 1.15. **Changes in the hydrogen isotope composition of water and methane in relation to two methanogenesis pathways.** In the hydrogenotrophic methanogenesis process, the hydrogen isotopes of methane and environmental water typically change in a 1:1 ratio, while in the acetotrophic methanogenesis process, the ratio is generally 1:4. (Figure taken from Whiticar (2020), with permission)

If the influence of substrate composition can be teased out, then the extent of isotope fractionation between the substrate and the product can be separated, which is a more conservative parameter, as it is only related to the processes that have occurred. Taking the CO_2 reduction pathway as an example, microbes preferentially utilize the lighter isotopologue, $^{12}CO_2$, resulting in methane with a more negative $\delta^{13}C$ compared to $\delta^{13}C$ of $^{12}CO_2$. There could be a consistent fractionation between CO_2 and CH_4 caused by methanogenesis. However, if CO_2 is continuously consumed without replenishment, its $\delta^{13}C$ of CO_2 will become progressively less

negative. This, in turn, will lead to the production of CH_4 with a less negative $\delta^{13}C$, provided that the fractionation between CO_2 and CH_4 remains unchanged. The fractionation factor, ${}^{13C}\alpha_{CO2\text{-}CH4}$ has the relationship of $10^3 \ln\left({}^{13C}\alpha_{CO2-CH4}\right) \approx \delta^{13}C_{CO2} - \delta^{13}C_{CH4}$ (see definition in Equation 1.9 and Equation 1.10), which provides a clearer reflection of the carbon isotopic fractionation process (carbon from CO_2 to CH_4) itself, since it cancels out the effect of the substrate composition (i.e., $\delta^{13}C_{CO2}$). Generally speaking, α values could offer a more effective means of distinguishing between different methanogenesis pathways than δ, especially in lab settings. A summary of fractionation factor (α) values for methanogenesis reported in the literature is listed in Table 1.3.

Table 1.3. **A summary of α values for methanogenesis.**

	Min	Max	Representative	References
${}^{13C}\alpha_{CO2\text{-}CH4}$	1.020	1.087	1.05	Whiticar et al. (1986) Valentine et al. (2004) and references therein Okumura et al. (2016) and references therein Li, Ash, et al. (2024)
${}^{13C}\alpha_{CH3COOH\text{-}CH4}$	1.007	1.022	1.02	Valentine et al. (2004) and references therein Li, Ash, et al. (2024)
${}^{D}\alpha_{H2O\text{-}CH4}$ hydrogenotrophic	1.11	1.66	1.50	Valentine et al. (2004) Okumura et al. (2016) and references therein Rhim and Ono (2022) and references therein Whiticar (2020)
${}^{D}\alpha_{H2O\text{-}CH4}$ acetotrophic			1.38	Whiticar (2020) Li, Ash, et al. (2024)

However, using the fractionation coefficient α to identify methanogenesis processes has a drawback: it requires that the substrate CO_2 (or CH_3COOH, H_2O, or H_2) are present simultaneously with CH_4 and that their isotopic compositions are not altered by subsequent processes. Therefore, this approach is more commonly applied in laboratory experiments, whereas it may be difficult to achieve in natural environments. Additionally, this α value is not fixed and can vary for several reasons. First, α is a function of temperature; generally, as temperature increases, α tends to approach 1. Second, different microbial species, growth stages, and substrate availability can also affect the α value. These biological factors influence the degree to which methanogenesis reactions proceed in a reversible manner – a concept commonly referred to as reversibility. For instance, Valentine et al. (2004) observed that the partial pressure of H_2 is a major factor controlling $\alpha_{H2\text{-}CH4}$ in the hydrogenotrophic pathway. The partial pressure of H_2 gas determines the free energy of the metabolic breakdown, thereby affecting the reversibility of individual enzymatic steps and, consequently, the extent of isotopic fractionation expressed at each step. Typically, when substrate availability is high, reactions becomes less reversible, allowing greater expression of kinetic isotope effects. As a result, the apparent α value deviates further from 1.

The variable range of the final product methane's $\delta^{13}C$ and δD values can far exceeds the variability seen in α values. This is because the isotopes of the substrate and product will also change as the reaction progresses. The specific pathways of change depend on whether the system is a closed (or reversible) system or an open (or closed irreversible) system, which can be simulated using Rayleigh distillation patterns (Rayleigh, 1902). For more detailed information, please refer to Hayes (2001b) and Whiticar (2020). As the substrate is consumed without

replenishment (i.e., a closed system), the $\delta^{13}C$ of the newly produced methane becomes progressively less negative (Figure 1.14, orange arrow). This substrate depletion effect is not as pronounced for the hydrogen isotope because the hydrogen source H_2O is typically abundantly available (Figure 1.14, orange arrow pointing downward but hardly to the right).

1.3.3.2. Microbial Methane Transportation

After methane generation by microbial metabolism, methane needs to go through transportation and may go through oxidation before reaching the atmosphere. At least five different mechanisms have been identified for methane emission: ebullition, diffusion, the release of stored methane due to water turnover, emissions through vegetation (Bastviken et al., 2004; Ström et al., 2012), and ice-bubble storage flux (Sepulveda-Jauregui et al., 2015). Each mechanism has different temporal and spatial characteristics. For example, diffusion flux could be relatively stable at least in summer in some areas, while the release of storage methane may show a big pulse in spring. A relatively consistent diel emission cycle from lakes was also observed (the strongest emission from 10 am to 4 pm) (Sieczko et al., 2020), although the reason for this pattern remains unclear. Rice paddies present a case; as a vascular plant, rice can transport gases through specialized air spaces known as *aerenchyma*. Consequently, methane in rice paddies can have a remarkably high proportion (reported up to 98%) released via the vegetation pathway (Tyler et al., 1997; Watanabe et al., 1999), suggesting that this methane likely undergoes less oxidation during its transport to the atmosphere. The different emission pathways indicate that the released methane may originate from various production zones, may have undergone different durations of methane oxidation, and therefore may exhibit distinct isotopic characteristics.

1.3.3.3. Methanotroph

Just as microbes produce methane, they also consume it, and the balance or imbalance between methane consumption and production determines the net emissions and the isotopic compositions of released methane. Microbial methane oxidation (also referred to as methanotrophy) is mediated by bacteria or archaea and is therefore also interfered with environmental factors. Anaerobic oxidation of methane (AOM) and aerobic oxidation of methane (AeOM) are two pathways. AOM is mediated by anaerobic methanotrophic archaea (ANME) in consortia with sulfate-reducing bacteria (Boetius et al., 2000). AOM typically occurs in the sulfate-methane transition zone (SMTZ) below the sediment surface, where sulfate and methane coexist (Alperin Marc & Reeburgh William, 1985; Boetius et al., 2000; Orphan et al., 2001; Valentine & Reeburgh, 2000):

$$CH_4 + {SO_4}^{2-} \rightarrow {HCO_3}^{-} + 2\,H_2O + HS^{-} \qquad (1.20)$$

Nitrite (Ettwig et al., 2010), ferric iron, and manganese (Beal et al., 2009) can also act as oxidizers (i.e., electron acceptors), but they are less common.

Aerobic oxidation of methane (AeOM) typically occurs on surfaces where sediment is exposed to air or just below the water surface. This process is primarily carried out by aerobic methanotrophic bacteria, with the key enzyme being methane monooxygenase (MMO), which converts methane to methanol (Hanson & Hanson, 1996):

$$CH_4 + O_2 + 2\,H^{+} \rightarrow CH_3OH + H_2O \qquad (1.21)$$

AeOM is the most thermodynamically favorable and has the fastest reaction rate. AOM occurs at much lower rates and relies on microbial consortia. The rate of methanogenesis likely falls

between these two processes. The fast speed of AeOM results in the surface layer of soil typically being methane-unsaturated, as aerobic methanotrophic bacteria in the soil continuously carrying out AeOM, which makes the soil a sink for atmospheric methane. A significant portion of methane generated in freshwater wetlands and lake sediments (approximately 22% to 100%) (Bastviken et al., 2008) is consumed by AeOM before it is released into the atmosphere. Although the rate of AOM is generally lower, it occurs over vast areas of marine sediments and may consume 75% to 95% of the methane generated in these sediments (Valentine, 2002).

Like methanogenesis, microbial methane oxidation is also strongly influenced by environmental factors such as temperature, precipitation, water table depth, salinity, atmospheric pressure, soil type, nearby urbanization, nearby agriculture, and vegetation cover. Ultimately, it is controlled by the availability of oxygen and other electron acceptors. However, the rate of methane production and the speed of its transportation also influence how much methane can be oxidized before being emitted, thereby influencing the signature of the released methane.

Microbial methane oxidation adds to the complexity of methane carbon and hydrogen isotope signals by preferentially removing lighter isotopes, thereby shifting the residual methane to less negative $\delta^{13}C$ and δD values. This not only complicates the use of isotopic signals to distinguish between the hydrogenotrophic and acetotrophic methanogenesis pathways but can also cause the isotopic signals of microbial methane to overlap with thermogenic signals (e.g., (Alperin et al., 1988; Whiticar, 1999)). The rate of change for carbon and hydrogen isotopes during methane oxidation is approximately in the range of 1:5 to 1:10 (Figure 1.14 red arrows, (Whiticar, 2020)). A summary of fractionation factor (α) values for methane oxidation reported in the literature is

listed in Table 1.4. Similarly, the expression of isotopic fractionation in AOM and AeOM is also influenced by reversibility (Liu, Harris, et al., 2023; Timmers et al., 2017).

Table 1.4. **A summary of α values for methanotroph.**

	Min	Max	References
$^{13C}\alpha_{AeOM}$	1.003	1.060	Happell et al. (1994) Templeton et al. (2006) Feisthauer et al. (2011) Wang et al. (2016) Krause et al. (2022)
$^{13C}\alpha_{AOM}$	1.002	1.038	Whiticar and Faber (1986) Alperin et al. (1988) Holler et al. (2009) Liu, Harris, et al. (2023)
$^{D}\alpha_{AeOM}$	1.050	1.938	Happell et al. (1994) Feisthauer et al. (2011) Wang et al. (2016) Krause et al. (2022)
$^{D}\alpha_{AOM}$	1.103	1.274	Alperin et al. (1988) Holler et al. (2009) Liu, Harris, et al. (2023)

Stepping back from the microscopic perspective, microbial methane exhibits certain distribution patterns on a global scale. Methane $\delta^{13}C$ values in tropical wetlands are less negative than those in temperate and boreal wetlands (Figure 1.16), a finding validated through both field studies (e.g., (Brownlow et al., 2017)) and modeling (e.g., (Ganesan et al., 2018; Oh et al., 2022)). This phenomenon may be attributed to a greater proportion of the hydrogenotrophic pathway in tropical regions, or it could simply be that the substrates in the tropics are less negative in $\delta^{13}C$ mainly due to the predominance of C4 plants which has a less negative $\delta^{13}C$ composition. Oxidation signals provide valuable insights for landfill methane emission studies, where $\delta^{13}C$ is

used to calculate site-specific oxidation efficiency; less negative $\delta^{13}C$ values indicate higher levels of oxidation (e.g., (Bakkaloglu et al., 2022)).

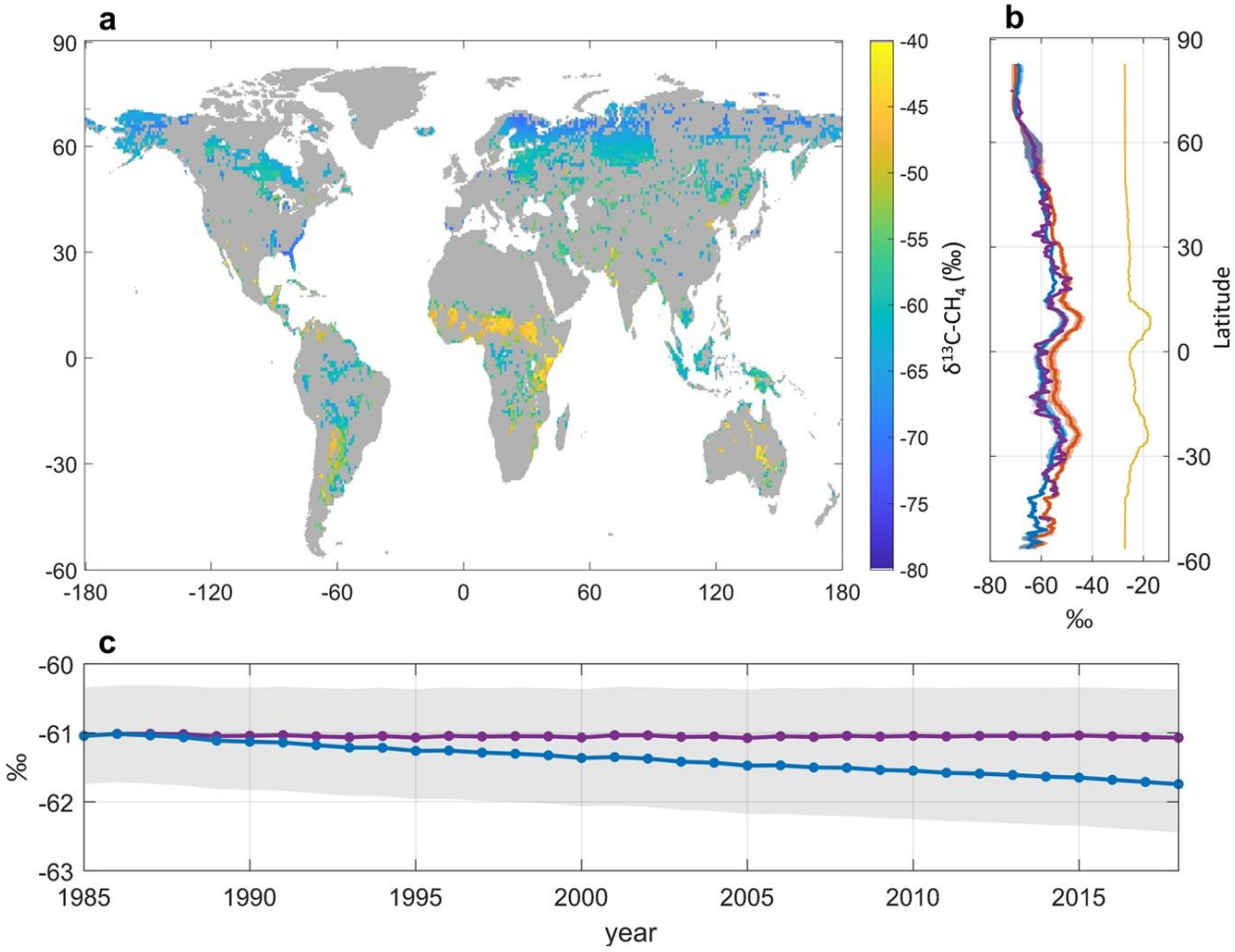

Figure 1.16. **Global wetland methane $\delta^{13}C$ isotopic signature map**. The map is simulated using a process-based biogeochemical model (isoTEM) that accounts for CH_4 production, oxidation, and transport mechanisms such as diffusion, ebullition, and plant-mediated transport between soil and the atmosphere. The model outputs are independently validated using field observation data. Additionally, the model provides information on how wetland $\delta^{13}C$ varies over time. (Figure taken from Oh et al. (2022), under CC BY 4.0).

In summary, based on the distribution of isotopic signatures, three types of methane can be defined: thermogenic, pyrogenic, and microbial. Influenced by various factors such as production pathways and substrate composition, each type of methane exhibits a different range of isotopic

signal variations, but they generally fall within three distinct areas on the $\delta^{13}C$-δD plot. Therefore, statistically, bulk isotopic signals of methane can be used to guide the differentiation of methane sources. However, as more data points were collected (Figure 1.7 and Figure 1.8), the boundaries between thermogenic, pyrogenic, and microbial methane have increasingly overlapped, highlighting the need for additional fingerprinting methods. The concentrations and isotopic compositions of associated gases and substrates with methane can provide supplementary information, as can the methane clumped isotopologues that will be introduced next (Section 1.4). A unique advantage of methane clumped isotopologues is that they do not require the presence of other gases or substrates. As long as there is enough methane, measurements can be taken, and two additional independent tracing proxies can be provided.

1.4. Methane Isotopologues

1.4.1. Background

Isotopologues refer to molecules that differ in isotopic composition, while isotopes are on the atomic level. Clumped isotopologues refer to molecules that have two or more atoms substituted by their rare isotopes. For methane, the singly-substituted isotopologues are: $^{12}CH_4$, $^{13}CH_4$, & $^{12}CH_3D$, and the clumped isotopologues are:$^{13}CH_3D$, $^{12}CH_2D_2$, $^{13}CH_2D_2$, $^{12}CHD_3$, $^{13}CHD_3$, $^{12}CD_4$, $^{13}CD_4$ if only stable isotopes are considered. The commonly measured methane clumped isotopologues are the doubly-substituted isotopologue, i.e., $^{13}CH_3D$, $^{12}CH_2D_2$. Other multiply-substituted isotopologues have extremely low natural abundances and currently have few

applications. Therefore, in this dissertation, as is customary in the literature of this research field, the term "methane clumped isotopologue" refers to the doubly-(heavy-isotope)-substituted methane isotopologues. Table 1.5 shows the hypothetical natural abundances of each isotopologue, assuming a purely random distribution of carbon and hydrogen atoms.

Table 1.5. **The hypothetical natural abundances of each methane isotopologue**, assuming carbon and hydrogen atoms are randomly distributed.

$^{12}CH_4$	$^{13}CH_4$	$^{12}CH_3D$	**$^{13}CH_3D$**	**$^{12}CH_2D_2$**
98.83%	1.11%	0.59‰	6.7ppm	0.13ppm
$^{13}CH_2D_2$	$^{12}CHD_3$	$^{13}CHD_3$	$^{12}CD_4$	$^{13}CD_4$
1.5ppb	13ppt	0.15ppt	50ppq	$5.6/10^{18}$

Traditional "bulk" carbon (or hydrogen) isotope analysis measures the abundance of ^{13}C (or D) atoms without distinguishing different isotopologues. The fraction of ^{13}C, $X(^{13}C)$, is effectively the sum of the fraction of isotopologues that contain ^{13}C, without differentiating isotopologues, i.e.:

$$X(^{13}C) = X(^{13}CH_4) + X(^{13}CH_3D) + X(^{13}CH_2D_2) + X(^{13}CHD_3) + X(^{13}CD_4) \qquad (1.22)$$

This is also why $\delta^{13}C$ and δD are referred to as "bulk" isotopes of methane. In cases where extremely high precisions (<1‰ of 1% level) are not required, it can be numerically treated that $X(^{13}C) \approx X(^{13}CH_4)$ because the abundances of the other isotopologues are much lower. Their low abundances make them hard to be measured.

The concept of clumped isotopologue was put forward by John Eiler (Eiler, 2007; Eiler & Schauble, 2004), with theoretical and computational studies supporting the enrichment of these isotopologues (Bigeleisen & Mayer, 1947; Liu & Liu, 2016; Urey, 1947; Wang, Schauble, et al., 2004; Webb & Miller, 2014). Recent technique breakthroughs have enabled the detection and

measurement of methane doubly-substituted isotopologues ($^{13}CH_3D$ and $^{12}CH_2D_2$) at natural abundances. It was not until 2013 that the total abundance of $^{13}CH_3D$ plus $^{12}CH_2D_2$ (without differentiation) was measured with a precision of 0.74‰ (±1 s.e. in 100s) (Eiler et al., 2013). The capacity of distinguishing $^{12}CH_2D_2$ from $^{13}CH_3D$ came a few years later, as instruments improved (Gonzalez et al., 2019; Young et al., 2016). Methane clumped isotopologue notation is defined similarly to carbon and hydrogen isotopes:

$$\delta^{13}CH_3D_{sample-standard} = \left(\frac{\left({}^{13}CH_3D / {}^{12}CH_4 \right)_{sample}}{\left({}^{13}CH_3D / {}^{12}CH_4 \right)_{standard}} - 1 \right) * 1000‰ \quad (1.23)$$

$$\delta^{12}CH_2D_2{}_{sample-standard} = \left(\frac{\left({}^{12}CH_2D_2 / {}^{12}CH_4 \right)_{sample}}{\left({}^{12}CH_2D_2 / {}^{12}CH_4 \right)_{standard}} - 1 \right) * 1000‰ \quad (1.24)$$

The reference standards are Vienna Pee Dee Belemnite (V-PDB) for carbon isotopes and Vienna Standard Mean Ocean Water (V-SMOW) for hydrogen isotopes (Coplen, 1994). The standard for clumped isotopologues ($^{13}CH_3D$ and $^{12}CH_2D_2$) is a hypothetical methane, which adopts the carbon isotope composition from V-PDB and the hydrogen isotope composition from V-SMOW, and assumes an intra-molecular stochastic distribution - purely random binding of ^{12}C, ^{13}C, H, and D: (Young et al., 2016)

$$^{13}CH_3D X_{substance,stochastic} = 4 * {}^{13}C X_{substance} * {}^{D}X_{substance} * \left({}^{H}X_{substance} \right)^3 \quad (1.25)$$

$$^{12}CH_2D_2 X_{substance,stochastic} = 6 * {}^{12}C X_{substance} * \left({}^{D}X_{substance} \right)^2 * \left({}^{H}X_{substance} \right)^2 \quad (1.26)$$

The coefficient 4 is derived from the four equivalent positions of hydrogen in methane molecules, and 6 is derived from 6 different combinations of two deuterium substituting two out of four hydrogen positions.

A more commonly adopted notation for clumped isotopologues describes the degree of enrichment or depletion of $^{13}CH_3D$ ($^{12}CH_2D_2$) relative to the pure random (stochastic) distribution of the sample itself (Eiler & Schauble, 2004; Young et al., 2016):

$$\Delta^{13}CH_3D_{sample} = \left(\frac{^{13}CH_3D X_{sample,measured}}{^{13}CH_3D X_{sample,stochastic}} - 1\right) * 1000‰ \quad (1.27)$$

$$\Delta^{12}CH_2D_{2\,sample} = \left(\frac{^{12}CH_2D_2 X_{sample,measured}}{^{12}CH_2D_2 X_{sample,stochastic}} - 1\right) * 1000‰ \quad (1.28)$$

Where $^{13}CH_3D X_{sample,measured}$ and $^{12}CH_2D_2 X_{sample,measured}$ are the measured proportions of $^{13}CH_3D$ and $^{12}CH_2D_2$ molecules in total methane molecules (i.e., all methane isotopologues). This definition makes methane clumped isotopologue signals independent from the bulk ^{13}C and D abundances because the reference coordinate is a relative coordinate system that removes the influence of bulk ^{13}C and D abundances.

In practical applications, we use approximate formulas to calculate $\Delta^{13}CH_3D$ and $\Delta^{12}CH_2D_2$ (Haghnegahdar et al., 2024; Haghnegahdar et al., 2023; Sun, Haghnegahdar, et al., 2025):

$$\Delta^{13}CH_3D_{sample} = \left(\left(1 + \delta^{13}CH_3D\right) \Big/ \left(1 + \delta^{13}CH_4\right) * \left(1 + \delta^{12}CH_3D\right) - 1\right) * 1000‰ \quad (1.29)$$

$$\Delta^{12}CH_2D_{2\,sample} = \left(\left(1 + \delta^{12}CH_2D_2\right) \Big/ \left(1 + \delta^{12}CH_3D\right)^2 - 1\right) * 1000‰ \quad (1.30)$$

The errors introduced by using these approximations are typically less than 0.05‰ for $\Delta^{13}CH_3D$ and less than 0.1‰ for $\Delta^{12}CH_2D_2$. In most cases, the deviations are smaller than these limits. These approximation-induced errors are generally an order of magnitude smaller than the 1σ measurement uncertainties.

Due to instrument limitation, many early-stage clumped isotopologue studies can only measure the total mass-18 intensity, but cannot distinguish $^{13}CH_3D$, $^{12}CH_2D_2$, and $^{13}CH_5$, so it is common to see Δ18 notation in the literature:

$$\Delta 18 = \left(\frac{^{18}X_{sample,measured}}{^{18}X_{sample,stochastic}} - 1\right) * 1000‰ \quad (1.31)$$

Where $^{18}X_{sample,measured}$ is the measured proportion of mass-18 molecules ($^{13}CH_3D$, $^{12}CH_2D_2$, and $^{13}CH_5$) in total methane molecules. Δ18 is numerically close to $\Delta^{13}CH_3D$ because the abundances of $^{12}CH_2D_2$ and $^{13}CH_5$ are two orders of magnitude lower than that of $^{13}CH_3D$.

1.4.2. Thermodynamic Equilibrium State and Intramolecular Thermometer

Methane clumped isotopologue measurements have been used to indicate the formation or equilibrium temperature of methane (Stolper, Lawson, et al., 2014; Stolper, Sessions, et al., 2014). Methane molecules are in constant thermal motion and collide with each other. Collision may or may not result in isotope exchange. When chemical energy is minimized for the system, we refer to it as being in an equilibrium state. The isotope effects leading to this state are called equilibrium isotope effects (EIEs). We take the formation of $^{13}CH_3D$ during intramolecular isotope exchange reaction as an example, and the theory can be applied to $^{12}CH_2D_2$:

$$^{13}CH_4 + {}^{12}CH_3D \leftrightarrow {}^{12}CH_4 + {}^{13}CH_3D \quad (1.32)$$

The equilibrium constant $^{^{13}CH_3D}K_{eq}$ is:

$$^{^{13}CH_3D}K_{eq} = \frac{[^{12}CH_4][^{13}CH_3D]}{[^{13}CH_4][^{12}CH_3D]} \quad (1.33)$$

$^{13CH_3D}K_{eq}$ is not equal to one. This is because the atoms forming ^{13}C-D bonds are heavier than atoms forming ^{12}C-D and ^{13}C-H bonds. As a result, the vibration frequency of the ^{13}C-D bond is lower than that of the ^{12}C-D bond, and the binding energy of ^{13}C-D bond is greater than that of ^{12}C-D bond. Consequently, the $^{13}CH_3D$ molecule is more stable than $^{12}CH_3D$ (and also $^{13}CH_4$) because breaking the^{13}C-D bond requires more energy than breaking the ^{12}C-D bond. This leads to a situation where, if methane is under thermodynamic equilibrium, the abundance of $^{13}CH_3D$ will be higher than its stochastic distribution (i.e. $\Delta^{13}CH_3D>0‰$) because $^{13}CH_3D$ is thermodynamically preferred. At a given temperature, if methane gas has not reached intramolecular thermal equilibrium, the isotope exchange reaction described above will tend to proceed in the forward direction, resulting in a higher proportion of doubly-substituted isotopologues (i.e., $^{13CH_3D}K_{eq} > 1$), a phenomenon also referred to as clumping. The stochastic distribution is a theoretical special case of the equilibrium distribution at infinite high temperatures. As temperature increases, entropy dominates and the distribution of isotopes among sites is randomized, leading to the reduction in isotopic fractionations and the tendency for molecules to approach a stochastic limit (i.e. $\Delta^{13}CH_3D=0$ and $^{13CH_3D}K_{eq\ at\ T=+\infty} = 1$).

K_{eq} can be calculated to a high level of certainty using first principles and thermodynamic laws. The first step is to calculate the potential energy surfaces of each methane isotopologue using the first principles. With the potential energy surface, the vibrational frequencies can be calculated. In this case, the standard approach has been to use the Bigeleisen-Mayer/Urey Model to calculate partition function ratios of an isotopologue pair (PFR) (Bigeleisen & Mayer, 1947; Eldridge et al., 2019; Urey, 1947). This approach assumes a rigid-rotor and harmonic-oscillator

approximation, but other methods that relax these constraints yield similar results (Eldridge et al., 2019):

$$PFR = \frac{Q^*}{Q} = \frac{\sigma}{\sigma^*} e^{-(E_0^* - E_0)/k_B T} \prod_{i=1}^{N} \left(\frac{m_i^*}{m_i}\right)^{\frac{3}{2}} \prod_{j=1}^{a} \frac{\omega_i^*}{\omega_i} \frac{1-e^{-\hbar\omega_j/k_B T}}{1-e^{-\hbar\omega_j^*/k_B T}} \quad (1.34)$$

where Q is the partition function of the isotopologue, σ is the rotational symmetry number, E_0 is zero-point energy, k_B is the Boltzmann constant, T is the temperature in kelvin, i from 1 to N represents the i[th] atom in a molecule of N atoms, m is the atomic mass, ω is the harmonic vibration frequency given in wavenumber, j from 1 to a is the vibrational modes, $\hbar$ is reduced Planck's constant, and the asterisk indicates substituted isotopologue. K_{eq} can be calculated from Q (or PFR):

$$^{13}CH_3D K_{eq} = \frac{Q^{12}CH_4 \, Q^{13}CH_3D}{Q^{13}CH_4 \, Q^{12}CH_3D} \quad (1.35)$$

Liu and Liu (2016) calculated the corrected partition function ratio (CPFR), which further considered six higher-order inharmonic energy terms.

Young, Kohl, Lollar, et al. (2017), for example, reported numerical approximations of K_{eq} as functions of temperature T in Kelvin (Figure 1.17):

$$^{13}CH_3D K_{eq} = 1 + \frac{0.0355502}{T} + \frac{-433.038}{T^2} + \frac{1270210.0}{T^3} + \frac{-5.94804*10^8}{T^4} + \frac{1.196630*10^{11}}{T^5} + \frac{-9.07230*10^{12}}{T^6} \quad (1.36)$$

$$\frac{8}{3} * {}^{12}CH_2D_2 K_{eq} = 1 + \frac{0.183798}{T} + \frac{-785.483}{T^2} + \frac{1056280.0}{T^3} + \frac{9.37307*10^7}{T^4} + \frac{-8.919480*10^{10}}{T^5} + \frac{9.901730*10^{12}}{T^6} \quad (1.37)$$

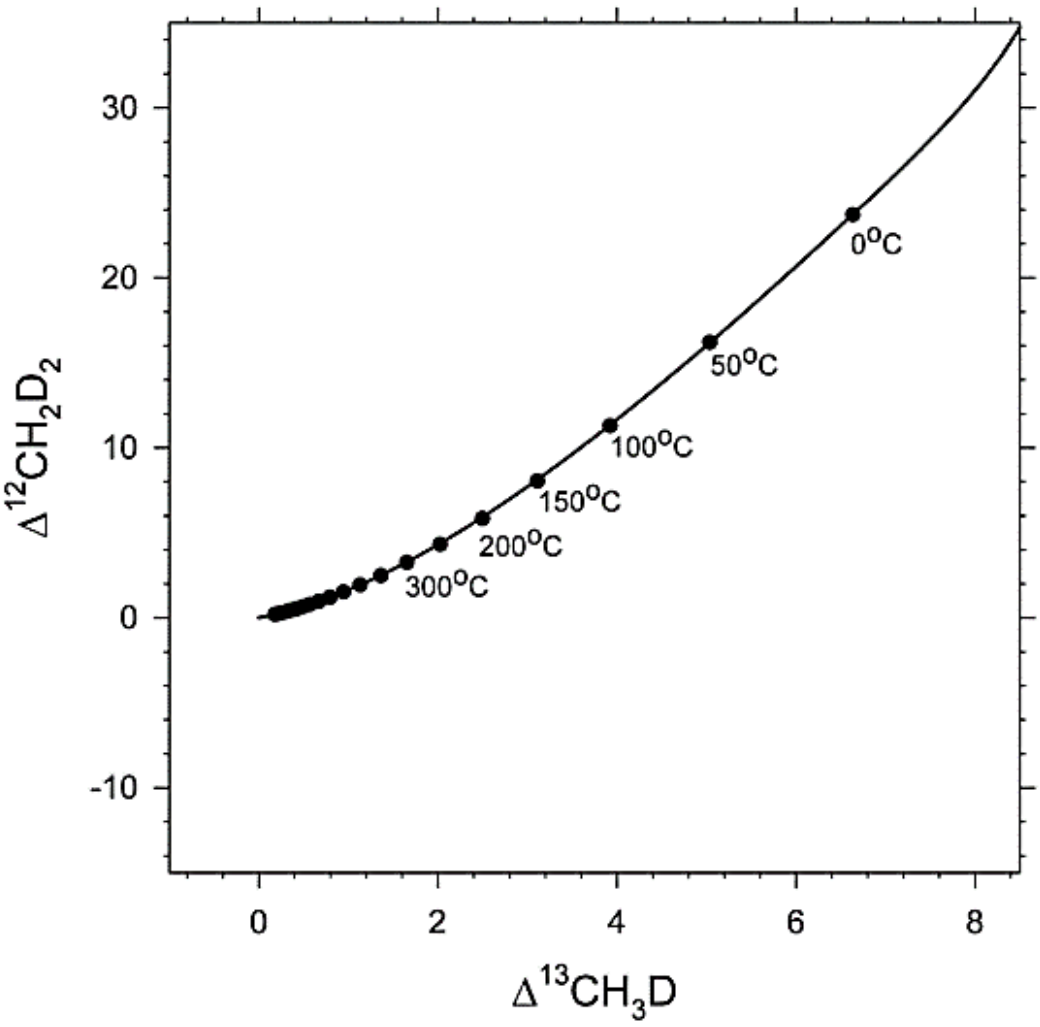

Figure 1.17. **Thermodynamic equilibrium curve in $\Delta^{12}CH_2D_2$ vs. $\Delta^{13}CH_3D$ space.** Both axes are in ‰. (Figure taken from Young (2019), under CC-BY-NC-SA 4.0)

The thermodynamic equilibrium curve (Eldridge et al., 2019; Young, Kohl, Lollar, et al., 2017) facilitates the use of methane clumped isotopologues as intramolecular thermometers. Both $^{13}CH_3D$ and $^{12}CH_2D_2$ can serve as independent thermometers, providing two separate temperature estimations. However, the premise of calculating temperature from clumped isotopologue signals is that the methane has already reached thermodynamic equilibrium. In many cases, this assumption does not hold, particularly for microbial methane. Earlier-stage studies used $\Delta 18$, or $\Delta^{13}CH_3D$ alone to calculate temperature due to the inability of

differentiating $^{12}CH_2D_2$ from $^{13}CH_3D$ or the inability of measuring $^{12}CH_2D_2$. For example, Stolper, Lawson, et al. (2014) used Δ18 to calculate the formation temperature of thermogenic and microbial methane in Haynesville Shale, Gulf of Mexico, and Potiguar Basin. Wang et al. (2015) used the relationship between $\Delta^{13}CH_3D$ and δD to point out that many lab cultures that produced microbial methane were not thermally equilibrated, so the derived temperature is not physically real. Figure 1.17 also provides a diagnostic criterion for assessing whether methane has reached thermodynamic equilibrium—namely, the $\Delta^{12}CH_2D_2$ and $\Delta^{13}CH_3D$ values should fall on the equilibrium curve, indicating that both clumped isotopologue signatures reflect the same equilibrium temperature. This criterion has been adopted in recent studies (e.g., (Young, Kohl, Lollar, et al., 2017; Zhang, Snyder, et al., 2021)). However, it is important to note that even if $\Delta^{12}CH_2D_2$ and $\Delta^{13}CH_3D$ values correspond to the same equilibrium temperature, this does not necessarily confirm that the methane has reached thermodynamic equilibrium or that it formed at that specific temperature. Various processes can alter these parameters, and in some cases, their values may appear to fall on the equilibrium curve, without necessarily indicating true equilibrium. These processes will be discussed in Section 1.4.3. Therefore, additional indicators are required to reliably determine whether methane has attained thermodynamic equilibrium. Based on current observations, a significant proportion of thermogenic methane, as well as some microbial methane in deep-sea sediments that has undergone methanogenesis-methanotrophy equilibrium at geological timescale, appears to meet thermodynamic equilibrium conditions.

1.4.3. Non-equilibrium Conditions

A large portion of natural and lab-produced methane samples has been found to deviate from thermodynamic equilibrium. For these methane samples, their non-equilibrium signals may convey other information about processes, such as mixing, combinatorial effect, and kinetic isotope fractionation caused by diffusion, atmospheric sink reactions, and microbial reaction networks. Some non-equilibrium signals arise from the way that processes like, but not limited to, mixing produce compositions that are revealed by the mathematical properties of the clumped Δ notations, while others result from deviations caused by physical and chemical processes. The kinetic isotope effect (KIE) is a notation often adopted to describe the kinetic isotope fractionation of a reaction/process. For a reaction involving methane isotopologues, KIE is typically defined as:

$$^{\mathrm{i}}\mathrm{KIE} = \frac{^{12}\mathrm{CH_4}_k}{^{\mathrm{i}}_k} \tag{1.38}$$

where $^{\mathrm{i}}k$ is the rate constant of the reaction/process with the isotopologue i as the reactant. In general, isotopologues with rare isotopes are more stable, resulting in a lower reaction rate constant compared to isotopologues without rare isotopes. Therefore, according to this definition, the KIE is always greater than or equal to 1.

The definition of KIE has some similarities with the definition of the isotope fractionation factor (α). However, α emphasizes the differences in isotopic composition between the product and the reactant, which is the result after the reaction is complete, while KIE focuses on the reaction rates of different isotopes during the conversion of the reactant to the product. For an irreversible

reaction in an open system, at each moment of the reaction, there is such a relationship between α and KIE:

$$^{i}\alpha_{\text{instantaneous product}-\text{reactant}} = {}^{i}\text{KIE of reaction reactant} \rightarrow \text{product} \qquad (1.39)$$

1.4.3.1. Mixing

The Δ notations are in a non-linear relative coordinate, unlike the δ notations, which are in a linear coordinate system. As a result, the mixing process of two different parcels of methane presents a curve rather than a straight line on the $\Delta^{13}CH_3D$-$\Delta^{12}CH_2D_2$ plot. For sample 1 and 2 mixing into a sample "mix" with a mixing ratio f_1 and f_2, the system has the following relationships:

$$A_{mix} = A_1 * f_1 + A_2 * f_2 \qquad (1.40)$$

$$f_1 + f_2 = 1 \qquad (1.41)$$

A can be any parameters on the linear coordinate, such as concentration, ^{13C}X, $\delta^{13}C$, ^{D}X, δD, $^{13CH3D}X$, $\delta^{13}CH_3D$, $^{12CH2D2}X$, and $\delta^{12}CH_2D_2$. But for $\Delta^{13}CH_3D$ and $\Delta^{12}CH_2D_2$, according to their definition:

$$\Delta^{13}CH_3D_{sample} = \left(\frac{^{13}CH_3D X_{sample,measured}}{^{13}CH_3D X_{sample,stochastic}} - 1\right) * 1000‰ \qquad (1.42)$$

$$\Delta^{12}CH_2D_{2\,sample} = \left(\frac{^{12}CH_2D_2 X_{sample,measured}}{^{12}CH_2D_2 X_{sample,stochastic}} - 1\right) * 1000‰ \qquad (1.43)$$

both denominators and numerators are being changed by the mixing process, so the ratios ($\Delta^{13}CH_3D$ and $\Delta^{12}CH_2D_2$) are no longer changing linearly. As the difference in $\delta^{13}C$ and δD between two mixing end members increases, the $\Delta^{13}CH_3D$-$\Delta^{12}CH_2D_2$ mixing trajectory of the mixture increasingly diverges from a linear relationship.

Mixing typically causes methane to deviate from the thermal equilibrium curve—only in very coincidental cases will the mixing of two parcels of methane result in a thermal equilibrium signal. The curved relationships observed in isotopologue compositions can serve as diagnostic indicators of mixing process and can further utilized to estimate mixing ratios. When more than two endmembers are mixed to cause ambiguity on the linear mixing fields such as the $\delta^{13}C$-δD plot, the curve mixing relationship may provide extra information. Figure 1.18 shows a mixing test done by Young, Kohl, Lollar, et al. (2017).

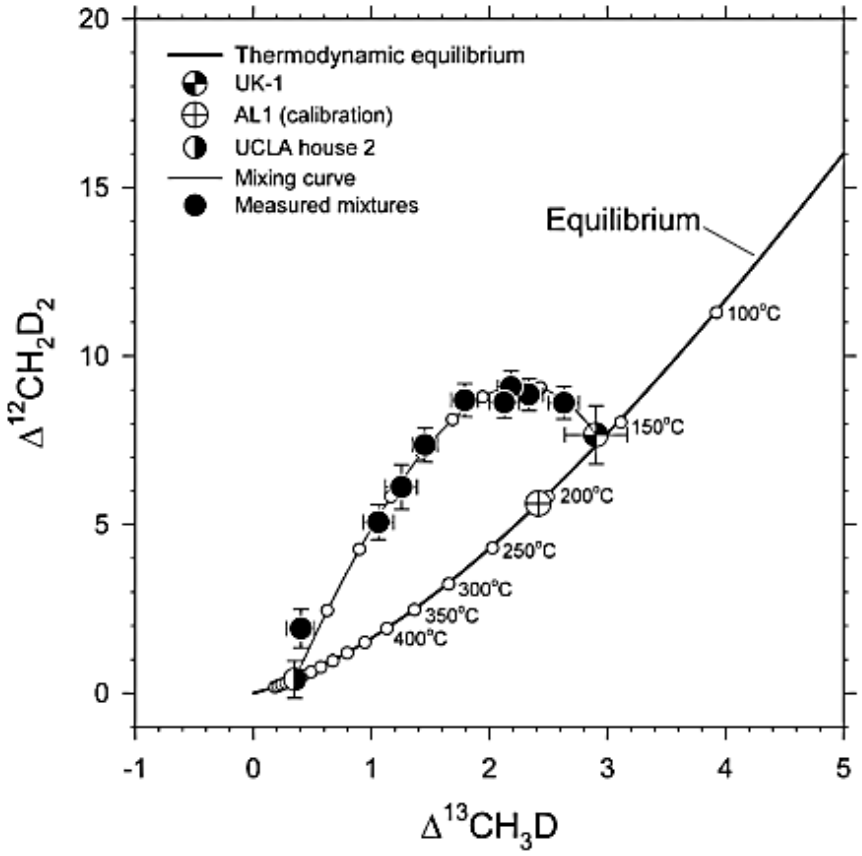

Figure 1.18. **The behavior of clumped isotopologues during mixing**. Black symbols are measured $\Delta^{13}CH_3D$ and $\Delta^{12}CH_2D_2$ in ‰ of the mixtures. The convex curve is the predicted mixing curve with small white points marking 10% intervals of mixing. (Figure from Young, Kohl, Lollar, et al. (2017), with permission)

1.4.3.2. Combinatorial Effects

While the mixing effect is the nonlinear changing of $\Delta^{13}CH_3D$ and $\Delta^{12}CH_2D_2$ when putting methane molecules with different isotope signatures together, the combinatorial effect only causes nonlinear changes in $\Delta^{12}CH_2D_2$ values. This effect arises during the assembling of individual methane molecules with hydrogen atoms derived from multiple hydrogen pools with different hydrogen isotope ratios. This effect is of particular interest for microbial methane studies (Labidi et al., 2024; Taenzer et al., 2020; Yeung, 2016) because the acetotrophic pathway could produce methane by combining the methyl group from the acetate with an external hydrogen from water. This process creates ideal conditions for the combinatorial effect, as the δD values of the methyl group in acetate and water are typically different:

$$^{*}CH_3COOH + {}^{\dagger}H\,{}^{\dagger}HO \rightarrow {}^{*}CH_3\,{}^{\dagger}H + CO_2 + H\,{}^{\dagger}HO \quad (1.44)$$

If I describe this system in a simplified way, we can assume that two hydrogen atoms combine in a ratio of $f_1 = f_2 = 0.5$, but these hydrogen atoms originate from two distinct hydrogen source pools, Pool 1 and Pool 2. The fraction of deuterium in Pool 1 is denoted as ${}^{D}X_1$, while in Pool 2, it is ${}^{D}X_2$. If the two pools are not mixed beforehand and the hydrogen atoms from Pool 1 and Pool 2 remain distinguishable, then the fraction of the (D,D) isotopologue formed is given by:

$$^{(D,D)}X_{mix,real} = {}^{D}X_1 * {}^{D}X_2 \quad (1.45)$$

However, if the two pools are mixed beforehand, making hydrogen atoms from Pool 1 and Pool 2 indistinguishable, the overall fraction of deuterium in the mixed pool becomes:

$$^{D}X_{mix} = \frac{{}^{D}X_1 + {}^{D}X_2}{2} \quad (1.46)$$

In this case, if hydrogen atoms combine randomly within the mixed pool, the fraction of the (D,D) isotopologue formed is:

$$^{(D,D)}X_{mix,stochastic} = (\frac{^{D}X_1 + ^{D}X_2}{2})^2 \quad (1.47)$$

It can be observed that $^{(D,D)}X_{mix,stochastic}$ is the square of arithmetic mean, while $^{(D,D)}X_{mix,real}$ is the square of geometric mean. Since the arithmetic mean is always greater than or equal to the geometric mean, we have:

$$^{(D,D)}X_{mix,stochastic} = (\frac{^{D}X_1 + ^{D}X_2}{2})^2 \geq {}^{D}X_1 * {}^{D}X_2 = {}^{(D,D)}X_{mix,real} \quad (1.48)$$

Thus, according to definition of the clumped isotopologue Δ notation:

$$\Delta'_{mix}(D,D) = (\frac{^{(D,D)}X_{mix,real}}{^{(D,D)}X_{mix,stochastic}} - 1) * 1000‰ \leq 0 \quad (1.49)$$

Equality holds only when $^{D}X_1 = {}^{D}X_2$. The prime symbol (‘) means that this formulation does not account the thermodynamic preference of doubly-substituted isotopologue. In other words, even in the absence of a kinetic isotope effect in the reaction, simply having different bulk isotopic compositions in the two pools leads to a downward deviation of the resulting isotopologue Δ value from its theoretically expected value.

It should be noted that this effect is generally very small. Only when the isotopic composition of the same element differs significantly between the two pools does the impact become noticeable. For example, in the case of methane, if the bulk hydrogen isotope composition of the two pools differs by 100‰, the combinatorial effect results in a deviation of less than 0.1‰ in Δ. If the difference reaches 1000‰, the combinatorial effect can cause a deviation of up to 5‰ in Δ. For methane formation, the primary scenario where this effect needs to be considered is acetotrophy. In natural environments, water can exhibit significant hydrogen isotopic variation. In laboratory

experiments, if deuterium-doped water is used to culture acetotrophic methanogenesis microbial communities, the effect becomes more pronounced (Taenzer et al., 2020). Theoretically, hydrogenotrophy involves the addition of four hydrogen atoms to CO_2 to form methane, with these four hydrogen atoms most likely originating from a single hydrogen pool. However, if each step of the process exhibits different isotopic fractionation, it could result in an effect equivalent to the combinatorial effect. The same applies to abiotically synthesized methane via the Fischer-Tropsch-Type pathway (Labidi et al., 2024).

The combinatorial effect will not produce an arithmetic anti-clumping signal in $\Delta^{13}CH_3D$ because the carbon from Pool 1 and the hydrogen from Pool 2 are fully resolved.

1.4.3.3. KIE caused by Diffusion

Heavy isotopes diffuse more slowly than light isotopes. There is typically a relationship as follows (Richter et al., 2006):

$$^{M2-M1}\mathrm{KIE} = \frac{^{M_1}D}{^{M_2}D} = \left(\frac{M_2}{M_1}\right)^{\beta} \quad (1.50)$$

where D is the diffusion coefficient, M_1 and M_2 represent isotopologues of the same species with different molecular masses, with $M_1 < M_2$, and β is the mass-dependent isotopic fractionation exponent, which is generally considered to be approximately 0.5. This equation applies to a single ideal gas under conditions where intermolecular forces and collisions can be neglected. For methane dissolved in water, solvent interactions influence the diffusion process, making the equation less applicable. However, it can be approximated by reducing β, meaning the KIE will be closer to 1. In systems containing multiple gases with similar molecular masses, the molecular

mass M can be replaced by the reduced mass μ, where: $\mu = M_1 * M_3/(M_1+M_3)$, M_3 is the molecular mass of another gas present in the system.

If we use the simplest equation for calculation, we obtain:

$$^{13}CH_4\text{KIE} = \frac{^{12}CH_4D}{^{13}CH_4D} = \left(\frac{13.00335+4*1.007825}{12+4*1.007825}\right)^{0.5} = 1.03082 \quad (1.51)$$

$$^{12}CH_3D\text{KIE} = \frac{^{12}CH_4D}{^{12}CH_3D_D} = \left(\frac{12+3*1.007825+2.0141}{12+4*1.007825}\right)^{0.5} = 1.03091 \quad (1.52)$$

$$^{13}CH_3D\text{KIE} = \frac{^{12}CH_4D}{^{13}CH_3D_D} = \left(\frac{13.00335+3*1.007825+2.0141}{12+4*1.007825}\right)^{0.5} = 1.06083 \quad (1.53)$$

$$^{12}CH_2D_2\text{KIE} = \frac{^{12}CH_4D}{^{12}CH_2D_{2D}} = \left(\frac{12+2*1.007825+2*2.0141}{12+4*1.007825}\right)^{0.5} = 1.06091 \quad (1.54)$$

The significant figures are intentionally taken to an unrealistically high precision to illustrate the subtle differences in values at high accuracy. Under these KIEs, we simulate the diffusion-driven isotope fractionation of pure methane gas with an initial composition typical of thermogenic methane (from natural gas samples) under ideal conditions. This evolution of the residue methane isotope composition can be approximated by a closed-system irreversible Rayleigh fractionation (Hayes, 2004):

$$\delta i_{\text{residue at t}} = \delta i_{\text{residue at t0}} * f_{\text{residue}}^{\left(\frac{1}{i}\text{KIE}-1\right)} \quad (1.55)$$

Where i refers to different isotopologues ($^{13}CH_4$, $^{12}CH_3D$, $^{13}CH_3D$, and $^{12}CH_2D_2$), $\delta i_{\text{residue at t}}$ and $\delta i_{\text{residue at t0}}$ are the isotopic composition of residue methane at time t and time 0 (initial), f_{residue} is the remaining fraction of (residue) methane. It should be noted that for clumped isotopologues, this equation can still only be applied to δ notation, not Δ notation. Δ must be

further calculated based on the previously defined formula. The results are presented in Figure 1.19.

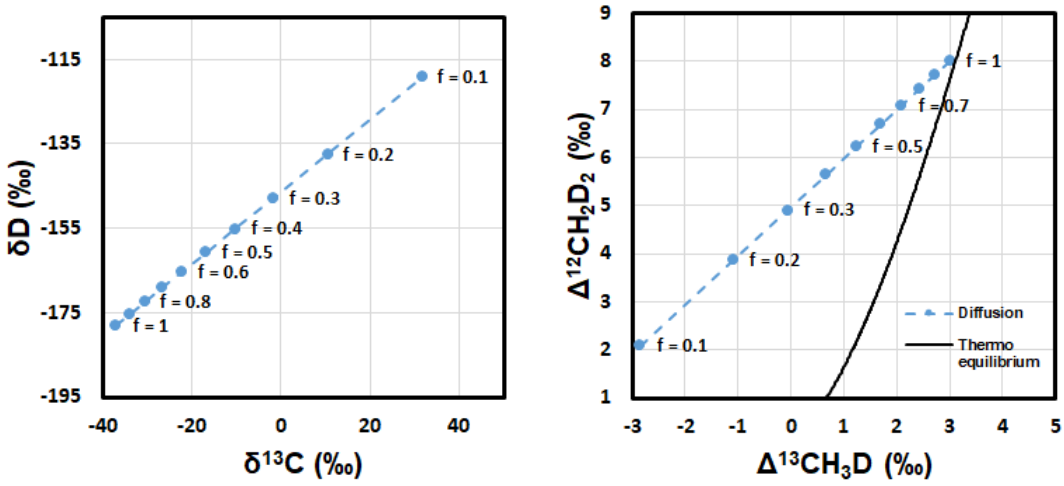

Figure 1.19. **Theoretical isotope fractionation caused by ideal pure gas diffusion.** *f* is the fraction of remaining methane. The x-axis and y-axis are set to have equal maximum ranges, with evenly spaced coordinate intervals.

From Figure 1.19, it can be observed that both bulk carbon and hydrogen isotope values become more positive in the residual methane. Moreover, the isotopic shifts of carbon and hydrogen occur in an almost 1:1 ratio. This is because $^{13}CH_4$KIE and $^{12}CH_3D$KIE are both greater than 1 and nearly equal. The same principle applies to $\delta^{13}CH_3D$ and $\delta^{12}CH_2D_2$, as their KIEs are also greater than 1 and nearly identical. Interestingly, $\Delta^{13}CH_3D$ and $\Delta^{12}CH_2D_2$ also exhibit an approximately 1:1 proportional change. However, the residual methane shifts toward a less clumped isotopologue composition, yet it still remains above the thermo-equilibrium curve.

The diffusion of methane occurs in various geological and environmental settings, including but not limited to: methane migration in marine sediments leading to gas hydrate accumulation

(Ginsburg & Soloviev, 1997); natural gas migration in sedimentary rocks (Zhang & Krooss, 2001); methane transport from sediments into the water column (Reeburgh, 2007); and methane diffusion across the cell membrane during microbial methanogenesis. Diffusion can also be artificially introduced in laboratory operations, such as during methane purification, where methane passes through a MolSieve (a porous polymer adsorbent) column in a Gas Chromatography (GC) (as described in detail in Section 2.3). Extreme isotopic fractionation could happen during this process. The nature of diffusion varies significantly across these processes, with some exhibiting minimal isotope fractionation and some following distinct mathematical relationships. Taking methane diffusion in porous adsorbent media as an example, in addition to the controlling factor of molecular mass, if the pore size approaches the molecular dimensions of methane, Knudsen diffusion or surface diffusion-induced pore effects will dominate. In such cases, isotopic fractionation does not follow Fick's law of molecular diffusion (e.g., (Moores & Sapers, 2024; Yeung et al., 2012)). Adsorption-desorption kinetics also play a role, leading to complex deviations from molecular diffusion (e.g., (Xia & Tang, 2012)). Nonetheless, the simulation in Figure 1.19 provides a general isotopic fractionation trend associated with methane diffusion.

1.4.3.4. KIE caused by Atmospheric Sink Reactions

The sink reactions of methane with OH and Cl, as described in Section 1.2.2, have strong tendencies to preferentially consume lighter methane molecules. As irreversible elementary reactions, the CH_4 + OH and CH_4 + Cl reactions are relatively straightforward, likely involving the formation of a single transition state followed by its decomposition to products. Therefore, the isotope effects in atmospheric sink reactions can be well described using KIEs.

Taking the CH_4 + OH reaction as an example, consider the following reaction in the atmosphere, each has a rate constant *k*:

$$^{12}\mathrm{CH_4} + \mathrm{OH}\cdot \rightarrow {}^{12}\mathrm{CH_3}\cdot + \mathrm{H_2O} \quad {}^{12\mathrm{CH_4}}k \tag{1.56}$$

$$^{13}\mathrm{CH_4} + \mathrm{OH}\cdot \rightarrow {}^{13}\mathrm{CH_3}\cdot + \mathrm{H_2O} \quad {}^{13\mathrm{CH_4}}k \tag{1.57}$$

$$^{12}\mathrm{CH_3D} + \mathrm{OH}\cdot \rightarrow {}^{12}\mathrm{CH_2D}\cdot + \mathrm{H_2O} \quad {}^{12\mathrm{CH_3D}}k^{s} \tag{1.58}$$

$$^{12}\mathrm{CH_3D} + \mathrm{OH}\cdot \rightarrow {}^{12}\mathrm{CH_3}\cdot + \mathrm{HDO} \quad {}^{12\mathrm{CH_3D}}k^{p} \tag{1.59}$$

$$^{13}\mathrm{CH_3D} + \mathrm{OH}\cdot \rightarrow {}^{13}\mathrm{CH_2D}\cdot + \mathrm{H_2O} \quad {}^{13\mathrm{CH_3D}}k^{s} \tag{1.60}$$

$$^{13}\mathrm{CH_3D} + \mathrm{OH}\cdot \rightarrow {}^{13}\mathrm{CH_3}\cdot + \mathrm{HDO} \quad {}^{13\mathrm{CH_3D}}k^{p} \tag{1.61}$$

$$^{12}\mathrm{CH_2D_2} + \mathrm{OH}\cdot \rightarrow {}^{12}\mathrm{CHD_2}\cdot + \mathrm{H_2O} \quad {}^{12\mathrm{CH_2D_2}}k^{s} \tag{1.62}$$

$$^{12}\mathrm{CH_2D_2} + \mathrm{OH}\cdot \rightarrow {}^{12}\mathrm{CH_2D}\cdot + \mathrm{HDO} \quad {}^{12\mathrm{CH_2D_2}}k^{p} \tag{1.63}$$

The cases that hydroxyl radicals could also have deuterium-substituted isotopologues are not listed here, to simplify the situation. In included, it would involve similar 8 equations and reaction rate constants. Among these, when methane isotopologues containing deuterium react with OH, either C-H bond cleavage or C-D bond cleavage can occur. The cleavage of the C-D bond leads to a primary isotope effect, where the isotope substitution directly affects the reaction rate, with the corresponding rate constant *k* marked with *p*; the cleavage of the C-H bond results in a secondary isotope effect, where the substitution indirectly influences the reaction through changes in the reaction environment, with the corresponding rate constant *k* marked with *s*. The overall rate constant *k* for the reaction of an isotopologue with OH is the weighted sum of k^p and k^s according to the stoichiometric coefficients. Taking $^{12}CH_3D$ as an example, it is:

$$^{12}\mathrm{CH_3D}k = \frac{3}{4}\,^{12}\mathrm{CH_3D}k^{s} + \frac{1}{4}\,^{12}\mathrm{CH_3D}k^{p} \quad (1.64)$$

The KIE is the ratio of the rate constant k for the light isotopologue to that of the heavy isotopologue. Tanking $^{12}CH_2D_2$ as an example, the KIE can be expressed as:

$$^{12}\mathrm{CH_2D_2}\mathrm{KIE}_{\mathrm{CH_4+OH}} = \frac{^{12}\mathrm{CH_4}k_{\mathrm{CH_4+OH}}}{^{12}\mathrm{CH_2D_2}k_{\mathrm{CH_4+OH}}} \quad (1.65)$$

Theoretically, these *k* values can be determined experimentally. However, conducting such experiments and measuring the parameters during the process is challenging, particularly when it comes to precisely determining the absolute reaction rates. Measuring the KIE might be somewhat simpler than measuring *k*, although it is still technically difficult. Since KIE is a ratio, the relative error in its measurement is likely to be smaller compared to measuring absolute rates. These *k* and KIE values can also be obtained through first-principles calculations. Calculating KIE can cancel out many computational terms, thereby achieving a more manageable level of uncertainty.

The KIE for OH with $^{13}CH_4$, $^{12}CH_3D$, $^{13}CH_3D$, and $^{12}CH_2D_2$ calculated using the second-order Møller-Plesset (MP2) method based on the cc-pVTZ basis sets are 1.0063, 1.32, 1.33, and 1.92, respectively at 20 °C (Haghnegahdar et al., 2017). However, the theoretical calculation results rely heavily on the choice of method that approximate the behavior of electrons in molecules. Generally, higher-accuracy approximation methods require more computational power. Nevertheless, the relative relationships of the KIE values are well-established. That is,

$$^{12}\mathrm{CH_4}k > {}^{13}\mathrm{CH_4}k \gg {}^{12}\mathrm{CH_3D}k > {}^{13}\mathrm{CH_3D}k \gg {}^{12}\mathrm{CH_2D_2}k \quad (1.66)$$

the OH sink reaction with $^{12}CH_4$ is the fastest, and the OH sink reaction with $^{12}CH_2D_2$ is the slowest, being almost half that of $^{12}CH_4$.

These conclusions also hold true for Cl. The KIEs for CH_4+Cl are larger than the corresponding KIEs for CH_4+OH. Table 1.6 summarizes these KIE values.

Table 1.6. **Summary of KIEs for methane sink reactions.** KIE calculated: KIEs at 20 °C, calculated using MP2 method with cc-pVTZ basis sets, and interpolated with forth-order polynomial fittings to 20 °C (Haghnegahdar et al., 2017; Sun, Haghnegahdar, et al., 2025). KIE experiment: KIEs measured from lab experiments (Haghnegahdar et al. (2017) and references therein).

	KIE calculated	KIE experiment	γ *
$^{13}CH_4$ + OH	1.006	1.0039 to 1.0059	
$^{12}CH_3D$ + OH	1.331	1.25, 1.30	
$^{13}CH_3D$ + OH	1.335	1.34	0.997
$^{12}CH_2D_2$ + OH	1.924	1.81	1.086
$^{13}CH_4$ + Cl	1.028	1.058	
$^{12}CH_3D$ + Cl	1.419	1.46	
$^{13}CH_3D$ + Cl	1.460	1.60	1.001
$^{12}CH_2D_2$ + Cl	2.215	1.40 to 2.43	1.100

* γ for $^{13}CH_3D$ is $KIE_{13CH3D}/(KIE_{13CH4}*KIE_{12CH3D})$, γ for $^{12}CH_2D_2$ is $KIE_{12CH2D2}/(KIE_{12CH3D})^2$.

See more introduction of γ in Section 1.4.3.4.

The OH in the atmosphere preferentially reacts with the lighter methane isotopologues, resulting in an atmospheric methane pool that is enriched in heavier isotopologues compared to the source. Specifically, $^{12}CH_2D_2$ shows the greatest enrichment, followed by moderately enrichment in $^{13}CH_3D$ and $^{12}CH_3D$, and a slight enrichment in $^{13}CH_4$. As for the exact magnitude of this

enrichment and the composition of atmospheric methane, it cannot be determined simply through a closed-system Rayleigh fractionation model. The simulation results of such models depend on how the atmospheric methane pool is treated—for example, whether it is modeled as a single box or multiple boxes, whether it is considered in a steady state or non-steady state, and the fluxes and compositions of each source. Of course, the KIEs of the sink reactions also play a direct role. These details will be discussed in Section 1.5.

1.4.3.5. Non-equilibrium Signal from Reaction Network

Unlike methane atmospheric sink reactions, microbial and abiotic processes related to methane production and consumption are not elementary reactions but rather continuous transformations involving a reaction network consisting of multiple reaction steps. Taking microbial methane formation and oxidation as an example, the equations presented in Section 1.3.3.1 and Section 1.3.3.3 represent net reactions; however, in reality, these processes consist of a series of enzymatic (sometimes could be non-enzymatic) reactions. For instance, hydrogenotrophic methanogenesis involves the stepwise reduction of CO_2 to methane through seven consecutive enzymatic reactions, four of which require the addition of electron carriers (Figure 1.20). All seven steps are reversible, as AOM, the reverse process of hydrogenotrophy, follows the same reaction steps but in the opposite direction. The degree of reversibility not only determines the reaction direction (i.e., methane production versus oxidation) but also governs the net expression of isotopic fractionation.

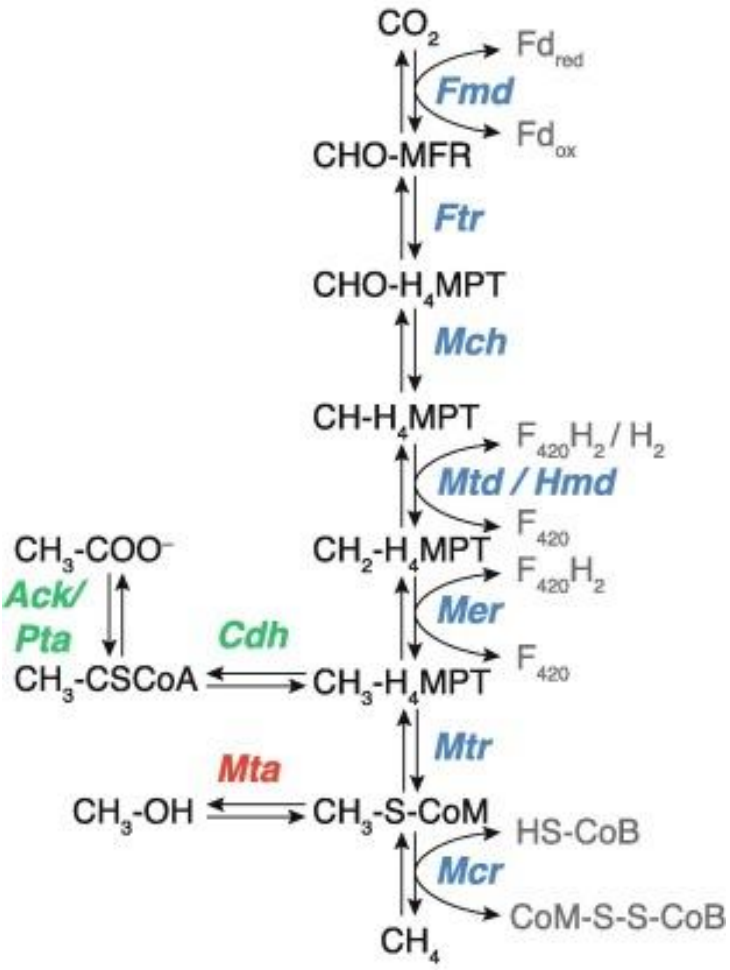

Figure 1.20. **Schematic diagram of microbial methanogenesis and methane oxidation metabolic pathways.** Metabolites are shown in bold black, electron carriers in gray. Enzymes that are applicable to hydrogenotrophic, acetoclastic, and methylotrophic pathways, as well as AOM pathways, are shown in blue. Enzymes unique to the methylotrophic pathway are highlighted in red, while those unique to the acetoclastic pathway are shown in green. For the full names of abbreviations, please refer to Gropp et al. (2021). (Figure taken from Gropp et al. (2021), with permission)

In a reaction network, some steps may not induce isotope fractionation, some steps that exhibit full reversibility follow equilibrium isotope fractionation (EIE), and some steps may be entirely unidirectional, leading to purely kinetic fractionation. More commonly, a step can proceed in both directions but may or may not be able to reach equilibrium or have not reached equilibrium,

making this step partially reversible. The reversibility (r) of a reaction $R \leftrightarrow P$, ranging from 0 to 1, is defined as the ratio of the backward and forward mass fluxes of the reaction and is related to its Gibbs free energy change (Wing & Halevy, 2014):

$$r_{P,R} = \frac{Flux_{P \to R}}{Flux_{R \to P}} = e^{\Delta G_r / RT} \quad (1.67)$$

Where R is the gas constant, T is the temperature, and ΔG_r is the Gibbs free energy change of the reaction. As a result, the extent to which KIE and EIE are expressed in a given step depends on its reversibility, leading to an intermediate fractionation value. Ultimately, the apparent isotope fractionation of the net reaction is the cumulative effect of all these individual steps. In microbial methanogenesis, methane often exhibits a non-equilibrium isotopic signature, making reversibility a key parameter in studying isotope fractionation in these systems.

The reaction pathway of Fischer-Tropsch-Type (FTT) abiotic methane formation is nearly identical to hydrogenotrophic methanogenesis, except that biological enzymes are replaced by metal catalysts. Therefore, the same isotopic fractionation considerations apply to both systems.

Several studies (Cao et al., 2019; Gropp et al., 2021; Stolper et al., 2015; Wang et al., 2015) have modeled isotopologue fractionation during the CO_2 reduction pathway (both microbial and abiotic). Cao et al. (2019) used a model with four rate-determining steps (i.e., steps in Figure 1.20 with electron carriers in gray) to estimate the possible range of $\Delta^{13}CH_3D$ and $\Delta^{12}CH_2D_2$ signals that the CO_2 reduction process may generate (Figure 1.21). Cao et al. (2019) proposed that the apparent $\Delta^{13}CH_3D$ and $\Delta^{12}CH_2D_2$ values are controlled by the reversibility scenarios of the four rate-determining steps (expressed as a four-digit binary code, e.g., 1100) and the hydrogen source. Gropp et al. (2021) further refined this model by constraining the EIE values,

which were left unconstrained in Cao et al. (2019), using first-principles calculations. This refinement resulted in a narrower predicted range than that presented by Cao et al. (2019) (Figure 1.21). It should be pointed out that while both the Cao et al. (2019) and Gropp et al. (2021) models appear theoretically and computationally sound, neither model successfully reproduces the range of observed methane clumped isotopologue compositions measured to date—whether from natural samples, pure culture incubations, or mixed laboratory incubations (Figure 1.21). The primary discrepancies between model predictions and empirical data are: 1) overestimation of $\Delta^{13}CH_3D$ values – The models predict exclusively positive values, whereas most measured values are negative; and 2) underestimation of $\Delta^{12}CH_2D_2$ values – The models predict values ranging from -50 to -120‰, whereas most measured values fall between -60 and -20‰. In the measured datasets, pure culture incubations exclusively reflect the hydrogenotrophic pathway. While natural and mixed laboratory incubation samples may have been altered by AOM, AOM itself is the reverse reaction of the hydrogenotrophic pathway. Thus, its isotopic effects should already be accounted for within the framework of reaction reversibility.

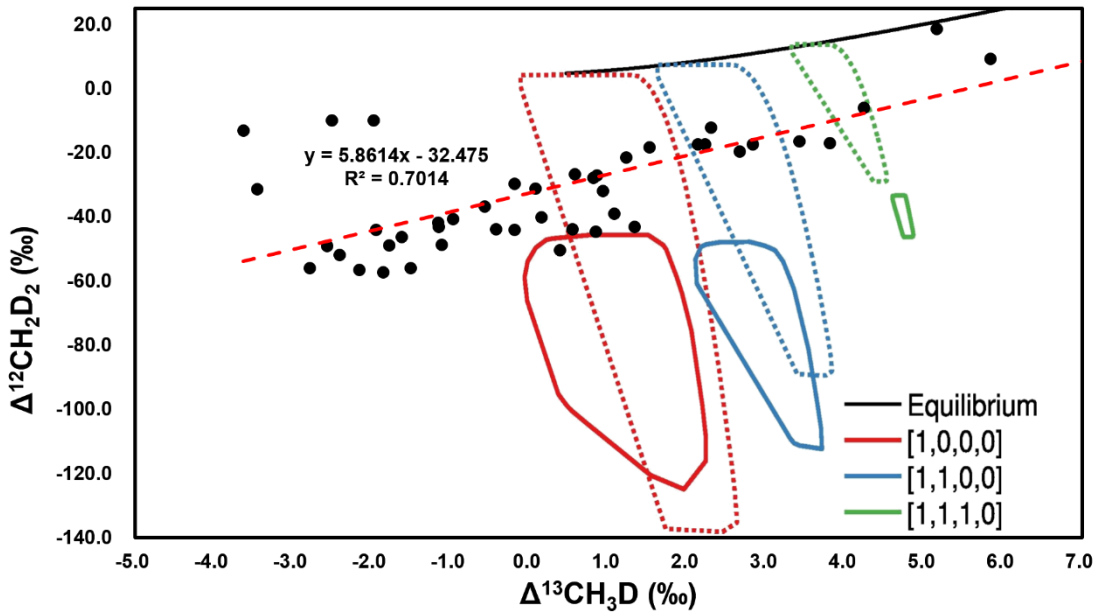

Figure 1.21. **Compiled methanogenesis methane clumped isotopologue signals, real measurement vs. theoretical calculations.** Black points are from real measurements, either from natural sample, lab pure culture, or lab incubations. Black line is the thermo-equilibrium curve. Colored boxes are possible $\Delta^{13}CH_3D$ and $\Delta^{12}CH_2D_2$ ranges of CO_2 reduction pathway, simulated by model presented by Gropp et al. (2021). (1000), (1100), and (1110) stand for different reversibility scenarios. (Figure adapted from Sun et al. (in revision) and Gropp et al. (2021), with permission)

Modeling each step in a microbial reaction network using first-principles calculations is challenging, and experimentally determining the isotope fractionation factors for individual steps is even more difficult. There are very limited works that reported experimental fractionation factors of each step. It is more common to measure the net fractionation resulting from the entire microbial reaction network and infer net fractionation factors (α values) for the overall reaction (refer to Section 1.3.3.1 and Section 1.3.3.3). This type of effort has recently been expanded to clumped isotopologues, reporting γ values aside from α values. The γ value is a parameter that quantifies the deviation of the clumped isotopologue fractionation factor from the product of corresponding bulk isotope fractionation factors. Take hydrogenotrophy as an example, it is defined as:

$$^{13CH3D}\gamma_{hydrogenotrphic} = \frac{^{13CH3D}\alpha_{hydrogenotrphic}}{^{13C}\alpha_{CO2-CH4,hydrogenotrphic} * {}^{D}\alpha_{H2O-CH4,hydrogenotrphic}} \quad (1.68)$$

$$^{12CH2D2}\gamma_{hydrogenotrphic} = \frac{^{12CH2D2}\alpha_{hydrogenotrphic}}{{}^{D}\alpha_{H2O-CH4,hydrogenotrphic} * {}^{D}\alpha_{H2O-CH4,hydrogenotrphic}} \quad (1.69)$$

If microbial methane exhibits $\Delta^{13}CH_3D = 0$ or $\Delta^{12}CH_2D_2 = 0$, this indicates that no additional isotopologue clumping or anti-clumping has occurred during fractionation process, and thus, the corresponding $^{13CH3D}\gamma$ or $^{12CH2D2}\gamma$ equals to 0.

While the bulk isotope α values have been summarized in Section 1.3.3.1 and Section 1.3.3.3, the experimentally measured γ values for clumped isotopologues are listed in Table 1.7.

Table 1.7. **A summary of γ values measured/calculated so far.**

	$^{13CH3D}\gamma$	$^{12CH2D2}\gamma$	References
Hydrogenotrophy	0.9943	0.9818	Ono et al. (2022)
Acetotrophy	0.9960	0.9990	Li, Ash, et al. (2024)
AOM	0.980 to 0.9952	0.912 0.935	Liu, Harris, et al. (2023) Ono et al. (2021)
AeOM	0.9919 to 1.0035	0.9013 0.7595 0.9745	Wang et al. (2016) Krause et al. (2022) Li, Ash, et al. (2024)
Catalyzed oxidation (high-Temperature)	0.9988	0.963	Sun, Haghnegahdar, et al. (2025)

1.4.4. Source Differentiation and Process Identification

Section 1.4.3 has introduced the possible processes that can generate equilibrium and various non-equilibrium isotope and clumped isotopologue signatures. As a result, clumped isotopologues serve as a tool for process identification, especially under strictly controlled laboratory conditions. Methane clumped isotopologues have been applied in observing mixing processes and combinatorial effects (Labidi et al., 2024; Labidi et al., 2020; Taenzer et al., 2020; Young, Kohl, Lollar, et al., 2017), investigating microbial methanogenesis (Gropp et al., 2021; Gropp et al., 2022; Gruen et al., 2018; Li, Ash, et al., 2024; Ono et al., 2022; Rhim & Ono, 2022; Wang et al., 2015) and microbial methane oxidations (Krause et al., 2022; Li, Chiu, et al., 2024; Liu, Harris, et al., 2023; Ono et al., 2021; Wang et al., 2016), understanding fossil fuel-related thermogenic processes (Dong et al., 2021; Shuai, Douglas, et al., 2018; Shuai, Etiope, et al., 2018; Thiagarajan et al., 2020), and studying atmospheric methane sink reactions (Haghnegahdar et al., 2017; Haghnegahdar et al., 2023; Joelsson et al., 2016; Whitehill et al., 2017).

Similarly, since methane formed through different processes—including thermogenic, abiotic, and microbial origins—is likely to exhibit distinct clumped isotopologue signatures, these signatures can also be used for source differentiation. Similar to the Schöll plot, which is based on bulk carbon and hydrogen isotopes, a $\Delta^{13}CH_3D$-$\Delta^{12}CH_2D_2$ plot can be used to distinguish sources. Since Δ values are independent of bulk isotope compositions, these two values offers a completely independent diagnostic framework for source differentiation. One of the applications of this approach is identifying the contributions of thermogenic methane and microbial methane in mixed gas samples, commonly seen in natural gas reservoirs and seafloor seeps (Douglas et

al., 2016; Giunta et al., 2019; Lalk et al., 2022; Lalk et al., 2023; Liu, Treude, et al., 2023; Stolper et al., 2015; Wang et al., 2018; Wang et al., 2024; Young, Kohl, Lollar, et al., 2017).

Methane from different sources tends to be distributed in different regions within the $\Delta^{13}CH_3D$-$\Delta^{12}CH_2D_2$ field. When combined with the $\delta^{13}C$-δD plot, the distribution in the $\Delta^{13}CH_3D$-$\Delta^{12}CH_2D_2$ plot appears to enhance the ability to determine methane sources, compared to relying solely on the $\delta^{13}C$-δD plot (Marcum et al.; Young, 2019).

Thermogenic methane is typically distributed along the thermo-equilibrium curve, aligning with its formation/equilibrium temperature. A laboratory experiment by Dong et al. (2021) produced thermogenic methane with negative $\Delta^{12}CH_2D_2$ through the thermal cracking of n-octadecane. This non-equilibrium methane was generated during the early stages of cracking (yield of methane <5%), possibly reflecting kinetic effects associated with thermal cracking. As decomposition progresses further, methane may eventually reach equilibrium. Under geological conditions, methane formed through thermal cracking is typically subjected to geological timescales of storage and equilibration in reservoirs after its formation. As a result, natural thermogenic methane is generally expected to exhibit a thermo-equilibrium signal. The boundary values of ($\Delta^{13}CH_3D$ ‰, $\Delta^{12}CH_2D_2$ ‰) pair for thermogenic methane are (5.1, 16.1) for 50°C and (2.1, 4.5) for 250°C, respectively.

Microbial methane can also have equilibrium characteristics, but at lower equilibrium temperatures. For instance, thermally equilibrated methane at 20°C has ($\Delta^{13}CH_3D$ ‰, $\Delta^{12}CH_2D_2$ ‰) values of (6.0, 20.1). Thermally equilibrated microbial methane is commonly found in

seafloor sediments. Laboratory experiments have demonstrated that this equilibrium signature in microbial methane can result from AOM fractionating fresh methane, a process that typically occurs in the SMTZ (Liu, Harris, et al., 2023). Additionally, equilibrium signals may arise from methanogenesis occurring at extremely low rates over geological timescales (Ono et al., 2022) or from rapid hydrogenotrophic methanogenesis under low hydrogen partial pressure and high hydrostatic pressure conditions (Mayumi et al., 2024).

However, when assessing the impact of microbial methane on the atmospheric methane budget, only the portion that is released into the atmosphere needs to be considered. In the context of the isotopic budget, the overall isotopic composition of the microbial source is represented by a flux-weighted average of various microbial sources. As a result, sources such as freshwater lakes, wetlands, rice fields, ruminants, and landfills carry greater weight, since they emit freshly produced methane that typically undergoes relatively little oxidation and therefore contributes a larger flux to the atmosphere. Laboratory cultures of methanogens at high H_2 pressure serve as a representative analog. This type of methane typically exhibits a pronounced anti-clumping characteristic (Gruen et al., 2018; Li, Ash, et al., 2024; Ono et al., 2022; Rhim & Ono, 2022; Taenzer et al., 2020; Wang et al., 2015; Young, Kohl, Lollar, et al., 2017), particularly with $\Delta^{12}CH_2D_2$ values reaching more negative than -40‰. The anti-clumping feature is associated with fast production rates and low reversibility (Gruen et al., 2018; Ono et al., 2022; Rhim & Ono, 2022) as well as the combinatorial effects of hydrogen from water and methyl precursors (Taenzer et al., 2020). When fresh microbial methane coexists with thermogenic methane, which is commonly observed in natural gas reservoirs, the differences in clumped isotopologue signals

and their mixing relationships can aid in distinguishing the contributions of these two methane sources (Stolper et al., 2015; Thiagarajan et al., 2020; Zhang, Snyder, et al., 2021).

Microbial oxidation is thought to gradually wipe out the anti-clumping signal of microbial methane (Giunta et al., 2019; Labidi et al., 2020; Li, Chiu, et al., 2024; Ono et al., 2021), and in some cases, it may even generate very positive $\Delta^{13}CH_3D$ and $\Delta^{12}CH_2D_2$ signals (Krause et al., 2022; Liu, Harris, et al., 2023). The isotope fractionation effects of AOM and AeOM may exhibit different directions on the $\Delta^{13}CH_3D$-$\Delta^{12}CH_2D_2$ field, even though they may overlap on the $\delta^{13}C$-δD field. This distinction provides a potential tool for differentiating between these two oxidation processes (Section 1.3.3.3 and Section 1.4.3.5, Figure 1.22). If a series of microbial oxidation laboratory cultures were conducted, the shifting pattern in clumped isotopologues could potentially reveal the degree of oxidation. However, identifying oxidation signals in natural samples presents challenges due to the lack of information on the presumed initial composition and the difficulty in modeling the entire system (e.g., closed vs. open system behavior, source supply dynamics, and transport effects). The key takeaway is that oxidation-induced secondary alteration must be carefully considered when interpreting clumped isotopologue signatures.

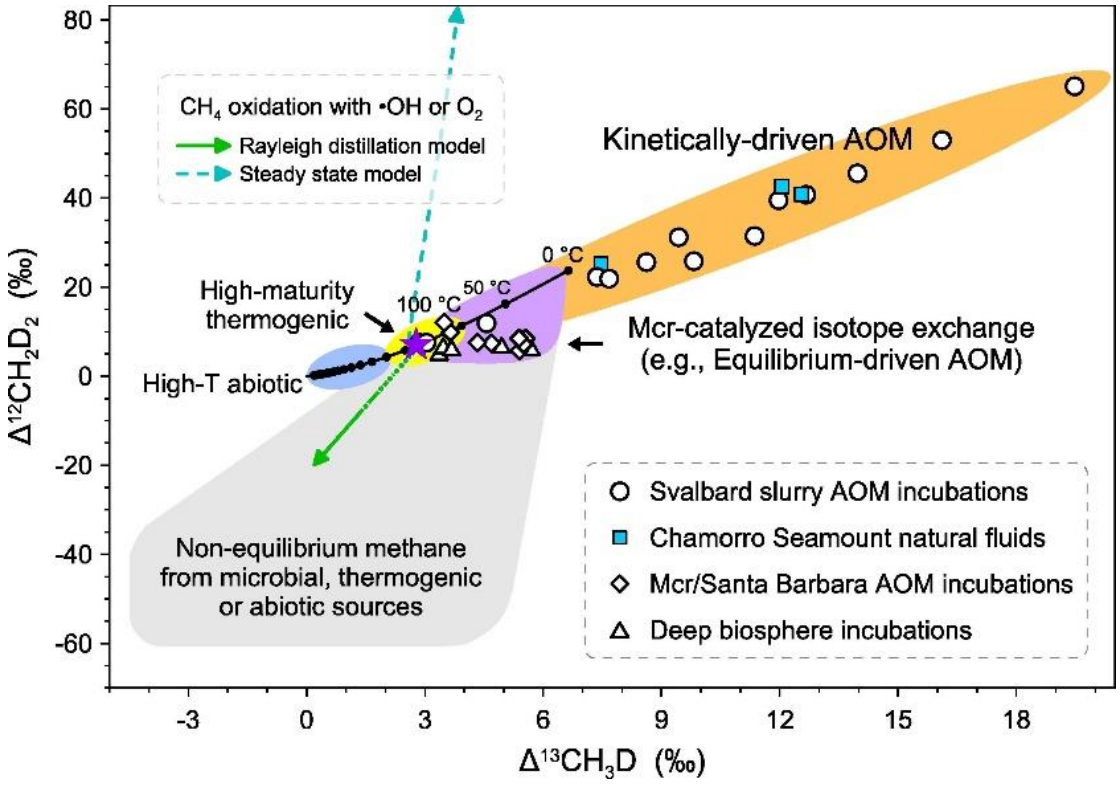

Figure 1.22. **AOM and AeOM appear to have different direction on the $\Delta^{13}CH_3D$-$\Delta^{12}CH_2D_2$ plot.** AOM is shown in orange band, and AeOM is shown in green and cyan lines. Both AOM and AeOM have the potential to generate extremely positive microbial methane clumped isotopologue signals. (Figure taken from Liu, Harris, et al. (2023), under CC BY 4.0)

As for pyrogenic methane, available data remain very limited. Labidi et al. (2024) investigated methane synthesized via laboratory FTT reactions, which exhibited a strong anti-clumping signature similar to that of hydrogenotrophic methane. This result is expected, as both processes share the same fundamental reaction network mechanisms (Section 1.4.3.5). Methane from biomass burning may exhibit a slight depletion in $\Delta^{12}CH_2D_2$ relative to the equilibrium line. In contrast, car exhaust methane (from fossil fuel combustion) displays either a thermal equilibrium signal or a slight enrichment in $\Delta^{12}CH_2D_2$ relative to the equilibrium line (Sun, Haghnegahdar, et al., 2025) (see Chapter 3).

To summarize Section 1.4.4, the representative clumped isotopologue values for different methane sources are summarized in Table 1.8 and Table 1.9.

Table 1.8. **Summary of methane source isotopologue compositions.** The values presented here will also be available in Sivan and Sun et al. (in prep.) (Chapter 6) (Sivan, Sun, et al., 2024), calculated from a compilation of published clumped isotopologue data. This table aims to provide an estimate of the global average. Due to current limitations in uncertainty quantification, the uncertainties reported here represent the 1SD of all values within the compiled database for each methane source type. At present, there is very little understanding of the temporal and spatial distribution of isotopologue compositions for different methane sources. Therefore, both the spatial and temporal columns in the table are marked as "NO" to indicate the lack of available information.

	$\Delta^{13}CH_3D$ (‰)	Uncertainty (‰)	$\Delta^{12}CH_2D_2$ (‰)	Uncertainty (‰)	Spatial?	Temporal?
Fossil-fuel	3.57	1.60	7.58	9.51	NO	NO
Wetland	1.74	4.06	-36.02	36.51	NO	NO
Agriculture	-0.16	1.34	-39.78	4.15	NO	NO
Waste	2.5	NA	-15	NA	NO	NO
Pyrogenic	1.19	0.85	9.49	18.4	NO	NO

Table 1.9. **Summary of the characteristic clumped isotopologue compositions of thermogenic, pyrogenic, and microbial methane.**

Thermogenic	($\Delta^{13}CH_3D$ ‰, $\Delta^{12}CH_2D_2$ ‰) = (2.1,4.5) to (5.1, 16.1) on thermo-equilibrium curve
Pyrogenic	$\Delta^{13}CH_3D$ ‰ from 0 to 4, $\Delta^{12}CH_2D_2$ ‰ from -55 to 1
Microbial	$\Delta^{13}CH_3D$ ‰ from -4 to 20, $\Delta^{12}CH_2D_2$ ‰ from -65 to 65 Usually around a $\Delta^{12}CH_2D_2$‰ = 5.86 *$\Delta^{13}CH_3D$‰ - 32.5 linear line

1.5. Atmosphere Methane

Atmospheric methane is a topic that warrants separated discussion. The atmosphere serves as a methane pool, and when we discuss methane sources and sinks, they are defined relative to this atmospheric reservoir. Compared to other methane reservoirs, such as natural gas deposits, gas hydrates, and soil, the atmospheric methane reservoir is relatively small, which is about one-thousandth of the sizes of other reservoirs (Whiticar, 2020). What's more, microbial oxidation in soil and water columns removes significantly more methane than atmospheric sinks do. Despite its relative small size and fluxes, atmospheric methane concentration exhibits large fluctuations, particularly over the past 200 years (Section 1.1), and methane in the atmosphere has a strong greenhouse effect, making it a critical focus of scientific research. The study of atmospheric methane primarily revolves around three key questions:

1) What are the characteristics of methane sources? This includes source types, fluxes, isotopic compositions, spatial distributions, and temporal variability.

2) What are the characteristics of methane sinks? This includes sink types, intensities, isotopic fractionation effects, spatial distributions, and temporal variability.

3) What modeling approaches are used? This includes whether models are one-box, two-box, or gridded, whether they are 2D or 3D, whether they incorporate transport and chemical reactions, and whether they use forward or inverse modeling.

Not every aspect of these questions has a well-defined answer.

For the first question regarding sources, Section 1.2.1 introduces methane sources associated with fossil fuels, agriculture and waste, biomass burning, and wetlands. Section 1.3 categorizes

methane into thermogenic, pyrogenic, and microbial sources based on their bulk isotopic compositions, summarizing the characteristic isotope values in Table 1.1 and Table 1.2. Section 1.4.4 extends this discussion to clumped isotopologues, providing a summary of characteristic values in Table 1.8 and Table 1.9. However, as discussed in these sections, significant uncertainties remain in our understanding of methane fluxes and isotopic compositions for each source. One of the most debated issues is whether fossil fuel-related methane emissions have been increasing or decreasing since 2000 (Franco et al., 2016; Hausmann et al., 2016; Helmig et al., 2016; Kai et al., 2011; Nisbet et al., 2016; Schaefer et al., 2016; Schwietzke et al., 2016). Another controversy concerns whether the current isotopic measurement data are sufficient to represent the global average isotopic composition of various sources and whether assuming a constant global average isotopic composition for each source over time is reasonable. This uncertainty can only be gradually reduced by continuously increasing the number of measurements and incorporating newly collected data into models. At present, one inference that can be made is that the isotopic values of fossil fuel-related methane have become less negative due to changes in the volume and locations of global fossil fuel extraction (e.g., (Schwietzke et al., 2016)). To be specific, rising coal production in China during 1999-2012 increased coal-related methane emissions, which is ^{13}C-enriched. Additionally, since around 2002, the rise in shale gas production in countries such as the US has also contributed, as shale gas methane tends to be relatively enriched in ^{13}C. In contrast, microbial methane may exhibit greater variability, and there is insufficient information to determine whether its average isotopic composition will change with climate variations. These uncertainties also affect estimates of other methane sources. Additionally, the spatial and temporal resolution of methane sources remains poorly constrained, limiting the accuracy and resolution of methane models.

The total source is to the sum of all types of methane sources across all locations, according to the mass balance equation:

$$\sum_i \sum_s {}_sF_i^t = F_{total}^t \quad (1.70)$$

Here, *F* represents the flux, *t* denotes time, and *i* refers to the methane source category. Sources can be classified based on emission sectors, such as wetlands, fossil fuels, agriculture, waste, biomass burning, and other sources, or based on formation mechanisms, such as thermogenic, pyrogenic, and microbial sources. The variable *s* represents the spatial distribution of source *i*, which can be defined by latitude and longitude, by country, by land type, or by hemispheric division (Northern and Southern Hemispheres), depending on the available data.

The principle of mass balance also applies to isotopes:

$$\sum_i \sum_s {}_sF_i^t * {}_s^x\delta_i^t = F_{total}^t * {}^x\delta_{total}^t \quad (1.71)$$

Here, ${}^x\delta$ is the isotopologue abundance of isotopologue *x*, where *x* for methane can be $^{12}CH_4$, $^{13}CH_4$, $^{12}CH_3D$, $^{13}CH_3D$, and $^{12}CH_2D_2$. In general, estimates for the total source isotopic composition are approximately $\delta^{13}C$ = -54.5 to -52.5‰ and δD = -286 to -270‰ (Lan et al., 2021; Whiticar, 2020), with $\Delta^{13}CH_3D$ = 1 to 3‰ and $\Delta^{12}CH_2D_2$ = -25 to -15‰ (Haghnegahdar et al., 2023; Sivan, Sun, et al., 2024), by weighted averaging of the compositions of each source given in Tables 1.1, 1.2, 1.8 and 1.9. The specific calculations involve extensive data compilation, data filtering and processing, assumptions or approximations, and interpolation/extrapolation based on limited information, which can be referenced in Schwietzke et al. (2016) and Lan et al. (2021). It is certain that these total source values are significantly lower than the current atmospheric measurements across all isotopic parameters, particularly for

δD and $\Delta^{12}CH_2D_2$. Current atmospheric values are approximately $\delta^{13}C$ = -47.5 to -47.1‰, δD = -92 to -88‰, $\Delta^{13}CH_3D \approx 1.5‰$, and $\Delta^{12}CH_2D_2 \approx 47.5‰$.

The inverse problem of the above equation, that is, estimating the F_i^t and δ_i^t of each source *i*, given known F_{total}^t and ${}^x\delta_{total}^t$, or simply called methane source apportionment, is a more challenging problem. When the uncertainties of measurements and assigned values are considered, this becomes a mathematical problem where statistical methods and unmixing algorithms are necessary. For a system like

$$\boldsymbol{Ax} = \boldsymbol{b} \quad \text{and} \quad \widehat{\boldsymbol{A}}\widehat{\boldsymbol{x}} = \widehat{\boldsymbol{b}} \tag{1.72}$$

Where $\boldsymbol{A}$ and $\widehat{\boldsymbol{A}}$ are the parameter matrices for actual values and assigned values with uncertainties of each source, $\boldsymbol{x}$ and $\widehat{\boldsymbol{x}}$ are the fraction matrices for actual fractions (of each source to the total source) and calculated fractions with uncertainties of each source, $\boldsymbol{b}$ and $\widehat{\boldsymbol{b}}$ are the parameter matrices for actual values and assigned values with uncertainties of the total source. For example,

$$\boldsymbol{A} = \begin{pmatrix} \delta^{13}\mathrm{C}_{\_\mathrm{thermogenic}} & \delta^{13}\mathrm{C}_{\_\mathrm{pyrogenic}} & \delta^{13}\mathrm{C}_{\_\mathrm{microbial}} \\ \delta\mathrm{D}_{\_\mathrm{thermogenic}} & \delta\mathrm{D}_{\_\mathrm{pyrogenic}} & \delta\mathrm{D}_{\_\mathrm{microbial}} \\ \delta^{13}\mathrm{CH_3D}_{\_\mathrm{thermogenic}} & \delta^{13}\mathrm{CH_3D}_{\_\mathrm{pyrogenic}} & \delta^{13}\mathrm{CH_3D}_{\_\mathrm{microbial}} \\ \delta^{12}\mathrm{CH_2D_2}_{\_\mathrm{thermogenic}} & \delta^{12}\mathrm{CH_2D_2}_{\_\mathrm{pyrogenic}} & \delta^{12}\mathrm{CH_2D_2}_{\_\mathrm{microbial}} \end{pmatrix} \tag{1.73}$$

$$\boldsymbol{x} = \begin{pmatrix} f_{\mathrm{thermogenic}} \\ f_{\mathrm{pyrogenic}} \\ f_{\mathrm{microbial}} \end{pmatrix} \tag{1.74}$$

$$\boldsymbol{b} = \begin{pmatrix} \delta^{13}\mathrm{C}_{\_\mathrm{total}} \\ \delta\mathrm{D}_{\_\mathrm{total}} \\ \delta^{13}\mathrm{CH_3D}_{\_\mathrm{total}} \\ \delta^{12}\mathrm{CH_2D_2}_{\_\mathrm{total}} \end{pmatrix} \tag{1.75}$$

Then,

$$\left(\widehat{\boldsymbol{A}}-\boldsymbol{A}\right)\widehat{\boldsymbol{x}}+\boldsymbol{A}(\widehat{\boldsymbol{x}}-\boldsymbol{x})=\widehat{\boldsymbol{b}}-\boldsymbol{b} \tag{1.76}$$

Assuming $\boldsymbol{A}$ is invertible, we have

$$\widehat{\boldsymbol{x}}-\boldsymbol{x}=\boldsymbol{A}^{-1}\left(\left(\widehat{\boldsymbol{b}}-\boldsymbol{b}\right)-(\widehat{\boldsymbol{A}}-\boldsymbol{A})\widehat{\boldsymbol{x}}\right) \tag{1.77}$$

Since we are interested in the relative error, we divide both sides by $\|\boldsymbol{x}\|$, where $\|\quad\|$ is the matrix norm which can be calculated by MATLAB function *norm()***.** The relative error is expressed as

$$\frac{\|\widehat{\boldsymbol{x}}-\boldsymbol{x}\|}{\|\boldsymbol{x}\|}\leq\kappa(\boldsymbol{A})\left(\frac{\|\widehat{\boldsymbol{A}}-\boldsymbol{A}\|\|\widehat{\boldsymbol{x}}\|}{\|\boldsymbol{A}\|\|\boldsymbol{x}\|}+\frac{\|\widehat{\boldsymbol{b}}-\boldsymbol{b}\|}{\|\boldsymbol{b}\|}\right) \tag{1.78}$$

Where $\kappa(\boldsymbol{A})$ is the condition number of $\boldsymbol{A}$, which can be calculated by MATLAB function *cond(A)*. Assuming $\left\|\boldsymbol{A}^{-1}\right\|\left\|\widehat{\boldsymbol{A}}-\boldsymbol{A}\right\|<\boldsymbol{1}$, we have

$$\frac{\|\widehat{\boldsymbol{x}}-\boldsymbol{x}\|}{\|\boldsymbol{x}\|}\leq\frac{\kappa(\boldsymbol{A})}{\boldsymbol{1}-\left\|\boldsymbol{A}^{-1}\right\|\left\|\widehat{\boldsymbol{A}}-\boldsymbol{A}\right\|}\left(\frac{\left\|\widehat{\boldsymbol{A}}-\boldsymbol{A}\right\|}{\|\boldsymbol{A}\|}+\frac{\|\widehat{\boldsymbol{b}}-\boldsymbol{b}\|}{\|\boldsymbol{b}\|}\right) \tag{1.79}$$

The left side of the inequality is the relative error of the fraction matrix. The right side of the inequality is the sum of the relative error of the parameter matrix for sources and the parameter matrix for air mixture, times a coefficient. Many inversion problems are based on the above unmixing mathematical theory. However, when dealing with real-world problems, it is often implicitly assumed that $\boldsymbol{A}=\widehat{\boldsymbol{A}}$, meaning that the isotopic compositions assigned to each source are considered to be accurate

For the second question regarding methane sinks, Section 1.2.2 introduces the major types of methane sinks and their intensities, while Section 1.4.3.4 discusses the kinetic isotope fractionation effects of methane sink reactions and summarizes the KIE values in Table 1.6. However, there are significant uncertainties in these estimates. One of the most prominent issues is how to determine the concentration of OH radicals to obtain a sink intensity estimate that is

independent of source emissions. Most models use a fixed methane lifetime, or scale it based on previous estimates to represent the strength of methane sink reactions (e.g., (Basu et al., 2022; Lan et al., 2021)). However, the estimation of lifetime is, to some extent, dependent on prior knowledge of source fluxes. A carefully chosen combination of sink intensity and source flux can be used to artificially force the model to fit observations. Therefore, if the sink intensity estimate is derived from the source flux, this parameter is not entirely independent. Another issue is that most KIE values are derived from first-principles calculations, with limited experimental validation. A well-crafted combination of sink intensity and KIE values can also force a model to fit observed isotopic characteristics. However, the uncertainty in KIE values is quite large, yet in models, KIE is often treated as a constant without uncertainty. Additionally, spatial and temporal information on methane sinks is extremely limited. Since KIE values are temperature-dependent, they should vary with altitude, yet a comprehensive 3D model incorporating this effect—along with altitude-dependent gradients in CH_4 and OH concentrations—is still lacking.

In the atmosphere, the rate of CH_4 sink reactions is proportional to the product of the reactant concentrations. In the absence of source replenishment, atmospheric methane concentration would decay exponentially:

$$-\frac{d[\mathrm{CH_4}]}{dt} = k_{\mathrm{CH_4+OH}} * [\mathrm{OH}\cdot] * [\mathrm{CH_4}] + k_{\mathrm{CH_4+Cl}} * [\mathrm{Cl}\cdot] * [\mathrm{CH_4}] + k_{\mathrm{CH_4+O\ ^1D}} * [\mathrm{O\ ^1D}] * [\mathrm{CH_4}] + k_{\mathrm{CH_4+other}} * [\mathrm{other}] * [\mathrm{CH_4}] \quad (1.80)$$

Where *k* is the corresponding rate constant of each sink reactions. The equation can be simplified to:

$$-\frac{d[\mathrm{CH_4}]}{dt} = k'_{total} * [\mathrm{CH_4}] \quad (1.81)$$

By rearranging the equation and integrating, we obtain:

$$[CH_4]_t = [CH_4]_0 * e^{-k'_{total}*t} \quad (1.82)$$

Defining the methane lifetime τ as the time it takes for the methane concentration to decrease to 1/e of its initial value, i.e., $[CH_4]_t = \frac{[CH_4]_0}{e}$, we derive:

$$\tau_{total} = \frac{1}{k'_{total}} \quad (1.83)$$

Lifetime τ is a key parameter in modeling atmospheric methane sinks and is generally assumed to be constant in models, with an approximate value of 9.1 years commonly adopted (e.g., (Lan et al., 2021)). This derivation can be extended to different methane isotopologues by treating each isotopologue as an independent molecule, each with its own corresponding reaction rate constants *k* and *k′* in sink reactions, leading to:

$$^i\tau = \frac{1}{^ik'} \quad (1.84)$$

where *i* represents different methane isotopologues, including $^{12}CH_4$, $^{13}CH_4$, $^{12}CH_3D$, $^{13}CH_3D$, and $^{12}CH_2D_2$. Refer to Section 1.4.3.4 for examples of isotopologue-specific reaction equations and the definition of the KIE. By introducing the KIE, we obtain:

$$^i\tau = {}^iKIE * {}^{^{12}CH_4}\tau \quad (1.85)$$

where *i* refers to methane isotopologues other than $^{12}CH_4$. Since KIE > 1, it follows that the lifetimes of all other isotopologues are longer than that of $^{12}CH_4$, as they react more slowly with atmospheric sinks. Notably, the lifetime of $^{12}CH_2D_2$ is more than twice that of $^{12}CH_4$, reaching 20.2 years.

Current estimates of sink reactions suggest that, under steady-state conditions where sources and sinks are balanced, the KIEs of sink reactions would enrich atmospheric methane $\delta^{13}C$, δD, Δ13CH_3D, and $\Delta^{12}CH_2D_2$ by approximately 5‰, 200‰, 0.4‰, and 100‰, respectively

(Haghnegahdar et al., 2017). When sources and sinks are not in steady state, the resulting isotope fractionation depends on the characteristics of the system (e.g., closed vs. open system, source supply dynamics, and transport processes). This leads directly to the third question, which concerns the choice of modeling approaches to represent these complexities.

For the third question regarding model structure, the simplest approach is to treat the atmosphere as a single-box with a total methane source and a total sink, represented by the equation:

$$\frac{d[\mathrm{CH_4}]}{dt} = F^t_{total} - {k'}^t_{total} * [\mathrm{CH_4}]_t \quad (1.86)$$

Or equivalently,

$$\frac{d[\mathrm{CH_4}]}{dt} = F^t_{total} - \frac{[\mathrm{CH_4}]_t}{\tau^t_{total}} \quad (1.87)$$

To some extent, this equation does not have an exact solution, as uncertainties exist in $[CH_4]$, F, and k. This transforms the problem into a parameter estimation problem, where relatively well-constrained parameters are used to infer those with higher uncertainty. Alternatively, it can be formulated as an inverse problem, where, given observations of $[CH_4]_t$ (Figure 1.2), we aim to infer $F(t)$ or $k(t)$. It can also be treated as a Bayesian inference (a combination of forward and inverse methods), where both prior knowledge (*prior*) and observational data (*likelihood*) are combined to estimate the posterior distributions of $F(t)$ and $k(t)$. These approaches inherently assume that $[CH_4]_t$ observations are accurate, but it introduces new choices: should we optimize $k(t)$ based on $F(t)$, or optimize $F(t)$ based on $k(t)$? The answer depends on which parameter we have greater confidence in based on prior knowledge. Typically, $k(t)$, or equivalently, $\tau(t)$, is assumed to be relatively well-constrained, and most models even treat k (or τ) as a constant.

An improved approach to obtaining a more optimal solution is to incorporate spatial information, transitioning from a single-box model to a two-box model, and eventually to a gridded atmospheric model, and from 2D to 3D:

$$\frac{d[\mathrm{CH_4}]}{dt}_{lat,lon,alt} = F^{t}_{total\,lat,lon} - k'^{\,t}_{total\,lat,lon,alt} * [\mathrm{CH_4}]_{t\,lat,lon,alt} + \text{transport} \qquad (1.88)$$

Methane in the atmosphere is not well-mixed on both spatial and temporal scales. Atmospheric methane concentrations are higher in the Northern Hemisphere and lower in the Southern Hemisphere (NOAA/GML) (Figure 1.23), reflecting higher emissions in the Northern Hemisphere. Air methane $\delta^{13}C$ and δD have similar latitudinal patterns to the $\delta^{13}C$ and δD patterns of wetlands methane emissions (Figure 1.16). Overprinting the global patterns are regional patterns such as urban plumes (Ren et al., 2018) (Figure 1.24), natural gas field plumes like Marcellus Shale (Ren et al., 2019), and permafrost (Łakomiec et al., 2021). The spatial distribution of air methane concentrations and isotope signals can be used to do source apportionment through numerical inversions (e.g., (Lowry et al., 2020; Townsend-Small et al., 2012)).

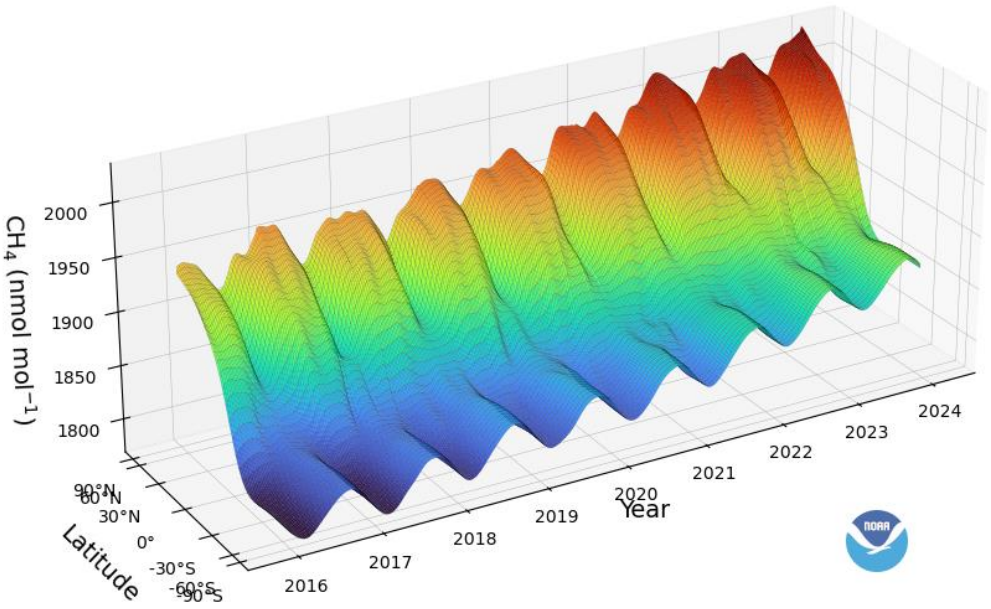

Figure 1.23. **Global distribution of surface atmosphere methane concentration**, from 2016 to 2024. (Figure taken from NOAA GML website)

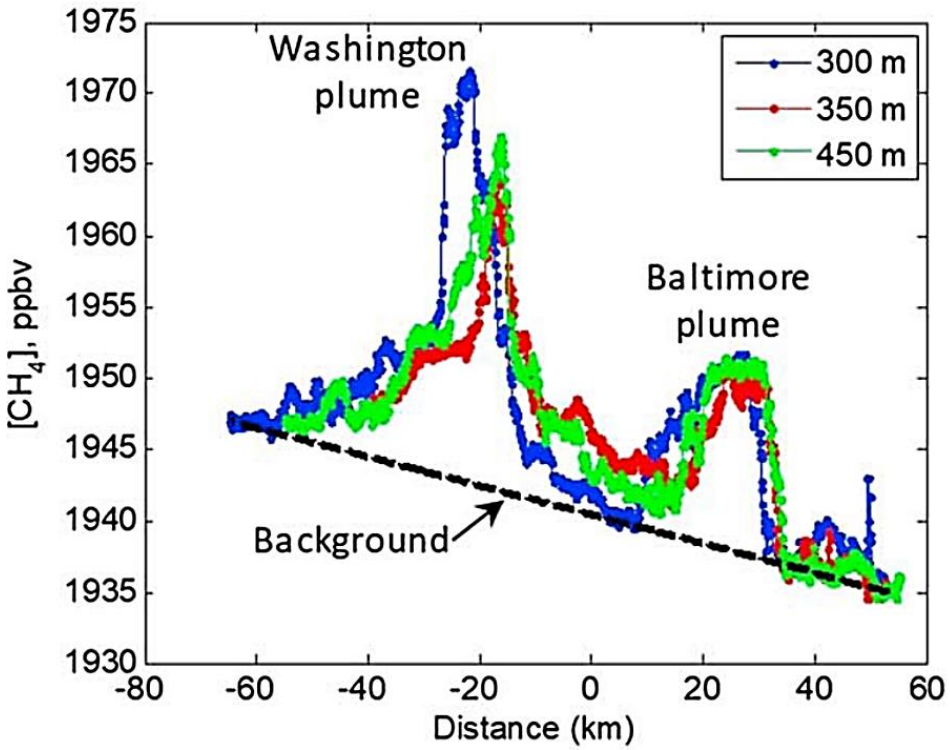

Figure 1.24. **Regional methane concentration distribution**, measured along three downwind flight transects at various altitudes on February 13, 2015 in DC-Baltimore metropolitan area. (Figure adapted from Ren et al. (2018), with permission)

By utilizing high-precision and high-resolution $[CH_4]_{t,loc}$ and $F_i(t,loc)$ data with geographic distribution information in a gridded atmospheric framework, it becomes possible to constrain the global-scale, lower-resolution estimates of $F_{total}(t)$ (Brown, 1993; Hein et al., 1997; Houweling et al., 1999; Tans et al., 1989). With the increasing availability of satellite observations (Jacob et al., 2022) and advancements in atmospheric transport modeling (Krol et al., 2005; Maasakkers et al., 2019; Meirink et al., 2008), the additional value provided by spatial distribution exceeds additional uncertainties brought by the transport term. This approach has led to significant progress in optimizing $F(t)$ and $k(t)$, as demonstrated in recent studies (e.g., (Qu et al., 2021; Saunois et al., 2020)).

Another approach is to incorporate isotopes (as well as other tracers) into the equation in an attempt to achieve a more optimized solution:

$$\frac{d[\ {}^{i}\mathrm{CH_4}]}{dt} = {}^{i}F^{t}_{total} - {}^{i}k'^{\,t}_{total} * \left[\ {}^{i}\mathrm{CH_4}\right]_t \tag{1.89}$$

where i represents various isotopologues. For each isotopologue i, a similar equation can be written. However, this introduces a new challenge:

$${}^{i}F^{t}_{total} = F^{t}_{total} * \left(\ {}^{i}\delta^{t}_{total} + 1\right) * \ {}^{i}Const. \tag{1.90}$$

which necessitates a decision on whether to optimize $\delta(t)$ based on $F(t)$, or $F(t)$ based on $\delta(t)$. Since source δ values are generally considered more reliable, isotope information is typically used to refine the estimation of $F(t)$. What's more, incorporating isotopes does not inherently make the numerical solution of the equation more accurate—unless the confidence in isotope data is higher than that of flux estimates. Several studies illustrate how isotopes have been used to constrain methane fluxes: Schwietzke et al. (2016) integrated updated $\delta^{13}C$ database into a

one-box model, concluding that fossil-fuel-related emissions remained flat over time. However, isotope balance led to a substantial upward revision of fossil-fuel-related CH_4 flux estimates. Lan et al. (2021) employed a 3D forward model with geographically resolved flux and $\delta^{13}C$ data, suggesting that recent atmospheric CH_4 growth was driven by increased microbial emissions, with little change in OH concentration. Basu et al. (2022) incorporated $\delta^{13}C$ into an inversion model, arguing that [CH_4]-only inversions were unlikely to reproduce observed $\delta^{13}C$ trends. Rice et al. (2016) added δD into the model. Riddell-Young et al. (2023) expanded on Lan et al. (2021) by integrating δD data with geographic resolution, reportedly improving source flux apportionment. Haghnegahdar et al. (2017); Haghnegahdar et al. (2023) returned to a one-box model to incorporate the latest clumped isotopologue measurements of contemporary air, significantly revising the estimated clumped isotopologue signals of the total source. Sivan and Sun et al. (in prep.) are extending the clumped isotopologue-involved model to a two-box framework (Sivan, Sun, et al., 2024), and integrating atmospheric methane clumped isotopologue profile from 1980 to 2020 to further validate the mass balance of clumped isotopologues. Aydin et al. (2011); Hausmann et al. (2016); Helmig et al. (2016); Simpson et al. (2012); Turner et al. (2019) leveraged the ethane-to-methane ratio to improve constraints on F_{fossil}. Worden et al. (2017) used CO measurements to give better estimations on biomass burning emissions. Rigby et al. (2017); Rigby et al. (2013) re-evaluated the influence of OH to methane sinks, using CH_3CCl_3 and major CFCs observations. Figure 1.25 from Turner et al. (2019) provide a nice summary of most of the available tracers. However, Turner et al. (2019); Turner et al. (2017) and Chung and Arnold (2021) concluded that the current observations are still insufficient for unambiguous source attribution. With the incorporation of δD and clumped isotopologue data, it is promising to achieve results with higher confidence.

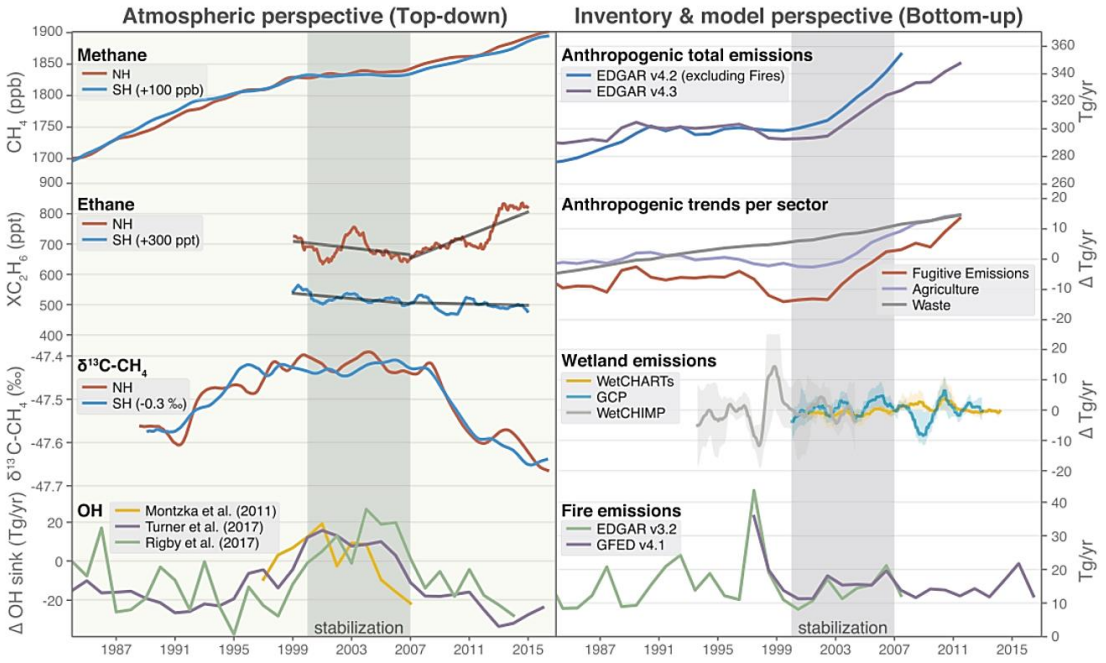

Figure 1.25. **Constraints on atmospheric methane over the past 40 years.** The left column from top to bottom is for atmospheric methane concentration, ethane concentration, methane carbon isotope, and derived OH concentration. The right column from top to bottom is for anthropogenic total emission fluxes, anthropogenic fluxes trends per sector, wetland emission fluxes, and fire emission fluxes in Tg CH_4 yr^{-1}. (Figure taken from Turner et al. (2019) without modification, under CC BY-NC-ND 4.0)

Figure 1.26 is a schematic representation of the atmospheric methane budget model structure.

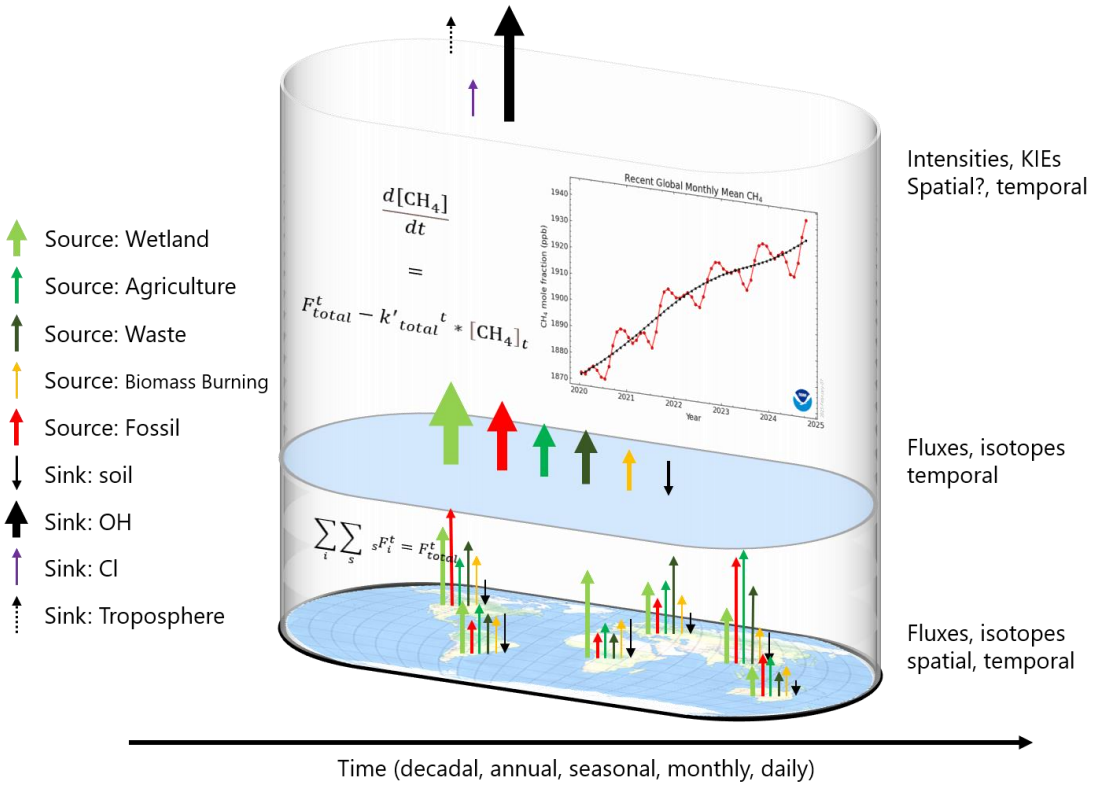

Figure 1.26. **Schematic diagram of the atmospheric methane source-sink model structure.**

1.6. Introduction to Chapter 2-7

Chapter 2 provides a detailed description of the novel measurement technique for methane clumped isotopologues. It covers the entire process, including sample collection, concentration measurement, methane extraction and purification from large-volume, low-methane-concentration air samples, as well as the final mass spectrometric analysis and isotope data calibration.

Chapters 3 to 6 present specific studies I have conducted, all of which have been or will be published as research articles in academic journals. The overarching goal of these studies is to

enhance our understanding of the global/regional methane budget. Each of these studies employs the methane clumped isotopologue measurement and can be placed within the framework of the atmospheric methane sink-source model introduced in Section 1.5.

Chapter 3 introduces a study on measuring the clumped isotopologue composition of methane in vehicle exhaust. The motivation for this project was twofold: First, in recent years, studies on methane clumped isotopologues have not clearly characterized the isotopic composition of the pyrogenic methane end-member. Most previous research has focused on fossil fuel-related methane as well as microbial methane from wetlands and laboratory cultures. Methane in vehicle exhaust is a product of incomplete combustion/oxidation of fossil fuels, originating from an extreme high-temperature abiotic process. To some extent, it represents the pyrogenic end-member, but with its own unique characteristics—it shares a formation process similar to thermogenic methane, an isotopic fractionation process akin to biomass burning, and an abiotic oxidation process that is the reverse of abiotic methane formation. By analyzing methane from vehicle exhaust, we aimed to improve the understanding of the isotopic composition of the pyrogenic end-member. Second, methane emissions from vehicle exhaust are generally considered a low-flux source and are often overlooked in global methane budget assessments. However, they may exhibit extreme isotopic signatures, potentially influencing isotope-involved mass balance calculations in methane budget studies. Therefore, direct measurements of vehicle methane emissions are necessary. Furthermore, in urban road methane leakage surveys, we frequently observe small methane peaks that cannot be readily attributed to known sources. We aimed to investigate whether clumped isotopologue analysis could help identify vehicle exhaust contributions in ambient air where such emissions may accumulate, and help distinguish vehicle

exhaust methane from other sources, such as thermogenic and microbial methane, which in urban areas are most likely associated with residential natural gas leaks and sewer line emissions.

However, the project did not progress as initially envisioned. Although methane concentrations in some vehicle exhaust samples were higher than expected, reaching >3000 ppb, the average methane emissions from the on-road vehicle fleet appeared to mix rapidly with ambient air, resulting in little to no detectable isotopic variation in the environment methane. Consequently, the study's original second motivation could not be realized. Instead, this study evolved into an effort to define the isotopic characteristics of vehicle exhaust methane and further incorporated an investigation into the mechanisms of isotopic fractionation during the methane emissions process from vehicles.

We deconstructed the methane generation and emission process in vehicles into four key steps: 1) Cracking of fossil fuels at high temperatures, producing methane; 2) Incomplete combustion of methane when exposed to oxygen at high temperatures; 3) Catalytic oxidation of methane when exhaust gases pass through the catalytic converter, further reducing methane emissions; and 4) Rapid mixing of the remaining released methane with ambient atmospheric methane. Based on these four steps, we developed an isotopic system model and discussed the KIE associated with high-temperature oxygen combustion of methane and catalytic oxidation of methane, involving first-principles calculations. The isotopic fractionation factors derived from these processes could have broader implications for understanding abiotic methane formation, atmospheric methane sink reactions, and microbial aerobic methane oxidation.

Chapter 4 presents the first study to analyze clumped isotopologues of methane in low-concentration atmospheric samples. This project was led by Mojhgan Haghnegahdar, a postdoctoral researcher in my lab, while I contributed significantly as the second author. Prior to this study, all research on methane clumped isotopologues focused on high-concentration (nearly pure) samples, such as natural gas, methane produced by microbial cultures in the lab, or bubbles emerging from wetlands/waters. This was due to the technical requirement that all instruments capable of measuring clumped isotopologues demand large volumes of nearly pure methane—whereas the methane concentration in air is only 2 ppm. Although modeling studies had predicted the clumped isotopologue composition of atmospheric methane, no direct measurements had been made.

To enable such measurements, we developed a gas pre-processing system capable of completely extracting and purifying only ~1.6 mL (approximately 70 µmol) of pure methane from 800 L of air. This process required ensuring no isotopic fractionation occurred, meaning that methane yield should to be sufficiently high (e.g., >99%), and the extraction workflow had to be standardized for reproducibility. The most time-consuming and tedious part of the study involved extensive testing and quality control to achieve this. Each extraction and purification process took approximately 8 hours, and even minor mistakes—such as failing to fully close a valve at the correct time—had a high chance of leading to extraction failure. Additionally, isotopologue measurement took even longer, approximately 40 hours for one sample.

Our final results reported that the atmospheric methane clumped isotopologue compositions were $\Delta^{13}CH_3D$ around 1.8‰ and $\Delta^{12}CH_2D_2$ around 48‰. The $\Delta^{12}CH_2D_2$ values were significantly

lower than previous model predictions, which generally suggested $\Delta^{12}CH_2D_2$ values above 80‰. Given this discrepancy, we revised the atmospheric methane budget model using the newly obtained measurements, leading to a substantial downward correction of the $\Delta^{12}CH_2D_2$ signature of the global total methane source. This finding indicates that either our understanding of the clumped isotopologue compositions of different methane sources is incomplete, i.e., one or more sources may have a lower $\Delta^{12}CH_2D_2$ than previously thought—or that we have underestimated the proportion of microbial methane in the total global methane flux.

Chapter 5 presents an attempt to use contemporary atmospheric clumped isotopologue measurements to infer methane sources and track source variations. This effort was inspired by similar studies that continuously monitor methane concentration and bulk carbon/hydrogen isotopes on mobile or stationary platforms, using the Keeling plot method to determine the isotopic composition of methane sources mixing into the background air. Such approaches are widely employed to identify sources of methane and other pollutants within a given region or plume. The key question was whether this method could be extended to methane clumped isotopologues. Several significant challenges arise when applying this approach to clumped isotopologues. Unlike bulk carbon isotope analysis—where in situ automated measurements at ambient concentrations are already feasible, achieving 10 Hz-level frequency—measuring methane clumped isotopologues is highly labor-intensive and time-consuming, with each measurement requires sampling 800 L of air, transporting the sample to the lab, 8 hours of pre-processing, and 40 hours of instrumental analysis.

Moreover, limited measurement precision presents a major hurdle. The uncertainty for $\Delta^{13}CH_3D$ is 0.5–0.8‰, yet even with 20% source mixing, the expected signal shift in 2.4 ppm CH_4 air is

only about 1‰. For $\Delta^{12}CH_2D_2$, the typical measurement uncertainty is ~1.5‰, but even with 20% source mixing, the expected variation is only 1 to 6‰. This implies that for air with methane concentrations below ~2.2 to 2.3 ppm, obtaining meaningful source information from clumped isotopologue data is nearly impossible.

Despite these challenges, we successfully conducted year-round intermittent measurements over a wetland site at Jug Bay and performed two samplings in a landfill plume. By applying the Keeling plot method, we successfully inferred the clumped isotopologue composition of methane emitted from the wetland and landfill sources. Notably, this study provides the first reported clumped isotopologue values for landfill methane, supplementing our understanding of methane source compositions. Furthermore, we observed seasonal patterns in wetland methane isotopic composition, which may reflect variations in methanotroph activity. These findings suggest that clumped isotopologue analysis of air could still provide information about regional-integrated methane emissions.

Chapter 6 presents a study on the measurement of methane clumped isotopologues in Arctic firn-trapped air. This project was inspired by the work in Chapter 4, as the modeling in that study incorporated historical methane emissions data from various databases to predict the changes in $\Delta^{12}CH_2D_2$ in atmospheric methane from 1985 to 2020. These databases differ in their estimations of historical methane source fluxes. For example, one dataset suggests that natural gas methane emissions began to decline from approximately 100 Tg/yr in 1985, while another dataset estimates that natural gas methane emissions have been increasing since 1985, but from a lower starting point of around 45 Tg/yr. These different historical estimates are referred to as emission

scenarios. We found that the predicted evolution of atmospheric $\Delta^{12}CH_2D_2$ varied significantly depending on the emission scenario used. If we back-calculate from the 2021 $\Delta^{12}CH_2D_2$ reported in Chapter 4, the reconstructed atmospheric $\Delta^{12}CH_2D_2$ values around 1985 show distinguishable differences under different emission scenarios—the maximum and minimum values differ by approximately 7‰, which is larger than the ±1.5‰ typical measurement uncertainty of $\Delta^{12}CH_2D_2$. In contrast, the bulk carbon and hydrogen isotope signatures do not show distinguishable differences among these emission scenarios. This means that if we can measure the historical atmospheric methane clumped isotopologue composition, we may be able to determine which historical emission scenario is more accurate.

Initially, we planned to conduct measurements on archived compressed air samples stored in cylinders, but we were informed that the remaining sample volumes were insufficient to support clumped isotopologue analysis. As an alternative, we collaborated with a research group from the Utrecht University to obtain firn-trapped air from the Arctic. This was a compromise approach, as firn-trapped air only represents a time-averaged composition over a certain period and requires additional firn diffusion modeling to determine the timeframe it reflects. Nevertheless, the availability of these samples provided us with a valuable opportunity.

We performed methane clumped isotopologue analysis on these precious samples, establishing the first atmospheric methane clumped isotopologue profile spanning from 1993 to 2021. This profile revealed that the 1993 atmospheric $\Delta^{12}CH_2D_2$ (approximately 40‰) was significantly lower than 2021 values (approximately 48‰), and gradually increased over time. We further used an atmospheric model to interpret the data. The updated model indicated that, given the

current measurement precision and data coverage, we still cannot determine with high confidence which historical emission scenario is more accurate. Instead, we found that the methane sink-source imbalance since 1990—where methane sources have increased quickly, outpacing the growth of sinks and preventing equilibrium—has primarily driven the observed trend. This conclusion holds regardless of which specific source contributed to the total increase in methane emissions. However, the observed trend in atmospheric $\Delta^{12}CH_2D_2$ places strict constraints on the relationship between total source composition $\Delta^{12}CH_2D_{2\ \text{total source}}$ and sink reaction $KIE_{12CH2D2}$. To refine these constraints, we compiled existing clumped isotopologue measurement data, providing a higher-confidence estimate of the total source composition $\Delta^{12}CH_2D_{2\ \text{total source}}$. Based on this, we derived a narrow range for the sink $KIE_{12CH2D2}$ to be between 1.78 and 1.82. Notably, this range does not align with current experimental measurements (~1.73) or theoretical calculations (~1.89), but instead falls between the two. Additionally, we used future methane emission scenarios to predict the future atmospheric clumped isotopologue signature. Our results suggest that different emission scenarios are likely to produce distinguishable isotopic trends, providing a potential tool for tracking future changes in methane sources and sinks if the analysis frequency can be higher and the uncertainty can be lower than current level.

Chapter 7 will summarize my work and, in addition, I would like to venture to propose some preliminary perspectives on the future directions of methane clumped isotopologue research. By doing so, I hope to stimulate further discussions and inspire future investigations in this field.

Chapter 2: Materials and Methods

The measurement of methane clumped isotopologues is technically challenging. This difficulty arises from the extremely low abundance of multiply substituted methane isotopologues in samples. The abundance of $^{13}CH_3D$ is approximately 6.7×10^{-6}, while that of $^{12}CH_2D_2$ is around 1.3×10^{-7} in a parcel of methane among all the methane molecules. In comparison, the abundances of $^{13}CH_4$ and $^{12}CH_3D$ are approximately 1.11×10^{-2} and 5.9×10^{-3}, respectively.

Ma et al. (2008) calculated the vibrational frequencies and corresponding infrared intensities of $^{13}CH_3D$, followed by the first infrared spectral measurement of $^{13}CH_3D$ (in artificial ^{13}C-D enriched methane) using Fourier Transform Infrared Spectroscopy (FTIR) at the California Institute of Technology (Caltech). Later, Tsuji et al. (2012) employed a widely tunable difference-frequency-generation spectrometer at the Tokyo Institute of Technology (TITECH) to measure $^{13}CH_3D$ in natural samples, achieving a reported uncertainty of approximately 20‰. Ono et al. (2014) further advanced the precision of $^{13}CH_3D$ measurements at the Massachusetts Institute of Technology (MIT) using tunable infrared laser direct absorption spectroscopy (TILDAS), reporting a precision of 0.2‰ (2σ) for 0.42 mmol of pure methane. The measurement of $^{12}CH_2D_2$ using spectroscopic techniques encountered some challenges and was successfully demonstrated by Gonzalez et al. (2019) at MIT. More recently, Zhang et al. (2025) at the Swiss Federal Laboratories for Materials Science and Technology (EMPA) improved spectroscopic methods, significantly reducing both sample and measurement time requirements. The challenges associated with spectroscopic measurements of methane clumped isotopologues stem

not only from their low abundance but also from the inherent difficulty in accurately calculating their spectral characteristics using theoretical models. Searching for the characteristic frequencies of doubly-substituted methane isotopologues is nearly impossible without theoretical predictions. Moreover, the primary spectral peaks of $^{13}CH_3D$ and $^{12}CH_2D_2$ overlap significantly with those of other methane isotopologues, while their characteristic absorption lines are weak and highly susceptible to interference from other molecules.

In contrast, mass spectrometers were introduced relatively late for measuring methane clumped isotopologues. The first tentative measurements were achieved by (2014) at Caltech using a prototype Thermo Scientific IRMS-253 Ultra (or "Ultra"). The word "tentative" is used here because the prototype Ultra instrument's mass resolving power (MRP) typically ranges between 20,000 and 25,000—sufficient to distinguish methane from interfering ions such as H_2O^+, OH^+, and NH_3^+ but insufficient to completely separate $^{13}CH_3D^+$, $^{13}CH_5^+$, $^{12}CH_2D_2^+$, and $^{12}CH_4D^+$. Consequently, early studies from Caltech and University of California, Berkeley (UCB), such as Stolper, Lawson, et al. (2014), reported the Δ^{18} value, which represents a combined signal of $^{13}CH_3D$ and $^{12}CH_2D_2$ without differentiation. Eldridge et al. (2019) later introduced post-processing methods to mathematically derive $\Delta^{13}CH_3D$ and $\Delta^{12}CH_2D_2$ on commercial Ultra, which could reach ~45,000 MRP but somehow $^{12}CH_2D_2$ is affected by the tail of $^{13}CH_5$. As a result, additional post-processing (peak stripping) is required to determine the $\Delta^{12}CH_2D_2$ value. Zhang, Snyder, et al. (2021) and Sivan, Röckmann, et al. (2024) measured $\Delta^{13}CH_3D$ and $\Delta^{12}CH_2D_2$ using the commercial Ultra located at the TITECH and Utrecht University, respectively, adopting this post-processing methods. The challenge posed by the prototype Ultra's insufficient MRP was theoretically predictable, as the mass-to-charge ratios (m/z) of

$^{13}CH_3D^+$, $^{13}CH_5^+$, $^{12}CH_2D_2^+$, and $^{12}CH_4D^+$ are extremely close—18.040927, 18.042475, 18.043854, and 18.045402, respectively. Additionally, the abundance of $^{13}CH_5^+$ is comparable to or significantly higher than that of $^{12}CH_2D_2^+$, whereas $^{13}CH_3D^+$ is far more abundant than both $^{13}CH_5^+$ and $^{12}CH_2D_2^+$. Depending on their relative abundances, an MRP of approximately 36,000–40,000 (maybe higher) is required to fully resolve these species and achieve interference-free measurements. Part of the issue with the commercial Ultra may stem from the inability to adjust the collector slit.

Young et al. (2016) at University of California, Los Angeles (UCLA) was the first to fully resolve $^{13}CH_3D$ and $^{12}CH_2D_2$ using the Nu Instruments Panorama mass spectrometer (or "Panorama"), which operates with an MRP exceeding 40,000. The third Panorama instrument (second in the U.S.) is housed at the University of Maryland, College Park (UMD), where we have followed the analytical approach established by Young et al. (2016) and began analyzing samples in 2021. Our primary advancement in this technique has been the development of preprocessing methods for low-methane-concentration samples, enabling the measurement of methane clumped isotopologues in atmospheric air (~2 ppm CH_4) and other low-concentration methane samples. The third Panorama used for methane clumped isotopologue measurements, as I know, is reported by Liu et al. (2024) at the Guangzhou Institute of Geochemistry (GIG), Chinese Academy of Sciences.

The measurement of methane clumped isotopologues is a comprehensive undertaking that requires far more than a well-calibrated, state-of-the-art mass spectrometer (or spectrometer). This chapter aims to provide a comprehensive description of the measurement process for

methane clumped isotopologues, with a particular focus on the additional procedures required for field sampling and the processing of air samples. These procedures include sample collection, concentration measurement, methane extraction and purification from large-volume, low-methane-concentration air samples, mass spectrometric analysis with calibration, and data quality control.

2.1. Sample Collection

Large sample volumes are required for $\Delta^{13}CH_3D$ and $\Delta^{12}CH_2D_2$ measurements. We generally collect samples to have ~ 70 μmol (i.e., 1.57 mL at STP) methane (after purification) if possible, which is the routinely required sample amount for the mass spectrometer to achieve the "desired" precision. We can technically measure as little as ~20 μmol of methane, but with the compromise of precision. For samples with a known approximate concentration range, we choose appropriate sampling methods and volume. For example, background air typically contains approximately 2 ppm of methane. To ensure sufficient sample volume for analysis, we collect air samples using 4 * 200 L Tedlar bags. For samples with unknown methane concentrations, such as vehicle exhaust, we first collect 5–20 mL samples using syringes to measure the methane concentration. Based on the measured concentration, we then determine the appropriate sampling volume for isotopologue analysis. Some samples, such as bubbles from wetland water surfaces, and natural gas, can generally be assumed to consist almost entirely of methane or contain more than 85% methane. In these cases, there is usually no difficulty in obtaining a sufficient sample volume for analysis.

2.1.1. Syringe Sampling

Syringe sampling is often used for collecting a batch of samples in a certain area for concentration mapping, or to predetermine concentrations before collecting a large volume sample for isotope measurement. A 5 ml or 20 ml BD® plastic syringe equipped with a Swagelok® three-way valve is used for sampling. We flush the syringe three times with the sample gas at the sampling location, then slowly pull the gas into the syringe until the piston reaches the maximum scale, and close the valve. An extension tube can be installed in front of the valve if the sampling location is not reachable by the syringe. The collected samples should usually be sent to the GC for concentration measurement within a day because the syringes and valves are not designed to store gas for a long time without leaking.

An example of syringe sampling is mapping the methane emissions of the UMD campus sewer manholes. Since we did not know the emission status of each sewer manhole, we collected samples from each available sewer manhole on campus and measured their methane concentrations. It turned out that a large proportion of the manholes does not have detectable methane accumulation, but a small proportion has more than 100 times the atmospheric concentration of methane. Another example is the sampling of vehicle exhaust. Since the methane concentration in the vehicle exhaust could vary largely (from below 1 ppm, to more than 3000 ppm), sampling small amount of the exhaust gases of various cars and obtaining their concentrations, before determining the sampling volumes for isotopologue analyses is necessary.

2.1.2. Tedlar Bag Sampling

Tedlar bag sampling is the most common sampling method, which is suitable for the vast majority of samples and is most commonly used for air sampling. We use CEL Scientific Corporation gas sampling bags made of DuPont's 2-mil Tedlar® PVF film, with polypropylene fitting. The required sample volumes are determined based on the sample concentration. For samples with [CH_4] > 50 ppm, we usually use 10-50 L Tedlar bags. For air samples and samples with similar concentration as air, we use 200 L Tedlar bags. Since the air methane concentration is generally around 2 ppm, we need 4 * 200 L bags to get about 71 μmol methane for clumped isotopologue analysis. The sample gas is pulled through a portable air mattress pump powered under 12 V direct current and pumped into the Tedlar bag (Figure 2.1 and Figure 2.2). It usually takes about 12-15 mins to fill a 200 L bag with the pump. Additional tube connections and extensions are sometimes necessary, but will slow down the flow rate.

Figure 2.1. **Using two mattress pumps to each fill one 200 L Tedlar bags.** Photo taken by Jiayang Sun on November 4, 2022, at 6:42 AM at Jug Bay Car Boat Launch (38.811565, -76.710501).

Figure 2.2. **Using one mattress pump to fill 2 * 200L Tedlar bags simultaneously.** Photo taken by Jiayang Sun on September 3, 2022, at 6:53 AM at Jug Bay Car Boat Launch (38.811565, -76.710501).

Sample extraction (Section 2.3) should be performed as soon as possible after sampling to extract methane from the collected gas. Tedlar bag is not ideal for long-term storage of gas samples. Our experience showed that a bulging Tedlar bag full of sample gas was no longer distended after being stored for 7 days. In addition, storing "dirty" gases (like car exhaust and sewer gas) for extended periods makes it more difficult to clean the bags. I typically do extraction right after or one day after the collection.

The sample bags should be cleaned immediately after the sample has been extracted. For air samples, no extra step is needed as long as the bag is fully evacuated during extraction. For high-concentration samples, a postdoc (Julianne Fernandez) in our lab had the experience that high methane concentration sample could leave some residue methane sticking on the inner surface of the bag and contaminate the next sample. I usually clean these bags by repeating the following procedures three times: pumping lab air into the bag, mixing the air well with any residue gas, and then evacuating the bag.

There is no evidence suggesting that leaving a sample in a sample bag for one day results in a detectable change in isotopic composition, nor is there evidence indicating that a bag flushed three times still causes a discernible level of sample contamination. However, similarly, there is no experimental data or literature explicitly proving that storing a sample in a bag for one day does not alter its isotopic composition, nor that a bag flushed three times is entirely free of residual samples. What is certain is that as storage time increases, the concentrations of various gases in the sample and their isotopic compositions become increasingly likely to undergo detectable changes—this assumption is based on permeation testing of polymer O-rings in sampling flasks by Sturm et al. (2004). Therefore, these tests are necessary but have long been overlooked.

2.1.3. Chamber Sampling

Chamber sampling can collect gas emitted from the soil surface. An aluminum chamber with the bottom side open can cover a certain area of wetland soil. The chamber is covered with a cap and

sealed by filling water in the gap (Figure 2.3). Gases released from the soil will accumulate in the chamber. A small hole drilled in the middle of the cap enables syringe sampling. Since the chamber has a known volume, it is one of the methods to get an estimation of the methane flux by checking the change of concentration over time.

Figure 2.3. **Photo of a chamber sampling from wetland.** Photo taken by Jiayang Sun on November 05, 2021 at noon, at University of Maryland Golf Course (38.996084, -76.955649).

2.1.4. Bubble Sampling

Bubble sampling can be achieved by floating a foam plastic embedded with an upside-down plastic bowl on the water surface. A small hole is drilled at the top of the bowl and a syringe was welded atop this and sealed with a valve, which enables syringe sampling. Bubbles are almost entirely methane but can include carbon dioxide. So, they usually require a much smaller sample volume (a few ml) for later isotope measurements.

2.1.5. Compressor Sampling

The large sample volume requirement poses significant challenges for sample collection and transportation. To address this, we are developing a method to collect air by compressing it into a tank using a compressor. The sampling system itself is relatively simple, with the only caveat being the necessity to use an oil-free compressor rather than any other type of compressor. However, thorough testing is necessary to ensure that the compression and subsequent decompression of air do not result in methane loss, contamination, or isotopic fractionation. For methane clumped isotopologue measurements, given the lengthy sample processing and measurement times, conducting such tests incurs a substantial time cost.

In fact, even tests that only examine methane concentration and bulk isotope composition are rarely reported in the literature. The only relevant study found is by Mak and Brenninkmeijer (1994), which tested gas sample collection using compressed gas cylinders for atmospheric carbon monoxide isotope analysis. They observed that an unclean pump and seal ring could introduce significant contamination. Additionally, mixing with ambient air (rather than the designated sampling source) could reach 1–10% unless a specialized piston was used. They also noted that when air was stored in a steel cylinder, CO concentrations tended to increase over time. Bender et al. (1994) discussed whether an aliquot of gas extracted from a larger sample could accurately represent the bulk sample composition—an issue that could be particularly significant for an aliquot of gas released from a high-pressure cylinder through a pressure regulator.

Although these issues have not been fully resolved, collecting air samples using compressed gas cylinders appears to be a common practice in the field (e.g., (Quay et al., 1999)) and is generally believed not to affect methane. This assumption is likely reasonable because methane is a non-polar molecule, non-sticky, photochemically inactive, present in the atmosphere at ppm levels rather than ppb or ppt levels, and thermodynamically stable under pressure, making it unlikely to undergo phase changes.

Between March and April 2022, our laboratory conducted some preliminary tests, although they were not systematically designed. The first set of tests involved collecting a lab air sample using the Tedlar bag sampling method, while simultaneously collecting the lab air sample into a gas cylinder using the compressor sampling method. The two samples were then subjected to extraction, purification, and measurement. Due to a significant difference in $\delta^{13}C$ values between the two samples, δD measurements for the Tedlar bag sample were not performed. The second set of tests utilized compressed air from the same gas tank. One sample was taken by directly filling Tedlar bags with the compressed tank air through the regulator, while the other sample was first stored in Tedlar bags and then further compressed into a cylinder using a compressor. Both samples then underwent extraction, purification, and measurement. However, discrepancies were still observed between the two results. Overall, we observed changes in methane concentration (not recorded) as well as fractionation of methane isotopes (Table 2.1). It remains uncertain whether the observed fractionation in the March–April 2022 tests was caused by the compression process, the inherent uncertainty of the sample extraction and purification methods,

or experimental errors introduced by the operator. Further testing is required to resolve these uncertainties.

Table 2.1. **Preliminary tests for compressor sampling.** 2σ is the mass spectrometer instrumental uncertainties, considering the error propagation but without considering the uncertainties brought by gas extraction and purification processes.

Run #	Description	Sample ID	Run Date	$\delta^{13}C$ (‰)	2σ (‰)	δD (‰)	2σ (‰)
Test #1							
1823-1825	Room Air to compressor	220209-Vent-CompressorTank	03/18/2022	-45.04	0.02	-113.14	0.89
1830	Room Air to bag	220321/220209 air vent bag check with compressor	03/21/2022	-46.86	0.01	/	/
Test #2							
1885-1889	Tank Air to bags	220330 AirTank (bags)	04/25/2022	-48.20	0.02	-108.13	0.24
1835-1838	Tank Air to compressor	220223 Acompr	03/25/2022	-48.81	0.02	-105.00	0.13
2023-2024	(new?) Tank Air to bags	220512AirTank	08/31/2022	-46.89	0.04	-98.03	0.33

The use of compressors will greatly facilitate sampling and allow us to deploy sampling apparatus to more locations under different conditions (e.g., towers and airplanes) if we can verify the reliability of compressor sampling.

2.2. Concentration Measurement

There are multiple methods I have used to measure methane concentration. One approach is using a Gas Chromatograph (GC) equipped with a Flame Ionization Detector (FID), while

another involves spectroscopic gas analyzers, with instruments from Picarro and Aeris being the ones I have used most frequently.

2.2.1. Gas Chromatograph (GC)

Methane concentrations are determined using a Shimadzu® GC-8AIF GC. Samples are injected from a 1 ml sample loop and carried by N_2 (about 60 ml/min) through the 1/8-inch inner diameter stainless steel GC column packed with 0.5 m Shimalite Q as the stationary phase. The column is kept at 80 °C. At this setting, different gases elute at different times due to their varying interactions with the stationary phase, which affects their travel rates through the column. Oxygen (O_2) elutes at 1.0 minutes, while methane elutes at 1.8 minutes. The Flame Ionization Detector (FID) records the peak signals. Air and hydrogen (H_2) gas flow rates for FID combustion are set at ~300 ml/min and ~50 ml/min, respectively. FID detects methane by burning it in a hydrogen flame, generating charged particles (ions and electrons). A high-voltage electrode captures these charged particles, producing an electrical current that corresponds to the methane concentration. The area under the methane peak in the chromatogram (which represents the time-integrated methane signal) is proportional to the average methane concentration in the sample.

Before measuring the sample, we ran the tank air standard ($[CH_4]$ = 1.984±0.010 ppm) three times to ensure that the instrument is in a stable state. Sometimes a “6 ppm” methane mixture was run twice after the tank air as a standard. This mixture had $[CH_4]$ = 6.253±0.0106 ppm on July 27, 2022, and had $[CH_4]$ = 5.840±0.016 ppm on Oct 6, 2022, due to leakage of the Tedlar

bag, and was used up at the end of October 2022. The leak rate is assumed to be constant. We bracket every four to five samples with a tank air measurement. After all the samples are measured, the tank air standard is measured three times. The sample methane concentration is calculated by scaling up/down the tank air assuming the GC responds linearly to methane concentrations. Sometimes we used a two-point calibration line given by the tank air standard (1.984 ppm) and "6 ppm" standard. The uncertainty is estimated by checking the standard error of the tank air runs. We estimate a typical uncertainty of 0.030 ppm (30 ppb) from the GC.

2.2.2. Spectroscopic Gas Analyzers

Methane molecules absorb light at specific wavelengths, a property that enables spectroscopic instruments to measure methane concentrations with high precision and high-frequency sampling.

One such instrument is the Mira Ultra LDS Infrared Multi-Pass Laser Gas Analyzer from Aeris Technologies Inc. (hereafter referred to as "Aeris"). This analyzer can simultaneously measure methane (CH_4) and ethane (C_2H_6) concentrations with fast time resolution, low latency, and high precision. The specific models I have used have serial numbers Aeris 302, 313, and 317. The manufacturer appears to have made continuous updates to the product based on user feedback, which may explain why instruments with higher serial numbers exhibit noticeably better performance and user experience (although this statement is based on personal experience rather than quantitative data). Improvements are observed in several aspects, including warm-up time,

data transmission stability, concentration measurement accuracy and precision, zero drift, and pressure dependence.

Aeris utilizes mid-infrared absorption, which detects the characteristic transition frequencies in the 3–3.5 μm wavelength range, where methane has strong infrared absorption features, although some overlap with water vapor absorption occurs. The absorption intensity at a fixed characteristic wavelength is proportional to the methane concentration and the optical path length. Aeris has an effective absorption path of 13 meters. While temperature and pressure are partially controlled, pressure in particular is susceptible to external variations. The manufacturer claims a typical precision of 1 ppb for CH_4 and 0.5 ppb for C_2H_6 at a 1-second integration time. However, based on actual use: Serial numbers 313 and 317 achieve ~1.1 ppb precision for CH_4 and ~0.3 ppb for C_2H_6. Serial number 302 has roughly twice the uncertainty for both CH_4 and C_2H_6 compared to 313 and 317.

All three Aeris instruments have undergone at least one slope calibration at the NOAA Air Resources Lab. The slope calibration procedure is as follows: a standard sample is directly introduced into the instrument for 5 minutes, and the average and standard deviation are calculated using the data from the last 4 minutes of measurements. A different standard sample is then used, and the same process is repeated. A total of at least three standard samples are used for one calibration. Following this, a zero air (i.e., air without CH_4, CO_2, or CO) standard sample is used to repeat the process and determine the zero point. The NOAA standard samples and zero air are stored in large compressed air cylinders and contain known reference concentrations of gases (CH_4, CO_2, and CO). The methane concentrations of the standard samples I used,

numbered #14, #18, #19, as well as #1, #2, #3, ranged from 1893.7 ppb to 3090.5 ppb. The measured values are then compared with the standard values, and a linear regression is performed to obtain the calibration equation: *True Concentration = a * Measured Concentration + b*. This equation corrects for both zero point offset and slope deviation, though typically only the slope correction (a) is used, as the zero point offset (b) is usually corrected through more frequent zero drifting calibrations. Strictly speaking, this calibration equation is valid only for methane concentrations in the range of 0 to 3.09 ppm, and recalibration is required periodically to obtain a new calibration equation. For a broader calibration range (e.g., 0 to 100 ppm), a known concentration of natural gas is used to mix with zero air, at a series of controlled flow rate controlled by mass flow controllers, to form a series of mixed gas with different mixing ratio and concentration. Such a calibration is typically performed with ten equally-gradiented concentrations in the desired concentration range.

In addition to slope calibration, corrections for zero drifting and span drifting are also necessary. Drifting refers to the gradual deviation of measurements for standard samples with fixed concentrations of 0 and x (where x is a relatively high value) as the instrument operates over time. Drifting typically goes in one direction. For the Aeris, drifting is quite noticeable. The methane drifting could reach 10 ppb in a day and may require zero drifting calibration once a day, while ethane concentration may require zero drifting calibration every hour.

In addition to various calibrations, close attention must also be paid to the spectrometer's response to temperature, pressure, absolute water vapor content, and relative humidity—factors that can cause significant deviations from the true values, and for which calibration is difficult.

The spectrometer's cavity typically has a strict temperature control system, and temperature variations during use are generally not significant. However, since the sample gas is directly sourced from the external environment, both pressure and water vapor content are highly influenced by external conditions. We observed approximately a 20 ppb CH_4 drift and a 10 ppb C_2H_6 drift with pressure variations from 1013 mbar (ambient pressure) to 500 mbar, on Aeris 317. The drift in the zero and span gases was fairly consistent on Aeris 317. And the drift is more significant and less consistent on Aeris 313 and Aeris 302. A lack of water in the sample will cause the Aeris to be unable to detect the spectral peaks for C_2H_6 and possibly CH_4, rendering the calculated concentration completely invalid. On the other hand, very high water vapor content can shift the spectral peak positions for ethane and methane, affecting the calculation results. More importantly, high water vapor content increases the risk of water condensation on the instrument's high reflectivity mirrors, and the droplets that form may leave contaminants on the mirrors after they evaporate. Therefore, it is recommended to flush the instrument's interior with zero air for one minute before each shutdown.

Picarro Inc. manufactures spectroscopic gas analyzers using a different principle, the cavity ring-down spectrometer (CRDS). Rather than measuring the intensity of light absorbed by the gas at specific wavelengths as it passes through an absorption cavity, CRDS measures the time it takes for an instantaneous laser to decay from its initial intensity to a threshold. The higher the methane concentration, the stronger the absorption, which causes the decay to occur faster, resulting in a shorter ring-down time. This mechanism converts the measurement of light intensity, which can have large uncertainty, into the measurement of time, which have smaller uncertainty, thereby improving instrument performance, particularly in reducing drifting and

temperature/pressure dependence. However, this mechanism requires a mirror with extremely high reflectivity (99.999%) and a powerful instantaneous laser to ensure the laser reflects more than 100,000 times within the cavity, resulting in an effective path length of around 20 km. As a result, the instrument is pricier. The Picarro models I have used include the G2301, G2401, G2401-m, and G2132-i. Among them, the G2401-m has additional pressure and temperature stabilization features and a design resistant to vibrations, making it suitable for deployment in moving vehicles and aircraft. The G2132-i can measure the carbon isotopes of methane and carbon dioxide. Each instrument has slightly different precision, but they can typically achieve precisions with 5 seconds integration of <15 ppb (typical 3.5 ppb) for CO, <50 ppb (typical 17 ppb) for CO_2; and <1 ppb (typically 0.1 ppb) for CH_4. The maximum drift at STP over 24 hours is 10 ppb for CO, 100 ppb for CO_2, and 1 ppb for CH_4, according to the manufacturer's specifications. External tests report long-term repeatability of 0.01-0.03 ppm for CO_2, 0.14-0.41 ppb for CH_4, and 0.3-2.2 ppb for CO (Yver Kwok et al., 2015), or 2-second precisions of 20 ppb for CO_2, 4.2 ppb for CO, and 0.2 ppb for CH_4 (Ren et al., 2019).

The calibration processes for slope, zero/span drift, and temperature, pressure, and water vapor dependency for the Picarro are similar to those of the Aeris described earlier. However, the Picarro G2401 and G2401-m have significantly less zero drift. The zero drift for methane is often not noticeable for up to a month. They are also significantly less affected by external temperature, pressure, and water vapor content.

Both Picarro and Aeris are portable and can be deployed in cars or aircraft. The Aeris Ultra is smaller, lighter, and does not rely on an independent external pump, making it more suitable for

portable use. They are often used for mapping methane emissions in urban areas or industrial facilities.

2.3. Extraction and Purification

The first step in the preconcentration of methane involves pumping air samples through a 400 ml moisture trap filled with dry silica gel, followed by a set of six 0.5-inch diameter liquid nitrogen cooled U-traps packed with 80-100 mesh Hayesep® DB Porous Polymer Adsorbent (Sigma-Aldrich®). The pressure is kept below the equilibrium vapor pressure of oxygen (~0.19 bar). This is to prevent oxygen condensation in the sealed environment, as condensed liquid oxygen is highly reactive and poses significant safety hazards, including explosion and fire risks. We use a rotary pump to provide suction, and under this setup, sample is drawn in at a rate of approximately 4 L/min. These U-traps quantitatively retain methane, krypton, and carbon dioxide and allow nitrogen and oxygen to partially bleed off. Once the sample has been transferred, the inlet valve is closed and the line is pumped to a pressure of ~100 torrs and then to ~2 torrs as a first step in removing nitrogen and oxygen while retaining methane and other condensable gases.

The sample is further concentrated by transferring to a second 3/8-inch diameter liquid nitrogen-cooled U-trap that is also packed with Hayesep DB. Originally, this step relied on the adsorption capacity of the second trap at liquid nitrogen temperature and the suction force generated by the pump positioned after the second U-trap. In February 2023, to further ensure complete transfer of the sample from the first set of U-traps to the second U-trap, an additional step was introduced,

using pure N_2 to flush both the first and second U-traps. In February 2025, nitrogen was replaced with helium for this flushing step. Although using N_2 is also feasible, it increases the time required for the subsequent step. The second trap is then warmed by replacing the liquid nitrogen trap with an ethanol slush bath at -120°C, while the pump continues to apply suction at one end. Nitrogen and oxygen are pumped out for 30 minutes (or until the pressure reaches 10 mbar). This step retains methane, while releasing most of the N_2 and O_2. The residue gas, after 3 to 5 hours of the above described extraction process, consists of concentrated methane and krypton, together with subequal amounts of N_2 and O_2. All U-traps in the purification line are heated up to about 80 °C and kept under vacuum overnight to remove any possible residues (especially water). Figure 2.4 is a schematic diagram of the extraction line. Figure 2.5 is a photo of the extraction line.

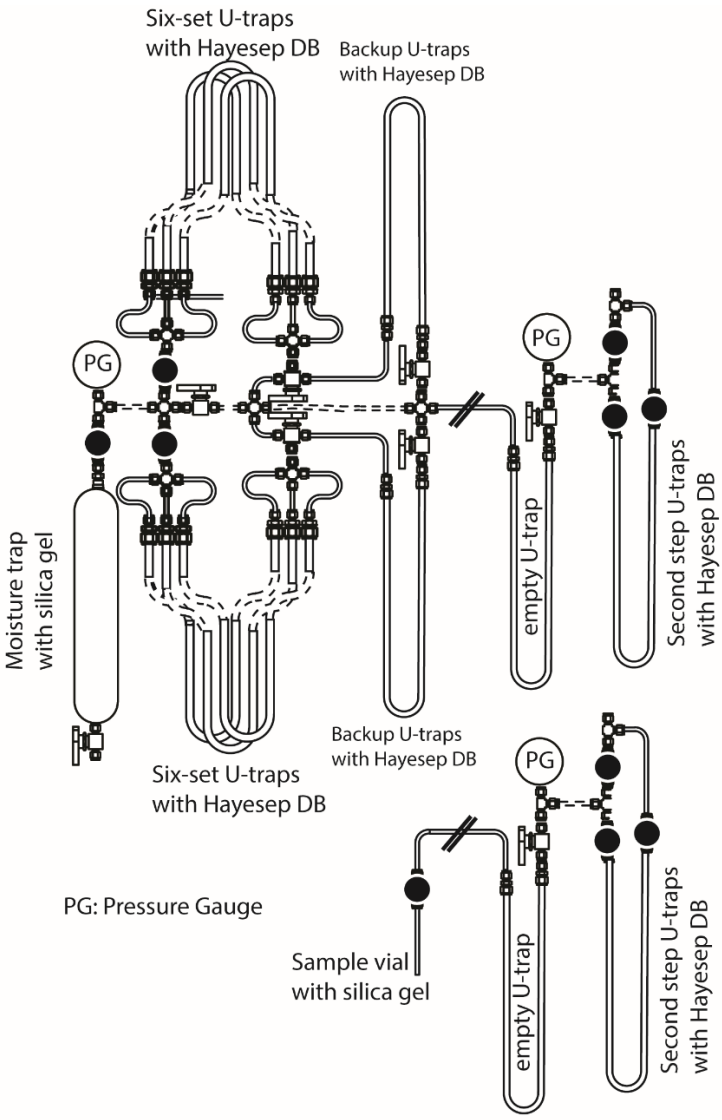

Figure 2.4. **Schematic diagram of the extraction line.** Diagram made by James Farquhar, labeled by Jiayang Sun.

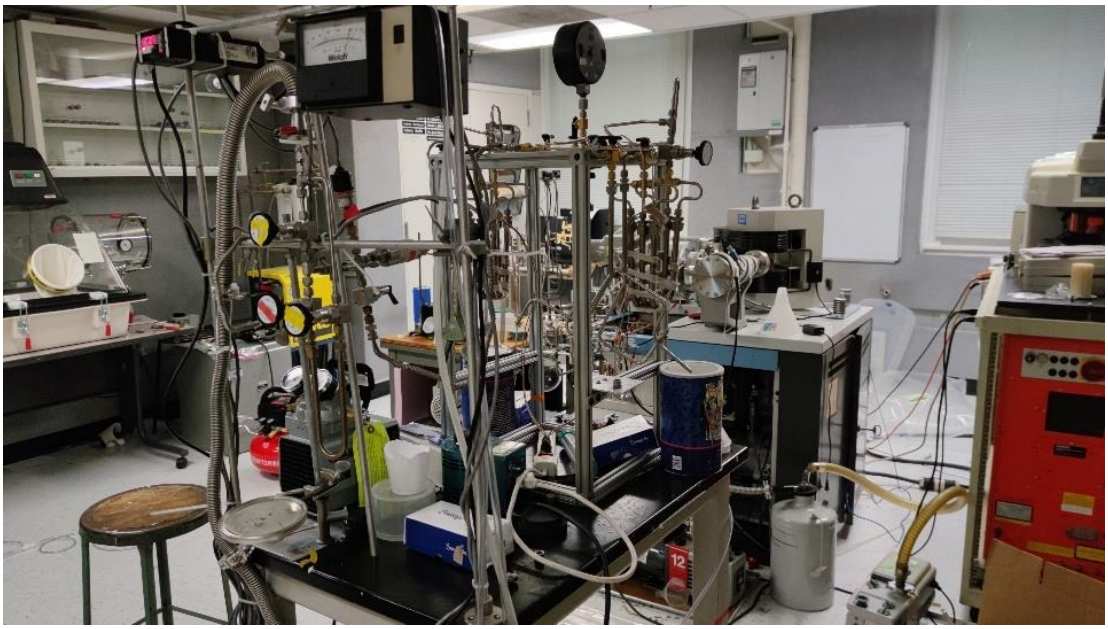

Figure 2.5. **Photo of the extraction line**, at the University of Maryland. Photo taken by Jiayang Sun on November 02, 2021 at 9:30 AM.

Extracting methane from vehicle exhaust requires the removal of substantial amounts of CO_2 and H_2O, this also applies to other samples with high CO_2 and water content. Failure to remove CO_2 and H_2O could result in process inefficiency and possibly cause sample fractionation. Removal of these gases is done in two steps. Before the sample gas is frozen onto the extraction big U-trap, it first passes through a dry ice bath to condense the water vapor, and then reacts with high-concentration (~50%w/v, ~20°C) NaOH aqueous solution by pulling the gas through a gas frit into the solution. The NaOH solution was aerated with N_2 for 3 hours before use, to remove CH_4 that has been reported to be adsorbed by solid NaOH pellets (Magen et al., 2014). Then a glass condenser cooled to liquid nitrogen temperature is used to trap any remaining CO_2 and H_2O. Subsequent air pressure monitoring on the purification line confirmed the efficiency of these added steps in removing CO_2 and H_2O. The vehicle exhaust samples also contained other impurities, which were removed during the bubbling process, as evidenced by the NaOH solution turning yellow and forming an oily layer. Given the substantial restriction on the gas

flow rate by the gas frit and NaOH solution, the extraction process could take more than 8 hours, instead of 5 hours for normal air samples. Hence, we rigorously inspected and reinforced the extraction line prior to use for optimal airtightness.

Transferring the sample from the extraction line to the purification line required first freezing the sample within a glass sample vial packed with silica beads under liquid nitrogen temperature on the extraction line and sealing it by closing the valve. The vial was then connected to the purification line and opened to release the sample. Final purification is accomplished using another GC separation. The He carrier gas set at 80 psi (about 80 ml/min) takes the sample in the injection loop through a 1/8-inch OD 2-mm ID stainless steel GC column packed with 25 feet (7.62 m) 60-80 mesh MolSieve 5A held at 56 °C. At this setting, the O_2 peak elutes at around 18 minutes, followed by N_2 at around 20 minutes, Kr at around 23 minutes, and methane at around 27 minutes. In most cases, the methane peak can be fully resolved from other gas peaks, except when the methane concentration and/or Kr concentration is too high. The methane peak is trapped in a liquid nitrogen-cooled collection loop filled with silica gel. The collection loop is then isolated from the GC, kept at liquid nitrogen temperature while kept pumping to remove Helium carrier gas. The amount of sample is then determined using a capacitance manometer in a calibrated volume and transferred to a sample tube containing silica gel that is cooled with liquid nitrogen. After elution of gas, the GC column is baked and back-flushed with helium flow at 200 °C for about an hour. All U-traps in the purification line are heated up to about 80 °C and kept under vacuum overnight to remove any possible residues (especially water). Figure 2.6 is a schematic diagram of the purification line. Figure 2.7 is a photo of the purification line.

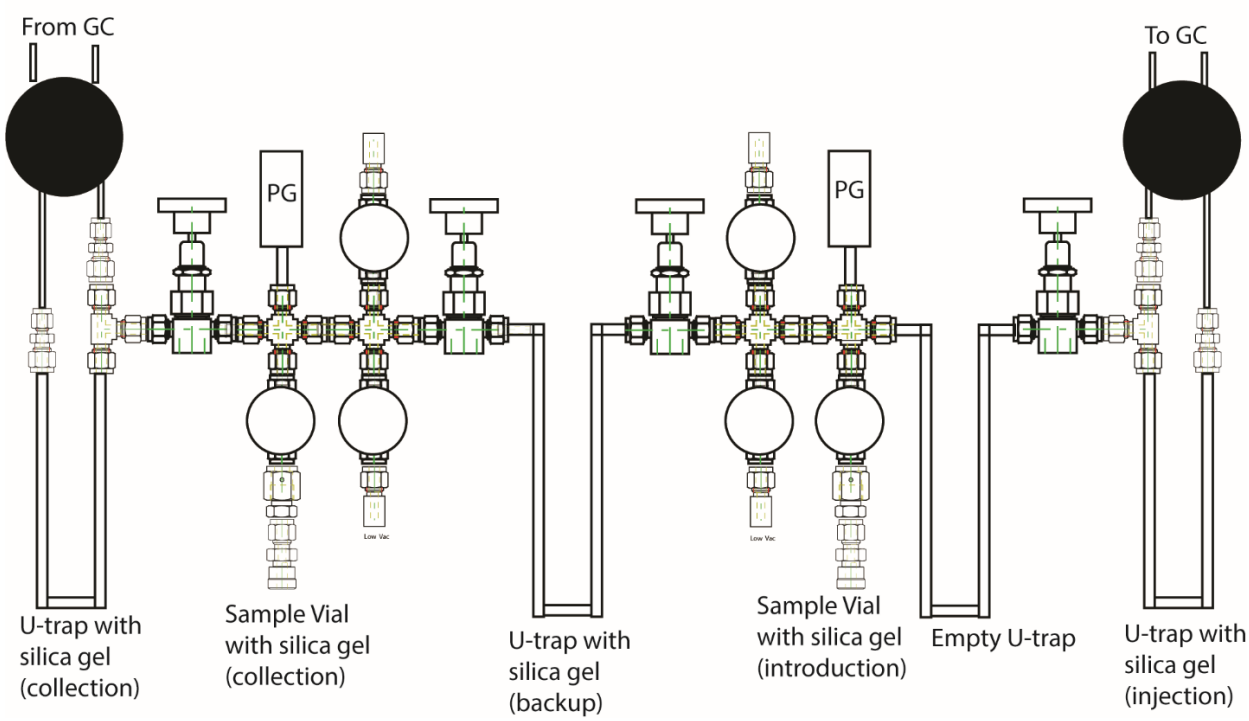

Figure 2.6. **Schematic diagram of the purification line.** Diagram made by James Farquhar, labeled by Jiayang Sun.

Figure 2.7. **Photo of the purification line**, at the University of Maryland. Photo taken by Jiayang Sun on November 02, 2021 at 9:30 AM.

2.4. Isotopologue Measurement

2.4.1. Introduction of Panorama

Methane isotopologues are measured using the Panorama (Nu Instruments Ltd.). The Panorama is a double-focusing high-sensitivity high-resolution gas-source mass spectrometer (Figure 2.8 and Figure 2.9) that can reach mass resolving power (MRP, defined as m/Δm, where m is the mass of the ion and Δm is the smallest mass difference between two peaks that can be separated) ~55,000, which is sufficient to separate peaks of $^{13}CH_3D^+$ and $^{12}CH_2D_2^+$ from adjacent methane adducts ($^{13}CH_5^+$ and $^{12}CH_4D^+$) on mass 18, as well as $^{12}CH_3D^+$ and $^{13}CH_4^+$ from $^{12}CH_5^+$ adduct on mass 17. The instrument attains this resolution with high signal strength due to a combination of factors that include:

(1) An acceleration potential of ~15-16 kV combined with a 1017.6 mm radius electrostatic analyzer (ESA), which reduces the energy spread (velocities) of ions entering the magnetic sector;

(2) A continuously variable source slit that allows for the beam to be optimized for mass resolution and large geometry since $MRP = {D}/{(X * s)}$ where D is the total mass dispersion which is about 630 mm for the Panorama, X is the magnification which is about 0.448, and s is the source slit width (With an MRP of 40000, the corresponding source slit width is about 35 μm);

(3) A number of quadrupole, hexapole, and octupole lenses, including a large quadrupole lens equipped between the ESA and the magnet, which allow increased transmission, because they

can be used to adjust bean shape (i.e., increases D/X), and reduce high-order aberrations. The Panorama has a D/X=1406 mm, which is comparable to large-geometry Secondary Ion Mass Spectrometry (SIMS) (e.g., CAMECA Instruments Inc. IMS 1280-HR);

(4) An 85° 800 mm radius magnetic sector, which allows for greater separation of ion beams;

(6) High vacuum (lower than $5*10^{-10}$ mbar) achieved in the instrument along the ion trajectory reduces scattering;

(7) Faraday collectors and an axial ion counter that are all moveable and with continuously variable slits, which allow for the collectors to be optimized to allow for fully resolved measurements; and

(8) The ion counter allows counting particle impacts with very low frequency (tens of times/second) with a precision close to counting statistics that makes the instrument a high sensitivity instrument in addition to a high mass resolution instrument.

The instrument is installed in a basement. The instrument has a relatively independent power supply to minimize interference from fluctuations in current frequency. It is also equipped with an uninterruptible power supply (UPS) to prevent damage caused by unexpected power outages. The room is fitted with a temperature control system, which typically maintains the temperature between 20 and 21 °C. However, the system may become less effective during spring and autumn, when there are large daily temperature variations in the external environment. The instrument is covered with a stainless-steel enclosure, which further reduces internal temperature fluctuations—particularly along the ion flight path and around the collector housing—and also helps protect the system from dust.

A detailed description of Panorama can be found in Young et al. (2016). The electrostatic sector – quadrupole – magnetic sector optical layout is designed by Matsuda (1974).

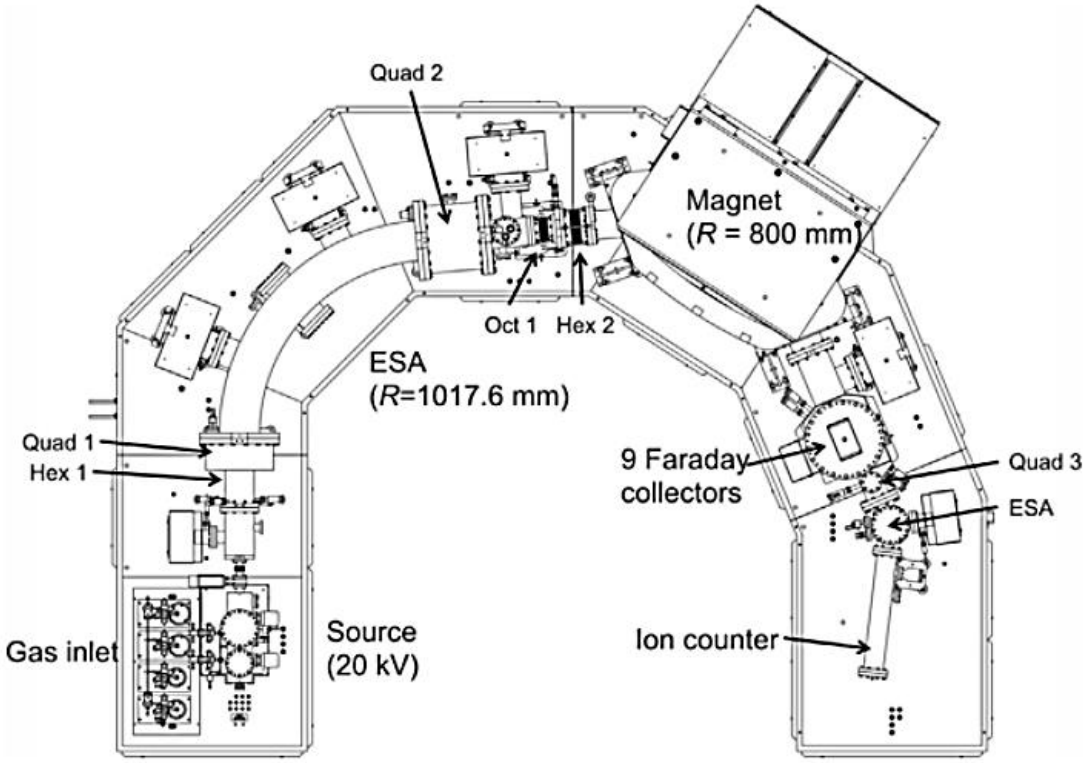

Figure 2.8. **The schematic layout of the Panorama mass spectrometer with major components labeled.** (Figure taken from Young et al. (2016), with permission)

Figure 2.9. **Photo of the Panorama mass spectrometer housed at University of Maryland.** Photo taken by Jiayang Sun. Except for the sample loading section on the far left, the rest part of the mass spectrometer is covered by metal shields to maintain temperature stability and prevent dust. Unshielded photos are not shown to avoid any patent disclosure conflicts.

2.4.2. Measurements

Figure 2.10 shows a peak scan of masses 15 (light blue), 16 (blue), 17 (red), and 18 (black) achieved under single scan mode scanning from magnet setting 17.85 to 17.86 with 200 steps. Better resolution and peak shape can be reached by careful tuning, higher scan frequency, and longer integration time. From Figure 2.10, we can distinguish $^{13}CH_4$ and $^{12}CH_3D$ (mass 17), as well as $^{13}CH_3D$, $^{12}CH_2D_2$, and $^{13}CH_5^+$ interference (mass 18).

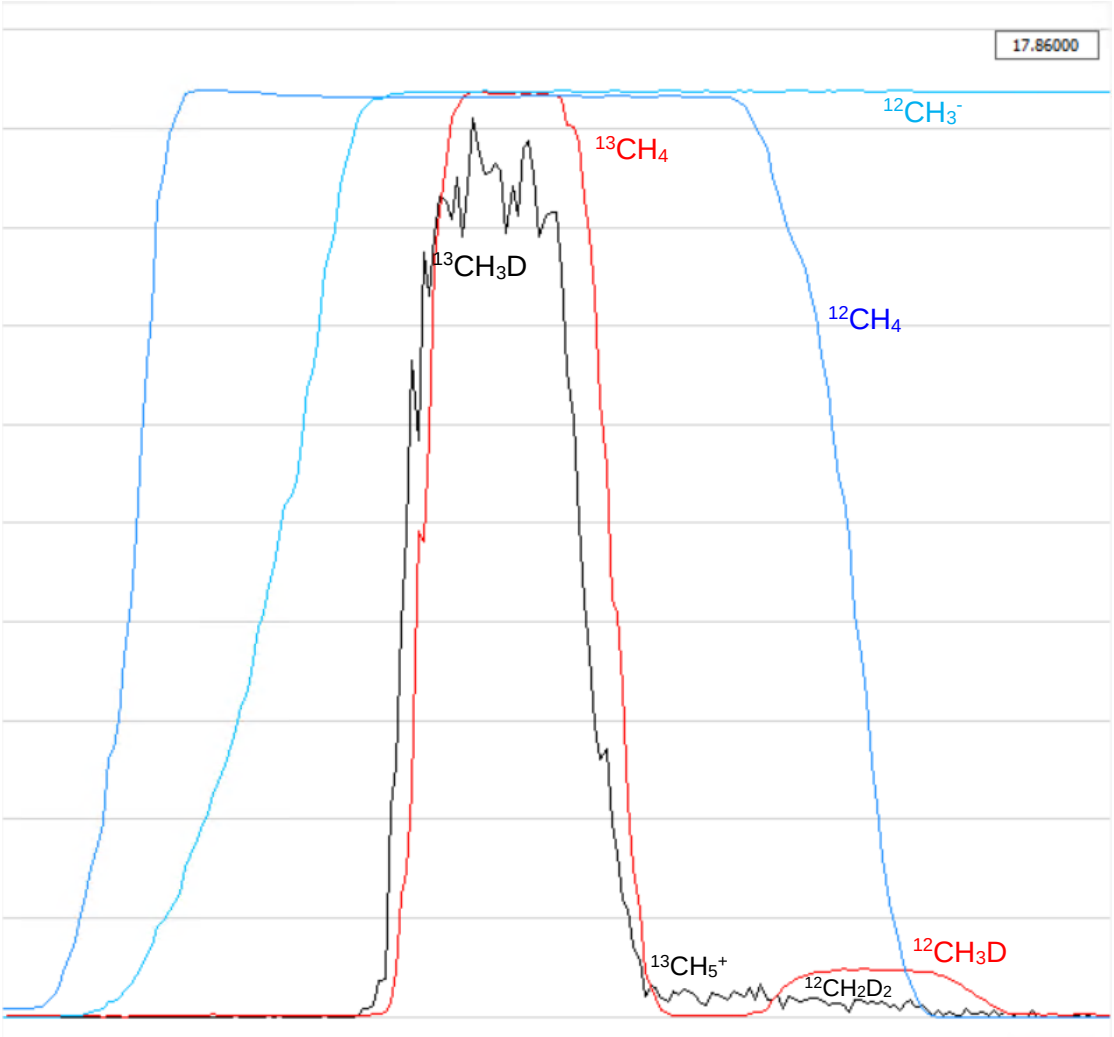

Figure 2.10. **Peak scan under single scan mode**, from magnet setting 17.85000 to 17.86000 with 200 steps. Peak heights are not to scale. Peak positions are moved to align and fit into a figure. Major beams are labeled. Light blue, blue, red, and black are for masses 15, 16, 17, and 18, respectively.

The collectors are set to simultaneously collect $^{12}CH_3$ (mass 15) & $^{12}CH_4$ (mass 16) & $^{13}CH_4$ (mass 17) & $^{13}CH_3D$ (mass 18), or $^{12}CH_3$ (mass 15) & $^{12}CH_4$ (mass 16) & $^{12}CH_3D$ (mass 17) & $^{12}CH_2D_2$ (mass 18). It means $^{13}CH_3D$ and $^{12}CH_2D_2$ cannot be measured simultaneously. Instead, we measure them in two separate runs (i.e., dynamic measurements). Mass 18 is counted using an ion counter. Mass 15, 16, and 17 are counted using Faraday cups. We use 10^9, 10^{10}, and 10^{11} Ω amplifiers for masses 15, 16, and 17, respectively.

Measurements are run at a balanced pressure and intensity between samples and references at about 10^{-8} mbar level in the analyzer housing (higher in the source) and about 10^{-10} Amp mass 16 signal intensity. For $^{13}CH_3D$, each run usually involves 40 blocks, where a block is 20 comparisons of sample-reference gas pairs. For $^{12}CH_2D_2$, each run usually involves 7 blocks, where a block is 100 comparisons of sample-reference gas pairs. The counting time for each single measurement (in a sample-reference pair) is set to be 40 seconds, followed by a delay time of 20 seconds for flushing the inlet. Peak centering using mass 17 and baseline monitoring on masses 16, 17, and 18 are performed between every block. Peak centering at a suitable interval is necessary because the peak position may drift as the sample pressure decreases and room temperature shifts. However, peak centering and baseline monitoring should not be too frequent because it can cause the fluctuation of measurement results, usually returning to normal within 1-2 minutes. This is probably due to the fact that the ionization house reaches a steady state with species and adducts generated in the ionization process during normal measurements, and when a peak centering is performed, it is followed by a baseline measurement without gas going into the ionization house. When the gas flow is restored, the source has to reestablish its steady state.

The instrument reports the intensity of targeted beams and the backgrounds. We calculate the intensity of the signal by subtracting the background:

$$I^x_{i,real} = I^x_{i,total} - I^x_{i,background} \quad (2.1)$$

Where I is the intensity, i is the targeted isotopologue, x can be 15, 16, 17, or 18. While $I^x_{i,real}$ will drift as the gas is consumed, the ratio of two masses will be more stable:

$$R^{y}_{sample\ or\ reference} = {I^{y}_{sample\ or\ reference}}\Big/{I^{16}_{sample\ or\ reference}} \quad (2.2)$$

Where R stands for the ratio, and y can be 15, 17, 18.

By calculating d^{y}, the ratio of the signal strengths of different mass for sample and reference, we get a more stable constant that mostly cancels out instrument fractionation and drift:

$$d^{y} = \frac{{I^{y}_{sam}}/{I^{16}_{sam}}}{{I^{y}_{ref}}/{I^{16}_{ref}}} \equiv const. \quad (2.3)$$

d^{y} can be converted to the commonly seen isotopic values format in per mil:

$$\delta^{y} = (d^{y} - 1) * 1000‰ \quad (2.4)$$

Typical instrument measurement uncertainties (1SD) for $d^{^{13}CH_4}$ (mass 17), $d^{^{13}CH_3D}$ (mass 18), $d^{^{12}CH_3D}$ (mass 17), $d^{^{12}CH_2D_2}$ (mass 18) are 0.005‰, 0.02‰, 0.05‰ and 0.8‰, respectively, for an 70 μmol sample being measured for about 8 hours for $^{13}CH_3D$ and 24 hours for $^{12}CH_2D_2$. The instrumental uncertainties are very close to Poisson counting statistics:

$$Relative\ Standard\ Deviation\ (RSD) = \frac{1}{\sqrt{Counts}} \quad (2.5)$$

When calculating the uncertainties of δ^{y}, we also consider the pressure imbalance calibration (see Section 2.4.3), and error propagation from the reference gas. When calculating the Δ, we also propagate the error of δ. The final reported isotopic values are usually 2SD propagated errors. Typical instrumentation internal uncertainties are about 0.01 to 0.04‰ for $\delta^{13}C$, 0.05 to 0.16‰ for δD, 0.3 to 0.6‰ for $\Delta^{13}CH_3D$, and 1.6 to 2.7‰ for $\Delta^{12}CH_2D_2$. Uncertainties are different for each sample. The available amount of the sample is the determining factor for uncertainty, followed by the instrument condition.

2.4.3. Calibration

We notice that sample/reference pressure imbalance will shift the measured isotope values (Figure 2.11). We apply calibration to pressure imbalance and propose that the formation of CH_3^+ byproduct during ionization can account for this phenomenon.

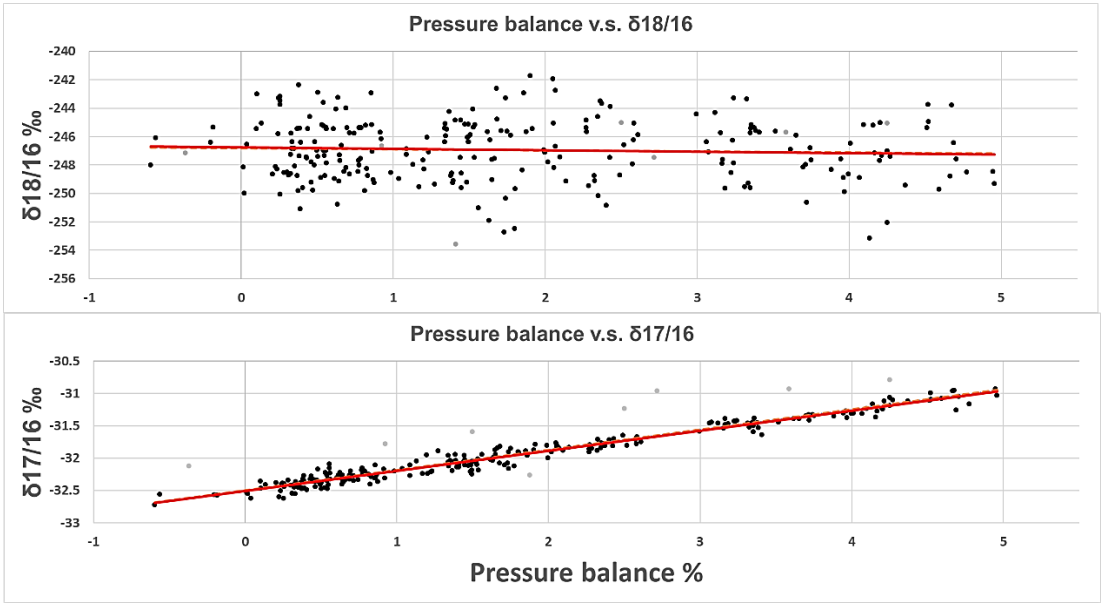

Figure 2.11. **An example of typical data calibration.** The definitions of pressure balance and d17/16 and d18/16 are described in Equations 2.6 and 2.7. The dots are the measured values, whereas gray represents the values being discarded according to the rules described in the Section 2.4.3 text. The red line is the linear fit of the black dots and the orange dashed line is the linear fit of all the dots.

We cannot always make the sample and reference pressure to be the same because 1) sometimes the sample volume is too small or too large for the reference side to match; 2) the two bellows compressing the gas on the sample and reference sides have different size and compression rates; 3) there may be hardware or software issues with the two bellows and the software, causing the volume and pressure controls to not fully functional. Sometimes the imbalance could be more

than 50%. This pressure imbalance causes the sample and reference to have different signal intensities during measurements, which are mostly reflected in mass 16. In other words:

$$r^{16} = {I_{sam}^{16}}/{I_{ref}^{16}} \neq 1 \tag{2.6}$$

and r^{16} increase or decrease as the measurement goes on. I stands for signal intensity.

Theoretically, although the sample and reference have different signal strengths, the ratio of the signal strengths ratio of different masses for sample and reference should not change with the development of the pressure imbalance, i.e.

$$d^{y} = \frac{{I_{sam}^{y}}/{I_{sam}^{16}}}{{I_{ref}^{y}}/{I_{ref}^{16}}} = \frac{r^{y}}{r^{16}} \equiv const. \tag{2.7}$$

Where y can be 15, 17, or 18. However, after processing the raw data, we find that most measurements show a linear relationship between pressure imbalance r^{16} and d^{y}, and most of them are positive correlations for mass 17 (i.e. d^{17}) while mass 18 (i.e. d^{18}) is less sensitive to pressure imbalance (Figure 2.11).

Panorama's default software program averages all the measured d^{y} values to get the final values in the report, which could be affected by this pressure dependency. Take Figure 2.11 as an example: most d^{y} values were measured under sample-working gas pressure imbalance conditions, where the sample pressure exceeded the working gas pressure by up to 5%. The average d^{y} value would be 0.75‰ higher than the projected value. When the pressure imbalance is large, the averaged value can largely deviate from the "true value". Our approach is to plot all the measured d^{y} against $r^{16} - 1$ (which represents pressure imbalance, 0 means sample and

reference pressure are the same), and perform linear fitting. When pressure imbalance is within 10% (i.e. $|r^{16} - 1| < 0.1$), d^y generally keeps a good linear relationship with pressure imbalance. This linearity can even be extended to 80% pressure imbalance or more, while still staying valid. The intercept, which should be the value when the sample and reference signal intensities are equal (i.e. $r^{16} - 1 = 0$), is the value we adopt in the final report. We take the variance of the intercept that propagated during the linear fitting to be the uncertainty, instead of the sample variance.

Certain data points are excluded from the regression based on the following criteria:

1. When r^{16} deviates too far from 1 and d^y no longer exhibits a linear relationship with r^{16}, the corresponding data points are removed.

2. When I_{sam}^{16} falls below a threshold—typically 5*10^{-11} A for large-volume samples and as low as 2*10^{-11} A for small-volume samples—the data points are excluded. This threshold is set because the uncertainty no longer decreases with the addition of more data once the signal falls below this limit.

3. Individual d^y values that fall outside the ±3σ range of all d^y measurements are also excluded.

4. The first measurement of each block is removed, since it was usually largely offset.

These filters usually have minor effects on the final results.

The phenomenon might be caused by the CH_3^+ byproduct produced during the ionization of methane. Processes that produced CH_3^+ might have different fractionation coefficients than those that produce CH_4^+, and the proportion of pathways that produced CH_3^+ might depend on the gas pressure. When the pressure of the sample and reference are not balanced, the measured signals

drift along with the degree of imbalance. After observing this phenomenon, we start to collect and monitor mass 15 simultaneously with masses 16, 17, and 18. The data may support this hypothesis to some extent. We notice that the intensity of the CH_3^+ peak is generally 0.81 to 0.83 times that of the CH_4^+ peak (which can fluctuate between 0.6-1 depending on the instrument status). There is a good negative linear relationship between d^{15} and pressure imbalance (Figure 2.12). A 5% increase in pressure imbalance corresponded to a 1.8‰ decrease in d^{15} and a 1.5‰ increase in d^{17}, which is in line with the mass balance. When the instrumental stability is poor, we observe a larger fluctuation of d^{15}, which might be an important contributor to the measurement uncertainty.

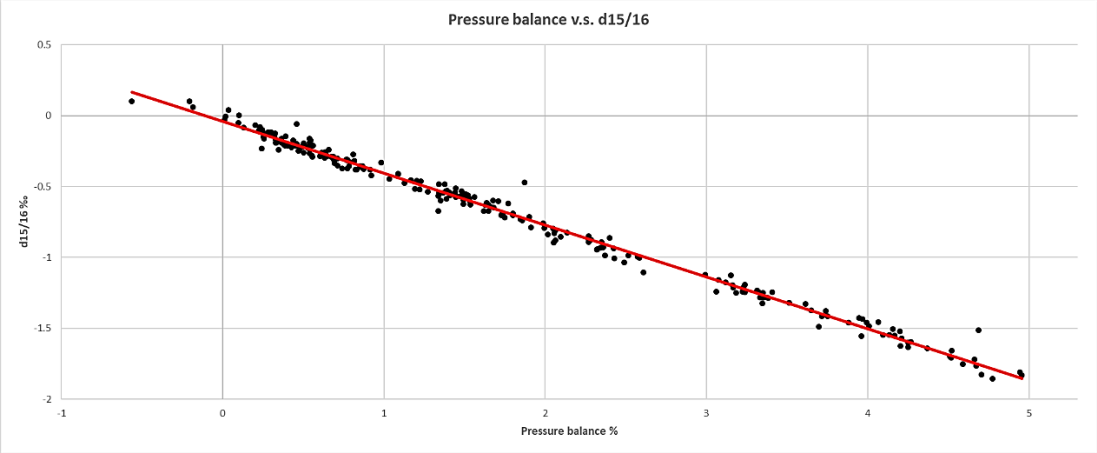

Figure 2.12. **Relationship between pressure balance and $d^{15/16}$**.

2.5. Quality Control

Multiple quality control measures should be implemented to ensure that the entire measurement process accurately represents the "true value" (i.e., accuracy) and that our workflow and measured values exhibit good reproducibility (i.e., precision). These measures include sample-

standard bracketing, continuously monitoring lab standards to assess external precision, conducting inter-laboratory comparisons, and establishing an absolute reference frame. Some of these measures have been implemented in our lab, while others are still lacking. The following sections (Sections 2.5.1 to 2.5.4) provide a detailed review.

2.5.1. Sample-Standard Bracketing

In isotope measurements, a commonly used sample sequencing strategy involves inserting standards with known isotope compositions at fixed intervals within a sample sequence. For example, when measuring sulfur isotopes using the Thermo Scientific MAT 253 mass spectrometer, the standard IAEA-S-1 is typically analyzed every 3–4 samples (J. W. Dottin et al., 2022; Sun & Farquhar, 2024). This sequencing strategy allows for the correction of instrumental drift (variations in repeated measurements of standard samples), reduction of (contamination) matrix effects (the presence of other substances affecting the ionization efficiency of the target substance), and minimization of memory effects (interference from a previous high-abundance sample on the subsequent sample).

However, this approach has not been routinely applied in our lab when using the Panorama to measure methane clumped isotopologues. The primary reason is the high time and sample cost associated with bracketing standards—each measurement takes approximately two days, not including sample preparation time. We have occasionally conducted zero testing, which partially serves the function of sample-standard bracketing. These zero tests are generally performed after major or minor instrument maintenance or after a significant tuning adjustment. During zero

testing, the working gas is introduced to both the sample and reference sides, rather than just the reference side, followed by a full measurement. Under these conditions, all measured d^y values are expected to be zero within the measurement uncertainty. If the test passes (i.e., d^y=0 within uncertainties), the instrument is considered to be in good working condition. If not, further maintenance or tuning is required.

Table 2.2 summarizes all runs identifiable as zero tests (or can be regarded equivalent to zero tests) conducted between October 2021 and October 2023. The results are listed in Table 2.3 and illustrated in Figure 2.13. In late April 2022, the Panorama instrument was used for sulfur isotope measurements. Between June and August 2022, the instrument underwent extended maintenance due to filament failure and sulfur contamination of the ion source. Notably, not all zero tests were successfully passed and zero testing criteria was not strictly enforced. In some cases where results were “close” to passing the zero test, additional adjustments were not performed. However, the results from runs 2185–2187 and 2188–2189 can serve as an example and indicate that if the instrument initially fails a zero test (run 2185–2187), it is possible to pass the zero test through additional tuning or by allowing the instrument to stabilize itself over time (run 2188–2189).

Table 2.2. **Compiled zero test and equivalent zero test runs and some descriptions.** All listed zero tests were performed by Jiayang Sun (JS) or James Farquhar (JF), sometimes for different purposes.

No.	Run #	Sample ID	Run Date MM/DD/YYYY	Operator	Description
1	1515-1516	ref vs ref	10/10/2021	JS	Working gas #B was simultaneously introduced into bellows A and B and uniformly mixed.
2	1643-1644	Marcellus run as zero in A and B	01/01/2022	JF	Sample Marcellus (natural gas) was simultaneously introduced into bellows A and B and uniformly mixed.
3	1723	ref. gas for calib. 220202b	03/02/2022	JF	Not sure.
4	1831	zero Marcellus A vs. B	03/22/2022	JF	Sample Marcellus (natural gas) was simultaneously introduced into bellows A and B and uniformly mixed.
5	1832	silica test A freeze back	03/23/2022	JS	Working gas #B was simultaneously introduced into bellows A and B and uniformly mixed. Then, gas in bellow A was frozen back to a clean sample tube with silica gel under liquid nitrogen temperature, and then warmed at room temperature for a long time to fully re-release gas. Fractionation might or might not have happened.
6	1856	new Reference	04/04/2022	JF	Not sure, but very likely working gas #D was simultaneously introduced into bellows A and B and uniformly mixed.
	Major repair after running sulfur samples				
7	1973-1974	Zero 1973 1ne 4	08/10/2022	JF	Not sure, but very likely working gas #D was simultaneously introduced into bellows A and B and uniformly mixed.

8	2127	Run Sample versus self from third capillary with air in one bellows	12/15/2022	JF	Sample X was simultaneously introduced into bellows A and C and uniformly mixed. Then one bellow was purposely allowed to be contaminated with some air. Differences were expected.
9	2167	zero, bellow reset	01/10/2023	JS	Working gas #D was simultaneously introduced into bellows A and B and uniformly mixed. Bellow B was replaced by a new bellow B before the testing. The run was to test if the new bellow was installed correctly or not.
10	2168	zero, bellow reset, autobalance	01/11/2023	JS	Working gas #D was simultaneously introduced into bellows A and B and uniformly mixed. Bellow B was replaced by a new bellow B before the testing. The run was to test if the new bellow auto-balancing function works or not.
11	2185-2187	zero ref vs ref	01/23/2023	JS	Working gas #D was simultaneously introduced into bellows A and B and uniformly mixed.
12	2188-2189	zero ref vs. ref	01/24/2023	JS	Working gas #D was simultaneously introduced into bellows A and B and uniformly mixed.

Table 2.3. **Compiled results of zero tests and equivalent zero tests.** If $^{12}CH_3D$-$^{12}CH_2D_2$ were not measured in the given run, it is marked as "/". All data processing was performed by Jiayang Sun or James Farquhar, who should have followed the same procedure. Uncertainties are reported as 1 se during the run, which only reflect the instrumental uncertainties and does not consider error propagations and human operation-introduced uncertainties. Sample ID labeled with * are expected to have human operation-introduced uncertainties or fractionations.

Run #	Sample ID	Run Date	d17 $^{13}CH_4$ (‰)	1 se (‰)	d18 $^{13}CH_3D$ (‰)	1 se (‰)	d17 $^{12}CH_3D$ (‰)	1 se (‰)	d18 $^{12}CH_2D_2$ (‰)	1 se (‰)
1515-1516	ref vs ref	10/10/2021	0.007	0.009	-0.02	0.283	-0.094	0.066	-0.765	1.091
1643-1644	Marcellus run as zero in A and B	01/01/2022	-0.161	0.026	-0.196	0.592	-0.103	0.245	-2.917	2.844
1723	ref. gas for calib. 220202b	03/02/2022	-0.192	0.006	-0.887	0.251	/	/	/	/
1831	zero Marcellus A vs. B	03/22/2022	0.049	0.015	0.298	0.714	/	/	/	/
1832	silica test A freeze back*	03/23/2022	-0.069	0.014	0.490	0.298	/	/	/	/
1856	new Reference	04/04/2022	-0.186	0.008	-0.218	0.119	/	/	/	/
Major repair after running sulfur samples										
1973-1974	Zero 1973 1ne 4	08/10/2022	-0.014	0.005	-0.094	0.138	0.010	0.060	1.428	0.898
2127	Run Sample versus self from third capillary with air in one bellows*	12/15/2022	0.503	0.004	0.902	0.153	/	/	/	/
2167	zero, bellow reset	01/10/2023	0.120	0.006	0.260	0.137	/	/	/	/
2168	zero, bellow reset, autobalance	01/11/2023	0.161	0.008	0.674	0.240	/	/	/	/
2185-2187	zero ref vs ref	01/23/2023	-0.044	0.010	-0.259	0.451	-0.334	0.190	-3.135	2.052
2188-2189	zero ref vs. ref	01/24/2023	-0.009	0.004	0.158	0.188	0.007	0.082	-0.233	1.124

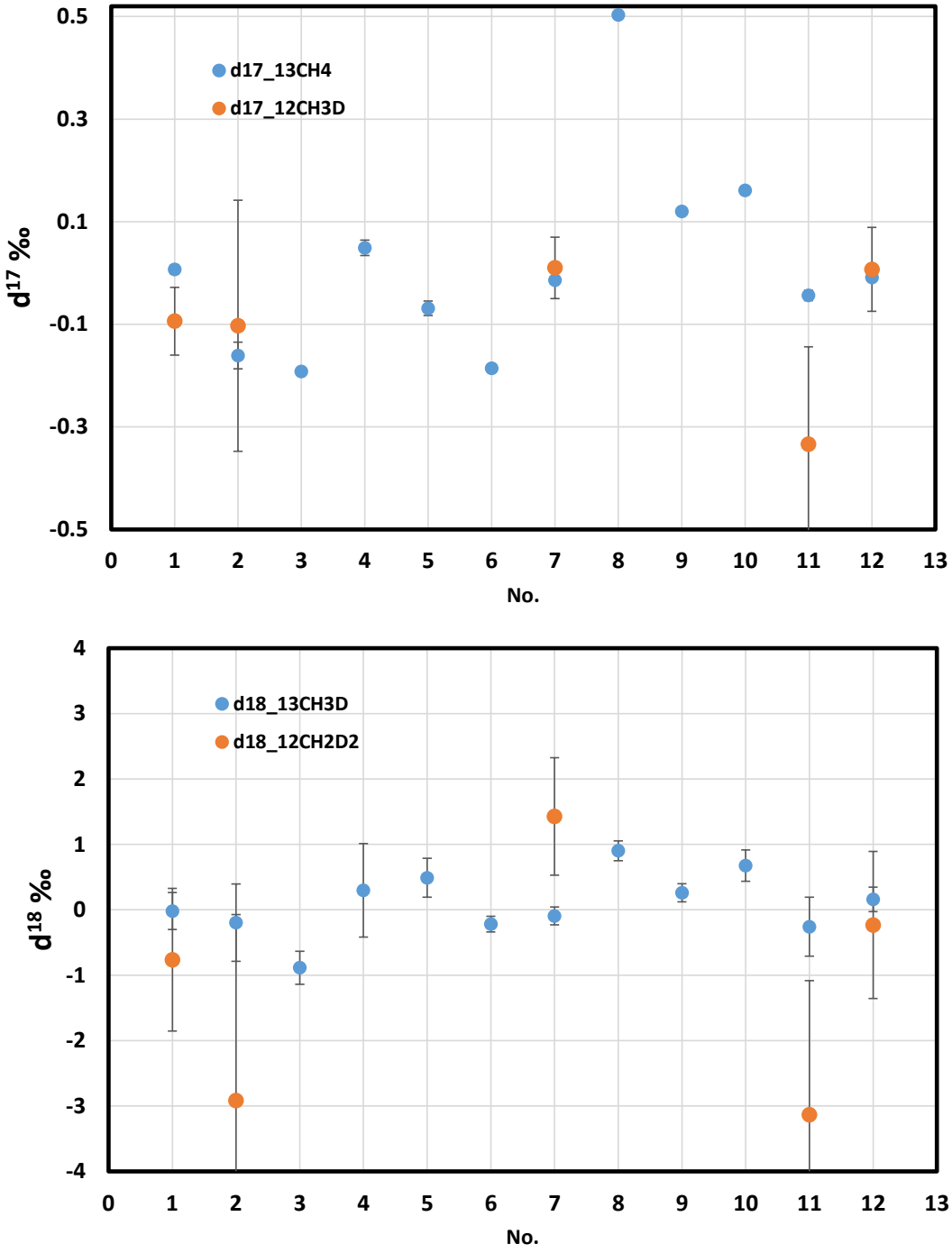

Figure 2.13. **Results of zero tests and equivalent zero tests.** All d17 and d18 values are expected to be within the error range of zero if the measurement was truly set for zero test. Test #12 is a perfect example of a "passed zero test."

2.5.2. Laboratory Standard Sample Acquisition and External Precision

Laboratories often measure a fixed sample intermittently over a long period (several years) to establish external precision. The standard used for bracketing in Section 2.5.1 can also be used for determining the lab external precision. This fixed sample can be an international standard, though it is typically pricy, or it can be a lab-prepared sample with a sufficiently large quantity. In a broader sense, external precision should also include the uncertainties stem from lab sample pretreatment processes. It is expected that, for methane clumped isotopologue measurements (and possibly methane bulk isotopes as well), the primary source of uncertainty comes from the sample pretreatment processes. This is because the extraction and purification process (Section 2.3) is time-consuming, involves complex steps, requires significant manual intervention, and lacks verification at each stage. As a result, determining the external precision of methane clumped isotopologue measurements remains a challenging issue. Each measurement requires 800 L of air, while a common Airgas Size 300 High Pressure Steel Cylinder can hold approximately 9,000 L of air, supporting only about ten measurements—even without considering the potential of isotopic fractionation as the cylinder nears depletion. This severely limits the ability to monitor external precision over an extended period due to sample availability constraints. Additionally, considering that each measurement requires approximately 8 hours for sample extraction and purification, followed by 40 hours of measurement time, the cost of such monitoring is quite high.

Table 2.4 compiles several identifiable tank air test runs. There were additional tank air tests conducted before and after those listed, but they evidently used different tanks, resulting in significant differences in the test results. Notably, among the five tests listed, Jiayang Sun performed the extraction and purification for two tests, while Cedric Magen handled the remaining three, potentially introducing different isotopic fractionation effects due to differences in operational details.

Table 2.4. **Compiled Tank Air Tests and Results.** The two samples labeled with "JS" in the Sample ID were prepared by Jiayang Sun, while the other three were prepared by Cedric Magen. All samples were measured by Jiayang Sun using the Panorama.

Run #	Sample ID	Run Date	$\delta^{13}C$ (‰)	2σ (‰)	δD (‰)	2σ (‰)	$\Delta^{13}CH_3D$ (‰)	2σ (‰)	$\Delta^{12}CH_2D_2$ (‰)	2σ (‰)
2023-2024	220512AirTank	08/31/2022	-46.89	0.04	-98.03	0.33	1.33	0.72	41.10	3.72
2103-2104	TankAir_JS1	11/15/2022	-47.59	0.01	-99.21	0.16	2.18	0.28	46.17	2.54
2133-2135	TankAir_JS2	12/22/2022	-47.06	0.10	-98.73	0.18	1.59	0.41	48.39	2.40
2137-2139	TankAir_Cedric1	12/23/2022	-47.27	0.04	-99.85	0.18	1.55	0.45	41.70	2.88
2163	TankAir_Cedric2	01/07/2023	-47.02	0.03	-97.93	0.16	2.39	0.61	47.11	2.20
	Average		-47.17	0.24 (1SD)	-98.75	0.72 (1SD)	1.81	0.40 (1SD)	44.89	2.94 (1SD)

2.5.3. Inter-laboratory Comparison

Inter-laboratory comparisons are necessary, especially for this new technique. The working gas we are using in our lab is a tank of natural gas from the Marcellus shale. The working gas has well-characterized $\delta^{13}C$ and δD values, but only has values measured by Young, Kohl, Lollar, et al. (2017) as references for $\Delta^{13}CH_3D$ and $\Delta^{12}CH_2D_2$. Therefore, additional work is needed to verify our measurement data are on the same scale as those from other labs. It is widely recognized that bulk hydrogen isotope data exhibit scale differences between different laboratories, making this a well-known issue in the field. According to the summary by Umezawa et al. (2018), laboratories capable of measuring hydrogen isotopes in methane across the globe can roughly be divided into two groups. Within each group, the measurement results are generally consistent; however, there is a difference of approximately 10‰ in the δD_{CH4} values for the same methane sample between the two groups. This discrepancy is likely due to the fact that each group calibrates its measurements using different hydrogen isotope reference materials.

Before February 2023, we had measured the AL-1 sample only once, on September 1, 2021. AL-1 is a working gas from Shuhei Ono's lab at MIT. Ono et al. (2014) have anchored AL-1 to the stochastic distribution coordinate, allowing us to normalize our values first to AL-1 and then to the stochastic distribution coordinate. It is important to note that the MIT lab employs TILDAS to measure methane clumped isotopologues, which operates on a different principle than mass spectrometry.

In February 2023, I tested a series of additional working gases, including AL-1 CD and AL-1 D3 (also from MIT), as well as CAL1549, AP613, and Std#3 from Utrecht University. These tests and their results, along with measurements of these standard samples from other laboratories, are compiled in Table 2.5.

Table 2.5. **Compiled methane clumped isotopologue measurements of standard working gases from different laboratories.** The measurements from MIT are reported in Ono et al. (2014) and Gonzalez et al. (2019), while those from UCLA are reported in Young et al. (2016). The UMD measurements are done in our lab. Some data (starting with AL1) were published in Haghnegahdar et al. (2023), and some remain unpublished. The Utrecht measurements are from Utrecht University and are a subset of data reported in Sivan, Röckmann, et al. (2024).

By	Sample	$\delta^{13}C$ (‰)	2σ (‰)	δD (‰)	2σ (‰)	$\Delta^{13}CH_3D$ (‰)	2σ (‰)	$\Delta^{12}CH_2D_2$ (‰)	2σ (‰)
MIT	AL1	-34.50	0.02	-147.70	0.06	2.33	0.05	4.40	0.50
	AL1-CD	-82.44	0.72	-158.00	0.18	15.79	0.45	5.50	1.90
	AL1-D3	-35.24	0.06	239.81	0.15	1.49	0.14	26.40	0.60
	AS2	-38.60	0.05	-153.70	0.30	2.33	0.14	5.70	0.50
	AS1-DY	-44.27	0.06	-403.34	0.43	5.06	0.17	324.30	1.10
UCLA	AL1	-34.65	0.01	-147.88	0.09	2.41	0.26	5.62	0.87
	AL1-CD	-82.01	0.03	-159.72	0.03	16.13	0.30	/	/
	AL1-D3	-34.76	0.00	242.55	0.01	1.55	0.12	/	/
UMD	AL1	-34.49	0.01	-147.64	0.05	2.72	0.28	5.00	0.79
	AL1-CD	-82.14	0.01	-159.30	0.06	16.07	0.21	10.98	1.18
	AL1-D3	-34.77	0.01	242.13	0.10	1.68	0.22	26.79	1.23
	AP613	-37.11	0.01	-171.64	0.09	2.23	0.25	2.35	1.52
	CAL1549	-17.73	0.01	-176.30	0.08	6.44	0.23	9.17	1.53
	Std3	-36.56	0.01	-209.62	0.07	2.06	0.25	-1.56	1.41
Utrecht	AP613	-37.50	0.10	-161.80	1.00	2.26	0.13	2.74	0.87
	CAL1549	-18.13	0.06	-171.27	0.87	6.37	0.42	7.66	1.49
	IMAU-3	-36.50	0.10	-200.10	1.00	2.84	0.34	1.25	1.80

Considering that different laboratories may use different reference scales for bulk carbon and hydrogen isotopes, we calculated the differences between two working gas standards within the same laboratory (e.g., the difference between AL1-CD and AL1 for $\delta^{13}C$, δD, $\Delta^{13}CH_3D$, and $\Delta^{12}CH_2D_2$) for comparison. The results are presented in Figure 2.14.

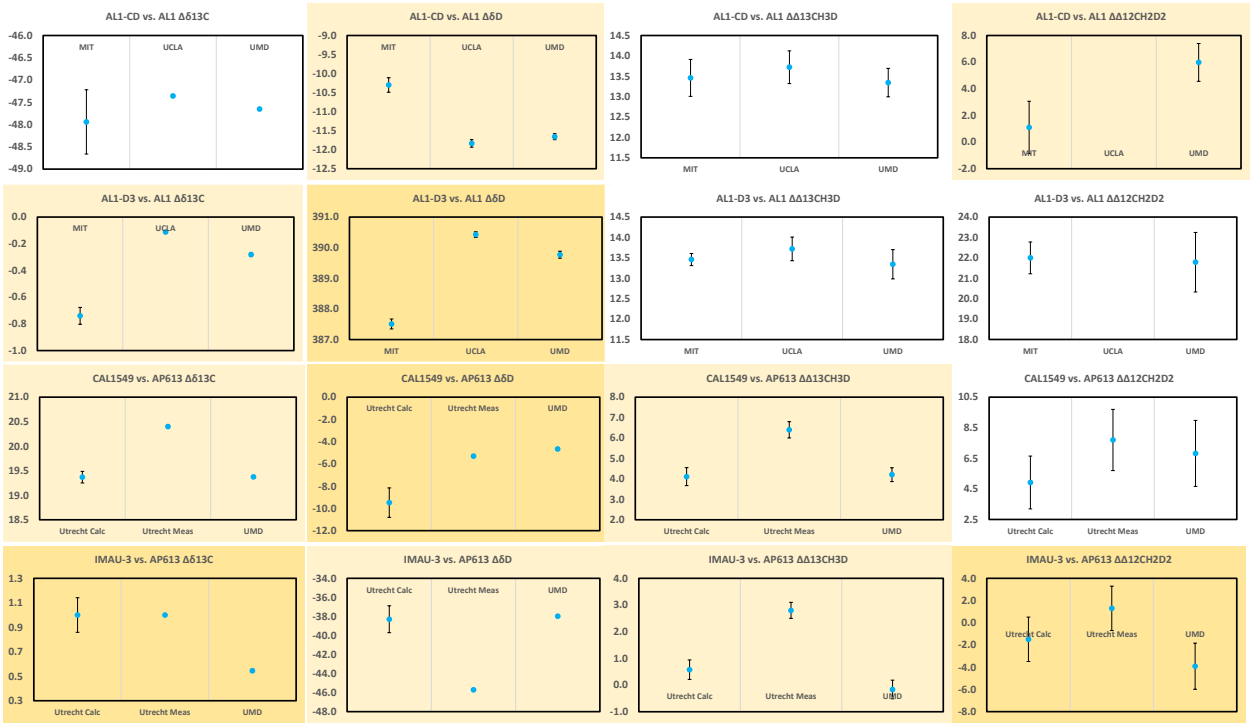

Figure 2.14. **Comparison of measurement differences for multiple standard samples across different laboratories.** The first two rows compare MIT, UCLA, and UMD, while the last two rows compare Utrecht and UMD. Each column, from left to right, represents the differences in $\delta^{13}C$, δD, $\Delta^{13}CH_3D$, and $\Delta^{12}CH_2D_2$ (i.e., $\Delta\delta^{13}C$, $\Delta\delta D$, $\Delta\Delta^{13}CH_3D$, $\Delta\Delta^{12}CH_2D_2$). Panels with darker background colors indicate higher inconsistency.

Overall, the measurements of MIT standard samples conducted by UMD and UCLA show good agreement within the uncertainty range, and both laboratories utilize the Panorama. The consistency between UMD and MIT is also reasonably good. However, UMD and Utrecht exhibit slightly poorer consistency. Notably, Utrecht's measured values deviate from the

theoretically expected values of their standard samples, whereas UMD's measurements of Utrecht's standard samples got values closer to the corresponding theoretically-estimated values.

2.5.4. Absolute Reference Frame

For clumped isotopologues, an additional quality control method can be applied, which does not rely on standard samples from other laboratories and, in theory, is independent of bulk isotope measurements. This method involves anchoring the measurements to the (absolute) stochastic distribution coordinate, as introduced in Section 1.4.2. Briefly speaking, when methane is in a thermo-equilibrium state, its clumped isotopologue Δ values are solely a function of temperature and can be theoretically calculated (see the curve in Figure 1.17). If a series of thermally equilibrated samples can be generated at known temperatures and their clumped isotopologue compositions are measured, we can verify whether the instrument correctly measures clumped isotopologue compositions. In practice, however, bulk carbon and hydrogen isotope compositions must still be known. This allows for simultaneous verification of the instrument's accuracy in measuring bulk isotope compositions, and since clumped isotopologue compositions are derived from bulk isotope values, this information remains essential.

To produce thermally equilibrated methane, pure methane of known volume, concentration, $\delta^{13}C$, and δD should be sealed in glass tubes together with activated γ-Al_2O_3, Pt, or Ni as a catalyst. The sealed tubes containing methane should be kept at various temperatures (e.g., 20°C, 50°C, 200°C, 500°C) for several days (or even tens of days if the temperature is low) to allow methane to reach thermal equilibrium. The $\Delta^{13}CH_3D$ and $\Delta^{12}CH_2D_2$ values of these samples can

be theoretically predicted, and since $\delta^{13}C$ and δD are known, their $X(^{13}CH_3D)$ and $X(^{12}CH_2D_2)$ can also be calculated. Measuring this series of samples will allow calibration of measurements and facilitates inter-lab comparisons. This test has been implemented to varying degrees in most of the previously mentioned labs and reported in literature (Eldridge et al., 2019; Haghnegahdar et al., 2023; Liu et al., 2024; Ono et al., 2014; Sivan, Röckmann, et al., 2024; Wang et al., 2015; Wang et al., 2020; Young, Kohl, Lollar, et al., 2017; Zhang et al., 2025; Zhang, Snyder, et al., 2021). However, current challenges include methane loss or failure to reach equilibrium when using Pt or Ni for low-temperature heated catalytic intramolecular equilibrium.

Chapter 3: Controls on Concentrations and Clumped Isotopologues of Vehicle Exhaust Methane

This chapter has been published in

Controls on concentrations and clumped isotopologues of vehicle exhaust methane. PLoS ONE 20(2): e0315304, (2025). https://doi.org/10.1371/journal.pone.0315304

Authors and Affiliations:

Jiayang Sun[1,2,3*], Mojhgan A. Haghnegahdar[1,4], Julianne M. Fernandez[1,5], Cédric Magen[1], James Farquhar[1,6]

[1] Department of Geology, University of Maryland, College Park, Maryland, USA

[2] Air Resources Laboratory, National Oceanic and Atmospheric Administration, College Park, Maryland, USA

[3] Cooperative Institute for Satellite Earth System Studies, University of Maryland, College Park, Maryland, USA

[4] Smithsonian Environmental Research Center, Edgewater, Maryland, USA

[5] Global Monitoring Laboratory, National Oceanic and Atmospheric Administration, Boulder, Colorado, USA

[6] Earth System Science Interdisciplinary Center, University of Maryland, College Park, Maryland, USA

* Corresponding author: Jiayang Sun

E-mail: jiayangs@umd.edu (JS)

Jiayang Sun is the first author of this paper and has made significant contributions, including but not limited to conceptualization, methodology, validation, formal analysis, investigation, resources, data curation, writing – original draft, writing - review & editing, and visualization.

3.1. Abstract

Methane emissions from vehicle exhaust, as a source of methane, are often overlooked. However, in areas with high vehicle activity, the emissions can be substantial. There is a notable lack of characterization regarding the variable concentrations and isotopic signatures of methane in vehicle exhaust. This gap in knowledge limits our understanding of the mechanisms of methane production in vehicles and the factors controlling concentration variations and isotopic fractionation, which also makes it difficult to identify and reduce methane emissions from vehicle exhaust.

This study characterized the methane concentration ($[CH_4]$), methane-to-ethane ratio (C_2:C_1), methane carbon and hydrogen isotopes ($\delta^{13}C$ and δD), and methane clumped isotopologues ($\Delta^{13}CH_3D$ and $\Delta^{12}CH_2D_2$) of the vehicle exhaust methane endmember. $[CH_4]$ varied widely from below 1 ppm to more than 3000 ppm, potentially influenced by vehicle maintenance and operational phases. Ethane concentrations ($[C_2H_6]$) correlated with $[CH_4]$, yet C_2:C_1 varied significantly from 0.1% to 18.3%. The $\delta^{13}C$ and δD values of exhaust methane were less

negative than those of natural gas. A large portion of samples showed a positive linear relationship between [CH_4], $\delta^{13}C$ from -22‰ to -11‰, and δD values from -170‰ to -120‰, while their clumped isotopologues exhibit ~0.8‰ clumping in $\Delta^{13}CH_3D$ and ~-2.4‰ anti-clumping in $\Delta^{12}CH_2D_2$. A small portion of the samples exhibited distinct isotopic characteristics, with their δ13C and δD values either becoming significantly more positive or aligning closer to the composition of ambient air, while their $\Delta^{12}CH_2D_2$ values showed a marked increase, reaching between +25‰ to +33‰.

These concentration and isotope characteristics show trends that can be explained by a combination of processes, including 1) methane formation in the engine, 2) methane combustion in the engine, 3) methane oxidation by the catalytic converter, and 4) mixing with air. The observed isotopic fractionation can be explained by thermo equilibrium and Rayleigh fractionations. These processes, elucidated through isotopic and clumped isotopologue analyses, underscore the intricate dynamics and controls of vehicular methane emissions.

Key words: vehicle exhaust; methane; clumped isotopologues; engine combustion; catalytic converter

3.2. Introduction

In addition to carbon dioxide (CO_2), vehicles emit other greenhouse gases (GHGs) such as methane (CH_4) and ethane (C_2H_6). CH_4 is a potent GHG and accounts for approximately 1/3 of added radiative forcing on climate with its global warming potential 80 times that of CO_2 over a

20-year period (IPCC, 2021). However, these short chain alkanes emissions from vehicle exhausts are not subject to regulation or routinely monitored. Studies on vehicle exhaust have focused more on pollutants like NO_x, SO_2, CO, and particulate matter (Herndon et al., 2005; Streets & Waldhoff, 2000; Sun et al., 2018; Winkler et al., 2018), with less attention given to methane and ethane (Da et al., 2020; Nam et al., 2004; Zhang, Sun, et al., 2021). Engine combustion models indicated that methane could be produced through pyrolysis of fuel and radical reactions, under a high-temperature engine environment (Battin-Leclerc, 2008; Mehl et al., 2011), although combustion with oxygen and subsequent catalytic oxidation at the surface of the catalytic converter should consume methane (Takigawa et al., 2005). Methane emissions from vehicle exhaust were often considered negligible and were rarely included in global methane inventories (Saunois et al., 2020). Previous studies estimated global automobile methane emissions between 0.45 ± 0.12 Tg CH_4 yr^{-1} (Nam et al., 2004) and 0.5-3.4 Tg CH_4 yr^{-1} (Chanton et al., 2000), representing about 0.06% to 0.6% of estimated global total methane emissions (Saunois et al., 2020). However, studies have highlighted that in certain urban areas, vehicular methane emissions can significantly impact the local methane budget. For instance, isotope data suggested that automobile exhaust contributed up to 30% of the near-surface air methane in Nagoya, Japan, in 1993 (Nakagawa et al., 2005). Two traffic air samples from the LAX parking garage and Sepulveda tunnel in Los Angeles, USA, displayed isotopic signals similar to those of vehicle exhaust methane but only had background methane concentrations ($[CH_4]$), suggesting the sampled areas were saturated with vehicle exhaust (Townsend-Small et al., 2012).

Better constraining vehicular methane emissions is necessary for supplementing the methane budget, especially in urban areas, which have been identified as methane emission hotspots (Chen et al., 2022; Plant, Kort, Murray, et al., 2022; Ren et al., 2019; Ren et al., 2018). Urban areas have stationary high-flux point sources like landfills (Bakkaloglu et al., 2021; Spokas et al., 2011), wastewater treatment plants (Fernandez et al., 2022), and natural gas infrastructure (McKain et al., 2015), and also prevalent mobile low-flux sources like vehicle exhaust. While an individual vehicle may contribute minimally, the collective effect of numerous vehicles can slightly elevate urban background [CH_4]. However, the low enhancement level makes it challenging to identify and quantify the contributions from vehicle sources, if proxies other than [CH_4] were not used.

Methane carbon and hydrogen isotopes ($\delta^{13}C$ and δD) and ethane-to-methane ratio (C_2:C_1) are frequently used for apportionment of major methane sources such as natural gas leaks, microbial emissions, and agricultural contributions (Allen, 2016; Townsend-Small et al., 2012; Whiticar, 1999; Yacovitch et al., 2014). These indicators are particularly effective in differentiating between methane of microbial and thermogenic origin, as these sources usually yield methane with distinct isotopic signatures (Schwietzke et al., 2016; Whiticar, 1999). Thermogenic methane, which is formed under high pressure and temperature and is often found in natural gas reserves, generally exhibits less negative $\delta^{13}C$ and δD values and higher C_2:C_1 (Liu et al., 2019; Townsend-Small et al., 2016). In contrast, microbial methane, such as those from wetlands, presents more negative $\delta^{13}C$ and δD (Whiticar, 1999), coupled with lower (if not zero) C_2:C_1. Although vehicle exhaust methane originates from fossil fuels, it cannot be simply classified as

thermogenic methane because the formation and subsequent alteration processes (pyrolysis, combustion, and catalytic oxidation) can strongly fractionate methane isotopes.

Recent advances in measurement techniques have enabled the measurement of the relative abundance of methane doubly-substituted isotopologues (i.e. $^{13}CH_3D$ and $^{12}CH_2D_2$, also referred to methane clumped isotopologues) (Eiler et al., 2013; Gonzalez et al., 2019; Haghnegahdar et al., 2023; Ono et al., 2014; Young et al., 2016). The capability of distinguishing methane from various sources using methane clumped isotopologues have been preliminarily explored (Young, 2019). Thermogenic methane usually exhibits thermodynamic equilibrium clumping signals (Shuai, Douglas, et al., 2018; Stolper et al., 2015; Thiagarajan et al., 2020; Young, 2019), whereas microbial methane from surface and lab environments may show strong anti-clumping signals (Gropp et al., 2022; Rhim & Ono, 2022; Young, 2019). Oxidation processes, including microbial aerobic oxidation (Giunta et al., 2022; Krause et al., 2022), microbial anaerobic oxidation (Giunta et al., 2022; Liu, Harris, et al., 2023), and atmospheric sink reactions with OH and Cl radicals (Haghnegahdar et al., 2017; Haghnegahdar et al., 2023; Joelsson et al., 2016; Whitehill et al., 2017), tend to cause stronger clumping signals in residual methane.

Existing data is sparse in defining the isotopic composition of the vehicular methane endmember (Nakagawa et al., 2005). The clumped isotopologue signals of vehicle exhaust methane have not been measured before. This limits our ability to identify the contributions of vehicle exhaust and refine global methane isotope budgets (Chung & Arnold, 2021; Haghnegahdar et al., 2023; Rice et al., 2016). It also restricts our understanding of methane-related reactions that happened in the engine and catalytic converter environments, where key isotopic fractionation parameters of

pyrolysis and catalytic oxidation could be obtained. These parameters are crucial for understanding methane geochemical processes such as thermogenic methane formation (Dong et al., 2021), microbial methane oxidation (Giunta et al., 2022; Liu, Harris, et al., 2023; Ono et al., 2021), and atmospheric sink reactions (Haghnegahdar et al., 2017; Haghnegahdar et al., 2023; Joelsson et al., 2016; Whitehill et al., 2017).

This study will fill this data gap by characterizing the isotopic ($\delta^{13}C$ and δD) and clumped isotopologue ($\Delta^{13}CH_3D$ and $\Delta^{12}CH_2D_2$) compositions of vehicle exhaust methane, while also collecting [CH_4] and ethane concentration ([C_2H_6]) information. The dataset enables us to define the isotopic signatures of the vehicular methane endmember, determine if clumped isotopologues can be used to distinguish vehicular methane from other methane emissions, and explore processes and controlling factors in vehicular methane production and isotopic fractionation.

3.3. Materials and Methods

3.3.1. Sampling Strategies and Procedures

Although methane emissions from vehicle exhaust are not regulated, studies on other vehicle exhaust pollutants like CO and NO_x suggested that emission profiles can vary substantially among vehicles (USEPA, 2020), which could also apply to methane. The variation is expected to be influenced by factors such as vehicle type, engine design, ignition method, fuel type, air-to-fuel ratio, catalytic converter conditions, and operating conditions (USEPA, 2020). To pinpoint

endmember signatures, our study involved collecting exhaust samples from a wide array of vehicles, which included different brands, years of manufacturing, engine configurations, and fuel types.

Two sampling and measurement campaigns were carried out and summarized in Table 3.1. The first campaign aimed to delineate a range of isotope and isotopologue signatures for vehicle exhaust methane. We intentionally collected exhaust gases from some old and poorly maintained vehicles, with the assumption that these vehicles have different exhaust methane compositions compared to newer vehicles. The second campaign did not involve gas collection for isotope measurements but focused on expanding the [CH_4] and [C_2H_6] profiles. We employed a Mira Ultra LDS Infrared multi-pass laser gas analyzer (Aeris#302) from Aeris Technologies Inc. for direct, real-time exhaust monitoring. Volunteer vehicles on the University of Maryland (UMD) campus were randomly sampled, predominantly consisting of common household vehicles aged between 0 to 15 years.

Figure 3.1 schematically illustrates the sampling and measurement settings. The large-volume sampling method and real-time monitoring procedures are described in Appendix A Note A.1. Descriptions of each sampled vehicle can be found in Appendix A Note A.2. In the subsequent text, we refer to each sampled vehicle and the corresponding sample using the format “year make model”, followed by a brief description of the state (“cold” or “hot”), sometimes an operation status (ignition, idling, revving, or post-acceleration), and sometimes a numerical suffix (1 or 2) when necessary. For example, “1981 BMW 528i cold2” refers to the second sample collected from the 1981 BMW 528i right after a cold start in the idling state). In the figures, the “year

make" information is omitted for clarity. Definitions of these vehicle states can be found in Appendix A Note A.2.

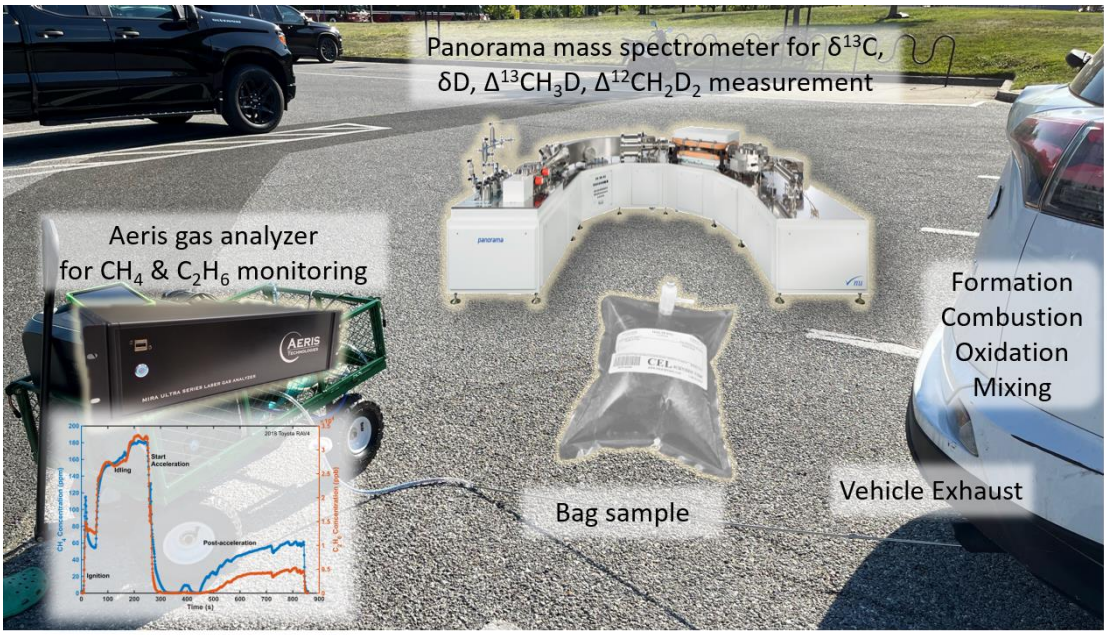

Figure 3.1. **Schematic diagram of sampling and measurement processes**.

Table 3.1. **Compiled information on sampled vehicles.** Samples collected or concentrations measured while the vehicles were idling, revving, after revving, right after a cold start, or after warmed up, were labeled as 'idle', 'accelerate', 'post-accelerate', 'cold', or 'hot', respectively. Detailed definitions of these vehicle conditions and operational phases can be found in Appendix A Note A.2.

	Model Year	Brand	Model	CH_4 (ppm) idle	C_2H_6 (ppb) idle					Collected?	Notes
Validation test sampling	1970	Dodge	Charger	299.3	20785.4[a]					Yes, Idle	No catalyst
	2017	Chevrolet	Sonic	9.8	24.4					Yes, Idle	/
	Model Year	Brand	Model	CH_4 (ppm) cold		C_2H_6 (ppb) cold	CH_4 (ppm) hot		C_2H_6 (ppb) hot	Collected?	Notes
First sampling campaign	1970	Dodge	Charger	1183.5		41412.5[a]	443.0			Yes, hot	No catalyst
	1981	BMW	528i	3101.8	1924.0		667.5	230.0		Yes, hot*2&cold*2	Poor condition
	2013	Kohler	XT675 (Mower)				204.0			Yes, hot	No catalyst
	1999	Volvo	S70	195.1			112.5			Yes, hot&cold	/
	1995	Mazda	MX-5 Miata				126.4			Yes, hot	/
	/	Ford	F-250				61.2			No	Long idling
	2017	Chevrolet	Sonic				2.0			Yes, hot	/
	2005	Gillig	Transit Bus				2.0			Yes, hot	Diesel
	2013	Gillig	Transit Bus				1.4			Yes, hot	Diesel
	2006	Ford	F-750 (Trash Truck)				9.2			Yes, hot	Diesel

	Model Year	Brand	Model	CH_4 (ppm) idle	C_2H_6 (ppb) idle	CH_4 (ppm) accelerate	C_2H_6 (ppb) accelerate	CH_4 (ppm) post-accelerate	C_2H_6 (ppb) post-accelerate	Collected?	Notes
Second sampling campaign	2015	Honda	Civic EX	5.2[a]	6.3	36.5[a]	697.9[a]	/	/	No	/
	2023	Chevrolet	Silverado	0.1	2.6	/	/	/	/		Brand new
	2017	Toyota	Prius Prime Hybrid	2.1	4.0	/	/	/	/		On electric engine
	2011	Hyundai	Elantra	15.7[a]	188.23[a]	77.36[a]	1183[a]	21.5[a]	125.5[a]		/
	2016	Toyota	Camry	35.9[a]	500.1[a]	154.8[a]	12973.5[a]	73.7[a]	7347.2[a]		/
	2013	Nissan	Altima	28.4[a]	1665.8[a]	217.6[a]	23739[a]	2.3	72.69[a]		Wet exhaust
	2019	Audi	A5	0.6	4.9	44.7	700.32[a]	7.1[a]	40.5		/
	2012	Honda	Civic coupe	20.3[a]	1271[a]	72.3[a]	5725.3[a]	1.0	4.8		/
	2009	Honda	Accord	58.1[a]	6816[a]	116.4[a]	20266.1[a]	4.03[a]	14.4		V6
	2015	Nissan	Altima	24.5[a]	148.73[a]	18.2	107.3[a]	9.3[a]	26.9		/
	2017	Alfa Romeo	Giulia Q4	25[a]	1460.9[a]	19.2	847.3[a]	10[a]	219.3[a]		Turbo
	2019	Hyundai	Kona	1.4	3.0	24.5	794.5[a]	0.1	3.0		/
	2023	Lexus	GX460	0.3	3.4	5.7	6.3	0.0	3.2		V8, brand new
	2018	Toyota	RAV4	180.2[a]	32815.7[a]	0.4	19.5	51.2[a]	4150.2[a]		/

[a]Concentrations were extrapolated with the assumption that the Aeris responded linearly to the concentration. These concentrations with label [a] could be considered as semi-quantitative. Concentrations without labels are strictly quantitative. See Section 3.2.2 for more details.

3.3.2. Methane and Ethane Concentration Measurements and Calibrations

Most of the methane concentration data, as well as all ethane concentration data, were acquired using the Aeris MIRA Ultra analyzers (#302). The Aeris employs mid-Infrared laser absorption spectroscopy, detecting the characteristic transition frequencies of target molecules. According to our tests, this Aeris #302 has a typical precision (1SD) of 1.6 ppb for CH_4 and 0.16 ppb for C_2H_6 with a one-second integration time.

The Aeris instrument was calibrated at the NOAA Air Resources Lab, College Park, Maryland. We used Aeris to measure three tank compressed standard gases with known methane concentrations (#19 at 1925.19 ppb, #14 at 2204.10 ppb, and #18 at 2528.95 ppb) and zero air for methane calibration. For ethane calibration, we used a mass flow controller to mix 2 standard litre per minute zero air with compressed house natural gas (known 4.83 ppm ethane) from 0 to 20 standard cubic centimeters per minute at 2 standard cubic centimeters per minute increments, to serve as standard gases. Each standard sample was measured for over 5 minutes to ensure thorough flushing and eliminate instrument delay. We used the average of the last 3 minutes of each measurement period to calculate the average. The measured averages were linearly fitted against theoretical concentrations to obtain a correction equation that would be applied to real measurements. The instrument uncertainty was derived from the 1SD of the last 3 minutes of zero air measurements. However, these calibration procedures are designed for ambient air monitoring, but not for direct vehicle exhaust measurements, which often exceed calibration ranges. For the data measured by Aeris, only methane concentrations between 0-2.53 ppm and ethane concentrations between 0-51.3 ppb can be considered strictly quantitative. Data beyond

this calibration range are extrapolated based on the assumption of the instrument's linear response to concentrations, with the upper limits of this linear response typically being 10,000 ppm for CH_4 and 1,000 ppm for C_2H_6, according to the manufacturer's specifications. Direct measurements of vehicle exhaust using Aeris are discouraged due to potential optical contamination and the possibility that concentrations may exceed the instrument's linear response range. In this study, no concentration values exceeded the manufacturer's reported upper limits for linear response. Thus, concentration measurements in this study are generally reliable. If the assumption of linear response is deemed invalid, then methane concentration data above 2.53 ppm and ethane concentration data exceeding 51.3 ppb measured by Aeris should be considered semi-quantitative.

For bag samples collected before we obtained the Aeris, methane concentrations were determined using a Shimadzu® GC-8AIF Gas Chromatograph (GC). Ethane concentrations were not measured. Injected from a 1 ml sample loop, samples were carried by N_2 carrier gas at approximately 60 ml/min through a stainless-steel GC column with an inner diameter (ID) of 1/8 inch, packed with 2.5 m of 80/100 pre-conditioned HayeSep Q. H_2, O_2, N_2, and CO were eluted, while CH_4 and CO_2 were retained in the column. Subsequently, N_2 carrier gas again carried residues in the column through another stainless-steel column with an ID of 1/8 inch, packed with 0.5 m of 100/100 Shimalite Q. The columns' temperatures were held at 80 °C. CH_4 peak signals were detected using a Flame Ionization Detector (FID), with air and H_2 gas flows set to approximately 300 ml/min and 50 ml/min, respectively, for combustion in the FID. Concentrations measured by GC are all quantitative.

3.3.3. Extraction and Purification of Bag Samples

Before taking measurements, each bag sample underwent extraction and purification processes to isolate pure methane from other gases, following the procedures outlined in Haghnegahdar et al. (2023). Briefly speaking, the sample gas was dried using silica gel and directed through a large U-trap filled with Hayesep DB, which was cooled with liquid nitrogen. This step effectively trapped almost all sample gas in the large U-trap except partially removing N_2 and O_2. Upon thawing the large U-trap, the trapped gas was redirected through a small U-trap filled with Hayesep DB, also cooled with liquid nitrogen. At this stage, the majority of N_2 and O_2 were removed, while CH_4 and Kr were fully retained. The trapped gas was warmed to -120°C using an ethanol slush and held at this temperature for 30 minutes to further remove N_2 and O_2. The residual gas underwent GC separation for final purification. The GC column was packed with 25 feet of 60-80 mesh MolSieve 5A and maintained at 56°C.

Compared to the method for normal air samples (Haghnegahdar et al., 2023), the extraction of vehicle exhaust samples requires two additional steps to remove substantial amounts of CO_2 and H_2O. Failure to remove CO_2 and H_2O could result in process inefficiency and possibly cause sample fractionation. The sample gas was first reacted with a high-concentration (~50%w/v, ~20°C) NaOH aqueous solution by pulling the gas through a gas frit into the solution. The NaOH solution was aerated with N_2 for 3 hours before use, to remove CH_4 that has been reported in NaOH pellets (Magen et al., 2014). A glass condenser cooled to liquid nitrogen temperature was utilized subsequently to trap any remaining CO_2 and H_2O. Pressure monitoring on the purification line confirmed the efficiency of these added steps in removing CO_2 and H_2O. The

vehicle exhaust samples also contained other impurities, which were removed during the bubbling process, as evidenced by the NaOH solution turning yellow and forming an oily layer. Given the substantial restriction on the gas flow rate by the gas frit and NaOH solution, the extraction process could take more than 8 hours, instead of 5 hours for normal air samples. Hence, we rigorously inspected and reinforced the extraction line prior to use for optimal airtightness.

3.3.4. Methane Isotopes and Isotopologues Measurement

The pure methane was analyzed using the Panorama mass spectrometer for isotope and isotopologue measurements. The Panorama is a high-resolution, high-sensitivity, double-focusing gas-source mass spectrometer with mass resolving power (MRP) that can exceed 50,000. This high MRP allows Panorama to distinguish between isotopologue ion beams with closely aligned masses such as $^{13}CH_3D^+$, $^{13}CH_5^+$, and $^{12}CH_2D_2^+$. Detailed specifications of the Panorama instrument are provided by Young et al. (2016). The methodologies and configurations used for methane clumped isotopologue measurements in the UMD lab are detailed in Haghnegahdar et al. (2023).

Bulk carbon and hydrogen isotopes are reported in ratio differences (δ notation):

$$\delta^{13}\mathrm{C}_{\mathrm{sample-standard}}(‰) = \left(\frac{\left({}^{13}\mathrm{C}/_{12}\mathrm{C}\right)_{\mathrm{sample}}}{\left({}^{13}\mathrm{C}/_{12}\mathrm{C}\right)_{\mathrm{standard}}} - 1 \right) * 1000 \qquad (3.1)$$

$$\delta\mathrm{D}_{\mathrm{sample-standard}}(‰) = \left(\frac{\left({}^{\mathrm{D}}/_{\mathrm{H}}\right)_{\mathrm{sample}}}{\left({}^{\mathrm{D}}/_{\mathrm{H}}\right)_{\mathrm{standard}}} - 1 \right) * 1000 \qquad (3.2)$$

Where the standards are usually Vienna Pee Dee Belemnite (V-PDB) for carbon isotopes and Vienna Standard Mean Ocean Water (V-SMOW) for hydrogen isotopes (Coplen, 1994, 1995).

Methane clumped isotopologue notations can be defined in a similar manner to carbon and hydrogen isotopes:

$$\delta^{13}\mathrm{CH_3D}(‰) = \left(\frac{\left({}^{13}\mathrm{CH_3D}/{}_{12}\mathrm{CH_4}\right)_{\mathrm{sample}}}{\left({}^{13}\mathrm{CH_3D}/{}_{12}\mathrm{CH_4}\right)_{\mathrm{standard}}} - 1 \right) * 1000 \quad (3.3)$$

$$\delta^{12}\mathrm{CH_2D_2}(‰) = \left(\frac{\left({}^{12}\mathrm{CH_2D_2}/{}_{12}\mathrm{CH_4}\right)_{\mathrm{sample}}}{\left({}^{12}\mathrm{CH_2D_2}/{}_{12}\mathrm{CH_4}\right)_{\mathrm{standard}}} - 1 \right) * 1000 \quad (3.4)$$

Where the standard could be methane characterized by V-PDB carbon isotope composition and V-SMOW hydrogen isotope composition, and followed intra-molecular stochastic distribution, which refers to the state of purely random combinations of ^{12}C, ^{13}C, H, and D intramolecularly to form methane molecules (Young et al., 2016), i.e.:

$$X_{^{13}CH_3D,\ stochastic} = 4 * X_{^{13}C} * X_D * (X_H)^3 \quad (3.5)$$

$$X_{^{12}CH_2D_2,\ stochastic} = 6 * X_{^{12}C} * (X_D)^2 * (X_H)^2 \quad (3.6)$$

$X_{^{13}\mathrm{C}}$ and X_{D} represent the proportions of ^{13}C and ^{2}H atoms in the total carbon and hydrogen atoms, respectively. The coefficients 4 and 6 are derived from the symmetry of the isotopically-substituted methane molecules.

A more commonly adopted notation for methane clumped isotopologue describes the level of enrichment or depletion of $^{13}CH_3D$ and $^{12}CH_2D_2$ relative to the stochastic distribution within the sample (Eiler & Schauble, 2004; Young et al., 2016):

$$\Delta^{13}CH_3D(‰) = \left(\frac{X_{^{13}CH_3D}}{X_{^{13}CH_3D,\ stochastic}} - 1\right) * 1000 \quad (3.7)$$

$$\Delta^{12}CH_2D_2(‰) = \left(\frac{X_{^{12}CH_2D_2}}{X_{^{12}CH_2D_2,\ stochastic}} - 1\right) * 1000 \quad (3.8)$$

$X_{^{13}CH_3D}$ and $X_{^{12}CH_2D_2}$ are the proportion of $^{13}CH_3D$ and $^{12}CH_2D_2$ molecules in the total methane molecules of the sample. Under these definitions, the clumped isotopologue cap-delta signals of methane are independent from the sample's bulk ^{13}C and D abundances. In practical applications, we use approximate formulas to calculate $\Delta^{13}CH_3D$ and $\Delta^{12}CH_2D_2$ (Haghnegahdar et al., 2023):

$$\Delta^{13}CH_3D(‰) = \left(\left(1 + \frac{\delta^{13}CH_3D}{1000}\right) \Big/ \left(1 + \frac{\delta^{13}CH_4}{1000}\right) * \left(1 + \frac{\delta^{12}CH_3D}{1000}\right) - 1\right) * 1000 \quad (3.9)$$

$$\Delta^{12}CH_2D_2(‰) = \left(\left(1 + \frac{\delta^{12}CH_2D_2}{1000}\right) \Big/ \left(1 + \frac{\delta^{12}CH_3D}{1000}\right)^2 - 1\right) * 1000 \quad (3.10)$$

The errors introduced by using these approximations are much smaller than the measurement uncertainties.

3.4. Results and Discussion

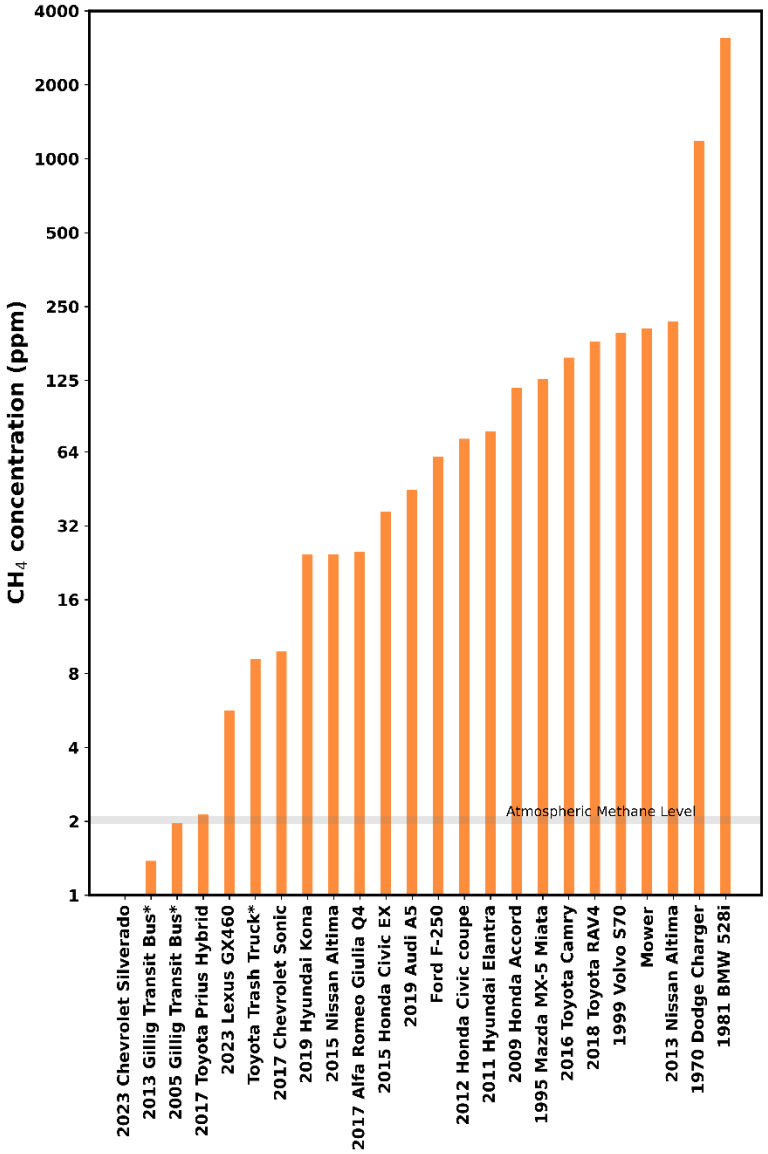

Figure 3.2**. Methane concentrations of vehicle exhaust samples.** The plotted concentrations are peak values among the vehicle operational cycle or states; therefore, the heights of the bars are not fully representative of the total emission fluxes from the corresponding vehicles. Asterisks (*) in labels mark diesel vehicles. The Y-axis is scaled logarithmically. Detailed information on individual vehicles can be found in Section 3.3.1, Table 3.1, and Appendix A Note A.2.

3.4.1. Methane Concentration of Vehicle Exhaust

Our dataset reveals that vehicular exhaust contains significant amounts of methane, contrary to the conventional assumption that high-temperature combustion in engines should oxidize nearly all methane. Methane concentrations are reported in Figure 3.2 and Table 3.1, with the highest exceeding atmospheric levels by a thousand times and the lowest below atmospheric levels. More discussions for each vehicle can be found in Appendix A Note A.3. While lacking quantitative parameters to assess vehicle condition, we infer that well-maintained and newer vehicles tend to have lower [CH_4], whereas vehicles in suboptimal conditions (for instance, right after cold start, with loose plug wires, or with malfunctioning catalytic converters) exhibit elevated [CH_4] in the exhaust.

Continuous monitoring of vehicle exhaust throughout the operation cycles (ignition-idling-revving-idling) revealed two key observations: 1) vehicles usually have transient [CH_4] spikes at the moment of ignition and the onset of revving (Figure A.2); 2) revving may result in either a moderate increase (Figure A.2b) or a substantial decrease (Figure A.2c) in [CH_4]. This behavior may reflect combustion dynamics within the engine influenced by fuel delivery systems. As extra fuel is added for acceleration, contemporary vehicles employ computerized control of fuel injection and ignition timings, optimizing air-to-fuel ratio and combustion efficiency (Ault et al., 1994), and may have smaller enhancements compared to older engines with carburetors.

Overall, [CH_4] data imply that vehicular exhaust emissions may follow a fat-tail distribution (i.e., a minority of events/units contribute most of the emissions), a pattern similar to that of natural

gas system emissions (Lyon et al., 2015). Even if vehicles in poor condition comprise only a small fraction of the total fleet, they could still account for a significant proportion of vehicular methane emissions.

3.4.2. Ethane Concentration of Vehicle Exhaust

A wide range of [C_2H_6] was observed in vehicle exhaust (Figure A.3), extending from a few ppb to more than 30,000 ppb. As can be seen from Figure A.2, [CH_4] and [C_2H_6] in vehicle exhaust increased and decreased almost simultaneously, indicating that they were generated and consumed by the same processes in vehicle engines and catalytic converters.

Despite the concentrations changing simultaneously, the [C_2H_6]-[CH_4] plot (Figure 3.3) reveals substantial variability in C_2:C_1, ranging from approximately 0.1% to 18.3% across different vehicles. Although the production mechanisms for CH_4 and C_2H_6 in vehicles are linked, preferences for producing CH_4 or C_2H_6 differ based on the vehicle's condition and operational state. Larger ratios often correlated with higher [C_2H_6], suggesting that vehicles in poorer conditions that produced more CH_4 also contributed higher amounts of C_2H_6. Very high [CH_4] and [C_2H_6] in some vehicles could yield spikes during roadside and/or on-road monitoring.

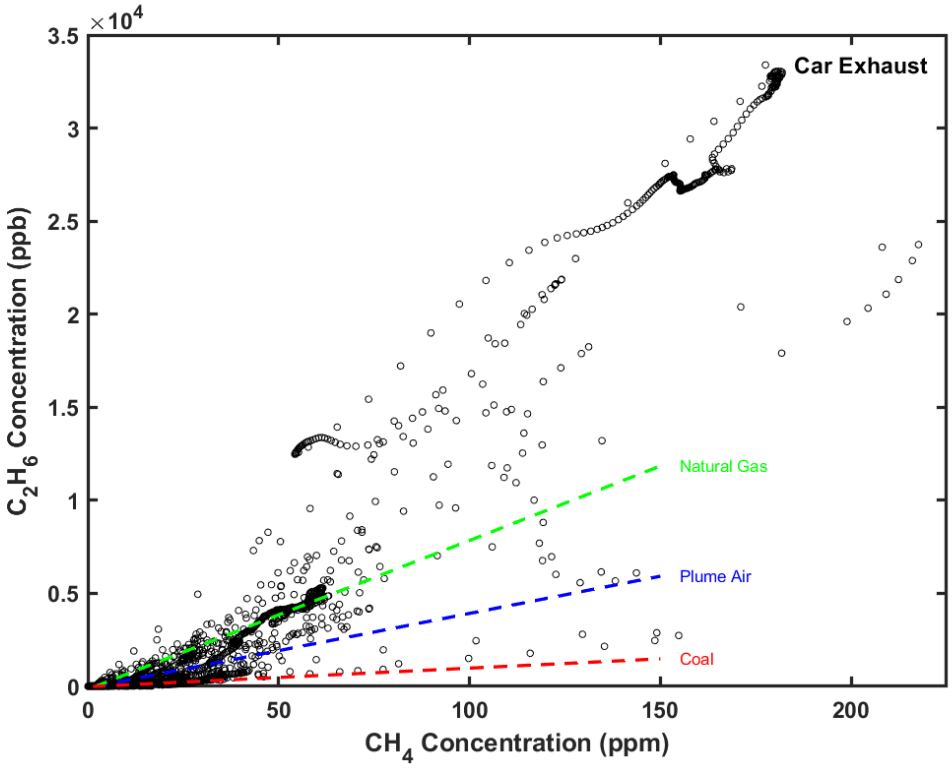

Figure 3.3**. [C_2H_6] vs. [CH_4] of all sampled vehicle exhausts in the second sampling campaign.** The campaign continuously monitored [CH_4] and [C_2H_6] of the exhaust during operation cycles (ignition, idling, acceleration, post-acceleration). Three reference lines indicate approximate C_2:C_1 for Baltimore natural gas (green), plume air observed in the air over the Baltimore-Washington Area (blue), and coal emissions (red).

Aircraft monitoring studies reported C_2:C_1 of 3.3% ± 0.35% and 4.31% ± 0.63% in the air over the Baltimore-Washington Area during the winters of 2015 and 2016, respectively (Ren et al., 2018). They also reported data from natural gas samples provided by the Baltimore Gas & Electric Company, showing C_2:C_1 of 8.40% and 7.81% for the same periods. A ratio of 2.3% has been reported in the air above the Marcellus Shale production region (Ren et al., 2019), with a ratio of 6.7% from direct Marcellus Shale well samples (Colón-Román & Ruppert, 2014). Stable coal vents in the San Juan Basin were reported to have C_2:C_1 of 1.28% ± 0.11% (Meyer et al., 2022). In general, coal emissions have a lower C_2:C_1 than natural gas, often less than 1 wt-% (Schwietzke et al., 2014). The highly variable C_2:C_1 in vehicle exhaust overlapped the range

from coal piles to natural gas wells, thus the ratio alone may not serve as an indicator for differentiating vehicle exhaust from thermogenic sources, but the variability in C_2:C_1 as vehicles transitioned through different operational states on the road might provide a signature for use during monitoring that distinguishes vehicle emissions from more homogenous sources like natural gas and coal.

3.4.3. Carbon and Hydrogen Isotopes of Vehicle Exhaust

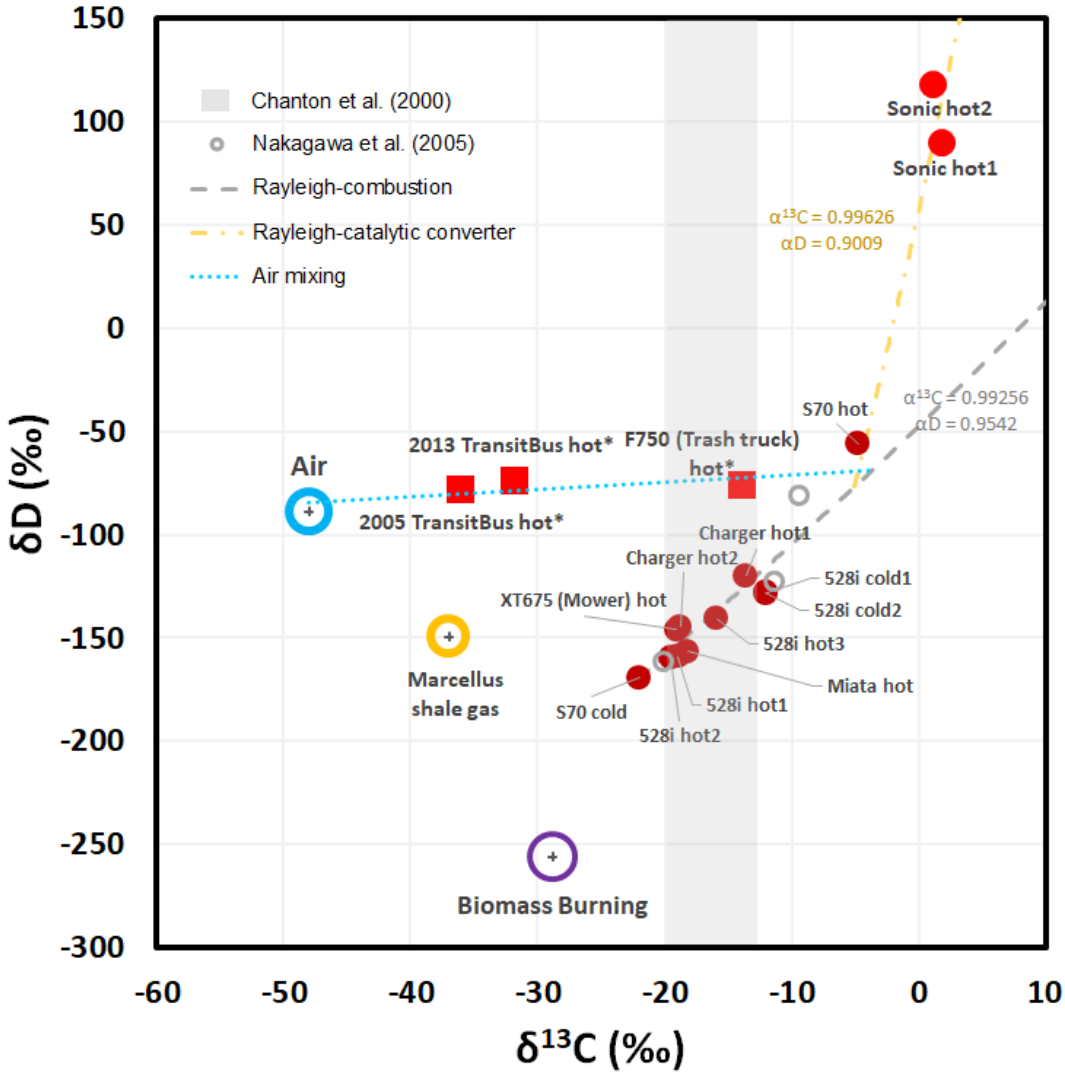

Figure 3.4. **δD-δ^{13}C plot of vehicle exhausts.** Red solid circles are for gasoline vehicles. The red squares are for diesel vehicles. Approximate compositions of air (blue ring), natural gas (yellow ring), and biomass burning (purple ring) methane are shown in the figure. Three averaged exhaust compositions derived from Nakagawa et al. (2005) are shown as gray circles. The gray shaded area marks the estimated range of exhaust carbon isotopes reported by Chanton et al. (2000). Error bars (2SD) with these measured data points are smaller than the symbols. The gray dashed line and the yellow dash-dotted line are isotopic compositions of the residue methane following the Rayleigh fractionation caused by combustion and catalytic converters, from different initial compositions, with different isotopic fractionation factors. The blue dotted line is the mixing line of air with an exhaust.

Table 3.2. **Methane concentrations, carbon isotopes, hydrogen isotopes, and clumped isotopologues of vehicle exhaust samples collected in the first sampling campaign**. Uncertainties reported in this table are 2SD.

	$[CH_4]$ ppm	$\delta^{13}C$ ‰	σ ‰	$\delta^{13}CH_3D$ ‰	σ ‰	δD ‰	σ ‰	$\delta^{12}CH_2D_2$ ‰	σ ‰	$\Delta^{13}CH_3D$ ‰	σ ‰	$\Delta^{12}CH_2D_2$ ‰	σ ‰
S70 hot	112.49	-4.76	0.15	-60.00	1.30	-56.06	0.49	-113.41	4.84	0.6	1.5	-5.0	5.5
S70 cold	195.09	-21.99	0.03	-186.14	0.72	-169.19	0.20	-310.99	1.81	1.6	0.9	-1.8	2.7
528i cold1	3101.78	-11.97	0.03	-138.62	0.67	-128.33	0.06	-239.96	0.97	0.2	0.8	0.3	1.3
528i cold2	1923.95	-12.02	0.03	-137.75	0.64	-127.90	0.22	-238.14	1.96	0.7	0.8	1.7	2.6
528i hot1	667.46	-18.93	0.02	-175.35	0.42	-159.06	0.09	-294.62	1.27	-0.4	0.5	-2.5	1.8
528i hot2	667.46	-19.51	0.05	-173.43	0.90	-159.44	0.62	-294.70	3.22	2.9	1.3	-1.8	4.8
528i hot3	230.00	-15.91	0.01	-154.26	0.29	-140.82	0.09	-265.26	1.45	0.3	0.4	-4.7	2.0
Charger hot1	/	-13.61	0.02	-130.91	0.82	-119.73	0.09	-224.32	1.40	0.9	1.0	1.0	1.8
Charger hot2	443.03	-18.76	0.46	-159.99	0.75	-144.58	1.56	-271.23	2.30	0.8	2.1	-4.1	4.8
Miata hot	126.39	-18.21	0.03	-170.99	0.62	-156.40	1.55	-290.94	1.81	0.9	2.0	-3.7	4.5
Sonic hot1	1.38	1.81	0.11	95.61	2.10	90.39	0.77	218.78	6.55	3.0	2.1	25.1	5.7
Sonic hot2	1.96	1.10	0.02	120.96	0.65	118.64	2.14	285.99	4.44	1.0	2.0	27.7	5.3
XT675 (Mower) hot	204.01	-19.07	0.05	-161.69	0.82	-145.91	0.26	-274.84	2.21	0.6	1.0	-5.9	3.1
2005 TransitBus hot*	1.96	-36.11	0.04	-110.05	0.15	-77.83	0.15	-123.96	1.98	1.2	0.2	30.1	2.4
2013 TransitBus hot*	1.38	-31.79	0.05	-101.85	1.00	-74.04	0.43	-114.39	3.15	1.8	1.2	32.9	3.8
F750 (Trash truck) hot*	9.15	-13.91	0.01	-87.93	0.28	-75.93	0.09	-138.32	1.33	0.9	0.3	9.1	1.6

The $\delta^{13}C$ and δD of vehicle exhaust exhibit considerable variability (Figure 3.4 and Table 3.2). Most vehicle exhaust methane samples are more enriched in ^{13}C than natural gas methane and biomass burning methane, and more enriched in deuterium (D) relative to biomass burning methane but similar to natural gas methane. In comparison to the $\delta^{13}C$ of gasoline, which has been reported to range from -34‰ to -21‰ with an average of approximately -27‰ (Smallwood et al., 2002), methane emissions from vehicle exhaust present different levels of enrichment in ^{13}C ($\delta^{13}C$ > -22‰ for all vehicle samples, with the highest $\delta^{13}C$ reaching 2‰) but show no significant difference in δD values compared to the range reported for a global set of gasoline, which varies between -70% and -145‰ (O'Sullivan & Kalin, 2008).

A positive linear correlation between $\delta^{13}C$ and δD values is observed in the majority of exhaust samples (Figure 3.4). This correlation aligns with a previous work (Nakagawa et al., 2005), which attributed this relationship to the effect of catalytic converters. A similar trend was observed with $\delta^{13}C$ values and [CH_4] (Chanton et al., 2000), where higher [CH_4] correlated with more negative $\delta^{13}C$ values, suggesting this pattern relates to combustion efficiency, which is also shown in our data (Figure 3.5). Exhaust samples from a few cleaner gasoline vehicles and all diesel vehicles proved to be exceptions from linear relationships, indicating that methane emitted from vehicle exhaust is the result of multiple processes that produce and consume it.

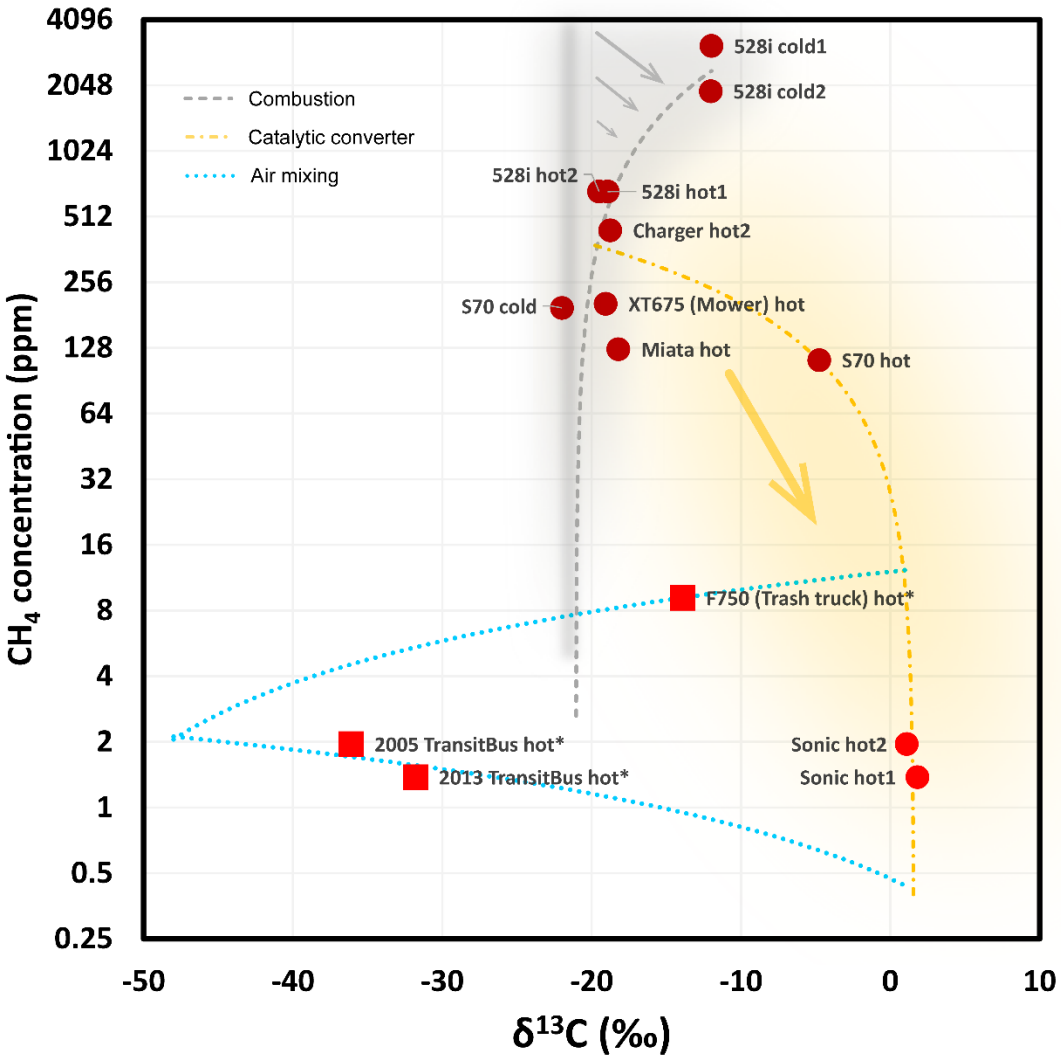

Figure 3.5. **[CH_4]-$\delta^{13}C$ plot of vehicle exhausts.** The [CH_4] axis is on the log scale. Symbols, colors, and error bars are the same as in Figure 3.4. The two blue dotted curves are linear mixing arrays for the trash truck, and two school shuttle buses, with air respectively. The gray dashed line is plotted by linear fittings of the majority of vehicles, and the yellow dash-dotted line is the linear fitting of samples from 2017 Chevrolet Sonic hot. The gray band indicates the methane produced during the high-temperature methane formation with consistent $\delta^{13}C$ but different [CH_4]. The formed methane underwent fractionation in the direction indicated by the gray arrow through combustion with $\alpha_{13C} = 0.9926$, resulting in compositions as suggested by the gray area. The yellow arrow shows the effect of methane oxidation on the catalytic converter with $\alpha_{13C} = 0.9985$, resulting in methane compositions represented by the yellow area. The gray and yellow areas are schematic ranges only.

We considered four processes to explain the observed trends and outliers, including (1) the formation of methane under high-temperature burning (Process #1 methane formation), followed by (2) the combustion of methane while still under high-temperature before expelled from the cylinder to the exhaust stroke (Process #2 methane combustion), (3) the oxidation of methane in the exhaust stroke by the catalytic converter (Process #3 catalytic oxidation), and (4) mixing of exhaust methane with air methane (Process #4 air mixing).

The formation of methane occurs primarily through collisions of methyl radicals with hydrogen radicals, following radical chain reactions starting from gasoline (Battin-Leclerc, 2008; Mehl et al., 2011). Although the reaction $CH_3 \cdot + H \cdot + M \leftrightarrow CH_4 + M$ thermodynamically favors the formation of methane, methane acts as a catalyst in the decomposition of small carbon-hydrogen-oxygen compounds such as H·, ·OH, HO2·, HCO·, CO·, and CH3O· (Mehl et al., 2011), causing newly formed methane to approach inter- and intramolecular isotope equilibrium, within such a high temperature closed system. There are no reference values available for the fractionation coefficient between gasoline and formed methane resulting from this step. If we assume the $\delta^{13}C$ of gasoline is -27‰ (Smallwood et al., 2002), then the fractionation for this step may be +4-5‰. If assuming minimal fractionation (Chanton et al., 2000), then local gasoline $\delta^{13}C$ composition is approximately -21‰.

In the later parts of the combustion process, the production of alkyl radicals slows due to the consumption of fuel, and the consumption of methane starts by combustion with O_2. The combustion process preferentially consumes $^{12}CH_4$ (Chanton et al., 2000), leading to the enrichment of $^{13}CH_4$ and $^{12}CH_3D$ in the residual methane. A higher combustion efficiency, and

possibly higher air-to-fuel ratio, signifies a greater proportion of methane being consumed, resulting in more pronounced isotopic fractionation in the residual methane. The isotopic effect of the combustion process can be simulated with Rayleigh fractionation (gray dashed line in Figure 3.4):

$$\delta^{13}C_{residue}(‰) + 1000 = \left(1000 + \delta^{13}C_{initial}\right) * f^{\alpha_{13C/12C}-1} \quad (3.11)$$

$$\delta D_{residue}(‰) + 1000 = (1000 + \delta D_{initial}) * f^{\alpha_{D/H}-1} \quad (3.12)$$

Here, f represents the proportion of residual methane relative to the initial amount of methane prior to combustion. We take the isotopic compositions of the 1999 Volvo S70 cold sample as the initial values. α is the kinetic isotope fractionation coefficient, which is the ratio of the rate constant of the heavy isotope to the light isotope in a reaction from the reactant to the product, i.e., k_{heavy}/k_{light}. We adopt kinetic isotope fractionation factors of ε_{13C} = +7.5‰ ($\alpha_{13C/12C}$ = 0.9926) and ε_{D} = +48‰ ($\alpha_{D/H}$ = 0.9542) as reported by Nakagawa et al. (2005). It should be noted that this set of α values was calculated with the assumption that the observed isotopic variations were attributed solely to the effect of the catalytic converter, while in this study we use them to describe the fractionation attributed to the combustion process. The mechanism would be different, but the approximate magnitude of the Kinetic Isotope Effect (KIE) could be a possible starting point.

Concentration may not show monotonic shifts as isotopes behave, for different exhaust samples that follow Rayleigh fractionation, because it is the proportion rather than the concentration of residual methane that matters. A higher [CH_4] in the exhaust does not necessarily imply lower combustion efficiency or smaller fractionation. Instead, it could be a consequence of substantial methane production in process #1 methane formation. As shown in Figure 3.5, process #1

methane formation can generate methane with isotope compositions close to that of gasoline but with varying [CH_4]. This is followed by process #2 methane combustion, which shifts unburnt methane to more positive $\delta^{13}C$ values following the gray arrows with fixed slopes proportional to $1/(\alpha_{13C,\ process\#1}-1)$. Process #2 combustion results in the gray area in Figure 3.5, with the gray dashed line depicting a case in which a higher proportion of methane is combusted if higher [CH_4] is produced in process #1, thus exhibiting greater fractionation from equilibrium value.

In process #3 catalytic oxidation, unburned methane is expelled into the exhaust system and is further oxidized if a catalytic converter is present. The isotopic effect caused by the catalytic converter might account for the distinct isotope compositions observed in the 1999 Volvo S70 hot sample and two 2017 Chevrolet Sonic hot samples, which have significantly positive $\delta^{13}C$ and δD values but low [CH_4]. This process can also be simulated with Rayleigh fractionation, as illustrated by the yellow dash-dotted line in Figure 3.4, starting with an initial composition of the 1999 Volvo S70 hot sample, coupled with $\alpha_{13C} = 0.9963$ and $\alpha_D = 0.9009$ to reach the composition of the 2017 Chevrolet Sonic hot when approximately 83% of methane are being oxidized. However, this is an underdetermined system where any values that meet the slope given by $(\alpha_D - 1)/(\alpha_{13C} - 1)$ will fit (Blunier et al., 2002). When considering concentrations, this Rayleigh fractionation process has a steeper slope proportional to $1/(\alpha_{13C,\ process2}-1)$, as shown by the yellow arrow in Figure 3.5, resulting in the yellow area. The greater proportion of methane consumed by the catalytic converter, the lower [CH_4] and the more positive isotopic composition it becomes. The yellow dash-dotted linear fitting curve does not have physical meaning but suggests that the 1999 Volvo S70 hot and 2017 Chevrolet Sonic hot samples likely have different

initial compositions and α values. Figure 3.4 and Figure 3.5 simplified the scenario by grouping them under one numerical context.

Diesel vehicles exhibit unique isotope profiles. Diesel engines rely on compression ignition of diesel fuel, which adiabatically heats and ignites the air-rich fuel-poor mixtures, while gasoline engines use spark ignition, which directly ignites the air-fuel mixture with sparks. The higher air-to-fuel ratios in diesel engines result in more complete combustions and notably lower [CH_4] in the exhaust. One time that diesel engines may operate with more fuel supply would be the trash truck under open throttle acceleration with load (2006 Ford F-750 trash truck hot sample).

Mixing a small amount of fresh air methane into the exhaust could impact the measured isotopic signatures, especially when the [CH_4] from the uncontaminated exhaust gas is low. This contamination could be the unburnt residue air methane that was sucked into the engine, or fresh air leaked into the sample bags from the outlet of the exhaust pipe during sampling. This mixing effect is supported by the linear fitting trend in Figure 3.5 (blue dotted line) between the air compositions and two diesel vehicle exhaust compositions, extending to possible compositions of exhaust after significant oxidation by the catalytic converter (yellow area in Figure 3.5). The isotopic patterns of $\delta^{13}C$-δD in Figure 3.4 also support a mixing trend, with the linear fitting (blue dotted line) pointing to an isotopically highly-enriched endmember. This potential interference of fresh air methane could apply to most of the vehicle samples but should have less impact on higher [CH_4] samples.

The analysis of isotopic fractionation processes allows us to define several ranges for the isotopic values of methane in vehicle exhaust based on the methane generation process. However, due to limitations in sample size and vehicle composition, these samples inevitably cannot represent the entire US fleet on the road. The methane isotopic signal in vehicle exhaust should not be assigned a single value; instead, it varies across different stages of formation, combustion, and catalytic conversion, ultimately influenced by vehicle operation and maintenance conditions. Generally, exhaust containing moderate concentrations of methane (100 to 1000 ppm) is predominantly influenced by high-temperature methane formation with low combustion consumption, tending to exhibit isotopic signals similar to that of gasoline, with $\delta^{13}C$ around -21‰ and δD near -170‰. In contrast, high-concentration methane (>1000 ppm) exhaust typically undergoes a higher proportion of methane combustion, resulting in less negative $\delta^{13}C$ and δD values, where $\delta^{13}C$ can reach -10‰ and δD approximately -120‰. Furthermore, low-concentration methane (<100 ppm) exhaust, due to the relatively greater contribution of catalytic oxidation effects, tends to have extreme positive isotopic compositions, with $\delta^{13}C$ possibly reaching 0‰ and δD reaching +100‰.

3.4.4. Methane Clumped Isotopologues of Vehicle Exhaust

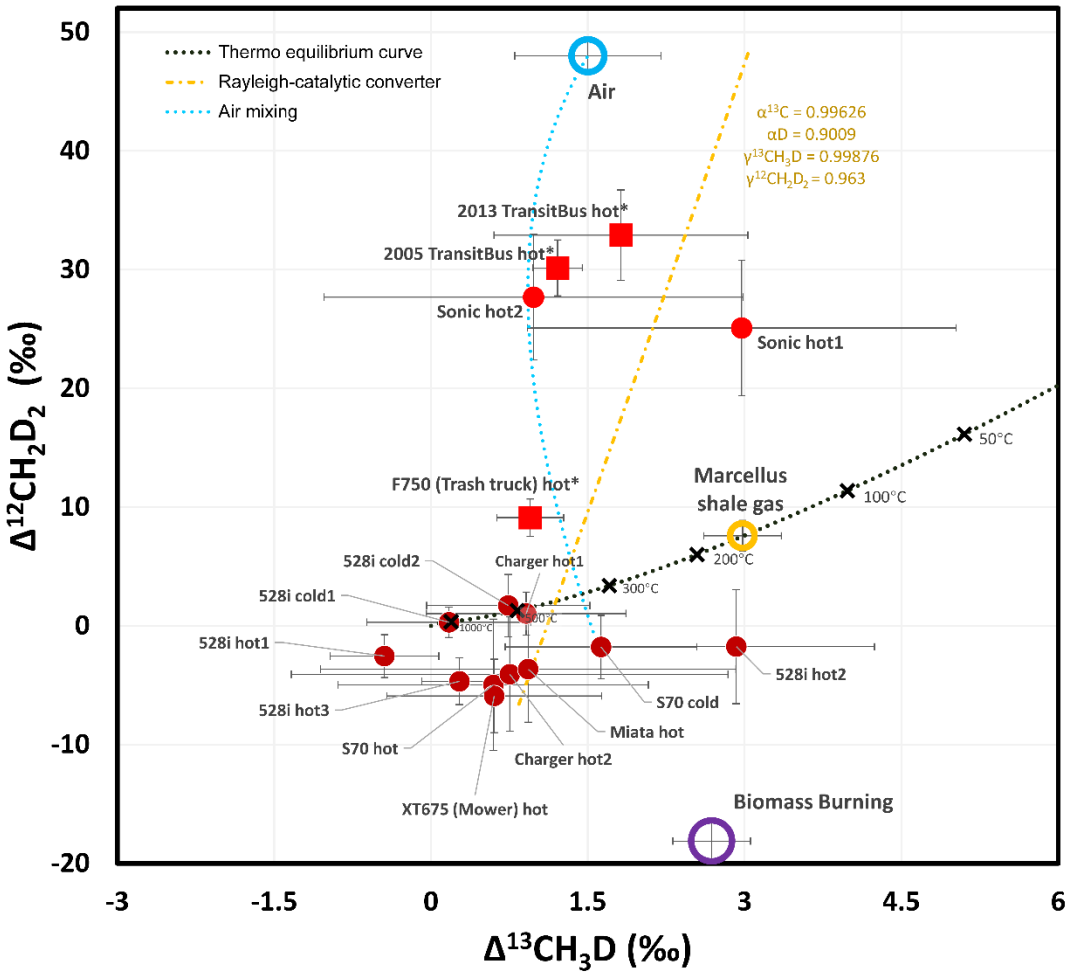

Figure 3.6. **$\Delta^{12}CH_2D_2$-$\Delta^{13}CH_3D$ plot of vehicle exhaust samples.** Symbols, curves, and colors are the same as in Figure 3.4. Error bars are showing 2SD uncertainties after propagation. The black dotted line is the thermo-equilibrium curve for methane clumped isotopologues taken from Young, Kohl, Lollar, et al. (2017).

The methane clumped isotopologue compositions in most vehicle exhaust samples are slightly anti-clumped in $^{12}CH_2D_2$, and slightly clumped in $^{13}CH_3D$ (Figure 3.6 and Table 3.2). This places vehicle exhaust methane clumped isotopologue compositions close to, but distinct from those of natural gas, and more clumped in $^{12}CH_2D_2$ than biomass burning, pyrolysis (Dong et al.,

2021), and microbial methanogenesis methane clumped signals (Gropp et al., 2022; Rhim & Ono, 2022; Young, 2019). Although direct measurements of vehicle exhaust methane yield distinct clumped isotope signals from other methane sources, it is currently not feasible to identify the contribution of vehicle emissions in a road survey by measuring clumped isotopes of methane in ambient air. Unlike nearly pure methane sources such as natural gas leaks and landfill emissions, vehicle exhaust presents concentrations at the ppm level. Incidents where vehicle emissions contribute to a 10% (i.e., ~0.2 ppm) enhancement in methane levels in the environment are quite rare; even when such instances occur, a 10% proportion of vehicle exhaust methane mixed with ambient methane would likely result in the methane isotopic signals being almost completely overwhelmed by the highly positive values of atmospheric methane. Even if we were to observe a slight decrease in $\Delta^{12}CH_2D_2$, we cannot rule out the possibility that this is due to the mixing of natural gas and/or biogenic methane. Therefore, clumped isotopologues currently cannot be used to distinguish vehicular methane from other methane emissions, and fundamentally, they are not suitable for this task.

Following on the framework proposed in the previous section, which explains the signals of the vehicular methane in four processes – methane formation, combustion, and oxidation via the catalytic converter, and mixing – we can extend this analysis to clumped isotopologues. Methane formation by proton addition to methyl radicals appears to generate anti-clumped compositions like that observed with the burning of wood (Haghnegahdar et al., 2023) (biomass burning data here) and pyrolysis of alkanes (Dong et al., 2021). According to the experimental results of n-octadecane pyrolysis, the methane production process from alkane pyrolysis could initially generate negative $\Delta^{12}CH_2D_2$ signals without significantly altering $\Delta^{13}CH_3D$ (Dong et al., 2021).

Once produced, methane will gradually return toward thermal-equilibrium clumped signals as collision and isotopic exchange happens. The low anti-clumping signals we observed imply the dominance of exchanging under high temperatures in the engine.

Process #2 methane combustion and process #3 methane oxidation by the catalytic converter can still be discussed under the framework of the Rayleigh fractionation process, with relationships given by:

$$\delta^{13}CH_3D_{residue}(‰) + 1000 = \left(1000 + \delta^{13}CH_3D_{initial}\right) * f^{\frac{\alpha_{13CH3D}-1}{12CH4}} \quad (3.13)$$

$$\delta^{12}CH_2D_{2\,residue}(‰) + 1000 = \left(1000 + \delta^{12}CH_2D_{2\,initial}\right) * f^{\frac{\alpha_{12CH2D2}-1}{12CH4}} \quad (3.14)$$

If we ignore the compounding additional decrease in zero point energy caused by the second rare isotope substitution on a singly-substituted isotopologue (ΔΔZPE, as defined in Whitehill et al. (2017) and similarly described in Eiler (2007)), according to the rule of the geometric mean (Bigeleisen, 1955), the KIE of doubly-substituted isotopologue equals to the product of KIEs of the two corresponding singly-substituted isotopologues, i.e. $\alpha_{13CH3D} = \alpha_{13C} * \alpha_D$ and $\alpha_{12CH2D2} = \alpha_D * \alpha_D$, given that α=1/KIE. In this scenario, there would be no cap-delta clumping signals, i.e. $\Delta^{13}CH_3D = 0$ and $\Delta^{12}CH_2D_2 = 0$. Clumping effects are likely small in the case of process #2 methane combustion, where the high-energy environment overwhelms the ΔΔZPE and thus limits clumping.

The presence of a catalytic converter which occurs at lower temperatures in process #3 catalytic oxidation might provide a special surface environment leading to the observed unusual clumping signals in the 2017 Chevrolet Sonic hot exhaust samples. To explain these signals, an additional adjustment coefficient γ for clumping has been introduced, where $\alpha_{13CH3D} = \alpha_{13C} * \alpha_D * \gamma_{13CH3D}$

and $\alpha_{12CH2D2} = \alpha_D * \alpha_D * \gamma_{12CH2D2}$. The physical basis for adding this γ coefficient relates to the ΔΔZPE. When deuterium (D) replaces hydrogen (H) in a singly-substituted isotopologue, the energy of the existing ^{13}C-H or ^{12}C-D bond is also affected, which further lowers the total energy of the molecule and makes it more stable, i.e. $\gamma < 1$. For $^{12}CH_2D_2$, H-abstraction, which is the main channel for methane oxidation compared to D-abstraction, its secondary isotope effect (Cao et al., 2019; Wang et al., 2015; Whitehill et al., 2017) is largely enhanced because of the existence of two D in the molecule, and is thus expected to cause a stronger clumping effect than $^{13}CH_3D$, i.e. usually $\gamma_{12CH2D2} < \gamma_{13CH3D} < 1$. To roughly align the yellow line in Figure 3.6 with the two 2017 Chevrolet Sonic hot samples, we employed $\gamma_{13CH3D} = 0.99867$ and $\gamma_{12CH2D2} = 0.963$. The γ_{13CH3D} value deduced in this study aligns numerically with those observed in aerobic oxidation of methane (AOM) experiments (Wang et al., 2016) and in anaerobic oxidation of methane (AeOM) experiments (Ono et al., 2021), yet is slightly smaller than the value calculated from the KIEs of gas phase CH_4+OH reactions (Haghnegahdar et al., 2017). The deduced is $\gamma_{12CH2D2}$ larger than the measured values in AOM and AeOM samples (Giunta et al., 2022), as well as the calculated value from the KIEs of CH_4+OH reactions at 25 °C (Haghnegahdar et al., 2017).

After determining the γ values, KIEs for methane oxidation with the presence of a catalytic converter at high temperature can be calculated: $KIE_{13CH3D} = 1.1156$ and $KIE_{12CH2D2} = 1.2794$. These values are significantly lower than those reported for CH_4+OH reactions at 25 °C (Haghnegahdar et al., 2017). Since the catalytic oxidation in vehicle exhaust requires a minimum operational temperature of about 400°C, it is improper to use the 25 °C values for comparison. By following established ab initio computational procedures (Haghnegahdar et al., 2017) with

the Gaussian 09 (EM64L-G09RevD.01) (Frisch et al., 2013) using the second-order Møller-Plesset (MP2) method (Møller & Plesset, 1934) with cc-pVTZ basis sets (Dunning, 1989), we calculated the KIEs for CH_4+OH and CH_4+Cl reactions at various temperatures (Table 3.3), and derived temperature-dependent KIE relationships with fourth-order polynomial fittings (Table 3.4). We interpolated the KIEs to temperatures of 1283 °C and 1116 °C, to match the derived $KIE_{^{13}CH_3D}$ and $KIE_{^{12}CH_2D_2}$ in this study, respectively. These temperatures exceed typical exhaust gas temperature when reaching the catalytic converter, which is usually about 600 °C.

Table 3.3. **Calculated KIEs of four methane isotopologues ($^{13}CH_4$, $^{12}CH_3D$, $^{13}CH_3D$, $^{12}CH_2D_2$) for CH_4+OH and CH_4+Cl reactions, at different temperatures**.

Species		Temperature (K)									
		150	200	253	273	293	298	323	373	500	1000
OH	$^{13}CH_4$	1.00217	1.00470	1.00602	1.00625	1.00637	1.00639	1.00642	1.00628	1.00541	1.00253
	$^{12}CH_3D$	1.31850	1.34051	1.33588	1.33137	1.32598	1.32452	1.31679	1.30000	1.25761	1.15381
	$^{13}CH_3D$	1.32347	1.34765	1.34452	1.34022	1.33490	1.33345	1.32565	1.30848	1.26463	1.15679
	$^{12}CH_2D_2$	2.02058	2.00236	1.96834	1.94754	1.92421	1.91811	1.88654	1.82188	1.67323	1.35927
Cl	$^{13}CH_4$	1.02879	1.02473	1.02209	1.02123	1.02042	1.02022	1.01930	1.01767	1.01460	1.00943
	$^{12}CH_3D$	1.58934	1.51341	1.46294	1.44489	1.42741	1.42314	1.40246	1.36479	1.29023	1.15734
	$^{13}CH_3D$	1.54460	1.47677	1.43110	1.41460	1.39855	1.39463	1.37558	1.34070	1.27120	1.14605
	$^{12}CH_2D_2$	2.73024	2.43593	2.25700	2.19441	2.13458	2.12010	2.05073	1.92768	1.69772	1.33611

Table 3.4. **Parameters of the derived fourth-order polynomial fittings for calculating KIEs of four methane isotopologues ($^{13}CH_4$, $^{12}CH_3D$, $^{13}CH_3D$, $^{12}CH_2D_2$) for CH_4+OH and CH_4+Cl reactions with temperatures T in Kelvin.** KIE = a / T^4 + b / T^3 + c / T^2 + d / T + e * T + f.

Species		T^{-4}	T^{-3}	T^{-2}	T^{-1}	T	1
		a	b	c	d	e	f
OH	$^{13}CH_4$	-3174600	152620	-1963.8	8.313	1.1173E-06	0.99491
	$^{12}CH_3D$	-359920000	7634100	-66793	274.11	0.000035924	0.90329
	$^{13}CH_3D$	-350160000	7638700	-68436	283.64	0.000037419	0.89688
	$^{12}CH_2D_2$	120570000	5036100	-107210	649.49	0.00010192	0.70991
Cl	$^{13}CH_4$	1.1703E+07	-113520	-186.91	6.8353	9.8809E-07	1.0019
	$^{12}CH_3D$	291190000	-2352300	-12346	196.3	0.000028557	0.94689
	$^{13}CH_3D$	254780000	-1878400	-13853	189.78	0.000027486	0.94426
	$^{12}CH_2D_2$	1920900000	-24939000	75250	307.09	0.000050941	0.92585

Several approaches could explain the discrepancy in KIE values. One simple explanation is that the KIE for methane catalytic oxidation in vehicle exhaust does have different KIEs than the gas phase CH_4+OH reaction, similar to how CH_4+Cl has different KIEs than CH_4+OH. Another approach might involve adjusting the α_{13C} and α_D values defined in the previous section and used in calculating KIEs for clumped isotopologues, which could be both increased while still aligning with measured $\delta^{13}C$ and δD values, potentially harmonizing the final KIE with those of the CH_4+OH reaction. Additionally, there could be a method to address the inconsistency without altering the existing values, by considering adsorption-desorption dynamics on the catalytic converter active Pt alloy coating. Methane in the exhaust stroke first adheres to the surface of the catalyst alloy, with part desorbing and another part oxidizing. This would yield a network with two CH_4 pools and a product:

$$\mathrm{CH4(exhaust)} \Leftrightarrow \mathrm{CH4(adsorbed)} \Rightarrow \mathrm{Product} \tag{3.15}$$

At any given moment, assume a fraction f of methane in the exhaust stroke is oxidized, and (1-f) desorbs. If the methane oxidation on the catalyst surface has KIE, then the net (apparent) KIE' for the entire network is modulated by the fraction f:

$$KIE' = (1 - f) * KIE + f \tag{3.16}$$

This equation allows the apparent KIE' to vary within the range of (1, KIE), controlled by the f. The deduced KIE' values in this study (KIE'_{13CH3D} = 1.1156 and $KIE'_{12CH2D2}$ = 1.2794) can be matched by f = 0.36 with interpolated KIE_{13CH3D} = 1.1752 at 600 °C and f = 0.32 with interpolated $KIE_{12CH2D2}$ = 1.4091 at 600 °C for CH_4+OH reaction, respectively. This consistency in f values across different isotopologues strengthens the reliability of using this approach to interpret the clumping effect of the catalytic oxidation process in vehicle exhaust.

If the modified Rayleigh fractionation model incorporating adsorption-desorption processes is adopted, the fractionation of bulk ^{13}C and D on the catalytic converter discussed in the previous section should also be explained using the modified model. The previous discussion remains valid as the model still utilizes the mathematical equations of Rayleigh fractionation but instead calculates an apparent fractionation coefficient α'.

Moving to the clumped isotopologue data for diesel vehicles, we find that the trend provided by these data is consistent with the hypothesis of air mixing with the exhaust. The mixing process generates a curve on the $\Delta^{12}CH_2D_2$-$\Delta^{13}CH_3D$ field, depicted by a blue dotted line in Figure 3.6. The 2006 Ford F-750 trash truck hot sample has a higher contribution from the original exhaust methane, compared to 2005 and 2013 Gillig transit bus hot samples, and thus the isotopic signals were less affected by the air mixing, resulting in a smaller increase in $\Delta^{12}CH_2D_2$.

To sum up, the observation from the clumped isotopologue data aligns with the conclusions drawn from carbon and hydrogen isotope data. That is, the observed isotopic and isotopologue data can be explained through four processes (formation, combustion, oxidation, and air mixing) combined with appropriate KIE values.

The clumped isotopic values of vehicular methane endmembers should be defined using the same process-based approach as traditional bulk isotopes. However, unlike bulk carbon and hydrogen isotopic data, clumped isotopologue measurements have high uncertainties, while the range of variation is relatively narrow. We observed that fractionation from Step 3 (catalytic conversion) and Step 4 (air mixing) caused the $\Delta^{12}CH_2D_2$ values of four low-methane

concentration samples to diverge significantly from others. Exhaust methane could have $\Delta^{12}CH_2D_2$ values that become extremely positive, reaching up to +30‰.

Excluding the four outliers, samples clustered near the (0,0) point in Figure 3.6, which happened to be samples predominantly influenced by Step 1 (formation) and Step 2 (combustion). Averaging these clustered samples yields values of $\Delta^{13}CH_3D$ = +0.8‰ and $\Delta^{12}CH_2D_2$ = -2.4‰. Considering that these samples generally have higher concentrations and may be more representative on the road, we recommend using this set of averaged values as the clumped isotopologue signatures for vehicle exhaust methane endmember.

This set of values is slightly away from the (0,0) point. This minor shift could be attributed to fractionation possibly caused by cracking during the high-temperature methane formation reaction. However, significant measurement uncertainties due to technical limitations, with average 2SD values of ±1.1‰ and ±3.2‰, hinder further quantitative analysis. Given the unique physical significance of the (0,0) in stochastic distribution, and the considerable measurement uncertainties, additional measurements are needed to determine whether the clumped isotopologue signals of vehicle exhaust methane are definitively deviating from (0,0).

To sum up, based on the data from this study, we suggest that the $\Delta^{13}CH_3D$ value for vehicle exhaust methane is primarily around 0.8‰ ± 1.1‰, while the $\Delta^{12}CH_2D_2$ value is approximately -2.4‰ ± 3.2‰, if not being largely affected by catalytic oxidation and air mixing. These values should be used with caution due to their representativeness limitations.

3.5. Conclusions

This study presents findings consistent with prior studies, showing that exhaust from studied vehicles exhibits a broad range of [CH_4] that vary depending on factors like vehicle age, state of repair, engine type, and operating conditions. [CH_4] in vehicle exhausts measured in this study ranged from <1 ppm to >1000 ppm. Older and poorly-maintained vehicles tend to emit more methane. Vehicles with compression-combustion (diesel) engines, allowing higher air/fuel, emitted lower [CH_4] compared to spark-combustion vehicles. Vehicular methane emissions are likely to follow a fat-tail distribution, meaning that a small portion of vehicles contribute the majority of emissions.

The C_2:C_1, $\delta^{13}C$ and δD of exhaust methane vary among vehicles, influenced by many of the same factors that concentrations scale with. C_2:C_1 varied from 0.1% to 18.3%. Vehicles emitting greater amounts of methane are generally those with higher C_2:C_1. $\delta^{13}C$ and δD could in principle be used to identify vehicular contributions, but low levels of [CH_4] enhancements on the road make this a challenging prospect. Vehicular methane typically has $\delta^{13}C$ values between -22 and -11‰ and δD values between -170 and -120‰, which are less negative than $\delta^{13}C$ and δD of natural gas. The majority of vehicle samples show a positive linear relationship among [CH_4], $\delta^{13}C$, and δD, although some samples significantly deviate from this trend.

After excluding some outliers, most samples show clumped isotopologue signals clustered near the (0,0) point, with average values of $\Delta^{13}CH_3D$ = +0.8 ± 1.1‰ and $\Delta^{12}CH_2D_2$ = -2.4‰ ± 3.2‰. More high-precision measurements are needed to determine whether these values consistently

deviate slightly from stochastic distributions. A small number of outliers can have $\Delta^{12}CH_2D_2$ values reaching +30‰. The clumped isotopologue signal of vehicle exhaust methane is significantly different from those of major methane sources, such as natural gas and microbial methane.

Despite the isotopic and isotopologue signatures of vehicle exhaust methane being different from other major methane sources, identifying vehicular methane emissions in urban air based on isotopes and isotopologues is still challenging due to the low enhancement level and the variability of isotopic signals from different sources.

The isotopic variations can be explained with four dominant processes: 1) formation of methane under high temperature during the first part of burning in the engine, 2) combustion of methane under high temperature in the engine before it is expelled from cylinder to exhaust stroke, 3) oxidation of methane by catalytic converter, and 4) mixing of exhaust methane with air methane. Process #1 methane formation aligns the $\delta^{13}C$ and δD values of generated methane with those of gasoline, while clumped isotopologue signals of generated methane are near-stochastic, or exhibit slight anti-clumping in $\Delta^{12}CH_2D_2$. This process may involve considerable intermolecular exchange of isotopes to yield a near-equilibrium signature. Process #2 methane combustion, described by the Rayleigh fractionation equation, is thought to produce the positive linear relationship observed among $[CH_4]$, $\delta^{13}C$, and δD in the majority of samples. Process #3 methane oxidation by the catalytic converter can also be simulated with a simple Rayleigh model, but a modified Rayleigh model that incorporates methane adsorption and desorption on the surface of the catalytic alloy allows better fit with literature values. The catalytic process

leads to extremely positive $\delta^{13}C$ and δD, as well as highly clumped $\Delta^{12}CH_2D_2$ signals with low $[CH_4]$. The exhaust of diesel vehicles typically shows very low $[CH_4]$ because compression combustion is generally under a higher air-to-fuel ratio. This low $[CH_4]$ exhaust is then mixed with ambient air while sampling to yield influenced $\delta^{13}C$, δD, and clumped isotopologue signals, which showed mixing trends with air. These processes collectively shape the concentration and isotope characteristics of vehicular methane, indicating vehicle emissions are primarily controlled by the operational states of the engine and catalytic converter. This study demonstrates the capability of isotopes and clumped isotopologues in tracing processes. Meanwhile, vehicle engines and catalytic converters provide a unique opportunity to obtain key isotopic fractionation factors for pyrolysis and methane catalytic oxidation. These parameters could provide a reference for studying other methane geochemical processes, such as microbial methane oxidation and atmospheric methane sink reactions.

3.6. Acknowledgment

The authors would like to thank Dr. David T. Wang and one anonymous reviewer for their insightful comments and constructive suggestions, which have greatly enhanced the quality of this manuscript. We express our gratitude to the staff of the University Park, MD town trash collection service for facilitating the collection of exhaust samples from trash trucks. Our thanks extend to the employees of the University of Maryland, College Park's Department of Transportation Services, for their assistance in collecting exhaust samples from campus shuttle buses. Additionally, we are thankful for the staff, graduate students, and undergraduates at the University of Maryland who provided their vehicles for our sampling endeavors. All electronic

structure calculations in this study are made using the Gaussian09 software package (Gaussian 09: AM6 4 L-G09RevB.01 12 August 2010) on the UCLA Hoffman2 cluster.

3.7. Data Availability

All measured data in this study are included in the main text and Appendix A. The clumped isotopologue data measured at UMD are also archived and available in the Digital Repository for the University of Maryland (DRUM, https://drum.lib.umd.edu/).

3.8. Supporting Information

Additional descriptions and figures of sampling details (Appendix A Note A.1, Figure A.1), descriptions of sampled vehicles (Appendix A Note A.2), descriptions of concentration measurement results (Appendix A Figure A.2, Figure A.3), and supplementary discussions of concentration results for some vehicles (Appendix A Note A.3) are provided in Appendix A.

Chapter 4: Tracing Sources of Atmospheric Methane Using Clumped Isotopes

This chapter has been published in

Proceedings of the National Academy of Sciences of the United States of America. 120 (47) e2305574120, (2023). https://doi.org/10.1073/pnas.2305574120

Authors and Affiliations:

Mojhgan A. Haghnegahdar[1,2,3]*, Jiayang Sun[1], Nicole Hultquist[1], Nora D. Hamovit[4], Nami Kitchen[5], John Eiler[5], Shuhei Ono[6], Stephanie A. Yarwood[4], Alan J. Kaufman[1,2], Russell R. Dickerson[7], Amaury Bouyon[1], Cedric Magen[1], and James Farquhar[1,2]

[1]Department of Geology, University of Maryland, College Park; College Park, MD, USA.

[2]Earth System Science Interdisciplinary Center, University of Maryland, College Park; College Park, MD, USA.

[3]Smithsonian Environmental Research Center; Edgewater, MD, USA.

[4]Department of Environmental Science and Technology, University of Maryland, College Park; College Park, MD, USA.

[5]Division of Geological and Planetary Sciences, California Institute of Technology; Pasadena, CA, USA.

[6]Department of Earth, Atmospheric and Planetary Sciences, Massachusetts Institute of Technology; Cambridge, MA, USA.

[7]Department of Oceanic and Atmospheric Science, University of Maryland, College Park; College Park, MD, USA.

*Corresponding author: Mojhgan A. Haghnegahdar

Email: mojhganh@umd.edu

Jiayang Sun is the second author of this paper and has made significant contributions, including but not limited to methodology, investigation, review, and editing. In particular, Jiayang contributed to the testing and quality control of the measurement methods. With the consent of the first author and the necessary approval from the graduate school, this paper has been included as a chapter in Jiayang Sun's dissertation. The content remains unchanged, but some formatting adjustments have been made to meet the dissertation's formatting requirements.

Keywords:

atmospheric methane,

methane isotopic composition and isotopologues,

CH_4 sources and sinks,

greenhouse gas emissions,

methane trends

4.1. Abstract

We apply a recently developed measurement technique for methane (CH_4) **isotopologues** (isotopic variants of CH_4 –$^{13}CH_4$, $^{12}CH_3D$, $^{13}CH_3D$, and $^{12}CH_2D_2$) to identify contributions to the atmospheric burden from fossil fuel and microbial sources. The aim of this study is to constrain factors that ultimately control the concentration of this potent greenhouse gas on global, regional, and local levels. While predictions of atmospheric methane isotopologues have been modeled, we present direct measurements that point to a different atmospheric methane composition and to a microbial flux with less **clumping** (greater deficits relative to stochastic) in both $^{13}CH_3D$ and $^{12}CH_2D_2$ than had been previously assigned. These differences make atmospheric isotopologue data sufficiently sensitive to variations in microbial to fossil fuel fluxes to distinguish between emissions scenarios such as those generated by different versions of EDGAR (the Emissions Database for Global Atmospheric Research), even when existing constraints on the atmospheric CH_4 concentration profile as well as traditional isotopes are kept constant.

4.2. Significance Statement

With an approximately ten-year lifetime and strong infrared absorption, methane is one of the most important greenhouse gases and a target for mitigation. Here we describe unique measurements of rare isotopic variants of methane (isotopologues, in particular, $^{13}CH_3D$ and $^{12}CH_2D_2$) in air, which when used in combination with traditional isotope and concentration constraints, add valuable new information about the balance of atmospheric CH_4 sources. Importantly, information from these isotopologue analyses distinguishes between different proposed histories of fossil fuel to microbial methane emissions, even when the traditional isotope and concentration records are the same. Consideration of these isotopologues also

supports recent assertions that increases in microbial emissions are driving the most recent rise in atmospheric methane.

4.3. Introduction

Methane (CH_4) is the second most important anthropogenic greenhouse gas in Earth's atmosphere with its residence time controlled primarily by loss to reaction with the •OH radical, and to a lesser extent by reaction with Cl• and $O(^1D)$ as well as oxidation in soils (Dlugokencky et al., 2011). These reactions result in a lifetime of ~10 years, meaning that >98% of the methane in the atmosphere was emitted in the past 40 years. The classification as a short-lived climate pollutant also means that increases in emission rates have thus supported an increase of >15% in its globally averaged atmospheric concentration over the same period (Lan et al., 2023).

Methane is a primary target to address climate change, in large part because of its short lifetime (and potential as a greenhouse gas), which translates to changes we make today will impact what most of us witness in our lifetimes (Dlugokencky et al., 2011). It has also been highlighted that methane mitigation may be one of our best opportunities to meet targets such as those outlined in the Paris Agreement (Nisbet, Jones, et al., 2021; Nisbet et al., 2019). A complicating factor in mitigating methane is uncertainty in its global budget, especially in sources, illustrated by disagreement between bottom-up vs. top-down models (Saunois et al., 2020); existing observations can be explained by different hypotheses relating changes in source fluxes, source compositions, and/or sink reactions (Lan et al., 2021; Milkov, Schwietzke, et al., 2020; Nisbet et al., 2023; Rigby et al., 2017; Schaefer et al., 2016; Turner et al., 2017). A need therefore exists

for the development of additional independent observations that can be used to increase the number of constraints controlling the processes that govern the rapid rise of methane in the atmosphere.

The rise in atmospheric methane from pre-industrial levels of ~700 ppb (Saunois et al., 2020) to ~1,900 ppb (Lan et al., 2023) in 2023, has not been monotonic. The buildup accelerated through most of the 20th century, only to taper off in the 1990's and then notably to stall between 1999 and 2006 (Lan et al., 2021); the early 21st century plateau was hypothesized to reflect the stabilization of sources due to a decrease in anthropogenic emissions (Bousquet et al., 2006). In 2007, methane resumed its rapid upward trajectory (~8-10 ppb/yr) indicating renewed strengthening of CH_4 sources, a weakening of its sinks, or both (Lan et al., 2021; Milkov, Schwietzke, et al., 2020; Nisbet et al., 2023; Rigby et al., 2017; Schaefer et al., 2016; Turner et al., 2017).

One approach used to improve our understanding of these temporal variations in atmospheric methane concentration, has been to study isotopic forms of CH_4 such as the $^{13}CH_4$ **isotopologue** (**isotopic variant** described by bulk **δ^{13}C** composition–also see Appendix B) (Lan et al., 2021; Milkov, Schwietzke, et al., 2020; Nisbet et al., 2023; Rigby et al., 2017; Schaefer et al., 2016; Turner et al., 2017). Biogenic sources tend to release less $^{13}CH_4$ relative to $^{12}CH_4$ compared to fossil sources (i.e., lighter $\delta^{13}C$). The proportion of atmospheric $^{13}CH_4$ to $^{12}CH_4$ increased (more positive $\delta^{13}C$) in the time leading up to the [CH_4] plateau between 1999 and 2006. Since that time, the $\delta^{13}C$ has shifted to more negative values, even as the rise in concentration resumed (compare **Figures B.3 and B.5A**). Understanding what drives the fluctuations in both

concentration and bulk carbon isotopic composition carries important implications for how society approaches the mitigation of this greenhouse gas–do we focus mitigation efforts on fossil sources such as natural gas leakage or on microbial sources such as landfills, agriculture, or wetlands? Other efforts have worked to use the $^{12}CH_3D$ isotopologue (variations recorded by **δD** compositions–see Appendix B) but this record is significantly less complete (Fujita et al., 2020; Rice et al., 2016). The need for more complete records of **δD** as well as for other independent measures provided by the rare isotopologues of methane has been documented (Rice et al., 2016).

In this study, we explore the use of two further isotopologues of methane, the doubly substituted species $^{13}CH_3D$ and $^{12}CH_2D_2$ with variations reported as, $\mathbf{\Delta^{13}CH_3D}$ [1] and $\mathbf{\Delta^{12}CH_2D_2}$ values as well as $\mathbf{\delta^{13}CH_3D}$ and $\mathbf{\delta^{12}CH_2D_2}$ values ((Fujita et al., 2020), also see Appendix B). The doubly-substituted isotopologues are colloquially referred to as **clumped**[2] because they have two heavy isotope substitutions and this clumping is associated with stronger bonds and makes them slightly more stable thermodynamically. Isotopes that are stochastically distributed are

[1] The Δ notation describes the enrichment (positive values) or depletion (negative values) in parts per thousand (‰) of an isotopologue ratio relative to the stochastic ratio. For example, $\Delta^{13}CH_3D$ (in ‰) = $1000 \times ((^{13}CH_3D/^{12}CH_4)_{sample} - (^{13}CH_3D/^{12}CH_4)_{stochastic})/(^{13}CH_3D/^{12}CH_4)_{stochastic}$). In a stochastic distribution all the stable isotopes in a given population of molecules are randomly distributed among all possible isotopologues.

[2] Gases comprised of different isotopologues are considered clumped when the $\mathbf{\Delta^{\#}X^{\#}Y}$ is positive and anti-clumped when $\mathbf{\Delta^{\#}X^{\#}Y}$ is negative.

represented according to their relative abundance as if randomly selected from the entire population.

Interest in methane clumped isotopologues has developed over the past 15 years, insofar as they can be used: 1) to document if isotopologue proportions are in equilibrium, and if so, at what temperature it was set; 2) to evaluate kinetics because these processes leave characteristic signatures between product and reactant (kinetic effects in both production and removal fractionate methane); and 3) to trace physical processes related to mixing of clumped isotopologues from specific sources into the surrounding air. All three of these processes play a part in the global atmospheric methane cycle, making the measurement of clumped isotopologues of methane a timely target for atmospheric research.

The use of clumped isotopes of methane in air has been enabled by the recent development of new instruments that can measure their ultra-low abundance at high mass resolution (Eiler et al., 2013; Gonzalez et al., 2019; Ono et al., 2014; Young et al., 2016). Also necessary were separation and purification of sufficient methane for analysis, which requires processing hundreds of liters of air (described in the materials and methods and also the Appendix B).

Measurements of the abundance of these isotopologues are considered in the context of the global methane budget to illustrate that the information is not only independent of that provided by traditional, singly substituted isotopologues given by $\delta^{13}C$ and δD, but that this information can test hypotheses relating to the apportionment of fossil fuel and microbial sources on global, regional, and local scales. This is possible because recent studies (e.g., (Dong et al., 2021;

Douglas et al., 2017; Stolper, Lawson, et al., 2014; Wang et al., 2015; Young, Kohl, Lollar, et al., 2017)) have been filling in critical information about clumped isotope compositions of various CH_4 sources and processes, the foundational information for making interpretations about methane in air.

The data presented here for singly and doubly substituted isotopologues demonstrate the applicability of this approach, which promises greater resolution of atmospheric CH_4 sources than is possible with only traditional bulk isotope techniques. We frame the information captured by various isotopic measurements using traditional isotope and isotopologue plots (Figure 4.1) (see also Appendix B Table B.1).

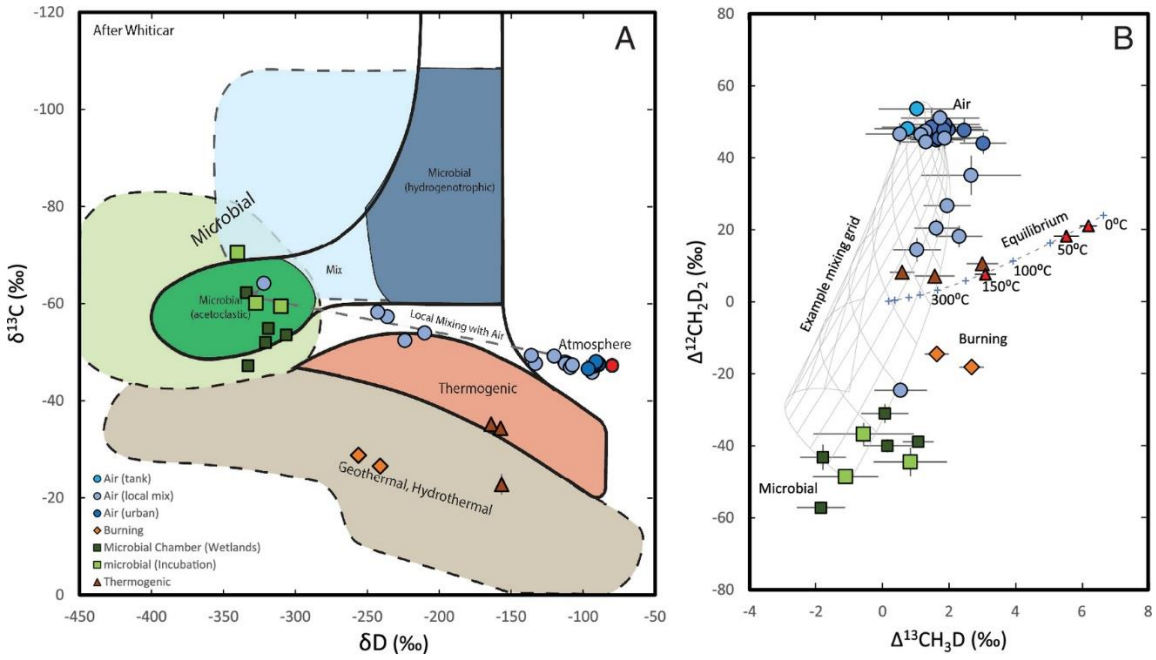

Figure 4.1. **(A) Plot of $\delta^{13}C$ and δD (‰) of methane samples measured in this study** (air–blue circles; microbial wetland related–green squares; natural gas–brown triangles; biomass burning–orange diamonds) overlain on the fields of Whiticar (2020). Dashed gray line shows possible trajectory for mixing of tropospheric air with local sources having microbial signatures. The red circle in Panel A is the composition of atmospheric methane given by Dong et al. (2021). **(B) Plot of $\Delta^{12}CH_2D_2$ vs. $\Delta^{13}CH_3D$ (‰)** illustrating the uniquely positive $\Delta^{12}CH_2D_2$ of air samples relative to the equilibrium curve (stippled gray curve labeled with temperatures from 0 to 330 °C) and samples equilibrated using with γ-alumina at 15 °C, 32 °C, and 150 °C (red triangles) following (Eldridge et al., 2019). Data for natural gas samples (brown triangles), (biomass) burning (orange diamonds), microbial methane (light green squares are incubations; darker green squares are chamber collections). A mixing net with end members broadly matching air mixed with microbial methane is plotted in dashed gray. Mixing of air with local sources such as air from wetlands (see Appendix B) is hypothesized to account for the variability that is seen. The global atmospheric (tropospheric) value is hypothesized to be near the cluster of air data points but could be slightly shifted since the sampling location is at ground level and within the urban dome (enhanced methane) of the Washington, DC region.

4.4. Samples

Methane was isolated from a variety of different types of samples for isotopologue measurements. Studied samples include methane extracted from near-surface air (500 to 1000 L) collected from urban sites on and near the University of Maryland campus, from compressed air

samples (commercial Airgas), and from sites located on or near the UMD campus associated with the local farm, and with wetlands. In addition to these samples, methane was extracted from smoke from a covered grill (burning wood and charcoal), from chambers deployed at the two studied wetlands, and from incubation experiments with wetland soils. Finally, methane collected from natural gas samples (Marcellus and Utica shale gas and natural gas from the UMD Chemistry Bldg) was analyzed. Additional detail about the sampling locations, collection procedures, and calibration are presented in the Supporting Information.

4.5. Using Isotopologue Data to Track Local Source Contributions and Mixing

In Figure 4.1A, the traditional isotopic compositions of various sources are illustrated as colored fields (Douglas et al., 2017); also on this panel is the much more narrowly defined and distinct composition for atmospheric methane (red circle). Data collected in this study largely falls within the defined fields, and data collected for ambient air (blue circles) extends from composition defined for air by Whiticar (2020) along an array that extends towards microbial sources. Air samples were all collected in the planetary boundary layer within 3 m of ground level. Those showing mixing (meaning influence of local sources) were generally collected in the early morning around sunrise near sites of methane emission and contained methane that accumulated overnight due to low nocturnal boundary layer height. These also have methane mixing ratios above the ~2,000 ppb (typical for 39°N in 2022). The mixing array is interpreted to reflect local mixing of microbially sourced methane into background air and a schematic mixing line is included on this diagram for illustrative purposes.

On this diagram, the isotopic composition of background tropospheric air (red circle) methane ($\delta^{13}C$ and δD values) is shifted from its source methane as a result of **KIE** (**Kinetic Isotope Effects**[3]—see Appendix B) associated with sink reactions for methane (predominantly reaction with the •OH radical, and to a lesser extent to sinks attributable to Cl•, $O(^1D)$, and soil oxidation reactions), and these KIE reflect different sink reaction rates for different isotopologues (Chung & Arnold, 2021; Haghnegahdar et al., 2017; Whitehill et al., 2017). The KIE for •OH + $^{13}CH_4$ is only about 1.0039, but •OH + $^{12}CH_3D$ is much slower with a KIE of ~1.3. This leads to different lifetimes (e.g., ~30% longer for $^{12}CH_3D$ compared to CH_4) for the isotopologues in air (Haghnegahdar et al., 2017). The effect for δD is more pronounced than for $\delta^{13}C$, and the difference in composition makes it possible to see, for instance, the effect of local contributions to atmospheric methane. Figure 4.1A shows little change in $\delta^{13}C$ relative to δD. There have been relatively few measurements of the other rate constants (e.g., (Whitehill et al., 2017)) and we have to calculate (model) KIE for other isotopologues using electronic structure methods; because this approach yields high-precision frequency shifts, the precision on the relative rates (KIE) is better than the accuracy (absolute rate constants).

Data for doubly substituted isotopologues ($\Delta^{12}CH_2D_2$ and $\Delta^{13}CH_3D$–Table B.1) for the same samples are presented in Figure 4.1B. A similar offset for the isotopic compositions of methane in tropospheric air compared to that of the sources is seen and reflects KIE that produces an enrichment in heavier isotopologues resulting from the lower rates of sink reactions involving

[3] KIE = k_{12CH4}/k_i, where k_i is the rate constant of the isotopologue of interest at a specific temperature.

isotopologues with progressively more heavy-isotope substitutions (e.g., (Chung & Arnold, 2021; Haghnegahdar et al., 2017; Whitehill et al., 2017)).

Evidence of mixing can also be seen with the doubly-substituted isotopologues. Figure 4.1B also includes a mixing grid for mixing of atmospheric methane with methane from sources with compositions like those produced by the two predominant microbial pathways that generate different isotopic signatures ((Whiticar, 2020) - See also Figure B.1 for a different mixing grid with natural gas and microbial sources). Mixing lines on this grid are curved because of the way that $\Delta^{12}CH_2D_2$ and $\Delta^{13}CH_3D$ are defined. Straight mixing lines are, however, seen on plots of $\delta^{12}CH_2D_2$ and $\delta^{13}CH_3D$ (See Figure B.2). Adding clumped isotopes to traditional isotopes and trace gas measurements will thus provide a way to significantly improve source identification and apportioning at local and regional levels. Prior to this result, there was no equivalent of the red circle (a prior measurement of air methane) for the doubly-substituted isotopologues.

While identifying contributions from local sources is a valuable application of isotopologue data, we first focus on the utility of isotopologue data for studies of the nature of global CH_4 sources and changes in the global methane cycle (sources and sinks) over decadal timescales.

4.6. Implications of Tropospheric Methane Isotopologue Data for Understanding Global Fluxes

As noted above, different rates of atmospheric sink reactions for isotopologues (KIE) exert a significant control over the resulting isotopic composition of methane in air. Enrichments of $^{12}CH_2D_2$, $^{13}CH_3D$, and $^{12}CH_3D$, leading to more positive $\delta^{13}CH_3D$, and $\delta^{12}CH_2D_2$ values on a global scale (Figure 4.1 and Figure B.1) result from several different kinetic isotope effects. The combined role of KIE for the sinks with •OH and Cl• generates ~5‰ increases in $\delta^{13}C$, ~130‰ increases for δD and $\delta^{13}CH_3D$, and ~200‰ increases for $\delta^{12}CH_2D_2$ for tropospheric methane relative to its primary sources (Haghnegahdar et al., 2017; Whitehill et al., 2017). KIE also produces the observed positive $\Delta^{12}CH_2D_2$ and $\Delta^{13}CH_3D$ values (clumped: $\Delta>0$) of methane in ambient (tropospheric) air (Haghnegahdar et al., 2017; Whitehill et al., 2017).

A potential added element for these two reactions is that the KIE for the reaction with the •OH radical lead to strong positive shifts for $\Delta^{12}CH_2D_2$ (enhanced clumping) but not for $\Delta^{13}CH_3D$ (Haghnegahdar et al., 2017; Whitehill et al., 2017). The reaction with Cl• however generates greater effects for the ^{13}C-containing isotopologues (Lan et al., 2021; Rigby et al., 2017; Turner et al., 2017). This combination raises the possibility that $\Delta^{13}CH_3D$ might also provide information about changes in the proportional contribution of the Cl• sink reaction.

4.7. Insight into Global Microbial Flux from Air Isotopologues

While the measurements of isotopologues in air have strongly positive $\Delta^{12}CH_2D_2$, like recent predictions (Chung & Arnold, 2021; Haghnegahdar, 2018; Haghnegahdar et al., 2017; Whitehill et al., 2017) using forward, bottom-up isotopologue models, an important difference is revealed. The predictions overestimated the degree of clumping for both doubly substituted isotopologues, a feature that can be traced to assignments of the isotopologic mix of methane emitted from microbial methanogenic sources such as wetlands.

At the time these modeling studies (e.g., (Chung & Arnold, 2021; Haghnegahdar, 2018; Haghnegahdar et al., 2017; Whitehill et al., 2017)) were undertaken, evidence existed that pure cultures of methanogens generate strongly anti-clumped methane (negative $\Delta^{12}CH_2D_2$ and $\Delta^{13}CH_3D$ values); however, it was also known that pure culture experiments may not capture the true signature of methanic microbial communities in situ. When cellular-level metabolic rates are slow, which is relevant in many natural environments, greater clumping is seen (Gropp et al., 2022; Jautzy et al., 2021). Furthermore, in nature, methanogens coexist with methanotrophs, microbes that consume (oxidize) methane produced by methanogens. Methanotrophs had been shown to shift isotopologues to more clumped (less negative) $\Delta^{12}CH_2D_2$ and $\Delta^{13}CH_3D$ values (Ash et al. (2019); Haghnegahdar (2018); Ono et al. (2021); Wang et al. (2015), but see Giunta et al. (2022); Krause et al. (2022) for recent exceptions). These two considerations led the modeling studies (e.g., (Chung & Arnold, 2021; Haghnegahdar, 2018; Haghnegahdar et al., 2017; Whitehill et al., 2017)) to assign more clumped (less negative) $\Delta^{12}CH_2D_2$ and $\Delta^{13}CH_3D$ values than those seen in pure culture to the global microbial source flux(es). In turn, these models

predicted strongly positive $\Delta^{12}CH_2D_2$ and $\Delta^{13}CH_3D$ values for air, more positive than our direct measurements (Figure 4.2).

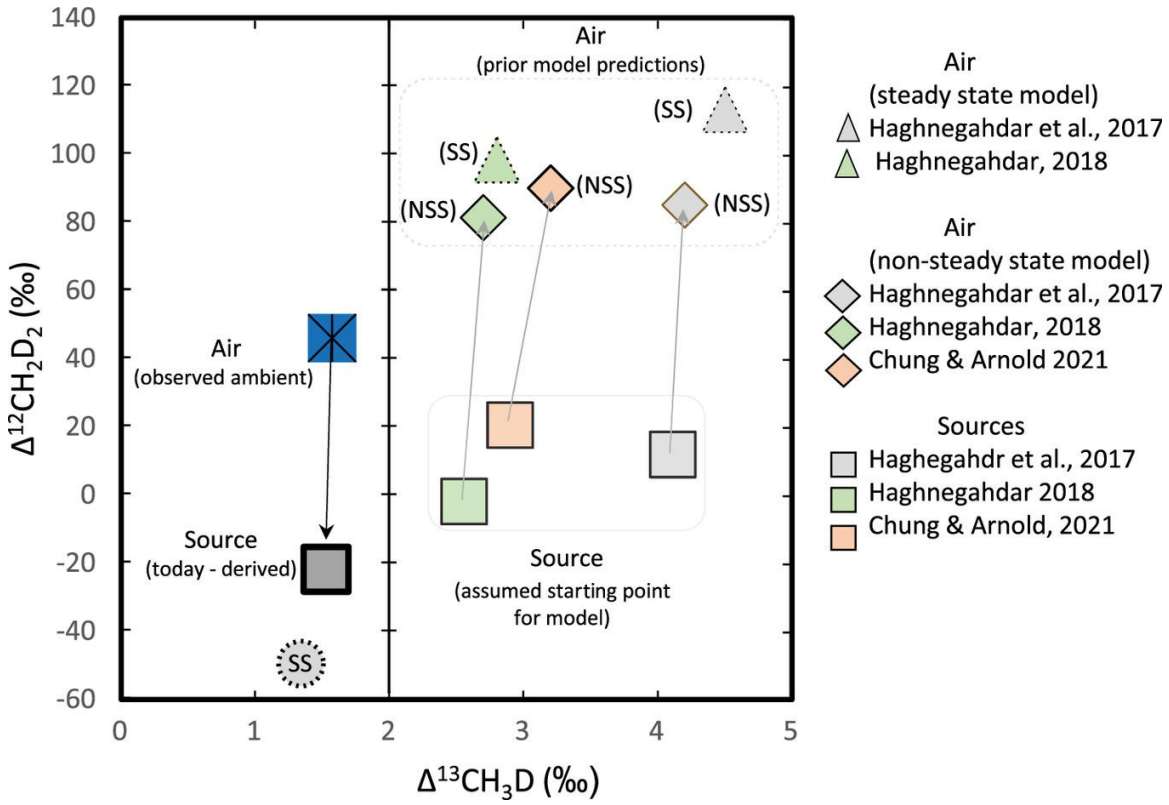

Figure 4.2. **Plot of $\Delta^{12}CH_2D_2$ vs. $\Delta^{13}CH_3D$ (‰) illustrating the fundamentally different structure and results of constraints imposed by modeling measurements of methane in tropospheric air versus predicting the composition from assumptions about sources.** The vertical line separates the observed measurement and derived source composition which have lower $\Delta^{13}CH_3D$ values from the prior model predictions which started with a source composition having higher $\Delta^{13}CH_3D$ values. The square symbol (blue with star) is the composition of observed ambient air methane (today). The gray square symbol is the derived composition of the source flux (today). The stippled grey circle (labeled SS) is what would be attained if the atmosphere and sources were in steady state (source flux = sink flux) for an atmospheric methane composition like the one observed. On the right side of the plot, at higher $\Delta^{13}CH_3D$, are plotted the assumed composition for the source flux used by (Whiticar (2020)–green), (Whitehill et al. (2017)–pink), (Chung and Arnold (2021)–tan). The diamond symbols are the derived (predicted) composition of air methane (same colors) and the stippled triangle symbols are the composition of air for the same sources when at steady state.

Using a box model (see Appendix B), we show here that the observed isotopologue composition of ambient tropospheric air requires a significantly less positive $\Delta^{12}CH_2D_2$ value (more anti-clumped) for the (total) source flux (Figure 4.2). This source flux has negative (anti-clumped) $\Delta^{12}CH_2D_2$ indicating that the major microbial sources (e.g., wetlands, landfills, and agriculture)[4] have anti-clumping, similar to gases collected in pure culture studies. The $\Delta^{13}CH_3D$ values are also lower, but not as low as those seen in pure culture studies. The reason for this less clumped source composition suggests that the most important pathways for methane emitted to the atmosphere are those where methanogenesis occurs at more rapid cellular rates and also that the signature is weighted toward methanogenesis because, in settings where methanotrophy dominates, emissions are lower.

The fact that the total source is fed by a combination of microbial contributions with strongly negative $\Delta^{12}CH_2D_2$ values and fossil fuel contributions with positive $\Delta^{12}CH_2D_2$ values amplifies the signal provided by $\Delta^{12}CH_2D_2$ values to track changes in their relative contributions. The smaller difference for $\Delta^{13}CH_3D$ values makes this tracer less sensitive to changes in microbial/fossil fuel flux ratios, but it may provide different constraints because the shifts generated by sink reactions with •OH radicals are small compared to the larger shifts for the sink reaction with Cl•. Thus, it may be possible to use $\Delta^{13}CH_3D$ values to track variations the Cl• sink reactions, should the proportional loss to the Cl• sink increase significantly above its present

[4] It is conceivable, if for instance landfill and or wetland sources are found to have less anti-clumping and agricultural sources are found to have greater anti-clumping, (or vice versa) that this analysis would point to one or the other as the primary reason for the observed compositions.

levels. Furthermore, some sources with similar $\Delta^{12}CH_2D_2$ have different $\Delta^{13}CH_3D$; for instance, those associated with microbially sourced methane compared to unequilibrated thermogenic methane (Dong et al., 2021), leading to the suggestions that on local scales, $\Delta^{13}CH_3D$ values may be a valuable asset for identifying which is most important.

4.8. Isotopologues Track Apportionment of Methane Fluxes on Decadal Timescales

The rise of atmospheric methane has been evaluated using bulk isotope measurements of atmospheric methane (e.g., (Lan et al., 2021; Milkov, Schwietzke, et al., 2020; Nisbet et al., 2023; Rice et al., 2016; Rigby et al., 2017; Schaefer et al., 2016; Turner et al., 2017)); however, the conclusions made in these studies differ; Rice et al. (2016) argues on the basis of time series δD measurements that fossil fuel sources were flat leading up to the plateau in methane concentration between 1999 and 2006 and only rose recently; whereas Milkov, Schwietzke, et al. (2020), Lan et al. (2021), and Basu et al. (2022) argue on the basis of $\delta^{13}C$ variations that recent enhancements in wetland emissions explain the most recent rise; other studies, Rigby et al. (2017), Turner et al. (2017) and Chung and Arnold (2021) have argued that other factors related to the strength of sinks and KIE also could play a role in controlling the recent rise of atmospheric methane. As argued by Rigby et al. (2017), it would appear clear that additional constraints and data with models are needed to fully understand the controls in the rapidly changing understanding of global atmospheric methane in the past, present, and future.

Here we use a box model to evaluate how much additional data from $\Delta^{12}CH_2D_2$ and $\Delta^{13}CH_3D$ may add to understanding the temporal trend in atmospheric methane, and specifically, whether they may differentiate the contributions of fossil fuel and microbial sources. **EDGAR** (**Emissions Database for Global Atmospheric Research** (Crippa et al., 2020)) provides high-quality constraints on methane fluxes from major anthropogenic sources, and different versions of EDGAR reflect uncertainty in understanding of the apportionment of these fluxes over the past few decades. We used two versions of EDGAR and also considered another model of fossil fuel flux (Höglund-Isaksson, 2017) to build four different scenarios for anthropogenic source fluxes for our box model. EDGAR does not include wetland emissions and those are calculated (a free variable) to close the flux balance needed by the model. Each scenario broadly follows one of four parameterizations[5] of anthropogenic source fluxes to obtain an estimate of the composition and evolution of $\Delta^{12}CH_2D_2$ and $\Delta^{13}CH_3D$ through time (Figure 4.3). The aim is to determine whether the isotopologue data would yield detectable signatures to distinguish among the four modeled scenarios.

[5] The parameterization of anthropogenic fluxes is described in more detail in Appendix B and includes the following: one scenario broadly matches fluxes of EDGAR 6.0, but smoothed to reduce artifacts of short term change; another broadly matches fluxes of EDGAR 5.0, also smoothed; a third substitutes a smoothed version of natural gas fluxes proposed by Höglund-Isaksson into the EDGAR 6.0 scenario; and the fourth substitutes a smoothed version of natural gas fluxes proposed by Höglund-Isaksson into EDGAR 5.0 scenario.

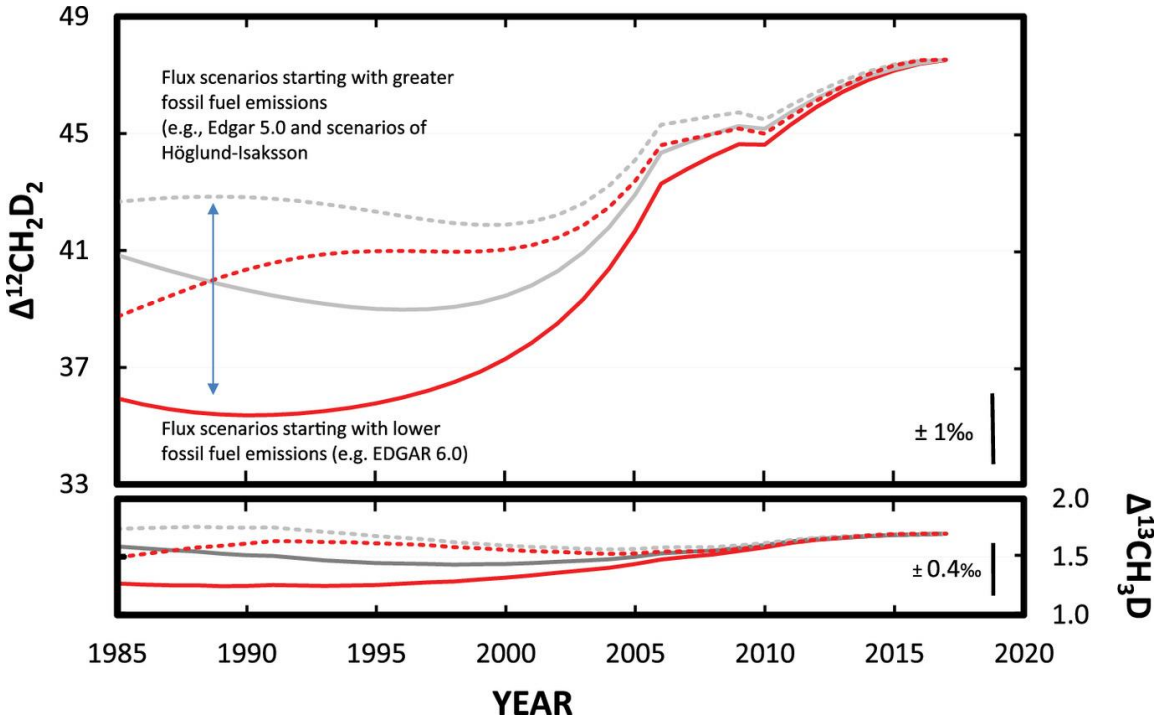

Figure 4.3. **Plot of model for variation of $\Delta^{12}CH_2D_2$ (top) and $\Delta^{13}CH_3D$ (bottom) scaled to have proportional signal compared to uncertainty** (bars on lower right of each plot). Four model scenarios are explored (see Appendix B for more detail) using different parameterization of sources, but the same parameterization for evolution of $\delta^{13}C$, δD, sink, and rise in concentration. Parameterizations are broadly matched to the EDGAR (Emissions Database for Global Atmospheric Research) versions 6.0 and 5.0 (Crippa et al., 2020) with and without substitution of a smoothed version of the natural gas fluxes proposed by Höglund-Isaksson (2017). The models are constrained to converge on the present-day composition for atmospheric methane and solved using an inverse approach. The models show that $\Delta^{12}CH_2D_2$ (top) and $\Delta^{13}CH_3D$ (bottom) vary in different ways for the different source flux parameterizations even when they reproduce the same evolution of $\delta^{13}C$, δD, sink, and rise in concentration. Solid red line is for fluxes broadly matched to EDGAR 6.0. Solid gray line is for fluxes broadly matched to EDGAR 5.0. Dashed lines are for fluxes that substitute the smoothed version of natural gas fluxes proposed by Höglund-Isaksson (2017) into the EDGAR 6.0 (red dashed) and EDGAR 5.0 (grey dashed) fluxes.

The temporal model evolution of atmospheric methane for the different scenarios is generally similar in form, with lower values of $\Delta^{12}CH_2D_2$ and $\Delta^{13}CH_3D$ in the 1980's, followed by a rise in values starting in the 1990's that levels off in the second decade of this century. This form is driven by the principles similar to those that drove the irregular rise of methane – the increase in $\Delta^{12}CH_2D_2$ and $\Delta^{13}CH_3D$ values is attributed to an approach to steady state as the rise tapered off.

As seen in Figure 4.3, both $\Delta^{12}CH_2D_2$ and $\Delta^{13}CH_3D$ are sensitive to the chosen test case scenarios for anthropogenic CH_4 sources, and since these scenarios are broadly similar to those that have been proposed by EDGAR, and because other model parameters (sink, concentration history, bulk isotopes, and KIE) are kept constant (the same), it can be concluded that the isotopologue approach adds information and improves the ability to refine understanding of the global methane cycle. Reaching this goal will be a challenge not only because of the difficulty and time involved in making these measurements, but also because of the scale of this global problem where methane and its isotopologues vary from pole to pole and on seasonal, annual, and decadal timescales (Basu et al., 2022; Bousquet et al., 2006; Fujita et al., 2020; Lan et al., 2021; Lan et al., 2023; Nisbet et al., 2019; Quay et al., 1999; Rice et al., 2016; Zhang et al., 2023; Zhang, Poulter, et al., 2022). It will therefore be important that more laboratories develop the instrumentation and capability to extract and analyze the isotopologue composition of atmospheric methane. Measurement of air from the past will prove more challenging because existing sample archives are highly precious and only contain small amounts of air. Trapped air samples from natural settings, like arctic firn (partially compacted granular snow that persists from prior years) should provide a means to explore methane isotopologue changes in the past, but these may become increasingly rare as global warming melts these icy archives.

Digging further into the underlying reason for the variation of $\Delta^{12}CH_2D_2$ among the four investigated model anthropogenic source flux scenarios, we hypothesize that this is in large part due to the greater contrast between negative $\Delta^{12}CH_2D_2$ for global microbial sources compared to fossil fuel sources. A critical part of this model exercise and this response to source was that the

derived composition of the total source would evolve differently, depending on whether fossil fuel or microbial wetland fluxes drove the rise in atmospheric methane concentration (Figure B.12). Further to this point, the D/H required of the wetland source must change significantly if the rise is due to fossil sources, but is stable if wetlands control the rise, which would lend support to recent findings that attribute the rise to increases in wetland fluxes on the basis of bulk ^{13}C abundances (Fujita et al., 2020; Gropp et al., 2022; Milkov, Schwietzke, et al., 2020; Rigby et al., 2017), but see Zhang, Poulter, et al. (2022) for arguments that the ^{13}C abundances permit alternate interpretations.

4.9. Conclusions

This study contributes three findings relating isotopologue data to atmospheric methane cycling. Isotopologue measurements of atmospheric methane provide additional, independent constraints on contributions from local sources that promise to strengthen source apportionment at regional and local levels. At a global level, the measurements of atmospheric methane isotopologues show that microbial CH_4 sources have clearly distinct (negative) $\Delta^{12}CH_2D_2$ values compared to fossil fuel sources, and this makes atmospheric methane isotopologue measurements more sensitive for source apportionment than previously suggested. In contrast, $\Delta^{13}CH_3D$ variations appear to be less sensitive for source apportionment, except in local source apportionment efforts where sources have distinctly different $\Delta^{13}CH_3D$. Finally, a model analysis shows that $\Delta^{12}CH_2D_2$ data and $\Delta^{13}CH_3D$ data will add to understanding of decadal changes in the global methane cycle (past and future), specifically as it relates to fluxes from fossil fuel and microbial contributions to global methane burden.

4.10. Materials and Methods

4.10.1. Sampling

Surface air, chamber, and smoke samples were collected into Tedlar bags (10, 20, or 200 L) using a Gast (P704) diaphragm pump. Methane from anaerobic incubations was extracted from the headspace using an air-tight syringe with a valve. Methane from bubbles released from a rice paddy was collected in a funnel and then into a 50-cc syringe with a valve.

For air samples, we generally use 600 to 800 L of sample, but we have worked with some samples as small as 200-400 L. For chamber and smoke samples, methane concentrations were higher and smaller samples were used. Sample size was determined to provide approximately 1.5 to 6 cc of purified methane, which was necessary for the low abundance isotopologue abundance measurements. For CO_2-rich samples, CO_2 and water were removed using a liquid nitrogen-cooled trap before introduction to the purification manifold.

4.10.2. Preconcentration and Purification

At the entrance to the purification manifold, the gas passes through a 400 cc canister trap filled with dehydrated silica gel (preheated to 150ºC overnight). The sample is then passed through a

set of liquid nitrogen-cooled U-traps (6 in total, ½ inch OD, ~40 cm length, packed with 100-120 mesh particle size HayeSep DB porous polymer (Sigma-Aldrich®)) by pumping with a mechanical vacuum pump on the far end of the manifold. The restriction of the canister trap holds the gas pressure before the set of HayeSep DB traps at ~200 mbar, thus allowing a 600 L sample to pass through in about 2 hours. Once the sample has been completely pumped through this canister trap, the upstream valve is closed, and the sample is pumped until the baseline stabilizes.

Following this, the sample is warmed to ~150 °C to transfer it to a second (smaller) liquid nitrogen cooled HayeSep DB filled trap (3/8" od, ~40 cm length), again, by pumping on the downstream side. For syringe samples, the samples are transferred directly to this second U trap because the concentration of balance gases (nitrogen and oxygen) is low. Once the transfer is complete and the pressure has dropped to about 10 mbar, this trap is warmed to ~−117°C using an ethanol slush to release most of the nitrogen, some oxygen, and possibly some krypton, but to retain the methane.

After 30 minutes, the trap is isolated and the preconcentrated sample is transferred using a sample tube with silica gel (freezing onto the silica gel by cooling with liquid nitrogen) to a purification manifold that is very similar in design to the manifold used at UCLA (Young et al., 2016). The sample is transferred to an injection loop filled with liquid nitrogen-cooled silica gel, which is subsequently warmed and injected using a 2-way Valco switching valve into an SRI 310C gas chromatograph. The chromatographic column is 1/8" diameter and 25' long filled with 5 Å mol sieve held at 54°C. The helium carrier gas flow of 35 mL/min separates methane from

krypton, nitrogen, and oxygen. A thermal conductivity detector is used to identify the start and end of the CH_4 peak, and the flow is manually diverted into a liquid nitrogen-cooled collection loop filled with silica gel through this interval. Additional details and schematics of our extraction and purification manifold can be found in Appendix B (Figure B.18 and Figure B.19).

Once the sample is collected, the collection loop contains methane and helium and it is necessary to remove the carrier gas without loss of methane. At UCLA this is done by slowly pumping the helium away. At UMD, we use a slightly different strategy by pumping through a second U trap (filled with silica gel) to trap any methane that might be drawn away as the helium is outgassed. Once the helium is quantitatively removed, the remaining methane is transferred to this second loop, which is then warmed and transferred to a sample tube filled with silica gel after the recovered yield is measured manometrically.

4.10.3. Measurements

The purified methane samples were then analyzed using the Panorama high-resolution mass spectrometer (Nu Instrument) at UMD. Ion currents of $^{12}CH_4^+$, $^{13}CH_4^+$, $^{12}CH_3D^+$, $^{13}CH_3D^+$, and $^{12}CH_2D_2^+$ were measured using a minimum mass resolving power (MRP) of 36,000 (5%-95%) for clean separation of $^{12}CH_2D_2$ from $^{13}CH_3D$, corresponding to an approximate entrance slit width of 35 μm (Young et al., 2016). Methane was measured using sample standard bracketing relative to a working gas (UMD-1). We see a minor dependence of isotopic composition on the pressure balance between the sample and reference that we hypothesize is related to production of both CH_3^+ and CH_4^+ in the source. We post process the data to determine the intercept where

sample and working gas pressures are equal. We also remove the first cycle from each set of sample standard bracketing pairs and any 3 σ outliers during each analytical session, which last between 24 and 36 hours. Precisions of the mass spectrometric measurements based on internal reproducibility (counting statistics for rare isotopologues) are reported in Table B.1.

Data are reported in standard notation (definitions and description in Appendix B). Calibrations reported here are done against AL-1 from MIT and the clumped isotopologues are calibrated by comparison with three thermal equilibrations using γ-alumina catalyst (Wang et al., 2015). We tested our reproducibility of samples with different $\Delta^{12}CH_2D_2$ and $\Delta^{13}CH_3D$ by sharing composite samples of methane separated from atmospheric air, methane from wetlands, and our reference gas with the California Institute of Technology, and by comparison of analyses of large methane samples provided for two other gases previously measured by MIT (Gonzalez et al., 2019; Ono et al., 2014) and UCLA (Young et al., 2016) (see Appendix B Table B.2 and Table B.3).

4.11. Acknowledgments

Funding for the UMD Panorama mass spectrometer has come from U.S. National Science Foundation (NSF MRI EAR-1725766 MRI: Acquisition of a High Mass Resolution/High Sensitivity Isotope Ratio Mass Spectrometer for Earth Sciences 2017-2020 (JF, AJK, RRD)) as well as infrastructure support for the facility from the Geology Department, the College of Computer, Mathematics, and Natural Sciences, and the Provost's Office at UMD. Funding for the establishment of protocols for air sampling were provided by Water Resources Research Act

Program Annual Base grant US Department of the Interior-US Geological Survey 2020, 2021 (JF and MH). Funding to support MH was provided by a UMD President's Postdoctoral Fellowship Program for providing funding that aided in supporting this work, and then by U.S. National Science Foundation grant (EAR-PF: 2052834) (MH). Finally, we thank Doug Rumble for providing samples of natural gas and for assistance during the commissioning of our mass spectrometer.

Chapter 5: Constraining Wetland and Landfill Methane Emission Signatures Through Atmospheric Methane Clumped Isotopologue Measurements

This chapter is a paper in press in

Journal of Geophysical Research: Biogeosciences (2025) http://doi.org/10.1029/2024JG008249

Authors and Affiliations:

Jiayang Sun[1,2,3*], Cédric Magen[1], Mojhgan A. Haghnegahdar[1,4], Jiarui Liu[5], Julianne M. Fernandez[1,6], and James Farquhar[1,7]

[1]Department of Geology, University of Maryland, College Park, MD 20742, USA.

[2]Air Resources Laboratory, National Oceanic and Atmospheric Administration, College Park, MD 20740, USA.

[3]Cooperative Institute for Satellite Earth System Studies (CISESS), University of Maryland, College Park, MD 20740, USA.

[4]Smithsonian Environmental Research Center, Edgewater, Maryland 21037, USA.

[5]Department of Earth, Planetary and Space Sciences, University of California, Los Angeles, CA 90095, USA.

[6]Global Monitoring Laboratory, National Oceanic and Atmospheric Administration, Boulder, CO 80305, USA.

[7]Earth System Science Interdisciplinary Center, University of Maryland, College Park, MD 20740, USA.

* Corresponding author: Jiayang Sun (jiayangs@umd.edu)

Jiayang Sun is the first author of this manuscript and has made significant contributions, including but not limited to conceptualization, methodology, validation, formal analysis, investigation, resources, data curation, writing – original draft, writing - review & editing, and visualization.

5.1. Key Points

1. Methane clumped isotopologues can fingerprint methane sources, using the Keeling plot method and a new mathematical method.
2. Methane clumped isotopologue signatures of background air, landfill, and wetland endmembers are defined and derived.
3. Wetland methane emission isotope signals show seasonal variations attributed to microbial oxidation.

Keywords

methane; clumped isotopologues; wetland; landfill; air measurement

5.2. Abstract

Microbial methane emissions are associated with a wide range of isotopic signatures, providing information about the sources and sinks of methane. Methods of directly sampling methane from environments such as wetlands may fail to capture the temporal and spatial variations in emissions at a specific site and time. The Keeling plot method is commonly used to infer the overarching isotopic signatures of methane sources. In this study, we have expanded the application of the Keeling plot from conventional stable isotope ratios to include novel clumped isotopologue compositions of methane. This advancement aims to provide more robust constraints on regional methane emission signatures. We analyzed methane isotopologue compositions from air samples collected above wetlands and landfills across Maryland, USA, and determined the endmember compositions for background air, wetland, and landfill sources. Our findings indicate that the isotopologue compositions of methane from regional wetland emissions exhibit seasonal variations — $\delta^{13}C$ and δD values become less positive as winter approaches, reflecting changes in methane oxidation and production rates. The continuous monitoring of air methane isotopologue signatures will deepen our understanding of the seasonal patterns in methane emissions and contribute to refining the global methane budget, as valuable insights can be extracted from these measurements.

5.3. Plain Language Summary

This study extends the method using air measurement to investigate methane emission signatures from wetlands and landfills. Our findings reveal seasonal changes in wetland emission signatures, which are attributed to microbial oxidation.

5.4. Introduction

Carbon and hydrogen isotopic compositions of methane have proven to be valuable tools for studying microbial methane emissions. Microbial methane refers to methane associated with microbial activities, involving both production and oxidation processes, such as methane from wetlands and landfills. Various factors collectively shape the bulk isotopic signatures of microbial methane emissions, including generation pathways (Hornibrook et al., 1997; Whiticar, 1999; Whiticar et al., 1986), oxidation processes (Alperin et al., 1988; Coleman et al., 1981; Happell et al., 1994), and transport mechanisms (Bastviken et al., 2004; Walter et al., 2008). Analyzing the isotopic signatures of the emitted methane can in turn reveal information about these processes. However, extracting information from bulk carbon and hydrogen isotopes alone could be challenging, as multiple processes could lead to overlapping isotopic characteristics (Liu, Treude, et al., 2023; Milkov & Etiope, 2018).

The measurements of doubly-substituted isotopologues ($^{13}CH_3D$ and $^{12}CH_2D_2$, hereafter referred to as methane clumped isotopologues) add independent constraints, allowing further exploration

of processes related to methane emissions. If the intra-molecular isotope exchange of methane reaches thermodynamic equilibrium, the clumped isotopologue signals can be used to constrain the temperatures at which methane formation or equilibration occurs (Stolper, Lawson, et al., 2014; Stolper et al., 2015; Stolper, Sessions, et al., 2014; Young, Kohl, Lollar, et al., 2017). However, the clumped signals of some natural methane samples deviate from thermodynamic equilibrium (Douglas et al., 2016; Douglas et al., 2020; Giunta et al., 2022; Giunta et al., 2019; Haghnegahdar et al., 2024; Haghnegahdar et al., 2023; Liu, Treude, et al., 2023; Wang et al., 2015; Young, Kohl, Lollar, et al., 2017). Lab-culture experiments and modeling have demonstrated that different methanogenesis pathways could result in different isotope fractionations of clumped isotopologues (Cao et al., 2019; Giunta et al., 2022; Gropp et al., 2021; Gropp et al., 2022; Gruen et al., 2018; Ono et al., 2021; Ono et al., 2022; Rhim & Ono, 2022; Young, Kohl, Lollar, et al., 2017). Methane oxidation can further cause fractionations (Haghnegahdar, 2018; Krause et al., 2022; Ono et al., 2021; Wang et al., 2016), with oxidation pathways and reversibility scenarios controlling the directions and extents of the fractionation (Giunta et al., 2022; Li, Chiu, et al., 2024; Liu, Harris, et al., 2023).

The diverse control mechanisms on microbial methane emissions pose challenges to using isotopes to investigate these methane sources, which exhibit substantial spatial and temporal variabilities (Burke et al., 1988; Ganesan et al., 2018; Johnson et al., 2022; Walter et al., 2008). For example, even within adjacent areas of the same wetland, or at the same sampling site but sampled at different times, the isotopic signatures of wetland methane can greatly differ. A single sample collected from a lake surface may not indicate whether it represents methane from ebullition or coincidently captures a water turnover event, without additional contextual

information (DelSontro et al., 2015; Wik et al., 2016). Point samples can be unrepresentative of overall emissions (DelSontro et al., 2015; Langenegger et al., 2019; Wik et al., 2016).

To overcome biases stemming from high spatial and temporal variability, studies have analyzed isotopes of methane in the air above targeted areas, aiming to provide a more representative snapshot of overall source signatures and their variations (e.g. (Bakkaloglu et al., 2022; Fisher et al., 2011; Sriskantharajah et al., 2012)). This method relies on the assumption that methane emissions from regional upwind sources mix with the atmosphere, with varying degrees of mixing depending mainly on distance. This mixing process is expected to induce linear changes in both methane concentration and its isotopic composition in the downwind air, reflecting the integrated signature of the sources. A common analytical approach to disentangle the mixing of source and background is the Keeling plot method (Bakwin et al., 1998; Keeling, 1958). This technique involves plotting $\delta^{13}C$ and/or δD against the reciprocal of methane concentration ($1/[CH_4]$) in air samples to interpolate the source $\delta^{13}C$ and/or δD values.

Incorporating clumped isotopologues would enhance our capability to differentiate methane sources through atmospheric measurements. Haghnegahdar et al. (2023) reported first measurements of air methane clumped isotopologues and incorporated the results into a global one-box model to delineate the contributions of microbial and thermogenic methane to the global methane budget. A recent study by Haghnegahdar et al. (2024) analyzed air samples collected at various heights from a few centimeters to several meters above the stream and demonstrated that the mixing of wetland methane with air can be traced through clumped isotopologues. Expanding the ideas of Haghnegahdar et al. (2024), this study applied the Keeling plot method to a series of

air samples from eastern Maryland to derive the unknown isotopologue signatures of landfills and regional wetlands. The objectives of this study were

1) To explore the variability of methane clumped isotopologue signatures in air influenced by sources, particularly when the air mixes with methane originating from wetlands or/and landfills,

2) To assess the potential of atmospheric methane clumped isotopologues for inferring source compositions in the absence of direct source information, and to determine if the variability in source signatures is reflected in the air measurements, and

3) To conducted atmospheric measurements at a small-scale site to infer methane source signatures, serving as a proof-of-concept to evaluate whether large-scale (e.g., global) atmospheric monitoring of methane clumped isotopologues can effectively provide meaningful insights into source compositions.

5.5. Samples and Methods

5.5.1. Sampling Area and Campaigns

The study area is the Patuxent River watershed of the Chesapeake Bay, Maryland, USA. Originating in Maryland's upland area, the Patuxent River flows through the D.C.-Baltimore urbanized corridor before merging into the Chesapeake Bay. This watershed is marked by the presence of abundant natural freshwater tidal wetlands, jousted by agriculture and urbanized areas. Progressing from north to south, there is a gradual increase in salinity levels, influenced by

the proximity to the bay and the ocean (Chesapeake Bay Program, https://www.chesapeakebay.net/what/maps/chesapeake-bay-mean-surface-salinity-1985-2018).

Our sampling focused on the Jug Bay Wetlands Sanctuary, with additional samples collected upstream and downstream along the Patuxent River (Figure 5.1 and Table C.1). The sampling events can be categorized as follows:

1. Time series sampling at the Jug Bay Car Top Boat Launch (hereafter referred to as the Jug Bay), from June 12, 2022, to May 7, 2023. Sampling intervals varied from two weeks to four months, with a major pause in sampling activities in early winter 2023;
2. A transect of samples taken along the Patuxent River, from upstream (Patuxent Research Refuge, Bowie, MD) through midstream (Chaneyville Rd, Lower Marlboro, MD), to downstream (Cruise to Patuxent River Station 3), conducted throughout Summer 2023. The Jug Bay is centrally located within this sampling series;
3. Two air samples collected downwind of the Brown Station landfill in Winter 2022 and 2023, during which high methane concentration plumes were detected in mobile greenhouse gas surveys.

Each sampling site is further described in Appendix C (Note C.1). In the following sections, samples collected above the wetlands from Jug Bay and along the Patuxent River are collectively referred to as "wetland air". Meanwhile, samples that are explicitly influenced by emissions from the Brown Station landfill are referred to as "landfill air".

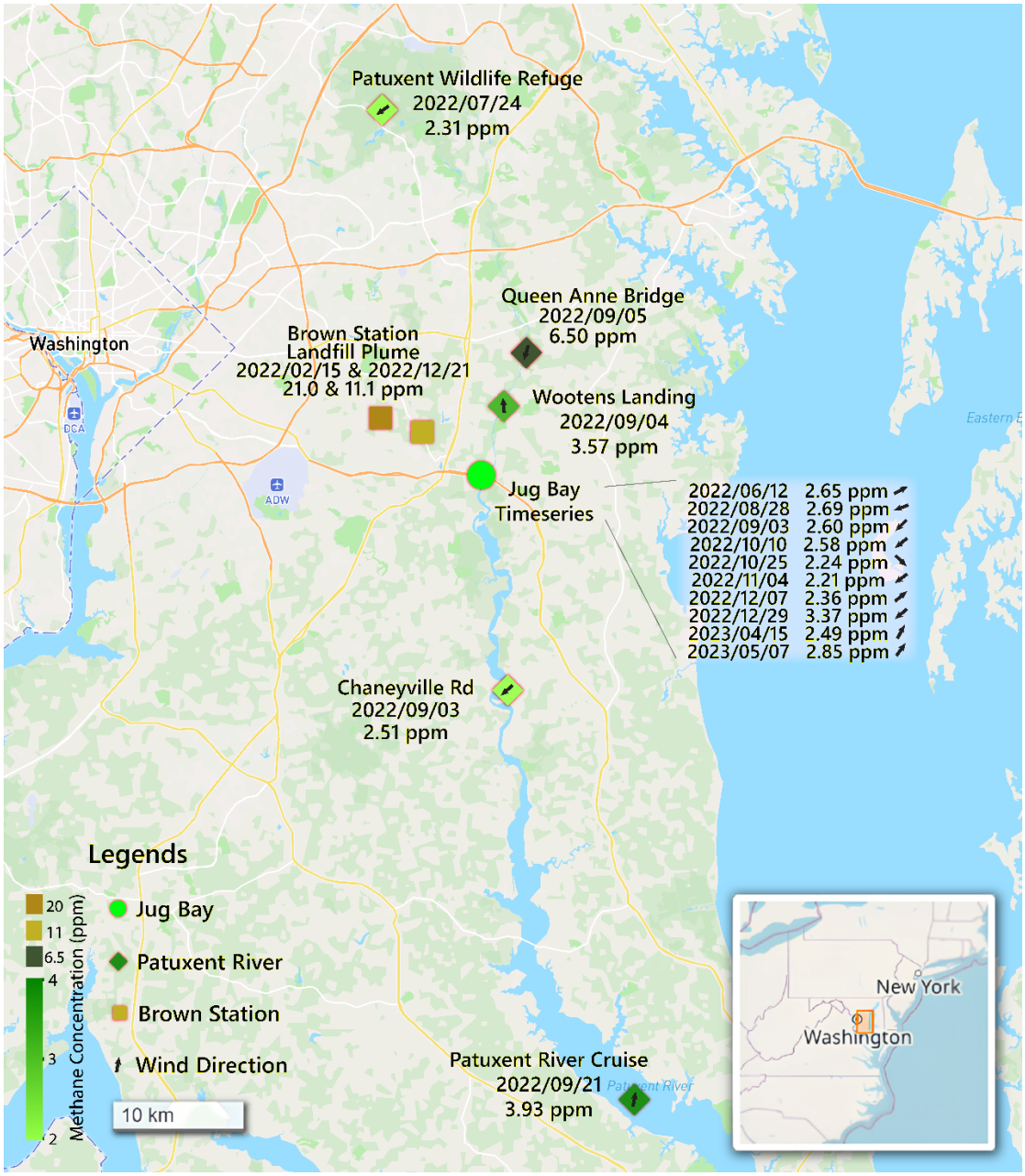

Figure 5.1. **Map of sampling locations.** The Jug Bay time series samples are represented by circles with 10 sampling events at the same location. The Patuxent River series samples are shown by diamonds, and landfill air samples by squares. Wetland air samples are in varying shades of green, with darker greens indicating higher methane concentrations. Landfill air is filled with light and dark brown shades. Prevailing wind directions at the time of sampling are indicated by black arrows on the map. The base map was customized using Mapbox. It was then called with the Python Folium package to overlay the base map, add a minimap, and plot data points. Annotations were added in Adobe Illustrator.

5.5.2. Sampling Methods

Sampling was carried out using portable air mattress pumps to inflate Tedlar Bags (CEL Scientific Corp.) (Figure C.1 and Figure C.2). Approximately 800 L of air were collected for each sample, for a duration of ~30 min. Sampling dates were picked so that the night before sampling had low wind velocities (<5 mph) to minimize possible horizontal mixing between different local sources. Most samples were collected at or just after sunrise, which provided the greatest likelihood of capturing methane samples before the nocturnal boundary layer dispersed, minimizing the chance of vertical convective mixing that was established during the day. Patuxent River Cruise sample was collected at noon because it was unsafe for the sampling boat to leave the dock before sunrise. Detailed sampling date, time, location information can be found in Table C.1.

5.5.3. Analytical Methods

The samples went through extraction and purification usually on the same day or the next day of sampling. The methodology for these procedures is specifically tailored to fully extracting methane from large volumes of air without causing fractionation (Haghnegahdar et al., 2023). In brief, a cryogenic separation technique is employed to remove substantial quantities of N_2 and O_2 while retaining CH_4 and Kr. A liquid nitrogen-cooled glass condenser was added before introducing the sample into the extraction line for humid samples (Sun, Haghnegahdar, et al., 2025). The preliminarily concentrated gas is then subjected to further separation via gas

chromatography (GC) to separate pure methane from other gases. Methane concentrations in each Tedlar Bag were measured using the Aeris MIRA Ultra Methane/Ethane Analyzer (Aeris302) or a GC (Shimadzu® GC-8AIF) before extraction.

We measured the abundances of $^{13}CH_4$, $^{12}CH_3D$, $^{13}CH_3D$, and $^{12}CH_2D_2$ isotopologues relative to $^{12}CH_4$, using the Panorama (Nu Instrument) at the University of Maryland (UMD), College Park, Maryland. Panorama is a high-sensitivity high-resolution gas-source mass spectrometer with a mass-resolving power that can distinguish between $^{13}CH_3D$, $^{13}CH_5$ (interference), and $^{12}CH_2D_2$. A comprehensive description of the Panorama instrument and the analytical procedures at UMD can be found in Young et al. (2016) and Haghnegahdar et al. (2023). The measured relative abundances are reported in ratio differences as δ notations:

$$\delta^{13}C_{sample-standard} = \frac{\left({}^{13}C/_{12}C\right)_{sample}}{\left({}^{13}C/_{12}C\right)_{standard}} - 1 \quad (5.1)$$

$$\delta D_{sample-standard} = \frac{({}^{D}/_{H})_{sample}}{({}^{D}/_{H})_{standard}} - 1 \quad (5.2)$$

$$\delta^{13}CH_3D_{sample-standard} = \frac{({}^{13}CH_3D/_{12}CH_4)_{sample}}{({}^{13}CH_3D/_{12}CH_4)_{standard}} - 1 \quad (5.3)$$

$$\delta^{12}CH_2D_2{}_{sample-standard} = \frac{({}^{12}CH_2D_2/_{12}CH_4)_{sample}}{({}^{12}CH_2D_2/_{12}CH_4)_{standard}} - 1 \quad (5.4)$$

The reference standards are Vienna Pee Dee Belemnite (V-PDB) for carbon isotopes and Vienna Standard Mean Ocean Water (V-SMOW) for hydrogen isotopes (Coplen, 1994). The standard for clumped isotopologues ($^{13}CH_3D$ and $^{12}CH_2D_2$) is a hypothetical methane, which adopts the carbon isotope composition from V-PDB and the hydrogen isotope composition from V-SMOW,

and assumes an intra-molecular stochastic distribution - purely random binding of ^{12}C, ^{13}C, H, and D: (Young et al., 2016)

$$X_{^{13}CH_3D,\ stochastic} = 4 * X_{^{13}C} * X_D * (X_H)^3 \quad (5.5)$$

$$X_{^{12}CH_2D_2,\ stochastic} = 6 * X_{^{12}C} * (X_D)^2 * (X_H)^2 \quad (5.6)$$

$X_{^{13}C}$ and X_D denote the fractions of ^{13}C and ^{2}H atoms among the total carbon and hydrogen atoms.

We could further calculate the Δ notations to address the deviations of clumped isotopologue abundances from the stochastic (purely random) state (Eiler & Schauble, 2004; Young et al., 2016):

$$\Delta^{13}CH_3D = \frac{1+\delta^{13}CH_3D}{(1+\delta^{13}CH_4)*(1+\delta^{12}CH_3D)} - 1 \quad (5.7)$$

$$\Delta^{12}CH_2D_2 = \frac{1+\delta^{12}CH_2D_2}{(1+\delta^{12}CH_3D)^2} - 1 \quad (5.8)$$

The equations presented above are approximations that simplify the calculations. The errors introduced by the approximation are negligible compared to the measurement precision (Haghnegahdar et al., 2023; Sun, Haghnegahdar, et al., 2025). The internal uncertainty is related to measurement duration and instrument conditions. Typically, longer measurement time leads to lower uncertainty, but this requires larger sample volume. The 1SD internal uncertainties are reported in Table C.1 for each sample, and are typically on the order of 0.03‰ for $\delta^{13}C$, 0.1‰ for δD, 0.4‰ for $\Delta^{13}CH_3D$, and 1.5‰ for $\Delta^{12}CH_2D_2$, with a few exceptions (Table C.1). The combined uncertainty is more difficult to estimate, but will be larger than the internal uncertainty as it includes a combination of uncertainty from the instrument and from gas handling and standardization.

5.5.4. Wind and Water Data

The wind speed and direction, water table depth, salinity, and dissolved oxygen concentration data were acquired from nearby monitoring stations operated by the NOAA National Estuarine Research Reserve System (NERRS) . Detailed descriptions can be found in Appendix C (Note C.2). Wind speeds and directions, and water table depths data are summarized in Table C.1. Salinity and dissolved oxygen concentration are plotted in Figures C.1 and Figure C.2.

5.6. Results

5.6.1. Methane Concentrations

Methane concentrations in wetland air samples spanned from 2.21 to 6.50 ppm (Table C.1). This range suggests varying degrees of source influence mixing with the air, since background air methane concentrations typically do not reach 2.2 ppm according to NOAA Global Monitoring Lab (GML) data (Lan et al.). One sample collected at the Queen Anne Bridge recorded an unusually high methane concentration of 6.50 ppm, the reason for which remains unclear but is unlikely to be contamination from the landfill plume, given the northward wind direction and the isotope data ($\delta^{13}CH_4$ = -52.4‰ and $\delta^{12}CH_3D$ = -139.0‰). Methane concentrations in other wetland air samples did not exceed 4 ppm and mostly ranged between 2.3 and 2.7 ppm, which

reflected mixing from the wetlands (see discussions in Section 5.7.1), albeit a minor contribution from the Brown Station landfill cannot be excluded. Two samples collected downwind of the Brown Station landfill recorded exceedingly higher methane concentrations of 11.1 ppm and 21.0 ppm, evidently indicating the landfill plume.

5.6.2. Carbon and Hydrogen Isotopes

The isotopic values of wetland air exhibit a wide range, extending from -48.6‰ to -55.4‰ for $\delta^{13}CH_4$, and from -98.4‰ to -181.4‰ for $\delta^{12}CH_3D$ (Table C.1 and Figure 5.2). While the $\delta^{13}CH_4$ values of landfill air fall within the same range as those of wetland air, the $\delta^{12}CH_3D$ values of landfill air are notably more negative, recorded at -258.7‰ and -286.4‰. Mixing trends for both wetland and landfill are apparent in the $\delta^{12}CH_3D$-$\delta^{13}CH_4$ plot (Figure 5.2), where a higher proportion of source mixing correlates with more negative $\delta^{12}CH_3D$ and $\delta^{13}CH_4$ values. These mixing scenarios are further discussed in Section 5.7.1.

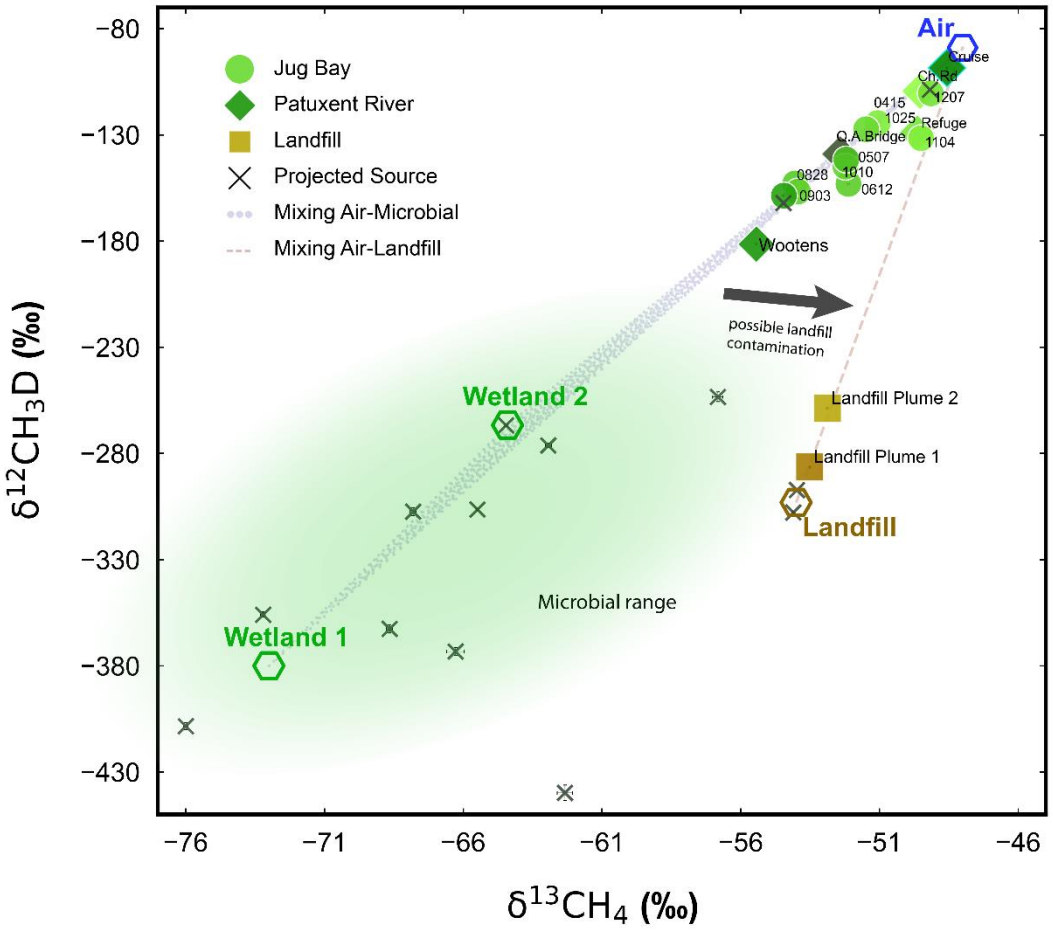

Figure 5.2. **$\delta^{12}CH_3D$-$\delta^{13}CH_4$ plot of samples, together with deduced endmembers, projected source compositions, and mixing lines and grids.** Hexagonal hollow symbols represent the deduced endmembers — blue stands for air, green for wetland, and brown for landfill. The wetland endmember encompasses a broad potential range, approximately shown in transparent green shade. Within this range, 'Wetland 1' and 'Wetland 2' are two representative compositions. Square solid symbols are two landfill air samples. Diamond-shaped solid symbols represent the Patuxent River series of wetland air samples. Circular solid symbols refer to the Jug Bay time series of wetland air samples. The color gradient of all solid symbols, transitioning from light green to dark green to brown, signifies methane concentrations ranging from near atmospheric levels of 2.2 ppm to the highest 20 ppm. Cross symbols are the projected source composition calculated based on the endmember values and individual sample values. Some crosses are positioned outside the range of the coordinate axis, exceeding the possible isotopic values for natural microbial methane (Liu, 2024). 1 Standard Deviation (SD) errors for each measurement are plotted on the figure but are smaller than the size of the symbols. Light brown dashed line is the mixing trend of air with landfill endmember. Light gray dots present a mixing grid of air and two microbial endmembers.

5.6.3. Methane Clumped Isotopologues

Clumped isotopologue data are presented in Table C.1, Figure 5.3, and Figure 5.4. For wetland air samples, $\Delta^{13}CH_3D$ values ranged between +1.6‰ and +3.2‰. The two landfill samples exhibit $\Delta^{13}CH_3D$ values of -0.8‰ and -0.4‰, which indicates an anti-clumping (negative) $\Delta^{13}CH_3D$ signal of the landfill endmember. The variability is more pronounced in $\Delta^{12}CH_2D_2$: wetland air $\Delta^{12}CH_2D_2$ vary from +41.5‰ to +51.6‰, except for the Queen Anne Bridge sample which has the highest methane concentration and $\Delta^{12}CH_2D_2$ = +33.4‰. The $\Delta^{12}CH_2D_2$ values of landfill air samples are +3.8‰ and -23.3‰. A greater proportion of wetland and/or landfill mixing leads to more negative $\Delta^{12}CH_2D_2$ values in the mixed air.

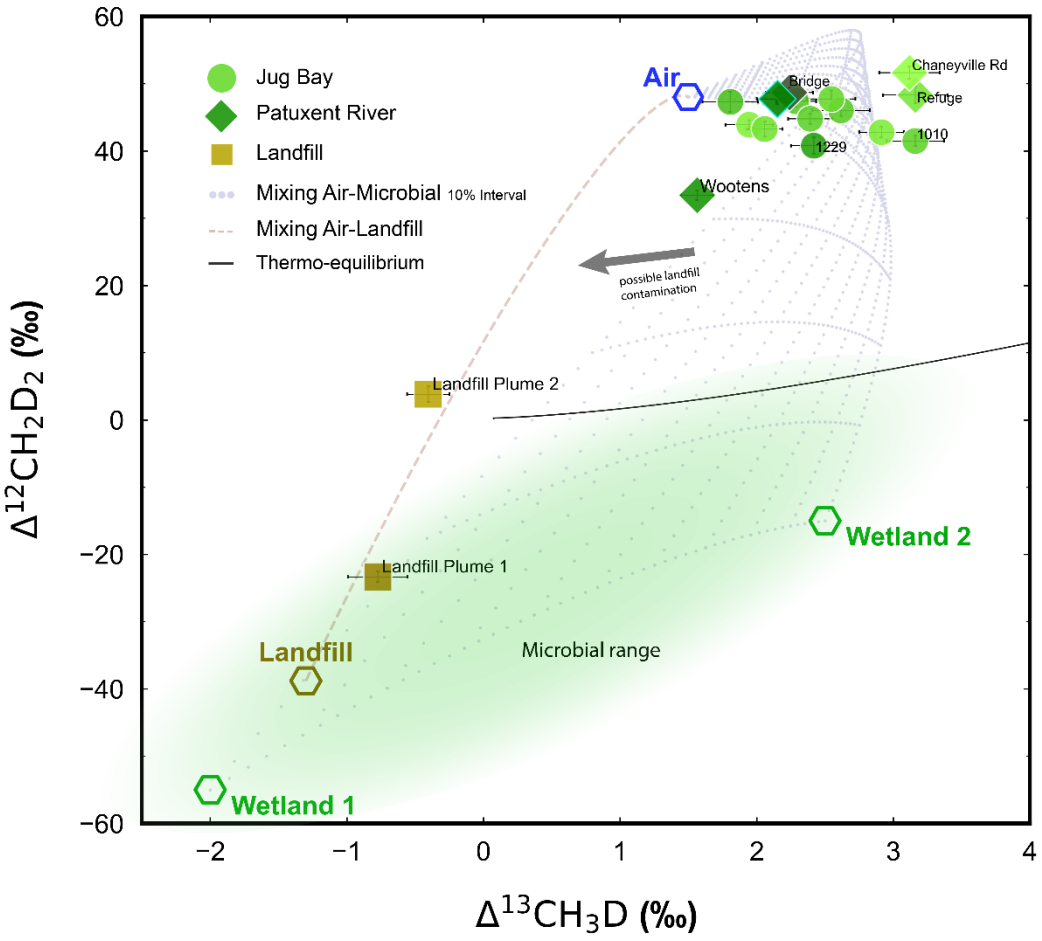

Figure 5.3. **$\Delta^{12}CH_2D_2$-$\Delta^{13}CH_3D$ plot of samples, together with deduced endmembers and mixing lines and grids.** The explanation of symbols can be found in Figure 5.2 caption.

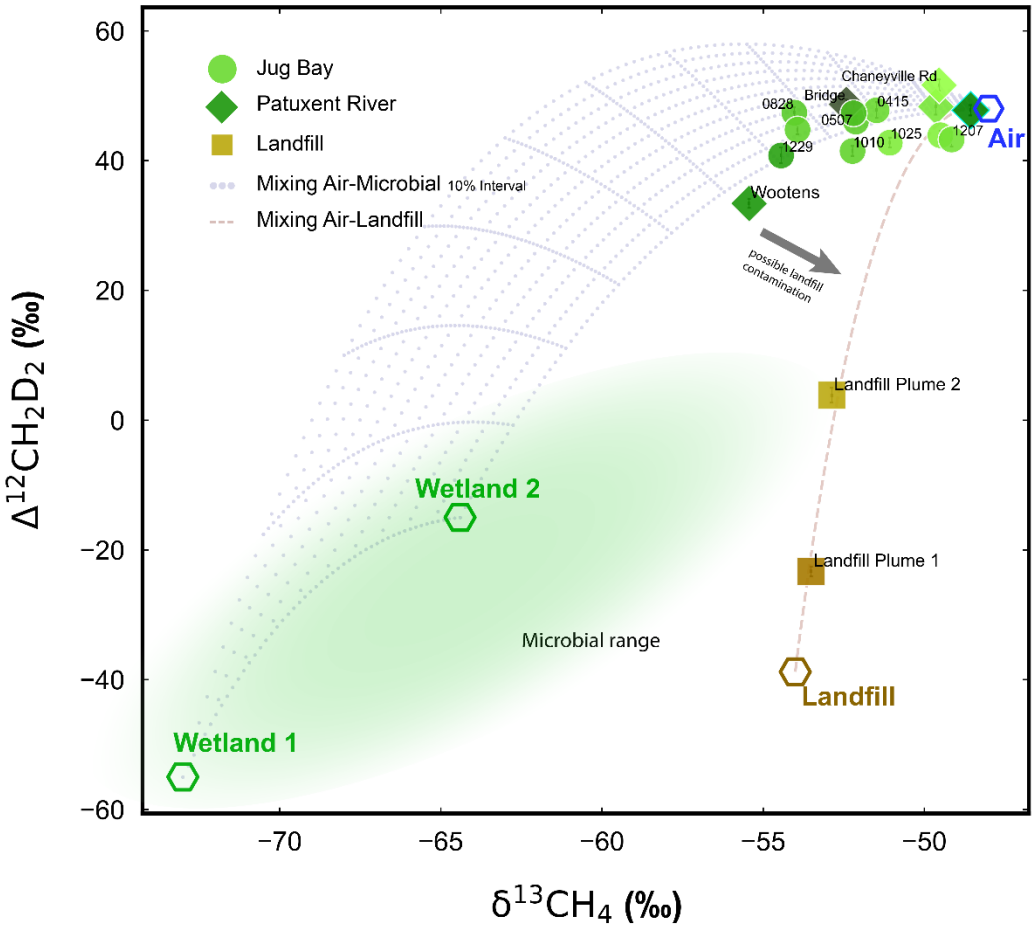

Figure 5.4. **$\Delta^{12}CH_2D_2$-$\delta^{13}CH_4$ plot of samples, together with deduced endmembers and mixing lines and grids.** The explanation of symbols can be found in Figure 5.2 caption.

5.7. Discussion

5.7.1. Mixing

The discussion of mixing is framed within an "Air-Landfill-Wetland three-endmember mixing" framework with five parameters (methane concentration, $\delta^{13}CH_4$, $\delta^{12}CH_3D$, $\Delta^{12}CH_2D_2$, and

$\Delta^{13}CH_3D$). The signatures of each endmember remain elusive, as it is usually challenging to acquire representative isotope and isotopologue signatures directly from each source. The mixing scenarios are illustrated in Figures 5.2-5.4. The compositions of each endmember are listed in Table 5.1.

Table 5.1. **The compositions of each end-member** that are used in the discussion.

Endmember	**[CH_4]**	**$\delta^{13}C$ ‰**	**δD ‰**	**$\Delta^{13}CH_3D$ ‰**	**$\Delta^{12}CH_2D_2$ ‰**
Air	2.05 ppm	-48.0	-89.0	1.5	48.0
Landfill		-54.0	-303.1	-1.3	-38.8
Microbial 1		-73.0	-380.0	-2.0	-55.0
Microbial 2		-64.4	-266.7	2.5	-15.0
Microbial		-68.7	-323.4	0.8	-24.9
Natural Gas		-37.0	-160.0	2.0	8.0
Total Source		-54.2	-295.0	1.5	-20.0

5.7.1.1. Defining Background Air End-Member Signatures

Defining the concentration and isotopic signatures of background air is the basis for subsequent discussions. Monitoring data from NOAA GML (Lan et al.) and NIST Northeast Corridor (Karion et al., 2020) stations in Washington DC (BWD), Baltimore (NWB and NEB), and northern Maryland (TMD) show that air methane concentrations are not static throughout the year, fluctuating between 1.95 ppm to 2.15 ppm. For our study, we have set 2.05 ppm as the background air methane concentration. Methane concentrations in our study area are elevated slightly above the northern hemisphere's tropospheric average because of the Washington D.C.-Baltimore urban plume (Ren et al., 2018) and the inputs from the Marcellus Shale region (Ren et al., 2019).

These urban and natural gas field influences are likely also impacting the isotopic compositions of the background air within the study area. Data from the NOAA GML station in Mauna Loa, Hawaii (MLO) shows that atmosphere $\delta^{13}C$ values are currently transitioning from -47.5‰ to -48‰. We can set the lower limit of background air's $\delta^{13}C$ as -48‰, assuming that urban air is a mixture of background air and some anthropogenic sources (such as natural gas), which typically have more positive isotopic values.

We conducted isotopologue analysis of "background air" at mid-day over one year at the UMD campus. Detailed descriptions of this collection of campus air samples and their compositions are available in Appendix C (Note C.3 and Table C.2). The averaged compositions from this set of campus air are $\delta^{13}CH_4$ = -47.1‰, $\delta^{12}CH_3D$ = -90.2‰, $\Delta^{13}CH_3D$ = +1.9‰, and $\Delta^{12}CH_2D_2$ = +46.3‰, with concentrations between 2.15 and 2.25 ppm. These campus air samples, while informative, may not be pure enough to represent background air at Jug Bay due to potential contamination from local methane sources such as natural gas leakage on campus. If we consider that UMD air is contaminated by natural gas leakage, $\delta^{13}CH_4$ = -47.1‰ and $\Delta^{13}CH_3D$ = +1.9‰ from the averaged UMD campus air can be regarded as the upper limit, while $\delta^{12}CH_3D$ = -90.2‰ and $\Delta^{12}CH_2D_2$ = +46.3‰ can be the lower limit of the background air.

In this study, we set methane concentration at 2.05 ppm, $\delta^{13}CH_4$ at -48.0‰, $\delta^{12}CH_3D$ at -89.0‰, $\Delta^{13}CH_3D$ at +1.5‰, and $\Delta^{12}CH_2D_2$ at +48.0‰, as regional background air methane compositions (Table 5.1). We will proceed by treating the air compositions as fixed in our subsequent discussions, which is a simplification that may introduce some errors. Nonetheless, the primary

goal of this study is to develop a methodology that incorporates clumped isotopologue data to deduce source characteristics from air measurements. Considering the limited precision and availability of data on air methane clumped isotopologue measurements, which restrict our ability to discern minor variations in the background air, this simplification is deemed acceptable.

5.7.1.2. Determining Landfill Emission Signatures

The isotopologue compositions of the Brown Station landfill endmember during winter were derived from the defined background air compositions and the measured values from landfill air sample values using a 3-point Keeling plot approach (Figure 5.5). It yields $\delta^{13}CH_4$ = -54.0‰, $\delta^{12}CH_3D$ = -303.1‰, $\delta^{13}CH_3D$ = -341.6‰, and $\delta^{12}CH_2D_2$ = -533.0‰. Subsequently, we can calculate $\Delta^{13}CH_3D$ = -1.3‰ and $\Delta^{12}CH_2D_2$ = -38.5‰ using the equations in Section 5.5.3. Two-point inversions for the 21.0 ppm and 11.1 ppm landfill air samples separately yield similar results. These projected $\delta^{13}CH_4$ and $\delta^{12}CH_3D$ values align with the range provided by on-site landfill measurements (Bakkaloglu et al., 2021). However, since we only sampled the plume outside one landfill, and both two samples were collected during winter, the seasonal and site-specific variabilities of the landfills (Spokas et al., 2021) are not within the scope of this study.

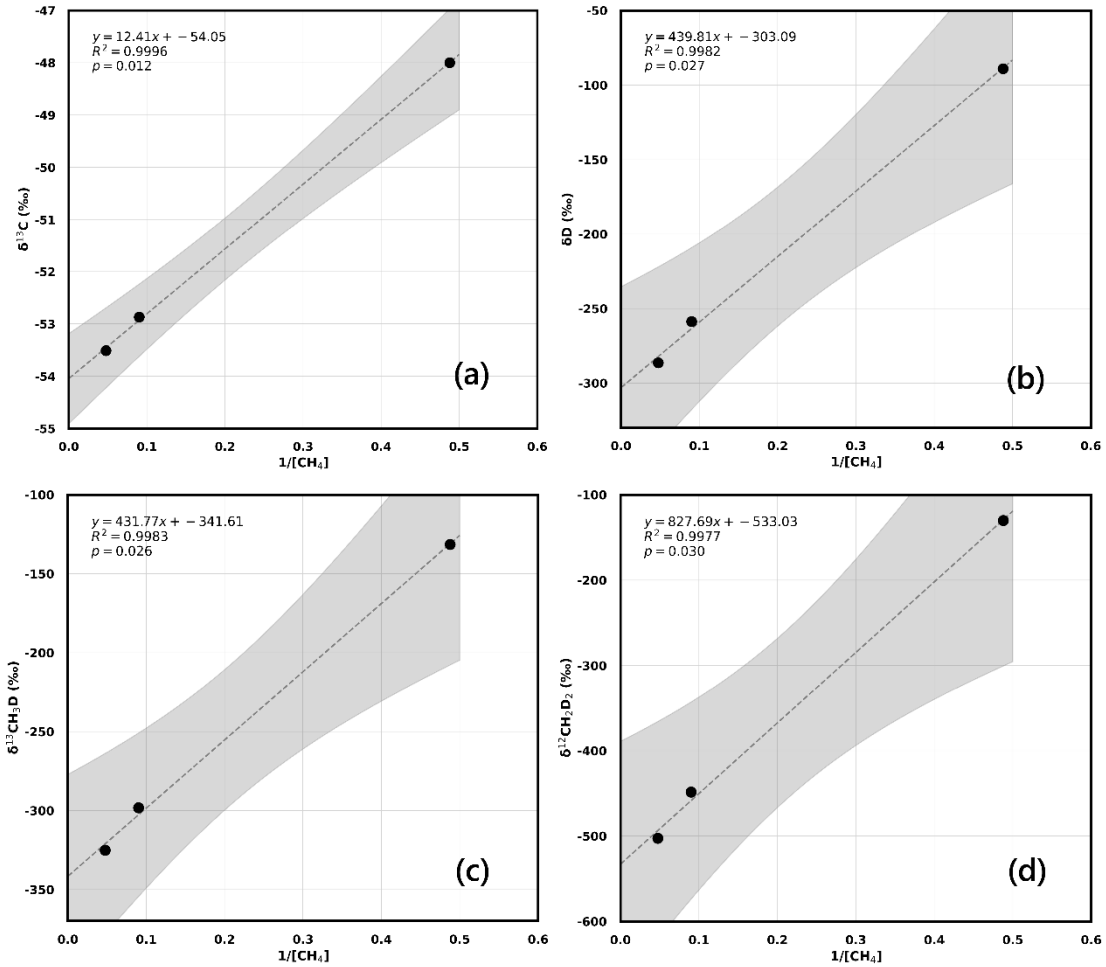

Figure 5.5. **a) $\delta^{13}CH_4$, b) $\delta^{12}CH_3D$, c) $\delta^{13}CH_3D$, d) $\delta^{12}CH_2D_2$ 3-point Keeling plots for landfill air samples.** The point in the upper right corner of each panel is the defined background air, and the two points in the lower left corner are landfill air samples. The gray bands represent the 95% confidence intervals of each linear fit.

5.7.1.3. Determining Wetland Emission Signatures

The Keeling plot method was also applied to wetland air samples (Jug Bay and Patuxent River series) (Figure 5.6). Most samples exhibit a positive linear correlation between $\delta^{13}CH_4$ and $\delta^{12}CH_3D$ with $1/[CH_4]$, yielding a derived wetland methane composition of $\delta^{13}CH_4$ = -64.7‰, $\delta^{12}CH_3D$ = -273.4‰, $\delta^{13}CH_3D$ = -321.2‰, and $\delta^{12}CH_2D_2$ = -480.7‰. These values fall in the mix and transition zone of two primary methanogenesis pathways (hydrogenotrophic and acetotrophic) (Conrad, 2005) as categorized by Whiticar (1999). Methanogenic pathways other

than CO_2-reduction and acetate-fermentation, such as methanogenesis using methanol and methyl amine, cannot be ruled out. However, these pathways are not predominant under natural freshwater wetland conditions, and there is no evidence to suggest substantial activity of such pathways in the study area (Haghnegahdar et al., 2024). We calculated $\Delta^{13}CH_3D$ = -1.1‰ and $\Delta^{12}CH_2D_2$ = -16.4‰. The derived $\Delta^{13}CH_3D$ aligns with typical characteristics of wetland methane. The $\Delta^{12}CH_2D_2$ value, while showing less anti-clumping compared to direct field methane samples from wetlands (Haghnegahdar et al., 2024), is consistent with methane produced in lab pure cultures using hydrogen and CO_2 as the substrates (Giunta et al., 2019; Young, 2019). This $\Delta^{12}CH_2D_2$ value may also reflect the influence of either aerobic or anaerobic oxidation in an open system, where the original anti-clumping signals are erased as oxidation proceeds (Krause et al., 2022; Liu, Harris, et al., 2023; Ono et al., 2021). Figure 5.6 also reveals that samples from the Queen Anne Bridge and the Patuxent River cruise deviate from the main linear array, suggesting the possible contribution of diverse methane sources or additional processes affecting the isotopic composition at these specific locations.

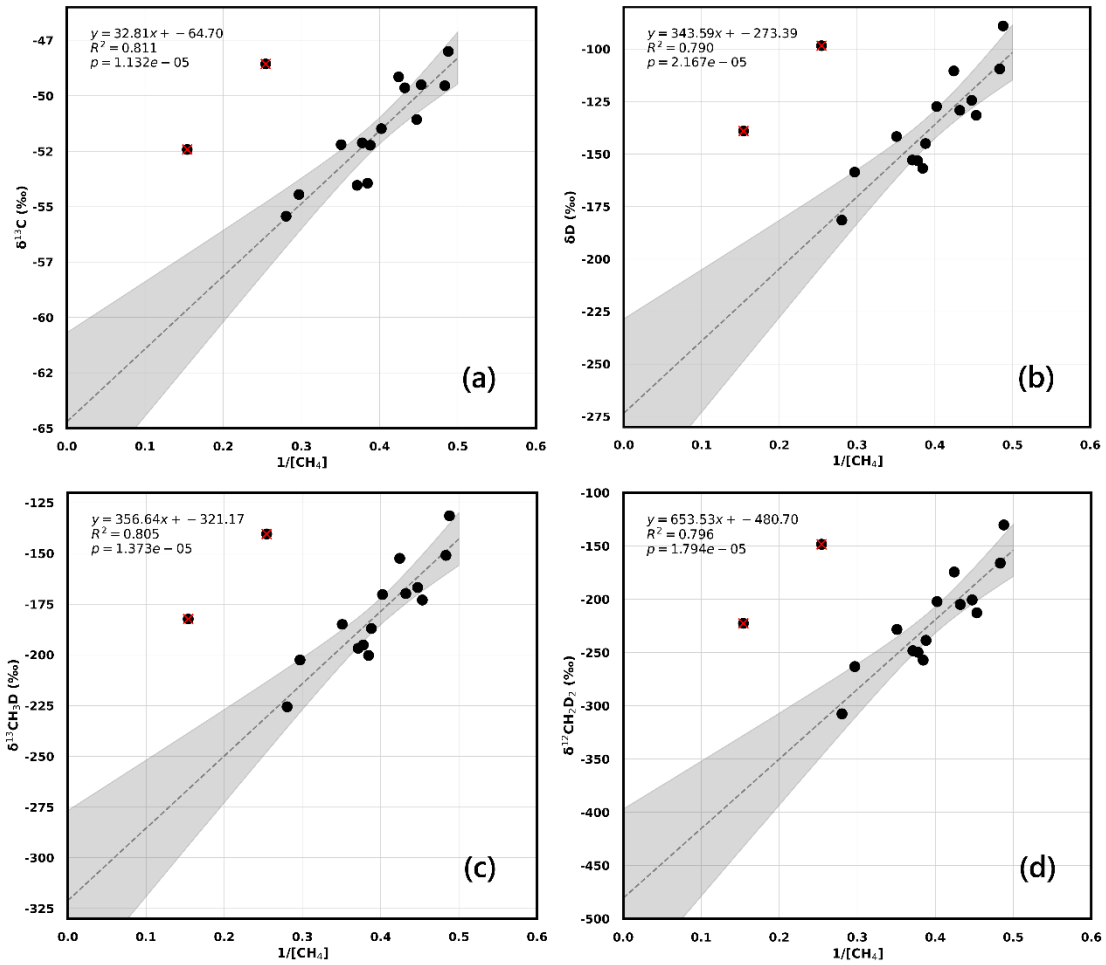

Figure 5.6. **a) $\delta^{13}CH_4$, b) $\delta^{12}CH_3D$, c) $\delta^{13}CH_3D$, d) $\delta^{12}CH_2D_2$ Keeling plots for all wetland air samples.** The one point in the upper right corner of each panel is the defined background air, and the rest of the points are wetland air samples. Two outliers (Queen Anne Bridge and Patuxent River cruise) off the major linear array are each marked with a red cross. The gray bands represent the 95% confidence intervals of each linear fit.

However, the application of the Keeling plot across all wetland air samples may be flawed due to the underlying oversimplification that the isotopic compositions of the wetland endmember are constant. To address this issue, we explored by applying the 2-point Keeling method to each individual wetland sample, treating each as a unique mixture of the previously determined constant background air and specific methane emissions at the time of sampling. The derived endmember compositions and associated uncertainties are listed in Table C.3, and the $\delta^{13}CH_4$ and $\delta^{12}CH_3D$ values are projected in Figure 5.2 if within the axis range. A notable limitation of

this method is the amplification of small measurement uncertainties, particularly when methane concentrations and isotopic compositions in the sample closely resemble those of the background air. The 2-point Keeling plot method seems to be less reliable when projecting clumped isotopologue signals, frequently yielding unrealistic compositions (Table C.3) due to the disproportionate amplification of biases and uncertainties in concentration, $\delta^{13}CH_4$, $\delta^{12}CH_3D$, $\Delta^{13}CH_3D$, and $\Delta^{12}CH_2D_2$ values during the inversion.

Although the Keeling plot method can yield unreliable results when applied to wetland air samples, particularly for clumped isotopologues, we still selected two sets of nominal values (listed in Table 5.1 and illustrated in Figure 5.2-5.4) to represent the wetland methane isotopic signatures while also reflecting the observed variability. The first set, labeled "Wetland 1", has $\delta^{13}CH_4$ = -73.0‰, $\delta^{12}CH_3D$ = -380.0‰, $\Delta^{13}CH_3D$ = -2.0‰, and $\Delta^{12}CH_2D_2$ = -55.0‰, referencing studies by Haghnegahdar et al. (2024) and Giunta et al. (2019). We hypothesize that this endmember represents methanogenesis using methyl compounds and acetate as substrates and/or involves low metabolic reversibility during methanogenesis (Giunta et al., 2019; Gropp et al., 2022; Ono et al., 2022). The second set, "Wetland 2", has $\delta^{13}CH_4$ = -64.4‰, $\delta^{12}CH_3D$ = -266.7‰, $\Delta^{13}CH_3D$ = +2.5‰, and $\Delta^{12}CH_2D_2$ = -15.0‰, cited from Giunta et al. (2022); Haghnegahdar (2018); Young (2019). This endmember may reflect methanogenesis using hydrogen and CO_2 as substrates and/or high metabolic reversibility during methanogenesis (Giunta et al., 2019; Gropp et al., 2022; Ono et al., 2022). It may also represent microbial methane that has undergone a higher degree of oxidation (Giunta et al., 2022; Liu, Harris, et al., 2023; Ono et al., 2021), thus exhibiting less negative $\delta^{13}C$ and δD, together with a less anti-clumping clumped signal. These values were chosen solely for facilitating discussions and

visualizations, while covering the majority of the derived wetland endmember compositions (Figure 5.2-5.4). This suggests that most samples likely represent different degrees of mixing between air and methane from wetlands, with varying methanogenesis pathways and reversibility, and/or oxidation levels.

5.7.1.4. Constraining bulk isotopic compositions with clumped isotopologues

In Section 5.7.1.3, we revealed that using measured wetland air compositions to determine source compositions could result in significant uncertainties and yield unreasonable outcomes, especially for clumped isotopologues. These inaccuracies are partly attributed to variability in air composition, where the assigned values may not accurately represent the actual background air compositions at each sampling event. Another source of error stems from inaccuracies in concentration measurements. Our sampling protocol involves collecting over 600 L of air per sample in three or four 200 L Tedlar bags. Filling each bag takes about 15 minutes, with two bags often being filled simultaneously. We have noted concentration discrepancies between bags as high as 0.2 ppm, exceeding the precision of the Aeris gas analyzer (1 SD = 1.6 ppb with 1-second integration). This suggests that the air above the sampling area might be heterogeneous, or that methane concentrations can fluctuate substantially over sampling periods. These inaccuracies and uncertainties will be amplified during the inversion processes used to calculate projected source compositions.

We can use the derived $\Delta^{13}CH_3D$ and $\Delta^{12}CH_2D_2$ from Section 5.7.1.3 as a check of the results. These derived $\Delta^{13}CH_3D$ and $\Delta^{12}CH_2D_2$ values were found to be unreasonable for samples: 20220612 Jug Bay, 20220724 Patuxent, 20220828 Jug Bay, 20220903 Jug Bay, 20220903

Patuxent, 20221010 Jug Bay, 20221025Jug Bay, and 20221104 Jug Bay. This underscores the necessity for more precise methane concentration profiles and more stringent constraints on air isotopologue compositions through more collection of background air samples. The checks provided by $\Delta^{13}CH_3D$ and $\Delta^{12}CH_2D_2$ are invaluable for evaluating data quality and the validity of extracted values.

To address the challenges, we explored a novel approach that leverages the additional constraints provided by methane clumped isotopologues (Δ values) to deduce the bulk (carbon and hydrogen) isotopic compositions (δ values) of the source methane, independently of concentration data. This methodology hinges on a critical assumption, supported by existing literature (Giunta et al., 2022; Giunta et al., 2019; Haghnegahdar, 2018; Haghnegahdar et al., 2024; Haghnegahdar et al., 2023; Liu, Harris, et al., 2023; Taenzer et al., 2020; Young, 2019; Young, Kohl, Lollar, et al., 2017), that the $\Delta^{12}CH_2D_2$ signature of microbial methane typically falls within a certain range. We allow a broad range for $\Delta^{12}CH_2D_2$ between -5‰ and -55‰ to cover most of the $\Delta^{12}CH_2D_2$ values reported for natural microbial methane. With this defined range, we are able to estimate the wetland's (bulk) hydrogen isotope composition ($\delta^{12}CH_3D_{source}$) using the following parameters: the presumed background air isotope and isotopologue compositions (R_{air}), and the measured isotope and isotopologue compositions of wetland air samples (R_{source}), without concentrations:

$$\left(1+\frac{\Delta^{12}CH_2D_{2\,source}}{1000}\right)*RD_{source}{}^{2}-\left(\frac{RD2_{mix}-RD2_{air}}{RD_{mix}-RD_{air}}\right)*RD_{source}$$
$$+\left(\frac{RD2_{mix}-RD2_{air}}{RD_{mix}-RD_{air}}\right)*RDair-RD2_{air}=0 \qquad (5.9)$$

R is the normalized ratio of isotopologue abundances. The definitions and mathematical derivations are detailed in Appendix C (Note C.4). This equation provides a way to infer $\delta^{12}CH_3D_{source}$ (results listed in Table C.5 and illustrated in Figure 5.7) by utilizing the constraints imposed by $\Delta^{12}CH_2D_{2\ source}$, hence offering a new perspective on source characterization without the direct need for concentration values. When the $\Delta^{12}CH_2D_2$ value approaches its minimum of -55‰, the calculated δD becomes more negative, with an average around -316‰. Conversely, when $\Delta^{12}CH_2D_2$ nears its maximum of -5‰, the calculated δD is less negative, averaging approximately -268‰. The 50‰ large variation range of $\Delta^{12}CH_2D_2$ propagates to an uncertainty of about 24‰ in δD, which is smaller than the inferred variation range of the methane δD signal in the studied wetland area (approximately 60‰, ranging from -300‰ to -240‰, see Figure 5.8) and significantly less than the variability of δD signals for natural microbial methane, which spans approximately 250‰ (from around -400‰ to -150‰).

Delving deeper following this idea, we consider that the $\Delta^{13}CH_3D$ and $\Delta^{12}CH_2D_2$ values of microbial methane are governed by a unified process, including changes in methanogenesis pathways and metabolic reversibility, and the involvement of microbial oxidation. We suggest that there exists a mathematical relationship between $\Delta^{13}CH_3D$ and $\Delta^{12}CH_2D_2$, i.e. $\Delta^{13}CH_3D_{microbial} = f\left(\Delta^{12}CH_2D_{2\,microbial}\right)$, for microbial methane. This hypothesis aligns with experimental and modeling research that seeks to elucidate the behavior of microbial methane clumped isotopologues (Cao et al., 2019; Gropp et al., 2021; Liu, Harris, et al., 2023; Ono et al., 2021; Wang et al., 2015). Generally, a more negative $\Delta^{12}CH_2D_2$ is associated with a more negative $\Delta^{13}CH_3D$. Compiling the available natural methane, incubation methane, and lab-culture methanogenesis methane clumped isotopologue data from Giunta et al. (2022); Giunta et

al. (2019); Haghnegahdar et al. (2024); Haghnegahdar et al. (2023); Li, Ash, et al. (2024); Liu, Harris, et al. (2023); Young (2019); Young, Kohl, Lollar, et al. (2017) (see Note C.4, Table C.4, and Figure C.5), without accounting for specific physical or biological processes, we establish a simplistic linear relationship between $\Delta^{13}CH_3D$ and $\Delta^{12}CH_2D_2$ values of microbial methane:

$$\Delta^{13}CH_3D_{\text{wetland methane}} = (5.70 \pm 0.26) * \Delta^{12}CH_2D_{2\,\text{wetland methane}} - (28.99 \pm 0.95) \quad (5.10)$$

With this established relationship, we can proceed to estimate the source's bulk carbon isotope composition using the designated $\Delta^{12}CH_2D_2$ range:

$$RC_{source} = \frac{RCD_{air} - \left(\frac{RCD_{mix} - RCD_{air}}{RC_{mix} - RC_{air}}\right) * RC_{air}}{\left(1 + \frac{f\left(\Delta^{12}CH_2D_{2\,source}\right)}{1000}\right) * RD_{source} - \left(\frac{RCD_{mix} - RCD_{air}}{RC_{mix} - RC_{air}}\right)} \quad (5.11)$$

The definitions and mathematical derivations are detailed in Appendix C (Note C.4). This equation can be used to infer $\delta^{13}CH_{4,\,source}$ (results listed in Table C.5 and illustrated in Figure 5.7) based on the assumed range of $\Delta^{12}CH_2D_{2\,source}$ and the assumed linear relationship between $\Delta^{13}CH_3D_{source}$ and $\Delta^{12}CH_2D_{2\,source}$. With 50‰ variation range of $\Delta^{12}CH_2D_2$, the corresponding uncertainty in $\delta^{13}C$, based on the aforementioned assumptions, averages only about 0.8‰. This uncertainty is less than the inferred variation range of the methane $\delta^{13}C$ signal in the studied wetland area (approximately 5.1‰, ranging from -53.5‰ to -48.4‰), and is significantly smaller than the variability of $\delta^{13}C$ signals for natural microbial methane, which spans approximately 40‰ (ranging from around -90‰ to -50‰).

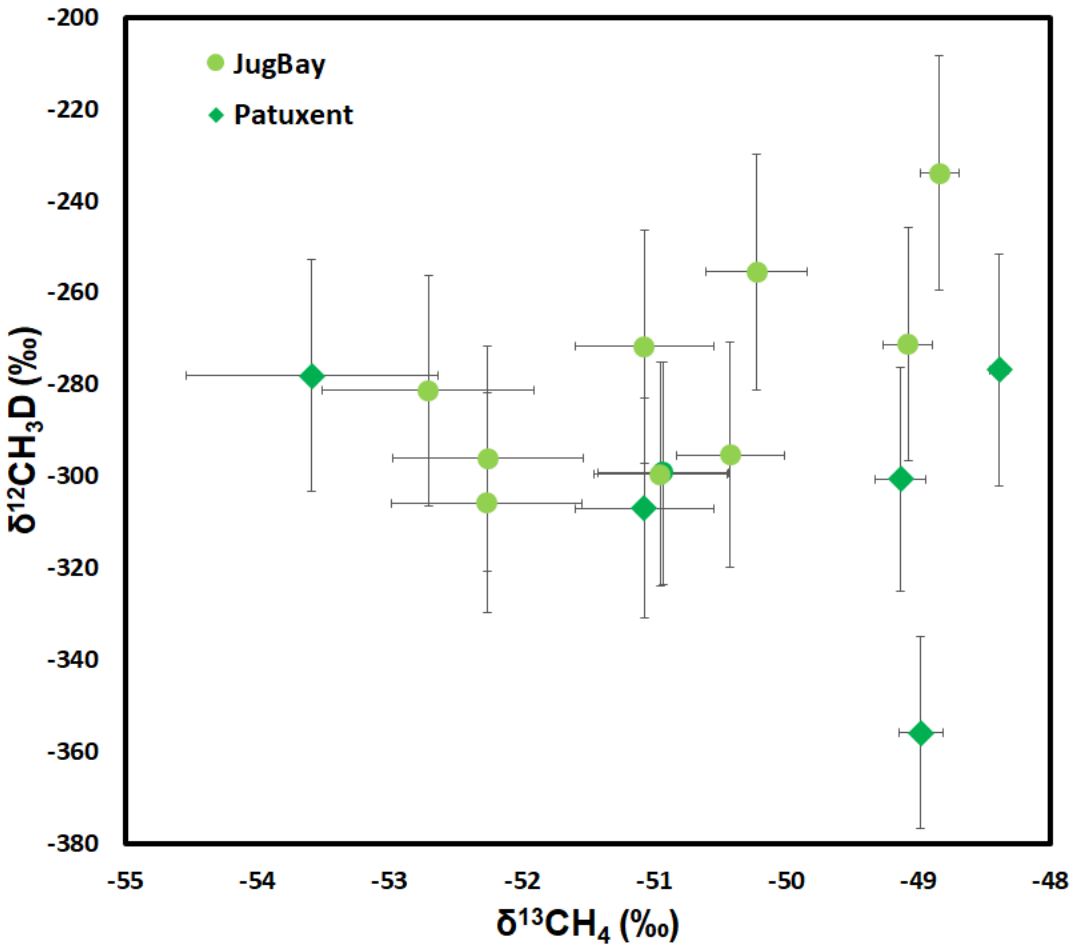

Figure 5.7. **Derived bulk hydrogen and carbon isotope compositions and uncertainties of the source methane ($\delta^{12}CH_3D_{source}$ and $\delta^{13}CH_{4,\,source}$) for each wetland air sample.** Source compositions derived from the Jug Bay air samples are in light green circles, and those derived from the Patuxent air samples are in dark green diamonds.

However, the calculations in Section 5.7.1.4, constrained by clumped isotopologues, derived wetland methane carbon and hydrogen isotopic signatures that are significantly less negative (δD approximately -290‰ and $\delta^{13}C$ approximately -51‰) compared to those calculated through the Keeling plot method in Section 5.7.1.3 (δD approximately -320‰ and $\delta^{13}C$ approximately -65‰). The signatures from Section 5.7.1.4 are more similar to those of the landfill endmember calculated in Section 5.7.1.2 using the Keeling plot method. While the results from Section 5.7.1.4 show notably smaller uncertainties and less unreasonable scattering, the method also

involves some assumptions. Future work will require more combined air and direct field sampling, along with high-precision concentration and isotopologue measurements, to determine which method yields the most reasonable results.

5.7.2. The Variability of Isotopic Composition of Wetland Methane Emissions

As mentioned in the introduction, multiple factors can influence the isotopic signatures of wetland methane emissions, including methanogenesis pathways and metabolic reversibility, oxidation processes, and transport mechanisms. Microbial methane can be generated through several different pathways: hydrogenotrophic, acetotrophic, and methylotrophic methanogenesis. Each pathway tends to yield different isotopic signatures (Hornibrook et al., 1997; Whiticar et al., 1986). For example, methane produced through the hydrogenotrophic pathway is generally more depleted in ^{13}C (with $\delta^{13}C$ values typically ranging from -110‰ to -60‰) and less depleted in D (with δD values usually ranging from -350‰ to -170‰). In contrast, methane generated through the acetotrophic pathway generally shows $\delta^{13}C$ values ranging from -70‰ to -50‰ and δD values from -400‰ to -250‰ (Liu, Treude, et al., 2023; Whiticar, 1999).

Microbial methane oxidation complicates the interpretation of carbon and hydrogen isotopic signatures, as it alters the signals (Alperin et al., 1988; Coleman et al., 1981; Happell et al., 1994). Aerobic oxidation of methane (AeOM) typically results in both $\delta^{13}C$ and δD values becoming less negative in the residue methane (Coleman et al., 1981; Hornibrook et al., 1997; Wang et al., 2016), while $\delta^{13}C$ and δD values may either increase or decrease during anaerobic oxidation of methane (AOM), depending on the reversibility of intracellular reactions (Holler et

al., 2009; Liu, Harris, et al., 2023; Yoshinaga et al., 2014). In terrestrial and coastal environments, the reversibility of AeOM is typically low due to the high availability of free energy, leading to less negative $\delta^{13}C$ and δD values (Liu, Harris, et al., 2023). Therefore, oxidation can cause overlapping isotopic signatures between microbial and thermogenic methane. Landfill, where high levels of AeOM activity frequently occur, exhibit varying degrees of oxidation depending on seasonal changes and landfill operations (Bakkaloglu et al., 2021; Chanton & Liptay, 2000; Spokas et al., 2021). The extent of methane oxidation determines how far the residual methane will fractionate from its original compositions (Chanton et al., 2008).

At least five different methane transport mechanisms have been identified (Bastviken et al., 2004; Johnson et al., 2022): ebullition, diffusion, the release of stored methane due to water turnover, emissions through aquatic vegetation (Sebacher et al., 1985), and ice-bubble storage flux (Walter et al., 2006). Each of these mechanisms has different temporal and spatial characteristics (DelSontro et al., 2011; Greene et al., 2014; Johnson et al., 2022; Sanches et al., 2019). For example, diffusion flux can be relatively stable at least in summer, while the release of storage methane can cause a big pulse in spring and autumn (Engle & Melack, 2000). The varying release mechanisms likely influence the isotopic signatures of the emitted methane (Walter et al., 2008).

The analysis in Section 5.7.1.4 reveals a seasonal pattern in the derived $\delta^{12}CH_3D_{source}$ values (Figure 5.8): from autumn through winter, the $\delta^{12}CH_3D$ values of methane emitted from wetlands in our study area became progressively less negative, and upon entering spring, these values shift back to more negative $\delta^{12}CH_3D$ values, with fluctuations of up to 40‰. Such a directional

change is also observed in $\delta^{13}CH_4$, $\delta^{12}CH_3D$, $\Delta^{13}CH_3D$, and $\Delta^{12}CH_2D_2$ values of the selected endmembers "Wetland 1" and "Wetland 2" in Section 5.7.1.3. Excluding the Chaneyville Rd. samples, which display significantly more negative $\delta^{12}CH_3D$ values, the remaining samples from the Patuxent River series have similar isotopic signatures to those from Jug Bay within the same season, suggesting a consistent seasonal trend across different locations within the study area.

Similar or different seasonal variations in the isotopic signals of wetland methane emissions have been observed in multiple studies. Happell et al. (1994) noted that during flooding periods, emitted methane had less negative $\delta^{13}C$ and δD, attributing to increased oxidation. Burke et al. (1992); Burke et al. (1988) observed a similar pattern for δD but an inverse pattern for $\delta^{13}C$ (i.e. $\delta^{13}C$ is inversely related to δD), suggesting that these opposing signals reflect differing contributions from acetotrophic and hydrogenotrophic methanogenesis pathways. Data from Sriskantharajah et al. (2012) and Fisher et al. (2017) might indicate a distinct seasonal pattern, controlled strongly by the freeze-thaw cycle in high-latitude wetlands. There are diverse factors that can contribute to seasonal variations in wetland methane emissions (France et al., 2022).

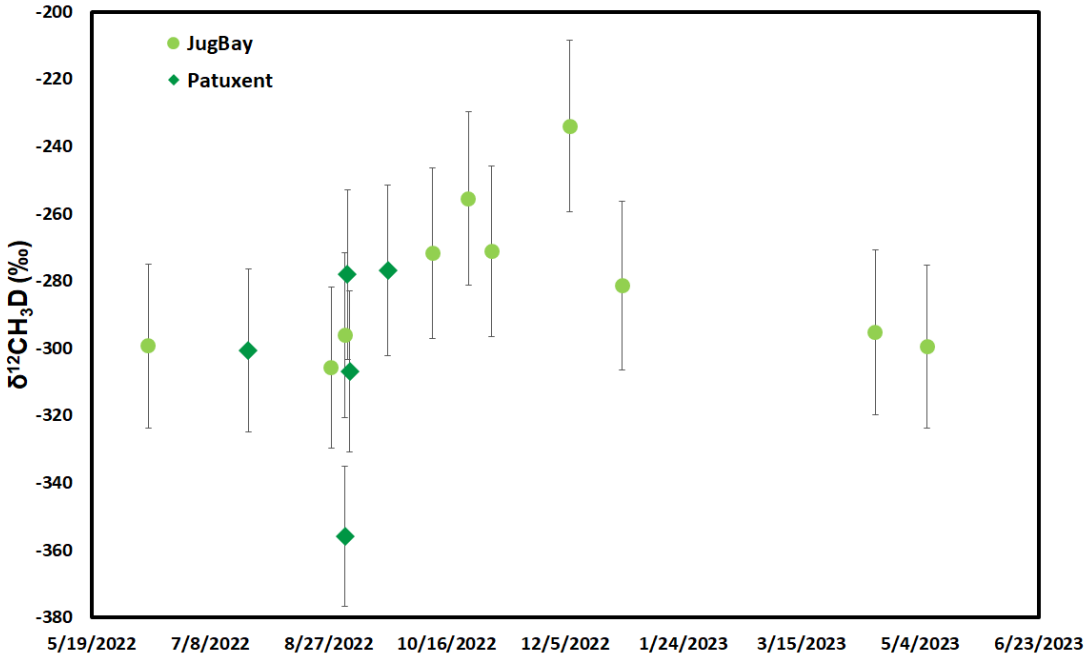

Figure 5.8. **Calculated bulk hydrogen isotopic composition ($\delta^{12}CH_3D_{source}$) vs. sampling time.** Source compositions derived from the Jug Bay air samples are in light green circles, and those derived from the Patuxent air samples are in dark green diamonds.

Unlike direct wetland sampling, the compositions we derived from air samples provide regionally integrated emission signals, which are anticipated to smooth out localized variances. Our analysis still revealed considerable variability in the derived wetland compositions, suggesting that regional controls rooted in process-based factors are governing the isotopic signals. We propose one hypothesis as an example to explain the observed variability in isotopic signals: the variability is caused by differing extents of microbial oxidation. Using the open-system models presented in Hayes (2001a) and Wang et al. (2016), we performed simulations to illustrate how the isotopic signals of methane change during AeOM and AOM, starting with the initial compositions of Wetland 1. The isotopic fractionation coefficient for AeOM were taken from Krause et al. (2022), while those for AOM were derived from Liu, Harris, et al. (2023). The modeling results (Figure 5.9) indicate that a combination of AOM and AeOM to a certain degree

can approximately replicate the composition of Wetland 2—at least in terms of the direction of isotope fractionation.

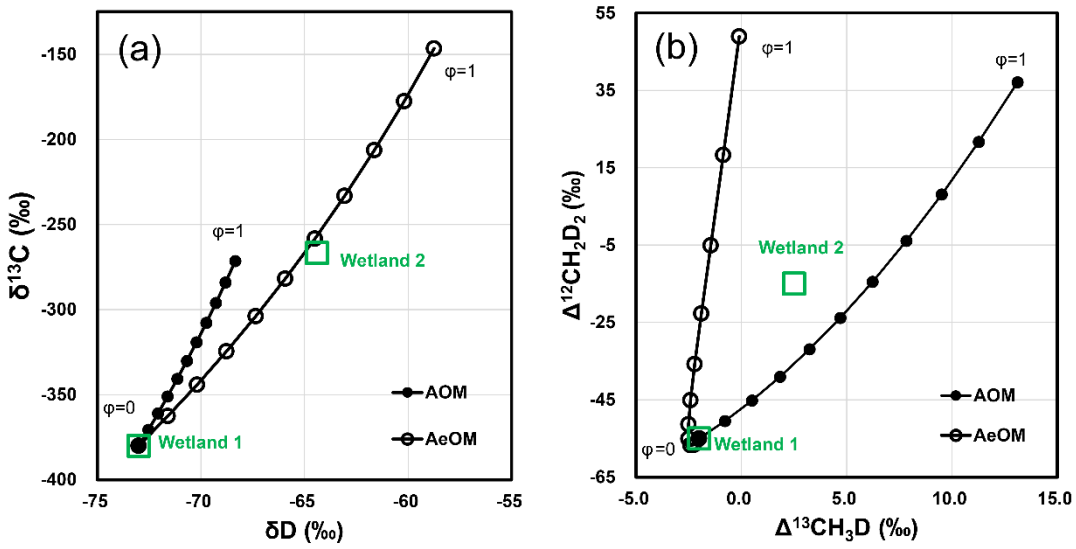

Figure 5.9. **The (a) isotopic and (b) isotopologue fractionation trends of methane undergoing varying degrees of open-system AOM (solid circles) and AeOM (hollow circles).** The initial composition is set to be Wetland 1. The fractionation factors for AOM are adopted from Krause et al. (2022), while those for AeOM are taken from Liu, Harris, et al. (2023). φ represents the fraction of methane removed through oxidation (as opposed to transport).

Quantitative PCR and pyrosequencing results conducted in the Jug Bay wetland area provide evidence that both aerobic and anaerobic methane-oxidizing microorganisms are present in this region (Haghnegahdar et al., 2024; Prasse et al., 2015). The water salinity and dissolved oxygen data described in Appendix C (Note C.2) are not in conflict with this hypothesis. During the summer, dissolved oxygen concentrations in wetland waters are lower than in winter (Figure C.3). There is also a slight increase in water salinity upon entering fall, (Figure C.4), suggesting an increased availability of sulfate to act as an oxidant. Wetland environment is more conducive to microbial oxidation in winter compared to summer. This is consistent with our derived

wetland endmember isotopic signatures which are less negative in $\delta^{13}C$ and δD in the winter, indicating that a higher proportion of the produced methane undergoes oxidation.

However, it is important to acknowledge that variations in methanogenesis pathways and differences in substrate compositions can influence the initial methane isotopic compositions. Moreover, the isotopic fractionation coefficients of AeOM and AOM can vary within a certain range. Many combinations of these factors can be used to numerically explain the observed variability in isotopic signals. The positive relationship between $\delta^{13}CH_4$ and $\delta^{12}CH_3D$ values (Figure 5.7) may suggest that a transition in methanogenesis pathways is unlikely to be the primary cause of the derived isotopic signal variations, as such transitions typically result in $\delta^{13}C$ and δD shifting in opposite directions (Burke et al., 1992; Burke et al., 1988). But the possibility that transitions in methanogenesis pathways have some influence on the observed isotopic signals cannot be ruled out. The specific microbial processes occurring in wetlands causing the observed isotopic signal variability should be further investigated by studies focusing on wetland methane-related microbiology.

5.7.3. Implications for Future Air Clumped Isotopologue Studies

The findings of this study present an exciting prospect: by analyzing air samples collected over emission sources, it is possible to deduce the source compositions, including clumped isotopologues. Wetland air samples appear to reveal seasonal variations in the isotopic signatures of regional wetlands (the Jug Bay). Understanding the drivers behind this variability in future studies will be essential for more precisely constraining methane emissions from wetlands on a

broader scale. To achieve this, more comprehensive field surveys and air samplings are needed. The efforts should involve collecting detailed meteorological, hydrological, and environmental data, combined with isotopic and isotopologue measurements of both direct wetland samples and air samples. Furthermore, given that different wetlands respond differently across seasons, sustained monitoring of multiple wetlands with diverse ecological settings could be valuable.

Another inference from this study is that the clumped isotopologue signals of air methane are relatively insensitive to low-proportion mixing from sources and this presents its own opportunities for information about atmospheric methane. To demonstrate this, we select four source endmembers: landfill, microbial, natural gas, and total source, with their compositions listed in Table 5.1. The landfill composition is the Brown Station emission composition derived in Section 5.7.1.2. The microbial composition is a 50/50 blend of "Wetland 1" and "Wetland 2" selected in Section 5.7.1.3. The natural gas composition is the Panorama measurement results of the Marcellus natural gas sample (Haghnegahdar et al., 2023). The $\delta^{13}C$ and δD values of the total source follow those defined by Chung and Arnold (2021), while $\Delta^{13}CH_3D$ and $\Delta^{12}CH_2D_2$ are derived from Haghnegahdar et al. (2023). These endmembers were mixed with background air (Figure 5.10). Although it is challenging to precisely define how low the mixing ratios are needed to not significantly affect air $\Delta^{12}CH_2D_2$ values, it appears that a 5% mix from microbial and natural gas sources does not cause changes in air $\Delta^{12}CH_2D_2$ beyond the current 1σ measurement uncertainty. For landfill methane, this proportion is 20%, and for the total source, it reaches up to 30%. In many instances, as long as air samples are collected away from known major methane emission sources, it is highly likely that these samples will meet the "clean" criteria where the clumped isotopologue signals are not significantly disturbed by the source.

Based on this working hypothesis, if we leverage the existing global greenhouse gas monitoring network (such as the NOAA GML monitoring sites), collect regional clean air samples from remote areas or upwind of cities, preferably from elevated altitudes, and measure their methane clumped isotopologue signatures, the observed spatial and/or temporal variations in $\Delta^{12}CH_2D_2$ values (if they exist) could be attributed solely to fluctuations in sink reactions. These variations could be due to spatial and temporal unevenness in OH concentrations (Anderson et al., 2021; Lu & Khalil, 1991), or fluctuations in the ratio of OH to Cl concentrations (Gromov et al., 2018; Platt et al., 2004; Solomon et al., 1997), such as during tropospheric intrusion events (Greenslade et al., 2017; Liang & Mahata, 2015). If we can obtain a sufficient number of high-precision measurements of methane clumped isotopologues in clean air, it may enable a more detailed investigation of atmospheric methane sink reactions from an isotopic perspective.

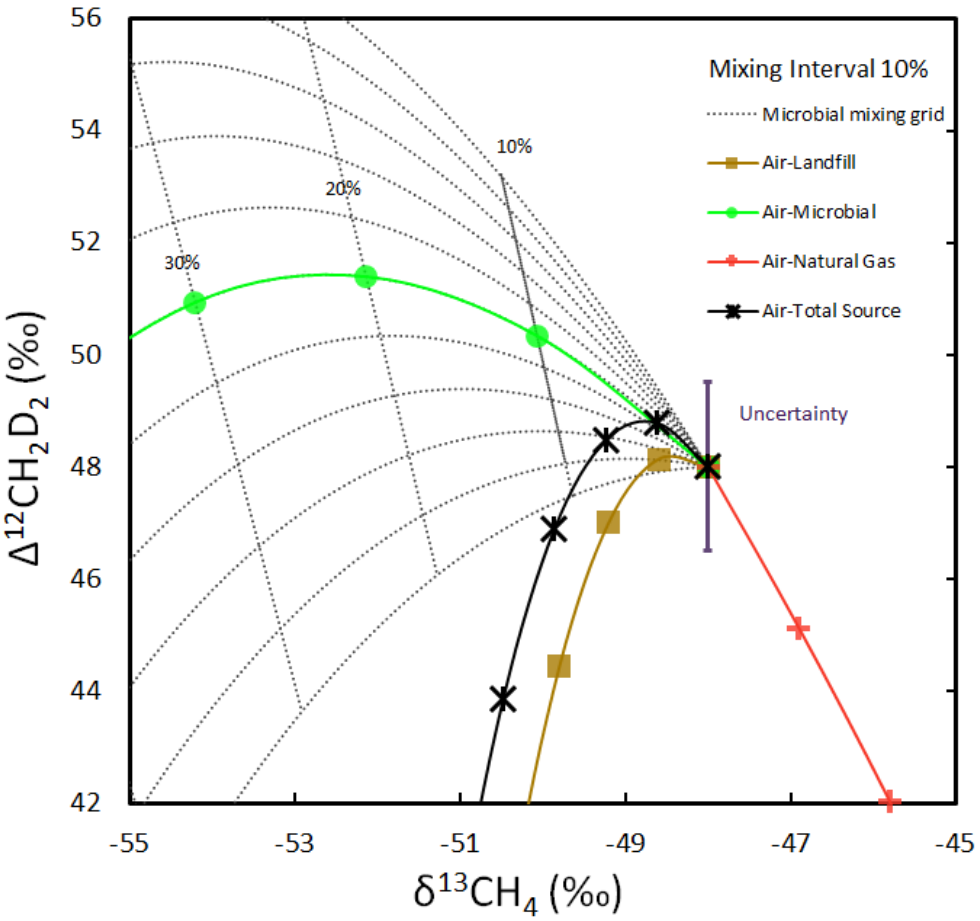

Figure 5.10. **The zoomed-in mixing curves of air with various sources, including landfill, microbial, natural gas, and total source.** The landfill mixing curve is brown with square markers. The microbial curve is green with circular markers. Natural gas is red with plus signs. The total source is black with star markers. The compositions of each source can be found in Table 5.1. The grey mixing grid is the same as the grid in Figure 5.4. The mixing intervals indicated in this figure are at 10%. The typical uncertainty for $\Delta^{12}CH_2D_2$ measurements (1σ) is represented in the figure with an error bar.

5.8. Summary

In this study, we investigated regional methane emissions, collecting air samples above wetlands and within landfill plumes to analyze the carbon and hydrogen isotope ratios, and clumped isotopologue compositions of methane. Employing a three-endmember (background air, landfill,

and wetland) mixing framework, we established the compositions of the background air and utilized the Keeling plot method to derive the compositions of landfill and wetland methane. Furthermore, we developed a mathematical approach leveraging methane clumped isotopologue data to estimate the bulk isotope compositions of wetland methane independently of concentration data. This method overcomes the amplification of uncertainties associated with concentration data, which is a major limitation of the Keeling plot method, resulting in lower uncertainties in derived wetland emission isotopic signatures.

Our findings reveal significant seasonal variations in the isotopic and isotopologue signatures of regionally integrated methane emissions, which we attribute to different oxidation levels, with a trend towards greater oxidation signatures in winter. This research advances our understanding of regional wetland methane dynamics and contributes to refining the global methane budget. Our results advocate for systematic isotopic and isotopologue monitoring of methane emissions from wetlands, coupled with fieldwork, to uncover seasonal emission patterns and gain more insights into their driving processes.

5.9. Acknowledgments

JS was supported by NOAA grant NA19NES4320002 (Cooperative Institute for Satellite Earth System Studies -CISESS) at UMD. Funding to support MH was provided by U.S. National Science Foundation grant (EAR-PF: 2052834). We thank Dr. William D. Leavitt and Jiawen Li for their valuable review and constructive feedback on this manuscript. We thank Dr. Alan Jay Kaufman for collecting the Brown Station landfill plume sample on February 15, 2022. We also

thank Dr. Laura Lapham and Anna Hildebrand for collecting and shipping the Patuxent River Cruise sample. We gratefully acknowledge the captain and crew of the *R/V Rachel Carson*, and the Patuxent River Science Cruises, which were funded by the Chesapeake Biological Laboratory, University of Maryland Center for Environmental Science.

5.10. Competing Interests

The authors declare no competing interests.

5.11. Open Research

All measured data in this study are included in Appendix C (Table C.1, Table C.2, Table C.4, Figure C.3, Figure C.4). Some are also plotted in the main text (Figure 5.1-5.6). The Excel tables used for this work, the code for generating some of the figures in this work, and the raw data tables from Panorama measurements are also available at the Digital Repository for the University of Maryland (DRUM) via http://hdl.handle.net/1903/33660 with free access (Sun, Magen, et al., 2025).

Chapter 6: Constraining the Clumped Isotope Budget of Atmospheric Methane using Firn Air Measurements

This chapter is a manuscript titled "*Constraining the clumped isotope budget of atmospheric methane using firn air measurements*", in preparation for submitting to *Science*.

Authors and Affiliations:

Malavika Sivan[1*†], Jiayang Sun[2,3*†], Patricia Martinerie[4], Maria Elena Popa[1], James Farquhar[2,5], Maarten Krol[1], Carina van der Veen[1], Bibhasvata Dasgupta[1], Mojhgan A. Haghnegahdar[2], Camilla Marie Jensen[6], Ji-Woong Yang[7], Johannes Freitag[8], Kévin Fourteau[9], Thomas Blunier[6], Thomas Röckmann[1]

[1]Institute for Marine and Atmospheric Research, Utrecht University; Utrecht, the Netherlands.

[2]Department of Geology, University of Maryland; College Park, Maryland 20742, USA.

[3]Air Resources Lab, National Oceanic and Atmospheric Administration; College Park, Maryland 20740, USA.

[4]Université Grenoble Alpes, CNRS, INRAE, IRD; Grenoble INP, IGE, 38000 Grenoble, France.

[5]Earth System Science Interdisciplinary Center, University of Maryland; College Park, Maryland 20740, USA.

[6]Physics of Ice Climate and Earth, Niels Bohr Institute, University of Copenhagen; Tagensvej 16, 2200, Copenhagen, Denmark.

[7]Laboratoire des Science du Climat et de l'Environnement, France.

[8]Alfred-Wegener-Institute; 27570 Bremerhaven, Germany.

[9]Géosciences Montpellier - CNRS, Université de Montpellier, France.

†These authors contributed equally to this work

*Corresponding authors. MS, JS. Email: m.sivan@uu.nl; jiayangs@umd.edu

Jiayang Sun is the co-first author of this manuscript and has made significant contributions, including but not limited to conceptualization, methodology, validation, formal analysis, investigation, data curation, writing – original draft, writing - review & editing, and visualization.

6.1. Abstract

The ongoing debate on the temporal evolution of atmospheric methane underscores gaps in our understanding of its global cycle. Here, we report the first reconstruction of clumped isotopic composition of atmospheric methane from firn air dating back to the 1990s. $\Delta^{12}CH_2D_2$ shows an increase of 10 ± 2 ‰ over the past 25 years. Models reveal that the observed $\Delta^{12}CH_2D_2$ trend arises due to the methane source-sink disequilibrium in the past. The Kinetic Isotope Effect of $^{12}CH_2D_2$ removal by OH needs to be smaller than theoretically calculated. We also show that atmospheric $\Delta^{12}CH_2D_2$ measurements will help distinguish possible methane emission and removal trajectories in the future.

6.2. Introduction

The increase in methane (CH_4) emissions since pre-industrial times is responsible for about half a degree of global warming. Furthermore, the continuing rising levels of atmospheric CH_4 are exacerbating global warming and climate change today (IPCC, 2021; Lan et al., 2023; MacFarling Meure et al., 2006). Over the past decades, atmospheric CH_4 concentrations were characterised by a brief stagnation period in the early 2000s, followed by an accelerated growth phase since 2007 (Lan et al., 2023). Variations in anthropogenic activities, particularly fossil fuel use and agricultural practices have contributed most significantly to this dynamic evolution, although climate feedback from natural sources like wetlands and changes in the atmospheric sink can also have an influence (Nisbet et al., 2023; Rigby et al., 2017; Turner et al., 2017). The tropospheric CH_4 concentration is influenced by the balance between the CH_4 sources, which include natural (e.g., wetlands, forest fires, and geological seeps) and anthropogenic (fossil fuels, ruminant farming, waste, and biomass burning) emissions, and the CH_4 sinks (oxidation by OH, Cl radicals, and uptake by surface soil) (Saunois et al., 2020). Previous studies investigated the short and long-term temporal and spatial variations in the bulk isotopic composition of CH_4 ($\delta^{13}C$ and δD) to assess natural variability and potential anthropogenic influences on atmospheric CH_4 concentrations (Basu et al., 2022; Feng et al., 2023; Kirschke et al., 2013; Nisbet et al., 2016; Schaefer et al., 2016; Thanwerdas et al., 2024; Worden et al., 2017). Unfortunately, a consensus on the controlling factors of atmospheric CH_4 concentration has not yet been reached (Rice et al., 2016).

In recent years, the clumped isotope signatures (Eiler, 2007; Young, Kohl, Sherwood Lollar, et al., 2017) of CH_4 - $\Delta^{13}CH_3D$ and $\Delta^{12}CH_2D_2$ - have been explored as additional tracers to characterize CH_4 sources (Douglas et al., 2017; Giunta et al., 2022; Giunta et al., 2019; Labidi et al., 2020; Lalk et al., 2022; Liu, Treude, et al., 2023; Shuai, Etiope, et al., 2018; Stolper et al., 2018; Stolper, Sessions, et al., 2014; Thiagarajan et al., 2020; Wang et al., 2015; Young, 2019; Young, Kohl, Sherwood Lollar, et al., 2017) and sinks (Haghnegahdar et al., 2017). $\Delta^{13}CH_3D$ and $\Delta^{12}CH_2D_2$ are defined as the deviations of the proportions of the respective doubly-substituted isotopologues among all the isotopologues compared to the stochastic distribution.

Thermogenic CH_4 and microbial CH_4 usually have different clumped isotopologue signals, where microbial CH_4 produced in surface environments and lab cultures often have much lower $\Delta^{12}CH_2D_2$ than thermogenic values. The clumped isotopologue signals of global total methane emissions are controlled by the proportions and compositions of each methane source. Atmospheric sink reactions will relatively enrich the heavier isotopologues of the residual CH_4. However, the Kinetic Isotope Fractionation (KIE) factors of clumped isotopologues in the removal reactions of CH_4 are not well constrained, with only a few theoretical and experimental studies available (Haghnegahdar et al., 2017; Joelsson et al., 2016; Whitehill et al., 2017). The first measurements of the atmospheric CH_4 clumped isotopic composition (Haghnegahdar et al., 2023; Sivan, Röckmann, et al., 2024) showed that $\Delta^{12}CH_2D_2$ values of ambient air CH_4 are distinct (around 45 ‰) compared to the values of any known CH_4 sources. This suggests a larger influence from the atmospheric sinks leading to a measurable signal of $\Delta^{12}CH_2D_2$ which is sensitive to variations in sink magnitude and/or source-sink imbalance, showing the potential to be used as tracers to study variations in the atmospheric CH_4 budget.

In this study, we report the first reconstructed profile of the atmospheric $\Delta^{13}CH_3D$ and $\Delta^{12}CH_2D_2$ in air retrieved from Greenland firn dating back to the 1990s. We use a two-box global atmosphere forward model to optimise key parameters of the CH_4 clumped isotope budget to interpret the measured isotopic signatures. We also investigate the difference in the bulk and clumped isotopic composition of CH_4 using different past emission scenarios, as well as possible future evolution scenarios assuming different emission trajectories until the end of the 21st century.

6.3. Reconstruction of Air Methane Clumped Isotopologues Dating Back to 1990s from Firn Air Samples

Figure 6.1 shows the measurements of CH_4 mole fraction, bulk and clumped isotope signatures for firn air samples collected at the East Greenland Ice-core Project site (EastGRIP) in 2018 (sampling and measurement details are provided in Appendix D, values in Table D.2). The CH_4 mole fraction increases by about 200 ppb from the lowest firn layer depth (~ 65 m) to the surface (0 m). The depth profiles show an overall range of 0.8 ‰ in $\delta^{13}C$ and 10 ‰ in δD values. The range in $\Delta^{13}CH_3D$ is about 2 ± 0.5 ‰, and no clear temporal trend can be determined. Whereas $\Delta^{12}CH_2D_2$ shows a clear and highly significant increase of 10 ‰ in the firn column from the lowest depth to the surface, much larger than our typical measurement error of 1-1.4 ‰ (1SD). For further quantitative analysis, the measurements were corrected for diffusion and gravitational settling in the firn layers (details in Appendix D).

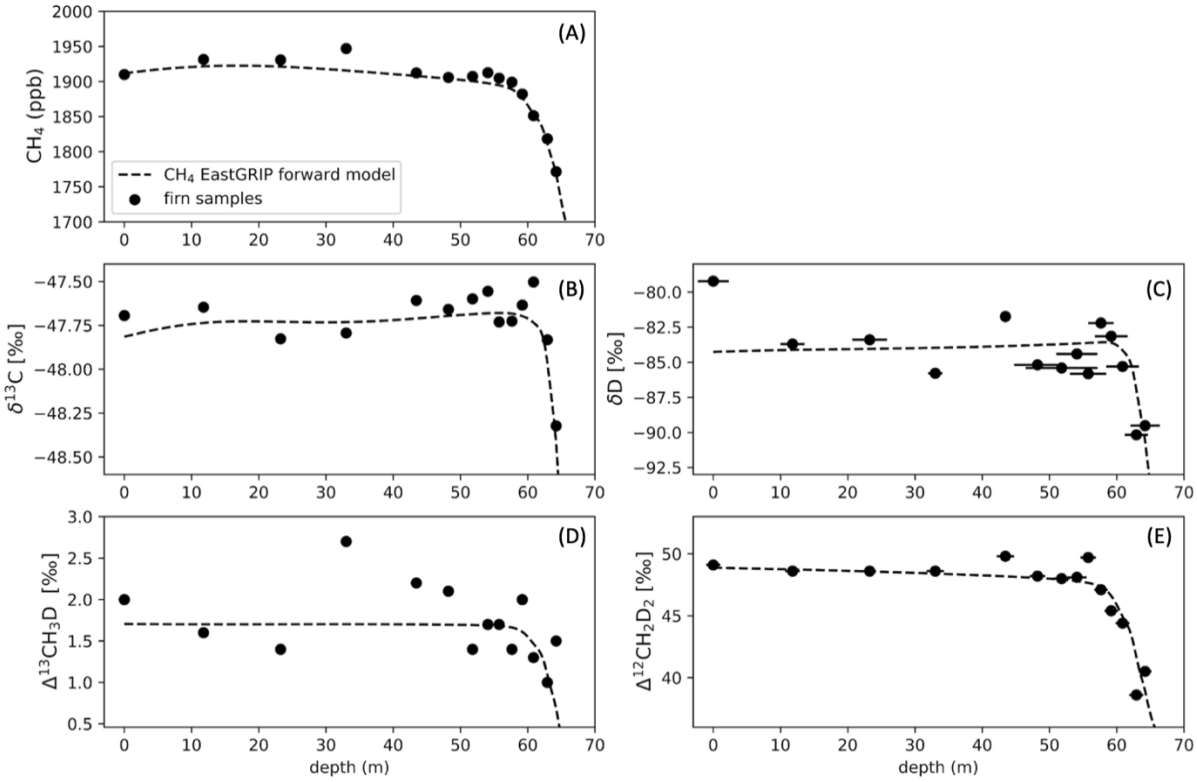

Figure 6.1. **Measured firn methane sample signals with depth.** Measurements of **(A)** CH_4 mole fraction, **(B)** $\delta^{13}C$, **(C)** δD, **(D)** $\Delta^{13}CH_3D$, and **(E)** $\Delta^{12}CH_2D_2$ of air collected from firn layers at the EastGRIP site in 2018. The black dashed lines in (A)-(E) show results from the firn model driven by the atmospheric histories presented in Figure 6.2.

The mole fraction and isotope depth profiles in the firn layers were converted into temporal atmospheric scenarios using an inverse mathematical model (Witrant et al., 2012). The firn air samples have CH_4 mean ages covering the period 1993 to 2018 (CH_4 age distributions are shown in Figure D.1) and thus allow us to derive the first information on temporal changes in the clumped isotope composition of historical atmospheric CH_4. $\delta^{13}C$ and δD measured in our study agree with previously published datasets for these years (Ferretti et al., 2005; Sapart et al., 2013). The evolution in $\Delta^{13}CH_3D$ is consistent with previous modelling studies showing little temporal variability (Chung & Arnold, 2021; Haghnegahdar et al., 2017). The large variation (10 ‰) in

$\Delta^{12}CH_2D_2$ from 1993 to 2018, however, is unexpected. A recent study (Farquhar et al., 2022) proposed the possibility that $\Delta^{12}CH_2D_2$ changes in the past could be large enough to be discerned with the current methods, but previous models predicted only about 3 to 4 ‰ change even over longer time scales (Chung & Arnold, 2021; Haghnegahdar et al., 2017).

6.4. Improvement of Key Parameters of the Methane Clumped Isotope Budget

We used a two-box atmosphere forward model, *clumped-forward-model* (see details in Appendix D), to investigate the factors influencing the reconstructed signals. The model uses optimised fluxes for five source categories - wetlands, waste, fossil, pyrogenic, and agriculture (see details in Appendix D) - between 1980 and 2024, which were derived from an inversion of long-time measurements of CH_4 and its bulk isotopic composition (details of *bulk-inverse-model* in Appendix D). Figure 6.2 shows the results of the measurements and the model output for the mole fraction, bulk, and clumped isotope compositions for the Northern Hemisphere (NH) (red line) and the existing NH measurements/observations from 1994-2019 (green line) for mole fraction and the bulk isotopic compositions (details in Appendix D). The corresponding model output for the Southern Hemisphere (SH) is shown in Figure D.5.

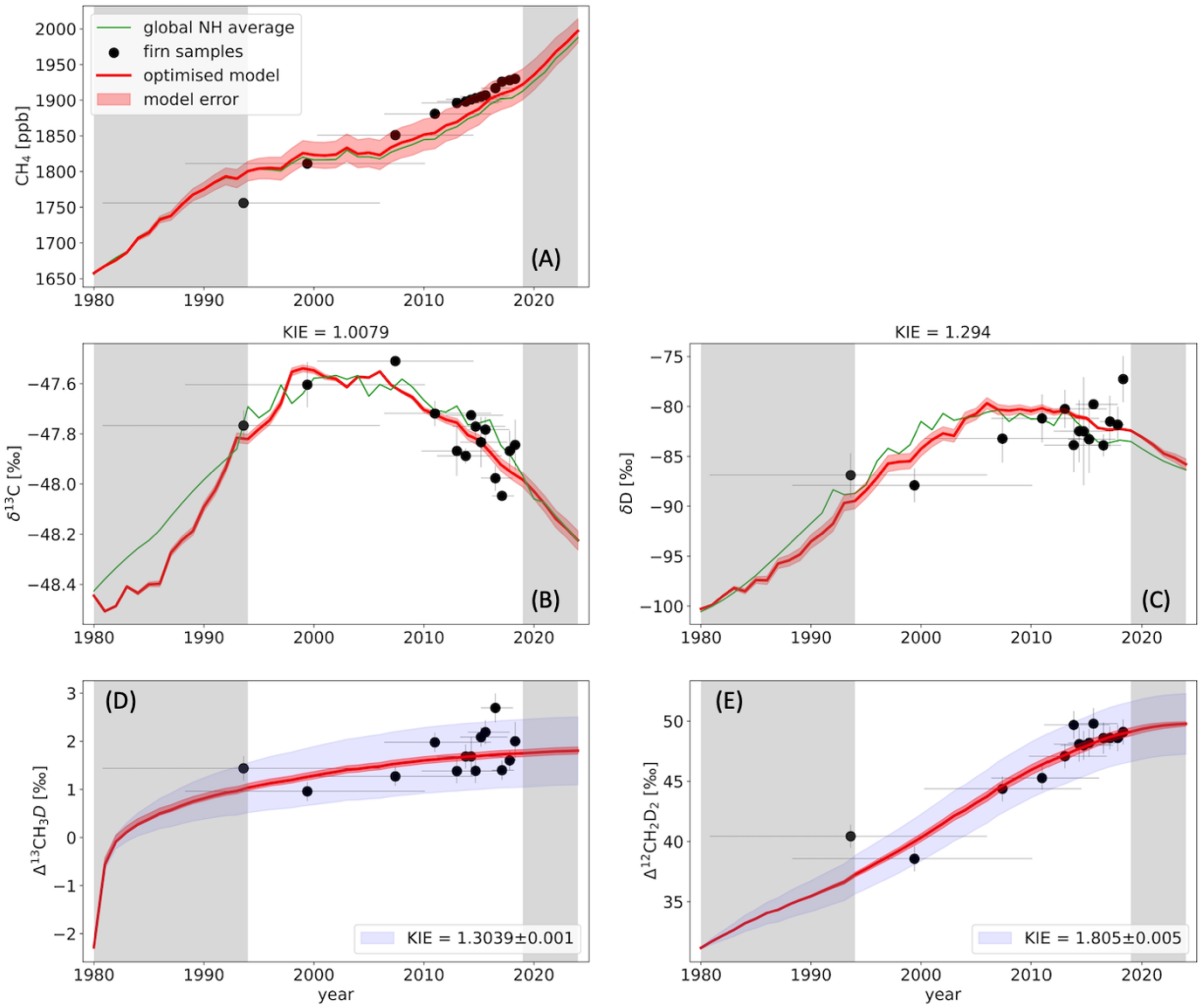

Figure 6.2. **Measurements (black circles) and model output of the two-box forward model using optimised fluxes (red) for (A) CH_4 mole fraction, (B) $\delta^{13}C$, (C) δD, (D) $\Delta^{13}CH_3D$ and (E) $\Delta^{12}CH_2D_2$.** The red-shaded areas in (A)-(E) show the error associated with the inverted fluxes (details in Appendix D). The green lines in (A)-(C) represent the NH averages calculated from NOAA GML monitoring stations (Lan et al.). The sink reaction KIEs for $^{13}CH_4$ and $^{12}CH_3D$ are given as titles in (B) and (C), respectively. The blue-shaded areas in (D) and (E) show the sensitivity of the KIEs used (±0.001 for $\Delta^{13}CH_3D$ and ±0.005 for $\Delta^{12}CH_2D_2$). The grey-shaded areas mark the spin-up and spin-down periods for optimising the fluxes.

The two key parameters that largely control the atmospheric bulk and clumped isotope budget are the source compositions of the individual source categories and the KIEs of the sink reactions. The hemisphere-specific $\delta^{13}C$ and δD of each source category were well-constrained based on existing literature, predominately from (Menoud et al., 2021; Sherwood et al., 2017) and optimised using *bulk-inversion model* simulations (details in Appendix D), assuming no

temporal variations. The corresponding KIEs for bulk isotopes are optimised using the forward model to match the existing NH observations (green line in Figure 6.2) and are found to be comparable with literature values (Fujita et al., 2020). However, for the clumped isotopologues, neither the source compositions of each source category nor the sink KIEs are well-constrained.

Figure 6.3A shows that different possible combinations of source compositions and sink reaction KIE values can produce similar $\Delta^{12}CH_2D_2$ histories. The source compositions and the sink KIEs form tight linear relationships for both $\Delta^{13}CH_3D$ (Figure D.6) and $\Delta^{12}CH_2D_2$ (Figure 6.3B). To provide constraints from one end, we compiled and categorised the CH_4 clumped isotopic composition measurements published so far (Dong et al., 2021; Douglas et al., 2020; Douglas et al., 2017; Eldridge et al., 2019; Giunta et al., 2022; Giunta et al., 2019; Gonzalez et al., 2019; Gruen et al., 2018; Haghnegahdar et al., 2023; Krause et al., 2022; Labidi et al., 2020; Lalk et al., 2024; Liu, Harris, et al., 2023; Liu, Treude, et al., 2023; Ono et al., 2021; Ono et al., 2014; Rhim & Ono, 2022; Shuai, Douglas, et al., 2018; Shuai, Etiope, et al., 2018; Stolper, Lawson, et al., 2014; Stolper et al., 2015; Stolper, Sessions, et al., 2014; Sun et al., 2023; Sun, Haghnegahdar, et al., 2025; Taenzer et al., 2020; Thiagarajan et al., 2020; Wang et al., 2015; Wang et al., 2018; Wang et al., 2016; Young, Kohl, Sherwood Lollar, et al., 2017; Young et al., 2016; Zhang, Snyder, et al., 2021) to estimate the clumped isotopologue compositions of each source category and the total atmospheric source mixture (details in Appendix D). The yellow shaded area in Figure 6.3B indicates the plausible range of KIEs is between 1.78 and 1.82, considering the possible range of $\Delta^{12}CH_2D_2$ values of the total CH_4 source (details in Appendix D).

The total sink KIE corresponding to the most probable source mixture (red dot in Figure 6.3B and Figure D.6) required to fit the firn air measurements were calculated to be 1.3039 ± 0.001 for $^{13}CH_3D$ and 1.805 ± 0.005 for $^{12}CH_2D_2$. These errors are the sensitivity of the KIEs for a particular source composition and are shown as blue-shaded areas in Figure 6.2D and Figure 6.2E. These independently constrained sink KIE values (1.805 ± 0.005), calculated from the isotope budget mass balance using our new measurements, differ significantly (for $^{12}CH_2D_2$) from previously published theoretical values (Chung & Arnold, 2021; Haghnegahdar et al., 2023) but are close to a published experimental result (Gierczak et al., 1997).

Alternately, the clumped isotope budget can be closed by redistributing global CH_4 fluxes to increase microbial CH_4 emissions, which have lower $\Delta^{12}CH_2D_2$ values, or strongly revising $\Delta^{12}CH_2D_2$ signatures of CH_4 sources towards more anti-clumping values, assuming that current measurements do not accurately represent global sources. However, these possibilities are considered unlikely. The global CH_4 budget is rather well constrained after an extensive community effort in the past decades, and a major repartitioning towards microbial sources is unlikely to fit with other constraints on the budget, such as the ^{14}C, ^{13}C, and D balances. Instead, the likely scenario is that the theoretical calculations of the isotopic fractionation in the CH_4 + OH reaction may need to be revised. The measurements of the temporal evolution of $\Delta^{12}CH_2D_2$ in this study better constrain this issue. It is important to note that for the bulk isotopes, the uncertainty in the sink fractionation has also been reported as one of the key uncertainties in further constraining the $\delta^{13}C$ budget (Basu et al., 2022).

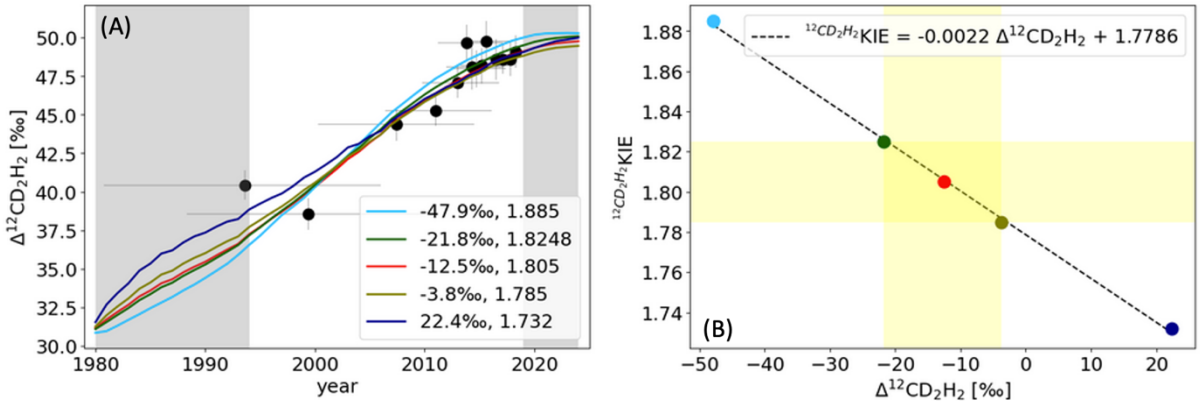

Figure 6.3. **The mutual constraint between the sink reaction KIE and the total source $\Delta^{12}CH_2D_2$. (A)** Model outputs of $\Delta^{12}CH_2D_2$ for different combinations of total source $\Delta^{12}CH_2D_2$ signatures and sink KIEs. Each combination is distinguished by a colour, as given in the legend (source mixture composition, sink KIE). The black dots represent the firn air samples measured in this study. **(B)** The strongly linear relationship between the total source $\Delta^{12}CH_2D_2$ signatures (x-axis) and sink KIEs (y-axis). The vertically shaded yellow region highlights the most probable range of values for $\Delta^{12}CH_2D_2$ deduced from existing datasets, and the horizontal, yellow-shaded region shows the required range of KIE values to fit the observation data.

6.5. Source and Sink Effects on the Clumped Isotopic Composition of Methane

Having constrained the source and sink characteristics, we further investigated the factors contributing to the measured temporal evolution of the $\Delta^{13}CH_3D$ and $\Delta^{12}CH_2D_2$, especially the 10‰ change in $\Delta^{12}CH_2D_2$. We first evaluated the role of the source fluxes by modelling scenarios in which one of the source categories was kept constant, and the optimised fluxes for four other categories were retained. The results (Figure D.7) show that even with these drastic synthetic source flux changes, which lead to clearly visible mismatches in the CH_4 mole fractions and the bulk isotopes, the trend in $\Delta^{12}CH_2D_2$ stays similar within the measurement precision. We then conducted simulations by keeping either fossil/wetland fluxes constant over time but adjusting the other sources to retain a realistic atmospheric CH_4 mole fraction (Figure D.8). These changes again significantly affect the bulk isotopes, while the change in the clumped

isotopic composition is still within the current measurement uncertainty. These tests show that changes in emission fluxes from individual source categories in the past 30 years cannot fully explain the measured evolution of $\Delta^{12}CH_2D_2$.

Following this, we investigated whether the large temporal variation observed in $\Delta^{12}CH_2D_2$ is due to the disequilibrium of atmospheric CH_4 sources and sinks. The atmospheric reservoir has changed rapidly over the past decades, and consequently, the isotopologues of CH_4 have not had sufficient time to adjust to the source-sink equilibrium (Tans, 1997). To qualitatively investigate this, we simulated a scenario with constant emissions since 1980 (grey line in Figure 6.4). It is evident that the atmospheric CH_4 mole fraction equilibrates quickly (Figure 6.4A), while the isotopic signatures take considerably longer to come to a steady state as was previously shown in (Haghnegahdar et al., 2017; Tans, 1997). Nevertheless, a scenario with constant sources already reproduces the measured temporal trends in δD, $\Delta^{13}CH_3D$ and $\Delta^{12}CH_2D_2$ (Figure 6.4C-6.4E), demonstrating that the source-sink disequilibrium is an important contribution to their temporal evolution. The reason for the disequilibrium effect being prominent for the signatures, including the hydrogen isotopes, is the strong sink fractionation of around 300 ‰ for $^{12}CH_3D$ and $^{13}CH_3D$ and 800 ‰ for $^{12}CH_2D_2$. The δ and Δ values at isotope stabilization depend on the chosen source composition and sink fractionation.

6.6. Methane Changes in the Future

Future atmospheric CH_4 levels are uncertain. On the one hand, unabated emissions from anthropogenic sources, coupled with potential climate feedback from natural sources, may lead

to the continuing rise of CH_4 levels (Dean et al., 2018). On the other hand, an increasing number of policies are recognising the importance of limiting CH_4 emissions. The Global Methane Pledge aims to reduce CH_4 emissions by 30 % by 2030 relative to 2020 (*Global Methane Pledge*), which, while challenging, could slow down or even reverse the increasing trend in CH_4 levels. Further sustained emission reductions and/or enhanced removal efforts may be necessary to achieve the goals of the Paris Agreement (United Nations Environment Programme and Climate and Clean Air Coalition, 2021). With this in mind, we performed simulations of future CH_4 scenarios that reflect different potential future CH_4 trajectories.

Figure 6.4 shows the model results for six different scenarios, representing "*constant sources*", "*unabated increase*", "*emission mitigation*", "*enhanced CH_4 removal*", and the IPCC's (IPCC, 2021) SSP1 and SSP5 scenarios (details in Appendix D). Additional IPCC-SSPx scenarios are in Figure D.9. Different isotope signatures are sensitive to different CH_4 budget parameters. $\delta^{13}C$ reacts strongly to source composition changes: in "*constant sources*", "*increase*", and "*removal*" scenarios, the relative shares of source categories remain largely unchanged, resulting in minor temporal $\delta^{13}C$ changes. The "*mitigation"* scenario, however, preferentially removes ^{13}C-enriched sources (fossil and waste), thereby lowering $\delta^{13}C$ values. The fossil source is also Deuterium-enriched, suggesting similar δD and $\delta^{13}C$ trends. However, after an initial decrease, δD increases again in '*emission mitigation"* and "*removal scenarios"* due to δD's higher sensitivity to sink fractionation. Reduced emissions or accelerated removal lead to atmospheric CH_4 being processed more by the sinks, increasing its "photochemical age". The KIE for δD is about 300 ‰, compared to only 8 ‰ for $\delta^{13}C$. Thus, the $\delta^{13}C$ temporal evolution is dominated by source

changes, while the evolution of δD is influenced by both source changes and the source-sink imbalance.

Our modelling results demonstrate that the novel isotope tracer $\Delta^{12}CH_2D_2$ is particularly sensitive to the source-sink imbalance. In the mitigation and removal scenarios, $\Delta^{12}CH_2D_2$ largely increases over the coming decades, driven by the strongest KIE of almost 800 ‰ (details in Appendix D). Thus, similar to the situation over the past decades reconstructed from our firn air measurements, $\Delta^{12}CH_2D_2$ will continue to record and integrate changes in the source-sink imbalance in the future. Figure D.10 shows that $\Delta^{12}CH_2D_2$ is negatively correlated (and time-shifted) to the annual CH_4 growth rate.

With the present measurement precision, $\Delta^{13}CH_3D$ may not be a useful tracer for atmospheric budget changes since the predicted variations are close to the measurement precision. The remaining three tracers will allow us to address the key components of the CH_4 budget: the sources ($\delta^{13}C$), the source-sink imbalance ($\Delta^{12}CH_2D_2$), and a mixed effect of both (δD).

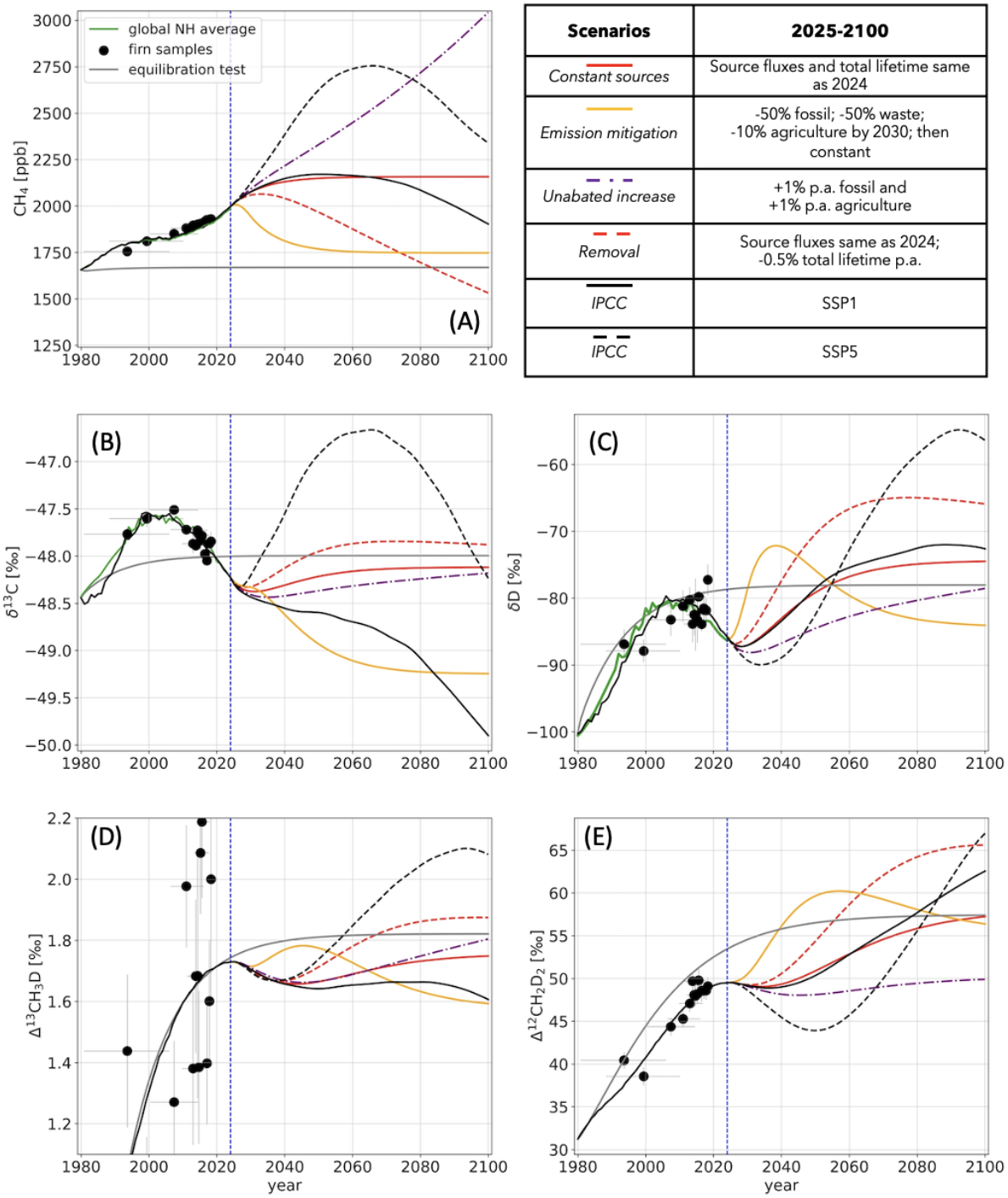

Scenarios	2025-2100
Constant sources	Source fluxes and total lifetime same as 2024
Emission mitigation	-50% fossil; -50% waste; -10% agriculture by 2030; then constant
Unabated increase	+1% p.a. fossil and +1% p.a. agriculture
Removal	Source fluxes same as 2024; -0.5% total lifetime p.a.
IPCC	SSP1
IPCC	SSP5

Figure 6.4. **Results of long-term simulations of various past and future scenarios. (A)** CH_4 mole fraction, **(B)** $\delta^{13}C$, **(C)** δD, **(D)** $\Delta^{13}CH_3D$ and **(E)** $\Delta^{12}CH_2D_2$. The vertical dashed blue line represents the current year (2024). The black dots represent the firn air samples measured in this study, and each line corresponds to the results of model scenario tests as given in the legend.

7. Summary and Outlook

7.1. Summary of current achievements

Over the past decade, the field of methane clumped isotopologues has seen progress.

7.1.1. Measurement Techniques

First, measurement techniques have gradually matured. The number of laboratories capable of measuring methane clumped isotopologues has increased from two in 2014 (MIT and Caltech) to five around 2021 (MIT, Caltech, UCLA, UMD, and TITECH), and further expanded to nine (or maybe more) by 2025 (with the addition of Utrecht University, GIG, EMPA, and the University of Edinburgh, among others).

However, neither spectroscopic nor mass spectrometric techniques have seen significant reductions in sample size requirements or improvements in precision. For spectroscopy, Ono et al. (2014) reported achieving a precision of 0.2‰ (2σ) for $\Delta^{13}CH_3D$ with a sample size of 0.42 mmol (10 ml STP), with a minimum sample size of 0.5 ml. Gonzalez et al. (2019) achieved a precision of 2‰ (2σ) for $\Delta^{12}CH_2D_2$ with a 20 ml STP sample. In Zhang et al. (2025), a precision of 0.14‰ (2σ) for $\Delta^{13}CH_3D$ and 2.6‰ (2σ) for $\Delta^{12}CH_2D_2$ was achieved with a 0.42 mmol (10 ml STP) sample. For mass spectrometry, only the Ultra and Panorama instruments are currently capable of such measurements (introduced in Chapter 2), and their sample requirements and

analytical precision remain strictly limited by counting statistics and MRPs, with no significant changes since their commercial deployment. For the Panorama instrument at UMD, a sample size of ~70 μmol (1.57 ml STP) is required to achieve a precision of ~0.4‰ (2σ) for $\Delta^{13}CH_3D$ and ~2.0‰ (2σ) for $\Delta^{12}CH_2D_2$, with a minimum sample size of ~20 μmol (~0.45 ml STP) (Haghnegahdar et al., 2023). For the Panorama at UCLA, $^{13}CH_3D/^{12}CH_4$ and $^{12}CH_2D_2/^{12}CH_4$ ratios are measured with precision of ~0.1‰ and ~0.5‰, respectively, with a bigger beam and slightly larger sample volume (Young, Kohl, Lollar, et al., 2017). The Ultra instrument requires larger sample sizes, and its $\Delta^{12}CH_2D_2$ values rely on post-processing.

Additionally, for high-concentration methane samples, automated methane purification lines (e.g., at MIT, the University of Edinburgh, and GIG) have significantly improved sample processing efficiency. For low-concentration methane samples, such as air, the combination of extraction and purification lines has made air measurements feasible (Haghnegahdar et al., 2023), though the extraction is still human labor-intensive. Recent publications have increasingly focused on the applications of methane clumped isotopologues rather than method development and validation.

7.1.2. Source Compositions

The clumped isotopologue composition ranges for various methane sources have become clearer, enabling clumped isotopologues to assist in methane source attribution. A Schöll plot-like diagram can be constructed for the $\Delta^{13}CH_3D$ - $\Delta^{12}CH_2D_2$ pair (Young, Kohl, Lollar, et al., 2017). On this diagram, thermogenic methane typically lies on the thermo-equilibrium curve,

representing its equilibrium temperature (usually between 50–250°C). Fresh microbial methane often exhibits significant anti-clumping signals in $\Delta^{12}CH_2D_2$ (typically <-20‰), with $\Delta^{13}CH_3D$ also being less than zero. Methane that has undergone methanogenesis-AOM balances (commonly found in deep-sea sediments) usually lies on the thermo-equilibrium curve but corresponds to lower equilibrium temperatures (e.g., lower than 50°C). Pyrogenic methane shows more variability but may exhibit anti-clumping $\Delta^{12}CH_2D_2$ and typically positive $\Delta^{13}CH_3D$.

Field sampling and clumped isotopologue analysis of methane from various sources have expanded and refined datasets based on activity/location classifications (e.g., wetlands, landfills, agriculture, biomass burning), particularly for previously unmeasured sources such as landfills (Sun et al., in revision) and vehicle exhaust methane (as a representative for biomass burning/pyrogenic sources) (Sun, Haghnegahdar, et al., 2025). Table 1.1 and Table 1.2 in Section 1.3 summarize the bulk carbon and hydrogen isotope characteristics of various methane sources, while Table 1.8 and Table 1.9 in Section 1.4.4 summarize their clumped isotopologue characteristics.

Incorporating clumped isotopologue signals with bulk carbon and hydrogen isotopes, as well as other geochemical proxies (e.g., ethane-to-methane ratios), generally improves confidence in methane source attribution.

7.1.3. Intramolecular Thermometer and Fossil-fuel Related Methane

The use of methane clumped isotopologues as an intramolecular thermometer has become more involved. After the simultaneous measurement of $\Delta^{13}CH_3D$ and $\Delta^{12}CH_2D_2$ became possible, the previous practice of calculating equilibrium temperatures based solely on $\Delta^{13}CH_3D$ was corrected (Wang et al., 2015; Young, Kohl, Lollar, et al., 2017). Now, if intramolecular thermometry is to be applied, the $\Delta^{13}CH_3D$-$\Delta^{12}CH_2D_2$ pair must lie on the thermo-equilibrium curve, and the possibility of non-equilibrium signals caused by processes described in Section 1.4.3 coincidentally achieving equilibrium must be ruled out. Within this framework, clumped isotopologue signals have carried information about the origin, migration, and equilibrium temperatures of fossil fuel-related methane.

7.1.4. Non-equilibrium Processes and Microbial Methane

Through laboratory microbial experiments and abiotic methane experiments, the pathways for generating non-equilibrium signals in methanogenesis, microbial methane oxidation, abiotic methane synthesis, and abiotic (catalyzed) methane oxidation have been largely clarified. Several studies have measured, calculated, and reported fractionation factors for these processes and explored controlling factors (e.g., (Krause et al., 2022; Labidi et al., 2024; Li, Ash, et al., 2024; Li, Chiu, et al., 2024; Liu, Harris, et al., 2023; Ono et al., 2022; Rhim & Ono, 2022; Sun, Haghnegahdar, et al., 2025)).

For methanogenesis and abiotic methane synthesis, the clumped isotopologue composition of the final methane product is controlled by the reversibility of each step in the enzymatic (or metal-catalyzed) reaction network. Under fully reversible conditions, EIE are expressed, while under fully irreversible conditions, KIE are expressed. The net fractionation is the cumulative effect of each reaction step. Typically, the reversibility of the final hydrogenation step is relatively low. Table 1.3 in Section 1.3.3.1 compiles the $^{13C}\alpha$ and $^{D}\alpha$ values reported in the literature, while Table 1.7 in Section 1.4.3.5 provides the $^{13CH3D}\gamma$ and $^{12CH2D2}\gamma$ values for methanogenesis, showing a relatively wide range of variation. Factors such as substrate availability (especially hydrogen sources), temperature, pressure, and the hydrogen isotope composition of water are critical in controlling reversibility and substrate isotope composition.

Methane oxidation has been found to enrich methane clumped isotopologue signals. AeOM and AOM may exhibit distinct directions on the $\Delta^{13}CH_3D$-$\Delta^{12}CH_2D_2$ plot (Liu, Harris, et al., 2023) (Figure 1.22 in Section 1.4.4). AOM can bring methane signals closer to the thermo-equilibrium line, even producing extremely positive values, while AeOM (also applicable to abiotic catalyzed oxidation and atmospheric oxidation) can shift methane signals toward the values observed in air. Compared to AeOM, AOM causes smaller changes in $\Delta^{13}CH_3D$. Table 1.4 in Section 1.3.3.3 provides the $^{13C}\alpha$ and $^{D}\alpha$ values for microbial oxidation processes, while Table 1.7 in Section 1.4.3.5 gives the $^{13CH3D}\gamma$ and $^{12CH2D2}\gamma$ values for oxidation processes.

7.1.5. Methane Atmospheric Sink Reactions

New insights have been gained into the isotopologue effects of atmospheric methane sink reactions—although there is no consensus on the exact KIE values for these reactions, it is agreed that sink reactions significantly enrich $\Delta^{12}CH_2D_2$ and slightly enrich $\Delta^{13}CH_3D$ (Haghnegahdar et al., 2017). Ongoing first-principles calculations are expected to provide updated KIE equations for CH_4+OH and CH_4+Cl reactions. And there are several known ongoing experimental efforts (Thomas Röckmann and Matthew Johnson at Utrecht University and University of Copenhagen, as well as Aparajeo Chattopadhyay, Lee Murray, and Vasilii Petrenko at the University of Rochester) to re-measure the clumped isotopologue KIEs of these reactions.

The first direct measurements of atmospheric clumped isotopologues (Haghnegahdar et al., 2023) and firn-trapped air (Sivan, Sun, et al., 2024) (Sivan and Sun et al., in prep) have provided strong constraints on sink KIEs. In particular, the 30-year trend in atmospheric methane clumped isotopologues derived from firn-trapped air strictly defines the linear relationship between total sink KIEs and total source composition, constraining sink KIE values for clumped isotopologues to lie between existing lab measurement value and theoretical calculation value.

7.1.6. Air Methane Compositions and Global Methane Budget Model with Clumped Isotopologues

Actual measurement data for atmospheric methane clumped isotopologues have been obtained (Haghnegahdar et al., 2023). Based on these real measurements, some previous global atmospheric methane models (Chung & Arnold, 2021; Haghnegahdar et al., 2017) have been significantly revised, particularly in their estimates of the total source clumped isotopologue composition. As estimates of clumped isotopologue compositions for various sources become more accurate, and with the analysis of firn-trapped air providing nearly 30 years of measured clumped isotopologue data (Sivan, Sun, et al., 2024) (Sivan and Sun et al., in prep), there have been attempts to incorporate clumped isotopologues into global box models.

7.2. Difficulties and Disadvantages

The main factors currently limiting the application of methane clumped isotopologues stem from two aspects.

7.2.1. Technical Difficulties

First, there are technical difficulties. Although Section 7.1 highlighted some technical advancements, there has been no qualitative leap. What remains unchanged is that, compared to bulk carbon and hydrogen isotopes, measuring clumped isotopologues requires a much larger

sample volume. As a result, most research to date has focused on lab cultures, natural gas, lab abiotic-synthesized samples, wetland bubbles, and sediment-trapped gases, which are almost pure methane or high-concentration methane. The measurement of atmospheric methane clumped isotopologues remains a technical challenge. The large sample volume requirements make sampling and transportation extremely difficult. Furthermore, the measurement process is still time-consuming, and the uncertainty remains high compared to bulk isotope measurements. This inevitably limits the number of data points that can be obtained for a given study. A paper reporting 10 data points likely means that at least 20–30, or even more, samples were collected, pre-processed, and measured. If all these are air samples, the duration of this project can be expected to be very long. limited data number and high uncertainty mean that statistical methods commonly used in environmental science or biochemistry cannot be effectively applied in this field.

7.2.2. Cost-effectiveness

Second, there is the issue of cost-effectiveness. For a specific scientific question, methane clumped isotopologues may not always be the best research tool. Take the problem of distinguishing contributions from thermogenic and microbial methane in a mixed gas as an example to explain. Clumped isotopologues are statistically useful for improving the confidence of differentiating thermogenic and microbial methane, if supplementing the clumped isotopologue information to bulk isotope information. Measuring clumped isotopologues in addition to bulk carbon and hydrogen isotopes requires several times more sample volume and significantly more effort, yet the additional parameters may improve source identification by a

few to tens of percentage points for some samples, while for others, there may be no improvement (Marcum et al.). And for samples with ambiguous bulk isotope signals (e.g., samples whose isotopic composition falls within the overlapping range typical of microbial methane and thermogenic methane), the effectiveness of isotopologue tools may also be limited (i.e., clumped isotopologue signals of this sample also give ambiguous information) (Young, 2019). In contrast, measuring the ethane content of the mixed gas—which requires negligible additional sample volume and effort—can provide highly confident methane source attribution and estimates of the proportions of the two sources.

The above statement can be illustrated using the Devonian Antrim Shale natural gas in the Michigan Basin as an example. The $\delta^{13}C$ of methane from this reservoir typically ranges between -50‰ and -53‰, falling within the overlapping range of thermogenic and microbial methane, making it hard to determine its origin based solely on methane bulk isotopes. Martini et al. (1996); Martini et al. (1998), based on the linear positive correlation between δD of CH_4 and δD of H_2O, concluded that microbial methane is the primary contributor, potentially accounting for up to 80% of the total. However, they also noted the presence of a thermogenic endmember based on the low C_1/C_{2-4} ratios (as low as 8) observed in some samples. Pore water incubation and molecular biological identification of sulfate-reducing bacteria provided microbiological evidence supporting the existence of a microbial endmember, and also suggested the influence of microbial oxidation. Some studies have measured the clumped isotopologues of Antrim Shale gas (Giunta et al., 2019; Stolper et al., 2015), with some data points lying slightly below the thermo-equilibrium curve at around 50 °C, while others exhibit $\Delta^{12}CH_2D_2$ values of approximately -15‰ and $\Delta^{13}CH_3D$ values of +4 to 5‰ (see Figure 3c of Giunta et al. (2019)). If

relying solely on clumped isotopologue compositions, it is not possible to as strongly conclude the existence of a thermogenic endmember as with the $C_1/C_{2\text{-}4}$ ratio (note that Stolper et al. (2015) inferred at least 25% contribution from ~140 °C thermogenic methane endmember based on the Δ^{18} thermometer, but the Δ^{18} thermometer was later found to be unreliable after $\Delta^{12}CH_2D_2$ measurements became possible, as methane may not always be in a thermo-equilibrium state (Section 1.4.2 and Section 1.4.3)). Only by incorporating the existence of a thermogenic endmember as a known condition into the analytical framework can the clumped isotopologue data support the conclusion of thermogenic endmember mixing and indicate that the microbial endmember has been altered by oxidation. That said, prior to obtaining the measurement results, we cannot estimate whether clumped isotopologues will provide new or more confident information. Therefore, such measurements remain necessary.

Similar cost-effectiveness issues apply to current microbial methane experimental research. Does measuring clumped isotopologue signals in microbial methane samples provide more information about microbial metabolic processes than bulk isotope measurements alone? Could other biological measurement techniques, such as DNA and sRNA sequencing (though also time and labor consuming), provide more straightforward insights? If methane clumped isotopologues are not the best tool for addressing a specific scientific question, the significance of such research diminishes (though it remains meaningful). An example that successfully highlights the unique capabilities of methane clumped isotopologues is their potential application in studying extraterrestrial methane. Since bulk carbon and hydrogen isotope information for methane on exoplanets may lack interpretative context, clumped isotopologues, as intramolecular features independent of bulk isotopes, could provide insights into the origin of extraterrestrial methane

(Labidi et al., 2024). This idea indeed addresses a problem that other research tools are unlikely to solve, although direct measurements of clumped isotopologues in extraterrestrial methane are not feasible in the short term. More targeted laboratory simulations and modeling could be pursued.

These disadvantages may be mitigated in the future through more advanced, faster, and automated measurement methods. Higher-precision isotopologue measurement technologies may enable the differentiation of some clumped isotopologue signals that cannot be distinguished with the current uncertainty levels. However, the most critical step is to accurately identify areas where clumped isotopologues have unique advantages and use them to address scientific questions that cannot be resolved by traditional bulk isotopes or other proxies.

7.3 Future Research Directions

Scientific progress is incremental. The outlook for future research directions in methane clumped isotopologues presented in this section is largely based on the current achievements in the field, as outlined in Section 7.1 (and Chapters 1–6), and extends from there.

7.3.1. Advancing Measurement Technologies for Methane Clumped Isotopologues

There is still significant room for improvement in measurement technology, but advancements should be driven by specific needs. For high methane concentration samples, current measurement techniques already provide sufficient performance for analysis. Sample pre-processing can also be largely automated. For low methane concentration samples, such as air, the main challenges are the lengthy pre-processing time and the large sample volume requirements.

I recommend **upgrading existing manual air sample extraction lines to achieve automation**, thereby freeing up researchers' time and energy. Air samples are relatively straightforward to automate because they are relatively "clean," lacking significant amounts of CO_2 or uncommon contaminants, and their methane concentration and water vapor content are relatively stable, with a common range of variation. Therefore, automated systems do not need excessive redundancy in design steps or capabilities.

Additionally, I suggest **conducting systematic and rigorous testing of compressor sampling** to demonstrate that this method can faithfully record methane concentrations and isotopic compositions in air, followed by standardizing this sampling method. Ideally, compressor sampling could become portable for single-person use—otherwise, it will likely still rely on specific compressors and gas cylinders/tanks, which are heavy.

For more challenging samples, such as those with even lower methane concentrations, limited total methane availability, or nearly impossible sampling conditions (e.g., methane trapped in ice cores or methane in the Martian atmosphere), more advanced instruments will need to be developed to allow for lower sample requirements or even in-situ measurements. Mass spectrometry may have greater potential for reducing sample volume requirements, while spectroscopy may be more promising for in-situ measurements. However, in the short term, neither mass spectrometry nor spectroscopy technology is likely to see significant breakthroughs.

7.3.2. Building a Comprehensive Global Source Isotopologue Database

Continuing to more accurately define the global average clumped isotopologue compositions of methane sources—and, if possible, **increasing spatial and temporal resolution**—is essential. This serves as the foundation for interpreting all other clumped isotopologue data. A parallel can be drawn with traditional bulk carbon isotopes: even after decades of methane carbon isotope measurements, there is still debate over the global average $\delta^{13}C$ value of fossil-fuel methane, despite the extensive databases compiled by Sherwood et al. (2017) and subsequent updates, as well as Menoud et al. (2022), which include thousands of measurements covering over 95% of oil and gas production regions. These databases themselves yield inconsistent results. Moreover, it is only in the last five years that studies like Lan et al. (2021) have begun to incorporate temporal and spatial information into models, as dividing global datasets by time and space drastically reduces the number of data points in each slice and creates uneven distributions. For example, there is abundant data from North America, with a long record in time, allowing us to identify that there are changes in US-averaged fossil-fuel methane $\delta^{13}C$ over time driven by

increased unconventional shale gas extraction. In contrast, data from South America and Africa, for example, are significantly scarcer, especially for earlier years, making it necessary to assume that source isotopic characteristics from these regions around the year 2000 can be represented by the global average and do not vary over time.

The above discussion pertains to $\delta^{13}C$; methane δD measurements are technically more challenging than $\delta^{13}C$, resulting in far fewer data points and even less understanding of global source δD values and their spatial and temporal variations.

Clumped isotopologue measurements are still in their infancy, with current data only sufficient to roughly estimate representative clumped compositions for each source. Fossil-fuel-related methane has the most clumped isotopologue measurements, possibly numbering in the hundreds. Microbial methane measurements are also numerous, but many are from lab cultures, which may not represent natural conditions. Field measurements from wetlands are limited, with only around 20 published data. Data from agriculture are even scarcer, with fewer than 10 measurements. Biomass burning and landfill (waste) methane measurements are essentially limited to one or two studies with only a few data points. I believe it is premature to perform statistical analyses with the current data, as the global averages derived from these limited measurements may not be representative. **Expanding source databases** by measuring methane from a broader spatial and temporal range of anthropogenic and natural sources, and investigating seasonal and regional variations in natural methane sources—particularly wetlands, landfills, and permafrost—is a long-term task that requires continuous updates and global collaborations.

7.3.3. Refining KIEs for Methane Sink Reactions

The values of sink KIEs still require confirmation through both theoretical calculations and experimental measurements. Current **first-principles calculations may need to be revisited** to consider which approximation theory could better describe the electron clouds of methane isotopologues and their corresponding transition states during the sink reactions. **Photochemical experiments** should be reproduced to systematically measure fractionation factors. It would be better if these lab experiments could include the reactions CH_4+OH and CH_4+Cl, covering the five most common methane isotopologues ($^{12}CH_4$, $^{13}CH_4$, $^{12}CH_3D$, $^{13}CH_3D$, and $^{12}CH_2D_2$) for each reaction, and should ideally be conducted at multiple temperatures. If possible, theoretical calculations and experimental measurements should also be performed for the CH^4+O(^{1}D) reaction.

The ultimate goal is to achieve consistency between theoretical values, experimental measurements, and values inferred from atmospheric measurements and models. Sink KIEs and total source isotope (and isotopologue) compositions form a linearly constrained pair. If KIEs can be accurately determined, they will provide stronger constraints on total source compositions. Currently, even the 1–3‰ discrepancy between experimental and theoretical values for the KIE of $^{13}CH_4$+OH introduces more than 10% uncertainty in the global allocation of thermogenic and microbial methane sources.

7.3.4. Exploring Isotopologue Fractionation in Microbial and Abiotic Processes

Continuing to **conduct controlled microbial and abiotic experiments** to establish robust isotopic fractionation factors and explore the factors controlling methane clumped isotopologue fractionation is essential. The analytical framework for microbial methane is now largely established: the cumulative isotopic expression of the (seven) enzymatic steps determines the final apparent isotopic fractionation. Reversibility controls the expression of KIE and EIE for each step. To bridge laboratory and field studies, it is crucial to clarify **how environmental factors influence reversibility.** Isotopic methods should be complemented by approaches from other disciplines, such as molecular biology and genomics (e.g., (Chadwick et al., 2022; Evans et al., 2015; Vorobev et al., 2014)), as well as thermodynamic and computational modeling (e.g., (Baik et al., 2003; Gherman et al., 2005)).

Additionally, **experiments and field sampling for abiotic methane synthesis and oxidation** remain scarce, yet abiotic methane may yield unique values. A significant question is whether methane clumped isotopologues can serve as a biomarker for life. Given that clumping is independent of bulk isotopes—whose interpretation relies on a relative reference frame—clumping may have greater potential than bulk isotopes as a biomarker (or abiomarker) in unknown environments, such as Mars.

The same logic applies to clumping in methoxy groups and site-specific clumping like ^{13}C-^{13}C clumping in organic molecules.

7.3.5. Establishing a Global Methane Clumped Isotopologue Observation Network and a Clumped Isotopologue incorporated Budget Model

Spatially and temporally resolved atmospheric methane clumped isotopologue measurements, along with improved global atmospheric methane models incorporating clumped isotopologues, are needed.

Current atmospheric measurements cannot **define the "background" clumped isotopologue values** or **global averages** because existing air data are limited to the air above the University of Maryland. We also tried two air samples from a NOAA observation site in Boulder, Colorado, but the project was not established due to limited funding and time. With the available data, we cannot determine whether air in different regions exhibits distinct methane clumped isotopologue signals or not. Drawing parallels to bulk carbon isotope observation networks, air $\delta^{13}C$ varies across regions. If a similar observation network could be extended to clumped isotopologues, similar variations might be observed.

Moreover, unlike $\delta^{13}C$, which is sensitive to source mixing, **$\Delta^{12}CH_2D_2$ is less sensitive to source mixing**; a 10–20% mixing ratio may not result in a discernible change in air $\Delta^{12}CH_2D_2$ (Sun et al., 2023; Sun et al., in revision). This provides an opportunity to decouple source mixing from sink effects—if a monitoring station observes a change in $\delta^{13}C$ without a significant change in $\Delta^{12}CH_2D_2$, it may indicate source mixing. If both $\delta^{13}C$ and $\Delta^{12}CH_2D_2$ change significantly, it could suggest the intrusion of air masses with different sink reaction histories.

Additionally, atmospheric models should be updated to **predict whether atmospheric methane clumped isotopologues will continue to change over time**. If they do and provide additional insights, an **observation network** should be established to regularly measure atmospheric methane clumped isotopologues. Temporally resolved measurements should begin now, as reconstructing past atmospheric methane clumped isotopologue profile would be very difficult (Sivan, Sun, et al., 2024) (Sivan and Sun et al., in prep).

Appendix A: Supporting Information for Controls on Concentrations and Clumped Isotopologues of Vehicle Exhaust Methane (Chapter 3)

This Appendix is the supporting information of a published paper:

Controls on concentrations and clumped isotopologues of vehicle exhaust methane. PLoS ONE 20(2): e0315304, (2025). https://doi.org/10.1371/journal.pone.0315304

Authors and Affiliations:

Jiayang Sun[1,2,3*], Mojhgan A. Haghnegahdar[1,4], Julianne M. Fernandez[1,5], Cédric Magen[1], James Farquhar[1,6]

[1] Department of Geology, University of Maryland, College Park, Maryland, USA

[2] Air Resources Laboratory, National Oceanic and Atmospheric Administration, College Park, Maryland, USA

[3] Cooperative Institute for Satellite Earth System Studies, University of Maryland, College Park, Maryland, USA

[4] Smithsonian Environmental Research Center, Edgewater, Maryland, USA

[5] Global Monitoring Laboratory, National Oceanic and Atmospheric Administration, Boulder, Colorado, USA

[6] Earth System Science Interdisciplinary Center, University of Maryland, College Park, Maryland, USA

* Corresponding author: Jiayang Sun

E-mail: jiayangs@umd.edu (JS)

Note A.1. Description of Sampling Procedures

In the first sampling campaign, methane concentrations in the exhaust were pre-determined before sampling to estimate the required sample volume for isotopic analysis. This involved analyzing methane concentration using a gas chromatograph (GC) of a few milliliters of exhaust gas collected with a syringe. Approximately 800 L of samples are required, if the exhaust is with air-level (2 ppm) methane concentration, to ensure that the amount of collected methane exceeds 70 μmol. Large-volume samplings were achieved using portable pumps to inflate Tedlar bags. The exhaust gas was pulled through a 1-meter metal tube that was partially inserted into the exhaust pipe, then a long (~ 2 m) rubber tube to the pump, and was pushed into bags. In this first sampling campaign, methane and ethane concentrations were measured post-collection. Hence, information on real-time concentration changes was not available.

During the first sampling campaign, we acquired a Mira Ultra LDS Infrared multi-pass laser gas analyzer (Aeris#302) from Aeris Technologies Inc. (referred to as Aeris hereafter). The acquisition of Aeris enabled us to obtain real-time concentration data for both methane and ethane.

In the second sampling campaign, a 1-meter metal tube was partially inserted into the vehicle's exhaust pipe, with the other end attached to a drying tube filled with 8-mesh desiccant-anhydrous indicating Drierite and a particle filter before being connected to the Aeris (Figure A.1). Participants were instructed to start the engine, initially keep the vehicle in an idling state until a stable concentration signal was recorded. Then they were instructed to rev the engine without load to reach and maintain 3000 rpm for approximately 20 seconds, before returning to an idling state.

Note A.2. Description of Sampled Vehicles

During the first sampling campaign, the 1999 Volvo S70 and 1981 BMW 528i exhaust gases were sampled immediately after a cold start in an idling state, as well as after vehicles warmed up and were revving at 3000 rpm. The rest of the vehicles were sampled after warming up in an idling state. Due to its extremely high concentration levels, the 1981 BMW 528i was sampled again both in cold and hot conditions. The 1970 Dodge Charger and 2017 Chevrolet Sonic exhausts were previously collected during an early validation experiment before the first major sampling campaign. The 2013 Kohler XT675 mower has a small single cylinder 4 stroke engine for domestic use and does not have a catalytic converter. The 1970 Dodge Charger is also not equipped with a catalytic converter due to its age and is one of two carburetor engines. The 1981 BMW 528i was in notably poor condition, exhibiting misfires in some tests, which was diagnosed as a result of a loose plug wire. The 1995 Mazda MX-5 Miata had been stored in the garage for a long term prior to measurement. The Ford F-250 (unknown year) was idling for at

least 20 minutes before being sampled. The 2005 and 2013 Gillig transit buses on the UMD campus and a 2006 Ford F-750 trash truck working at University Park, Maryland are diesel-fueled, and equipped with compression-ignition engines which differ from the other vehicles with spark-ignition engines running on gasoline.

In the second sampling campaign, the 2017 Prius Prime Hybrid was operating solely on its battery engine, with no option to switch to the gasoline engine if not moving. The 2013 Nissan Altima expelled some liquid water from the exhaust pipe at the end of acceleration. The 2017 Alfa Romeo Giulia Q4 has a turbocharged engine. The 2009 Honda Accord features a V6 engine, and the 2023 Lexus GX460 is equipped with a V8 engine. Two 2023-model vehicles (2023 Lexus GX460 and 2023 Chevrolet Silverado) were being used for less than a month before joining the test. According to our information, the 2019 Audi A5 had been well-maintained by its owner, however, the 2013 Nissan Altima, 2016 Toyota Camry, and 2018 Toyota RAV4 had poor maintenance histories.

All vehicles not specifically mentioned were gasoline-fueled vehicles with I4 cylinders in normal conditions. We lack data to quantify the conditions of all vehicles.

For multiple samples from the same vehicle under identical conditions, numerical suffixes indicated sampling sequence (e.g., 1970 Dodge Charger 1 for the first sample from the 1970 Dodge Charger, 1970 Dodge Charger 2 for the second). When sampling the same vehicle under different conditions, brief descriptors were used (e.g., 1999 Volvo S70 hot and 1999 Volvo S70 cold). The vehicle conditions were qualitatively described: for the bag samples from the first

sampling campaign, "cold" referred to samples taken immediately after the vehicle starts and idles in winter, while "hot" referred to samples taken after at least 10 minutes of driving and then idling. If not labeled "cold" or "hot," the samples were still "hot" but lacked a corresponding "cold" sample. For the second sampling campaign, we measured real-time concentrations during "ignition, idling, revving, and post-acceleration" operational states without distinguishing between "cold" and "hot."

Note A.3. Additional Discussion of Methane Emission from Each Sampled Vehicle

The highest methane concentration, exceeding atmospheric levels by a factor of a thousand, was recorded during the cold start and warm up of the 1981 BMW 528i which turned out to have a loose plug wire and misfire. Some vehicles emitted methane at concentrations below ambient levels at certain operation phase, such as the 2023 Chevrolet Silverado with a 2.7L Turbo I4 engine and the 2019 Hyundai Kona while idling. The 1981 BMW 528i provides an example of a vehicle emitting due to age and poor maintenance. In this case, a loose plug wire resulted in an engine misfire allowed unburnt fuel to bypass the combustion process and be routed directly to the catalytic converter. Under normal conditions, the catalytic converter facilitates the conversion of unburned hydrocarbons to CO_2. In the presence of substantial unburned gasoline, catalytic converter still operates, but the process can instead lead to incomplete conversion of gasoline into CO_2 and instead produce lower hydrocarbons, such as ethane and methane, thereby functioning as a methane generator, and this was the case with this 1981 BMW 528i. The 2013

Kohler XT675 mower and 1970 Dodge Charger, both lack catalytic converters, demonstrated exhaust methane concentrations representative of post-combustion gases under their respective operating conditions. Based on our familiarity with poor maintenance histories of the 2013 Nissan Altima, 2016 Toyota Camry, and 2018 Toyota RAV4, we surmise that inadequate maintenance contributed to elevated emissions. In contrast, the 2023 Chevrolet Silverado and 2023 Lexus GX460, both in pristine condition, have the lowest emissions. The 2019 Audi A5 and 2019 Hyundai Kona were known for having good maintenance, also showed low methane emissions. Notably, some vehicles manufactured between 2015 and 2018, which make up a significant part of current urban fleets, have high emission levels. This suggests that vehicle's maintenance status, rather than its manufacturing year, plays a more crucial role in determining emission levels.

Diesel vehicles generally emit exhaust with low methane concentrations, potentially because they are equipped with compression-ignition engines, which have higher air-to-fuel ratios compared to spark-ignition gasoline engines, thereby achieving enhanced combustion efficiency. However, heavy-duty diesel engines, such as the 2006 Ford F-750 trash truck that frequently operate under loads, have elevated emissions.

However, this dataset should not be used to quantitatively estimate the average exhaust methane concentration, given that our sampling design was biased on purpose and was constrained to accessible vehicles.

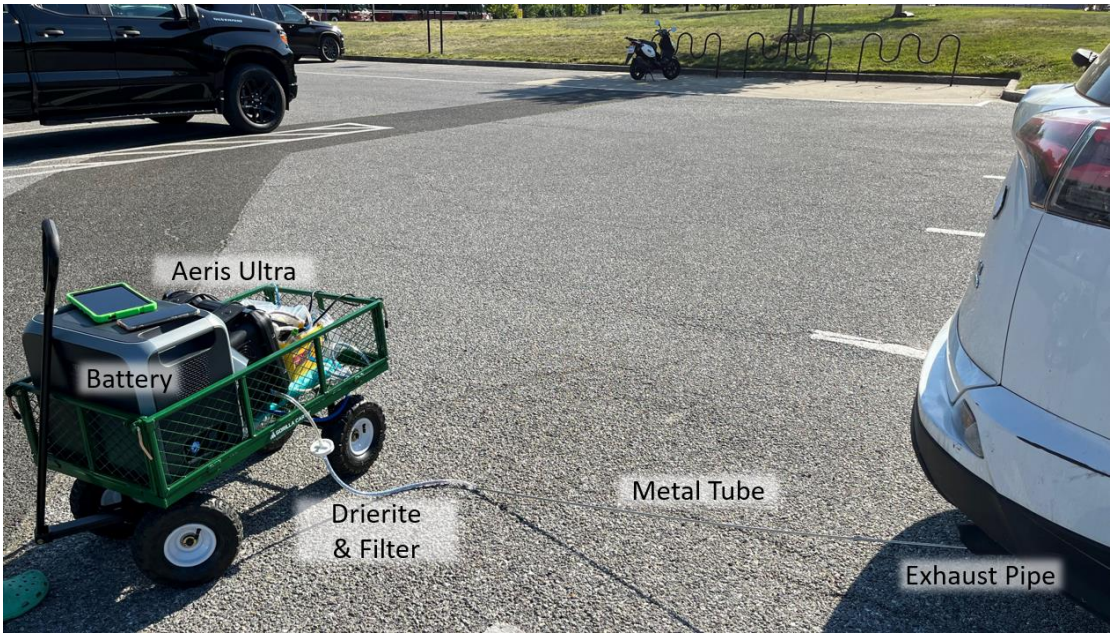

Figure A.1. **Photo while monitoring the real-time methane and ethane emissions from the 2018 Toyota RAV4 using Aeris**, during the second sampling campaign.

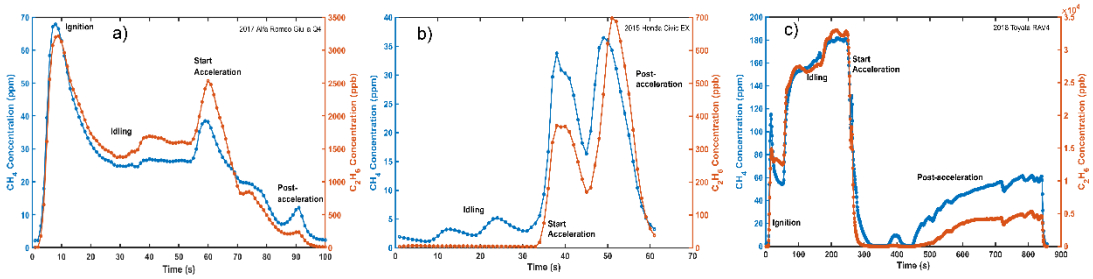

Figure A.2. **Continuous monitoring of a) 2017 Alfa Romeo Giulia Q4, b) 2015 Honda Civic EX, c) 2018 Toyota RAV4 exhaust methane and ethane concentration throughout operation cycles** (ignition, idling, revving, and post-revving).

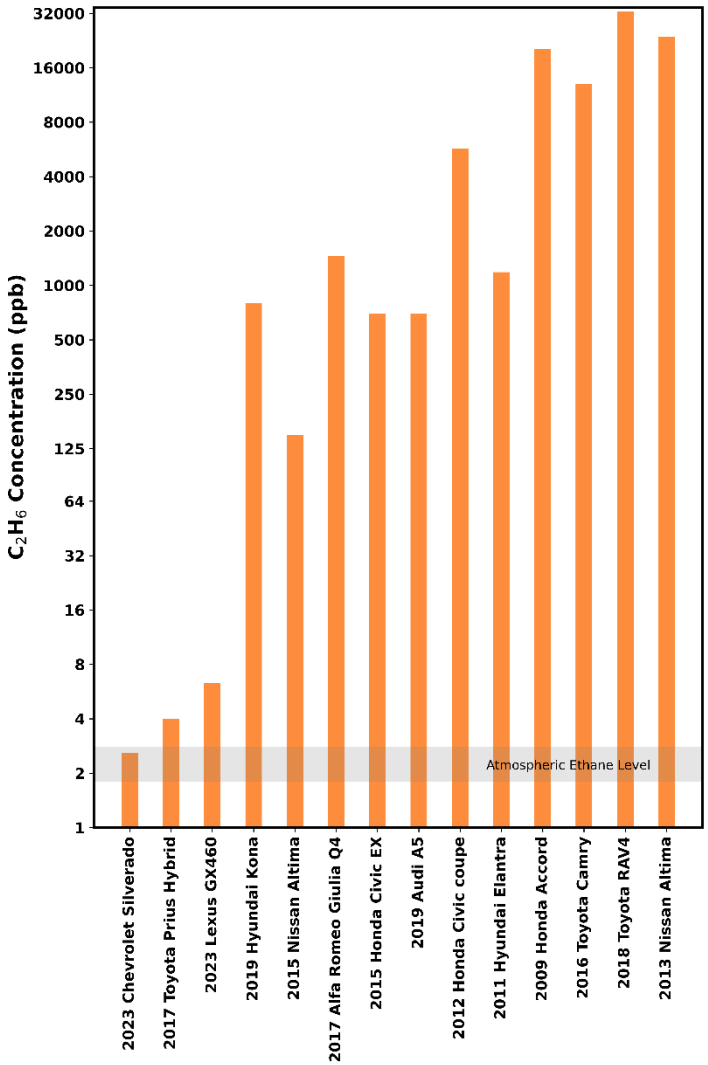

Figure A.3. **Ethane concentrations of vehicle exhaust samples.** The sequence on X-axis is basically consistent with the sequence in Figure 3.2, except that the vehicles in the first campaign have no ethane information and are not included. The plotted concentrations are peak values among the vehicle operational cycles; therefore, the heights of the bars are not fully representative of the total emission fluxes from the corresponding vehicles. Asterisks (*) in labels mark diesel vehicles. The Y-axis is scaled logarithmically. Detailed information on individual vehicles can be found in Section 3.3.1, Table 3.1, and Appendix A Note A.2.

Appendix B: Supporting Information for Tracing Sources of Atmospheric Methane Using Clumped Isotopes (Chapter 4)

This Appendix is the supporting information of a published paper:

Proceedings of the National Academy of Sciences of the United States of America. 120 (47) e2305574120, https://doi.org/10.1073/pnas.2305574120 (2023).

Authors and Affiliations:

Mojhgan A. Haghnegahdar[1,2,3]*, Jiayang Sun[1], Nicole Hultquist[1], Nora D. Hamovit[4], Nami Kitchen[5], John Eiler[5], Shuhei Ono[6], Stephanie A. Yarwood[4], Alan J. Kaufman[1,2], Russell R. Dickerson[7], Amaury Bouyon[1], Cedric Magen[1], and James Farquhar[1,2]

[1]Department of Geology, University of Maryland, College Park; College Park, MD, USA.

[2]Earth System Science Interdisciplinary Center, University of Maryland, College Park; College Park, MD, USA.

[3]Smithsonian Environmental Research Center; Edgewater, MD, USA.

[4]Department of Environmental Science and Technology, University of Maryland, College Park; College Park, MD, USA.

[5]Division of Geological and Planetary Sciences, California Institute of Technology; Pasadena, CA, USA.

[6]Department of Earth, Atmospheric and Planetary Sciences, Massachusetts Institute of Technology; Cambridge, MA, USA.

[7]Department of Oceanic and Atmospheric Science, University of Maryland, College Park; College Park, MD, USA.

*Corresponding author: Mojhgan A. Haghnegahdar

Email: mojhganh@umd.edu

B.1. Notation

The mass spectrometric measurement gives the following delta values normalized to the working reference gas using the following equations:

$$\delta^{13}\mathrm{CH_4}(\text{in ‰}) = 1000 \times \left(\frac{\left(\frac{^{13}\mathrm{CH_4}}{^{12}\mathrm{CH_4}}\right)_{sample}}{\left(\frac{^{13}\mathrm{CH_4}}{^{12}\mathrm{CH_4}}\right)_{reference}} - 1 \right) \quad \text{(B.1)}$$

$$\delta^{12}\mathrm{CH_3}D(\text{in ‰}) = 1000 \times \left(\frac{\left(\frac{^{12}\mathrm{CH_3}D}{^{12}\mathrm{CH_4}}\right)_{sample}}{\left(\frac{^{12}\mathrm{CH_3}D}{^{12}\mathrm{CH_4}}\right)_{reference}} - 1 \right) \quad \text{(B.2)}$$

$$\delta^{13}\mathrm{CH_3D}(\text{in ‰}) = 1000 \times \left(\frac{\left(\frac{^{13}\mathrm{CH_3D}}{^{12}\mathrm{CH_4}}\right)_{sample}}{\left(\frac{^{13}\mathrm{CH_3D}}{^{12}\mathrm{CH_4}}\right)_{reference}} - 1 \right) \quad \text{(B.3)}$$

$$\delta^{12}\mathrm{CH_2D_2}(\text{in ‰}) = 1000 \times \left(\frac{\left(\frac{^{12}\mathrm{CH_2D_2}}{^{12}\mathrm{CH_4}}\right)_{sample}}{\left(\frac{^{12}\mathrm{CH_2D_2}}{^{12}\mathrm{CH_4}}\right)_{reference}} - 1 \right) \quad \text{(B.4)}$$

We use the first two equations to represent $\delta^{13}C$ and δD. These are approximations because some ^{13}C and D are also in other isotopologues (like $^{13}CH_3D$, $^{12}CH_2D_2$) and are thus not accounted for. This introduces a shift much smaller than the analytical uncertainty relative to the actual definitions:

$$\delta^{13}\mathrm{C}(\text{in }‰) = 1000 \times \left(\frac{\left(\frac{^{13}\mathrm{C}}{^{12}\mathrm{C}}\right)_{sample}}{\left(\frac{^{13}\mathrm{C}}{^{12}\mathrm{C}}\right)_{reference}} - 1 \right) \quad \text{(B.5)}$$

$$\delta D(\text{in }‰) = 1000 \times \left(\frac{\left(\frac{D}{\mathrm{H}}\right)_{sample}}{\left(\frac{\mathrm{D}}{\mathrm{H}}\right)_{reference}} - 1 \right) \quad \text{(B.6)}$$

We also use:

$$\Delta^{13}\mathrm{CH_3D} = 1000 \times \left(\frac{\left(1+\frac{\delta^{13}\mathrm{CH_3D}}{1000}\right)}{\left(1+\frac{\delta^{12}\mathrm{CH_3D}}{1000}\right)\left(1+\frac{\delta^{13}\mathrm{CH_4}}{1000}\right)} - 1 \right) \quad \text{(B.7)}$$

, and

$$\Delta^{12}\mathrm{CH_2D_2} = 1000 \times \left(\frac{\left(1+\frac{\delta^{12}\mathrm{CH_2D_2}}{1000}\right)}{\left(1+\frac{\delta^{12}\mathrm{CH_3D}}{1000}\right)^2} - 1 \right) \quad \text{(B.8)}$$

to represent $\Delta^{13}CH_3D$ and $\Delta^{12}CH_2D_2$ respectively, and these also approximate to a high degree (much smaller than analytical uncertainty) the actual definitions:

$$\Delta^{13}\mathrm{CH_3D}(\text{in }‰) = 1000 \times \left(\frac{\left(\frac{^{13}\mathrm{CH_3D}}{^{12}\mathrm{CH_4}}\right)_{sample}}{\left(\frac{^{13}\mathrm{CH_3D}}{^{12}\mathrm{CH_4}}\right)_{stochastic}} - 1 \right) \quad \text{(B.9)}$$

$$\Delta^{12}\mathrm{CH_2D_2}(\text{in }‰) = 1000 \times \left(\frac{\left(\frac{^{12}\mathrm{CH_2D_2}}{^{12}\mathrm{CH_4}}\right)_{sample}}{\left(\frac{^{12}\mathrm{CH_2D_2}}{^{12}\mathrm{CH_4}}\right)_{stochastic}} - 1 \right) \quad \text{(B.10)}$$

The approximations greatly simplify interconversion of Δ and isotopologue ratios that we use for the model calculations. In our exploration of the approximation, we have so far not found that the difference is expressed in the value well below the hundredths of a permil level.[6]

B.2. Sample Types

B.2.1. Methane from Air

B.2.1.1. Compressed air samples

Two samples of compressed air from a commercial air tank (Airgas) were analyzed (210419, 210421). The Airgas tanks are filled locally before sunrise, we were told by the facility. The facility is located at (38.92894 (ºN), -76.93319 (ºE)) which is next to a reconstructed wetland on the Anacostia river.

B.2.1.2. Urban air

Nine samples (210329, 210408, 21503, 21504, 210506, 211021, 210901, 210511, 210514) were collected in the UMD chemistry building by directly pumping from the makeup air duct. This air

[6] We directly compared the two ways of calculating the values for combinations of $\delta^{13}C$, δD, and $\Delta^{12}CH_2D_2$ between 100‰ and -100‰ and $\Delta^{13}CH_3D$ between 5 ‰ and -5 ‰. We found that the difference between approximation and 'exact' was less than 0.00000001‰ for this range of values.

is actively blown into the makeup air ducts from an inlet outside the front door of the building (38.98938 (ºN), -76.94021 (ºE)). These samples were either connected directly to the preconcentration manifold or pumped into Tedlar bags that were then extracted. Most samples were extracted in the late morning after the nocturnal boundary layer had dispersed. One sample was collected into Tedlar bags from the parking lot behind the College Park Shoppers Food warehouse (39.01690 (ºN), -76.92823 (ºE)) close to the freeway in the afternoon during a rush hour.

B.2.1.3. UMD Campus Farm location

Four samples were collected in the early morning by pumping air through tubes suspended from the silo at the UMD campus farm (38.99252 (ºN), -76.94038 (ºE)) at heights of 4 (210803-S4, 210720B, 210904s4) and 10 feet: (210803S10). At this time, the nocturnal surface boundary layer has not dispersed, which allows locally generated methane to accumulate. A fifth sample (210720S) was collected just across from the silo (38.99259 (ºN), -76.93983 (ºE)) in the afternoon. The samples were pumped into 200 L Tedlar bags. In these cases, the samples were only 200 liters which leads to greater uncertainty on the measurements. In addition, four samples were collected inside a three sided (open on one side) dairy barn (38.99252 (ºN), -76.94062 (ºE)) where cattle are kept in pens (210803b3, 210803b2, 210801B1, 210423) in the morning. Due to limited air circulation and proximity to livestock and manure, these samples had higher proportions of local added methane. Note that a strong methane leak (from natural gas) was subsequently identified under the roadway by mobile surveys and the gas company. It is possible that this local leak could affect the samples, however the isotopologue data point to microbial sources. These samples were pumped into 200 L Tedlar bags using the Gast diaphragm pump.

B.2.1.4. Wetland sites

Two samples of air (210429, 210430/29) from a location on campus (38.99437 (ºN), -76.94431 (ºE)) by a regenerative stormwater conveyance and a third sample from a location at the Jackson Lane wetland (210418) (39.05744 (ºN), -75.75226 (ºE)) were collected by pumping air into 200 L Tedlar bags. The bags were returned to the lab and processed in the same way as other air samples. The samples collected on campus were collected at sunrise (before the nocturnal boundary layer had dissipated and convection up to cloud layers (planetary boundary layer) had been established). This allows for the locally sourced methane to accumulate to slightly higher concentration (a few hundred ppb above ambient). The sample from Jackson Lane was collected within a zone of flooded reed grass using off of a floating small platform in the late morning, which reduced mixing with ambient air. The Jackson Lane wetlands is an example of a type of seasonally-flooded freshwater wetland (a Delmarva Bays wetland) for which thousands are known across the Delmarva peninsula.

B.2.2. Other Methane Samples

B.2.2.1. Methane from Combustion

Two samples (210515a, 210515b/23) were collected from a covered grill by drawing smoke and air through a length of metal tube, attached to Tygon tubing using a Gast diaphragm pump and pushed into 10 L Tedlar bags. The bags were flushed twice with smoke before collecting the

samples. For one sample, the grill was fed with oak logs and for the second sample, the grill was fed with charcoal.

B.2.2.2. Methane from chambers (wetlands and rice paddies)

Three samples (210420BC, 210420d/e, 210420H) were collected at the Jackson Lane Delmarva Bays wetland (39.05744 (ºN), -75.75226 (ºE)) and a fourth sample was collected in at the UMD campus (210409) (38.99437 (ºN), -76.94431) in two-piece chambers (14 inches wide, 24 inches long and 10 inches high when assembled that have an inlet and an outlet). The base of the chamber is pressed into the ground and left to sit before putting the top on. The top was put on and sealed. After a few hours, air was pulled from the chamber using a pump through the inlet with the outlet open (we used two pumps – a peristaltic pump and a Gast diaphragm pump. One sample (210819) was collected in an inverted funnel bubble sample from rice paddies east of Little Rock Arkansas, near 34.95659 (ºN), -91.30682 (ºE). For this sample, methane bubbles were collected in a 50 cc syringe.

B.2.2.3. Incubations

Three samples (210429i, 210430i, 210524i) were collected as incubations. The samples 210429i and 210430i were collected at the Jackson Lane wetland (39.05744 (ºN), -75.75226 (ºE)) and sample 210524i was collected at the campus regenerative stormwater conveyance location (38.99437 (ºN), -76.94431 (ºE)). For the first two incubation samples (210429i, 210430i) 100 cc of homogenized soil was loaded into autoclaved 200 cc serum bottles that were stoppered with blue silica stoppers. The serum bottles were successively evacuated, shaken, and filled with helium, and this was repeated three times. Once prepared the samples with helium headspace

were placed in incubators at 32ºC (210429i) or 25ºC (210430i). The third incubation sample (210524i) was prepared by loading approximately 50 cc of mud with an additional 50 cc of water into an autoclaved 200 cc serum bottle sealed with blue silica stoppers. This sample was kept in 20ºC. These three samples were left to incubate until sufficient methane accumulated in the headspace for analysis.

B.2.2.4. Natural Gas Samples

Three samples of natural gas were analyzed. Two of these were supplied by D. Rumble from the Marcellus (210516n) and Utica (212211n) shales and a third was collected from the wall of the lab (210506n) and was natural gas used for glassblowing. Because of their high purity the first two of these samples were not processed through the purification line but were instead introduced directly into the Panorama. The third was purified and then analyzed.

B.2.2.5. Thermally-equilibrated samples

Three samples of gas were transferred by expanding at atmospheric pressure from a bag into sample tubes (with glass O-ring valves) containing 4-8 pellets of activated γ-alumina. Activation was done by heating the γ-alumina pellets in the tubes to >550ºC. The tubes were then left for ~80 days at temperature to equilibrate. Temperatures of equilibration were 15ºC, 32ºC and 150ºC. A fourth tube was set up at a temperature of 75ºC, but the incubator containing the tube failed during the 80 days, cooling to room temperature.

Measured isotopic compositions of all samples are given in Tables B.1, B.2, and B.3.

B.3. Standardization of Isotopic and Isotopologue Data

We standardized our isotopic data through analysis of calibrated samples from MIT ($\delta^{13}C$ and δD) and combined this with three thermal equilibration experiments undertaken using γ-alumina. Using this hybrid calculation, our measurements of the MIT reference gases are within error of most reported MIT values. The one exception is our measurement of $\Delta^{12}CH_2D_2$ for AL1-CD which is outside of the 2σ overlap of the respective measurements. We do not have an explanation for this outlier. We found the thermal equilibration experiments to be challenging due to small shifts in the $\delta^{13}C$ and δD of our gases for experiments with γ-alumina and larger shifts for experiments we undertook with Pt wire and Ni metal. Our working hypothesis is that there are reactions between CH_4 with (or promoted by) the catalysts that we were unable to avoid, and this implies that further refinement in our calibrations may occur in our future work. See Tables B.2, B.3, and B.4 for isotopic data related to standardization and comparison with other labs.

B.4. Using Δ and δ Notation to Reveal Evidence of Mixing

Plotting clumped isotope data using delta notation provides information in a different way than the plots of $\Delta^{12}CH_2D_2$ vs. $\Delta^{13}CH_3D$ (compare **Figure 4.1 and B.1 with Figure B.2**). On the $\delta^{12}CH_2D_2$ vs. δD plot the offsets for $\Delta^{12}CH_2D_2$ are not obvious; however, the residuals (offset from the mixing line for air samples – which are straight lines on this plot) provide an illustration of mixing and how some components do not fit. The principle is very similar to that seen for

plots of $\delta^{13}C$ vs δD (e.g., main text **Figure 4.1**), but provides additional information about mixing endmembers and proportions. In this case, the compositions reflect mixing of methane from microbial sources into background tropospheric air.

B.5. Atmospheric Model

We used a box model to evaluate whether information from clumped isotopologues has the potential to provide information about changes in contributions from various (global-scale) sources. The model used simplified inputs for historical methane concentration data and for isotope compositions ($\delta^{13}C$ and δD). It assigns a single value for the sink by assuming a constant lifetime of 9.5 years. It also assigns smoothed (over time) values for various anthropogenic CH_4 fluxes (sources) that broadly follow those from two versions of EDGAR (Crippa et al., 2020) and modifies the natural gas fluxes for these two using Höglund-Isaksson (2017) to explore four different scenarios. The use of the same major isotope compositions and fluxes in all tests allows exploration of how changes in the proportion of fossil fuel methane (with positive $\Delta^{12}CH_2D_2$) to microbial methane (with negative $\Delta^{12}CH_2D_2$). The use of smoothed 5^{th} order fits for most ($\delta^{13}C$ excepted -see below) inputs reduces expression of non-steady-state model response that generate short term shifts in $\Delta^{12}CH_2D_2$.

B.6. Concentration Data used for Atmospheric Model

We fit a 5th order polynomial to the annual global methane concentration data [reference data found at: https://gml.noaa.gov/webdata/ccgg/trends/ch4/ch4_annmean_gl.txt] that broadly follows the year resolution NOAA data record (Lan et al., 2023) from 1984 to 2019 and used this as the starting point for the model. See **Figure B.3** for fit.

B.7. Total Source Flux and Flux of Unsubstituted (Major) Isotopologue

We simplify the treatment of isotopic compositions and their relationship to mixing proportions by assuming that methane concentration and the concentration of $^{12}CH_4$ are identical. This is not the case, but Lan et al. (2023) have shown that this assumption can be used to calculate relationships between isotopes with only a small shift relating isotopes and concentration of the elemental species (e.g., methane in this case).

We solved for the total flux of methane into the atmosphere (E) by solving the equation for a box model with a first-order sink[7] (e.g. controlled only by methane concentration and with a constant lifetime) in terms of the flux (E) into the box: the following equation:

[7]The sink assumes that the combined reactions with •OH, Cl•, O(^{1}D), as well as oxidation in soils does not vary with time. Preliminary exploration of our model shows less sensitivity to changes in the strength of sinks than to changes in sources. This is an area that warrants future investigation with more complex atmospheric models.

$$E = \frac{k(n_t - n_{t-1}e^{-kt})}{(1-e^{-kt})} \quad \text{(B.11)}$$

where n_t is the amount in the box at time (t), n_{t-1} is the amount in the box at the prior time step (t-1), and k is the first order rate constant for the sink reactions. For the global atmosphere, to follow the evolution of concentration seen in Figure B.3, the total flux into the atmosphere solved using this box model is given by **Figure B.4**.

B.7. Component Source Fluxes

Four models (scenarios) of anthropogenic source fluxes were used (**Figure B.5**). Two models were run with source fluxes that are smoothed versions that broadly fit the flux of anthropogenic sources as outlined in the Emissions Database for Global Atmospheric Research (EDGAR), EDGAR 5.0 and 6.0 (Crippa et al., 2020). Another two model runs were run with source fluxes that broadly fit EDGAR 5.0 and 6.0 but with substituting the natural gas fluxes of Höglund-Isaksson (2017) (labeled as HI). **Figure B.6.** Illustrates the different profiles of the natural gas fluxes of the E50 and E50HI and the E6 and E60HI.

The way that the model works, this also means that the part of the fluxes for natural (wetlands) will be different to make up a different amount of the total flux. The EDGAR component fluxes were divided into classes that were then assigned their own isotopic compositions (described later in this section). These yield the same profiles for E60 and E60HI and then also for the E50 and E50HI, but different between the E50 and E60 pairs (**Figure B.7)**. The classification strategy is described in **Table B.5** and while it likely can be improved, provides a way to account for

different contributions that can be used to evaluate the way the system broadly responds to changes in model scenarios. The principal assigned difference between the different scenarios is the natural gas flux. **Figure B.6** illustrates the difference in the natural gas flux term between the four different scenarios.

B.8. Carbon and Hydrogen Isotopes

The atmospheric burden of $^{13}CH_4$ and $^{12}CH_3D$ are determined by considering records of $\delta^{13}C$ (**Figure B.8A)** and δD (**Figure B.8B)** in combination with the atmospheric concentration of total methane (**Figure B.3)**. The fluxes of $^{13}CH_4$ and $^{12}CH_3D$ are solved by adjusting the lifetime using information about kinetic isotope effects associated with the sink reactions. The carbon isotope profiles broadly matched that used by Turner et al. (2017) and is not fit to a 5^{th} order polynomial (smoothed) to illustrate how derived model results such as $\Delta^{13}CH_3D$ are affected by short term uncertainties in isotopic composition that arise the calculation of $\Delta^{13}CH_3D$ for sources, and its dependence on $\delta^{13}C$. The hydrogen isotope evolution of atmospheric methane was fit using the curve in **Figure B.8B** which broadly matched Rice et al. (2016), but with an extension for the most recent decade showing no subsequent change. This evolution follows a smoothed curve from 1984 to 2006 and then a rise to 2010, and constant values thereafter. Like the evolution of $\delta^{13}C$, the assigned evolution of δD is approximate.

B.9. Derived $\delta^{13}C$ and δD of Source Methane

Solving for fluxes requires additional information about the kinetics of sink reactions for each isotopologue, which are used in combination with the constraints on sink for the major isotopologue ($^{12}CH_4$) to derive the k for each isotopologue. While this simplification would not be used in a more sophisticated model, it is valid and allows us to simplify the model. The rate data (KIE and ratios of rates relative to major isotopologue) used in our calculations are given in **Table B.6.** These values assume the major contribution to the KIE is ●OH with a small contribution from Cl●. Small changes in these KIE (within the range of the difference from experimental determinations can have an effect on the model-derived ^{13}C-containing isotopologues because they have values near unity (see **Figure B.17**), but the effects related to D- substitutions do not significantly affect the model results because these values differ from unity.

Constraints on kinetic isotope effects (KIE=k_{12CH4}/k_i, where k_i is the rate constant of the isotopologue of interest) of Haghnegahdar et al. (2017) were used to constrain the rates of these sink reactions for $^{13}CH_4$ ($\delta^{13}C$) and $^{12}CH_3D$ (δD) as well as other isotopologues (described in sections below). These electronic structure calculations are made with the Gaussian 09 software package (EM64L-G09RevD.01) (Frisch et al., 2013). The calculated values match experiments reasonably well for the best constrained values when high level Møller-Plesset theory (MP2) are coupled with large basis sets. Using these KIE with the model isotopic evolution yields an evolution of the CH_4 flux (total methane emissions, integrated or total source) with the $\delta^{13}C$ and

δD of **Figure B.9**. This isotopic composition reflects the ratio of fluxes for $^{13}CH_4$ and $^{12}CH_3D$ relative to $^{12}CH_4$. (e.g., $\delta^{13}C$ relates to $^{13}CH_4/^{12}CH_4$)

B.10. Isotopic Compositions of Anthropogenic Fluxes

The isotopic composition of the anthropogenic flux for the different model scenarios was calculated by considering the individual component contributions to the flux as listed in tables from EDGAR and then reassigned to a category with an assigned isotopic composition (**Table B.5**). The isotopic compositions for the categories (**Table B.7**) were assigned based on values provided in Sherwood et al. (2017) for the δD and $\delta^{13}C$ and Haghnegahdar et al. (2017) for clumped isotopologues, with the exception that microbial sources clumped isotopologues were all set to a single model determined value. Using these isotopic compositions, the isotopic compositional evolution of the anthropogenic sources is given in **Figure B.10**.

B.11. Isotopes and Isotopologues of Natural (Wetland) Part of Methane Flux

Calculation of the individual isotopologue fluxes of the natural (wetland) part was done in the same way as for the total flux, but by considering adjustments to the anthropogenic component fluxes that scale with isotopic compositions of Sherwood et al. (2017) and then by calculating the needed isotopologue fluxes from the natural (wetland) part to close the mass balance (difference) relating the total (integrated) flux for each isotopologue. These were then converted into isotopic compositions using standard definitions. The resulting isotopic compositions for the natural

(wetland) source are given in **Figure B.11** and yields a source with variable isotopic composition with time. While the clumped isotopologue composition of the natural (wetland) part of the flux is calculated as a constant value to allow each model scenario to end with the air isotopic composition matching the assigned valued (**Table B.8**), the $\delta^{13}C$ and δD are allowed to vary with time (**Figure B.11** shows the resulting variation). This is required by the treatment and could in principle be justified as possible if one considers that there could be changes in the types of wetlands or proportions of high latitude, mid latitude, and equatorial wetlands.

B.12. Isotopologues of Methane in Air

The remaining part of the model calculation is the clumped isotopologue composition of CH_4 fluxes (anthropogenic part, natural (wetland) part, and total) as well as the methane in air. These are given in **Figures B.12, B.13,** and text **Figure 4.3**. The model evolution in **Figure B.13**, shows that different scenarios start at different $\Delta^{12}CH_2D_2$ and $\Delta^{13}CH_3D$, with those having a greater proportion of fossil fuel sources starting at higher values than those with a smaller proportion of fossil fuel sources. All model scenarios have a steep rise in $\Delta^{12}CH_2D_2$ and $\Delta^{13}CH_3D$ which is attributed to the weakening of CH_4 fluxes which allowed a greater expression of the KIE. The flattening seen in the second decade of this century likely reflects the waning growth of methane in the 1990's. The reason for the difference in phasing (delay) for the flattening of the CH_4 concentration profile (**Figure B.3**) and the flattening of the clumped isotopologue profiles (**Figures B.12 and B.13**) reflects the longer lifetimes of the doubly-substituted isotopologues. The broad conclusion is that the different scenarios with different histories of emissions (fluxes) from fossil fuels, altered the proportion of fossil/microbial

methane and can be detected by measuring clumped isotopologues. Such measurements should be possible either with archived samples or samples of air that are isolated from the atmosphere, such as in Arctic firn.

B.13. Further Exploration of Clumped Isotopologues and Their Relationship to Fossil and Microbial Methane

To explore the role of fossil fuels further, a second set of scenarios was examined that starts with an anthropogenic endmember with proportions broadly similar to those of the smoothed E60 scenario (Black dashed line in **Figure B.14A**) having a steady rise in the anthropogenic contributions from 1984 to 2018. Additional scenarios were set up to flatten this profile (colored lines in **Figure B.14A**), while maintaining the same total flux by shifting the natural (wetland) component (**Figure B.11B**) This second set of models was solved for the isotopic compositions in the same way as the previous model scenarios were solved and yields the $\Delta^{12}CH_2D_2$ for air and source in **Figure B.15** and for δD in the total flux (single solution) and the natural(wetland) part of the flux in **Figure B.16.**

While these models are very simple, they yield results that suggest the derived $\Delta^{12}CH_2D_2$ and the δD of the total sources will be more constant in scenarios that include a rising influence of microbial CH_4 sources. If constancy is a more parsimonious state, it would suggest that the clumped isotopes and the δD support a rise in wetland fluxes as the explanation for the most recent rise in atmospheric methane concentration. This is analogous to the recent proposals (Basu

et al., 2022; Fujita et al., 2020; Lan et al., 2021; Milkov, Schwietzke, et al., 2020) based on $\delta^{13}C$ (and δD). These test scenarios also show the potential of $\Delta^{12}CH_2D_2$ in distinguishing between different scenarios and the accompanying $\delta^{13}C$ and δD.

B.14. Note on KIE and Uncertainty

The main results reported in this study are based on second-order Møller-Plesset theory (MP2) (Møller & Plesset, 1934) determined in Haghnegahdar et al. (2017). The KIE used for the calculations play a role in the results of the models and determination of KIE at high enough precision to be used in the calculations experiments has proven to be challenging. For example, experimental determination of the KIE for the $^{12}CH_2D_2$ + •OH and $^{13}CH_3D$ + •OH sink reactions at 298 K are 1.81± 0.28 (Gierczak et al., 1997) and 1.34± 0.03 (Joelsson et al., 2016), respectively. The KIE of the $^{12}CH_2D_2$+Cl· (Boone et al., 2001; Feilberg et al., 2005; Matsumi et al., 1997; Sauer et al., 2015; Wallington & Hurley, 1992) have been determined to be 1.60±0.03 for $^{13}CH_3D$+Cl· (Joelsson et al., 2014). Whitehill et al. (2017) define a term ${}^{i,j}\gamma_{OH}$ (${}^{i,j}k*k/({}^{i}k*{}^{j}k)$ = ${}^{i}KIE*{}^{j}KIE/{}^{i,j}KIE$) that can be used to relate the KIE uncertainties to uncertainty on $\Delta^{13}CH_3D$ and $\Delta^{12}CH_2D_2$. Using Monte Carlo techniques, uncertainties for experimental determinations of KIE propagate to ±150‰ and ±20‰ for ${}^{2,2}\gamma_{OH}$ and ${}^{13,2}\gamma_{OH}$ (representing $\Delta^{12}CH_2D_2$ and $\Delta^{13}CH_3D$, respectively).

Ab Initio techniques offer another way to determine KIE which may be more precise for term ${}^{i,j}\gamma_{OH}$ (${}^{i,j}k*k/({}^{i}k*{}^{j}k)$ = ${}^{i}KIE*{}^{j}KIE/{}^{i,j}KIE$) (and $\Delta^{13}CH_3D$ and $\Delta^{12}CH_2D_2$) because of cancellation of effects due to frequencies for all isotopologues (and resulting partition functions) are related by a

single electronic structure model. The uncertainty for the KIE derived using ab initio techniques are evaluated by comparing results of calculations done at second-order Møller-Plesset theory (MP2) (Møller & Plesset, 1934) and couple cluster single and double excitation (CCSD) (Purvis & Bartlett, 1982) level of theory, yielding a difference on the order of 10‰ and 3‰, for $^{2,2}\gamma_{OH}$ and $^{13,2}\gamma_{OH}$ (respectively $\Delta^{12}CH_2D_2$ and $\Delta^{13}CH_3D$). Tunnel corrections for the •OH reaction made in previous studies (e.g., (Sessions & Hayes, 2005)) amount to a smaller difference than the difference between MP2 and CCSD. Work to refine the KIE will improve the quality of results that doubly-substituted isotopologue measurements will ultimately have the potential to provide.

We undertook one calculation where we arbitrarily varied the KIE for the $^{13}CH_4$ sink reaction from 1.005 to 1.010, which is within the range of the experimental and theoretical studies. The KIE determined from ab initio studies used here is 1.006. What we find (**Figure B.17**) is that a small shift in the KIE for the $^{13}CH_4$ sink reaction has an ~12‰ effect on the $\delta^{13}C$ generated by the model for the natural (wetland) part of the source flux. This suggests that further investigation into the KIE is warranted because it has the potential to significantly reduce uncertainty associated with models considering $\delta^{13}C$.

B.15. Description of Apparatus

The manifolds that we used for preconcentration and purification are illustrated in **Figure B.18**. These were built as prototypes for air separation and purification. The manifold for preconcentration is in panel A. It consists of: a part for drying the air and restricting flow (canister with silica gel); a part for capturing methane (set of 6 ½ inch OD traps filled with

HayeSep DB and cooled to liquid nitrogen temperature; a second set of HayeSep DB traps (not used); a U-trap to reduce CO_2, immediately before a final 3/8 inch OD Trap filled with HayeSep DB that is liquid nitrogen cooled for transfer of methane and air and then warmed with a -116ºC ethanol slush while pumping for 30 minutes to finish the preconcentration. The system has been checked for methane by flow by connecting a bag with a T to an Aeris gas analyzer to ensure no loss of methane during the preconcentration steps. The biggest issue we have encountered is incomplete transfer of methane from the HayeSep DB traps due to incomplete warming. The HayeSep DB is recommended, however, because for some samples with a nitrogen balance (incubations) we found that we were not able to reproducibly determine the isotopic composition if the trapping on silica gel resulted in saturation with nitrogen (had a residual pressure). Our hypothesis is that the competition by nitrogen for locations that would normally trap methane led to incomplete trapping of methane and fractionation. This was increasingly more important for low concentration methane samples. This has been addressed by flushing with dry nitrogen (the large traps) on transfer to the second trap, and by heating the second trap to 250ºC when transferring the sample to the sample tube (panel B illustrates configuration). Panel C illustrates the purification manifold, which is similar to the manifold used by Young et al. (2016)) with three modifications. The GC, not pictured, is equipped with a molecular Sieve column that allows separation of oxygen, nitrogen, and Kr, from methane (**Figure B.19**), the collection silica gel trap can be actively pumped when carrier is flowing, and the collection silica gel U-trap can be pumped through the central silica gel trap because of the rough pump configuration. In addressing the issue of Kr, we first set up the GC with a composite Mol sieve 5A column followed by a HayeSep D column and found that for separation of Kr, we needed to cool the column well below what the GC was designed for. This was done by drawing air and vapors

from above a standing liquid nitrogen reservoir. We then switched to a longer molecular sieve 5A column because of its properties for separation. The HayeSep DB trap is better for trapping and separating methane from nitrogen than silica gel.

B.16. Tests of Isotopic Fractionation During Processing

We conducted two recent tests of recovery of methane as follows. We injected 1 cc of methane (40 micromoles) into a 200 L Tedlar bag filled with dry nitrogen. The contents of the bag were then drawn through the same procedure used to process air samples. Results are in **Table B.9**. The larger uncertainty results from the smaller sample size. This sample size is 500 L of air. Tests of recovery with the purification line show recovery is better than 99%.

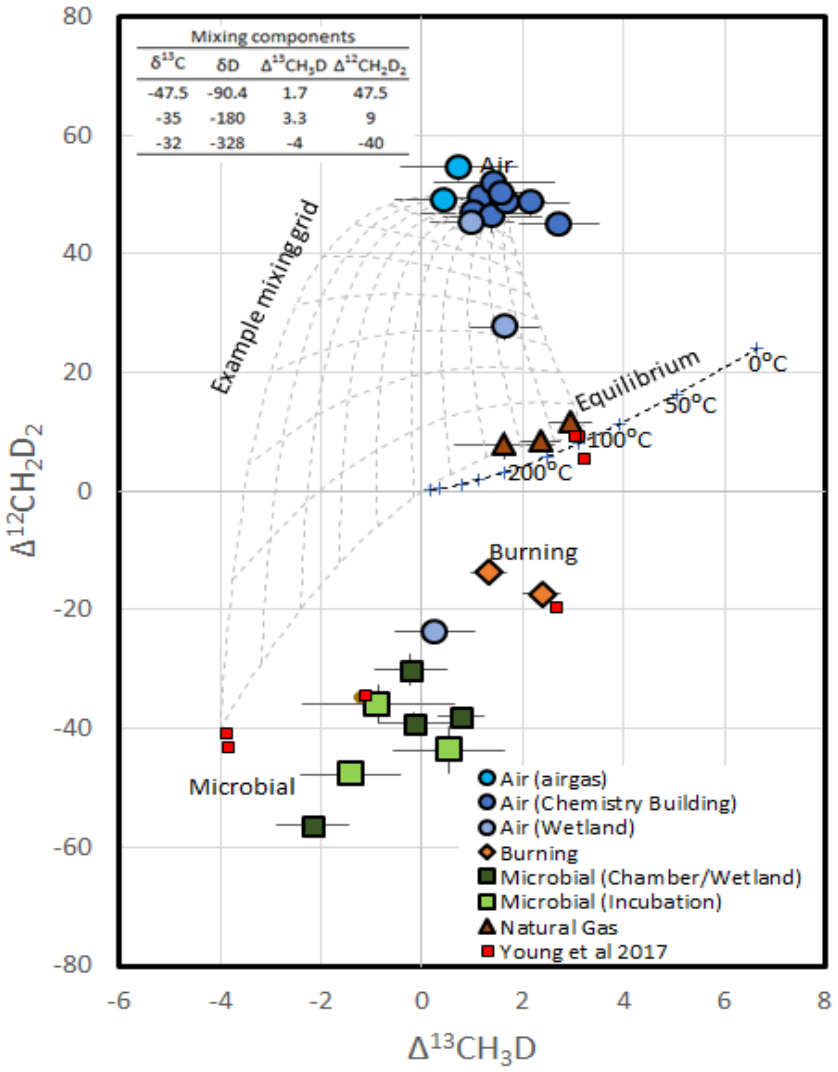

Figure B.1. Plot of $\Delta^{12}CH_2D_2$ vs. $\Delta^{13}CH_3D$ of methane samples measured in this study with a mixing grid added for mixing air with microbial and natural gas, both from Young, Kohl, Lollar, et al. (2017). Also plotted on this figure in red are analyses from Young, Kohl, Lollar, et al. (2017) for microbial cultures and natural gas samples. The air samples labeled wetland with low $\Delta^{12}CH_2D_2$ can be used for source composition identification and apportionment.

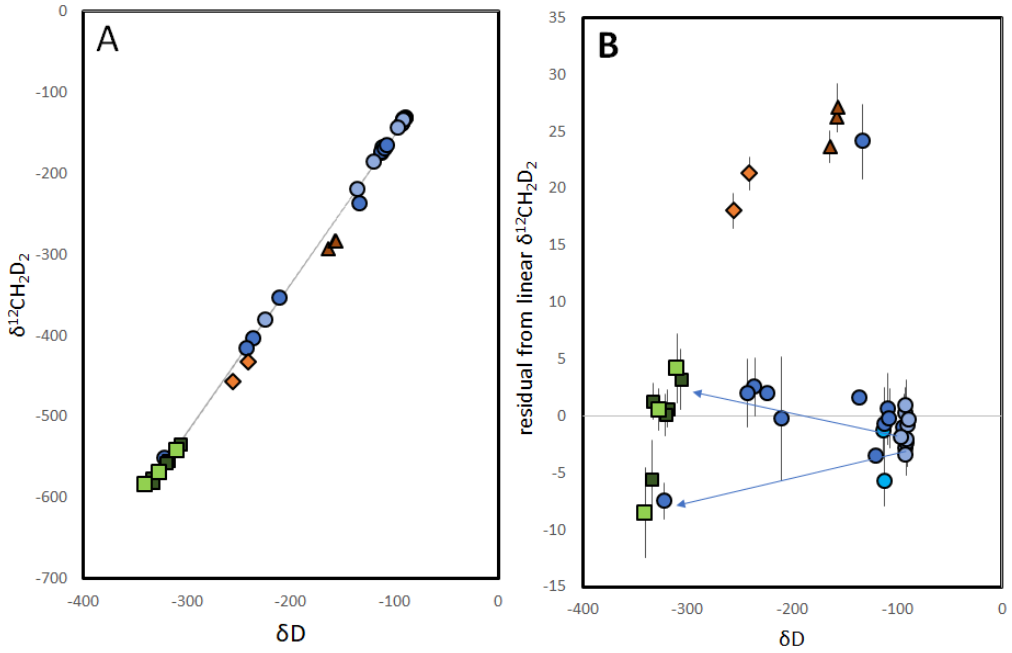

Figure B.2. (**A)** Plot of δ $^{12}CH_2D_2$ vs. δ D with mixing line fit for air samples. Note that data for natural gas and (biomass) burning lie away from this line. (Mixing is linear when isotopologues are plotted as delta values versus delta values.) (**B**) Plot of the residuals relative to the mixing line to show that the different types of air mixing plot along different arrays. Symbols as in **Figure B.1**.

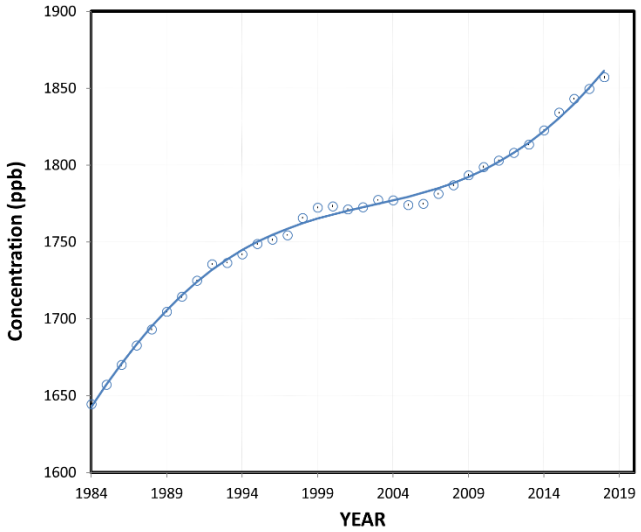

Figure B.3. Plot of methane concentration vs. time used for the model (5th order polynomial fit to data from https://gml.noaa.gov/webdata/ccgg/trends/ch4/ch4_annmean_gl.txt). Model is a line, data is presented as circles. Size of circles is approximately 3σ of the uncertainty on the data.

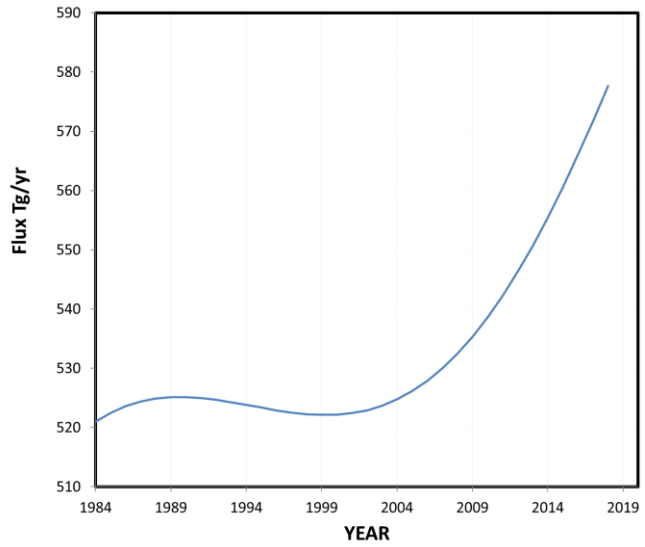

Figure B.4. Global CH_4 flux calculated from the concentration profile in **Figure B.3.** These fluxes are assumed as the total for the major methane isotopologue ($^{12}CH_4$). While this is not strictly valid as the solution for the major methane isotopologue, it introduces only a small systematic uncertainty.

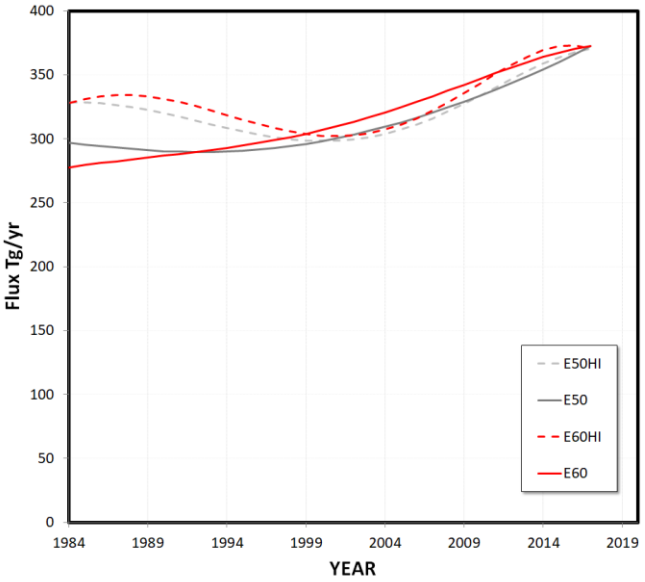

Figure B.5. Plot of the anthropogenic component of the flux (Tg/yr) for the four scenarios explored in the model. E50 and E60 broadly reproduce smoothed (5th order) fits to fluxes in EDGAR 6.0 and 5.0 (Crippa et al., 2020). The lines labeled E60HI and E50HI use natural gas flux that broadly reproduces a 5th order fit to the natural gas flux of Höglund-Isaksson (2017), but with other fluxes similar to those in the EDGAR.

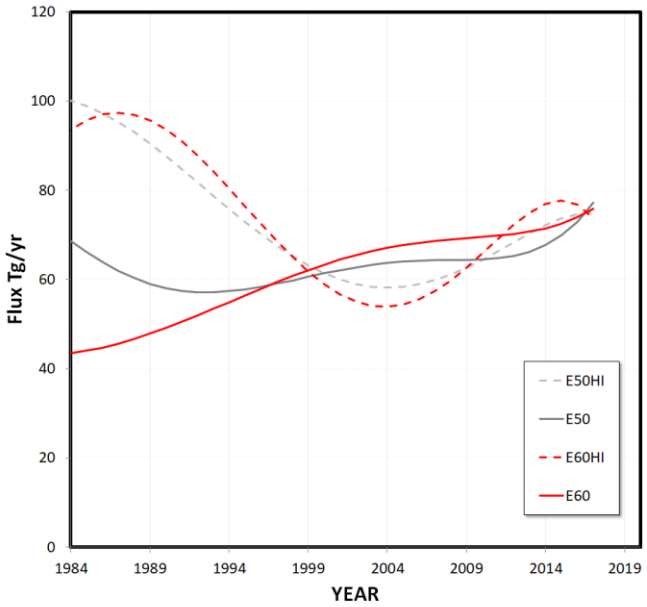

Figure B.6. Flux of methane from natural gas for the four different scenarios explored in the model. E50 and E60 broadly reproduce smoothed (5th order) fits to fluxes in EDGAR 6.0 and 5.0 (1), and HI broadly reproduces a 5th order fit to the Natural Gas flux of Crippa et al. (2020); Höglund-Isaksson (2017), but with other fluxes similar to those in the EDGAR.

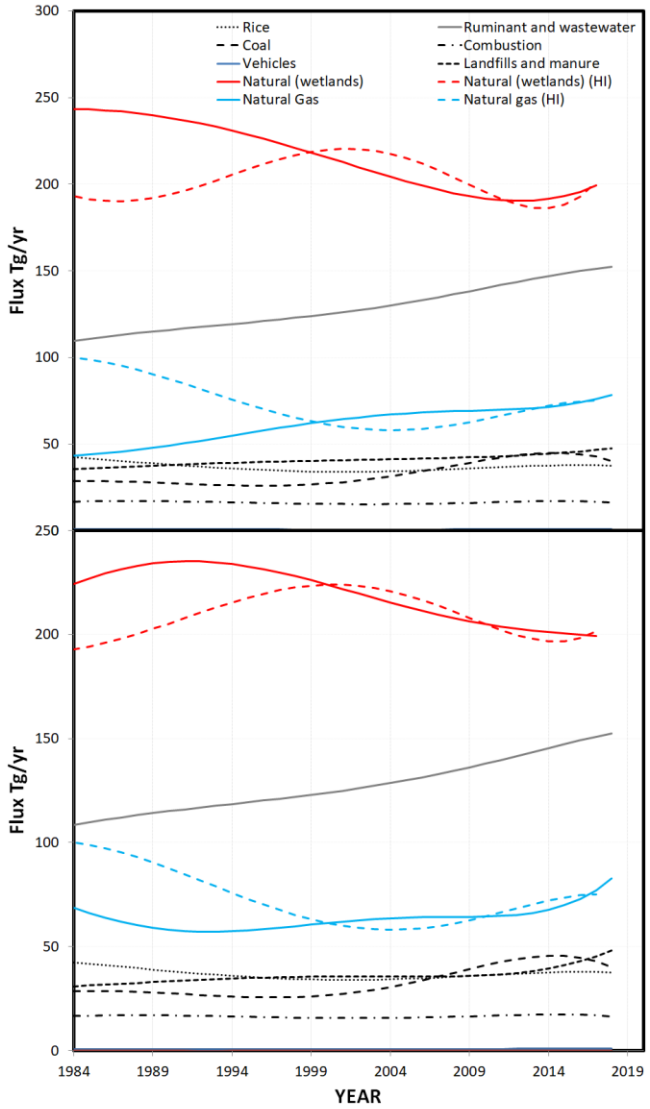

Figure B.7. Plot of the flux of methane (Tg/yr) for natural sources (treated as wetlands) and component anthropogenic sources for the four model scenarios (defined as in prior figures and captions). The flux from natural sources for our different scenarios was determined by subtracting total anthropogenic flux from the total flux. Where there are no (HI) curves, the flux profiles are the same. Panel A. is E50 and E50HI fluxes. Panel B. is E60 and E60HI fluxes.

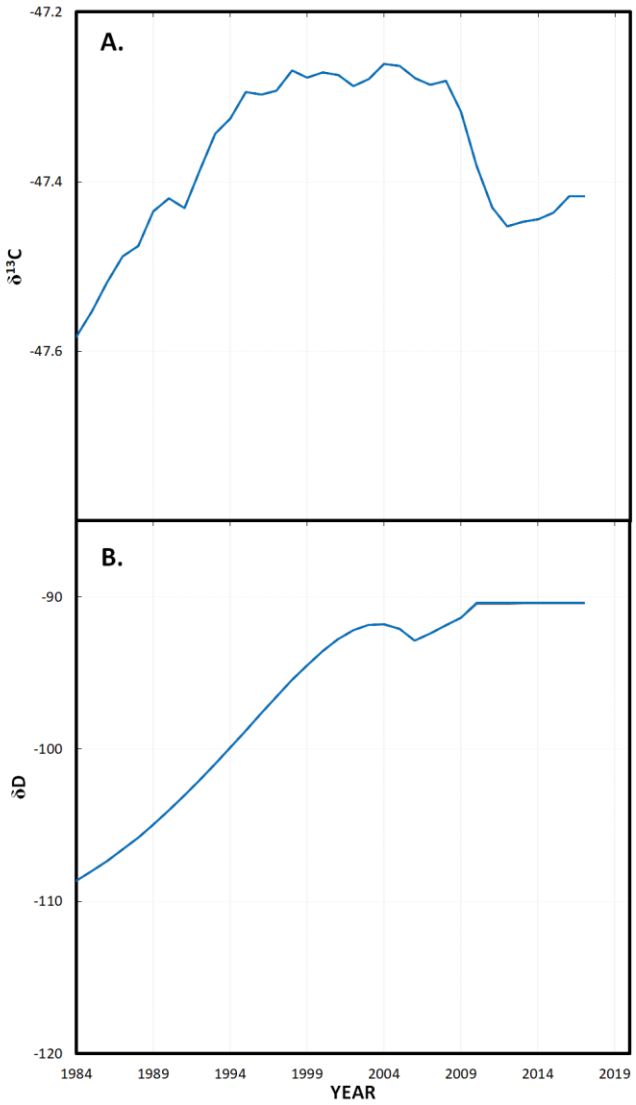

Figure B.8. **(A)** Plot of $\delta^{13}C$ for methane in air used as a constraint for the model. The evolution broadly follows that presented by Turner et al. (2017) and is derived by tracing his curve. **(B)** Plot of δD for methane in air used as a constraint for the model. The evolution broadly follows that presented by Rice et al. (2016) until 2010 (derived by tracing his curve).

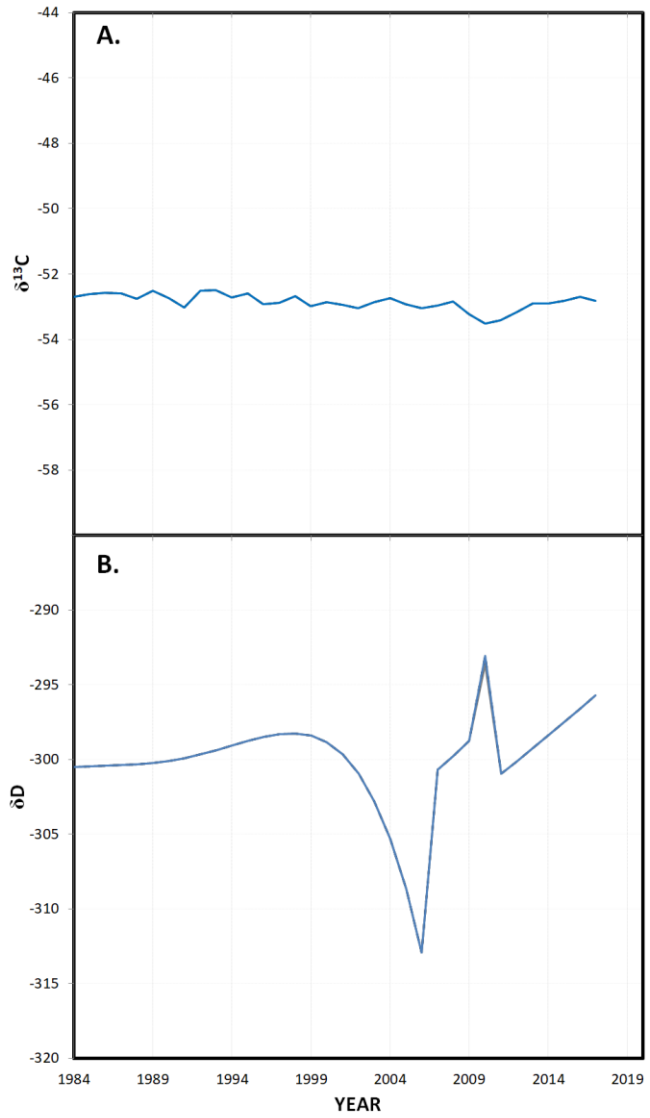

Figure B.9. (**A)** Plot of $\delta^{13}C$ for source CH_4 to air derived using Equation B.5. (**B)** Plot of δD for source CH_4 (methane flux) to air derived using Equation B.5. Shape of each is influenced by changes in profiles of $\delta^{13}C$ and δD of methane in air (**Figure B.8**)

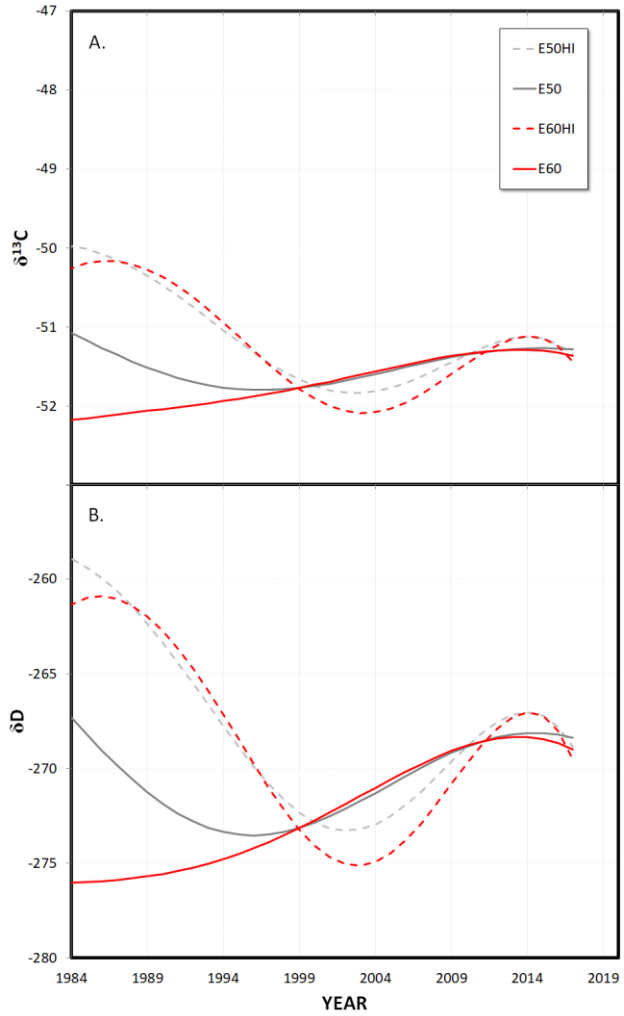

Figure B.10. Isotope profiles for anthropogenic part of total flux of model scenarios (**A)** Plot of carbon isotope compositions used in model for anthropogenic endmember. (**B)** Plot of deuterium/hydrogen isotope compositions used in models for anthropogenic endmember. These values are calculated using source apportionment in the four scenarios which are smoothed (5^{th} order functions) that broadly follow the flux apportionment given in EDGAR 6.0 (E60), EDGAR 5.0 (E50), EDGAR 6.0 with natural gas fluxes of Höglund-Isaksson (2017) (E60HI) and EDGAR 5.0 with natural gas fluxes of Höglund-Isaksson (2017) (E50HI).

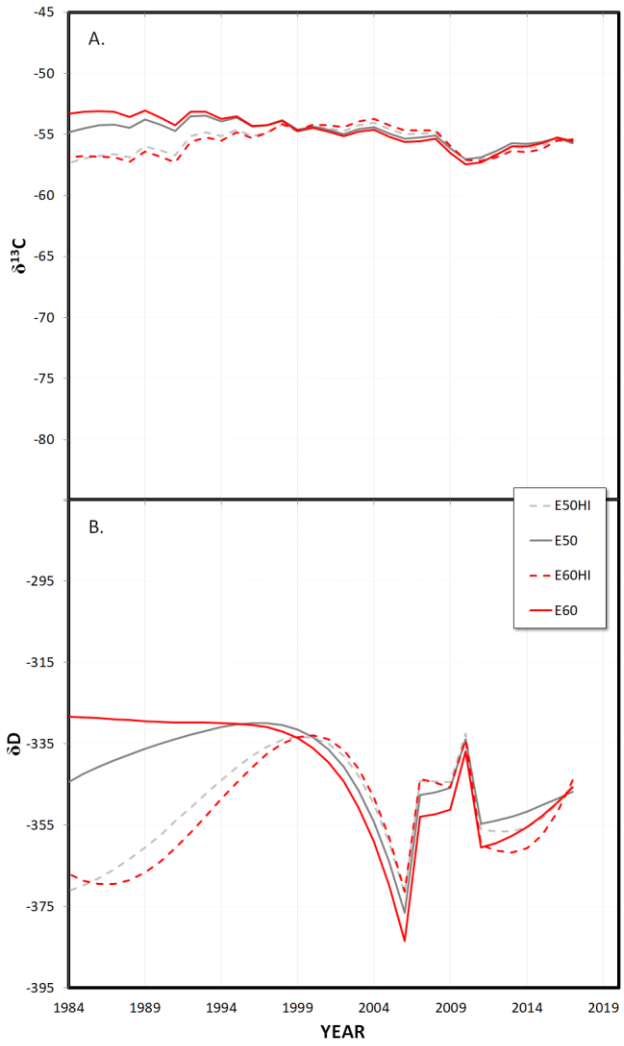

Figure B.11. Plot of $\delta^{13}C$ (**Panel A.**) and δD (**Panel B.**) for the natural (wetland) methane part of the flux generated by the model. The isotopic compositions are those required to make up the isotopic balance needed to reproduce the isotopic compositions of the total flux (**Figure B.4**) after the isotopic composition of the anthropogenic part (**Figures B.7**) of the flux is accounted for.

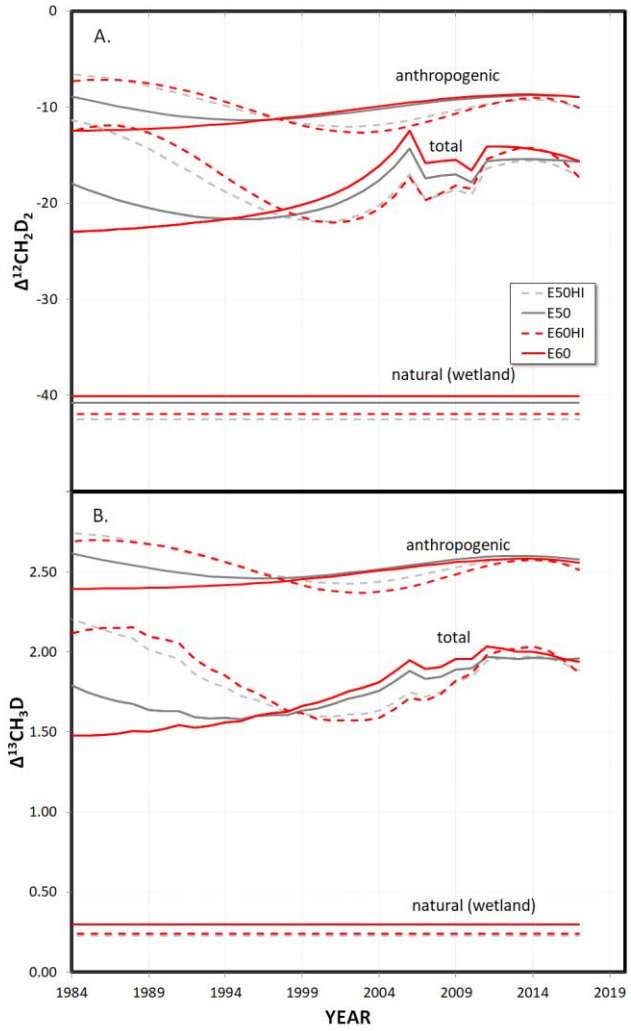

Figure B.12. Plot of $\Delta^{12}CH_2D_2$ (**Panel. A**) and $\Delta^{13}CH_3D$ (**Panel. B**) for methane of sources (fluxes) to air for the four model scenarios from the anthropogenic part, the natural (wetland) part, and of the total. The total for $\Delta^{12}CH_2D_2$ shows small breaks in slope which reflect the fit to δD because δD is part of the calculation of $\Delta^{12}CH_2D_2$. Likewise, similar variations and a less smooth relationship shows up for total $\Delta^{13}CH_3D$ because of the added effect of variability in the fit for $\delta^{13}C$.

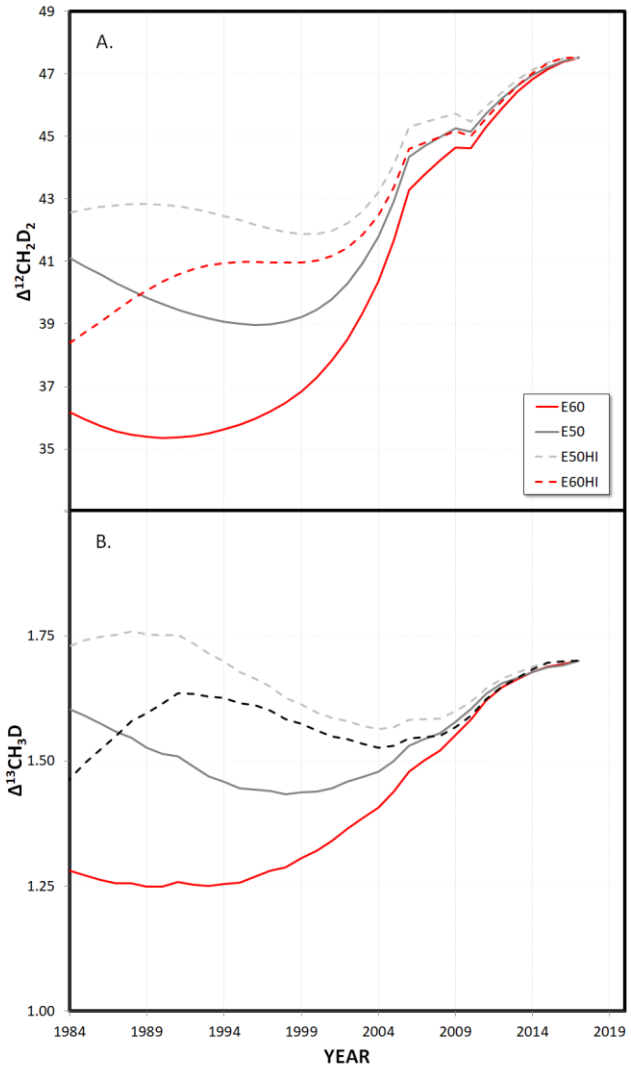

Figure B.13. Plot of $\Delta^{12}CH_2D_2$ (**Panel. A**) and $\Delta^{13}CH_3D$ (**Panel. B**) for methane of air for the four model scenarios.

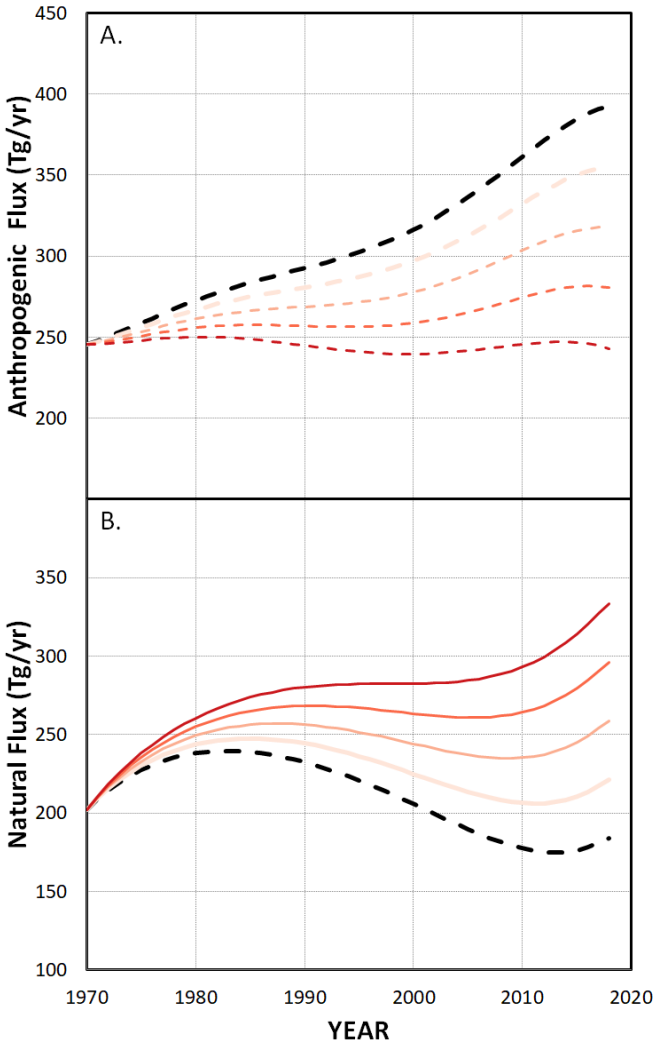

Figure B.14. Plot of fluxes used in the second set of models. Total source is kept constant. **A.** Fluxes from anthropogenic components. **B.** fluxes from the natural (wetland) component.

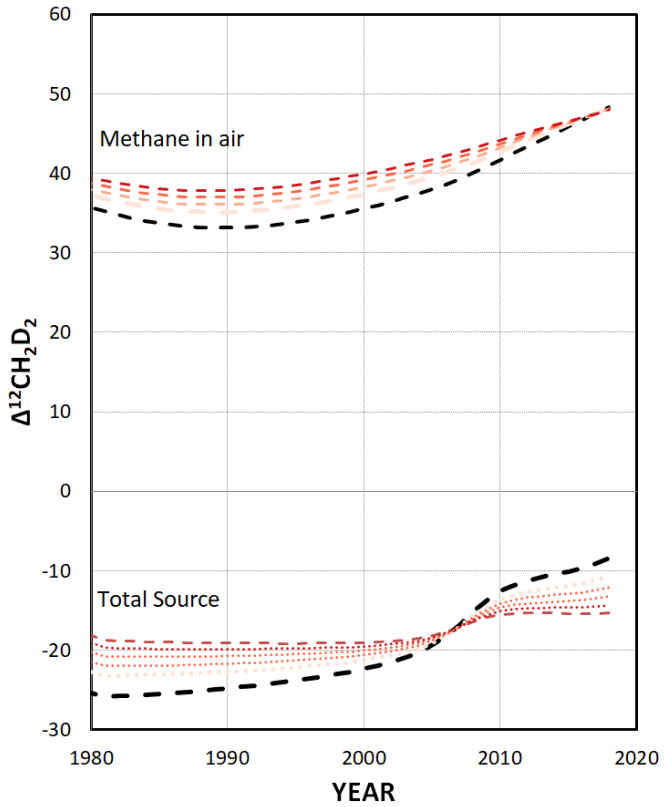

Figure B.15. Plot of $\Delta^{12}CH_2D_2$ for model scenarios ranging from rising anthropogenic CH_4 flux and stable wetlands CH_4 flux (black dashed) to flat anthropogenic methane and rising wetland CH_4 flux (red curves).

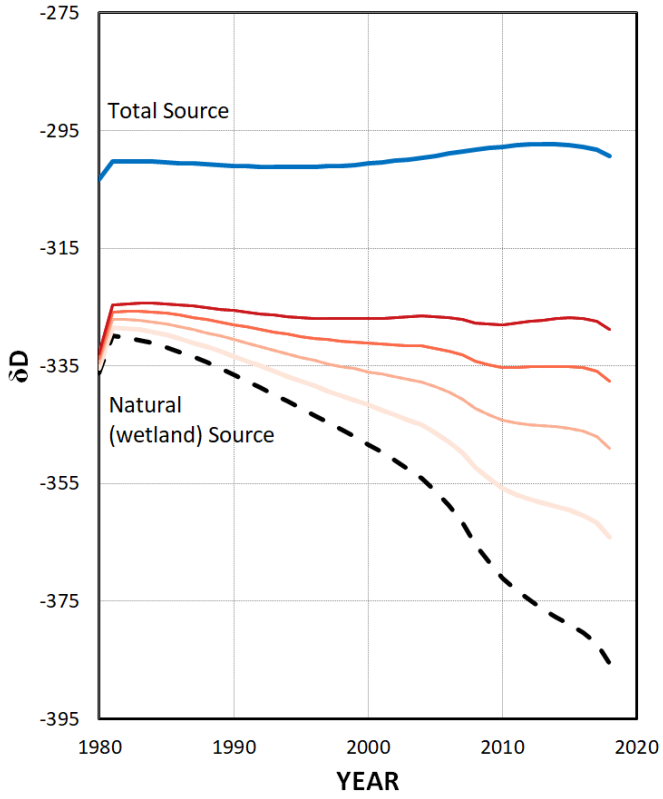

Figure B.16. Plot of δD for total source (blue line) and for the natural (wetland) portion of the total source (black and red lines as defined in previous plots). The dashed black line is for a rising anthropogenic flux and stable natural flux and the red lines progress to a rising natural (wetland) flux.

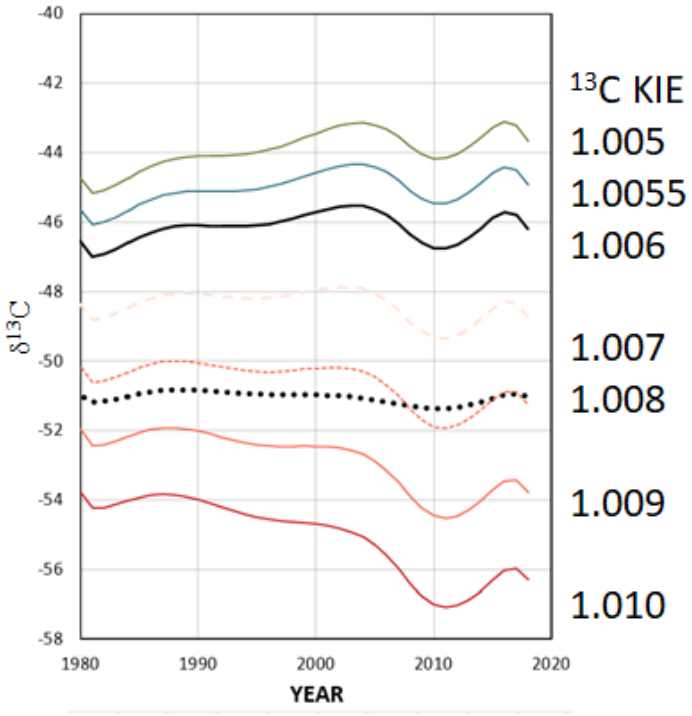

Figure B.17. Plot of model result calculated using different values for the $^{13}CH_4$ sink reaction. A value of 1.006 used in this study based on ab initio methods yields values that are less negative for the natural (wetland) part of the source flux than the total flux. A KIE value closer to 1.010 would reverse this.

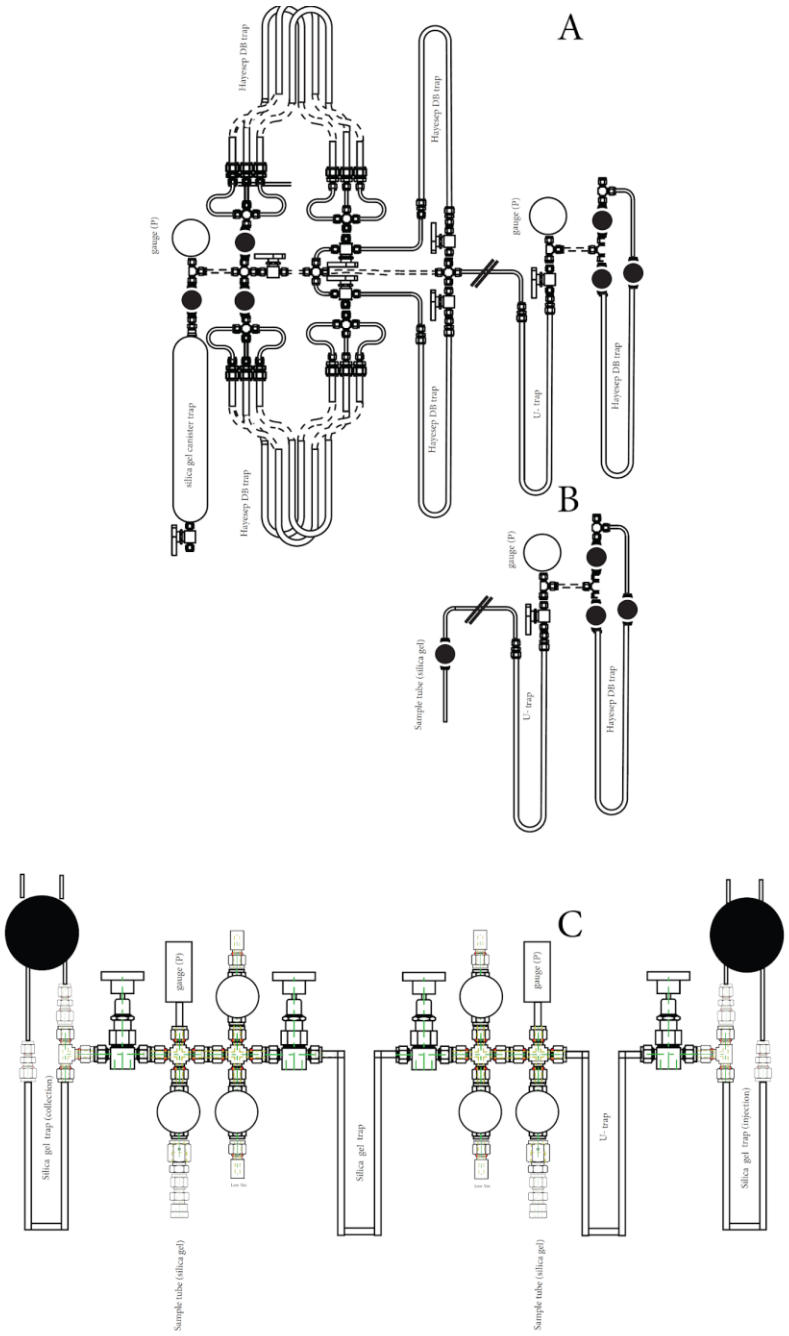

Figure B.18 Schematic of air preconcentration manifold and purification manifold. Pumps used during preconcentration are Gast two stage diaphragm pumps, followed by a rotary vane pump for final pumping. Pumps used on the purification manifold are a rotary vane pump for rough vacuum and a small turbo pump repurposed from a decommissioned mass spectrometer. The GC is an SRI with TCD.

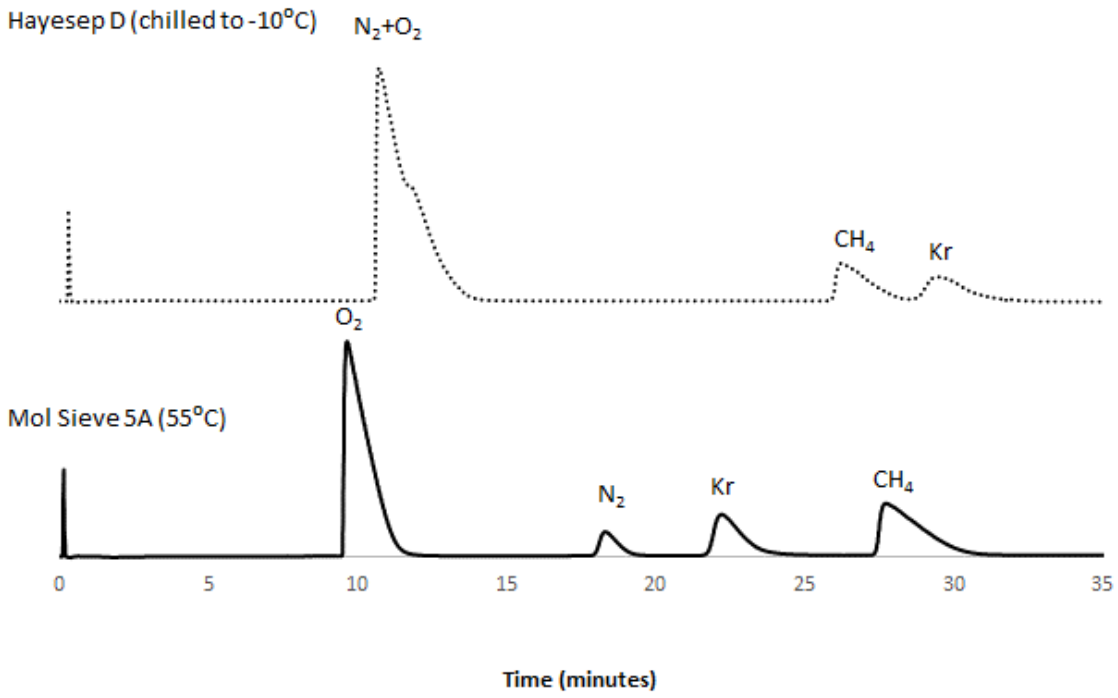

Figure B.19. Sample chromatograms illustrating separation of pre-concentrated gases (N2, O2, Kr, CH4) using HayeSep D column and Molecular Sieve Column. The HayeSep D column did not separate the CH_4 and Kr when used at temperatures >20ºC. The column was cooled by modifying the inlet fan to the oven with a U shape in ducting that was filled with a small amount of liquid nitrogen (a kluge for testing and separating/confirming the second peak as Kr). The lower trace is for a molecular sieve 5A column at 55ºC and the separation of all permanent gases is better and more predictable.

Table B.1. Measured isotopologue data of samples

Sample type	Sample number	$\delta^{13}CH_4$ (‰)	2σ	$\delta^{12}CH_3D$ (‰)	2σ	$\delta^{13}CH_3D$ (‰)	2σ	$\delta^{12}CH_2D_2$ (‰)	2σ	$\Delta^{13}CH_3D$ (‰)	2σ	$\Delta^{12}CH_2D_2$ (‰)	2σ
Air (Airgas tank)	210419	-47.84	0.03	-111.64	0.13	-153.27	0.96	-168.51	1.73	1.03	1.15	53.60	2.21
Air (Airgas tank)	210421	-47.93	0.03	-112.72	0.11	-154.61	0.84	-174.88	1.60	0.76	1.00	48.09	2.05
Air (local mix - Barn)	210423	-64.16	0.02	-321.79	0.04	-364.96	0.50	-551.34	0.74	0.55	0.79	-24.57	1.61
Air (local mix - Barn)	210803b2	-53.94	0.07	-210.10	0.40	-250.72	1.05	-354.14	3.33	2.67	1.50	35.13	5.44
Air (local mix - Barn)	210803b3	-57.30	0.02	-236.01	0.08	-278.62	0.47	-404.37	1.47	1.62	0.66	20.47	2.53
Air (local mix - Barn)	210803B1	-58.24	0.02	-242.67	0.10	-285.14	0.49	-416.03	1.69	2.31	0.69	18.19	2.96
Air (local mix - campus Farm)	210720S	-47.61	0.04	-112.11	0.34	-153.29	0.74	-174.32	2.54	1.29	0.95	47.36	3.32
Air (local mix - campus Farm)	210720B	-45.84	0.05	-93.60	0.41	-134.70	0.80	-140.17	2.33	0.52	1.03	46.59	2.98
Air (local mix - campus Farm)	210803S10	-46.83	0.06	-108.81	0.22	-148.96	0.86	-169.67	2.43	1.87	1.05	45.48	3.11
Air (local mix - campus Farm)	210803-S4	-47.68	0.02	-133.02	0.22	-173.50	0.55	-237.46	2.42	1.03	0.72	14.49	3.25
Air (local mix - campus Farm)	210904s4	-47.35	0.02	-107.32	0.18	-148.61	0.45	-166.12	2.02	1.16	0.56	46.44	2.57
Air (local mix - wetland)	210429	-49.17	0.03	-120.07	0.13	-161.89	0.98	-186.18	1.74	1.74	1.18	51.08	2.28

Air (local mix -wetland)	210429	-52.41	0.02	-223.82	0.07	-263.07	0.52	-381.46	1.22	1.95	0.71	26.71	2.03
Air (local mix -wetland)	210418	-49.31	0.02	-135.94	0.06	-177.48	0.67	-220.24	1.13	1.31	0.82	44.43	1.52
Air (urban - chemistry bldg.)	210901	-47.13	0.03	-92.21	0.15	-133.59	0.71	-138.87	1.84	1.63	0.84	44.96	2.26
Air (urban - chemistry bldg.)	210329	-47.44	0.03	-91.41	0.09	-133.24	0.72	-134.41	1.49	1.48	0.83	48.53	1.81
Air (urban - chemistry bldg.)	210408	-47.39	0.04	-89.33	0.12	-131.32	0.92	-132.59	1.66	1.34	1.07	45.93	2.02
Air (urban - chemistry bldg.)	21503	-47.28	0.03	-91.73	0.10	-132.05	0.67	-138.72	1.45	3.03	0.79	44.04	1.77
Air (urban - chemistry bldg.)	21504	-47.58	0.03	-89.01	0.17	-130.88	0.84	-132.42	2.10	1.70	0.98	45.39	2.57
Air (urban - chemistry bldg.)	210506	-47.93	0.02	-90.37	0.12	-132.25	0.64	-132.94	1.72	1.99	0.75	47.91	2.09
Air (urban - chemistry bldg.)	210511	-47.65	0.02	-91.46	0.09	-133.12	0.52	-133.89	1.61	1.88	0.61	49.26	1.96
Air (urban - chemistry bldg.)	210514	-48.06	0.02	-90.98	0.10	-132.54	0.65	-134.32	1.60	2.46	0.76	47.64	1.95
Air (urban - shoppers parking lot)	210805	-46.56	0.05	-96.32	0.31	-136.81	0.65	-144.31	2.57	1.85	0.83	47.83	3.22
Burning (charcoal)	210515b	-28.80	0.01	-256.12	0.05	-275.60	0.26	-456.68	0.86	2.69	0.37	-18.12	1.55

Burning (Oak)	210515A/23	-26.54	0.02	-241.04	0.04	-259.97	0.26	-432.32	0.83	1.63	0.36	-14.49	1.45
Chamber (wetland - rice paddy)	210819	-62.28	0.01	-334.07	0.08	-376.67	0.43	-575.69	1.55	-1.80	0.69	-43.17	3.50
Chamber (wetland)	210420d/e	-53.56	0.05	-306.37	0.15	-343.47	0.44	-533.80	1.24	0.07	0.71	-31.02	2.61
Chamber (wetland)	210420BC	-54.91	0.02	-318.82	0.05	-355.53	0.29	-554.02	0.77	1.08	0.46	-38.85	1.66
Chamber (wetland)	210420H	-52.02	0.02	-320.85	0.05	-356.09	0.46	-557.21	0.84	0.15	0.72	-39.99	1.83
Chamber (wetland)	210409	-47.23	0.02	-332.88	0.05	-365.57	0.46	-580.40	0.71	-1.86	0.72	-57.16	1.61
Incubation	210429i	-59.43	0.07	-309.97	0.18	-351.34	0.96	-541.34	1.44	-0.57	1.51	-36.72	3.07
Incubation	210430i	-60.08	0.02	-327.32	0.06	-368.44	0.62	-569.48	0.83	-1.11	0.98	-48.57	1.85
Incubation	210524i	-70.48	0.04	-340.30	0.24	-386.29	0.64	-584.16	1.69	0.84	1.10	-44.49	3.95
Natural gas	210506n	-35.19	0.02	-163.92	0.07	-190.91	0.38	-293.56	0.99	3.01	0.48	10.59	1.42
Natural gas	211218n	-34.33	0.03	-157.34	0.08	-185.79	0.29	-284.09	0.92	0.59	0.37	8.23	1.31
Natural gas	211221n	-22.79	0.03	-156.66	0.13	-174.59	0.47	-283.70	1.48	1.57	0.59	7.14	2.11

Table B.2. Thermal Equilibration data

Sample number	$\delta^{13}CH_4$ (‰)	2σ	$\delta^{13}CH_3D$ (‰)	2σ	$\delta^{12}CH_3D$ (‰)	2σ	$\delta^{12}CH_2D_2$ (‰)	2σ	$\Delta^{13}CH_3D$ (‰)	2σ	$\Delta^{12}CH_2D_2$ (‰)	2σ
Starting Methane	-37.00		-178.24		-149.20		-270.66		2.98		7.58	
230424 150	-34.29	0.01	-172.86	0.26	-146.14	0.05	-265.35	1.25	3.10	0.32	7.65	1.71
230424 32	-37.00	0.02	-175.92	0.31	-148.97	0.05	-262.54	1.09	5.54	0.38	18.23	1.51
230424-15	-36.98	0.02	-175.13	0.20	-148.73	0.05	-260.08	0.92	6.20	0.26	21.06	1.28

Table B.3. Isotopologue values comparison for samples analyzed by UCLA (Young et al., 2016)) and MIT (Gonzalez et al., 2019), and UMD.

	Sample	$\delta^{13}CH_4$ (‰)	2σ	$\delta^{12}CH_3D$ (‰)	2σ	$\Delta^{13}CH_3D$ (‰)	2σ	$\Delta^{12}CH_2D_2$ (‰)	2σ
MIT	AL1	-34.50	0.02	-147.70	0.06	2.33	0.05	4.40	0.50
	AL1-CD	-82.44	0.72	-158.00	0.18	15.79	0.45	5.50	1.90
	AL1-D3	-35.24	0.06	239.81	0.15	1.49	0.14	26.40	0.60
UCLA	AL1	-34.65	0.01	-147.88	0.09	2.41	0.26	5.62	0.87
	AL1-CD	-82.01	0.03	-159.72	0.03	16.13	0.30		
	AL1-D3	-34.76	0.00	242.55	0.01	1.55	0.12		
UMD	AL1[8]	-34.5	0.01	-147.7	0.14	2.62	0.41	5.68	1.56
	AL1-CD	-82.14	0.01	-159.30	0.06	16.07	0.21	10.98	1.18
	AL1-D3	-34.77	0.01	242.13	0.10	1.68	0.22	26.79	1.23

Table B.4. Isotopologue values comparison for three different composite samples including a reference gas, wetland sample and air sample analyzed by Caltech and UMD.

	Sample	$\delta^{13}CH_4$ (‰)	2σ	$\delta^{12}CH_3D$ (‰)	2σ	$\Delta^{13}CH_3D$ (‰)	2σ	$\Delta^{12}CH_2D_2$ (‰)	2σ
Caltech	220202a	-37.01	0.02	-145.04	0.32	3.07	0.96	9.1	3.20
	220122a	-49.91	0.04	-325.52	0.34	0.77	1.22	-46.4	4.60
	220121a	-46.67	0.02	-91.03	0.54	0.01	1.04	53	4.00
UMD	220202a[9]	-36.95		-149.0		2.98		7.58	
	220122a	-49.30	0.01	-333.30	0.06	-1.85	0.27	-50.74	1.78
		-49.28	0.01	-332.80	0.02	-2.69	0.75	-50.66	3.61
	220121a	-46.21	0.02	-93.92	0.11	2.17	0.57	45.01	2.04
		-46.19	0.03	-93.85	0.14	0.56	0.37	47.93	2.40
		-45.90	0.02	-94.08	0.12	1.23	0.71	47.56	2.26

[8] Assigned based on MIT Value and three thermal equilibration experiments because used as basis for standardization

[9] Assigned based on MIT Value and three thermal equilibration experiments because used as basis for standardization

Table B.5. Conversions to transform EDGAR data into isotopic compositions for models.

This study	ipcc_code_2006_for_standard_report	ipcc_code_2006_for_standard_report_name
Combustion	1.A.1.a	Main Activity Electricity and Heat Production
Combustion	1.A.1.a	Main Activity Electricity and Heat Production
Combustion	1.A.1.bc	Petroleum Refining - Manufacture of Solid Fuels and Other Energy Industries
Combustion	1.A.1.bc	Petroleum Refining - Manufacture of Solid Fuels and Other Energy Industries
Combustion	1.A.2	Manufacturing Industries and Construction
Combustion	1.A.2	Manufacturing Industries and Construction
Combustion	1.A.3.a	Civil Aviation
Vehicles	1.A.3.b_noRES	Road Transportation no resuspension
Vehicles	1.A.3.b_noRES	Road Transportation no resuspension
Vehicles	1.A.3.c	Railways
Vehicles	1.A.3.c	Railways
Vehicles	1.A.3.d	Water-borne Navigation
Vehicles	1.A.3.d	Water-borne Navigation
Vehicles	1.A.3.e	Other Transportation
Vehicles	1.A.3.e	Other Transportation
Combustion	1.A.4	Other Sectors
Combustion	1.A.4	Other Sectors
Combustion	1.A.5	Non-Specified
Combustion	1.A.5	Non-Specified
COAL Fugitive	1.B.1	Solid Fuels
COAL Fugitive	1.B.1	Solid Fuels
Natural gas Fugitive	1.B.2	Oil and Natural Gas

Natural gas Fugitive	1.B.2	Oil and Natural Gas
production and fugitive	2.B	Chemical Industry
Hight-T	2.C	Metal Industry
Rumen	3.A.1	Enteric Fermentation
Manure	3.A.2	Manure Management
Biomass Burning	3.C.1	Emissions from biomass burning
Rice	3.C.7	Rice cultivations
biogenic Landfill	4.A	Solid Waste Disposal
biogenic Landfill	4.B	Biological Treatment of Solid Waste
Burning	4.C	Incineration and Open Burning of Waste
Burning	4.C	Incineration and Open Burning of Waste
Wastewater treatment	4.D	Wastewater Treatment and Discharge
Other	5.B	Other

Table B.6. KIE used in model simulations

	KIE	k'/k
$^{12}CH_4$	1.0000	1.00000
$^{13}CH_4$	1.0060	0.99400
$^{12}CH_3D$	1.3213	0.75683
$^{13}CH_3D$	1.3135	0.76135
$^{12}CH_2D_2$	1.8613	0.53726

Table B.7. Isotopic compositions of Category

	$\delta^{13}C$	$\delta^{13}CH_3D$	δD	$\delta^{12}CH_2D2$	$\Delta^{13}CH_3D$	$\Delta^{12}CH_2D2$
E60						
Rice	-63.0	-362.7	-320.0	-556.2	0.30	-40.3
Ruminants and wastewater	-60.5	-370.3	-330.0	-569.2	0.30	-40.3
Natural gas	-39.6	-210.1	-180.0	-322.5	3.00	7.6
Coal	-37.0	-169.3	-140.0	-254.8	3.00	7.6
Combustion	-24.6	-241.9	-225.0	-409.0	2.80	-16.0
Vehicles	-24.6	-242.6	-225.0	-396.4	2.00	5.0
High T	-24.6	-243.7	-225.0	-398.8	0.50	1.0
Landfills and manure	-55.0	-347.8	-310.0	-543.1	0.30	-40.3
Biomass burning	-41.0	-254.7	-225.0	-409.0	2.80	-16.0
E60HI						
Rice	-63.0	-362.7	-320.0	-557.0	0.24	-41.9
Ruminants and wastewater	-60.5	-370.4	-330.0	-569.9	0.24	-41.9
Natural gas	-39.6	-210.1	-180.0	-322.5	3.00	7.6
Coal	-37.0	-169.3	-140.0	-254.8	3.00	7.6
Combustion	-24.6	-241.9	-225.0	-409.0	2.80	-16.0
Vehicles	-24.6	-242.6	-225.0	-396.4	2.00	5.0
High T	-24.6	-243.7	-225.0	-398.8	0.50	1.0
Landfills and manure	-55.0	-347.8	-310.0	-543.9	0.24	-41.9
Biomass burning	-41.0	-254.7	-225.0	-409.0	2.80	-16.0
E50						
Rice	-63.0	-362.7	-320.0	-556.5	0.30	-40.8
Ruminants and wastewater	-60.5	-370.3	-330.0	-569.4	0.30	-40.8
Natural gas	-39.6	-210.1	-180.0	-322.5	3.00	7.6
Coal	-37.0	-169.3	-140.0	-254.8	3.00	7.6
Combustion	-24.6	-241.9	-225.0	-409.0	2.80	-16.0
Vehicles	-24.6	-242.6	-225.0	-396.4	2.00	5.0
High T	-24.6	-243.7	-225.0	-398.8	0.50	1.0
Landfills and manure	-55.0	-347.8	-310.0	-543.3	0.30	-40.8
Biomass burning	-41.0	-254.7	-225.0	-409.0	2.80	-16.0
E50HI						
Rice	-63.0	-362.7	-320.0	-557.2	0.23	-42.5
Ruminants and wastewater	-60.5	-370.4	-330.0	-570.2	0.23	-42.5
Natural gas	-39.6	-210.1	-180.0	-322.5	3.00	7.6
Coal	-37.0	-169.3	-140.0	-254.8	3.00	7.6
Combustion	-24.6	-241.9	-225.0	-409.0	2.80	-16.0
Vehicles	-24.6	-242.6	-225.0	-396.4	2.00	5.0
High T	-24.6	-243.7	-225.0	-398.8	0.50	1.0
Landfills and manure	-55.0	-347.8	-310.0	-544.1	0.23	-42.5
Biomass burning	-41.0	-254.7	-225.0	-409.0	2.80	-16.0

Grey fields are determined by model fit for wetlands and assigned to all microbial sources.

Table B.8. Derived clumped isotopologue compositions for different model scenarios.

	$\Delta^{13}CH_3D$	$\Delta^{12}CH_2D2$
E60	0.30	-40.13
E60HI	0.24	-41.96
E50	0.30	-40.77
E50HI	0.23	-42.49

Table B.9. Tests of recovery of 40 micromole (1cc) methane from 200 L nitrogen

Sample number	$\delta^{13}CH_4$ (‰)	2σ	$\delta^{12}CH_3D$ (‰)	2σ	$\Delta^{13}CH_3D$ (‰)	2σ	$\Delta^{12}CH_2D_2$ (‰)	2σ
Starting	-37.00		-149.20		2.98		7.58	
230330	-36.84	0.01	-148.54	0.16	2.76	0.35	8.36	2.66
230221	-36.82	0.02	-148.44	0.22	2.72	0.45	9.24	3.18

Appendix C: Supporting Information for Constraining Wetland and Landfill Methane Emission Signatures Through Atmospheric Methane Clumped Isotopologue Measurements

This Appendix is the supporting information of an in-press paper:

Journal of Geophysical Research: Biogeosciences (2025) http://doi.org/10.1029/2024JG008249

Authors and Affiliations:

Jiayang Sun[1,2,3*], Cédric Magen[1], Mojhgan A. Haghnegahdar[1,4], Jiarui Liu[5], Julianne M. Fernandez[1,6], and James Farquhar[1,7]

[1]Department of Geology, University of Maryland, College Park, MD 20742, USA.

[2]Air Resources Laboratory, National Oceanic and Atmospheric Administration, College Park, MD 20740, USA.

[3]Cooperative Institute for Satellite Earth System Studies (CISESS), University of Maryland, College Park, MD 20740, USA.

[4]Smithsonian Environmental Research Center, Edgewater, Maryland 21037, USA.

[5]Department of Earth, Planetary and Space Sciences, University of California, Los Angeles, CA 90095, USA.

[6]Global Monitoring Laboratory, National Oceanic and Atmospheric Administration, Boulder, CO 80305, USA.

[7]Earth System Science Interdisciplinary Center, University of Maryland, College Park, MD 20740, USA.

* Corresponding author: Jiayang Sun (jiayangs@umd.edu)

Note C.1. Descriptions of Sampling Sites

The Jug Bay Wetlands Sanctuary is located in southern Anne Arundel County, Maryland. The Patuxent River traverses through the Jug Bay Wetlands Sanctuary in a north-south direction. The sampling site, Jug Bay Car Top Boat Launch (coordinates: 38.81158, -76.71055) is located at the southeast corner of the Patuxent Wetlands Park, right north of Maryland Route 4. The sampling location is at a small tributary of the Patuxent River, less than 500 feet from its confluence with the main river. A wooden platform is constructed along the shore, extending over the water where sampling took place approximately 30 cm above the water surface, one meter away from the shore (Figure C.1 and Figure C.2).

The Patuxent Research Refuge sampling site (coordinates: 39.04494, -76.78869) is less than 20 miles upstream(north) along the Patuxent River from Jug Bay. Sampling took place on a wooden trail platform elevated 1-2 meters above the ground, but below the tree canopy. The Queen Anne Bridge is 6 miles north of Jug Bay. This sampling site (coordinates: 38.88866, -76.67119) is near the river, surrounded by dead ash trees. The Wootens Landing Trail (coordinates: 38.8563, -76.6891) is about 3.5 miles north of the Jug Bay in the Wooton's Landing Wetland Park, with a similar environment as the Jug Bay.

Approximately 10 miles downstream from the Jug Bay along the Patuxent River, we sampled at Chaneyville Rd (coordinates: 38.66245, -76.68256) in Lower Marlboro, MD. At this location, the Patuxent River takes on a U-shape. Our sampling point is nestled within a forested area on the riverbank. We traveled further downstream by boat to Patuxent River Station 3 (PAX, coordinates: 38.41215, -76.58377). The Patuxent River Station 3 sample is a special one as it was collected in the middle of the Bay directly above the water, while the rest samples were collected on the shore. The sampling series presents a north-to-south transition from terrestrial to estuarine environments, with increasing influence from the tidal flows of the Chesapeake Bay.

Located 5.3 miles to the northwest of the Jug Bay is the Brown Station Road Sanitary Landfill. According to a report released by the Environmental Integrity Project on June 9, 2021 (Environmental Integrity Project, 2021), the Brown Station Landfill is the largest greenhouse gas emitter among all landfills in Maryland. Its annual emissions in 2017 were recorded as high as 86,066 tons of carbon dioxide and 6,129 tons of methane. We conducted two mobile greenhouse gas surveys downwind of the Brown Station in the 2022 and 2023 winter. The surveys indicated that the Brown Station was continuing to release a significant amount of methane, with its plume extending to the Jug Bay.

Figure C.1. **A general view of the Jug Bay sampling site.** The photo was taken on December 7, 2022, at 6:39 AM. The light source in the image is the beam from a car's headlights. Two sampling bags are being inflated by a portable pump to collect air samples.

Figure C.2. **A closer view of the sampling bags and the pump.** The photo was taken on November 4, 2022, at 6:43 AM. Two sampling bags are simultaneously being inflated by two portable pumps to collect air samples. Dense fog was present.

Note C.2. Wind and Water Data

The wind speed and direction, water table depth, salinity, and dissolved oxygen concentration data were acquired from nearby monitoring stations (station code: CBMJBMET, CBMIPWQ, CBMRRWQ) operated by the NOAA National Estuarine Research Reserve System (https://cdmo.baruch.sc.edu/) (NOAANERRS). Average wind speeds were calculated from midnight to 7 am, representing the wind speeds at the time of sampling. Prevailing wind directions were determined from averages taken 2-3 hours before sampling. Water table depth readings were taken from the reading at 7 am on each sampling date. Despite the exact locations not perfectly aligning with our sampling sites, these monitoring sites are very close to our sampling site at Jug Bay and share the same water flow, the proximity is close enough that the differences can be considered negligible for the scale of this study. Wind speeds and directions, and water table depths data are summarized in Table C.1.

Table C.1. **Compiled sample information of the sampling date, time, location, wind and water table depth data, concentration profile, and isotope measurement results.**

Type	Location	Longitude °	Latitude °	Start time AM	End time AM	Wind Speed m/s	Wind Direction °	Tidal m ↑/↓	CH_4 ppm	CO_2 ppm	C_2H_6 ppb	$\delta^{13}C$ ‰	2σ ‰	δD ‰	2σ ‰	$\Delta^{13}CH_3D$ ‰	2σ ‰	$\Delta^{12}CH_2D_2$ ‰	2σ ‰
Brown Station	North of Brown Station	38.8477	-76.7903	5:00	5:30				21.0			-53.51	0.03	-286.40	0.20	-0.8	0.4	-23.3	1.5
Jug Bay	Car Top Boat Launch	38.8115	-76.7105	7:00	7:30	0.6	242	1.89 ↓	2.647			-52.12	0.07	-153.11	0.08	2.6	0.4	46.0	1.6
Patuxent River	Patuxent Wildlife Refuge	39.0449	-76.7887	8:00	8:50	0.3	54	1.63 ↓	2.315	495.558		-49.64	0.03	-129.11	0.21	3.2	0.5	48.3	2.5
Jug Bay	Car Top Boat Launch	38.8115	-76.7105	7:00	7:30	0.3	70	1.89 ↓	2.695	600.292		-54.03	0.01	-152.86	0.02	2.3	0.3	47.4	1.6
Jug Bay	Car Top Boat Launch	38.8115	-76.7105	6:30	7:00	0.3	45	1.87 ↑	2.602	459.298		-53.94	0.01	-156.74	0.02	2.4	0.3	44.8	1.5
Patuxent River	Chaneyville Rd.	38.6626	-76.6821	7:00	7:40	0.4	49	1.93 ↑	2.069	480.334		-49.54	0.01	-109.45	0.02	3.1	0.4	51.6	1.7
Patuxent River	Wootens Landing Trail	38.8558	-76.6906	7:04	8:00	0.1	175	1.57 ↑	3.566	1250.789		-55.44	0.01	-181.44	0.05	1.6	0.2	33.4	1.4
Patuxent River	Queen Anne Bridge	38.8887	-76.6712	7:00	7:30	0.5	253	1.47 ↑	6.497	710.239		-52.42	0.02	-139.02	0.07	2.2	0.3	48.7	1.4
Patuxent River	River Cruise	38.4121	-76.5838	12:21	12:26	0.6	190		3.934			-48.57	0.01	-98.43	0.07	2.2	0.3	47.7	1.6
Jug Bay	Car Top Boat Launch	38.8115	-76.7105	6:30	7:00	0.2	51	1.97 ↓	2.577	467.025		-52.22	0.01	-144.97	0.07	3.2	0.4	41.5	1.5
Jug Bay	Car Top Boat Launch	38.8115	-76.7105	6:50	7:20	0.3	314	1.91 ↓	2.236	474.208		-51.07	0.01	-124.42	0.08	2.9	0.3	42.8	1.6
Jug Bay	Car Top Boat Launch	38.8115	-76.7105	6:30	7:00	0.5	53	1.59 ↓	2.207	490.615		-49.50	0.01	-131.51	0.02	1.9	0.3	43.9	1.3
Jug Bay	Car Top Boat Launch	38.8115	-76.7105	6:45	7:15	2.0	230	1.81 ↓	2.357		5.8	-49.15	0.02	-110.40	0.14	2.1	0.3	43.3	2.2
Brown Station	Road 202	38.8389	-76.7567	7:30	8:00	0.4	50	1.55 ↓	11.098		15.3	-52.87	0.03	-258.75	0.13	-0.4	0.3	3.8	2.3
Jug Bay	Car Top Boat Launch	38.8115	-76.7105	7:20	7:35	0.2	50	1.60 ↑	3.369		9.0	-54.44	0.01	-158.59	0.17	2.4	0.3	40.8	2.5
Jug Bay	Car Top Boat Launch	38.8115	-76.7105	7:00	7:35	1.4	208	Low	2.487		2.4	-51.48	0.01	-127.36	0.16	2.5	0.4	47.8	2.4
Jug Bay	Car Top Boat Launch	38.8115	-76.7105	7:00	7:35	0.4	216	Low	2.851		6.3	-52.20	0.03	-141.61	0.23	1.8	0.4	47.3	3.0

Water salinity and dissolved oxygen concentrations for the period from January 1, 2022, to Dec 31, 2023, are depicted in Figure C.3 and Figure C.4, illustrating the annual cycles over the two years.

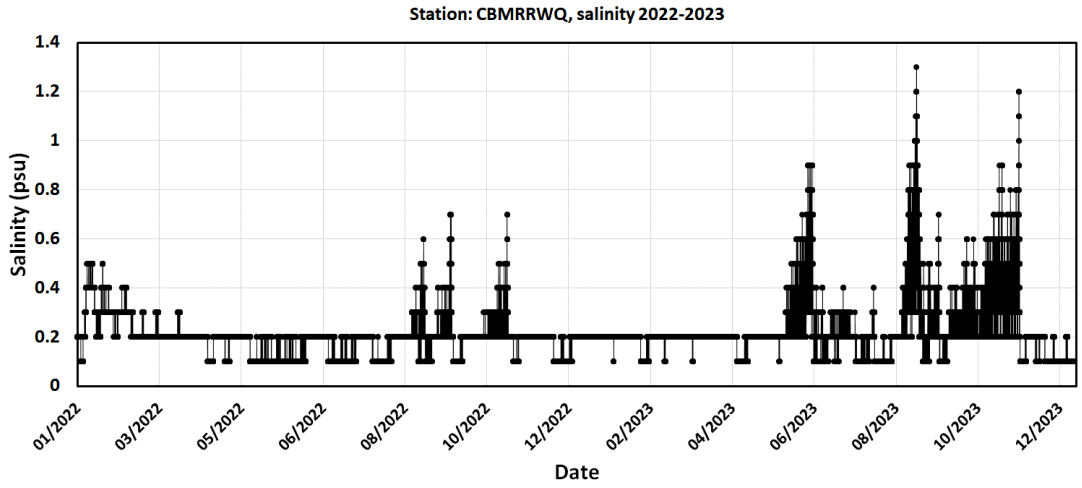

Figure C.3. **Water salinity during 2022-2023**, from NOAA NERRS station CBMRRWQ.

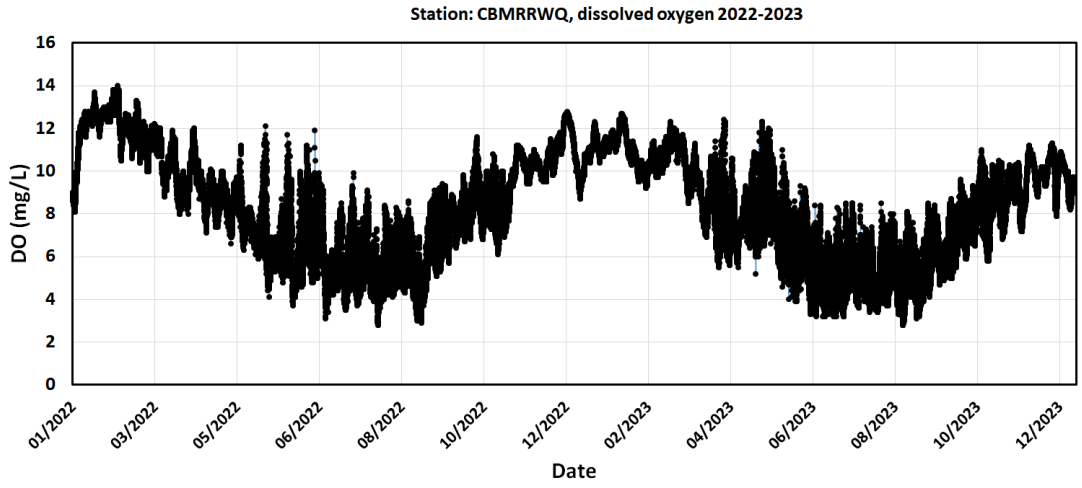

Figure C.4. **Water dissolved oxygen concentration during 2022-2023**, from NOAA NERRS station CBMRRWQ.

Note C.3. Campus Air Samples

Campus air samples consist of a series of collections at fixed sampling locations within the University of Maryland (UMD) campus for methane clumped isotopologue analysis. Table C.2 summarizes the sampling information (sample names, sampling dates, and locations), the measurement information (measurement run number and run dates), and the measured isotopic signals ($\delta^{13}C$, δD, $\delta^{13}CH_3D$, $\delta^{12}CH_2D_2$, $\Delta^{13}CH_3D$, and $\Delta^{12}CH_2D_2$, and their respective 2SD uncertainties).

Table C.2. **Compiled information on campus air samples.**

Run	Run Date	Sample	Sample Date	Type	$\delta^{13}C$ ‰	2σ ‰	$\delta^{13}CH_3D$ ‰	2σ ‰	δD ‰	2σ ‰	$\delta^{12}CH_2D_2$ ‰	2σ ‰	$\Delta^{13}CH_3D$ ‰	2σ ‰	$\Delta^{12}CH_2D_2$ ‰	2σ ‰	Note
1227	2021-04-19	210408 air	2021-04-08	CHEM air	-47.39	0.04	-131.32	0.92	-89.33	0.12	-132.59	1.663	1.3	1.1	45.9	2.0	
1247	2021-04-27	210329 air	2021-03-29	CHEM air	-47.44	0.03	-133.24	0.72	-91.41	0.09	-134.41	1.488	1.5	0.8	48.5	1.8	
~~1260~~	~~2021-05-02~~	~~2104029 air~~	~~2021-04-29~~	~~CHEM air~~	~~-49.17~~	~~0.03~~	~~-161.89~~	~~0.98~~	~~-120.07~~	~~0.13~~	~~-186.18~~	~~1.745~~	~~1.7~~	~~1.2~~	~~51.1~~	~~2.3~~	δD out of 3σ
1269	2021-05-07	210503 air	2021-05-03	CHEM air	-47.28	0.03	-132.05	0.67	-91.73	0.10	-138.72	1.451	3.0	0.8	44.0	1.8	
1271	2021-05-07	210504 air	2021-05-04	CHEM air	-47.58	0.03	-130.88	0.84	-89.01	0.17	-132.42	2.105	1.7	1.0	45.4	2.6	
1274	2021-05-08	210506 air	2021-05-06	CHEM air	-47.93	0.02	-132.25	0.64	-90.37	0.12	-132.94	1.720	2.0	0.8	47.9	2.1	
1280	2021-05-09	210402 air	2021-04-02	~~CHEM air~~	-47.76	0.02	-132.91	0.53	-91.16	0.07	-133.38	1.269	1.9	0.6	49.2	1.5	
~~1291~~	~~2021-05-15~~	~~210507 air~~	~~2021-05-07~~	~~CHEM air~~	~~-47.20~~	~~0.05~~	~~-140.40~~	~~0.98~~	~~-99.77~~	~~0.17~~	~~-131.12~~	~~2.028~~	~~2.2~~	~~1.2~~	~~72.1~~	~~2.5~~	$\Delta^{12}CH_2D_2$ out of 3σ
1301	2021-05-18	210511 air	2021-05-11	CHEM air	-47.65	0.02	-133.12	0.52	-91.46	0.09	-133.89	1.610	1.9	0.6	49.3	2.0	
1314	2021-05-22	210514 air	2021-05-14	CHEM air	-48.06	0.02	-132.54	0.65	-90.98	0.10	-134.32	1.597	2.5	0.8	47.6	1.9	
1338	2021-06-04	210601/210530 air	2021-05-30	CHEM air	-46.30	0.05	-127.79	1.18	-88.83	0.18	-129.82	2.087	3.7	1.4	48.1	2.5	
1341	2021-06-06	210602/210530 air	2021-05-30	CHEM air	-45.48	0.04	-121.25	0.91	-81.46	0.17	-119.79	2.153	2.3	1.1	43.2	2.6	
1346	2021-06-08	210607/210603 air	2021-06-03	CHEM air	-46.08	0.02	-128.11	0.58	-87.06	0.15	-127.62	1.887	1.2	0.7	46.7	2.3	
1351	2021-06-09	210603/210530 air	2021-05-30	CHEM air	-47.20	0.11	-131.92	2.52	-91.08	0.30	-132.77	3.229	2.4	2.9	49.7	4.0	
1354	2021-06-10	210605/210605 air	2021-06-05	CHEM air	-46.16	0.03	-126.82	0.58	-86.38	0.12	-126.88	1.739	2.0	0.7	46.0	2.1	
1214	2021-07-14	210712 atl roof 2	2021-07-12	ATL air	-48.29	0.02	-129.51	0.41	-87.03	0.23	-128.81	2.033	1.8	0.5	45.2	2.5	
1417	2021-07-16	210712 atl roof 1	2021-07-12	ATL air	-45.18	0.06	-128.18	0.89	-88.48	0.44	-134.00	3.201	1.7	1.1	42.3	4.0	
1435	2021-07-27	210719AtlRoof	2021-07-19	ATL air	-45.99	0.03	-130.48	0.58	-89.66	0.29	-133.84	2.639	1.2	0.7	45.2	3.3	
1478	2021-09-13	20210901 StormIDA	2021-09-01	CHEM air	-47.13	0.03	-133.59	0.71	-92.21	0.15	-138.87	1.840	1.6	0.8	45.0	2.3	
1649	2022-01-02	211103 ATL BLDG 11:00-11:15	2021-11-13	ATL air	-47.78	0.24	-134.86	0.79	-94.37	0.13	-141.66	4.070	3.2	1.0	46.5	5.0	
~~1652~~	~~2022-01-03~~	~~211119 Atl Bldg roof 4:00-4:45 pm~~	~~2021-11-19~~	~~ATL air~~	~~-49.97~~	~~0.42~~	~~-148.13~~	~~0.46~~	~~-103.94~~	~~0.03~~	~~-157.04~~	~~1.739~~	~~0.7~~	~~0.7~~	~~49.9~~	~~2.2~~	δD out of 3σ
~~1726~~	~~2022-02-07~~	~~211217 ATL Roof 10:15-11:15~~	~~2021-12-17~~	~~ATL air~~	~~-46.30~~	~~0.04~~	~~-135.43~~	~~0.86~~	~~-89.38~~	~~0.03~~	~~-139.25~~	~~1.856~~	~~-4.5~~	~~1.0~~	~~38.0~~	~~2.2~~	$\Delta^{13}CH_3D$ out of 3σ

1728	2022-02-09	220106 ATL Roof 12:30pm-13:15pm	2022-01-06	ATL air	-47.53	0.04	-138.11	0.65	-96.52	0.15	-145.58	1.925	1.6	0.8	46.7	2.4	
1820	2022-03-15	220217 atl bld roof 11:30 12:15	2022-02-17	ATL air	-47.42	0.01	-132.25	0.26	-90.72	0.12	-135.52	1.520	1.8	0.3	45.6	1.9	
1890	2022-04-26	220311-AtlBuildingRoof	2022-03-11	ATL air	-47.22	0.02	-135.76	0.45	-94.17	0.03	-141.10	1.552	1.4	0.5	46.8	1.9	
1981	2022-08-14	220414 atl bldg air 230-330	2022-04-14	ATL air	-46.64	0.04	-128.80	0.66	-88.37	0.23	-130.25	2.429	2.4	0.8	46.5	3.0	
1984	2022-08-16	220429 atl air	2022-04-29	ATL air	-47.41	0.02	-131.65	0.37	-89.69	0.18	-129.45	1.425	1.4	0.5	50.5	1.8	
1987	2022-08-18	220331 atl building	2022-03-31	ATL air	-46.88	0.04	-132.43	0.37	-90.98	0.13	-136.41	1.590	1.4	0.4	45.1	1.9	
1993	2022-08-21	220815 air atl 345-430	2022-08-15	ATL air	-47.81	0.02	-136.55	0.30	-94.46	0.13	-142.10	1.511	1.4	0.4	46.2	1.9	
2010	2022-08-27	220623 air atl	2022-06-23	ATL air	-46.75	0.02	-127.98	0.39	-86.46	0.13	-125.31	1.688	1.4	0.5	48.1	2.0	
2057	2022-09-19	ATL20220914 1510-1610	2022-09-14	ATL air	-47.90	0.02	-138.14	0.42	-96.71	0.10	-147.18	1.561	2.1	0.5	45.2	1.9	
~~2089~~	~~2022-10-31~~	~~20221020-1320 ATL BLDG~~	~~2022-10-20~~	~~ATL air~~	~~-52.32~~	~~0.01~~	~~-148.57~~	~~0.30~~	~~-104.56~~	~~0.02~~	~~-158.37~~	~~1.421~~	~~3.3~~	~~0.4~~	~~49.6~~	~~1.8~~	Extraction Fractionated

The CHEM air samples were collected at the ventilation shaft entrance of the UMD Chemistry Building. This shaft, located at ground level, is responsible for supplying air to the interior of the Chemistry Building. Positioned at the heart of the campus, the building fronts the main campus road, Regent Drive, with a semi-enclosed parking garage situated across the street. ATL air samples were collected from the fourth-floor roof of the UMD Atlantic Building. The Atlantic Building is also centrally located within the campus, not far from the intersection of two major campus roads. Surrounding the building are a large sports stadium, a dining hall, a semi-enclosed parking garage, a campus farm housing cattle, horses, and sheep, along with various academic buildings and dormitories. Low concentrations of methane plumes are often detected around the campus farm. High concentrations (but low flux) of methane have been occasionally recorded in sewer manholes on these two main roads, which some could be attributed to natural gas leakage.

The sampling dates were chosen randomly depending on availability. Sampling times were primarily concentrated in the midday to early afternoon period. During these hours, the surface temperature is higher, and the boundary layer is relatively elevated, which is conducive to collecting well-mixed tropospheric air and minimizing the influence of potential nearby sources. Throughout the sampling period, atmospheric methane concentrations typically fluctuated within the range of 2.15 to 2.25 ppm.

The methods for collecting and analyzing these background air samples were consistent with those described in the main text for wetland air samples.

It is important to note that this set of samples is experimental for several reasons:

1) Meteorological conditions such as weather, wind direction, and temperature were not considered during sampling, introducing numerous variable factors. The primary purpose of collecting these samples was to validate the analytical method and to obtain preliminary data on the variability of atmospheric methane clumped isotopologue values.

2) The timing of the sampling was not at regular intervals but depended on the availability of personnel and equipment.

3) Due to limitations in manpower and time, the processes of sampling, extraction, purification, and Panorama measurement were not always carried out by the same individual. Although all participants aimed to follow the same standard operating procedures, the introduction of additional variables was possible. For example, different individuals may use the heat gun differently while heating for transfer, leading to variations in heating temperatures or durations.

4) Due to constraints on manpower and time, there could be extended intervals between different processes. For instance, samples might not be extracted immediately after collection but several days later, potentially allowing for minor mixing with lab air due to Tedlar Bag leakage.

5) The analytical method was continuously optimized. Given the extensive duration covered by this set of samples, there were changes in our extraction line, purification line, and the way we operated the Panorama over two years. For example, the pump in the extraction line was replaced several times, and the method of connecting the pump tubing was modified.

Within this dataset, one record has known issues that happened during the extraction process that could cause fractionation and warrant its exclusion. It is highlighted in dark gray and marked with a strikethrough in Table C.2). For the remaining records, although no known issues were identified, we applied 3σ tests to determine potential outliers. If any of the four parameters ($\delta^{13}C$,

δD, $\Delta^{13}CH_3D$, and $\Delta^{12}CH_2D_2$) in a data record exceeds the mean of all records by more than $\pm 3\sigma$, that entire record is excluded from the dataset used to calculate the UMD campus air average. These samples, highlighted in light gray and marked with a strikethrough in Table C.2, are:

2104029 air (Run 1260)

210507 air (Run 1291)

211119 Atl Bldg roof 4:00-4:45 pm (Run 1652)

221217 ATL Roof 10:15-11:15 (Run 1726)

After applying these filters, the surviving data records were averaged to determine the UMD campus air average compositions, which are:

$\delta^{13}C$ = -47.1‰, δD = -90.2‰, $\Delta^{13}CH_3D$ = 1.9‰, and $\Delta^{12}CH_2D_2$ = 46.3‰

Table C.3. This table details **the derived source compositions and associated uncertainties corresponding to each wetland air sample, using the 2-point Keeling plot method.** The uncertainties of the background air compositions are set to be $2\sigma\delta^{13}C$ = 0.02‰, $2\sigma\delta D$ = 0.1‰, $2\sigma\delta^{13}CH_3D$ = 0.27‰, and $2\sigma\delta^{12}CH_2D_2$ = 1.3‰. Uncertainties on concentrations are not considered in the propagation of uncertainties.

Date	Area	Location	$\delta^{13}CH_4$	$2\sigma\delta^{13}C$	$\delta^{12}CH_3D$	$2\sigma\delta D$	$\Delta^{13}CH_3D$	$2\sigma\Delta^{13}CH_3D$	$\Delta^{12}CH_2D_2$	$2\sigma\Delta^{12}CH_2D_2$
2022-06-12	Jug Bay	Car Top Boat Launch	-66.27	0.32	-373.27	1.72	1.4	3.3	-135.1	11.7
2022-07-24	Patuxent	Wildlife Refuge	-62.33	0.27	-439.85	3.61	15.9	8.3	-309.4	35.9
2022-08-28	Jug Bay	Car Top Boat Launch	-73.21	0.08	-355.91	1.30	-2.7	2.4	-93.4	10.6
2022-09-03	Jug Bay	Car Top Boat Launch	-76.00	0.08	-408.47	1.58	-5.3	3.2	-223.8	12.9
2022-09-03	Patuxent	Swan Lane	-216.63	2.57	-2323.60	50.30	217.8	52.4	-2731.9	162.8
2022-09-04	Patuxent	Wootons Landing Trail	-65.49	0.03	-306.40	0.55	-1.7	1.0	-59.0	4.4
2022-09-05	Patuxent	Queen Anne Bridge	-54.46	0.02	-162.08	0.42	2.4	0.6	46.6	2.1
2022-09-21	Patuxent	River Cruise	-49.18	0.03	-108.69	0.60	2.9	0.8	47.2	3.6
2022-10-10	Jug Bay	Car Top Boat Launch	-68.65	0.10	-362.63	1.93	5.0	3.6	-163.0	12.4
2022-10-25	Jug Bay	Car Top Boat Launch	-84.89	0.25	-515.05	4.32	0.8	11.3	-898.5	45.6
2022-11-04	Jug Bay	Car Top Boat Launch	-69.16	0.28	-687.23	5.34	-21.2	20.9	-3957.5	77.8
2022-12-07	Jug Bay	Car Top Boat Launch	-56.82	0.18	-253.39	2.25	4.9	3.9	-47.9	22.5
2022-12-29	Jug Bay	Car Top Boat Launch	-64.45	0.05	-266.73	0.69	1.6	1.3	-13.7	7.0
2023-04-15	Jug Bay	Car Top Boat Launch	-67.81	0.12	-307.40	1.90	3.6	3.6	-40.2	18.7
2023-05-07	Jug Bay	Car Top Boat Launch	-62.93	0.11	-276.21	1.11	-0.2	2.3	-5.9	12.5

Note C.4. Derivation of the Formula to Estimate δ_{source} from Δ_{source}

The first part will derive the formula to calculate $\delta^{12}CH_3D_{source}$ from the assumed $\Delta^{12}CH_2D_{2_{source}}$.

Convert hydrogen isotope δ values to a normalized ratio RD would be:

$$RD = \left(\frac{^{12}CH_3D}{^{12}CH_4}\right)_{sample} \Big/ \left(\frac{^{12}CH_3D}{^{12}CH_4}\right)_{reference} = \left(1 + \frac{\delta^{12}CH_3D}{1000}\right) \quad (C.1)$$

We can have a similar definition for $^{12}CH_2D_2$ to a normalized ratio RD2:

$$RD2 = \left(\frac{^{12}CH_2D_2}{^{12}CH_4}\right)_{sample} \Big/ \left(\frac{^{12}CH_2D_2}{^{12}CH_4}\right)_{reference} = \left(1 + \frac{\delta^{12}CH_2D_2}{1000}\right) \quad (C.2)$$

We can start with two equations describing the mixing relationships:

$$RD_{mix} = (1 - f) * RD_{air} + f * RD_{source} \quad (C.3)$$

$$RD2_{mix} = (1 - f) * RD2_{air} + f * RD2_{source} \quad (C.4)$$

Where f is the mixing ratio of the source. We can solve for f for each of the above equations:

$$f = \frac{RD_{mix} - RD_{air}}{RD_{source} - RD_{air}} \quad (C.5)$$

$$f = \frac{RD2_{mix} - RD2_{air}}{RD2_{source} - RD2_{air}} \quad (C.6)$$

If we set these equal, we get:

$$\frac{RD_{mix} - RD_{air}}{RD_{source} - RD_{air}} = \frac{RD2_{mix} - RD2_{air}}{RD2_{source} - RD2_{air}} \quad (C.7)$$

Which we can rearrange to:

$$RD2_{source} - \left(\frac{RD2_{mix}-RD2_{air}}{RD_{mix}-RD_{air}}\right) * RD_{source} + \left(\frac{RD2_{mix}-RD2_{air}}{RD_{mix}-RD_{air}}\right) * RD_{air} - RD2_{air} = 0 \quad (C.8)$$

Noting that there is a relationship between the $\Delta^{12}CH_2D_2$ and $\delta^{12}CH_3D$, which is numerically very similar to δD:

$$\Delta^{12}CH_2D_2 = {(1+\delta^{12}CH_2D_2)}/{(1+\delta^{12}CH_3D)^2} - 1 \quad (C.9)$$

We can assign a $\Delta^{12}CH_2D_2$ for the source, and then express $RD2_{source}$ in terms of RD_{source}, we can write the above equation into:

$$\left(1+\frac{\Delta^{12}CH_2D_{2_{source}}}{1000}\right) * (RD_{source})^2 - \left(\frac{RD2_{mix}-RD2_{air}}{RD_{mix}-RD_{air}}\right) * RD_{source} + \left(\frac{RD2_{mix}-RD2_{air}}{RD_{mix}-RD_{air}}\right) * RD_{air} - RD2_{air} = 0 \quad (C.10)$$

This is a quadratic equation of form $ax^2 + bx + c = 0$, where a can be calculated based on an assumed value of $\Delta^{12}CH_2D_{2_{source}}$, b and c are calculated from the measured/assigned $\Delta^{12}CH_2D_2$ and δD of the wetland sample and the background air, and x can be solved using the quadratic equation:

$$x = \frac{-b \pm \sqrt{b^2-4ac}}{2a} \quad (C.11)$$

RD_{source} is then converted back to $\delta^{12}CH_3D_{source}$.

We can further calculate $\delta^{13}CH_{4_{source}}$ if we adopt an exploratory assumption. This assumption suggests that the $\Delta^{13}CH_3D$ and $\Delta^{12}CH_2D_2$ values of microbial methane are governed by a unified process, thus there exists a mathematical expression between $\Delta^{13}CH_3D$ and $\Delta^{12}CH_2D_2$ for microbial methane. We compiled the available natural and lab-culture microbial methane

clumped isotopologue data from Douglas et al. (2020); Giunta et al. (2022); Giunta et al. (2019); Haghnegahdar et al. (2024); Haghnegahdar et al. (2023); Li, Ash, et al. (2024); Liu, Harris, et al. (2023); Young (2019); Young, Kohl, Sherwood Lollar, et al. (2017) in Table C.4, and made a linear regression of all these data shown in Figure C.5.

Table C.4. **Compiled microbial methane (natural sample and lab-culture) isotope ($\delta^{13}C$ and δD) and isotopologue ($\Delta^{13}CH_3D$ and $\Delta^{12}CH_2D_2$) values and uncertainties** from published literature.

References	Sample ID/description	$\delta^{13}C$	2σ	δD	2σ	$\Delta^{13}CH_3D$	2σ	$\Delta^{12}CH_2D_2$	2σ	Type
Young et al., 2017	*M. acetivorans* CH3OH 30°C	-32.768	0.007	-328.407	0.019	-3.880	0.203	-40.858	0.364	culture
	M. acetivorans CH3OH 30°C	-32.763	0.005	-328.448	0.017	-3.837	0.091	-43.239	0.308	culture
	M. thermolithotrophicus H2+CO2 65°C	-49.355	0.011	-394.368	0.015	2.661	0.098	-19.437	0.304	culture
	M. barkeri CH3OH 30°C	-56.550	0.007	-340.178	0.016	-1.108	0.127	-34.327	0.346	culture
Giunta et al., 2019	*M. aeolicus* H2+CO2 46°C	-53.221	0.007	-390.902	0.015	2.830	0.219	-17.343	0.337	culture
	M. aeolicus H2+CO2 46°C	-51.451	0.003	-399.598	0.014	3.804	0.302	-16.937	0.296	culture
	M. maripaludis H2+CO2 37°C	-50.259	0.003	-372.563	0.021	2.300	0.122	-12.108	0.387	culture
	M. barkeri CH3OH 37°C	-53.703	0.004	-250.103	0.011	-2.373	0.011	-54.488	0.356	culture
	M. barkeri CH3OH 37°C	-53.356	0.005	-249.879	0.013	-2.261	0.013	-55.340	0.342	culture
Douglas et al., 2020	Mac_B2 *M. acetivorans* CH3OH 28°C	-29.160	0.005	-343.220	0.108	-4.200	0.278	-30.000	1.540	culture
	Mac_B5 *M. acetivorans* CH3OH 28°C	-88.220	0.005	-372.490	0.087	-6.400	0.320	-38.000	2.610	culture
	Mac_B7 *M. acetivorans* CH3OH 28°C	-29.170	0.005	-343.030	0.071	-3.800	0.277	-35.000	1.690	culture
Young, 2019	methanogenesis	-47.305	0.005	-393.976	0.017	3.415	0.091	-16.345	0.314	culture
	methanogenesis	-89.474	0.003	-379.519	0.024	-3.452	0.141	-31.291	0.789	culture
	M. mazei MeOH 39°C	-108.639	0.004	-287.120	0.029	-3.510	0.155	-51.847	0.826	culture
	M. shengliensis MeOH 65°C	-79.114	0.003	-275.578	0.034	-4.174	0.142	-45.796	0.656	culture
	M. shengliensis TMB 65°C	-86.652	0.005	-282.044	0.022	0.355	0.209	-34.288	0.719	culture

M. shengliensis diluted TMB 65°C	-98.640	0.006	-298.756	0.020	0.420	0.223	-35.844	0.724	culture
M. luminyensis TMA+H2 37°C	-64.911	0.003	-358.997	0.017	-0.256	0.125	-17.858	0.636	culture
M. luminyensis MeOH+H2 37°C	-97.959	0.004	-271.945	0.014	-2.145	0.152	-44.503	0.580	culture
M. luminyensis diluted MeOH+H2 37°C	-99.711	0.003	-272.344	0.017	-2.255	0.122	-44.482	0.637	culture
M. luminyensis diluted TMA+H2 37°C	-69.995	0.003	-361.769	0.020	-0.485	0.133	-17.202	0.745	culture
M. shengliensis diluted MeOH 65°C	-91.980	0.003	-285.745	0.016	-3.571	0.112	-46.732	0.608	culture
methanogenesis	-98.364	0.004	-307.783	0.033	1.332	0.174	-42.919	0.819	culture
methanogenesis	-98.097	0.007	-308.642	0.048	0.384	0.203	-50.197	1.390	culture
methanogenesis	-79.429	0.014	-419.169	0.020	1.514	0.082	-18.222	0.281	culture
methanogenesis	-76.158	0.017	-408.019	0.078	-0.193	0.172	-29.568	0.253	culture
methanogenesis	-61.207	0.011	-380.523	0.019	0.569	0.121	-26.671	0.282	culture
methanogenesis	-55.523	0.018	-312.766	0.020	5.160	0.122	18.669	0.350	culture
methanogenesis	-62.580	0.003	-379.372	0.023	0.926	0.111	-31.754	0.307	culture
methanogenesis	-71.117	0.003	-319.642	0.026	2.225	0.092	-17.290	0.378	culture
methanogenesis	-70.882	0.003	-379.880	0.018	0.853	0.086	-27.000	0.289	culture
methanogenesis	-77.355	0.003	-397.096	0.016	0.808	0.077	-27.748	0.271	culture
methanogenesis	-73.343	0.004	-399.761	0.020	-1.161	0.100	-41.624	0.281	culture
methanogenesis	-82.141	0.004	-342.032	0.021	4.235	0.101	-5.905	0.281	culture
methanogenesis	-66.374	0.004	-367.781	0.021	2.130	0.086	-17.242	0.336	culture
methanogenesis	-70.706	0.006	-346.144	0.017	5.834	0.088	9.369	0.300	culture

	methanogenesis	-83.990	0.016	-452.182	0.019	1.226	0.113	-21.311	0.248	culture
	methanogenesis	-53.822	0.007	-261.531	0.028	-2.568	0.249	-48.943	0.832	culture
	methanogenesis	-47.037	0.023	-257.010	0.029	-2.789	0.252	-55.761	0.915	culture
AOM Liu et al., 2023	HD941-IGT6-VT7 Chamorro Seamount	-26.091	0.004	-110.323	0.023	7.463	0.138	25.185	0.617	natural
	HD945-IGT6-VT6 Chamorro Seamount	-36.981	0.004	-101.557	0.020	12.051	0.134	42.639	0.573	natural
	HD947-IGT5-VT5 Chamorro Seamount	-36.637	0.004	-100.645	0.021	12.550	0.147	40.814	0.602	natural
AOM and AeOM Giunta et al., 2022	Black Sea- GC01_S2	-75.439	0.005	-120.846	0.033	15.688	0.212	74.626	0.886	natural
	Black Sea- GC01_S3	-74.823	0.003	-227.911	0.028	7.901	0.139	24.668	0.884	natural
	Black Sea- GC01_S4	-73.335	0.010	-229.817	0.033	7.514	0.172	19.735	1.072	natural
	Black Sea- GC02_S3	-72.052	0.009	-103.856	0.040	14.604	0.290	61.142	0.866	natural
	Black Sea- GC02_S6	-70.980	0.005	-230.337	0.025	6.795	0.185	14.783	0.886	natural
	Black Sea- GC02_S4	-71.956	0.003	-203.212	0.027	6.768	0.157	18.255	0.865	natural
	Pavin Lake_sediment 2 - 40cm (T.giunta)	-64.592	0.005	-252.320	0.024	5.007	0.180	7.222	0.782	natural
	Pavin Lake_PV-90-1 (T.giunta)	-66.577	0.005	-304.428	0.029	2.793	0.299	-12.321	0.937	natural
	Pavin Lake_PV-70-2 (T.giunta)	-61.568	0.006	-307.188	0.040	2.318	0.222	-17.507	1.669	natural
	Pavin Lake PV-60-500	-60.005	0.005	-310.410	0.018	1.779	0.163	-17.644	0.763	natural
	Pavin Lake PV-55-1000 TG	-56.186	0.007	-285.804	0.053	0.738	0.243	-20.320	1.380	natural
	Pavin Lake sed 1	-64.143	0.004	-251.668	0.025	5.149	0.226	8.547	0.860	natural
Haghnegahdar et al., 2023	210819 Chamber (wetland - rice paddy)	-62.254	0.013	-333.973	0.128	-1.944	0.247	-43.931	1.387	natural

	210420d/e Chamber (wetland)	-53.558	0.048	-306.371	0.155	0.072	0.354	-31.016	1.307	natural
	210420BC Chamber (wetland)	-54.912	0.017	-318.821	0.052	1.075	0.232	-38.846	0.829	natural
	210420H Chamber (wetland)	-52.023	0.017	-320.853	0.053	0.146	0.361	-39.994	0.915	natural
	210409 Chamber (wetland)	-47.231	0.021	-332.883	0.051	-1.859	0.362	-57.165	0.806	natural
	210409i Incubation	-59.425	0.067	-309.967	0.175	-0.569	0.755	-36.717	1.534	incubation
	210430i Incubation	-60.083	0.021	-327.323	0.063	-1.112	0.492	-48.568	0.923	incubation
	210524i Incubation	-70.484	0.044	-340.303	0.236	0.837	0.550	-44.489	1.977	incubation
Haghnegahdar et al., 2024	210619 bubbles	-57.330	0.090	-329.550	0.040	-0.430	0.555	-43.750	0.770	natural
	210619 bubbles	-60.430	0.090	-340.010	0.090	-0.190	0.700	-43.920	1.350	natural
	210703 bubbles	-57.470	0.090	-341.340	0.050	-1.150	0.570	-42.930	0.905	natural
	chamber	-58.390	0.090	-353.010	0.070	-1.620	0.575	-46.210	1.145	natural
	chamber	-47.230	0.090	-332.880	0.050	-2.160	0.615	-56.350	0.965	natural
	chamber	-48.230	0.100	-332.810	0.040	-1.510	0.245	-55.920	1.070	natural
	incubation	-70.480	0.100	-340.300	0.240	0.540	0.740	-43.660	2.920	incubation
	incubation	-67.010	0.100	-317.210	0.250	-0.970	0.735	-40.650	2.925	incubation
	incubation	-63.420	0.100	-331.810	0.240	-1.780	0.740	-48.680	2.910	incubation
	incubation	-69.270	0.100	-325.790	0.250	-2.410	0.740	-51.790	2.920	incubation
Li et al., preprint	*M. luminyensis* MeOH + H2 37 °C	-97.307	0.005	-271.380	0.019	-2.514	0.151	-44.851	0.622	culture
	M. luminyensis TMA + H2 37 °C	-69.639	0.005	-362.562	0.029	-0.484	0.206	-16.486	1.018	culture
	M. luminyensis TMA + H2 37 °C	-67.953	0.005	-361.870	0.026	0.077	0.175	-16.553	0.938	culture

M. shengliensis MeOH 65 °C	-72.148	0.003	-270.375	0.031	-5.509	0.117	-47.815	0.559	culture
M. shengliensis MeOH 65 °C	-65.998	0.005	-269.489	0.028	-3.218	0.210	-45.703	0.803	culture
M. mazei CO2 + H2 39 °C	-38.650	0.005	-523.122	0.030	-3.626	0.184	-12.982	0.969	culture
M. mazei MeOH 39 °C	-108.734	0.006	-287.000	0.029	-3.951	0.222	-48.100	1.036	culture
M. mazei TMA 39 °C	-89.474	0.003	-379.519	0.024	-3.452	0.141	-31.291	0.789	culture
M. luminyensis dilute MeOH + H2 37 °C	-99.419	0.007	-272.081	0.025	-2.588	0.131	-44.982	0.751	culture
M. luminyensis dilute TMA + H2 37 °C	-69.351	0.005	-362.229	0.027	0.989	0.203	-16.197	0.860	culture
M. shengliensis dilute MeOH 65 °C	-93.176	0.003	-286.154	0.029	-3.839	0.138	-47.036	0.789	culture
M. barkeri H2+CO2 35 °C	-73.153	0.004	-536.753	0.028	-1.975	0.215	-9.876	0.981	culture
M. barkeri H2+CO2 35 °C	-71.834	0.005	-536.883	0.003	-2.509	0.215	-9.857	0.963	culture
M. barkeri MeOH 35 °C	-103.899	0.005	-295.189	0.022	-4.432	0.121	-47.647	0.682	culture
M. barkeri MeOH 35 °C	-98.504	0.005	-290.482	0.037	-9.235	0.193	-47.879	0.873	culture
M. barkeri MeOH 35 °C	-85.930	0.005	-279.402	0.019	-5.210	0.219	-49.478	0.749	culture
M. barkeri Acetate 35 °C	-47.773	0.003	-318.490	0.022	-1.961	0.244	-39.768	0.774	culture
M. barkeri Acetate 35 °C	-48.577	0.029	-319.383	0.023	-1.906	0.238	-41.240	0.728	culture

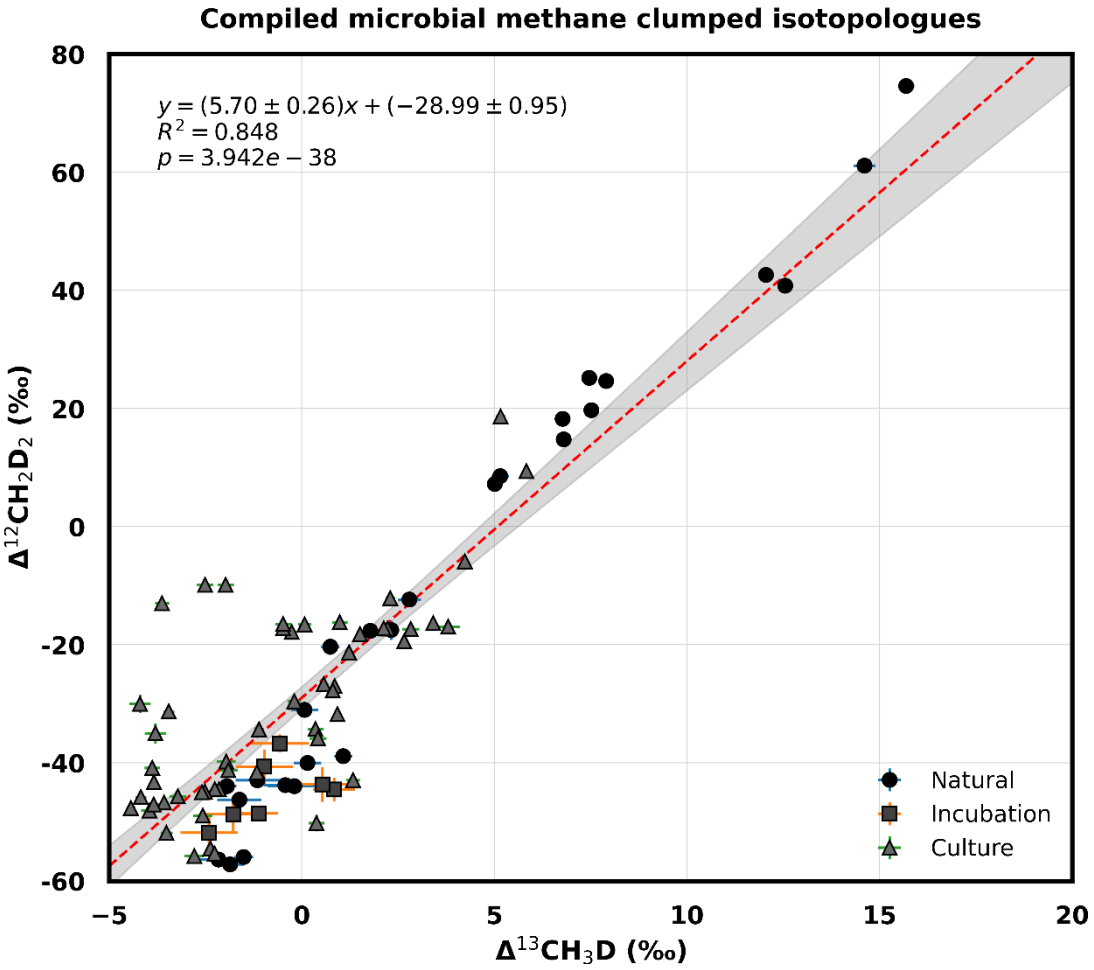

Figure C.5. **Compiled microbial methane clumped isotopologue ($\Delta^{13}CH_3D$ and $\Delta^{12}CH_2D_2$) data from published literature, with a linear fitting line** in red. Natural samples are in solid black circle. Lab incubation samples are in solid dark gray square. Lab pure culture samples are in solid light gray triangle. The gray band represents the 95% confidence interval of the linear fit.

In the derivation, we use this simple linear mapping to represent this relationship:

$$\Delta^{13}\mathrm{CH_3D}_{\text{wetland methane}} = f\left(\Delta^{12}\mathrm{CH_2D_2}_{\text{wetland methane}}\right) = (5.70 \pm 0.26) * \Delta^{12}\mathrm{CH_2D_2}_{\text{wetland methane}} - (28.99 \pm 0.95) \quad \text{(C.12)}$$

Following the derivation in the previous section, we can convert δ values to a normalized ratio

RC and RCD:

$$RC = \left(\frac{^{13}CH_4}{^{12}CH_4}\right)_{sample} \Big/ \left(\frac{^{13}CH_4}{^{12}CH_4}\right)_{reference} = \left(1 + \frac{\delta^{13}CH_4}{1000}\right) \quad (C.13)$$

$$RCD = \left(\frac{^{13}CH_3D}{^{12}CH_4}\right)_{sample} \Big/ \left(\frac{^{13}CH_3D}{^{12}CH_4}\right)_{reference} = \left(1 + \frac{\delta^{13}CH_3D}{1000}\right) \quad (C.14)$$

And the mixing relationships, followed by the same rearranging process:

$$RC_{mix} = (1 - f) * RC_{air} + f * RC_{source} \quad (C.15)$$

$$RCD_{mix} = (1 - f) * RCD_{air} + f * RCD_{source} \quad (C.16)$$

$$\frac{RC_{mix} - RC_{air}}{RC_{source} - RC_{air}} = \frac{RCD_{mix} - RCD_{air}}{RCD_{source} - RCD_{air}} \quad (C.17)$$

$$RCD_{source} - \left(\frac{RCD_{mix} - RCD_{air}}{RC_{mix} - RC_{air}}\right) * RC_{source} + \left(\frac{RCD_{mix} - RCD_{air}}{RC_{mix} - RC_{air}}\right) * RC_{air} - RCD_{air} = 0 \quad (C.18)$$

We can express $\Delta^{13}CH_3D$ with $\delta_{^{13}CH_4}$ and $\delta_{^{12}CH_3D}$:

$$\Delta^{13}CH_3D = (1 + \delta^{13}CH_3D) \Big/ (1 + \delta^{13}CH_4) * (1 + \delta^{12}CH_3D) - 1 \quad (C.19)$$

The RCD_{source} can be substituted, and the equation becomes:

$$\left(1 + \frac{\Delta^{13}CH_3D\ source}{1000}\right) * RC_{source} * RD_{source} - \left(\frac{RCD_{mix} - RCD_{air}}{RC_{mix} - RC_{air}}\right) * RC_{source} +$$

$$\left(\frac{RCD_{mix} - RCD_{air}}{RC_{mix} - RC_{air}}\right) * RC_{air} - RCD_{air} = 0 \quad (C.20)$$

And adopting the relationship to express $\Delta^{13}CH_3D_{source}$ with $\Delta^{12}CH_2D_{2\ source}$:

$$\left(1 + \frac{5.70 * \Delta^{12}CH_2D_{2\ wetland\ methane} - 28.99}{1000}\right) * RD_{source} * RC_{source} - \left(\frac{RCD_{mix} - RCD_{air}}{RC_{mix} - RC_{air}}\right) * RC_{source} +$$

$$\left(\frac{RCD_{mix} - RCD_{air}}{RC_{mix} - RC_{air}}\right) * RC_{air} - RCD_{air} = 0 \quad (C.21)$$

This is a linear equation, where RD_{source} has been calculated in the previous section. Therefore:

$$RC_{source} = \frac{RCD_{air} - \left(\frac{RCD_{mix} - RCD_{air}}{RC_{mix} - RC_{air}}\right) * RC_{air}}{\left(1 + \frac{5.70 * \Delta^{12}CH_2D_2\ \text{wetland methane} - 28.99}{1000}\right) * RD_{source} - \left(\frac{RCD_{mix} - RCD_{air}}{RC_{mix} - RC_{air}}\right)} \quad \text{(C.22)}$$

Up to this point, by assigning a range for the source's $\Delta^{12}CH_2D_2$, we have calculated the source's bulk carbon and hydrogen isotope compositions without using concentration data, listed in Table C.5 and plotted in Figure 5.7 in the main text.

Table C.5. **Derived bulk hydrogen and carbon isotope compositions and uncertainties of the source methane ($\delta^{12}CH_3D_{source}$ and $\delta^{13}CH_{4,\,source}$) for each wetland air sample**, with assumptions described in the text.

Date	Area	Location	$\delta^{12}CH_3D$	$2\sigma\delta D$	$\delta^{13}CH_4$	$2\sigma\delta^{13}C$
20220612	Jug Bay	Car Top Boat Launch	-299.2	24.3	-50.9	0.5
20220724	Patuxent	Wildlife Refuge	-300.5	24.3	-49.1	0.2
20220828	Jug Bay	Car Top Boat Launch	-305.7	24.0	-52.3	0.7
20220903	Jug Bay	Car Top Boat Launch	-296.0	24.5	-52.3	0.7
20220903	Patuxent	Swan Lane	-355.8	20.9	-49.0	0.2
20220904	Patuxent	Wootons Landing Trail	-278.0	25.2	-53.6	1.0
20220905	Patuxent	Queen Anne Bridge	-306.9	24.0	-51.1	0.5
20220921	Patuxent	River Cruise	-276.7	25.2	-48.4	0.1
20221010	Jug Bay	Car Top Boat Launch	-271.7	25.4	-51.1	0.5
20221025	Jug Bay	Car Top Boat Launch	-255.4	25.7	-50.2	0.4
20221104	Jug Bay	Car Top Boat Launch	-271.2	25.4	-49.1	0.2
20221207	Jug Bay	Car Top Boat Launch	-233.9	25.5	-48.8	0.1
20221229	Jug Bay	Car Top Boat Launch	-281.2	25.1	-52.7	0.8
20230415	Jug Bay	Car Top Boat Launch	-295.2	24.5	-50.4	0.4
20230507	Jug Bay	Car Top Boat Launch	-299.5	24.3	-51.0	0.5

Appendix D: Supplementary Information for Constraining the Clumped Isotope Budget of Atmospheric Methane using Firn Air Measurements

This Appendix is the supplementary information for a manuscript titled "*Constraining the clumped isotope budget of atmospheric methane using firn air measurements*", in preparation for submitting to *Science*.

Authors and Affiliations:

Malavika Sivan[1*†], Jiayang Sun[2,3*†], Patricia Martinerie[4], Maria Elena Popa[1], James Farquhar[2,5], Maarten Krol[1], Carina van der Veen[1], Bibhasvata Dasgupta[1], Mojhgan A. Haghnegahdar[2], Camilla Marie Jensen[6], Ji-Woong Yang[7], Johannes Freitag[8], Kévin Fourteau[9], Thomas Blunier[6], Thomas Röckmann[1]

[1]Institute for Marine and Atmospheric Research, Utrecht University; Utrecht, the Netherlands.

[2]Department of Geology, University of Maryland; College Park, Maryland 20742, USA.

[3]Air Resources Lab, National Oceanic and Atmospheric Administration; College Park, Maryland 20740, USA.

[4]Université Grenoble Alpes, CNRS, INRAE, IRD; Grenoble INP, IGE, 38000 Grenoble, France.

[5]Earth System Science Interdisciplinary Center, University of Maryland; College Park, Maryland 20740, USA.

[6]Physics of Ice Climate and Earth, Niels Bohr Institute, University of Copenhagen; Tagensvej 16, 2200, Copenhagen, Denmark.

[7]Laboratoire des Science du Climat et de l'Environnement, France.

[8]Alfred-Wegener-Institute; 27570 Bremerhaven, Germany.

[9]Géosciences Montpellier - CNRS, Université de Montpellier, France.

†These authors contributed equally to this work

*Corresponding authors. MS, JS. Email: m.sivan@uu.nl; jiayangs@umd.edu

D.1. Isotope Notation and Calculations

The bulk isotopic compositions of CH_4, denoted as $\delta^{13}C$ and δD, are defined as:

$$\delta^{13}C_{sample} = \frac{R^{13C}_{sample}}{R^{13C}_{VPDB}} - 1 \quad \text{(D.1)}$$

$$\delta D_{sample} = \frac{R^{D}_{sample}}{R^{D}_{VSMOW}} - 1 \quad \text{(D.2)}$$

where, R^{13C}_{sample} and R^{D}_{sample} are the $^{13}C/^{12}C$ and D/H ratios of the sample, $R^{13C}_{VPDB} = 0.011180$ is the $^{13}C/^{12}C$ ratio of the international carbon isotope standard Vienna Pee Dee Belemnite, and $R^{D}_{VSMOW} = 0.00015576$ is the D/H ratio of the international hydrogen isotope standard Vienna Standard Mean Ocean Water (Gonfiantini, 1978).

The clumped isotopic composition of CH_4 in a sample is expressed as $\Delta^{13}CH_3D$ and $\Delta^{12}CH_2D_2$. It quantifies the deviation of the measured ratio of clumped isotopologues compared to the ratio

that would be obtained if the heavy isotopes ^{13}C and D were distributed randomly across all isotopologues in the same sample:

$$\Delta^{13}CH_3D_{sample} = \frac{R_{sample}^{^{13}CH_3D}}{(4*R_{sample}^{^{13}C}*R_{sample}^{D})} - 1 \quad (D.3)$$

$$\Delta^{12}CH_2D_{2\,sample} = \frac{R_{sample}^{^{12}CH_2D_2}}{(6*(R_{sample}^{D})^2)} - 1 \quad (D.4)$$

$R_{sample}^{^{13}CH_3D}$ and $R_{sample}^{^{12}CH_2D_2}$ are the isotopologue ratios of $^{13}CH_3D/^{12}CH_4$ and $^{12}CH_2D_2/^{12}CH_4$ of the sample. $R_{sample}^{^{13}C}$ and R_{sample}^{D} are isotope ratios of $^{13}C/^{12}C$ and D/H of the sample. The denominators in the above formulae give the expected stochastic distribution of the heavier isotopes in a sample, where 4 and 6 are symmetry factors (Young, Kohl, Sherwood Lollar, et al., 2017).

In practice, we use the following approximate equations to simplify the calculation of $\Delta^{13}CH_3D$ and $\Delta^{12}CH_2D_2$ (Haghnegahdar et al., 2023):

$$\Delta^{13}CH_3D = \frac{1+\delta^{13}CH_3D}{(1+\delta^{13}CH_4)*(1+\delta^{12}CH_3D)} - 1 \quad (D.5)$$

$$\Delta^{12}CH_2D_2 = \frac{1+\delta^{12}CH_2D_2}{(1+\delta^{12}CH_3D)^2} - 1 \quad (D.6)$$

The approximation is done by using the bulk isotopologue ratios, $^{13}CH_4/^{12}CH_4$ instead of $^{13}C/^{12}C$ and $^{12}CH_3D/^{12}CH_4$ instead of D/H. The errors introduced by these approximations are much smaller than the analytical precision.

The Kinetic Isotope Effect (KIE) is the rate coefficient ratio for chemical reactions involving different isotopologues and can be calculated as

$$KIE = \frac{k_{light}}{k_{heavy}} \quad \text{(D.7)}$$

Where k_{light} and k_{heavy} are the reaction rate coefficients of the reactions involving lighter and heavier isotopologues, respectively.

D.2. Sampling and Measurement Methods

D.2.1. Firn Air Sampling

The firn air samples used for this study were collected at the East Greenland Ice-Core Project (EastGRIP) site in 2018. The firn air camp was located approximately 1 km east (upwind of the main wind direction) of the main EastGRIP camp to avoid possible contamination from activity at the camp. The firn air sampling is described in detail in Westhoff et al. (2023). In short, the firn hole was drilled to a certain depth, then the firn sampling assembly was inserted into the borehole. The assembly consisted of a 5 m long bladder and a set of three tubes, one to inflate the bladder and two to pump up air from two different "compartments" below the bladder. The two compartments are separated by a stainless-steel disc with the same width as the borehole. First, the bladder is inflated via the fill tube so that it tightly seals the borehole, and the bottom of the borehole is isolated from the overlying atmosphere. The purge line pulls air from the first compartment below the bladder to further eliminate possible contamination from the bladder. The sample line pumps up the sample air from the lower second compartment. Continuous online CO_2 and CH_4 concentration measurements were performed to verify that no

contamination with contemporary air occurred during the extraction procedure. After the contaminating air had been pumped away, firn air was collected into various containers for different analyses. The large volume samples required for CH_4 clumped isotope analysis were compressed into 5L volume aluminium cylinders using two compressors in series, a metal bellows compressor and a piston compressor. The RIX piston compressor can compress the air into the high-pressure cylinders up to a pressure of 140 bar, yielding up to 560 L of air for analysis. However, the average volume of these samples are 430 L, with some as low as 250 L.

D.2.2. Measurement Methods for Methane Mole Fraction and Isotope Analysis

After transport to the laboratory, the CH_4 mole fraction in the cylinders was measured using a G2301 greenhouse gas analyser (Picarro Inc.) at the Institute for Marine and Atmospheric Research (IMAU), Utrecht. The bulk isotopic composition ($\delta^{13}C$ and δD) was measured directly from the cylinders using a continuous flow isotope ratio mass spectrometry technique at IMAU (Menoud et al., 2021).

For the clumped isotopic composition measurements, CH_4 was extracted and purified by using up the remaining air in the cylinders. Air was pulled through a water trap with dry silica beads at room temperature, then into a large 6-loop U-trap filled with silica beads and cooled by liquid nitrogen, where CH_4, Kr, and remaining H_2O and CO_2 were trapped, but most N_2 and O_2 were pumped away. The large U-trap was then heated up to 150 °C, and the trapped gases were pulled through a small U-trap filled with HayeSep DB Porous Polymer Adsorbent cooled to liquid

nitrogen temperature, further removing N_2 and O_2 while retaining CH_4. Ultra-pure N_2 from a cylinder was used to flush the large U-trap, pushing and pulling the sample gas through the small U-trap to ensure complete transfer of CH_4. The small U-trap was then heated to -120°C using an ethanol slush bath and kept pumped for about 30 minutes, allowing further release of N_2 and O_2 without CH_4 breaking through the HayeSep DB column. The remaining gases, including CH_4, Kr, and traces of N_2, O_2, H_2O, and CO_2, were transferred to the purification line.

The sample was further purified using Gas Chromatography (GC) separation. Helium carrier gas was used to transfer the concentrated sample gas into a GC column packed with MolSieve 5A held at 56 °C. Under this condition, O_2, N_2, Kr, and CH_4 peaks eluted sequentially, so the CH_4 could be trapped selectively. Finally, the purified methane was frozen into a glass sample vial with silica beads, sealed, and transferred to the Panorama for measurement.

The clumped isotopologue signals were measured using the Nu Panorama mass spectrometer, at the University of Maryland, College Park. Panorama is a double-focusing, high-sensitivity, high-resolution gas-source electron-impact isotope-ratio mass spectrometer. It can achieve a mass resolving power (MRP) of ~55,000, sufficient to separate peaks of $^{13}CH_3D$ and $^{12}CH_2D_2$ from adjacent methane adducts $^{13}CH_5$ and $^{12}CH_4D$, which are all at mass 18. Each sample measurement is conducted using two measurement protocols. In the first run, $^{12}CH_3$ is measured on mass 15, $^{12}CH_4$ on mass 16, $^{13}CH_4$ on mass 17, and $^{13}CH_3D$ on mass 18. The second run, $^{12}CH_3$ on mass 15, $^{12}CH_4$ on mass 16, $^{12}CH_3D$ on mass 17, and $^{12}CH_2\ D_2$ on mass 18. Masses 15, 16, and 17 are collected by Faraday cups, while mass 18 is counted by an ion counter. Measurements are performed at balanced pressure and signal intensity between sample and

reference pairs. The signal intensity of mass 16 is controlled at 10^{-10} Amps, and signal intensities of mass 15, 17, and 18 are reported relative to mass 16. The detailed analytical process is described in Haghnegahdar et al. (2023).

Due to the firn air sample volume (usually around 500L, with some samples around 300L) being less than the ideal volume for Panorama measurements (800L), the limited sample amount forces measurements to be completed within a reduced counting time. This results in higher measurement uncertainties than other samples analyzed on the Panorama. For firn air samples, the 1SD for $\Delta^{13}CH_3D$ is between 0.2 - 0.4 ‰ with about 5 - 7 hours measurement time, and for $\Delta^{12}CH_2D_2$, it is between 1 - 1.5 ‰ with about 12 - 20 hours measurement time.

D.3. Modelling Trace Gas Transport in Firn

Gas transport in firn is primarily driven by molecular diffusion, with additional mixing components in the upper layers and possibly deep firn (Battle et al., 1996; Buizert et al., 2012; Martinerie et al., 2009; Trudinger et al., 2002). Gravity also induces an increased sinking of heavier molecules, resulting in isotopic fractionation. Forward firn models use atmospheric trends as an upper boundary condition to simulate trace gas profiles versus depth in firn. Here, we use a firn model (Witrant et al., 2012), which showed excellent performances in a firn model inter-comparison study (Buizert et al., 2012). A site-specific tuning is necessary to determine a firn diffusivity profile based on constraints provided by multiple reference gases for which both atmospheric trend and depth profile in firn are available (Buizert et al., 2012; Witrant et al.,

2012). Here, we use CH_4, SF_6, CFC-12, CFC-113, CH_3CCl_3, and HFC-134, as in (Westhoff et al., 2023).

Inverse modelling methods may be used to reconstruct atmospheric trends from depth profiles of tracers measured in firn air samples, but isotopic ratios require specific model developments as they are not mass-conservative (Sapart et al., 2013). Such specific development is not yet available for the clumped isotope Δ values. In a previous study of $\Delta^{18}O^{18}O$ (Yeung et al., 2019), a simplification based on the absence of atmospheric trend for $\delta^{18}O$ allowed the use of an approximate inverse approach, but this cannot be used for the clumped isotopes of CH_4. Thus, we implemented a forward firn model approach using as input harmonised CH_4 mole fraction and bulk isotope time series from 6 high northern latitude stations covering 3 decades (Dasgupta et al, in preparation). Emissions from the five main source sectors (fossil, pyrogenic, wetlands, waste, and agriculture, see definitions in Section D.5) were optimised to reproduce these measurements in a two-box inverse model (Section D.4, Dasgupta et al, in preparation). Clumped isotope time series were then generated by assigning clumped isotope source signatures to the sectors (Section D.5) and adjusting the KIEs so that the model output fits the observed trends. These time series are used as the surface constraint of the forward firn model, which then calculates vertical profiles of stable isotope composition in the firn that can be compared to the measurements (Figure 6.1). Similar approaches were used, for example, in Battle et al. (1996); Martinerie et al. (2009).

A graphical comparison of atmospheric trends with firn data can also be made by plotting firn data corrected for the effects of gravitational setting and diffusional fractionation versus mean

gas age (Trudinger et al., 2002). However, this introduces an additional uncertainty due to the significant width of the gas age distribution in deep firn (Figure D.1), represented as horizontal grey lines in Figures 6.2-6.4.

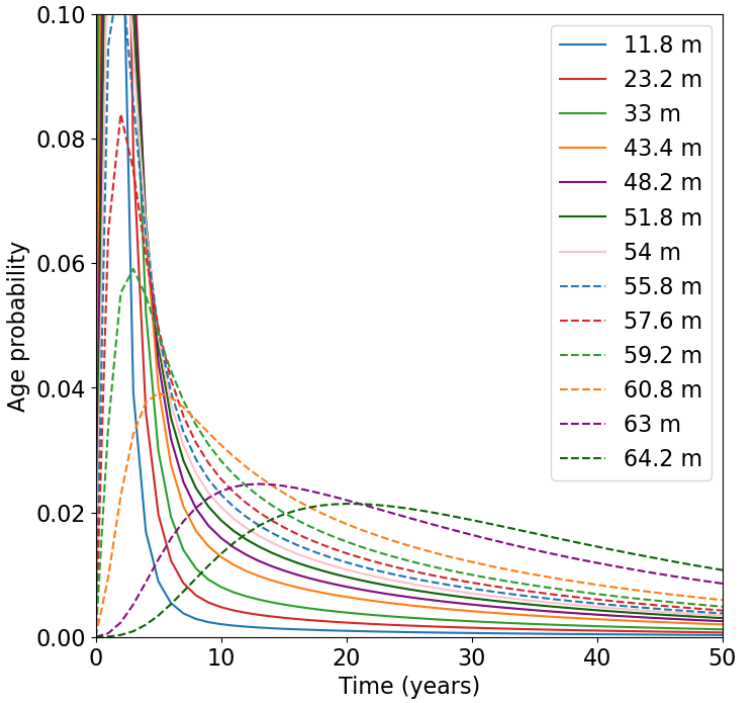

Figure D.1. **Modelled methane age distribution for the air samples collected at the EastGRIP site.** Each line represents the age probability distribution at the sampling depth given in the legend. The x-axis shows the time (in years) before 2018 (the firn drilling year).

The age distribution of CH_4 in the firn column is evaluated using a Green's function approach: a Dirac delta function is used as a surface constraint of the firn model. The resulting matrix versus time and depth represents the age probability distribution function. Due to the effect of gravitational settling, the sum of all age probabilities at a given depth is slightly different from one and a small correction was applied to normalise the sum of probabilities to one at each depth. Figure D.1 illustrates the wide and asymmetrical CH_4 age distributions in deep firn. For example, at the last measurement depth (64.2 m), the difference between mode age (age of maximum

probability) and mean age is 9 years. The age uncertainties are calculated as ± 1σ equivalent age width - the ages at which the sum of ages at a given depth reaches 15% and 85% cumulated probability.

Several firn model tests were performed to evaluate the robustness of our results. The large age widths shown in Figure D.1 imply that initialising the firn model simulations in 1980 may produce results that are still dependent on model initialisation in deep firn. Results from firn model simulations from 1980 are shown as green dashed lines in the left panels of Figure D.2. The best guess model simulations (black continuous lines in left panels of Figure D.2) were initialised in 1800 with an atmospheric CH_4 trend evaluated as described in (Buizert et al., 2012), and with constant isotopic ratios before 1980 (black continuous lines in right panels of Figure D.2). Simulations starting in 1980 (green dashed lines in Figure D.2) only significantly differ from the best guess model solution (black continuous lines in Figure D.2) and firn data near the lowest sampling depth and only for CH_4 and $\delta^{13}C$. Other isotopic ratios are not affected by the long-term CH_4 trend. Extrapolating trends also tested the impact of model initialisation in isotopic ratios with constant slopes before 1980 (black dashed lines in right panels of Figure D.2). This initial slope is unrealistically steep for $\Delta^{13}CH_3D$ but still only affects the model results below 60 m depth. Other isotope ratios are unaffected. A final input scenario test compares the results obtained with the two-box atmospheric isotope model (described in Section D.4) taking CH_4 trend in recent years and referencing the CH_4 trend before 1980 (green continuous lines in Figure D.2) to the best guess CH_4 trend for Greenland (black continuous lines in Figure D.2). The best guess trend includes seasonal variations in recent years, whereas the two-box model trends represent annual and hemispheric means. EGRIP CH_4 concentrations in firn (this study)

are slightly underestimated with the two-box model hemispheric methane trend, whereas only $\delta^{13}C$ is affected among isotopologues. Relative to its weak atmospheric variations (a few 0.1 ‰), $\delta^{13}C$ in firn is strongly affected by the steep CH_4 trend and fractionation in firn. The wiggle in the top ~40m of the firn for the reference simulation reflects the effect of seasonal variations of CH_4.

On the right panels of Figure D.2, original firn data (open circles) are compared with data corrected for the effects of gravitational settling and diffusional fractionation. Compared to atmospheric variations, the effect of firn processes is only important for $\delta^{13}C$. Hydrogen isotope and clumped isotopologue signals remain largely unaffected. The high sensitivity of $\delta^{13}C$ to firn processes in recent decades, driven by the strong trend in methane concentration and weak trend in $\delta^{13}C$, was a phenomenon already identified by Sapart et al. (2013).

Two additional tests in Figure D.2 were done to evaluate the impact of firn structure parameters on the behaviour of CH_4 isotopic ratios. For the first test (red line in left panels of Figure D.2), only CH_4 was used to constrain the firn diffusivity profile instead of six different gases. This results in a much less reliable diffusivity profile (Buizert et al., 2012; Witrant et al., 2012). Only $\delta^{13}C$, which is highly sensitive to firn processes, is significantly affected (Sapart et al., 2013). Another important parameter in deep firn is the open/closed porosity ratio, which is poorly constrained (Westhoff et al., 2023). The blue lines in the left panels of Figure D.2 illustrate the effect of using the modified Goujon open/closed porosity ratio described in Westhoff et al. (2023). The results obtained are nearly the same as the reference simulations (black continuous lines in left panels of Figure D.2).

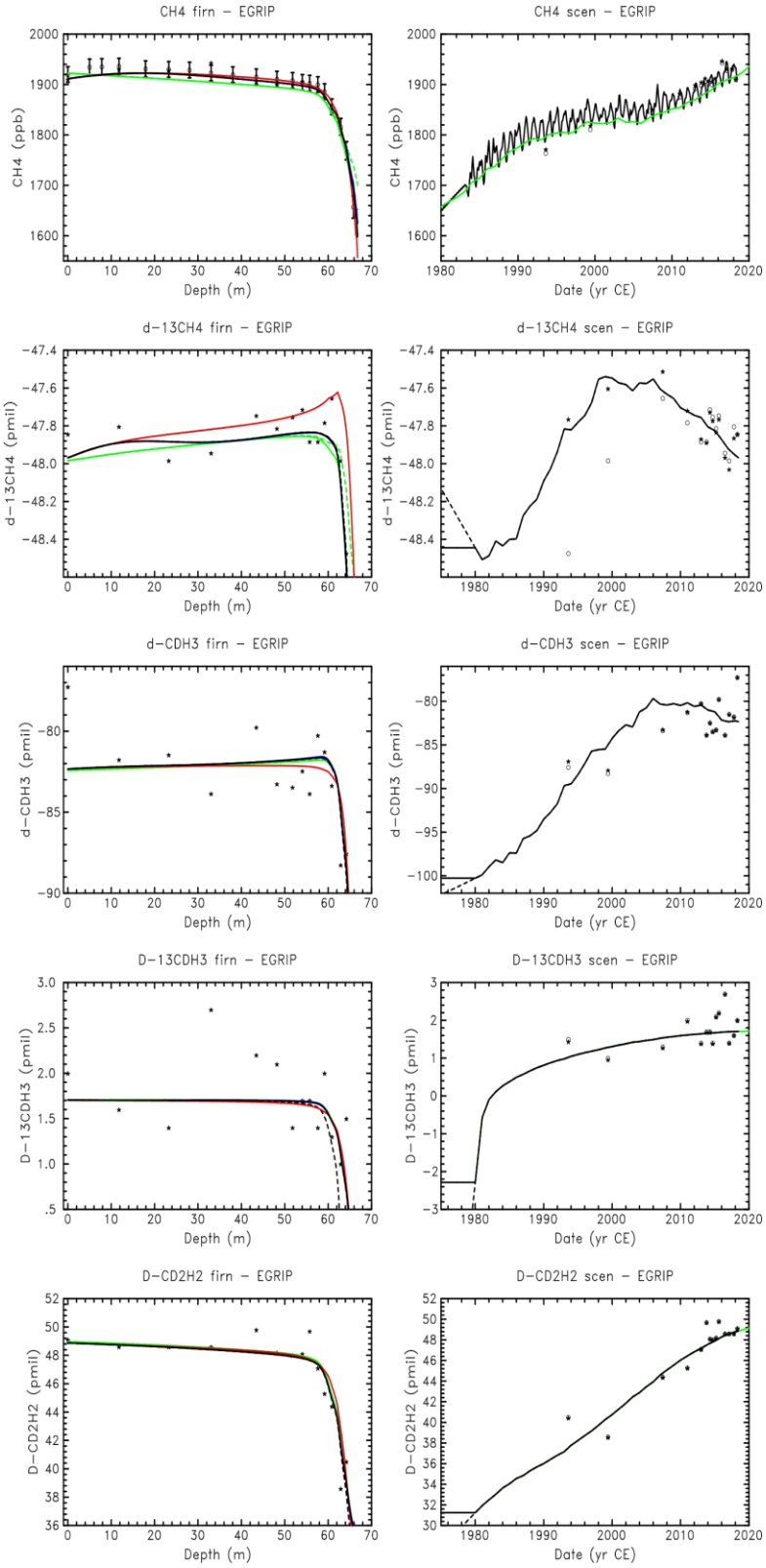
CH4 firn – EGRIP
CH4 (ppb)
Depth (m)
CH4 scen – EGRIP
CH4 (ppb)
Date (yr CE)
d–13CH4 firn – EGRIP
d–13CH4 (pmil)
Depth (m)
d–13CH4 scen – EGRIP
d–13CH4 (pmil)
Date (yr CE)
d–CDH3 firn – EGRIP
d–CDH3 (pmil)
Depth (m)
d–CDH3 scen – EGRIP
d–CDH3 (pmil)
Date (yr CE)
D–13CDH3 firn – EGRIP
D–13CDH3 (pmil)
Depth (m)
D–13CDH3 scen – EGRIP
D–13CDH3 (pmil)
Date (yr CE)
D–CD2H2 firn – EGRIP
D–CD2H2 (pmil)
Depth (m)
D–CD2H2 scen – EGRIP
D–CD2H2 (pmil)
Date (yr CE)

Figure D.2. **Firn model sensitivity tests.** Left panels: comparison of firn model results (lines) with firn data (symbols) versus depth. Measurements at Utrecht University on the samples presented in this study data are shown as stars, CH_4 concentrations measured at IGE and published in Westhoff et al. (2024) are shown as open circles with error bars. Reference simulations with atmospheric trends starting in 1800 shown as continuous black lines. results of sensitivity tests (described in the SI text) are shown as black dashed lines, green continuous and dashed lines, red and blue continuous lines. Right panels: comparison of atmospheric trends (lines) with firn data versus mean age uncorrected (open circles) and corrected (stars) for the effects of gravitational settling and diffusional fractionation in firn. Reference scenarios (starting in 1800) are shown as black continuous lines. The two-box model hemispheric annual scenario for CH_4 appears in green. Isotope ratio trends extrapolated with constant slopes before 1980 are shown as dashed black lines.

D.4. Two-box Model for Atmospheric Methane Isotopologues

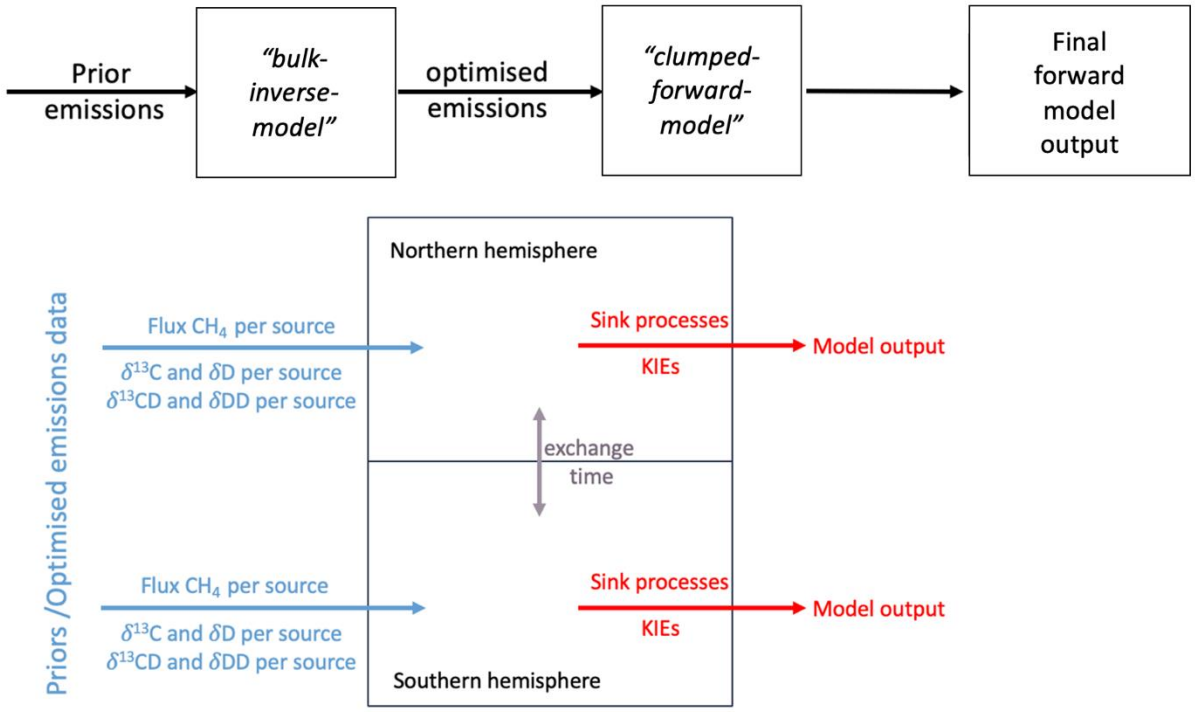

Figure D.3. **Schematic of the two-box atmosphere model used in this study**.

The clumped isotope forward model, '*clumped-forward-model*', developed for this work uses optimised source fluxes per source category (see model descriptions below, and source category

definitions in Section D.5) and optimised lifetime from an inverse modelling study (Dasgupta et al., 2024 (in prep)), hereafter referred to as the '*bulk-inverse-model*' that was constrained by the bulk isotopic composition from high latitude sites in both hemispheres over the past 30 years. The errors associated with the inverted source fluxes and lifetimes from the '*bulk-inverse-model*' are also incorporated into the '*clumped-forward-model*' and shown as the red-shaded region in Figure 6.2. Both the '*bulk-inverse-model*' and the '*clumped-forward-model*' have the same model framework as described below.

A two-box model is a simplified method used to study atmospheric CH_4 variability, dividing the atmosphere into NH and SH and balancing CH_4 sources and sinks to estimate its residence time (Figure D.3). It assumes that the CH_4 concentration in each hemisphere is well-mixed, with intra-hemispheric gradients applied to account for the differences between polar and hemispheric values, and it helps to understand the observed variations in atmospheric CH_4 concentrations and their sources (Sapart et al., 2012; Worden et al., 2017). Using input data for emission rates and isotopic compositions of different CH_4 source sectors, mixing between the hemispheres, and the removal by the sinks, it simulates the temporal evolution of the different isotopic composition of atmospheric CH_4 in NH and SH separately.

It is important to note that the model simulates individual isotopologue concentrations of $^{12}CH_4$, $^{13}CH_4$, $^{12}CH_3D$, $^{13}CH_3D$ and $^{12}CH_2D_2$. Thus, for each source flux, the total flux is separated into the individual isotopologue fluxes using the isotopic source signatures. Then, isotopologues are added, transported, and removed (by applying the KIE to simulate isotopologue-specific removal rate coefficients) in the model. The δ and Δ values are calculated again from the isotopologue

abundances. The model assumes an interhemispheric exchange time of 0.75 years, constrained by independent model studies with SF_6. The source categories of CH_4 are fossil, pyrogenic, wetlands, waste, and agriculture (see Section D.5), while the sinks include chemical reactions with OH and Cl radicals in the troposphere, stratosphere, and soil sinks.

The model defines the relationship of the observed mole fractions *y* (of each species) to the state vector *x* (emission sources in Tg/y) such as $y = F(x) \pm \sigma_\epsilon$, where σ_ϵ^2 is the observational error variance, defined as the sum of observations and model errors.

For the '*bulk-inverse-model*', the prior flux dataset was obtained from a combination of data from several inventories: Emissions Database for Global Atmospheric Research (EDGAR, (Janssens-Maenhout et al., 2019)), Atmospheric Chemistry and Climate Model Intercomparison (ACCMIP)/MACC and CityZen projects (MACCity), Global Fire Assimilation System (GFAS, (Kaiser et al., 2012)), Lund–Potsdam–Jena Wald Schnee und Landscaft version (LPJ-wsl, (Calle & Poulter, 2021)) and Trends in Precipitation and its Predictability (TIPP, (Nguyen et al., 2014)). The state vector *x* of emission rates was optimised by minimising the cost function:

$$J(x) = \frac{(x - x_{\text{prior}})^2}{(\sigma_a)^2} + \frac{(y - F(x))^2}{(\sigma_\epsilon)^2} \qquad \text{(D.8)}$$

with x_{prior} the a-priori emission rates in Tg/y, based on bottom-up inventories, and their variance σ_a^2. The inversion was performed to fit the atmospheric CH_4 mole fraction and bulk isotopic composition. This optimised inverted source fluxes and lifetimes output (Figure D.3) was used as the input for the '*clumped-forward-model*' to study the evolution of clumped isotopologues.

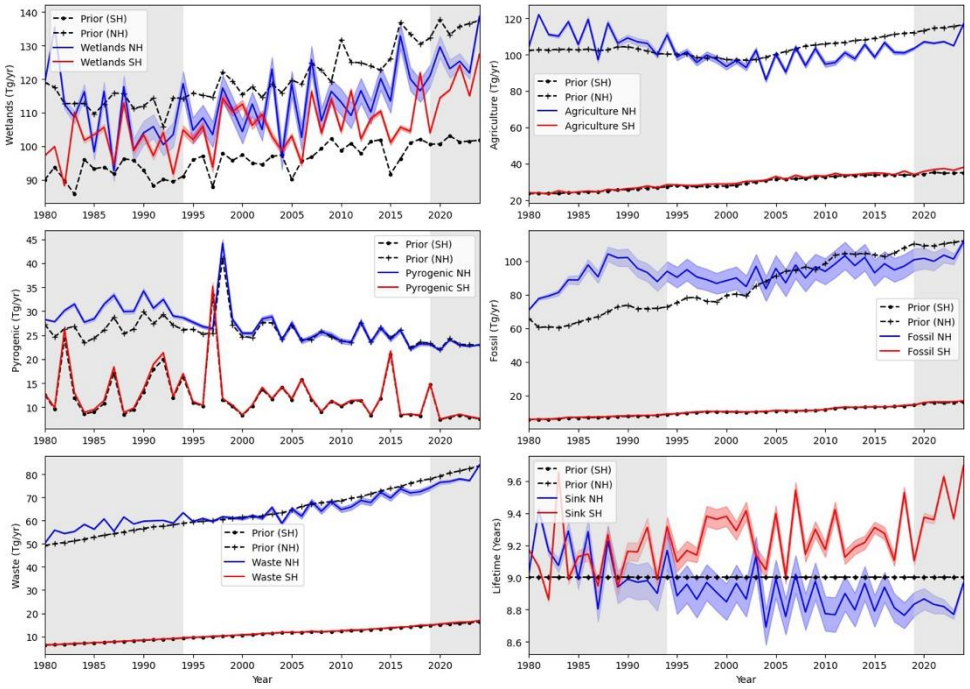

Figure D.4. **Prior and posterior emission rates with 3 sigma error bands.** Prior estimated rates from EDGAR, ACCMIP/MACCity, GFAS, LPJ-wsl and TIPP computed from the '*bulk-inverse-model*' are plotted in black dots for southern hemisphere and black plus symbols for northern hemisphere. Posterior emission rates are plotted in blue for northern hemisphere and in red for southern hemisphere.

D.5. Definition of Source Categories and Source Compositions

For our evaluation, CH_4 sources are separated into 5 categories: fossil, pyrogenic, wetlands, waste, and agriculture. Different inventories and scientific studies classify CH_4 emissions differently, so clarification is necessary. Generally, there are two overlapping classification methods: process-based and activity-based. The process-based method categorises CH_4 as microbial, thermogenic, or abiotic (pyrogenic). The activity-based method classifies CH_4 emissions as anthropogenic or natural and may further specify them by geographic location or economic activity, such as fossil fuel-related, agriculture, waste, biomass burning, wetlands, waters, geological sources, oceans, termites, wild animals, and permafrost. Each specific CH_4

source category can be further subdivided. For example, fossil fuel-related emissions may come from oil, natural gas, and coal and in inventories, they are further categorised into production, gathering, processing, transmission and storage, local distribution, oil refining, and transportation (e.g., (Alvarez et al., 2018)). Global CH_4 emission inventories typically use this classification method: the Global Carbon Project (GCP) (Saunois et al., 2020), EDGAR (Crippa et al., 2020), and the Intergovernmental Panel on Climate Change (IPCC) Assessment Report (IPCC AR6) (IPCC, 2021). GCP focuses specifically on CH_4, whereas IPCC and EDGAR cover all greenhouse gases, leading to slight differences in classification but generally consistent categories. Forward models often use a combination of classifications from large databases. For example, the reference Lan et al. (2021) primarily relied on EDGAR 4.3. whereas references East et al. (2024); Janssens-Maenhout et al. (2019) are based on the GCP.

We employed a mixed definition approach where fossil, wetlands, waste, and agriculture sources follow the definitions in GCP (Saunois et al., 2020), while the pyrogenic category represents the remaining sources. When using EDGAR and IPCC datasets, re-categorisation is necessary. The following rules were followed:

We classify the IPCC-defined category "1 Energy" as *fossil*, although "1A Fuel Combustion Activities" might fit under *pyrogenic*. IPCC categories "2 Industrial Processes and Product Use," "3C1 Biomass Burning," and "5 Other" are categorised as *pyrogenic*, although some microbial emissions (e.g., termites, oceans) are also included in "5 Other". Categories "3B4 Wetlands," "3B1 Forest Land," and "3B3 Grassland," along with any residual fluxes, are categorized under *wetlands*. This adjustment is necessary because IPCC and EDGAR focus on anthropogenic

emissions. "3A2 Manure Management" and "4 Waste" are classified as *waste*, while "3A1 Enteric Fermentation" and "3B2 Cropland" (mainly rice) fall under *agriculture*. For detailed definitions of specific sources, such as what type of land can be defined as wetlands, we refer to the IPCC guidelines (IPCC, 2006, 2019), which are beyond our discussion scope.

Based on our current understanding of fossil, pyrogenic, wetlands, waste, and agriculture sources, we assigned $\delta^{13}C$, δD, $\Delta^{13}CH_3D$ and $\Delta^{12}CH_2D_2$ values to each source. $\delta^{13}C$ and δD values were differentiated between the NH and SH, while a global value was assigned for $\Delta^{13}CH_3D$ and $\Delta^{12}CH_2D_2$.

The isotopic signatures, $\delta^{13}C$ and δD, in CH_4 are specific to the type of emission. The initial values are assigned to each emission category. Most values are averages derived from the global isotope database (Menoud et al., 2022; Sherwood et al., 2017) and weighted by emission rates used as prior in the model. In the case of fossil fuels and biomass burning, the $\delta^{13}C$ values were taken from Schwietzke et al. (2016). We also used literature values for the $\delta^{13}C$-CH_4 from enteric fermentation, based on Chang et al. (2021). The isotopic signature of wetland and freshwater CH_4 is latitude-dependent (Brownlow et al., 2017; Ganesan et al., 2018). Therefore, we used averaged hemispheric $\delta^{13}C$ and δD values computed with a global model by Stell et al. (2021), based on up-to-date observations of CH_4 isotopic composition from sites at different latitudes. Several sensitivity tests were run on the '*bulk-inverse-model*', varying input parameters such as the source isotope signatures obtained from literature, and evaluating the posterior results (Dasgupta et al., 2024 (in prep)). Based on these simulations, some of the source signatures were

revised to optimise the model output, i.e., to match between posterior outputs and atmospheric observations. The optimised hemisphere-specific source signatures are given in Table D.1.

For the source signatures of the clumped isotopologues, we compiled currently published CH_4 clumped isotopologue measurements (Dong et al., 2021; Douglas et al., 2020; Douglas et al., 2017; Eldridge et al., 2019; Giunta et al., 2022; Giunta et al., 2019; Gonzalez et al., 2019; Gruen et al., 2018; Haghnegahdar et al., 2024; Haghnegahdar et al., 2023; Krause et al., 2022; Labidi et al., 2020; Lalk et al., 2024; Liu, Harris, et al., 2023; Liu, Treude, et al., 2023; Ono et al., 2021; Ono et al., 2014; Rhim & Ono, 2022; Shuai, Douglas, et al., 2018; Shuai, Etiope, et al., 2018; Stolper, Lawson, et al., 2014; Stolper et al., 2015; Stolper, Sessions, et al., 2014; Sun, Haghnegahdar, et al., 2025; Sun, Magen, et al., 2025; Taenzer et al., 2020; Thiagarajan et al., 2020; Wang et al., 2015; Wang et al., 2018; Wang et al., 2016; Young, Kohl, Sherwood Lollar, et al., 2017; Young et al., 2016; Zhang, Snyder, et al., 2021). Samples from oil and natural gas well sites, hydrothermal vents, seeps, steam vents, residential natural gas, and gas hydrates are categorised as fossil-related, regardless of whether clumped isotopologues indicate microbial or thermogenic origins or microbial alteration. Samples from vehicle exhaust, biomass burning, lab pyrolysis experiments, and lab coal heating experiments are considered pyrogenic. Natural samples from ponds, swamps, permafrost, lake and ocean sediments, lake bubble ebullition, wetlands, and derived values from wetland air plumes, along with lab pure-culture methanogenesis, aerobic oxidation of methane (AOM), and anaerobic oxidation of CH_4 (AeOM), are categorised as wetlands. Samples from cow rumen and rice paddies are categorised as agriculture. Landfill compositions derived from landfill plume air samples are used for waste. Measurements for each category were averaged or weighted.

Due to the disproportionate number of lab synthetic samples in the pyrogenic category, averages for natural and lab samples were calculated separately and then averaged at an 80:20 ratio. This method also applies to the wetland category, with a 75:25 ratio for natural to lab samples. Given the high number of AOM and AeOM samples in the wetland category, which are typically low in concentration and trapped deep in the sediment in natural conditions, they likely do not represent the true emission signals from wetlands. Therefore, we adjusted the ratio of methanogenesis-produced CH_4 to oxidised CH_4 to 85:15. The agriculture and waste categories had few measurements, possibly lacking representativeness. While these classifications, weightings, and final values are limited, they represent our best understanding of CH_4 clumped isotopologues.

Some studies only measured Δ_{18}, which is a combination of $^{13}CH_3D$ and $^{12}CH_2D_2$, due to the limitations of the mass spectrometer resolution. These Δ_{18} values were approximated as $\Delta^{13}CH_3D$, as $^{12}CH_2D_2$ abundance is two orders of magnitude lower than $^{13}CH_3D$, and its influence should be negligible. Additionally, some studies only measured $\Delta^{13}CH_3D$ using laser spectrometers, thus lacking $\Delta^{12}CH_2D_2$ values. Systematic differences may exist between different labs and instruments, but these variations are not considered in this study.

Table D.4 shows the final average clumped isotope source signatures per category. Fossil CH_4 has $\Delta^{13}CH_3D$ = 3.57 ‰ and $\Delta^{12}CH_2D_2$ = 7.58 ‰, slightly below the thermodynamic equilibrium line. This is because fossil methane includes both thermogenic and microbial methane (e.g., (Young, Kohl, Sherwood Lollar, et al., 2017)). Pyrogenic methane is assigned values of $\Delta^{13}CH_3D$ = 1.19 ‰ and $\Delta^{12}CH_2D_2$ = -9.49 ‰, consistent with biomass burning and lab pyrolysis

measurements, which have shown slightly anti-clumping signals in $\Delta^{12}CH_2D_2$ (Dong et al., 2021; Haghnegahdar et al., 2023).Wetland CH_4 is assigned $\Delta^{13}CH_3D$ = 1.74 ‰ and $\Delta^{12}CH_2D_2$ = -36 ‰, agriculture CH_4 is assigned $\Delta^{13}CH_3D$ = -0.16 ‰ and $\Delta^{12}CH_2D_2$ = -39.78 ‰, and waste CH_4 is assigned $\Delta^{13}CH_3D$ = 2.26 ‰ and $\Delta^{12}CH_2D_2$ = -27.15 ‰. These results align with the understanding that microbial methanogenesis produces strong anti-clumping in $\Delta^{12}CH_2D_2$ (Gruen et al., 2018; Young, Kohl, Sherwood Lollar, et al., 2017) and that waste CH_4, having undergone more oxidation, shows less anti-clumping (Giunta et al., 2022; Liu, Treude, et al., 2023; Sun et al., in revision). The $\Delta^{13}CH_3D$ and $\Delta^{12}CH_2D_2$ of the total source mixture using the above signatures is around 2.8 ‰ for $\Delta^{13}CH_3D$ and -12.5 ‰ for $\Delta^{12}CH_2D_2$.

Table D.1. **Isotopic signatures of $\delta^{13}C$, δD, and designated $\Delta^{13}CH_3D$ and $\Delta^{12}CH_2D_2$ of the source categories and the total sink KIEs** used as the input for the '*clumped-forward-model*' for the optimised case. The values of $\delta^{13}C$ and δD corresponding to NH and SH are given separately.

Sources/Sinks	$\delta^{13}C$ SH (‰)	$\delta^{13}C$ NH (‰)	δD SH (‰)	δD NH (‰)	$\Delta^{13}CH_3D$ (‰)	$\Delta^{12}CH_2D_2$ (‰)
Wetlands	-58.3	-63.9	-297.0	-339.0	1.8	-36.0
Agriculture	-64.0	-63.0	-302.0	-309.0	-0.2	-39.8
Waste	-54.5	-54.5	-292.2	-292.2	2.5	-15.0
Fossil	-44.0	-44.0	-192.0	-194.0	3.6	7.6
Pyrogenic	-22.3	-22.4	-213.0	-183.0	1.2	-9.5

D.6. Measurement Results and Model Outputs

Table D.2. **Sampling depth, measured CH_4 mole fraction, $\delta^{13}C$, δD, $\Delta^{13}CH_3D$ and $\Delta^{12}CH_2D_2$ of the firn samples presented in this study**.

Sample ID	Volume (L)	Depth (m)	CH_4 mole fraction (ppb)	$\delta^{13}C$ (‰)	δD (‰)	$\Delta^{13}CH_3D$ (‰)	$\Delta^{12}CH_2D_2$ (‰)
1	350	0	1910.0	-47.69	-79.2	2.0 (±0.4)	49.1 (±1.1)
3	465	11.78	1931.4	-47.65	-83.7	1.6 (±0.2)	48.6 (±1.1)
6	535	23.25	1930.8	-47.83	-83.4	1.4 (±0.2)	48.6 (±1.0)
18	280	33.01	1947.0	-47.79	-85.8	2.7 (±0.3)	48.6 (±1.3)
16	350	43.44	1912.2	-47.61	-81.7	2.2 (±0.3)	49.8 (±1.3)
13	560	48.20	1905.8	-47.66	-85.2	2.1 (±0.2)	48.2 (±1.2)
12	315	51.80	1907.2	-47.60	-85.4	1.4 (±0.3)	48.0 (±1.2)
11	250	54.07	1912.5	-47.56	-84.4	1.7 (±0.4)	48.1 (±1.5)
14	425	55.75	1904.7	-47.73	-85.8	1.7 (±0.3)	49.7 (±1.2)
15	425	57.65	1898.9	-47.73	-82.2	1.4 (±0.3)	47.1 (±1.0)
10	555	59.18	1882.1	-47.63	-83.2	2.0 (±0.2)	45.3 (±1.0)
9	475	60.86	1851.2	-47.50	-85.3	1.3 (±0.2)	44.4 (±1.1)
8	525	62.92	1818.4	-47.83	-90.2	1.0 (±0.2)	38.6 (±1.1)
7	500	64.22	1771.4	-48.32	-89.5	1.5 (±0.3)	40.5 (±1.0)

Table D.3. **Mean age, age at 15% and 85% of the age distribution, and the diffusion – and gravitation** - corrected isotopic signatures using the CH_4 EastGRIP forward model as described above.

Sample	depth	Mean year	age at 15%	age at 85%	Corrected $\delta^{13}C$ (‰)	Corrected δD (‰)	Corrected $\Delta^{13}CH_3D$ (‰)	Corrected $\Delta^{12}CH_2D_2$ (‰)
1	0	2018.3	n.a.	n.a.	-47.69	-79.2	2.0 (±0.4)	49.1 (±1.1)
3	11.78	2017.8	2018.4	2017.5	-47.71	-83.7	1.6 (±0.2)	48.6 (±1.1)
6	23.25	2017.1	2018.2	2016.2	-47.876	-83.4	1.4 (±0.2)	48.6 (±1.0)
18	33.01	2016.5	2018.1	2015.2	-47.813	-85.8	2.7 (±0.3)	48.6 (±1.3)
16	43.44	2015.6	2017.8	2014	-47.629	-81.7	2.2 (±0.3)	49.8 (±1.3)
13	48.2	2015.2	2017.6	2013.3	-47.68	-85.2	2.1 (±0.2)	48.2 (±1.2)
12	51.8	2014.7	2017.4	2012.6	-47.619	-85.4	1.4 (±0.3)	48.0 (±1.2)
11	54.07	2014.3	2017.2	2012	-47.574	-84.4	1.7 (±0.4)	48.1 (±1.5)
14	55.75	2013.8	2017.1	2011.2	-47.735	-85.8	1.7 (±0.3)	49.7 (±1.2)
15	57.65	2013	2016.8	2009.8	-47.715	-82.2	1.4 (±0.3)	47.1 (±1.0)
10	59.18	2011	2016.1	2006.4	-47.566	-83.1	2.0 (±0.2)	45.3 (±1.0)
9	60.86	2007.4	2014.5	2000.3	-47.358	-85.2	1.3 (±0.2)	44.4 (±1.1)
8	62.92	1999.4	2010.1	1988.3	-47.449	-89.8	1.0 (±0.2)	38.6 (±1.1)
7	64.22	1993.6	2006	1980.8	-47.611	-88.8	1.4 (±0.3)	(±1.0)

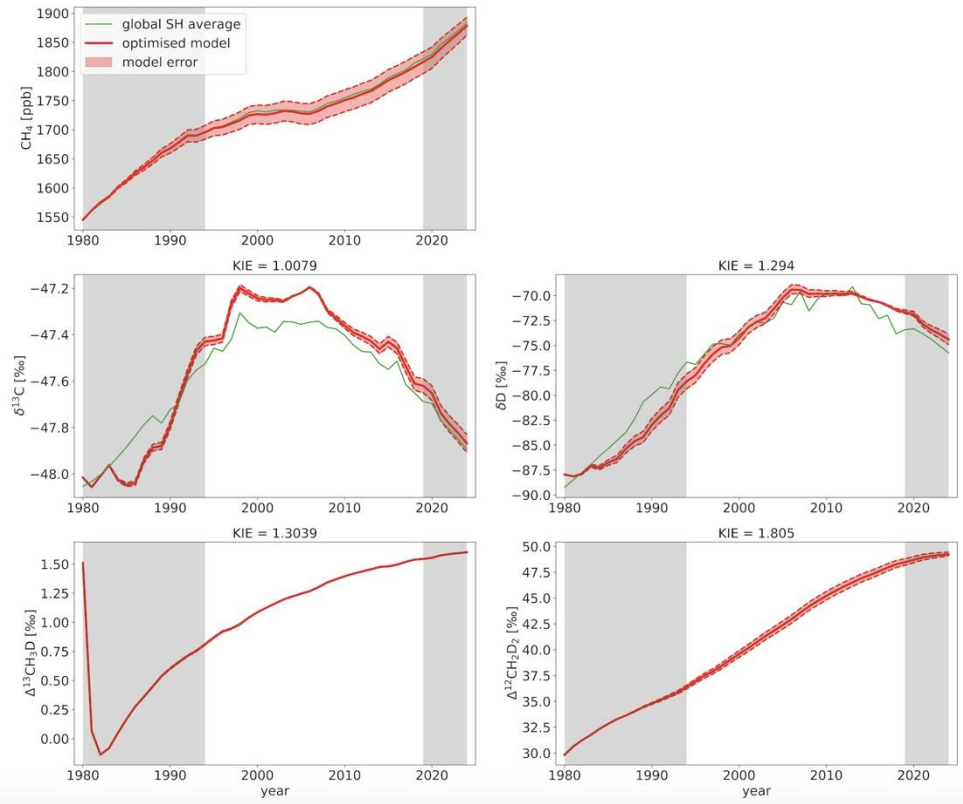

Figure D.5. **Model output of the two-box forward model.** Optimised fluxes are plotted in red for **(A)** CH_4 mole fraction, **(B)** $\delta^{13}C$, **(C)** δD, **(D)** $\Delta^{13}CH_3D$, and **(E)** $\Delta^{12}CH_2D_2$. The red-shaded areas show the errors associated with the inverted fluxes. The green lines in (A)-(C) represent the SH averages calculated from NOAA GML monitoring stations. The KIEs are given as panel titles. The grey-shaded areas mark the spin-up and spin-down periods.

D.7. Source-Sink Relationship for the Clumped Isotopologues

We varied the isotopic signatures of $\Delta^{13}CH_3D$ and $\Delta^{12}CH_2D_2$ for the different source categories over a relatively wide range and determined the KIE for each corresponding assumed source signatures, for which the modelled trend in $\Delta^{13}CH_3D$ and $\Delta^{12}CH_2D_2$ match best with the observations. The results show a tight relationship between the clumped isotope source signatures and the KIEs. The lower limit of the source range assumes the KIEs from ab initio calculations (Haghnegahdar et al., 2017), which can only be reconciled with the measurements

when we assume a very depleted $\Delta^{12}CH_2D_2$ source signature of approximately -50 ‰ (light blue dot in Figure 6.3 and Figure D.5). This is virtually impossible to reconcile with the available observations since individual microbial sources would need to be as low as -85 ‰ to close the measured ambient air CH_4 clumped isotope budget. As the upper limit, we use the clumped isotopic composition of sources at thermodynamic equilibrium (4 ‰ for $\Delta^{13}CH_3D$ and 20 ‰ for $\Delta^{12}CH_2D_2$), as predicted in Haghnegahdar et al. (2017) (dark blue dot in Figure D.3 and Figure D.5). The most probable range for $\Delta^{12}CH_2D_2$ of the source mixture (-21 ‰ to -4 ‰) highlighted in Figure 6.3B (shaded yellow) is calculated using the most common reported range of compositions measured for the microbial samples to date, -50 ‰ to -20 ‰ for $\Delta^{12}CH_2D_2$. The shaded region in Figure D.6B shows the most probable range for the total source $\Delta^{13}CH_3D$ (1.8 ‰ to 3 ‰), which is calculated assuming that most of the non-equilibrium signatures measured for sources are around 0 to 2 ‰.

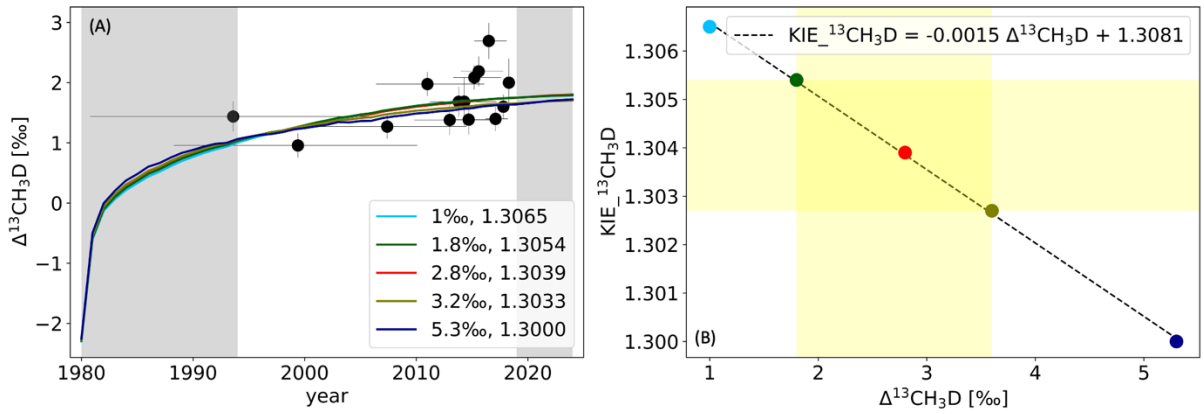

Figure D.6. **The mutual constraint between the sink reaction KIE and the total source $\Delta^{13}CH_3D$.** Panel **(A)**: Model outputs of $\Delta^{13}CH_3D$ for different combinations of total source $\Delta^{13}CH_3D$ signatures and sink KIEs that fit the observed trends from the firn air measurements well when used in the two-box model. Each combination is distinguished by a colour, as given in the legend (source mixture composition, sink KIE). The black circles represent the firn air samples measured in this study. Panel **(B)** shows the linear relationship between the simulated total source $\Delta^{13}CH_3D$ signatures (x-axis) and sink KIEs (y-axis). The vertically shaded yellow region highlights the most probable range of values for $\Delta^{13}CH_3D$ deduced from existing datasets, and the horizontal, yellow-shaded region shows the required range of KIE values to fit the observation data.

D.8. Sensitivity Analysis: Source Mixture

The sensitivity of the CH_4 mole fraction and isotopic composition to the contributions from individual source categories was investigated by keeping one source flux constant over time (as in 1980) and keeping the optimised fluxes for others unchanged. This was done for all the five source categories. The optimised lifetimes were used in all calculations. Figure D.7 shows that these tests change the CH_4 mole fraction in the atmosphere, which is expected if increases in one source category are excluded. The different scenarios also lead to clear changes in $\delta^{13}C$, especially between constant fossil and other scenarios. The changes in δD are much smaller, but still significant and distinguishable with the currently available analytical precision. However, the difference in $\Delta^{13}CH_3D$ and $\Delta^{12}CH_2D_2$ between these different scenarios is small, and within

the current achievable measurement uncertainty. This test shows that atmospheric methane clumped isotopologue signals are not sensitive to the change of flux of a specific source, when the total source flux is optimized.

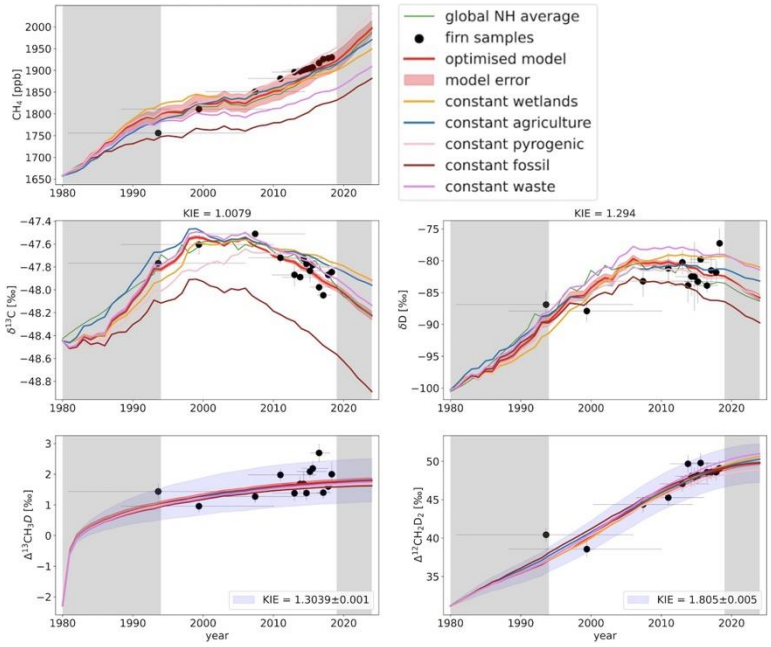

Figure D.7. **Results of model sensitivity tests to individual source contributions.** Outputs of **(A)** CH_4 mole fraction, **(B)** $\delta^{13}C$, **(C)** δD, **(D)** $\Delta^{13}CH_3D$, and **(E)** $\Delta^{12}CH_2D_2$ are plotted. The colours represent the scenarios when one of the sources is kept constant from 1980-2024, as given in the legend. The green line represents the high northern latitude average values compiled from 6 high northern latitude stations over the past 30 years (see Section D.4, Dasgupta et al., in prep). The solid black circles represent the firn samples measured in this study.

We did another sensitivity test on the wetland-fossil fuel sources pair, by keeping one source flux constant and changing the flux of the other source to still match the measured atmospheric CH_4 mole fractions. Figure D.8 shows that $\delta^{13}C$ and δD, react most strongly to these changes. $\Delta^{12}CH_3D$ and $\Delta^{12}CH_2D_2$, on the other hand, show only minor changes, and the differences are within the measurement error.

Both the two sensitivity tests show that the measured 10 ‰ change in $\Delta^{12}CH_2D_2$ cannot be explained solely by the change in the individual source flux from 1980.

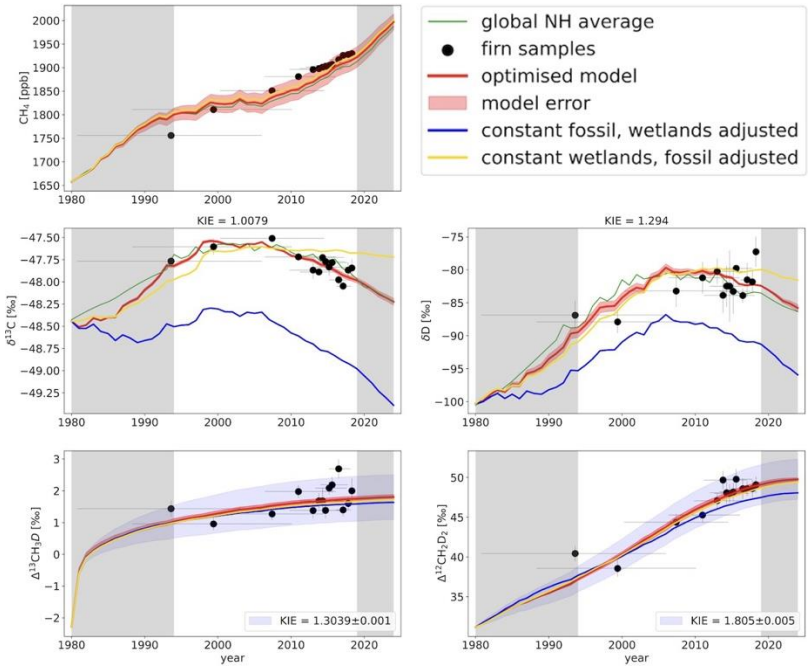

Figure D.8. **Results of model sensitivity tests of wetland-fossil fuel source category fluxes.** Outputs of **(A)** CH_4 mole fraction, **(B)** $\delta^{13}C$, **(C)** δD, **(D)** $\Delta^{13}CH_3D$, and **(E)** $\Delta^{12}CH_2D_2$ are plotted. The colours represent the scenarios when fossil or wetland emission is kept constant but the other category emission is adjusted to fit the real atmospheric methane mole fraction. The green line represents the high northern latitude average values compiled from 6 high northern latitude stations over the past 30 years (see Section D.4, Dasgupta et al., in prep). The solid black circles represent the firn samples measured in this study.

D.9. Future Emission Scenarios

We evaluate the CH_4 mole fraction and the isotopic composition for several future emission scenarios. The *constant sources* scenario kept flux of each source between 2024 and 2100 at the 2024 levels (solid red line in Figure 6.4).

The *emission mitigation* scenario (solid yellow line in Figure 6.4) shows the evolution of CH_4 mole fraction and isotope signatures for a 50 % reduction of fossil fuel emissions and 10 % of agriculture (including ruminants) emissions by 2030, assuming a linear decrease per year from 2024 to 2030. This scenario aligns with what the Global Methane Pledge (*Global Methane Pledge*) promotes. In this case, we assume that the fluxes stay constant after 2030.

The *removal* scenario (dashed red line in Figure 6.4) brings down the mole fraction to 1500 ppb in 2100 by keeping the source fluxes constant as of 2024, and by decreasing the total lifetime of atmospheric CH_4 by 0.5% every year.

The *unabated increase* scenario (dashed purple line in Figure 6.4) assumes an increase of the main anthropogenic (fossil and agriculture) sources by 1 % every year from 2024 till 2100. In this scenario, the CH_4 mole fraction reached about 3000 ppb in 2100.

We also used the IPCC-defined Representative Concentration Pathways (RCPs), with future emission fluxes from the IPCC AR6 Scenarios Database (Byers et al., 2022; Intergovernmental Panel on Climate, 2023; Riahi et al., 2023). We selected five SSPx-Baseline scenarios run by the IMAGE3.0.1 (Stehfest et al., 2014) model, which provides methane emissions specific to source categories. SSP represents Shared Socio-Economic Pathways, with higher numbers indicating higher target radiative forcing levels by 2100. To align with our model, we reclassified IPCC's future emission inventories according to our source categories, as explained in Section D.5. The emission fluxes were scaled to match our model's 2015 emission fluxes for each source, using cubic interpolation to convert five-year flux estimations to annual values. The emissions were

then adjusted to match the 2024 emission fluxes in our model. Finally, each category's total emissions were divided into SH and NH based on the 2015 NH/SH emission ratio. This process ensures that RCP inputs fit the observational data up to 2024 while retaining the temporal evolution of the RCP estimates for future emission trends. We keep the wetlands emissions constant from 2024 to 2100 in all the scenarios. The evolution of CH_4 mole fraction, $\delta^{13}C$, δD, $\Delta^{13}CH_3D$ and $\Delta^{12}CH_2D_2$ resulting from the emission time series of SSP1 and SSP5 are shown in Figure 6.4, the other scenarios are shown in Figure D.9.

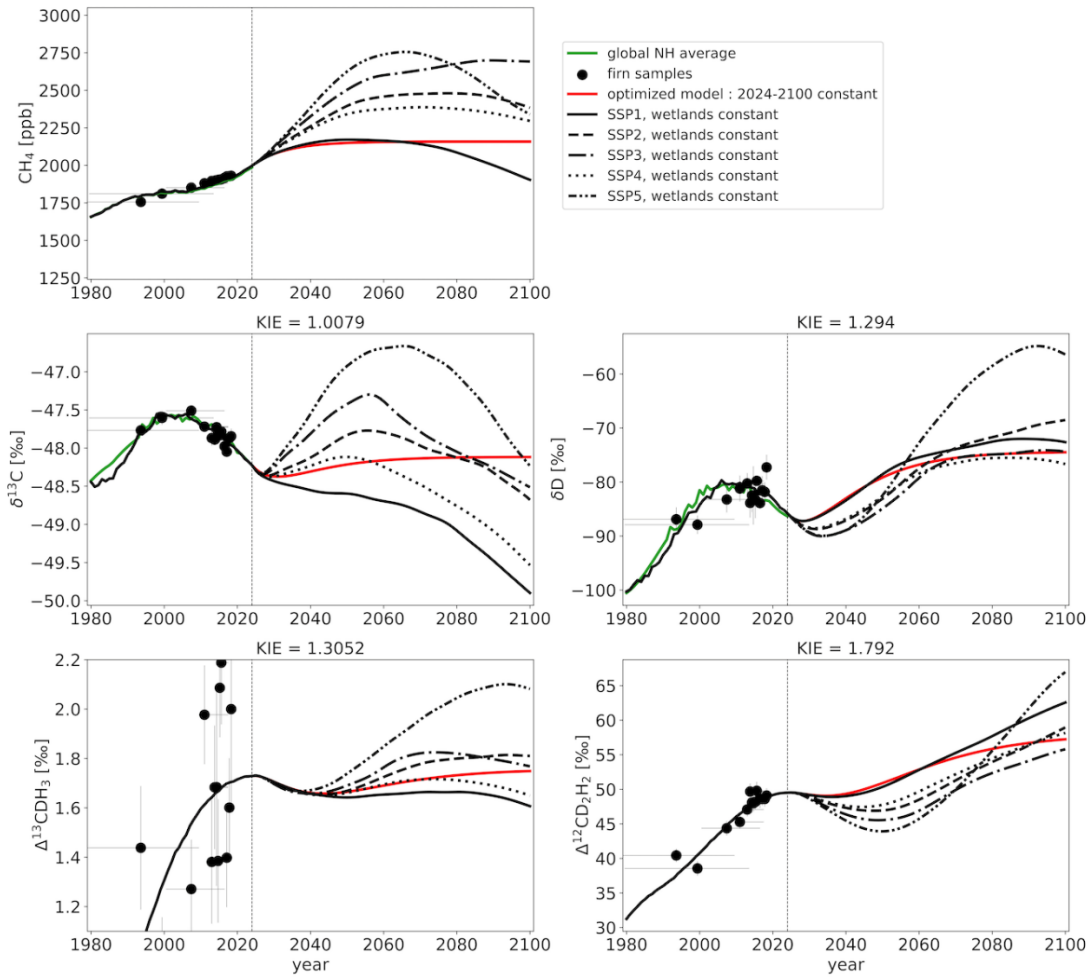

Figure D.9. **Results of model simulation with future emission scenarios.** Simulated results of **(A)** CH_4 mole fraction, **(B)** $\delta^{13}C$, **(C)** δD, **(D)** $\Delta^{13}CH_3D$ and **(E)** $\Delta^{12}CH_2D_2$ using the five IPCC SSPx scenarios as given in the legend as input for the two-box model are plotted.

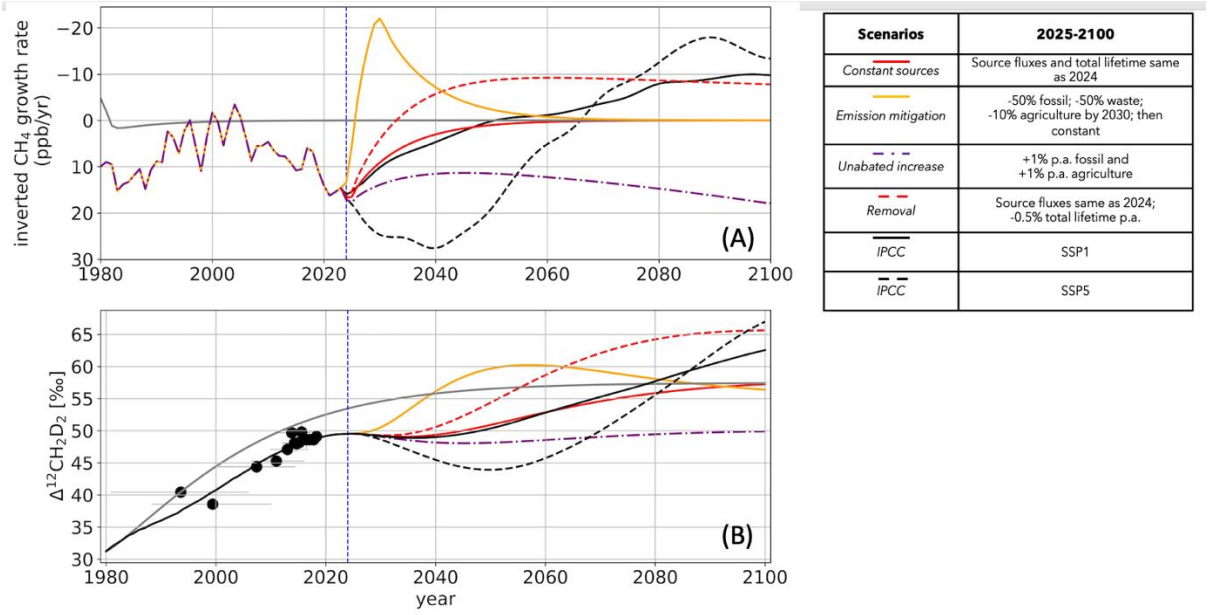

Figure D.10. **(A)** inverted growth rate of CH_4 in ppb/year from 2024-2100; **(B)** evolution of $\Delta^{12}CH_2D_2$.

Bibliography

40 CFR 60.18. https://www.ecfr.gov/current/title-40/chapter-I/subchapter-C/part-60/subpart-A/section-60.18

40 CFR Part 258. https://www.ecfr.gov/current/title-40/chapter-I/subchapter-I/part-258

Allan, W., Lowe, D. C., & Cainey, J. M. (2001). Active chlorine in the remote marine boundary layer: Modeling anomalous measurements of δ13C in methane. *Geophysical Research Letters*, *28*(17), 3239-3242. https://doi.org/10.1029/2001gl013064

Allan, W., Manning, M. R., Lassey, K. R., Lowe, D. C., & Gomez, A. J. (2001). Modeling the variation of δ13C in atmospheric methane: Phase ellipses and the kinetic isotope effect. *Global Biogeochemical Cycles*, *15*(2), 467-481. https://doi.org/10.1029/2000GB001282

Allan, W., Struthers, H., & Lowe, D. (2007). Methane carbon isotope effects caused by atomic chlorine in the marine boundary layer: Global model results compared with Southern Hemisphere measurements. *Journal of Geophysical Research: Atmospheres*, *112*(D4).

Allen, D. (2016). Attributing Atmospheric Methane to Anthropogenic Emission Sources. *Accounts of Chemical Research*, *49*(7), 1344-1350. https://doi.org/10.1021/acs.accounts.6b00081

Alperin Marc, J., & Reeburgh William, S. (1985). Inhibition Experiments on Anaerobic Methane Oxidation. *Applied and Environmental Microbiology*, *50*(4), 940-945. https://doi.org/10.1128/aem.50.4.940-945.1985

Alperin, M. J., Reeburgh, W. S., & Whiticar, M. J. (1988). Carbon and hydrogen isotope fractionation resulting from anaerobic methane oxidation. *Global Biogeochemical Cycles*, *2*(3), 279-288. https://doi.org/10.1029/GB002i003p00279

Alvarez, R. A., Zavala-Araiza, D., Lyon, D. R., Allen, D. T., Barkley, Z. R., Brandt, A. R., Davis, K. J., Herndon, S. C., Jacob, D. J., Karion, A., Kort, E. A., Lamb, B. K., Lauvaux, T., Maasakkers, J. D., Marchese, A. J., Omara, M., Pacala, S. W., Peischl, J., Robinson, A. L.,…Hamburg, S. P. (2018). Assessment of methane emissions from the U.S. oil and gas supply chain. *Science*, *361*(6398), 186-188. https://doi.org/10.1126/science.aar7204

American Petroleum Institute. (2021). *Compendium of greenhouse gas emissions methodologies for the natural gas and oil industry*.

Andela, N., Morton, D. C., Giglio, L., Chen, Y., van der Werf, G. R., Kasibhatla, P. S., DeFries, R. S., Collatz, G. J., Hantson, S., Kloster, S., Bachelet, D., Forrest, M., Lasslop, G., Li, F., Mangeon, S., Melton, J. R., Yue, C., & Randerson, J. T. (2017). A human-driven decline in global burned area. *Science*, *356*(6345), 1356-1362. https://doi.org/10.1126/science.aal4108

Anderson, D. C., Duncan, B. N., Fiore, A. M., Baublitz, C. B., Follette-Cook, M. B., Nicely, J. M., & Wolfe, G. M. (2021). Spatial and temporal variability in the hydroxyl (OH) radical: understanding the role of large-scale climate features and their influence on OH through its dynamical and photochemical drivers. *Atmos. Chem. Phys.*, *21*(8), 6481-6508. https://doi.org/10.5194/acp-21-6481-2021

Ash, J. L., Egger, M., Treude, T., Kohl, I., Cragg, B., Parkes, R. J., Slomp, C. P., Lollar, B. S., & Young, E. D. (2019). Exchange catalysis during anaerobic methanotrophy revealed by 12CH2D2 and 13CH3D in methane. *Geochemical Perspectives Letters*, *10*, 26-30. https://doi.org/10.7185/geochemlet.1910

Ault, B. A., Jones, V. K., Powell, J. D., & Franklin, G. F. (1994). Adaptive Air-Fuel Ratio Control of a Spark-Ignition Engine. *SAE Transactions*, *103*, 442-451. http://www.jstor.org/stable/44632807

Aydin, M., Verhulst, K. R., Saltzman, E. S., Battle, M. O., Montzka, S. A., Blake, D. R., Tang, Q., & Prather, M. J. (2011). Recent decreases in fossil-fuel emissions of ethane and methane derived from firn air. *Nature*, *476*(7359), 198-201. https://doi.org/10.1038/nature10352

Baik, M.-H., Newcomb, M., Friesner, R. A., & Lippard, S. J. (2003). Mechanistic Studies on the Hydroxylation of Methane by Methane Monooxygenase. *Chemical Reviews*, *103*(6), 2385-2420. https://doi.org/10.1021/cr950244f

Bakkaloglu, S., Lowry, D., Fisher, R. E., France, J. L., Brunner, D., Chen, H., & Nisbet, E. G. (2021). Quantification of methane emissions from UK biogas plants. *Waste Management*, *124*, 82-93. https://doi.org/10.1016/j.wasman.2021.01.011

Bakkaloglu, S., Lowry, D., Fisher, R. E., Menoud, M., Lanoisellé, M., Chen, H., Röckmann, T., & Nisbet, E. G. (2022). Stable isotopic signatures of methane from waste sources through atmospheric measurements. *Atmospheric Environment*, *276*, 119021. https://doi.org/10.1016/j.atmosenv.2022.119021

Bakwin, P. S., Tans, P. P., White, J. W. C., & Andres, R. J. (1998). Determination of the isotopic(13C/12C) discrimination by terrestrial biology from a global network of observations. *Global Biogeochemical Cycles*, *12*(3), 555-562. https://doi.org/10.1029/98GB02265

Baldocchi, D., Detto, M., Sonnentag, O., Verfaillie, J., Teh, Y. A., Silver, W., & Kelly, N. M. (2012). The challenges of measuring methane fluxes and concentrations over a peatland pasture. *Agricultural and Forest Meteorology*, *153*, 177-187. https://doi.org/10.1016/j.agrformet.2011.04.013

Bastviken, D., Cole, J., Pace, M., & Tranvik, L. (2004). Methane emissions from lakes: Dependence of lake characteristics, two regional assessments, and a global estimate. *Global Biogeochemical Cycles*, *18*(4). https://doi.org/10.1029/2004GB002238

Bastviken, D., Cole, J. J., Pace, M. L., & Van de Bogert, M. C. (2008). Fates of methane from different lake habitats: Connecting whole-lake budgets and CH4 emissions. *Journal of Geophysical Research: Biogeosciences*, *113*(G2). https://doi.org/10.1029/2007JG000608

Basu, S., Lan, X., Dlugokencky, E., Michel, S., Schwietzke, S., Miller, J. B., Bruhwiler, L., Oh, Y., Tans, P. P., Apadula, F., Gatti, L. V., Jordan, A., Necki, J., Sasakawa, M., Morimoto, S., Di Iorio, T., Lee, H., Arduini, J., & Manca, G. (2022). Estimating emissions of methane consistent with atmospheric measurements of methane and $\delta^{13}C$ of methane. *Atmos. Chem. Phys.*, *22*(23), 15351-15377. https://doi.org/http://doi.org/10.1002/rcm.886710.5194/acp-22-15351-2022

Battin-Leclerc, F. (2008). Detailed chemical kinetic models for the low-temperature combustion of hydrocarbons with application to gasoline and diesel fuel surrogates. *Progress in Energy and Combustion Science*, *34*(4), 440-498. https://doi.org/10.1016/j.pecs.2007.10.002

Battle, M., Bender, M., Sowers, T., Tans, P. P., Butler, J. H., Elkins, J. W., Ellis, J. T., Conway, T., Zhang, N., Lang, P., & Clarket, A. D. (1996). Atmospheric gas concentrations over the past century measured in air from firn at the South Pole. *Nature*, *383*(6597), 231-235. https://doi.org/10.1038/383231a0

Beal, E. J., House, C. H., & Orphan, V. J. (2009). Manganese- and Iron-Dependent Marine Methane Oxidation. *Science*, *325*(5937), 184-187. https://doi.org/10.1126/science.1169984

Bender, M. L., Tans, P. P., Ellis, J. T., Orchardo, J., & Habfast, K. (1994). A high precision isotope ratio mass spectrometry method for measuring the O2N2 ratio of air. *Geochimica Et Cosmochimica Acta*, *58*(21), 4751-4758. https://doi.org/10.1016/0016-7037(94)90205-4

Berchet, A., Bousquet, P., Pison, I., Locatelli, R., Chevallier, F., Paris, J.-D., Dlugokencky, E. J., Laurila, T., Hatakka, J., & Viisanen, Y. (2016). Atmospheric constraints on the methane emissions from the East Siberian Shelf. *Atmospheric Chemistry and Physics*, *16*(6), 4147-4157.

Berner, U., & Faber, E. (1988). Maturity related mixing model for methane, ethane and propane, based on carbon isotopes. *Organic Geochemistry*, *13*(1-3), 67-72.

Biastoch, A., Treude, T., Rüpke, L. H., Riebesell, U., Roth, C., Burwicz, E. B., Park, W., Latif, M., Böning, C. W., Madec, G., & Wallmann, K. (2011). Rising Arctic Ocean temperatures cause gas hydrate destabilization and ocean acidification. *Geophysical Research Letters*, *38*(8). https://doi.org/10.1029/2011GL047222

Bigeleisen, J. (1955). Statistical Mechanics of Isotopic Systems with Small Quantum Corrections. I. General Considerations and the Rule of the Geometric Mean. *The Journal of Chemical Physics*, *23*(12), 2264-2267. https://doi.org/10.1063/1.1740735

Bigeleisen, J., & Mayer, M. G. (1947). Calculation of Equilibrium Constants for Isotopic Exchange Reactions. *The Journal of Chemical Physics*, *15*(5), 261-267. https://doi.org/10.1063/1.1746492

Bloom, A. A., Bowman, K. W., Lee, M., Turner, A. J., Schroeder, R., Worden, J. R., Weidner, R. J., McDonald, K. C., & Jacob, D. J. (2021). CMS: Global 0.5-deg Wetland Methane Emissions and Uncertainty (WetCHARTs v1.3.1). In: ORNL Distributed Active Archive Center.

Bloom, A. A., Bowman, K. W., Lee, M., Turner, A. J., Schroeder, R., Worden, J. R., Weidner, R. J., McDonald, K. C., & Jacob, D. J. (2024). CMS: Global 0.5-deg Wetland Methane Emissions and Uncertainty (WetCHARTs v1.3.3). In: ORNL Distributed Active Archive Center.

Blunier, T., Barnett, B., Bender, M. L., & Hendricks, M. B. (2002). Biological oxygen productivity during the last 60,000 years from triple oxygen isotope measurements. *Global Biogeochemical Cycles*, *16*(3), 3-1-3-13. https://doi.org/10.1029/2001GB001460

Boetius, A., Ravenschlag, K., Schubert, C. J., Rickert, D., Widdel, F., Gieseke, A., Amann, R., Jørgensen, B. B., Witte, U., & Pfannkuche, O. (2000). A marine microbial consortium apparently mediating anaerobic oxidation of methane. *Nature*, *407*(6804), 623-626. https://doi.org/10.1038/35036572

Boone, G. D., Agyin, F., Robichaud, D. J., Tao, F.-M., & Hewitt, S. A. (2001). Rate Constants for the Reactions of Chlorine Atoms with Deuterated Methanes: Experiment and Theory. *The Journal of Physical Chemistry A*, *105*(9), 1456-1464. https://doi.org/10.1021/jp0027290

Boschetti, T., Etiope, G., & Toscani, L. (2013). Abiotic Methane in the Hyperalkaline Springs of Genova, Italy. *Procedia Earth and Planetary Science*, *7*, 248-251. https://doi.org/10.1016/j.proeps.2013.02.004

Botz, R., Pokojski, H.-D., Schmitt, M., & Thomm, M. (1996). Carbon isotope fractionation during bacterial methanogenesis by CO2 reduction. *Organic Geochemistry*, *25*(3-4), 255-262. https://doi.org/10.1016/s0146-6380(96)00129-5

Bousquet, P., Ciais, P., Miller, J. B., Dlugokencky, E. J., Hauglustaine, D. A., Prigent, C., Van der Werf, G. R., Peylin, P., Brunke, E. G., Carouge, C., Langenfelds, R. L., Lathière, J., Papa, F., Ramonet, M., Schmidt, M., Steele, L. P., Tyler, S. C., & White, J. (2006). Contribution of anthropogenic and natural sources to atmospheric methane variability. *Nature*, *443*(7110), 439-443. https://doi.org/10.1038/nature05132

Brand, U., Blamey, N., Garbelli, C., Griesshaber, E., Posenato, R., Angiolini, L., Azmy, K., Farabegoli, E., & Came, R. (2016). Methane Hydrate: Killer cause of Earth's greatest mass extinction. *Palaeoworld*, *25*(4), 496-507.

Brandt, A. R., Heath, G. A., & Cooley, D. (2016). Methane leaks from natural gas systems follow extreme distributions. *Environmental Science & Technology*, *50*(22), 12512-12520. https://doi.org/10.1021/acs.est.6b04303

Brown, M. (1993). Deduction of emissions of source gases using an objective inversion algorithm and a chemical transport model. *Journal of Geophysical Research: Atmospheres*, *98*(D7), 12639-12660. https://doi.org/10.1029/93JD01003

Brownlow, R., Lowry, D., Fisher, R., France, J., Lanoisellé, M., White, B., Wooster, M., Zhang, T., & Nisbet, E. (2017). Isotopic ratios of tropical methane emissions by atmospheric measurement. *Global Biogeochemical Cycles*, *31*(9), 1408-1419.

Buizert, C., Martinerie, P., Petrenko, V. V., Severinghaus, J. P., Trudinger, C. M., Witrant, E., Rosen, J. L., Orsi, A. J., Rubino, M., Etheridge, D. M., Steele, L. P., Hogan, C., Laube, J. C., Sturges, W. T., Levchenko, V. A., Smith, A. M., Levin, I., Conway, T. J., Dlugokencky, E. J.,…Blunier, T. (2012). Gas transport in firn: multiple-tracer characterisation and model intercomparison for NEEM, Northern Greenland. *Atmospheric Chemistry and Physics*, *12*(9), 4259-4277. https://doi.org/10.5194/acp-12-4259-2012

Burke, R. A., Barber, T. R., & Sackett, W. M. (1992). Seasonal variations of stable hydrogen and carbon isotope ratios of methane in subtropical freshwater sediments. *Global Biogeochemical Cycles*, *6*(2), 125-138. https://doi.org/10.1029/92GB00155

Burke, R. A., Martens, C. S., & Sackett, W. M. (1988). Seasonal variations of D/H and 13C/12C ratios of microbial methane in surface sediments. *Nature*, *332*(6167), 829-831. https://doi.org/10.1038/332829a0

Burruss, R. C., & Laughrey, C. D. (2010). Carbon and hydrogen isotopic reversals in deep basin gas: Evidence for limits to the stability of hydrocarbons. *Organic Geochemistry*, *41*(12), 1285-1296. https://doi.org/10.1016/j.orggeochem.2010.09.008

Byers, E., Krey, V., Kriegler, E., Riahi, K., Schaeffer, R., Kikstra, J., Lamboll, R., Nicholls, Z., Sanstad, M., Smith, C., Wijst, K.-I. v. d., Khourdajie, A. A., Lecocq, F., Portugal-Pereira, J., Saheb, Y., Strømann, A., Winkler, H., Auer, C., Brutschin, E.,…Vuuren, D. v. (2022). AR6 Scenarios Database hosted by IIASA. In: International Institute for Applied Systems Analysis.

Calle, L., & Poulter, B. (2021). Ecosystem age-class dynamics and distribution in the LPJ-wsl v2.0 global ecosystem model. *Geosci. Model Dev.*, *14*(5), 2575-2601. https://doi.org/10.5194/gmd-14-2575-2021

Cao, X., Bao, H., & Peng, Y. (2019). A kinetic model for isotopologue signatures of methane generated by biotic and abiotic CO2 methanation. *Geochimica Et Cosmochimica Acta*, *249*, 59-75. https://doi.org/10.1016/j.gca.2019.01.021

Caulton, D. R., Shepson, P. B., Santoro, R. L., Sparks, J. P., Howarth, R. W., Ingraffea, A. R., Cambaliza, M. O., Sweeney, C., Karion, A., Davis, K. J., Stirm, B. H., Montzka, S. A., & Miller, B. R. (2014). Toward a better understanding and quantification of methane emissions from shale gas development. *Proceedings of the National Academy of Sciences*, *111*(17), 6237-6242. https://doi.org/10.1073/pnas.1316546111

Chadwick, G. L., Skennerton, C. T., Laso-Pérez, R., Leu, A. O., Speth, D. R., Yu, H., Morgan-Lang, C., Hatzenpichler, R., Goudeau, D., Malmstrom, R., Brazelton, W. J., Woyke, T., Hallam, S. J., Tyson, G. W., Wegener, G., Boetius, A., & Orphan, V. J. (2022). Comparative genomics reveals electron transfer and syntrophic mechanisms differentiating methanotrophic and methanogenic archaea. *PLOS Biology*, *20*(1), e3001508. https://doi.org/10.1371/journal.pbio.3001508

Chang, J., Peng, S., Ciais, P., Saunois, M., Dangal, S. R., Herrero, M., Havlík, P., Tian, H., & Bousquet, P. (2019). Revisiting enteric methane emissions from domestic ruminants and their δ13CCH4 source signature. *Nature Communications*, *10*(1), 1-14.

Chang, J., Peng, S., Yin, Y., Ciais, P., Havlik, P., & Herrero, M. (2021). The Key Role of Production Efficiency Changes in Livestock Methane Emission Mitigation. *AGU Advances*, *2*(2), e2021AV000391. https://doi.org/10.1029/2021AV000391

Chanton, J., & Liptay, K. (2000). Seasonal variation in methane oxidation in a landfill cover soil as determined by an in situ stable isotope technique. *Global Biogeochemical Cycles*, *14*(1), 51-60. https://doi.org/10.1029/1999GB900087

Chanton, J. P., Powelson, D. K., Abichou, T., & Hater, G. (2008). Improved Field Methods to Quantify Methane Oxidation in Landfill Cover Materials Using Stable Carbon Isotopes. *Environmental Science & Technology*, *42*(3), 665-670. https://doi.org/10.1021/es0710757

Chanton, J. P., Rutkowski, C. M., Schwartz, C. C., Ward, D. E., & Boring, L. (2000). Factors influencing the stable carbon isotopic signature of methane from combustion and biomass burning. *Journal of Geophysical Research: Atmospheres*, *105*(D2), 1867-1877. https://doi.org/10.1029/1999JD900909

Chen, H., Zhu, Q., Peng, C., Wu, N., Wang, Y., Fang, X., Jiang, H., Xiang, W., Chang, J., Deng, X., & Yu, G. (2013). Methane emissions from rice paddies natural wetlands, and lakes in China: synthesis and new estimate. *Global Change Biology*, *19*(1), 19-32. https://doi.org/10.1111/gcb.12034

Chen, Y., Hall, J., van Wees, D., Andela, N., Hantson, S., Giglio, L., van der Werf, G. R., Morton, D. C., & Randerson, J. T. (2023). Multi-decadal trends and variability in burned area from the fifth version of the Global Fire Emissions Database (GFED5). *Earth Syst. Sci. Data*, *15*(11), 5227-5259. https://doi.org/10.5194/essd-15-5227-2023

Chen, Z., El Abbadi, S. H., Sherwin, E. D., Burdeau, P. M., Rutherford, J. S., Chen, Y., Zhang, Z., & Brandt, A. R. (2024). Comparing Continuous Methane Monitoring Technologies for High-Volume Emissions: A Single-Blind Controlled Release Study. *ACS ES&T Air*, *1*(8), 871-884. https://doi.org/10.1021/acsestair.4c00015

Chen, Z., Jacob, D. J., Nesser, H., Sulprizio, M. P., Lorente, A., Varon, D. J., Lu, X., Shen, L., Qu, Z., Penn, E., & Yu, X. (2022). Methane emissions from China: a high-resolution inversion of TROPOMI satellite observations. *Atmos. Chem. Phys.*, *22*(16), 10809-10826. https://doi.org/10.5194/acp-22-10809-2022

ChesapeakeBayProgram. *https://www.chesapeakebay.net/what/maps/chesapeake-bay-mean-surface-salinity-1985-2018*

Chong, Z. R., Pujar, G. A., Yang, M., & Linga, P. (2016). Methane hydrate formation in excess water simulating marine locations and the impact of thermal stimulation on energy recovery. *Applied Energy*, *177*, 409-421.

Chung, E., & Arnold, T. (2021). Potential of Clumped Isotopes in Constraining the Global Atmospheric Methane Budget. *Global Biogeochemical Cycles*, *35*(10), e2020GB006883. https://doi.org/10.1029/2020GB006883

Coleman, D. D., Risatti, J. B., & Schöll, M. (1981). Fractionation of carbon and hydrogen isotopes by methane-oxidizing bacteria. *Geochimica Et Cosmochimica Acta*, *45*(7), 1033-1037. https://doi.org/10.1016/0016-7037(81)90129-0

Collins, W. J., Lamarque, J. F., Schulz, M., Boucher, O., Eyring, V., Hegglin, M. I., Maycock, A., Myhre, G., Prather, M., Shindell, D., & Smith, S. J. (2017). AerChemMIP: quantifying the effects of chemistry and aerosols in CMIP6. *Geosci. Model Dev.*, *10*(2), 585-607. https://doi.org/10.5194/gmd-10-585-2017

Colón-Román, Y. A., & Ruppert, L. F. (2014). Central Appalachian basin natural gas database—Distribution, composition, and origin of natural gases: U.S. Geological Survey Open-File Report 2014–1207. *13 p., 1 app.* https://doi.org/https://dx.doi.org/10.3133/ofr20141207

Conrad, R. (2005). Quantification of methanogenic pathways using stable carbon isotopic signatures: a review and a proposal. *Organic Geochemistry*, *36*(5), 739-752. https://doi.org/10.1016/j.orggeochem.2004.09.006

Conrad, R. (2009). The global methane cycle: recent advances in understanding the microbial processes involved. *Environmental Microbiology Reports*, *1*(5), 285-292. https://doi.org/10.1111/j.1758-2229.2009.00038.x

Conrad, R. (2020). Importance of hydrogenotrophic, aceticlastic and methylotrophic methanogenesis for methane production in terrestrial, aquatic and other anoxic environments: A mini review. *Pedosphere*, *30*(1), 25-39. https://doi.org/10.1016/S1002-0160(18)60052-9

Coplen, T. B. (1994). Reporting of stable hydrogen, carbon, and oxygen isotopic abundances (Technical Report). *66*(2), 273-276. https://doi.org/10.1351/pac199466020273 (Pure and Applied Chemistry)

Coplen, T. B. (1995). Letter to the Editor: New IUPAC guidelines for the reporting of stable hydrogen, carbon, and oxygen isotope-ratio data. *J Res Natl Inst Stand Technol*, *100*(3), 285. https://doi.org/10.6028/jres.100.021

Craig, H., & Lupton, J. E. (1976). Primordial neon, helium, and hydrogen in oceanic basalts. *Earth and Planetary Science Letters*, *31*(3), 369-385. https://doi.org/10.1016/0012-821X(76)90118-7

Crippa, M., Guizzardi, D., Pagani, F., Banja, M., Muntean, M., Schaaf, E., Monforti-Ferrario, F., Becker, W. E., Quadrelli, R., Risquez Martin, A., Taghavi-Moharamli, P., Köykkä, J., Grassi, G., Rossi, S., Melo, J., Oom, D., Branco, A., San-Miguel, J., Manca, G.,…Pekar, F. (2024). *GHG emissions of all world countries*. P. O. o. t. E. Union.

Crippa, M., Solazzo, E., Huang, G., Guizzardi, D., Koffi, E., Muntean, M., Schieberle, C., Friedrich, R., & Janssens-Maenhout, G. (2020). High resolution temporal profiles in the Emissions Database for Global Atmospheric Research. *Scientific Data*, *7*(1), 121. https://doi.org/10.1038/s41597-020-0462-2

Curry, C. L. (2007). Modeling the soil consumption of atmospheric methane at the global scale. *Global Biogeochemical Cycles*, *21*(4). https://doi.org/10.1029/2006GB002818

Cusworth, D. H., Duren, R. M., Ayasse, A. K., Jiorle, R., Howell, K., Aubrey, A., Green, R. O., Eastwood, M. L., Chapman, J. W., Thorpe, A. K., Heckler, J., Asner, G. P., Smith, M. L., Thoma, E., Krause, M. J., Heins, D., & Thorneloe, S. (2024). Quantifying methane emissions from United States landfills. *Science*, *383*(6690), 1499-1504. https://doi.org/10.1126/science.adi7735

Da, P., Tao, L., Sun, K., Golston, L. M., Miller, D. J., Zhu, T., Qin, Y., Zhang, Y., Mauzerall, D. L., & Zondlo, M. A. (2020). Methane emissions from natural gas vehicles in China. *Nature Communications*, *11*(1), 4588. https://doi.org/10.1038/s41467-020-18141-0

Dean, J. F., Middelburg, J. J., Röckmann, T., Aerts, R., Blauw, L. G., Egger, M., Jetten, M. S. M., de Jong, A. E. E., Meisel, O. H., Rasigraf, O., Slomp, C. P., in't Zandt, M. H., & Dolman, A. J. (2018). Methane Feedbacks to the Global Climate System in a Warmer World [https://doi.org/10.1002/2017RG000559]. *Reviews of Geophysics*, *56*(1), 207-250. https://doi.org/10.1002/2017RG000559

Defratyka, S. M., Paris, J.-D., Yver-Kwok, C., Fernandez, J. M., Korben, P., & Bousquet, P. (2021). Mapping urban methane sources in Paris, France. *Environmental Science & Technology*, *55*(13), 8583-8591. https://doi.org/10.1021/acs.est.1c00859

DelSontro, T., Kunz, M. J., Kempter, T., Wüest, A., Wehrli, B., & Senn, D. B. (2011). Spatial Heterogeneity of Methane Ebullition in a Large Tropical Reservoir. *Environmental Science & Technology*, *45*(23), 9866-9873. https://doi.org/10.1021/es2005545

DelSontro, T., McGinnis, D. F., Wehrli, B., & Ostrovsky, I. (2015). Size Does Matter: Importance of Large Bubbles and Small-Scale Hot Spots for Methane Transport. *Environmental Science & Technology*, *49*(3), 1268-1276. https://doi.org/10.1021/es5054286

DeMore, W. B., & Raper, O. F. (1967). Reaction of O(1D) with Methane. *The Journal of Chemical Physics*, *46*(7), 2500-2505. https://doi.org/10.1063/1.1841075

Des Marais, D. J., Donchin, J. H., Nehring, N. L., & Truesdell, A. H. (1981). Molecular carbon isotopic evidence for the origin of geothermal hydrocarbons. *Nature*, *292*(5826), 826-828. https://doi.org/10.1038/292826a0

Dlugokencky, E., Walter, B., Masarie, K., Lang, P., & Kasischke, E. (2001). Measurements of an anomalous global methane increase during 1998. *Geophysical Research Letters*, *28*(3), 499-502.

Dlugokencky, E. J., Dutton, E., Novelli, P., Tans, P., Masarie, K., Lantz, K. O., & Madronich, S. (1996). Changes in CH4 and CO growth rates after the eruption of Mt. Pinatubo and their link with changes in tropical tropospheric UV flux. *Geophysical Research Letters*, *23*(20), 2761-2764.

Dlugokencky, E. J., Nisbet, E. G., Fisher, R., & Lowry, D. (2011). Global atmospheric methane: budget, changes and dangers. *Philosophical Transactions of the Royal Society A: Mathematical, Physical and Engineering Sciences*, *369*(1943), 2058-2072. https://doi.org/doi:10.1098/rsta.2010.0341

Dong, G., Xie, H., Formolo, M., Lawson, M., Sessions, A., & Eiler, J. (2021). Clumped isotope effects of thermogenic methane formation: Insights from pyrolysis of hydrocarbons. *Geochimica Et Cosmochimica Acta*, *303*, 159-183. https://doi.org/10.1016/j.gca.2021.03.009

Douglas, P., Stolper, D., Smith, D., Anthony, K. W., Paull, C., Dallimore, S., Wik, M., Crill, P. M., Winterdahl, M., & Eiler, J. (2016). Diverse origins of Arctic and Subarctic methane point source emissions identified with multiply-substituted isotopologues. *Geochimica Et Cosmochimica Acta*, *188*, 163-188. https://doi.org/10.1016/j.gca.2016.05.031

Douglas, P. M. J., Gonzalez Moguel, R., Walter Anthony, K. M., Wik, M., Crill, P. M., Dawson, K. S., Smith, D. A., Yanay, E., Lloyd, M. K., Stolper, D. A., Eiler, J. M., & Sessions, A. L. (2020). Clumped Isotopes Link Older Carbon Substrates With Slower Rates of Methanogenesis in Northern Lakes. *Geophysical Research Letters*, *47*(6). https://doi.org/10.1029/2019gl086756

Douglas, P. M. J., Stolper, D. A., Eiler, J. M., Sessions, A. L., Lawson, M., Shuai, Y., Bishop, A., Podlaha, O. G., Ferreira, A. A., Santos Neto, E. V., Niemann, M., Steen, A. S., Huang, L., Chimiak, L., Valentine, D. L., Fiebig, J., Luhmann, A. J., Seyfried, W. E., Etiope, G.,…Kitchen, N. (2017). Methane clumped isotopes: Progress and potential for a new isotopic tracer. *Organic Geochemistry*, *113*, 262-282. https://doi.org/10.1016/j.orggeochem.2017.07.016

Douglas, P. M. J., Stratigopoulos, E., Park, S., & Phan, D. (2021). Geographic variability in freshwater methane hydrogen isotope ratios and its implications for global isotopic source signatures. *Biogeosciences*, *18*(11), 3505-3527. https://doi.org/10.5194/bg-18-3505-2021

Dow, W. G. (1977). Kerogen studies and geological interpretations. *Journal of Geochemical Exploration*, *7*, 79-99. https://doi.org/10.1016/0375-6742(77)90078-4

Dunning, T. H., Jr. (1989). Gaussian basis sets for use in correlated molecular calculations. I. The atoms boron through neon and hydrogen. *The Journal of Chemical Physics*, *90*(2), 1007-1023. https://doi.org/10.1063/1.456153

East, J. D., Jacob, D. J., Balasus, N., Bloom, A. A., Bruhwiler, L., Chen, Z., Kaplan, J. O., Mickley, L. J., Mooring, T. A., Penn, E., Poulter, B., Sulprizio, M. P., Worden, J. R., Yantosca, R. M., & Zhang, Z. (2024). Interpreting the Seasonality of Atmospheric Methane. *Geophysical Research Letters*, *51*(10), e2024GL108494. https://doi.org/10.1029/2024GL108494

Eiler, J. M. (2007). "Clumped-isotope" geochemistry—The study of naturally-occurring, multiply-substituted isotopologues. *Earth and Planetary Science Letters*, *262*(3-4), 309-327. https://doi.org/10.1016/j.epsl.2007.08.020

Eiler, J. M., Clog, M., Magyar, P., Piasecki, A., Sessions, A., Stolper, D., Deerberg, M., Schlueter, H.-J., & Schwieters, J. (2013). A high-resolution gas-source isotope ratio mass spectrometer. *International Journal of Mass Spectrometry*, *335*, 45-56. https://doi.org/10.1016/j.ijms.2012.10.014

Eiler, J. M., & Schauble, E. (2004). 18O13C16O in Earth's atmosphere. *Geochimica Et Cosmochimica Acta*, *68*(23), 4767-4777. https://doi.org/10.1016/j.gca.2004.05.035

Eldridge, D. L., Korol, R., Lloyd, M. K., Turner, A. C., Webb, M. A., Miller, T. F., & Stolper, D. A. (2019). Comparison of Experimental vs Theoretical Abundances of 13CH3D and 12CH2D2 for Isotopically Equilibrated Systems from 1 to 500 °C. *ACS Earth and Space Chemistry*, *3*(12), 2747-2764. https://doi.org/10.1021/acsearthspacechem.9b00244

Engle, D., & Melack, J. M. (2000). Methane emissions from an Amazon floodplain lake: Enhanced release during episodic mixing and during falling water. *Biogeochemistry*, *51*(1), 71-90. https://doi.org/10.1023/A:1006389124823

Environmental Integrity Project. (2021). *Greenhouse Gases from Maryland's Landfills Underestimated and Under Regulated.* https://environmentalintegrity.org/wp-content/uploads/2021/06/MD-Landfill-Methane-Report-6.9.2021-unembargoed_with-Attachments.pdf

Etiope, G., Ciotoli, G., Schwietzke, S., & Schöll, M. (2019). Gridded maps of geological methane emissions and their isotopic signature. *Earth Syst. Sci. Data*, *11*(1), 1-22. https://doi.org/10.5194/essd-11-1-2019

Etiope, G., Schöll, M., & Hosgörmez, H. (2011). Abiotic methane flux from the Chimaera seep and Tekirova ophiolites (Turkey): Understanding gas exhalation from low temperature serpentinization and implications for Mars. *Earth and Planetary Science Letters*, *310*(1), 96-104. https://doi.org/10.1016/j.epsl.2011.08.001

Etiope, G., & Sherwood Lollar, B. (2013). Abiotic Methane on Earth. *Reviews of Geophysics*, *51*(2), 276-299. https://doi.org/10.1002/rog.20011

Etiope, G., & Whiticar, M. J. (2019). Abiotic methane in continental ultramafic rock systems: Towards a genetic model. *Applied Geochemistry*, *102*, 139-152. https://doi.org/10.1016/j.apgeochem.2019.01.012

Ettwig, K. F., Butler, M. K., Le Paslier, D., Pelletier, E., Mangenot, S., Kuypers, M. M. M., Schreiber, F., Dutilh, B. E., Zedelius, J., de Beer, D., Gloerich, J., Wessels, H. J. C. T., van Alen, T., Luesken, F., Wu, M. L., van de Pas-Schoonen, K. T., Op den Camp, H. J. M., Janssen-Megens, E. M., Francoijs, K.-J.,…Strous, M. (2010). Nitrite-driven anaerobic methane oxidation by oxygenic bacteria. *Nature*, *464*(7288), 543-548. https://doi.org/10.1038/nature08883

Evans, P. N., Parks, D. H., Chadwick, G. L., Robbins, S. J., Orphan, V. J., Golding, S. D., & Tyson, G. W. (2015). Methane metabolism in the archaeal phylum Bathyarchaeota revealed by genome-centric metagenomics. *Science*, *350*(6259), 434-438. https://doi.org/10.1126/science.aac7745

FAO. *Food and Agriculture Organization of the United Nations FAOSTAT* https://www.fao.org/faostat/en/#data/QCL/visualize

Farquhar, J., Sun, J., Haghnegahdar, M. A., & Magen, C. (2022). Using Clumped Isotopes to Constrain Factors Influencing Trends in Atmospheric Methane. 2022 Goldschmidt Conference,

Feilberg, K. L., Griffith, D. W. T., Johnson, M. S., & Nielsen, C. J. (2005). The 13C and D kinetic isotope effects in the reaction of CH4 with Cl. *International Journal of Chemical Kinetics*, *37*(2), 110-118. https://doi.org/10.1002/kin.20058

Feisthauer, S., Vogt, C., Modrzynski, J., Szlenkier, M., Krüger, M., Siegert, M., & Richnow, H.-H. (2011). Different types of methane monooxygenases produce similar carbon and hydrogen isotope fractionation patterns during methane oxidation. *Geochimica Et Cosmochimica Acta*, *75*(5), 1173-1184. https://doi.org/10.1016/j.gca.2010.12.006

Feng, L., Palmer, P. I., Parker, R. J., Lunt, M. F., & Bösch, H. (2023). Methane emissions are predominantly responsible for record-breaking atmospheric methane growth rates in 2020 and 2021. *Atmos. Chem. Phys.*, *23*(8), 4863-4880. https://doi.org/10.5194/acp-23-4863-2023

Feng, L., Palmer, P. I., Zhu, S., Parker, R. J., & Liu, Y. (2022). Tropical methane emissions explain large fraction of recent changes in global atmospheric methane growth rate. *Nature Communications*, *13*(1), 1378. https://doi.org/10.1038/s41467-022-28989-z

Fernandez, J. M., Maazallahi, H., France, J. L., Menoud, M., Corbu, M., Ardelean, M., Calcan, A., Townsend-Small, A., van der Veen, C., Fisher, R. E., Lowry, D., Nisbet, E. G., & Röckmann, T. (2022). Street-level methane emissions of Bucharest, Romania and the dominance of urban wastewater. *Atmospheric Environment: X*, *13*, 100153. https://doi.org/10.1016/j.aeaoa.2022.100153

Ferretti, D. F., Miller, J. B., White, J. W., Etheridge, D. M., Lassey, K. R., Lowe, D. C., Macfarling Meure, C. M., Dreier, M. F., Trudinger, C. M., van Ommen, T. D., & Langenfelds, R. L. (2005). Unexpected changes to the global methane budget over the past 2000 years. *Science*, *309*(5741), 1714-1717. https://doi.org/10.1126/science.1115193

Fetzer, S., Bak, F., & Conrad, R. (1993). Sensitivity of methanogenic bacteria from paddy soil to oxygen and desiccation. *FEMS Microbiology Ecology*, *12*(2), 107-115. https://doi.org/10.1111/j.1574-6941.1993.tb00022.x

Fiore, A. M., Horowitz, L. W., Dlugokencky, E. J., & West, J. J. (2006). Impact of meteorology and emissions on methane trends, 1990–2004. *Geophysical Research Letters*, *33*(12).

Fisher, R. E., France, J. L., Lowry, D., Lanoisellé, M., Brownlow, R., Pyle, J. A., Cain, M., Warwick, N., Skiba, U. M., Drewer, J., Dinsmore, K. J., Leeson, S. R., Bauguitte, S. J. B., Wellpott, A., O'Shea, S. J., Allen, G., Gallagher, M. W., Pitt, J., Percival, C. J.,…Nisbet, E. G. (2017). Measurement of the 13C isotopic signature of methane emissions from northern European wetlands. *Global Biogeochemical Cycles*, *31*(3), 605-623. https://doi.org/10.1002/2016GB005504

Fisher, R. E., Sriskantharajah, S., Lowry, D., Lanoisellé, M., Fowler, C., James, R., Hermansen, O., Lund Myhre, C., Stohl, A., & Greinert, J. (2011). Arctic methane sources: Isotopic evidence for atmospheric inputs. *Geophysical Research Letters*, *38*(21). https://doi.org/10.1029/2011GL049319

France, J. L., Lunt, M. F., Andrade, M., Moreno, I., Ganesan, A. L., Lachlan-Cope, T., Fisher, R. E., Lowry, D., Parker, R. J., Nisbet, E. G., & Jones, A. E. (2022). Very large fluxes of methane measured above Bolivian seasonal wetlands. *Proceedings of the National Academy of Sciences*, *119*(32), e2206345119. https://doi.org/10.1073/pnas.2206345119

Franco, B., Mahieu, E., Emmons, L. K., Tzompa-Sosa, Z. A., Fischer, E. V., Sudo, K., Bovy, B., Conway, S., Griffin, D., Hannigan, J. W., Strong, K., & Walker, K. A. (2016). Evaluating ethane and methane emissions associated with the development of oil and natural gas extraction in North America. *Environmental Research Letters*, *11*(4), 044010. https://doi.org/10.1088/1748-9326/11/4/044010

Frankenberg, C., Thorpe, A. K., Thompson, D. R., Hulley, G., Kort, E. A., Vance, N., Borchardt, J., Krings, T., Gerilowski, K., Sweeney, C., Conley, S., Bue, B. D., Aubrey, A. D., Hook, S., & Green, R. O. (2016). Airborne methane remote measurements reveal heavy-tail flux distribution in Four Corners region. *Proceedings of the National Academy of Sciences*, *113*(35), 9734-9739. https://doi.org/10.1073/pnas.1605617113

Frisch, M. J., Trucks, G. W., Schlegel, H. B., Scuseria, G. E., Robb, M. A., Cheeseman, J. R., Scalmani, G., Barone, V., Petersson, G. A., Nakatsuji, H., Li, X., Caricato, M., Marenich, A., Bloino, J., Janesko, B. G., Gomperts, R., Mennucci, B., Hratchian, H. P., Ortiz, J. V.,…Fox, D. J. (2013). Gaussian 09: EM64L-G09RevD.01, Gaussian, Inc., Wallingford CT.

Frost, B. R. (1979). Mineral equilibria involving mixed-volatiles in a COH fluid phase: the stabilities of graphite and siderite.

Fujita, R., Morimoto, S., Maksyutov, S., Kim, H.-S., Arshinov, M., Brailsford, G., Aoki, S., & Nakazawa, T. (2020). Global and Regional CH4 Emissions for 1995–2013 Derived From Atmospheric CH4, δ13C-CH4, and δD-CH4 Observations and a Chemical Transport Model. *Journal of Geophysical Research: Atmospheres*, *125*(14), e2020JD032903. https://doi.org/10.1029/2020JD032903

Gålfalk, M., Olofsson, G., Crill, P., & Bastviken, D. (2016). Making methane visible. *Nature Climate Change*, *6*(4), 426-430. https://doi.org/10.1038/nclimate2877

Ganesan, A., Stell, A., Gedney, N., Comyn‐Platt, E., Hayman, G., Rigby, M., Poulter, B., & Hornibrook, E. (2018). Spatially resolved isotopic source signatures of wetland methane emissions. *Geophysical Research Letters*, *45*(8), 3737-3745. https://doi.org/10.1002/2018GL077536

Gherman, B. F., Lippard, S. J., & Friesner, R. A. (2005). Substrate Hydroxylation in Methane Monooxygenase: Quantitative Modeling via Mixed Quantum Mechanics/Molecular Mechanics Techniques. *Journal of the American Chemical Society*, *127*(3), 1025-1037. https://doi.org/10.1021/ja049847b

Gierczak, T., Talukdar, R. K., Herndon, S. C., Vaghjiani, G. L., & Ravishankara, A. R. (1997). Rate Coefficients for the Reactions of Hydroxyl Radicals with Methane and Deuterated Methanes. *The Journal of Physical Chemistry A*, *101*(17), 3125-3134. https://doi.org/10.1021/jp963892r

Ginsburg, G. D., & Soloviev, V. A. (1997). Methane migration within the submarine gas-hydrate stability zone under deep-water conditions. *Marine Geology*, *137*(1), 49-57. https://doi.org/10.1016/S0025-3227(96)00078-3

Giunta, T., Young, E. D., Labidi, J., Sansjofre, P., Jézéquel, D., Donval, J.-P., Brandily, C., & Ruffine, L. (2022). Extreme methane clumped isotopologue bio-signatures of aerobic and anaerobic methanotrophy: Insights from the Lake Pavin and the Black Sea sediments. *Geochimica Et Cosmochimica Acta*, *338*, 34-53. https://doi.org/10.1016/j.gca.2022.09.034

Giunta, T., Young, E. D., Warr, O., Kohl, I., Ash, J. L., Martini, A., Mundle, S. O. C., Rumble, D., Pérez-Rodríguez, I., Wasley, M., LaRowe, D. E., Gilbert, A., & Sherwood Lollar, B. (2019). Methane sources and sinks in continental sedimentary systems: New insights from paired clumped isotopologues 13CH3D and 12CH2D2. *Geochimica Et Cosmochimica Acta*, *245*, 327-351. https://doi.org/10.1016/j.gca.2018.10.030

Global Methane Pledge. Global Methane Pledge. https://www.globalmethanepledge.org/resources/global-methane-pledge

Gloor, M., Gatti, L. V., Wilson, C., Parker, R. J., Boesch, H., Popa, E., Chipperfield, M. P., Poulter, B., Zhang, Z., Basso, L., Miller, J., McNorton, J., Jimenez, C., & Prigent, C. (2021). Large Methane Emissions From the Pantanal During Rising Water-Levels Revealed by Regularly Measured Lower Troposphere CH4 Profiles. *Global Biogeochemical Cycles*, *35*(10), e2021GB006964. https://doi.org/10.1029/2021GB006964

Gold, T. (1979). TERRESTRIAL SOURCES OF CARBON AND EARTHQUAKE OUTGASSING. *Journal of Petroleum Geology*, *1*(3), 3-19. https://doi.org/10.1111/j.1747-5457.1979.tb00616.x

Gonfiantini, R. (1978). Standards for stable isotope measurements in natural compounds. *Nature*, *271*(5645), 534-536. https://doi.org/http://doi.org/10.1038/271534a0

Gonzalez, Y., Nelson, D. D., Shorter, J. H., McManus, J. B., Dyroff, C., Formolo, M., Wang, D. T., Western, C. M., & Ono, S. (2019). Precise Measurements of 12CH2D2 by Tunable Infrared Laser Direct Absorption Spectroscopy. *Analytical Chemistry*, *91*(23), 14967-14974. https://doi.org/10.1021/acs.analchem.9b03412

Goss, M., Swain, D. L., Abatzoglou, J. T., Sarhadi, A., Kolden, C. A., Williams, A. P., & Diffenbaugh, N. S. (2020). Climate change is increasing the likelihood of extreme autumn wildfire conditions across California. *Environmental Research Letters*, *15*(9), 094016. https://doi.org/10.1088/1748-9326/ab83a7

Greene, S., Walter Anthony, K. M., Archer, D., Sepulveda-Jauregui, A., & Martinez-Cruz, K. (2014). Modeling the impediment of methane ebullition bubbles by seasonal lake ice. *Biogeosciences*, *11*(23), 6791-6811. https://doi.org/10.5194/bg-11-6791-2014

Greenslade, J. W., Alexander, S. P., Schofield, R., Fisher, J. A., & Klekociuk, A. K. (2017). Stratospheric ozone intrusion events and their impacts on tropospheric ozone in the Southern Hemisphere. *Atmos. Chem. Phys.*, *17*(17), 10269-10290. https://doi.org/10.5194/acp-17-10269-2017

Gromov, S., Brenninkmeijer, C. A., & Jöckel, P. (2018). A very limited role of tropospheric chlorine as a sink of the greenhouse gas methane. *Atmospheric Chemistry and Physics*, *18*(13), 9831-9843. https://doi.org/10.5194/acp-18-9831-2018

Gropp, J., Iron, M. A., & Halevy, I. (2021). Theoretical estimates of equilibrium carbon and hydrogen isotope effects in microbial methane production and anaerobic oxidation of methane. *Geochimica Et Cosmochimica Acta*, *295*, 237-264. https://doi.org/10.1016/j.gca.2020.10.018

Gropp, J., Jin, Q., & Halevy, I. (2022). Controls on the isotopic composition of microbial methane. *Science Advances*, *8*(14), eabm5713. https://doi.org/10.1126/sciadv.abm5713

Gruen, D. S., Wang, D. T., Könneke, M., Topçuoğlu, B. D., Stewart, L. C., Goldhammer, T., Holden, J. F., Hinrichs, K.-U., & Ono, S. (2018). Experimental investigation on the controls of clumped isotopologue and hydrogen isotope ratios in microbial methane. *Geochimica Et Cosmochimica Acta*, *237*, 339-356. https://doi.org/10.1016/j.gca.2018.06.029

Haghnegahdar, M. (2018). *Theoretical Study of Tellurium Isotope Fractionations in Ore-Forming Systems, and Studies of Doubly Substituted Isotopologues of Methane* (Publication Number Haghnegahdar_ucla_0031D_17475) UCLA]. https://escholarship.org/uc/item/7bd5c85d

Haghnegahdar, M. A., Hultquist, N., Hamovit, N. D., Yarwood, S. A., Bouyon, A., Kaufman, A. J., Sun, J., Magen, C., & Farquhar, J. (2024). A Better Understanding of Atmospheric Methane Sources Using $^{13}CH3D$ and $^{12}CH_2D_2$ Clumped Isotopes. *Journal of Geophysical Research: Biogeosciences*, *129*(11). https://doi.org/10.1029/2024JG008172

Haghnegahdar, M. A., Schauble, E. A., & Young, E. D. (2017). A model for 12CH2D2 and 13CH3D as complementary tracers for the budget of atmospheric CH4. *Global Biogeochemical Cycles*, *31*(9), 1387-1407. https://doi.org/10.1002/2017GB005655

Haghnegahdar, M. A., Sun, J., Hultquist, N., Hamovit, N. D., Kitchen, N., Eiler, J., Ono, S., Yarwood, S. A., Kaufman, A. J., Dickerson, R. R., Bouyon, A., Magen, C., & Farquhar, J. (2023). Tracing sources of atmospheric methane using clumped isotopes. *Proceedings*

of the National Academy of Sciences, *120*(47), e2305574120. https://doi.org/10.1073/pnas.2305574120
Hanson, R. S., & Hanson, T. E. (1996). Methanotrophic bacteria. *Microbiological Reviews*, *60*(2), 439-471. https://doi.org/10.1128/mr.60.2.439-471.1996
Hao, W. M., & Ward, D. E. (1993). Methane production from global biomass burning. *Journal of Geophysical Research: Atmospheres*, *98*(D11), 20657-20661. https://doi.org/10.1029/93JD01908
Happell, J. D., Chanton, J. P., & Showers, W. S. (1994). The influence of methane oxidation on the stable isotopic composition of methane emitted from Florida swamp forests. *Geochimica Et Cosmochimica Acta*, *58*(20), 4377-4388. https://doi.org/10.1016/0016-7037(94)90341-7
Hausmann, P., Sussmann, R., & Smale, D. (2016). Contribution of oil and natural gas production to renewed increase in atmospheric methane (2007–2014): top–down estimate from ethane and methane column observations. *Atmospheric Chemistry and Physics*, *16*(5), 3227-3244. https://doi.org/10.5194/acp-16-3227-2016
Hayes, J. M. (2001a). Fractionation of Carbon and Hydrogen Isotopes in Biosynthetic Processes*. *Reviews in Mineralogy and Geochemistry*, *43*(1), 225-277. https://doi.org/10.2138/gsrmg.43.1.225
Hayes, J. M. (2001b). Stable Isotope Geochemistry
3. Fractionation of Carbon and Hydrogen Isotopes in Biosynthetic Processes. In J. W. Valley & D. R. Cole (Eds.), (pp. 225-278). De Gruyter. https://doi.org/doi:10.1515/9781501508745-006
Hayes, J. M. (2004). An introduction to isotopic calculations. *Woods Hole Oceanographic Institution, Woods Hole, MA, 2543*.
Hein, R., Crutzen, P. J., & Heimann, M. (1997). An inverse modeling approach to investigate the global atmospheric methane cycle. *Global Biogeochemical Cycles*, *11*(1), 43-76. https://doi.org/10.1029/96GB03043
Helmig, D., Rossabi, S., Hueber, J., Tans, P., Montzka, S. A., Masarie, K., Thoning, K., Plass-Duelmer, C., Claude, A., Carpenter, L. J., Lewis, A. C., Punjabi, S., Reimann, S., Vollmer, M. K., Steinbrecher, R., Hannigan, J. W., Emmons, L. K., Mahieu, E., Franco, B.,…Pozzer, A. (2016). Reversal of global atmospheric ethane and propane trends largely due to US oil and natural gas production. *Nature Geoscience*, *9*(7), 490-495. https://doi.org/10.1038/ngeo2721
Herndon, S. C., Shorter, J. H., Zahniser, M. S., Wormhoudt, J., Nelson, D. D., Demerjian, K. L., & Kolb, C. E. (2005). Real-Time Measurements of SO2, H2CO, and CH4 Emissions from In-Use Curbside Passenger Buses in New York City Using a Chase Vehicle. *Environmental Science & Technology*, *39*(20), 7984-7990. https://doi.org/10.1021/es0482942
Höglund-Isaksson, L. (2017). Bottom-up simulations of methane and ethane emissions from global oil and gas systems 1980 to 2012. *Environmental Research Letters*, *12*(2), 024007.
Holler, T., Wegener, G., Knittel, K., Boetius, A., Brunner, B., Kuypers, M. M. M., & Widdel, F. (2009). Substantial 13C/12C and D/H fractionation during anaerobic oxidation of methane by marine consortia enriched in vitro. *Environmental Microbiology Reports*, *1*(5), 370-376. https://doi.org/10.1111/j.1758-2229.2009.00074.x
Hornibrook, E. R. C., Longstaffe, F. J., & Fyfe, W. S. (1997). Spatial distribution of microbial methane production pathways in temperate zone wetland soils: Stable carbon and

hydrogen isotope evidence. *Geochimica Et Cosmochimica Acta*, *61*(4), 745-753. https://doi.org/10.1016/S0016-7037(96)00368-7

Hossaini, R., Chipperfield, M. P., Saiz‐Lopez, A., Fernandez, R., Monks, S., Feng, W., Brauer, P., & Von Glasow, R. (2016). A global model of tropospheric chlorine chemistry: Organic versus inorganic sources and impact on methane oxidation. *Journal of Geophysical Research: Atmospheres*, *121*(23), 14,271-214,297.

Houweling, S., Kaminski, T., Dentener, F., Lelieveld, J., & Heimann, M. (1999). Inverse modeling of methane sources and sinks using the adjoint of a global transport model. *Journal of Geophysical Research: Atmospheres*, *104*(D21), 26137-26160. https://doi.org/10.1029/1999JD900428

Hunt, J. (1995). Petroleum Geochemistry and Geology (Textbook). *Petroleum Geochemistry and Geology (Textbook).(2nd Ed.), WH Freeman Company*.

IEA. *Global conventional biofuel production, 2011-2023* https://www.iea.org/data-and-statistics/charts/global-conventional-biofuel-production-2011-2023

IEA. (2024). *Global Methane Tracker 2024* https://www.iea.org/reports/global-methane-tracker-2024

Intergovernmental Panel on Climate, C. (2023). *Climate Change 2022 – Impacts, Adaptation and Vulnerability: Working Group II Contribution to the Sixth Assessment Report of the Intergovernmental Panel on Climate Change*. Cambridge University Press. https://doi.org/DOI: 10.1017/9781009325844

IPCC. (2006). *IPCC Guidelines for National Greenhouse Gas Inventories*. The Intergovernmental Panel on Climate Change, IPCC TSU NGGIP, IGES, Institute for Global Environmental Strategy. http://www.ipcc-nggip.iges.or.jp/support/Primer_2006GLs.pdf

IPCC. (2013). *Climate Change 2013: The Physical Science Basis. Contribution of Working Group I to the Fifth Assessment Report of the Intergovernmental Panel on Climate Change* (T. F. Stocker, D. Qin, G.-K. Plattner, M. Tignor, S.K. Allen, J. Boschung, A. Nauels, Y. Xia, V. Bex， , & P. M. Midgley, Eds.). Cambridge University Press.

IPCC. (2019). *2019 Refinement to the 2006 IPCC Guidelines for National Greenhouse Gas Inventories*. IPCC. https://www.ipcc.ch/report/2019-refinement-to-the-2006-ipccguidelines-for-national-greenhouse-gas-inventories/

IPCC. (2021). *Climate Change 2021: The Physical Science Basis. Contribution of Working Group I to the Sixth Assessment Report of the Intergovernmental Panel on Climate Change*. Cambridge University Press. https://doi.org/doi:10.1017/9781009157896

Ito, A., & Inatomi, M. (2012). Use of a process-based model for assessing the methane budgets of global terrestrial ecosystems and evaluation of uncertainty. *Biogeosciences*, *9*(2), 759-773. https://doi.org/10.5194/bg-9-759-2012

J. W. Dottin, I., Farquhar, J., Kim, S. T., Shearer, C., Wing, B., Sun, J., & Ni, P. (2022). Isotopic evidence of sulfur photochemistry during lunar regolith formation. *Geochemical Perspectives Letters*, *23*, 38-42. https://doi.org/10.7185/geochemlet.2235

Jackson, R. B., Down, A., Phillips, N. G., Ackley, R. C., Cook, C. W., Plata, D. L., & Zhao, K. (2014). Natural gas pipeline leaks across Washington, DC. *Environmental Science & Technology*, *48*(3), 2051-2058. https://doi.org/10.1021/es404474x

Jacob, D. J., Turner, A. J., Maasakkers, J. D., Sheng, J., Sun, K., Liu, X., Chance, K., Aben, I., McKeever, J., & Frankenberg, C. (2016). Satellite observations of atmospheric methane

and their value for quantifying methane emissions. *Atmos. Chem. Phys.*, *16*(22), 14371-14396. https://doi.org/10.5194/acp-16-14371-2016

Jacob, D. J., Varon, D. J., Cusworth, D. H., Dennison, P. E., Frankenberg, C., Gautam, R., Guanter, L., Kelley, J., McKeever, J., Ott, L. E., Poulter, B., Qu, Z., Thorpe, A. K., Worden, J. R., & Duren, R. M. (2022). Quantifying methane emissions from the global scale down to point sources using satellite observations of atmospheric methane. *Atmos. Chem. Phys.*, *22*(14), 9617-9646. https://doi.org/10.5194/acp-22-9617-2022

Janssens-Maenhout, G., Crippa, M., Guizzardi, D., Muntean, M., Schaaf, E., Dentener, F., Bergamaschi, P., Pagliari, V., Olivier, J. G. J., Peters, J. A. H. W., van Aardenne, J. A., Monni, S., Doering, U., Petrescu, A. M. R., Solazzo, E., & Oreggioni, G. D. (2019). EDGAR v4.3.2 Global Atlas of the three major greenhouse gas emissions for the period 1970–2012. *Earth Syst. Sci. Data*, *11*(3), 959-1002. https://doi.org/10.5194/essd-11-959-2019

Jautzy, J. J., Douglas, P. M. J., Xie, H., Eiler, J. M., & Clark, I. D. (2021). CH4 isotopic ordering records ultra-slow hydrocarbon biodegradation in the deep subsurface. *Earth and Planetary Science Letters*, *562*, 116841. https://doi.org/10.1016/j.epsl.2021.116841

Joelsson, L. M. T., Forecast, R., Schmidt, J. A., Meusinger, C., Nilsson, E. J. K., Ono, S., & Johnson, M. S. (2014). Relative rate study of the kinetic isotope effect in the 13CH3D+Cl reaction. *Chemical Physics Letters*, *605-606*, 152-157. https://doi.org/10.1016/j.cplett.2014.05.022

Joelsson, L. M. T., Schmidt, J. A., Nilsson, E. J. K., Blunier, T., Griffith, D. W. T., Ono, S., & Johnson, M. S. (2016). Kinetic isotope effects of 12CH3D + OH and 13CH3D + OH from 278 to 313 K. *Atmospheric Chemistry and Physics*, *16*(7), 4439-4449. https://doi.org/10.5194/acp-16-4439-2016

Johnson, M. S., Matthews, E., Du, J., Genovese, V., & Bastviken, D. (2022). Methane Emission From Global Lakes: New Spatiotemporal Data and Observation-Driven Modeling of Methane Dynamics Indicates Lower Emissions. *Journal of Geophysical Research: Biogeosciences*, *127*(7), e2022JG006793. https://doi.org/10.1029/2022JG006793

Kai, F. M., Tyler, S. C., Randerson, J. T., & Blake, D. R. (2011). Reduced methane growth rate explained by decreased Northern Hemisphere microbial sources. *Nature*, *476*(7359), 194-197. https://doi.org/10.1038/nature10259

Kaiser, J. W., Heil, A., Andreae, M. O., Benedetti, A., Chubarova, N., Jones, L., Morcrette, J. J., Razinger, M., Schultz, M. G., Suttie, M., & van der Werf, G. R. (2012). Biomass burning emissions estimated with a global fire assimilation system based on observed fire radiative power. *Biogeosciences*, *9*(1), 527-554. https://doi.org/10.5194/bg-9-527-2012

Karion, A., Callahan, W., Stock, M., Prinzivalli, S., Verhulst, K. R., Kim, J., Salameh, P. K., Lopez-Coto, I., & Whetstone, J. (2020). Greenhouse gas observations from the Northeast Corridor tower network. *Earth Syst. Sci. Data*, *12*(1), 699-717. https://doi.org/10.5194/essd-12-699-2020

Karion, A., Sweeney, C., Pétron, G., Frost, G., Michael Hardesty, R., Kofler, J., Miller, B. R., Newberger, T., Wolter, S., & Banta, R. (2013). Methane emissions estimate from airborne measurements over a western United States natural gas field. *Geophysical Research Letters*, *40*(16), 4393-4397.

Kawagucci, S., Kobayashi, M., Hattori, S., Yamada, K., Ueno, Y., Takai, K., & Yoshida, N. (2014). Hydrogen isotope systematics among H2–H2O–CH4 during the growth of the hydrogenotrophic methanogen Methanothermobacter thermautotrophicus strain ΔH.

Geochimica Et Cosmochimica Acta, *142*, 601-614. https://doi.org/10.1016/j.gca.2014.07.020

Keeling, C. D. (1958). The concentration and isotopic abundances of atmospheric carbon dioxide in rural areas. *Geochimica Et Cosmochimica Acta*, *13*(4), 322-334. https://doi.org/10.1016/0016-7037(58)90033-4

Kelley, D. S., & Früh-Green, G. L. (1999). Abiogenic methane in deep-seated mid-ocean ridge environments: Insights from stable isotope analyses. *Journal of Geophysical Research: Solid Earth*, *104*(B5), 10439-10460. https://doi.org/10.1029/1999JB900058

Kelley, D. S., Karson, J. A., Früh-Green, G. L., Yoerger, D. R., Shank, T. M., Butterfield, D. A., Hayes, J. M., Schrenk, M. O., Olson, E. J., Proskurowski, G., Jakuba, M., Bradley, A., Larson, B., Ludwig, K., Glickson, D., Buckman, K., Bradley, A. S., Brazelton, W. J., Roe, K.,…Sylva, S. P. (2005). A Serpentinite-Hosted Ecosystem: The Lost City Hydrothermal Field. *Science*, *307*(5714), 1428-1434. https://doi.org/10.1126/science.1102556

Kim, J., Verma, S. B., & Billesbach, D. P. (1999). Seasonal variation in methane emission from a temperate Phragmites-dominated marsh: effect of growth stage and plant-mediated transport. *Global Change Biology*, *5*(4), 433-440. https://doi.org/10.1046/j.1365-2486.1999.00237.x

Kim, J., Verma, S. B., Billesbach, D. P., & Clement, R. J. (1998). Diel variation in methane emission from a midlatitude prairie wetland: Significance of convective throughflow in Phragmites australis. *Journal of Geophysical Research: Atmospheres*, *103*(D21), 28029-28039. https://doi.org/10.1029/98JD02441

Kirschke, S., Bousquet, P., Ciais, P., Saunois, M., Canadell, J. G., Dlugokencky, E. J., Bergamaschi, P., Bergmann, D., Blake, D. R., Bruhwiler, L., Cameron-Smith, P., Castaldi, S., Chevallier, F., Feng, L., Fraser, A., Heimann, M., Hodson, E. L., Houweling, S., Josse, B.,…Zeng, G. (2013). Three decades of global methane sources and sinks. *Nature Geoscience*, *6*(10), 813-823. https://doi.org/10.1038/ngeo1955

Kiyosu, Y., Asada, N., & Yoshida, Y. (1992). Origin of light hydrocarbon gases from the Matsukawa geothermal area in Japan. *Chemical Geology: Isotope Geoscience section*, *94*(4), 321-329. https://doi.org/10.1016/0168-9622(92)90007-W

Kohn, M. J. (2010). Carbon isotope compositions of terrestrial C3 plants as indicators of (paleo)ecology and (paleo)climate. *Proceedings of the National Academy of Sciences*, *107*(46), 19691-19695. https://doi.org/10.1073/pnas.1004933107

Krause, S. J. E., Liu, J., Young, E. D., & Treude, T. (2022). Δ13CH3D and Δ12CH2D2 signatures of methane aerobically oxidized by Methylosinus trichosporium with implications for deciphering the provenance of methane gases. *Earth and Planetary Science Letters*, *593*, 117681. https://doi.org/10.1016/j.epsl.2022.117681

Krol, M., Houweling, S., Bregman, B., van den Broek, M., Segers, A., van Velthoven, P., Peters, W., Dentener, F., & Bergamaschi, P. (2005). The two-way nested global chemistry-transport zoom model TM5: algorithm and applications. *Atmos. Chem. Phys.*, *5*(2), 417-432. https://doi.org/10.5194/acp-5-417-2005

Krzycki, J. A., Kenealy, W. R., DeNiro, M. J., & Zeikus, J. G. (1987). Stable Carbon Isotope Fractionation by Methanosarcina barkeri during Methanogenesis from Acetate, Methanol, or Carbon Dioxide-Hydrogen. *Applied and Environmental Microbiology*, *53*(10), 2597-2599. https://doi.org/10.1128/aem.53.10.2597-2599.1987

Labidi, J., McCollom, T. M., Giunta, T., Sherwood Lollar, B., Leavitt, W. D., & Young, E. D. (2024). Clumped Isotope Signatures of Abiotic Methane: The Role of the Combinatorial Isotope Effect. *Journal of Geophysical Research: Solid Earth*, *129*(7), e2023JB028194. https://doi.org/10.1029/2023JB028194

Labidi, J., Young, E. D., Giunta, T., Kohl, I. E., Seewald, J., Tang, H., Lilley, M. D., & Früh-Green, G. L. (2020). Methane thermometry in deep-sea hydrothermal systems: Evidence for re-ordering of doubly-substituted isotopologues during fluid cooling. *Geochimica Et Cosmochimica Acta*, *288*, 248-261. https://doi.org/10.1016/j.gca.2020.08.013

Łakomiec, P., Holst, J., Friborg, T., Crill, P., Rakos, N., Kljun, N., Olsson, P.-O., Eklundh, L., Persson, A., & Rinne, J. (2021). Field-scale CH 4 emission at a subarctic mire with heterogeneous permafrost thaw status. *Biogeosciences*, *18*(20), 5811-5830.

Lalk, E., Pape, T., Gruen, D. S., Kaul, N., Karolewski, J. S., Bohrmann, G., & Ono, S. (2022). Clumped methane isotopologue-based temperature estimates for sources of methane in marine gas hydrates and associated vent gases. *Geochimica Et Cosmochimica Acta*, *327*, 276-297. https://doi.org/10.1016/j.gca.2022.04.013

Lalk, E., Seewald, J. S., Bryndzia, L. T., & Ono, S. (2023). Kilometer-scale Δ13CH3D profiles distinguish end-member mixing from methane production in deep marine sediments. *Organic Geochemistry*, *181*, 104630. https://doi.org/10.1016/j.orggeochem.2023.104630

Lalk, E., Velez, A., & Ono, S. (2024). Methane Clumped Isotopologue Variability from Ebullition in a Mid-latitude Lake. *ACS Earth and Space Chemistry*, *8*(4), 689-701. https://doi.org/10.1021/acsearthspacechem.3c00282

Lamb, B. K., Cambaliza, M. O., Davis, K. J., Edburg, S. L., Ferrara, T. W., Floerchinger, C., Heimburger, A. M., Herndon, S., Lauvaux, T., & Lavoie, T. (2016). Direct and indirect measurements and modeling of methane emissions in Indianapolis, Indiana. *Environmental Science & Technology*, *50*(16), 8910-8917.

Lan, X., Basu, S., Schwietzke, S., Bruhwiler, L. M. P., Dlugokencky, E. J., Michel, S. E., Sherwood, O. A., Tans, P. P., Thoning, K., Etiope, G., Zhuang, Q., Liu, L., Oh, Y., Miller, J. B., Pétron, G., Vaughn, B. H., & Crippa, M. (2021). Improved Constraints on Global Methane Emissions and Sinks Using δ13C-CH4. *Global Biogeochemical Cycles*, *35*(6), e2021GB007000. https://doi.org/10.1029/2021GB007000

Lan, X., K.W. Thoning, & Dlugokencky, E. J. (2023). Trends in globally-averaged CH4, N2O, and SF6 determined from NOAA Global Monitoring Laboratory measurements. *Version 2024-04*. https://doi.org/10.15138/P8XG-AA10

Lan, X., Thoning, K. W., & Dlugokencky, E. J. *Trends in globally-averaged CH4, N2O, and SF6 determined from NOAA Global Monitoring Laboratory measurements. Version 2025-01* https://doi.org/10.15138/P8XG-AA10

Langenegger, T., Vachon, D., Donis, D., & McGinnis, D. F. (2019). What the bubble knows: Lake methane dynamics revealed by sediment gas bubble composition. *Limnology and Oceanography*, *64*(4), 1526-1544. https://doi.org/10.1002/lno.11133

le Texier, H., Solomon, S., & Garcia, R. R. (1988). The role of molecular hydrogen and methane oxidation in the water vapour budget of the stratosphere. *Quarterly Journal of the Royal Meteorological Society*, *114*(480), 281-295. https://doi.org/10.1002/qj.49711448002

Leaney, F. W., Osmond, C. B., Allison, G. B., & Ziegler, H. (1985). Hydrogen-isotope composition of leaf water in C3 and C4 plants: its relationship to the hydrogen-isotope composition of dry matter. *Planta*, *164*(2), 215-220. https://doi.org/10.1007/BF00396084

Lebel, E. D., Finnegan, C. J., Ouyang, Z., & Jackson, R. B. (2022). Methane and NOx Emissions from Natural Gas Stoves, Cooktops, and Ovens in Residential Homes. *Environmental Science & Technology*, *56*(4), 2529-2539. https://doi.org/10.1021/acs.est.1c04707

Li, J., Ash, J. L., Cobban, A., Kubik, B. C., Rizzo, G., Thompson, M., Guibourdenche, L., Berger, S., Morra, K., Lin, Y., Mueller, E. P., Masterson, A. L., Stein, R., Fogel, M., Torres, M. A., Feng, X., Holden, J. F., Martini, A., Welte, C. U.,…Leavitt, W. D. (2024). The clumped isotope signatures of multiple methanogenesis metabolisms. *bioRxiv*, 2024.2012.2018.629299. https://doi.org/10.1101/2024.12.18.629299

Li, J., Chiu, B. K., Piasecki, A. M., Feng, X., Landis, J. D., Marcum, S., Young, E. D., & Leavitt, W. D. (2024). The evolution of multiply substituted isotopologues of methane during microbial aerobic oxidation. *Geochimica Et Cosmochimica Acta*, *381*, 223-238. https://doi.org/10.1016/j.gca.2024.06.032

Liang, M.-C., & Mahata, S. (2015). Oxygen anomaly in near surface carbon dioxide reveals deep stratospheric intrusion. *Scientific Reports*, *5*(1), 11352. https://doi.org/10.1038/srep11352

Liu, J. (2024). *The Biogeochemistry of Methane Cycling and Its Clumped Isotope Effects* (Publication Number 31637159) [Ph.D., University of California, Los Angeles]. ProQuest Dissertations & Theses Global. United States -- California. https://escholarship.org/uc/item/62d7r8rs

Liu, J., Harris, R. L., Ash, J. L., Ferry, J. G., Krause, S. J. E., Labidi, J., Prakash, D., Sherwood Lollar, B., Treude, T., Warr, O., & Young, E. D. (2023). Reversibility controls on extreme methane clumped isotope signatures from anaerobic oxidation of methane. *Geochimica Et Cosmochimica Acta*, *348*, 165-186. https://doi.org/10.1016/j.gca.2023.02.022

Liu, J., Treude, T., Abbasov, O. R., Baloglanov, E. E., Aliyev, A. A., Harris, C. M., Leavitt, W. D., & Young, E. D. (2023). Clumped isotope evidence for microbial alteration of thermogenic methane in terrestrial mud volcanoes. *Geology*, *52*(1), 22-26. https://doi.org/10.1130/G51667.1

Liu, Q., Li, J., Jiang, W., Li, Y., Lin, M., Liu, W., Shuai, Y., Zhang, H., Peng, P. a., & Xiong, Y. (2024). Application of an absolute reference frame for methane clumped-isotope analyses. *Chemical Geology*, *646*, 121922. https://doi.org/10.1016/j.chemgeo.2024.121922

Liu, Q., & Liu, Y. (2016). Clumped-isotope signatures at equilibrium of CH4, NH3, H2O, H2S and SO2. *Geochimica Et Cosmochimica Acta*, *175*, 252-270. https://doi.org/10.1016/j.gca.2015.11.040

Liu, Q., Wu, X., Wang, X., Jin, Z., Zhu, D., Meng, Q., Huang, S., Liu, J., & Fu, Q. (2019). Carbon and hydrogen isotopes of methane, ethane, and propane: A review of genetic identification of natural gas. *Earth-Science Reviews*, *190*, 247-272. https://doi.org/10.1016/j.earscirev.2018.11.017

Lowry, D., Fisher, R. E., France, J. L., Coleman, M., Lanoisellé, M., Zazzeri, G., Nisbet, E. G., Shaw, J. T., Allen, G., & Pitt, J. (2020). Environmental baseline monitoring for shale gas development in the UK: Identification and geochemical characterisation of local source emissions of methane to atmosphere. *Science of The Total Environment*, *708*, 134600. https://doi.org/10.1016/j.scitotenv.2019.134600

Lu, H., Xi, D., Xiang, Y., Su, Z., & Cheng, Y. F. (2025). Vehicle–canine collaboration for urban pipeline methane leak detection. *Nature Cities*. https://doi.org/10.1038/s44284-024-00183-w

Lu, Y., & Khalil, M. A. K. (1991). Tropospheric OH: model calculations of spatial, temporal, and secular variations. *Chemosphere*, *23*(3), 397-444. https://doi.org/10.1016/0045-6535(91)90194-I

Lyon, D. R., Zavala-Araiza, D., Alvarez, R. A., Harriss, R., Palacios, V., Lan, X., Talbot, R., Lavoie, T., Shepson, P., Yacovitch, T. I., Herndon, S. C., Marchese, A. J., Zimmerle, D., Robinson, A. L., & Hamburg, S. P. (2015). Constructing a Spatially Resolved Methane Emission Inventory for the Barnett Shale Region. *Environmental Science & Technology*, *49*(13), 8147-8157. https://doi.org/10.1021/es506359c

Lyon, G. L., & Giggenbach, W. F. (1994). The isotopic and chemical composition of natural gases from the South Island, New Zealand.

Ma, Q., Wu, S., & Tang, Y. (2008). Formation and abundance of doubly-substituted methane isotopologues (13CH3D) in natural gas systems. *Geochimica Et Cosmochimica Acta*, *72*(22), 5446-5456. https://doi.org/10.1016/j.gca.2008.08.014

Maasakkers, J. D., Jacob, D. J., Sulprizio, M. P., Scarpelli, T. R., Nesser, H., Sheng, J. X., Zhang, Y., Hersher, M., Bloom, A. A., Bowman, K. W., Worden, J. R., Janssens-Maenhout, G., & Parker, R. J. (2019). Global distribution of methane emissions, emission trends, and OH concentrations and trends inferred from an inversion of GOSAT satellite data for 2010–2015. *Atmos. Chem. Phys.*, *19*(11), 7859-7881. https://doi.org/10.5194/acp-19-7859-2019

MacFarling Meure, C., Etheridge, D., Trudinger, C., Steele, P., Langenfelds, R., van Ommen, T., Smith, A., & Elkins, J. (2006). Law Dome CO2, CH4 and N2O ice core records extended to 2000 years BP. *Geophysical Research Letters*, *33*(14). https://doi.org/10.1029/2006GL026152

Machel, H. G. (2001). Bacterial and thermochemical sulfate reduction in diagenetic settings — old and new insights. *Sedimentary Geology*, *140*(1), 143-175. https://doi.org/10.1016/S0037-0738(00)00176-7

Magen, C., Lapham, L. L., Pohlman, J. W., Marshall, K., Bosman, S., Casso, M., & Chanton, J. P. (2014). A simple headspace equilibration method for measuring dissolved methane. *Limnology and Oceanography: Methods*, *12*(9), 637-650.

Mak, J. E., & Brenninkmeijer, C. A. (1994). Compressed air sample technology for isotopic analysis of atmospheric carbon monoxide. *Journal of Atmospheric and Oceanic Technology*, *11*(2), 425-431.

Marcum, S., Young, E. D., Li, J., Leavitt, W., & Liu, J. (2023). A Bayesian Approach to Developing Methane as a Biosignature. AGU Fall Meeting,

Martinerie, P., Nourtier-Mazauric, E., Barnola, J. M., Sturges, W. T., Worton, D. R., Atlas, E., Gohar, L. K., Shine, K. P., & Brasseur, G. P. (2009). Long-lived halocarbon trends and budgets from atmospheric chemistry modelling constrained with measurements in polar firn. *Atmos. Chem. Phys.*, *9*(12), 3911-3934. https://doi.org/10.5194/acp-9-3911-2009

Martini, A. M., Budai, J. M., Walter, L. M., & Schoell, M. (1996). Microbial generation of economic accumulations of methane within a shallow organic-rich shale. *Nature*, *383*(6596), 155-158. https://doi.org/10.1038/383155a0

Martini, A. M., Walter, L. M., Budai, J. M., Ku, T. C. W., Kaiser, C. J., & Schoell, M. (1998). Genetic and temporal relations between formation waters and biogenic methane: Upper Devonian Antrim Shale, Michigan Basin, USA. *Geochimica Et Cosmochimica Acta*, *62*(10), 1699-1720. https://doi.org/10.1016/S0016-7037(98)00090-8

Matsuda, H. (1974). Double focusing mass spectrometers of second order. *International Journal of Mass Spectrometry and Ion Physics*, *14*(2), 219-233. https://doi.org/10.1016/0020-7381(74)80009-4

Matsumi, Y., Izumi, K., Skorokhodov, V., Kawasaki, M., & Tanaka, N. (1997). Reaction and Quenching of Cl(2Pj) Atoms in Collisions with Methane and Deuterated Methanes. *The Journal of Physical Chemistry A*, *101*(7), 1216-1221. https://doi.org/10.1021/jp962064v

Mayumi, D., Mochimaru, H., Tamaki, H., Yamamoto, K., Yoshioka, H., Suzuki, Y., Kamagata, Y., & Sakata, S. (2016). Methane production from coal by a single methanogen. *Science*, *354*(6309), 222-225. https://doi.org/10.1126/science.aaf8821

Mayumi, D., Tamaki, H., Kato, S., Igarashi, K., Lalk, E., Nishikawa, Y., Minagawa, H., Sato, T., Ono, S., Kamagata, Y., & Sakata, S. (2024). Hydrogenotrophic methanogens overwrite isotope signals of subsurface methane. *Science*, *386*(6728), 1372-1376. https://doi.org/10.1126/science.ado0126

McCollom, T. M., Lollar, B. S., Lacrampe-Couloume, G., & Seewald, J. S. (2010). The influence of carbon source on abiotic organic synthesis and carbon isotope fractionation under hydrothermal conditions. *Geochimica Et Cosmochimica Acta*, *74*(9), 2717-2740. https://doi.org/10.1016/j.gca.2010.02.008

McKain, K., Down, A., Raciti, S. M., Budney, J., Hutyra, L. R., Floerchinger, C., Herndon, S. C., Nehrkorn, T., Zahniser, M. S., Jackson, R. B., Phillips, N., & Wofsy, S. C. (2015). Methane emissions from natural gas infrastructure and use in the urban region of Boston, Massachusetts. *Proceedings of the National Academy of Sciences*, *112*(7), 1941-1946. https://doi.org/10.1073/pnas.1416261112

McNorton, J., Chipperfield, M. P., Gloor, M., Wilson, C., Feng, W., Hayman, G. D., Rigby, M., Krummel, P. B., O'Doherty, S., Prinn, R. G., Weiss, R. F., Young, D., Dlugokencky, E., & Montzka, S. A. (2016). Role of OH variability in the stalling of the global atmospheric CH₄ growth rate from 1999 to 2006. *Atmospheric Chemistry and Physics*, *16*(12), 7943-7956. https://doi.org/10.5194/acp-16-7943-2016

McNorton, J., Wilson, C., Gloor, M., Parker, R. J., Boesch, H., Feng, W., Hossaini, R., & Chipperfield, M. P. (2018). Attribution of recent increases in atmospheric methane through 3-D inverse modelling. *Atmospheric Chemistry and Physics*, *18*(24), 18149-18168. https://doi.org/10.5194/acp-18-18149-2018

Mehl, M., Pitz, W. J., Westbrook, C. K., & Curran, H. J. (2011). Kinetic modeling of gasoline surrogate components and mixtures under engine conditions. *Proceedings of the Combustion Institute*, *33*(1), 193-200. https://doi.org/10.1016/j.proci.2010.05.027

Meirink, J. F., Bergamaschi, P., & Krol, M. C. (2008). Four-dimensional variational data assimilation for inverse modelling of atmospheric methane emissions: method and comparison with synthesis inversion. *Atmos. Chem. Phys.*, *8*(21), 6341-6353. https://doi.org/10.5194/acp-8-6341-2008

Menoud, M., van der Veen, C., Lowry, D., Fernandez, J. M., Bakkaloglu, S., France, J. L., Fisher, R. E., Maazallahi, H., Stanisavljević, M., Nęcki, J., Vinkovic, K., Łakomiec, P., Rinne, J., Korbeń, P., Schmidt, M., Defratyka, S., Yver-Kwok, C., Andersen, T., Chen, H., & Röckmann, T. (2022). New contributions of measurements in Europe to the global inventory of the stable isotopic composition of methane. *Earth Syst. Sci. Data*, *14*(9), 4365-4386. https://doi.org/10.5194/essd-14-4365-2022

Menoud, M., van der Veen, C., Necki, J., Bartyzel, J., Szénási, B., Stanisavljević, M., Pison, I., Bousquet, P., & Röckmann, T. (2021). Methane (CH4) sources in Krakow, Poland:

insights from isotope analysis. *Atmos. Chem. Phys.*, *21*(17), 13167-13185. https://doi.org/10.5194/acp-21-13167-2021
Meyer, A. G., Lindenmaier, R., Heerah, S., Benedict, K. B., Kort, E. A., Peischl, J., & Dubey, M. K. (2022). Using Multiscale Ethane/Methane Observations to Attribute Coal Mine Vent Emissions in the San Juan Basin From 2013 to 2021. *Journal of Geophysical Research: Atmospheres*, *127*(18), e2022JD037092. https://doi.org/10.1029/2022JD037092
Milkov, A. V., & Etiope, G. (2018). Revised genetic diagrams for natural gases based on a global dataset of >20,000 samples. *Organic Geochemistry*, *125*, 109-120. https://doi.org/10.1016/j.orggeochem.2018.09.002
Milkov, A. V., Faiz, M., & Etiope, G. (2020). Geochemistry of shale gases from around the world: Composition, origins, isotope reversals and rollovers, and implications for the exploration of shale plays. *Organic Geochemistry*, *143*, 103997. https://doi.org/10.1016/j.orggeochem.2020.103997
Milkov, A. V., Schwietzke, S., Allen, G., Sherwood, O. A., & Etiope, G. (2020). Using global isotopic data to constrain the role of shale gas production in recent increases in atmospheric methane. *Scientific Reports*, *10*(1), 4199. https://doi.org/10.1038/s41598-020-61035-w
Møller, C., & Plesset, M. S. (1934). Note on an Approximation Treatment for Many-Electron Systems. *Physical Review*, *46*(7), 618-622. https://doi.org/10.1103/PhysRev.46.618
Montreal protocol on substances that deplete the ozone layer, 128-136 (1987).
Montzka, S. A., Krol, M., Dlugokencky, E., Hall, B., Jöckel, P., & Lelieveld, J. (2011). Small interannual variability of global atmospheric hydroxyl. *Science*, *331*(6013), 67-69. https://doi.org/10.1126/science.1197640
Moores, J. E., & Sapers, H. M. (2024). Isotopic fractionation of methane on Mars via diffusive separation in the subsurface. *Planetary and Space Science*, *251*, 105971. https://doi.org/10.1016/j.pss.2024.105971
Morin, T. H., Bohrer, G., Naor-Azrieli, L., Mesi, S., Kenny, W. T., Mitsch, W. J., & Schäfer, K. V. R. (2014). The seasonal and diurnal dynamics of methane flux at a created urban wetland. *Ecological Engineering*, *72*, 74-83. https://doi.org/10.1016/j.ecoleng.2014.02.002
Mukhopadhyay, P. K. (1994). Vitrinite reflectance as maturity parameter: petrographic and molecular characterization and its applications to basin modeling. In. ACS Publications.
Naik, V., Voulgarakis, A., Fiore, A. M., Horowitz, L. W., Lamarque, J.-F., Lin, M., Prather, M. J., Young, P., Bergmann, D., & Cameron-Smith, P. (2013). Preindustrial to present-day changes in tropospheric hydroxyl radical and methane lifetime from the Atmospheric Chemistry and Climate Model Intercomparison Project (ACCMIP). *Atmospheric Chemistry and Physics*, *13*(10), 5277-5298.
Nakagawa, F., Tsunogai, U., Komatsu, D. D., Yamada, K., Yoshida, N., Moriizumi, J., Nagamine, K., Iida, T., & Ikebe, Y. (2005). Automobile exhaust as a source of 13C- and D-enriched atmospheric methane in urban areas. *Organic Geochemistry*, *36*(5), 727-738. https://doi.org/10.1016/j.orggeochem.2005.01.003
Nam, E. K., Jensen, T. E., & Wallington, T. J. (2004). Methane Emissions from Vehicles. *Environmental Science & Technology*, *38*(7), 2005-2010. https://doi.org/10.1021/es034837g
National Academies of Sciences Engineering and Medicine. (2018). *Improving Characterization of Anthropogenic Methane Emissions in the United States* [Book]. National Academies

Press. http://search.ebscohost.com/login.aspx?direct=true&db=nlebk&AN=1883976&site=ehost-live

Nguyen, N.-p., Mirarab, S., Liu, B., Pop, M., & Warnow, T. (2014). TIPP: taxonomic identification and phylogenetic profiling. *Bioinformatics*, *30*(24), 3548-3555. https://doi.org/10.1093/bioinformatics/btu721

Nisbet, E. G. (2023a). Climate feedback on methane from wetlands. *Nature Climate Change*, *13*(5), 421-422. https://doi.org/10.1038/s41558-023-01634-3

Nisbet, E. G. (2023b). Slaying the methane minotaur. *Proceedings of the National Academy of Sciences*, *120*(49), e2318019120. https://doi.org/10.1073/pnas.2318019120

Nisbet, E. G., Allen, G., Fisher, R. E., France, J. L., Lee, J. D., Lowry, D., Andrade, M. F., Bannan, T. J., Barker, P., Bateson, P., Bauguitte, S. J. B., Bower, K. N., Broderick, T. J., Chibesakunda, F., Cain, M., Cozens, A. E., Daly, M. C., Ganesan, A. L., Jones, A. E.,…E. Wilde, S. (2021). Isotopic signatures of methane emissions from tropical fires, agriculture and wetlands: the MOYA and ZWAMPS flights. *Philosophical Transactions of the Royal Society A: Mathematical, Physical and Engineering Sciences*, *380*(2215), 20210112. https://doi.org/10.1098/rsta.2021.0112

Nisbet, E. G., Dlugokencky, E. J., Manning, M. R., Lowry, D., Fisher, R. E., France, J. L., Michel, S. E., Miller, J. B., White, J. W. C., Vaughn, B., Bousquet, P., Pyle, J. A., Warwick, N. J., Cain, M., Brownlow, R., Zazzeri, G., Lanoisellé, M., Manning, A. C., Gloor, E.,…Ganesan, A. L. (2016). Rising atmospheric methane: 2007–2014 growth and isotopic shift. *Global Biogeochemical Cycles*, *30*(9), 1356-1370. https://doi.org/10.1002/2016GB005406

Nisbet, E. G., Jones, A. E., Pyle, J. A., & Skiba, U. (2021). Rising methane: is there a methane emergency? *Philosophical Transactions of the Royal Society A: Mathematical, Physical and Engineering Sciences*, *380*(2215), 20210334. https://doi.org/10.1098/rsta.2021.0334

Nisbet, E. G., Manning, M., Dlugokencky, E., Fisher, R., Lowry, D., Michel, S., Myhre, C. L., Platt, S. M., Allen, G., & Bousquet, P. (2019). Very strong atmospheric methane growth in the 4 years 2014–2017: Implications for the Paris Agreement. *Global Biogeochemical Cycles*, *33*(3), 318-342.

Nisbet, E. G., Manning, M. R., Dlugokencky, E. J., Michel, S. E., Lan, X., Röckmann, T., Denier van der Gon, H. A. C., Schmitt, J., Palmer, P. I., Dyonisius, M. N., Oh, Y., Fisher, R. E., Lowry, D., France, J. L., White, J. W. C., Brailsford, G., & Bromley, T. (2023). Atmospheric Methane: Comparison Between Methane's Record in 2006–2022 and During Glacial Terminations. *Global Biogeochemical Cycles*, *37*(8). https://doi.org/10.1029/2023gb007875

NOAANERRS. *System-wide Monitoring Program. Data accessed from the NOAA NERRS Centralized Data Management Office website: http://www.nerrsdata.org/*

The Nord Stream pipelines have stopped leaking. But the methane emitted broke records. (2022, October 4). *National Public Radio*. https://www.npr.org/2022/10/04/1126562195/the-nord-stream-pipelines-have-stopped-leaking-but-the-methane-emitted-broke-rec

O'Neill, H. S. C. (1987). Quartz-fayalite-iron and quartz-fayalite-magnetite equilibria and the free energy of formation of fayalite (Fe 2 SiO 4) and magnetite (Fe 3 O 4). *American Mineralogist*, *72*(1-2), 67-75.

O'Sullivan, G., & Kalin, R. M. (2008). Investigation of the range of carbon and hydrogen isotopes within a global set of gasolines. *Environmental Forensics*, *9*(2-3), 166-176.

OECD. (2018). *Waste - Municipal waste: generation and treatment* https://data-explorer.oecd.org/vis?df[ds]=DisseminateFinalDMZ&df[id]=DSD_MUNW%40DF_MUNW&df[ag]=OECD.ENV.EPI&dq=.A.MUNICIPAL.T%2BKG_PS&pd=2015%2C&to[TIME_PERIOD]=false

OGMP. (2023). *Oil and Gas Methane Partnership 2.0 Technical Guidance Document*. https://ogmpartnership.com/guidance-documents-and-templates/

Oh, Y., Zhuang, Q., Welp, L. R., Liu, L., Lan, X., Basu, S., Dlugokencky, E. J., Bruhwiler, L., Miller, J. B., Michel, S. E., Schwietzke, S., Tans, P., Ciais, P., & Chanton, J. P. (2022). Improved global wetland carbon isotopic signatures support post-2006 microbial methane emission increase. *Communications Earth & Environment*, *3*(1), 159. https://doi.org/10.1038/s43247-022-00488-5

Okumura, T., Kawagucci, S., Saito, Y., Matsui, Y., Takai, K., & Imachi, H. (2016). Hydrogen and carbon isotope systematics in hydrogenotrophic methanogenesis under H2-limited and H2-enriched conditions: implications for the origin of methane and its isotopic diagnosis. *Progress in Earth and Planetary Science*, *3*(1). https://doi.org/10.1186/s40645-016-0088-3

Ono, S., Rhim, J. H., Gruen, D. S., Taubner, H., Kölling, M., & Wegener, G. (2021). Clumped isotopologue fractionation by microbial cultures performing the anaerobic oxidation of methane. *Geochimica Et Cosmochimica Acta*, *293*, 70-85. https://doi.org/10.1016/j.gca.2020.10.015

Ono, S., Rhim, J. H., & Ryberg, E. C. (2022). Rate limits and isotopologue fractionations for microbial methanogenesis examined with combined pathway protein cost and isotopologue flow network models. *Geochimica Et Cosmochimica Acta*, *325*, 296-315. https://doi.org/10.1016/j.gca.2022.03.017

Ono, S., Wang, D. T., Gruen, D. S., Sherwood Lollar, B., Zahniser, M. S., McManus, B. J., & Nelson, D. D. (2014). Measurement of a doubly substituted methane isotopologue, 13CH3D, by tunable infrared laser direct absorption spectroscopy. *Anal Chem*, *86*(13), 6487-6494. https://doi.org/10.1021/ac5010579

Orphan, V. J., Hinrichs, K. U., Ussler, W., Paull, C. K., Taylor, L. T., Sylva, S. P., Hayes, J. M., & Delong, E. F. (2001). Comparative Analysis of Methane-Oxidizing Archaea and Sulfate-Reducing Bacteria in Anoxic Marine Sediments. *Applied and Environmental Microbiology*, *67*(4), 1922-1934. https://doi.org/10.1128/AEM.67.4.1922-1934.2001

Parker, R. J., Boesch, H., McNorton, J., Comyn-Platt, E., Gloor, M., Wilson, C., Chipperfield, M. P., Hayman, G. D., & Bloom, A. A. (2018). Evaluating year-to-year anomalies in tropical wetland methane emissions using satellite CH4 observations. *Remote Sensing of Environment*, *211*, 261-275. https://doi.org/10.1016/j.rse.2018.02.011

Peischl, J., Ryerson, T., Brioude, J., Aikin, K., Andrews, A., Atlas, E., Blake, D., Daube, B., De Gouw, J., & Dlugokencky, E. (2013). Quantifying sources of methane using light alkanes in the Los Angeles basin, California. *Journal of Geophysical Research: Atmospheres*, *118*(10), 4974-4990.

Peng, S., Lin, X., Thompson, R. L., Xi, Y., Liu, G., Hauglustaine, D., Lan, X., Poulter, B., Ramonet, M., Saunois, M., Yin, Y., Zhang, Z., Zheng, B., & Ciais, P. (2022). Wetland emission and atmospheric sink changes explain methane growth in 2020. *Nature*, *612*(7940), 477-482. https://doi.org/10.1038/s41586-022-05447-w

Penning, H., Plugge, C. M., Galand, P. E., & Conrad, R. (2005). Variation of carbon isotope fractionation in hydrogenotrophic methanogenic microbial cultures and environmental

samples at different energy status. *Global Change Biology*, *11*(12), 2103-2113. https://doi.org/10.1111/j.1365-2486.2005.01076.x

Petit, J.-R., Jouzel, J., Raynaud, D., Barkov, N. I., Barnola, J.-M., Basile, I., Bender, M., Chappellaz, J., Davis, M., & Delaygue, G. (1999). Climate and atmospheric history of the past 420,000 years from the Vostok ice core, Antarctica. *Nature*, *399*(6735), 429-436.

Phillips, N. G., Ackley, R., Crosson, E. R., Down, A., Hutyra, L. R., Brondfield, M., Karr, J. D., Zhao, K., & Jackson, R. B. (2013). Mapping urban pipeline leaks: Methane leaks across Boston. *Environmental pollution*, *173*, 1-4. https://doi.org/10.1016/j.envpol.2012.11.003

Pisso, I., Myhre, C. L., Platt, S. M., Eckhardt, S., Hermansen, O., Schmidbauer, N., Mienert, J., Vadakkepuliyambatta, S., Bauguitte, S., & Pitt, J. (2016). Constraints on oceanic methane emissions west of Svalbard from atmospheric in situ measurements and Lagrangian transport modeling. *Journal of Geophysical Research: Atmospheres*, *121*(23), 14,188-114,200.

Plant, G., Kort, E. A., Brandt, A. R., Chen, Y., Fordice, G., Gorchov Negron, A. M., Schwietzke, S., Smith, M., & Zavala-Araiza, D. (2022). Inefficient and unlit natural gas flares both emit large quantities of methane. *Science*, *377*(6614), 1566-1571. https://doi.org/10.1126/science.abq0385

Plant, G., Kort, E. A., Murray, L. T., Maasakkers, J. D., & Aben, I. (2022). Evaluating urban methane emissions from space using TROPOMI methane and carbon monoxide observations. *Remote Sensing of Environment*, *268*, 112756. https://doi.org/10.1016/j.rse.2021.112756

Platt, U., Allan, W., & Lowe, D. (2004). Hemispheric average Cl atom concentration from 13C/12C ratios in atmospheric methane. *Atmospheric Chemistry and Physics*, *4*(9/10), 2393-2399. https://doi.org/10.5194/acp-4-2393-2004

Plummer, D., Nagashima, T., Tilmes, S., Archibald, A., Chiodo, G., Fadnavis, S., Garny, H., Josse, B., Kim, J., & Lamarque, J.-F. (2021). CCMI-2022: A new set of Chemistry-Climate Model Initiative (CCMI) community simulations to update the assessment of models and support upcoming ozone assessment activities. *SPARC Newsletter*, *57*, 22-30.

Prasse, C. E., Baldwin, A. H., & Yarwood, S. A. (2015). Site History and Edaphic Features Override the Influence of Plant Species on Microbial Communities in Restored Tidal Freshwater Wetlands. *Applied and Environmental Microbiology*, *81*(10), 3482-3491. https://doi.org/10.1128/AEM.00038-15

Purvis, G. D., III, & Bartlett, R. J. (1982). A full coupled‐cluster singles and doubles model: The inclusion of disconnected triples. *The Journal of Chemical Physics*, *76*(4), 1910-1918. https://doi.org/10.1063/1.443164

Qu, Z., Jacob, D. J., Shen, L., Lu, X., Zhang, Y., Scarpelli, T. R., Nesser, H., Sulprizio, M. P., Maasakkers, J. D., Bloom, A. A., Worden, J. R., Parker, R. J., & Delgado, A. L. (2021). Global distribution of methane emissions: a comparative inverse analysis of observations from the TROPOMI and GOSAT satellite instruments. *Atmos. Chem. Phys.*, *21*(18), 14159-14175. https://doi.org/10.5194/acp-21-14159-2021

Qu, Z., Jacob, D. J., Zhang, Y., Shen, L., Varon, D. J., Lu, X., Scarpelli, T., Bloom, A., Worden, J., & Parker, R. J. (2022). Attribution of the 2020 surge in atmospheric methane by inverse analysis of GOSAT observations. *Environmental Research Letters*, *17*(9), 094003. https://doi.org/10.1088/1748-9326/ac8754

Quay, P., Stutsman, J., Wilbur, D., Snover, A., Dlugokencky, E., & Brown, T. (1999). The isotopic composition of atmospheric methane [https://doi.org/10.1029/1998GB900006]. *Global Biogeochemical Cycles*, *13*(2), 445-461. https://doi.org/10.1029/1998GB900006

Rayleigh, L. (1902). LIX. On the distillation of binary mixtures. *The London, Edinburgh, and Dublin Philosophical Magazine and Journal of Science*, *4*(23), 521-537. https://doi.org/10.1080/14786440209462876

Reeburgh, W. S. (2007). Oceanic Methane Biogeochemistry. *Chemical Reviews*, *107*(2), 486-513. https://doi.org/10.1021/cr050362v

Ren, X., Hall, D. L., Vinciguerra, T., Benish, S. E., Stratton, P. R., Ahn, D., Hansford, J. R., Cohen, M. D., Sahu, S., & He, H. (2019). Methane emissions from the Marcellus Shale in Southwestern Pennsylvania and Northern West Virginia based on airborne measurements. *Journal of Geophysical Research: Atmospheres*, *124*(3), 1862-1878. https://doi.org/10.1029/2018JD029690

Ren, X., Salmon, O. E., Hansford, J. R., Ahn, D., Hall, D., Benish, S. E., Stratton, P. R., He, H., Sahu, S., Grimes, C., Heimburger, A. M. F., Martin, C. R., Cohen, M. D., Stunder, B., Salawitch, R. J., Ehrman, S. H., Shepson, P. B., & Dickerson, R. R. (2018). Methane Emissions From the Baltimore-Washington Area Based on Airborne Observations: Comparison to Emissions Inventories. *Journal of Geophysical Research: Atmospheres*, *123*(16), 8869-8882. https://doi.org/10.1029/2018JD028851

Rhim, J. H., & Ono, S. (2022). Combined carbon, hydrogen, and clumped isotope fractionations reveal differential reversibility of hydrogenotrophic methanogenesis in laboratory cultures. *Geochimica Et Cosmochimica Acta*, *335*, 383-399. https://doi.org/10.1016/j.gca.2022.07.027

Riahi, K., Schaeffer, R., Arango, J., Calvin, K., Guivarch, C., Hasegawa, T., Jiang, K., Kriegler, E., Matthews, R., Peters, G. P., Rao, A., Robertson, S., Sebbit, A. M., Steinberger, J., Tavoni, M., & Vuuren, D. P. v. (2023). Mitigation Pathways Compatible with Long-term Goals. In C. Intergovernmental Panel on Climate (Ed.), *Climate Change 2022: Mitigation of Climate Change. Contribution of Working Group III to the Sixth Assessment Report of the Intergovernmental Panel on Climate Change* (pp. 295-408). Cambridge University Press. https://doi.org/http://doi.org/10.1017/9781009157926.005

Rice, A. L., Butenhoff, C. L., Teama, D. G., Röger, F. H., Khalil, M. A. K., & Rasmussen, R. A. (2016). Atmospheric methane isotopic record favors fossil sources flat in 1980s and 1990s with recent increase. *Proceedings of the National Academy of Sciences*, *113*(39), 10791. https://doi.org/10.1073/pnas.1522923113

Rice, D. D., & Claypool, G. E. (1981). Generation, accumulation, and resource potential of biogenic gas. *AAPG bulletin*, *65*(1), 5-25.

Richter, F. M., Mendybaev, R. A., Christensen, J. N., Hutcheon, I. D., Williams, R. W., Sturchio, N. C., & Beloso, A. D. (2006). Kinetic isotopic fractionation during diffusion of ionic species in water. *Geochimica Et Cosmochimica Acta*, *70*(2), 277-289. https://doi.org/10.1016/j.gca.2005.09.016

Riddell-Young, B., Tans, P. P., Michel, S., Miller, J. B., & Lan, X. (2023, 2023). A high-resolution, global dataset of atmospheric δD-CH4: Identifying signals and their implications. AGU Fall Meeting,

Ridgwell, A. J., Marshall, S. J., & Gregson, K. (1999). Consumption of atmospheric methane by soils: A process-based model. *Global Biogeochemical Cycles*, *13*(1), 59-70. https://doi.org/10.1029/1998GB900004

Riedel, T. P., Wagner, N. L., Dubé, W. P., Middlebrook, A. M., Young, C. J., Öztürk, F., Bahreini, R., VandenBoer, T. C., Wolfe, D. E., Williams, E. J., Roberts, J. M., Brown, S. S., & Thornton, J. A. (2013). Chlorine activation within urban or power plant plumes: Vertically resolved ClNO2 and Cl2 measurements from a tall tower in a polluted continental setting. *Journal of Geophysical Research: Atmospheres*, *118*(15), 8702-8715. https://doi.org/10.1002/jgrd.50637

Rigby, M., Montzka, S. A., Prinn, R. G., White, J. W. C., Young, D., O'Doherty, S., Lunt, M. F., Ganesan, A. L., Manning, A. J., Simmonds, P. G., Salameh, P. K., Harth, C. M., Mühle, J., Weiss, R. F., Fraser, P. J., Steele, L. P., Krummel, P. B., McCulloch, A., & Park, S. (2017). Role of atmospheric oxidation in recent methane growth. *Proceedings of the National Academy of Sciences*, *114*(21), 5373. https://doi.org/10.1073/pnas.1616426114

Rigby, M., Prinn, R., O'Doherty, S., Montzka, S., McCulloch, A., Harth, C., Mühle, J., Salameh, P., Weiss, R., & Young, D. (2013). Re-evaluation of the lifetimes of the major CFCs and CH 3 CCl 3 using atmospheric trends. *Atmospheric Chemistry and Physics*, *13*(5), 2691-2702.

Röckmann, T., Brass, M., Borchers, R., & Engel, A. (2011). The isotopic composition of methane in the stratosphere: high-altitude balloon sample measurements. *Atmospheric Chemistry and Physics*, *11*(24), 13287-13304. https://doi.org/10.5194/acp-11-13287-2011

Roque, B. M., Venegas, M., Kinley, R. D., de Nys, R., Duarte, T. L., Yang, X., & Kebreab, E. (2021). Red seaweed (Asparagopsis taxiformis) supplementation reduces enteric methane by over 80 percent in beef steers. *PLOS ONE*, *16*(3), e0247820. https://doi.org/10.1371/journal.pone.0247820

Rowland, F. S. (1989). Chlorofluorocarbons and the Depletion of Stratospheric Ozone. *American Scientist*, *77*(1), 36-45. http://www.jstor.org/stable/27855550

Ruppel, C. D., & Kessler, J. D. (2017). The interaction of climate change and methane hydrates [https://doi.org/10.1002/2016RG000534]. *Reviews of Geophysics*, *55*(1), 126-168. https://doi.org/10.1002/2016rg000534

Sachs, T., Giebels, M., Boike, J., & Kutzbach, L. (2010). Environmental controls on CH4 emission from polygonal tundra on the microsite scale in the Lena river delta, Siberia. *Global Change Biology*, *16*(11), 3096-3110. https://doi.org/10.1111/j.1365-2486.2010.02232.x

Sanches, L. F., Guenet, B., Marinho, C. C., Barros, N., & de Assis Esteves, F. (2019). Global regulation of methane emission from natural lakes. *Scientific Reports*, *9*(1), 255. https://doi.org/10.1038/s41598-018-36519-5

Sapart, C. J., Martinerie, P., Witrant, E., Chappellaz, J., van de Wal, R. S. W., Sperlich, P., van der Veen, C., Bernard, S., Sturges, W. T., Blunier, T., Schwander, J., Etheridge, D., & Röckmann, T. (2013). Can the carbon isotopic composition of methane be reconstructed from multi-site firn air measurements? *Atmos. Chem. Phys.*, *13*(14), 6993-7005. https://doi.org/10.5194/acp-13-6993-2013

Sapart, C. J., Monteil, G., Prokopiou, M., van de Wal, R. S. W., Kaplan, J. O., Sperlich, P., Krumhardt, K. M., van der Veen, C., Houweling, S., Krol, M. C., Blunier, T., Sowers, T., Martinerie, P., Witrant, E., Dahl-Jensen, D., & Rockmann, T. (2012). Natural and anthropogenic variations in methane sources during the past two millennia. *Nature*, *490*(7418), 85-88. https://doi.org/Doi 10.1038/Nature11461

Sargent, M. R., Floerchinger, C., McKain, K., Budney, J., Gottlieb, E. W., Hutyra, L. R., Rudek, J., & Wofsy, S. C. (2021). Majority of US urban natural gas emissions unaccounted for in

inventories. *Proceedings of the National Academy of Sciences*, *118*(44), e2105804118. https://doi.org/10.1073/pnas.2105804118

Sauer, F., Portmann, R. W., Ravishankara, A. R., & Burkholder, J. B. (2015). Temperature Dependence of the Cl Atom Reaction with Deuterated Methanes. *The Journal of Physical Chemistry A*, *119*(19), 4396-4407. https://doi.org/10.1021/jp508721h

Saunois, M., Martinez, A., Poulter, B., Zhang, Z., Raymond, P., Regnier, P., Canadell, J. G., Jackson, R. B., Patra, P. K., Bousquet, P., Ciais, P., Dlugokencky, E. J., Lan, X., Allen, G. H., Bastviken, D., Beerling, D. J., Belikov, D. A., Blake, D. R., Castaldi, S.,…Zhuang, Q. (2024). Global Methane Budget 2000-2020. *Earth Syst. Sci. Data Discuss.*, *2024*, 1-147. https://doi.org/10.5194/essd-2024-115

Saunois, M., Stavert, A. R., Poulter, B., Bousquet, P., Canadell, J. G., Jackson, R. B., Raymond, P. A., Dlugokencky, E. J., Houweling, S., Patra, P. K., Ciais, P., Arora, V. K., Bastviken, D., Bergamaschi, P., Blake, D. R., Brailsford, G., Bruhwiler, L., Carlson, K. M., Carrol, M.,…Zhuang, Q. (2020). The Global Methane Budget 2000–2017. *Earth System Science Data*, *12*(3), 1561-1623. https://doi.org/10.5194/essd-12-1561-2020

Sayedi, S. S., Abbott, B. W., Thornton, B. F., Frederick, J. M., Vonk, J. E., Overduin, P., Schädel, C., Schuur, E. A. G., Bourbonnais, A., Demidov, N., Gavrilov, A., He, S., Hugelius, G., Jakobsson, M., Jones, M. C., Joung, D., Kraev, G., Macdonald, R. W., David McGuire, A.,…Frei, R. J. (2020). Subsea permafrost carbon stocks and climate change sensitivity estimated by expert assessment. *Environmental Research Letters*, *15*(12), 124075. https://doi.org/10.1088/1748-9326/abcc29

Schaefer, H., Fletcher Sara, E. M., Veidt, C., Lassey Keith, R., Brailsford Gordon, W., Bromley Tony, M., Dlugokencky Edward, J., Michel Sylvia, E., Miller John, B., Levin, I., Lowe Dave, C., Martin Ross, J., Vaughn Bruce, H., & White James, W. C. (2016). A 21st-century shift from fossil-fuel to biogenic methane emissions indicated by 13CH4. *Science*, *352*(6281), 80-84. https://doi.org/10.1126/science.aad2705

Schneising, O., Burrows, J. P., Dickerson, R. R., Buchwitz, M., Reuter, M., & Bovensmann, H. (2014). Remote sensing of fugitive methane emissions from oil and gas production in North American tight geologic formations. *Earth's Future*, *2*(10), 548-558.

Schöll, M. (1980). The hydrogen and carbon isotopic composition of methane from natural gases of various origins. *Geochimica Et Cosmochimica Acta*, *44*(5), 649-661. https://doi.org/10.1016/0016-7037(80)90155-6

Schöll, M. (1988). Multiple origins of methane in the Earth. *Chemical Geology*, *71*(1), 1-10. https://doi.org/10.1016/0009-2541(88)90101-5

Schuler, P., Rehmann, O., Vitali, V., Saurer, M., Oettli, M., Cernusak, L. A., Gessler, A., Buchmann, N., & Lehmann, M. M. (2024). Hydrogen isotope fractionation in plants with C, C, and CAM CO fixation. *New Phytologist*, *244*(2), 477-495. https://doi.org/10.1111/nph.20057

Schwietzke, S., Griffin, W. M., Matthews, H. S., & Bruhwiler, L. M. P. (2014). Global Bottom-Up Fossil Fuel Fugitive Methane and Ethane Emissions Inventory for Atmospheric Modeling. *ACS Sustainable Chemistry & Engineering*, *2*(8), 1992-2001. https://doi.org/10.1021/sc500163h

Schwietzke, S., Sherwood, O. A., Bruhwiler, L. M. P., Miller, J. B., Etiope, G., Dlugokencky, E. J., Michel, S. E., Arling, V. A., Vaughn, B. H., White, J. W. C., & Tans, P. P. (2016). Upward revision of global fossil fuel methane emissions based on isotope database. *Nature*, *538*(7623), 88-91. https://doi.org/10.1038/nature19797

Scott, H. P., Hemley, R. J., Mao, H.-k., Herschbach, D. R., Fried, L. E., Howard, W. M., & Bastea, S. (2004). Generation of methane in the Earth's mantle: In situ high pressure–temperature measurements of carbonate reduction. *Proceedings of the National Academy of Sciences*, *101*(39), 14023-14026. https://doi.org/10.1073/pnas.0405930101

Sebacher, D. I., Harriss, R. C., & Bartlett, K. B. (1985). Methane Emissions to the Atmosphere Through Aquatic Plants. *Journal of Environmental Quality*, *14*(1), 40-46. https://doi.org/10.2134/jeq1985.00472425001400010008x

Sepulveda-Jauregui, A., Walter Anthony, K., Martinez-Cruz, K., Greene, S., & Thalasso, F. (2015). Methane and carbon dioxide emissions from 40 lakes along a north–south latitudinal transect in Alaska. *Biogeosciences*, *12*(11), 3197-3223.

Sessions, A. L., & Hayes, J. M. (2005). Calculation of hydrogen isotopic fractionations in biogeochemical systems. *Geochimica Et Cosmochimica Acta*, *69*(3), 593-597. https://doi.org/10.1016/j.gca.2004.08.005

Shakhova, N., Semiletov, I., Leifer, I., Sergienko, V., Salyuk, A., Kosmach, D., Chernykh, D., Stubbs, C., Nicolsky, D., Tumskoy, V., & Gustafsson, Ö. (2013). Ebullition and storm-induced methane release from the East Siberian Arctic Shelf. *Nature Geoscience*, *7*(1), 64-70. https://doi.org/10.1038/ngeo2007

Shaw, J. T., Allen, G., Barker, P., Pitt, J. R., Pasternak, D., Bauguitte, S. J. B., Lee, J., Bower, K. N., Daly, M. C., Lunt, M. F., Ganesan, A. L., Vaughan, A. R., Chibesakunda, F., Lambakasa, M., Fisher, R. E., France, J. L., Lowry, D., Palmer, P. I., Metzger, S.,…Nisbet, E. G. (2022). Large Methane Emission Fluxes Observed From Tropical Wetlands in Zambia. *Global Biogeochemical Cycles*, *36*(6), e2021GB007261. https://doi.org/10.1029/2021GB007261

Shen, N., Tan, J., Wang, W., Xue, W., Wang, Y., Huang, L., Yan, G., Song, Y., & Li, L. (2024). Long-term changes of methane emissions from rice cultivation during 2000 – 2060 in China: Trends, driving factors, predictions and policy implications. *Environment International*, *191*, 108958. https://doi.org/10.1016/j.envint.2024.108958

Sherwin, E. D., El Abbadi, S. H., Burdeau, P. M., Zhang, Z., Chen, Z., Rutherford, J. S., Chen, Y., & Brandt, A. R. (2024). Single-blind test of nine methane-sensing satellite systems from three continents. *Atmos. Meas. Tech.*, *17*(2), 765-782. https://doi.org/10.5194/amt-17-765-2024

Sherwood Lollar, B., Westgate, T. D., Ward, J. A., Slater, G. F., & Lacrampe-Couloume, G. (2002). Abiogenic formation of alkanes in the Earth's crust as a minor source for global hydrocarbon reservoirs. *Nature*, *416*(6880), 522-524. https://doi.org/10.1038/416522a

Sherwood, O. A., Schwietzke, S., Arling, V. A., & Etiope, G. (2017). Global Inventory of Gas Geochemistry Data from Fossil Fuel, Microbial and Burning Sources, version 2017. *Earth System Science Data*, *9*(2), 639-656. https://doi.org/10.5194/essd-9-639-2017

Sherwood, O. A., Schwietzke, S., & Lan, X. (2021). *Global δ13C-CH4 Source Signature Inventory 2020* https://doi.org/10.15138/qn55-e011

Shuai, Y., Douglas, P. M. J., Zhang, S., Stolper, D. A., Ellis, G. S., Lawson, M., Lewan, M. D., Formolo, M., Mi, J., He, K., Hu, G., & Eiler, J. M. (2018). Equilibrium and non-equilibrium controls on the abundances of clumped isotopologues of methane during thermogenic formation in laboratory experiments: Implications for the chemistry of pyrolysis and the origins of natural gases. *Geochimica Et Cosmochimica Acta*, *223*, 159-174. https://doi.org/10.1016/j.gca.2017.11.024

Shuai, Y., Etiope, G., Zhang, S., Douglas, P. M. J., Huang, L., & Eiler, J. M. (2018). Methane clumped isotopes in the Songliao Basin (China): New insights into abiotic vs. biotic hydrocarbon formation. *Earth and Planetary Science Letters*, *482*, 213-221. https://doi.org/10.1016/j.epsl.2017.10.057

Sieczko, A. K., Duc, N. T., Schenk, J., Pajala, G., Rudberg, D., Sawakuchi, H. O., & Bastviken, D. (2020). Diel variability of methane emissions from lakes. *Proceedings of the National Academy of Sciences*, *117*(35), 21488-21494. https://doi.org/doi:10.1073/pnas.2006024117

Siese, M., Becker, K. H., Brockmann, K. J., Geiger, H., Hofzumahaus, A., Holland, F., Mihelcic, D., & Wirtz, K. (2001). Direct Measurement of OH Radicals from Ozonolysis of Selected Alkenes: A EUPHORE Simulation Chamber Study. *Environmental Science & Technology*, *35*(23), 4660-4667. https://doi.org/10.1021/es010150p

Simpson, I. J., Rowland, F. S., Meinardi, S., & Blake, D. R. (2006). Influence of biomass burning during recent fluctuations in the slow growth of global tropospheric methane. *Geophysical Research Letters*, *33*(22). https://doi.org/10.1029/2006GL027330

Simpson, I. J., Sulbaek Andersen, M. P., Meinardi, S., Bruhwiler, L., Blake, N. J., Helmig, D., Rowland, F. S., & Blake, D. R. (2012). Long-term decline of global atmospheric ethane concentrations and implications for methane. *Nature*, *488*(7412), 490-494. https://doi.org/10.1038/nature11342

Sivan, M., Röckmann, T., van der Veen, C., & Popa, M. E. (2024). Extraction, purification, and clumped isotope analysis of methane (Δ13CDH3 and Δ12CD2H2) from sources and the atmosphere. *Atmos. Meas. Tech.*, *17*(9), 2687-2705. https://doi.org/10.5194/amt-17-2687-2024

Sivan, M., Sun, J., Röckmann, T., Martinerie, P., Farquhar, J., Krol, M. C., Paandey, S., Menoud, M., Dasgupta, B., Hagnegedar, M. A., Veen, C. V. D., & Popa, M. E. (2024, 14–19 Apr). *Evolution of atmospheric methane clumped isotope anomalies since the 1990s reconstructed from firn air measurements* EGU General Assembly, Vienna, Austria.

Smallwood, B. J., Paul Philp, R., & Allen, J. D. (2002). Stable carbon isotopic composition of gasolines determined by isotope ratio monitoring gas chromatography mass spectrometry. *Organic Geochemistry*, *33*(2), 149-159. https://doi.org/10.1016/S0146-6380(01)00142-5

Snover, A. K., Quay, P. D., & Hao, W. M. (2000). The D/H content of methane emitted from biomass burning. *Global Biogeochemical Cycles*, *14*(1), 11-24. https://doi.org/10.1029/1999GB900075

Solomon, S., Borrmann, S., Garcia, R. R., Portmann, R., Thomason, L., Poole, L. R., Winker, D., & McCormick, M. P. (1997). Heterogeneous chlorine chemistry in the tropopause region. *Journal of Geophysical Research: Atmospheres*, *102*(D17), 21411-21429. https://doi.org/10.1029/97JD01525

Song, C., Luan, J., Xu, X., Ma, M., Aurela, M., Lohila, A., Mammarella, I., Alekseychik, P., Tuittila, E.-S., Gong, W., Chen, X., Meng, X., & Yuan, W. (2020). A Microbial Functional Group-Based CH4 Model Integrated Into a Terrestrial Ecosystem Model: Model Structure, Site-Level Evaluation, and Sensitivity Analysis. *Journal of Advances in Modeling Earth Systems*, *12*(4), e2019MS001867. https://doi.org/10.1029/2019MS001867

Spokas, K., Bogner, J., & Chanton, J. (2011). A process‐based inventory model for landfill CH4 emissions inclusive of seasonal soil microclimate and CH4 oxidation. *Journal of Geophysical Research: Biogeosciences*, *116*(G4).

Spokas, K., Bogner, J., & Corcoran, M. (2021). Modeling landfill CH4 emissions: CALMIM international field validation, using CALMIM to simulate management strategies, current and future climate scenarios. *Elem Sci Anth*, *9*(1), 00050. https://doi.org/10.1525/elementa.2020.00050

Sriskantharajah, S., Fisher, R., Lowry, D., Aalto, T., Hatakka, J., Aurela, M., Laurila, T., Lohila, A., Kuitunen, E., & Nisbet, E. (2012). Stable carbon isotope signatures of methane from a Finnish subarctic wetland. *Tellus B: Chemical and Physical Meteorology*, *64*(1), 18818. https://doi.org/10.3402/tellusb.v64i0.18818

Stehfest, E., van Vuuren, D., Kram, T., Bouwman, L., Alkemade, R., Bakkenes, M., Biemans, H., Bouwman, A., den Elzen, M., Janse, J., Lucas, P., van Minnen, J., Müller, C., & Prins, A. (2014). Integrated Assessment of Global Environmental Change with IMAGE 3.0. Model description and policy applications. (The Hague: PBL Netherlands Environmental Assessment Agency).

Stell, A. C., Western, L. M., Sherwen, T., & Rigby, M. (2021). Atmospheric-methane source and sink sensitivity analysis using Gaussian process emulation. *Atmos. Chem. Phys.*, *21*(3), 1717-1736. https://doi.org/10.5194/acp-21-1717-2021

Stern, J. C., Chanton, J., Abichou, T., Powelson, D., Yuan, L., Escoriza, S., & Bogner, J. (2007). Use of a biologically active cover to reduce landfill methane emissions and enhance methane oxidation. *Waste Management*, *27*(9), 1248-1258. https://doi.org/10.1016/j.wasman.2006.07.018

Stewart, G. A., Sharp, S. J., Taylor, A. K., Williams, M. R., & Palmer, M. A. (2024). High spatial variability in wetland methane fluxes is tied to vegetation patch types. *Biogeochemistry*, *167*(12), 1589-1607. https://doi.org/10.1007/s10533-024-01188-2

Stolper, D. A., Lawson, M., Davis, C. L., Ferreira, A. A., Neto, E. V. S., Ellis, G. S., Lewan, M. D., Martini, A. M., Tang, Y., Schöll, M., Sessions, A. L., & Eiler, J. M. (2014). Formation temperatures of thermogenic and biogenic methane. *Science*, *344*(6191), 1500-1503. https://doi.org/10.1126/science.1254509

Stolper, D. A., Lawson, M., Formolo, M. J., Davis, C. L., Douglas, P. M. J., & Eiler, J. M. (2018). The utility of methane clumped isotopes to constrain the origins of methane in natural gas accumulations. *Geological Society, London, Special Publications*, *468*(1), 23. https://doi.org/10.1144/SP468.3

Stolper, D. A., Martini, A. M., Clog, M., Douglas, P. M., Shusta, S. S., Valentine, D. L., Sessions, A. L., & Eiler, J. M. (2015). Distinguishing and understanding thermogenic and biogenic sources of methane using multiply substituted isotopologues. *Geochimica Et Cosmochimica Acta*, *161*, 219-247. https://doi.org/10.1016/j.gca.2015.04.015

Stolper, D. A., Sessions, A. L., Ferreira, A. A., Santos Neto, E. V., Schimmelmann, A., Shusta, S. S., Valentine, D. L., & Eiler, J. M. (2014). Combined 13C–D and D–D clumping in methane: Methods and preliminary results. *Geochimica Et Cosmochimica Acta*, *126*, 169-191. https://doi.org/10.1016/j.gca.2013.10.045

Strąpoć, D., Mastalerz, M., Dawson, K., Macalady, J., Callaghan, A. V., Wawrik, B., Turich, C., & Ashby, M. (2011). Biogeochemistry of microbial coal-bed methane. *Annual Review of Earth and Planetary Sciences*, *39*(1), 617-656.

Streets, D. G., & Waldhoff, S. T. (2000). Present and future emissions of air pollutants in China:: SO2, NOx, and CO. *Atmospheric Environment*, *34*(3), 363-374. https://doi.org/10.1016/S1352-2310(99)00167-3

Ström, L., Tagesson, T., Mastepanov, M., & Christensen, T. R. (2012). Presence of Eriophorum scheuchzeri enhances substrate availability and methane emission in an Arctic wetland. *Soil Biology and Biochemistry*, *45*, 61-70. https://doi.org/10.1016/j.soilbio.2011.09.005

Sturm, P., Leuenberger, M., Sirignano, C., Neubert, R. E. M., Meijer, H. A. J., Langenfelds, R., Brand, W. A., & Tohjima, Y. (2004). Permeation of atmospheric gases through polymer O-rings used in flasks for air sampling. *Journal of Geophysical Research: Atmospheres*, *109*(D4). https://doi.org/10.1029/2003JD004073

Suda, K., Ueno, Y., Yoshizaki, M., Nakamura, H., Kurokawa, K., Nishiyama, E., Yoshino, K., Hongoh, Y., Kawachi, K., & Omori, S. (2014). Origin of methane in serpentinite-hosted hydrothermal systems: The CH4–H2–H2O hydrogen isotope systematics of the Hakuba Happo hot spring. *Earth and Planetary Science Letters*, *386*, 112-125.

Sun, J., & Farquhar, J. (2024). Fully resolved high-precision measurement of ^{36}S for sulfur reference materials. *Rapid Communications in Mass Spectrometry*, *38*(14), e9768. https://doi.org/10.1002/rcm.9768

Sun, J., Farquhar, J., & Haghnegahdar, M. A. (2023). The Behavior of Methane Clumped Isotopologues in a Wetland-Landfill-Air Mixing System. Goldschmidt Abstract, Lyon.

Sun, J., Haghnegahdar, M. A., Fernandez, J. M., Magen, C., & Farquhar, J. (2025). Controls on concentrations and clumped isotopologues of vehicle exhaust methane. *PLOS ONE*, *20*(2), e0315304. https://doi.org/10.1371/journal.pone.0315304

Sun, J., Magen, C., Haghnegahdar, M., Liu, J., Fernandez, J., & Farquhar, J. (in revision). Constraining Wetland and Landfill Methane Emission Signatures Through Atmospheric Methane Clumped Isotopologue Measurements. *Journal of Geophysical Research - Biogeosciences*.

Sun, J., Magen, C., Haghnegahdar, M. A., Liu, J., Fernandez, J. M., & Farquhar, J. (2025). *Dataset for Constraining Wetland and Landfill Methane Emission Signatures Through Atmospheric Methane Clumped Isotopologue Measurements (Version 1) [Dataset]* (Digital Repository for the University of Maryland. http://hdl.handle.net/1903/33660

Sun, W., Shao, M., Granier, C., Liu, Y., Ye, C. S., & Zheng, J. Y. (2018). Long-Term Trends of Anthropogenic SO2, NOx, CO, and NMVOCs Emissions in China. *Earth's Future*, *6*(8), 1112-1133. https://doi.org/10.1029/2018EF000822

Szopa, S., V. Naik, B. Adhikary, P. Artaxo, T. Berntsen, W.D. Collins, S. Fuzzi, L. Gallardo, A. Kiendler-Scharr, Z. Klimont, H. Liao, N. Unger, & Zanis, P. (2021). Short-Lived Climate Forcers Supplementary Material. In V. Masson-Delmotte, P. Zhai, A. Pirani, S. L. Connors, C. Péan, S. Berger, N. Caud, Y. Chen, L. Goldfarb, M. I. Gomis, M. Huang, K. Leitzell, E. Lonnoy, J. B. R. Matthews, T. K. Maycock, T. Waterfield, O. Yelekçi, R. Yu, & B. Zhou (Eds.), *Climate Change 2021: The Physical Science Basis Contribution of Working Group I to the Sixth Assessment Report of the Intergovernmental Panel on Climate Change*. https://www.ipcc.ch/

Taenzer, L., Labidi, J., Masterson, A. L., Feng, X., Rumble, D., Young, E. D., & Leavitt, W. D. (2020). Low Δ12CH2D2 values in microbialgenic methane result from combinatorial isotope effects. *Geochimica Et Cosmochimica Acta*, *285*, 225-236. https://doi.org/10.1016/j.gca.2020.06.026

Takigawa, A., Matsunami, A., & Arai, N. (2005). Methane emission from automobile equipped with three-way catalytic converter while driving. *Energy*, *30*(2), 461-473. https://doi.org/10.1016/j.energy.2004.04.016

Tans, P. P. (1997). A note on isotopic ratios and the global atmospheric methane budget. *Global Biogeochemical Cycles*, *11*(1), 77-81. https://doi.org/10.1029/96GB03940

Tans, P. P., Conway, T. J., & Nakazawa, T. (1989). Latitudinal distribution of the sources and sinks of atmospheric carbon dioxide derived from surface observations and an atmospheric transport model. *Journal of Geophysical Research: Atmospheres*, *94*(D4), 5151-5172. https://doi.org/10.1029/JD094iD04p05151

Taran, Y. A., Varley, N. R., Inguaggiato, S., & Cienfuegos, E. (2010). Geochemistry of H2- and CH4-enriched hydrothermal fluids of Socorro Island, Revillagigedo Archipelago, Mexico. Evidence for serpentinization and abiogenic methane. *Geofluids*, *10*(4), 542-555. https://doi.org/10.1111/j.1468-8123.2010.00314.x

Tassi, F., Fiebig, J., Vaselli, O., & Nocentini, M. (2012). Origins of methane discharging from volcanic-hydrothermal, geothermal and cold emissions in Italy. *Chemical Geology*, *310-311*, 36-48. https://doi.org/10.1016/j.chemgeo.2012.03.018

Templeton, A. S., Chu, K.-H., Alvarez-Cohen, L., & Conrad, M. E. (2006). Variable carbon isotope fractionation expressed by aerobic CH4-oxidizing bacteria. *Geochimica Et Cosmochimica Acta*, *70*(7), 1739-1752. https://doi.org/10.1016/j.gca.2005.12.002

Thanwerdas, J., Saunois, M., Berchet, A., Pison, I., & Bousquet, P. (2024). Investigation of the renewed methane growth post-2007 with high-resolution 3-D variational inverse modeling and isotopic constraints. *Atmos. Chem. Phys.*, *24*(4), 2129-2167. https://doi.org/10.5194/acp-24-2129-2024

Thiagarajan, N., Xie, H., Ponton, C., Kitchen, N., Peterson, B., Lawson, M., Formolo, M., Xiao, Y., & Eiler, J. (2020). Isotopic evidence for quasi-equilibrium chemistry in thermally mature natural gases. *Proceedings of the National Academy of Sciences*, *117*(8), 3989. https://doi.org/10.1073/pnas.1906507117

Tian, H., Lu, C., Ciais, P., Michalak, A. M., Canadell, J. G., Saikawa, E., Huntzinger, D. N., Gurney, K. R., Sitch, S., Zhang, B., Yang, J., Bousquet, P., Bruhwiler, L., Chen, G., Dlugokencky, E., Friedlingstein, P., Melillo, J., Pan, S., Poulter, B.,…Wofsy, S. C. (2016). The terrestrial biosphere as a net source of greenhouse gases to the atmosphere. *Nature*, *531*(7593), 225-228. https://doi.org/10.1038/nature16946

Timmers, P. H. A., Welte, C. U., Koehorst, J. J., Plugge, C. M., Jetten, M. S. M., & Stams, A. J. M. (2017). Reverse Methanogenesis and Respiration in Methanotrophic Archaea. *Archaea*, *2017*(1), 1654237. https://doi.org/10.1155/2017/1654237

Townsend-Small, A., Tyler, S. C., Pataki, D. E., Xu, X., & Christensen, L. E. (2012). Isotopic measurements of atmospheric methane in Los Angeles, California, USA: Influence of "fugitive" fossil fuel emissions. *Journal of Geophysical Research: Atmospheres*, *117*(D7). https://doi.org/10.1029/2011JD016826

Townsend‐Small, A., Ferrara, T. W., Lyon, D. R., Fries, A. E., & Lamb, B. K. (2016). Emissions of coalbed and natural gas methane from abandoned oil and gas wells in the United States. *Geophysical Research Letters*, *43*(5), 2283-2290.

Trudinger, C. M., Etheridge, D. M., Rayner, P. J., Enting, I. G., Sturrock, G. A., & Langenfelds, R. L. (2002). Reconstructing atmospheric histories from measurements of air composition in firn. *Journal of Geophysical Research: Atmospheres*, *107*(D24), ACH 15-11-ACH 15-13. https://doi.org/https://doi.org/10.1029/2002JD002545

Tsuji, K., Teshima, H., Sasada, H., & Yoshida, N. (2012). Spectroscopic isotope ratio measurement of doubly-substituted methane. *Spectrochimica Acta Part A: Molecular and Biomolecular Spectroscopy*, *98*, 43-46. https://doi.org/10.1016/j.saa.2012.08.028

Turner, A. J., Frankenberg, C., & Kort, E. A. (2019). Interpreting contemporary trends in atmospheric methane. *Proceedings of the National Academy of Sciences*, *116*(8), 2805. https://doi.org/10.1073/pnas.1814297116

Turner, A. J., Frankenberg, C., Wennberg, P. O., & Jacob, D. J. (2017). Ambiguity in the causes for decadal trends in atmospheric methane and hydroxyl. *Proceedings of the National Academy of Sciences*, *114*(21), 5367. https://doi.org/10.1073/pnas.1616020114

Tyler, S. C., Bilek, R. S., Sass, R. L., & Fisher, F. M. (1997). Methane oxidation and pathways of production in a Texas paddy field deduced from measurements of flux, δl3C, and δD of CH4. *Global Biogeochemical Cycles*, *11*(3), 323-348. https://doi.org/10.1029/97GB01624

Umezawa, T., Brenninkmeijer, C. A. M., Röckmann, T., van der Veen, C., Tyler, S. C., Fujita, R., Morimoto, S., Aoki, S., Sowers, T., Schmitt, J., Bock, M., Beck, J., Fischer, H., Michel, S. E., Vaughn, B. H., Miller, J. B., White, J. W. C., Brailsford, G., Schaefer, H.,…Levin, I. (2018). Interlaboratory comparison of δ13C and δD measurements of atmospheric CH4 for combined use of data sets from different laboratories. *Atmos. Meas. Tech.*, *11*(2), 1207-1231. https://doi.org/10.5194/amt-11-1207-2018

United Nations Environment Programme and Climate and Clean Air Coalition. (2021). *Global Methane Assessment: Benefits and Costs of Mitigating Methane Emissions.*

Urey, H. C. (1947). The thermodynamic properties of isotopic substances [10.1039/JR9470000562]. *Journal of the Chemical Society (Resumed)*(0), 562-581. https://doi.org/10.1039/JR9470000562

USEPA. *US Greenhouse Gas Inventory* https://ghgdata.epa.gov

USEPA. (2020). *Motor Vehicle Emission Simulator: MOVES3. Office of Transportation and Air Quality. US Environmental Protection Agency. Ann Arbor, MI. November*. Retrieved from https://www.epa.gov/moves

Valentine, D. L. (2002). Biogeochemistry and microbial ecology of methane oxidation in anoxic environments: a review. *Antonie van Leeuwenhoek*, *81*(1), 271-282. https://doi.org/10.1023/A:1020587206351

Valentine, D. L., Chidthaisong, A., Rice, A., Reeburgh, W. S., & Tyler, S. C. (2004). Carbon and hydrogen isotope fractionation by moderately thermophilic methanogens 1 1Associate editor: N. E. Ostrom. *Geochimica Et Cosmochimica Acta*, *68*(7), 1571-1590. https://doi.org/10.1016/j.gca.2003.10.012

Valentine, D. L., & Reeburgh, W. S. (2000). New perspectives on anaerobic methane oxidation. *Environmental Microbiology*, *2*(5), 477-484. https://doi.org/10.1046/j.1462-2920.2000.00135.x

van der Werf, G. R., Randerson, J. T., Giglio, L., van Leeuwen, T. T., Chen, Y., Rogers, B. M., Mu, M., van Marle, M. J. E., Morton, D. C., Collatz, G. J., Yokelson, R. J., & Kasibhatla, P. S. (2017). Global fire emissions estimates during 1997–2016. *Earth Syst. Sci. Data*, *9*(2), 697-720. https://doi.org/10.5194/essd-9-697-2017

van Wees, D., van der Werf, G. R., Randerson, J. T., Rogers, B. M., Chen, Y., Veraverbeke, S., Giglio, L., & Morton, D. C. (2022). Global biomass burning fuel consumption and emissions at 500 m spatial resolution based on the Global Fire Emissions Database (GFED). *Geosci. Model Dev.*, *15*(22), 8411-8437. https://doi.org/10.5194/gmd-15-8411-2022

Vernooij, R., Dusek, U., Popa, M. E., Yao, P., Shaikat, A., Qiu, C., Winiger, P., van der Veen, C., Eames, T. C., Ribeiro, N., & van der Werf, G. R. (2022). Stable carbon isotopic

composition of biomass burning emissions – implications for estimating the contribution of C3 and C4 plants. *Atmos. Chem. Phys.*, *22*(4), 2871-2890. https://doi.org/10.5194/acp-22-2871-2022

Vicente, E. D., Duarte, M. A., Tarelho, L. A. C., Nunes, T. F., Amato, F., Querol, X., Colombi, C., Gianelle, V., & Alves, C. A. (2015). Particulate and gaseous emissions from the combustion of different biofuels in a pellet stove. *Atmospheric Environment*, *120*, 15-27. https://doi.org/10.1016/j.atmosenv.2015.08.067

Vogel, F., Ars, S., Wunch, D., Lavoie, J., Gillespie, L., Maazallahi, H., Röckmann, T., Nęcki, J., Bartyzel, J., Jagoda, P., Lowry, D., France, J., Fernandez, J., Bakkaloglu, S., Fisher, R., Lanoiselle, M., Chen, H., Oudshoorn, M., Yver-Kwok, C.,…Calcan, A. (2024). Ground-Based Mobile Measurements to Track Urban Methane Emissions from Natural Gas in 12 Cities across Eight Countries. *Environmental Science & Technology*, *58*(5), 2271-2281. https://doi.org/10.1021/acs.est.3c03160

von Fischer, J. C., Cooley, D., Chamberlain, S., Gaylord, A., Griebenow, C. J., Hamburg, S. P., Salo, J., Schumacher, R., Theobald, D., & Ham, J. (2017). Rapid, vehicle-based identification of location and magnitude of urban natural gas pipeline leaks. *Environmental Science & Technology*, *51*(7), 4091-4099. https://doi.org/10.1021/acs.est.6b06095

Vorobev, A., Jagadevan, S., Jain, S., Anantharaman, K., Dick Gregory, J., Vuilleumier, S., & Semrau Jeremy, D. (2014). Genomic and Transcriptomic Analyses of the Facultative Methanotroph Methylocystis sp. Strain SB2 Grown on Methane or Ethanol. *Applied and Environmental Microbiology*, *80*(10), 3044-3052. https://doi.org/10.1128/AEM.00218-14

Wallington, T. J., & Hurley, M. D. (1992). A kinetic study of the reaction of chlorine atoms with CF3CHCl2, CF3CH2F, CFCl2CH3, CF2ClCH3, CHF2CH3, CH3D, CH2D2, CHD3, CD4, and CD3Cl at 295±2 K. *Chemical Physics Letters*, *189*(4), 437-442. https://doi.org/10.1016/0009-2614(92)85228-3

Walter, K. M., Chanton, J. P., Chapin Iii, F. S., Schuur, E. A. G., & Zimov, S. A. (2008). Methane production and bubble emissions from arctic lakes: Isotopic implications for source pathways and ages. *Journal of Geophysical Research: Biogeosciences*, *113*(G3). https://doi.org/10.1029/2007JG000569

Walter, K. M., Zimov, S. A., Chanton, J. P., Verbyla, D., & Chapin, F. S. (2006). Methane bubbling from Siberian thaw lakes as a positive feedback to climate warming. *Nature*, *443*(7107), 71-75. https://doi.org/10.1038/nature05040

Wang, D. T., Gruen, D. S., Lollar, B. S., Hinrichs, K.-U., Stewart, L. C., Holden, J. F., Hristov, A. N., Pohlman, J. W., Morrill, P. L., Könneke, M., Delwiche, K. B., Reeves, E. P., Sutcliffe, C. N., Ritter, D. J., Seewald, J. S., McIntosh, J. C., Hemond, H. F., Kubo, M. D., Cardace, D.,…Ono, S. (2015). Nonequilibrium clumped isotope signals in microbial methane. *Science*, *348*(6233), 428. https://doi.org/10.1126/science.aaa4326

Wang, D. T., Reeves, E. P., McDermott, J. M., Seewald, J. S., & Ono, S. (2018). Clumped isotopologue constraints on the origin of methane at seafloor hot springs. *Geochimica Et Cosmochimica Acta*, *223*, 141-158. https://doi.org/10.1016/j.gca.2017.11.030

Wang, D. T., Sattler, A., Paccagnini, M., & Chen, F. G. (2020). Method for calibrating methane clumped isotope measurements via catalytic equilibration of methane isotopologues on γ-alumina. *Rapid Communications in Mass Spectrometry*, *34*(10), e8555. https://doi.org/10.1002/rcm.8555

Wang, D. T., Welander, P. V., & Ono, S. (2016). Fractionation of the methane isotopologues 13CH4, 12CH3D, and 13CH3D during aerobic oxidation of methane by Methylococcus capsulatus (Bath). *Geochimica Et Cosmochimica Acta*, *192*, 186-202. https://doi.org/10.1016/j.gca.2016.07.031

Wang, X., Chen, B., Dong, G., Zhang, N., Liu, W., Han, J., Liu, C.-Q., Li, S.-L., Eiler, J. M., & Xu, S. (2024). Microbial contribution estimated by clumped isotopologues (13CH3D and 12CH2D2) characteristics in a CO2 enhanced coal bed methane reservoir. *Science of The Total Environment*, *922*, 170926. https://doi.org/10.1016/j.scitotenv.2024.170926

Wang, X., Huang, X., Zuo, C., & Hu, H. (2004). Kinetics of quinoline degradation by O3/UV in aqueous phase. *Chemosphere*, *55*(5), 733-741. https://doi.org/10.1016/j.chemosphere.2003.11.019

Wang, X., Jacob, D. J., Downs, W., Zhai, S., Zhu, L., Shah, V., Holmes, C. D., Sherwen, T., Alexander, B., Evans, M. J., Eastham, S. D., Neuman, J. A., Veres, P. R., Koenig, T. K., Volkamer, R., Huey, L. G., Bannan, T. J., Percival, C. J., Lee, B. H., & Thornton, J. A. (2021). Global tropospheric halogen (Cl, Br, I) chemistry and its impact on oxidants. *Atmos. Chem. Phys.*, *21*(18), 13973-13996. https://doi.org/10.5194/acp-21-13973-2021

Wang, Z., Schauble, E. A., & Eiler, J. M. (2004). Equilibrium thermodynamics of multiply substituted isotopologues of molecular gases. *Geochimica Et Cosmochimica Acta*, *68*(23), 4779-4797. https://doi.org/10.1016/j.gca.2004.05.039

Watanabe, A., Takeda, T., & Kimura, M. (1999). Evaluation of origins of CH4 carbon emitted from rice paddies. *Journal of Geophysical Research: Atmospheres*, *104*(D19), 23623-23629. https://doi.org/10.1029/1999JD900467

Webb, M. A., & Miller, T. F. (2014). Position-Specific and Clumped Stable Isotope Studies: Comparison of the Urey and Path-Integral Approaches for Carbon Dioxide, Nitrous Oxide, Methane, and Propane. *The Journal of Physical Chemistry A*, *118*(2), 467-474. https://doi.org/10.1021/jp411134v

Westhoff, J., Freitag, J., Orsi, A., Martinerie, P., Weikusat, I., Dyonisius, M., Faïn, X., Fourteau, K., & Blunier, T. (2023). Combining traditional and novel techniques to increase our understanding of the lock-in depth of atmospheric gases in polar ice cores - results from the EastGRIP region. *EGUsphere*, *2023*, 1-26. https://doi.org/10.5194/egusphere-2023-1904

Whitehill, A. R., Joelsson, L. M. T., Schmidt, J. A., Wang, D. T., Johnson, M. S., & Ono, S. (2017). Clumped isotope effects during OH and Cl oxidation of methane. *Geochimica Et Cosmochimica Acta*, *196*, 307-325. https://doi.org/10.1016/j.gca.2016.09.012

Whiticar, M. J. (1999). Carbon and hydrogen isotope systematics of bacterial formation and oxidation of methane. *Chemical Geology*, *161*(1-3), 291-314. https://doi.org/10.1016/S0009-2541(99)00092-3

Whiticar, M. J. (2020). The Biogeochemical Methane Cycle. In H. Wilkes (Ed.), *Hydrocarbons, Oils and Lipids: Diversity, Origin, Chemistry and Fate* (pp. 1-78). Springer International Publishing. https://doi.org/10.1007/978-3-319-54529-5_5-1

Whiticar, M. J., & Faber, E. (1986). Methane oxidation in sediment and water column environments—Isotope evidence. *Organic Geochemistry*, *10*(4), 759-768. https://doi.org/10.1016/S0146-6380(86)80013-4

Whiticar, M. J., Faber, E., & Schöll, M. (1986). Biogenic methane formation in marine and freshwater environments: CO2 reduction vs. acetate fermentation—Isotope evidence.

Geochimica Et Cosmochimica Acta, *50*(5), 693-709. https://doi.org/10.1016/0016-7037(86)90346-7

Wik, M., Thornton, B. F., Bastviken, D., Uhlbäck, J., & Crill, P. M. (2016). Biased sampling of methane release from northern lakes: A problem for extrapolation. *Geophysical Research Letters*, *43*(3), 1256-1262. https://doi.org/10.1002/2015GL066501

Wing, B. A., & Halevy, I. (2014). Intracellular metabolite levels shape sulfur isotope fractionation during microbial sulfate respiration. *Proceedings of the National Academy of Sciences*, *111*(51), 18116-18125. https://doi.org/10.1073/pnas.1407502111

Winiberg, F. A. F., Dillon, T. J., Orr, S. C., Groß, C. B. M., Bejan, I., Brumby, C. A., Evans, M. J., Smith, S. C., Heard, D. E., & Seakins, P. W. (2016). Direct measurements of OH and other product yields from the HO2 + CH3C(O)O2 reaction. *Atmospheric Chemistry and Physics*, *16*(6), 4023-4042. https://doi.org/10.5194/acp-16-4023-2016

Winkler, S. L., Anderson, J. E., Garza, L., Ruona, W. C., Vogt, R., & Wallington, T. J. (2018). Vehicle criteria pollutant (PM, NOx, CO, HCs) emissions: how low should we go? *npj Climate and Atmospheric Science*, *1*(1), 26. https://doi.org/10.1038/s41612-018-0037-5

Witrant, E., Martinerie, P., Hogan, C., Laube, J. C., Kawamura, K., Capron, E., Montzka, S. A., Dlugokencky, E. J., Etheridge, D., Blunier, T., & Sturges, W. T. (2012). A new multi-gas constrained model of trace gas non-homogeneous transport in firn: evaluation and behaviour at eleven polar sites. *Atmos. Chem. Phys.*, *12*(23), 11465-11483. https://doi.org/10.5194/acp-12-11465-2012

Worden, J. R., Bloom, A. A., Pandey, S., Jiang, Z., Worden, H. M., Walker, T. W., Houweling, S., & Röckmann, T. (2017). Reduced biomass burning emissions reconcile conflicting estimates of the post-2006 atmospheric methane budget. *Nature Communications*, *8*(1), 2227. https://doi.org/10.1038/s41467-017-02246-0

World Bank. (2023). *Global Gas Flaring Tracker Report*. https://www.worldbank.org/en/topic/extractiveindustries/publication/2023-global-gas-flaring-tracker-report

Xia, X., & Tang, Y. (2012). Isotope fractionation of methane during natural gas flow with coupled diffusion and adsorption/desorption. *Geochimica Et Cosmochimica Acta*, *77*, 489-503. https://doi.org/10.1016/j.gca.2011.10.014

Xiao, H., Song, C., Li, S., Lu, X., Liang, M., Xia, X., & Yuan, W. (2024). Global Wetland Methane Emissions From 2001 to 2020: Magnitude, Dynamics and Controls. *Earth's Future*, *12*(9), e2024EF004794. https://doi.org/10.1029/2024EF004794

Yacovitch, T. I., Herndon, S. C., Roscioli, J. R., Floerchinger, C., McGovern, R. M., Agnese, M., Pétron, G., Kofler, J., Sweeney, C., Karion, A., Conley, S. A., Kort, E. A., Nähle, L., Fischer, M., Hildebrandt, L., Koeth, J., McManus, J. B., Nelson, D. D., Zahniser, M. S., & Kolb, C. E. (2014). Demonstration of an Ethane Spectrometer for Methane Source Identification. *Environmental Science & Technology*, *48*(14), 8028-8034. https://doi.org/10.1021/es501475q

Yamada, K., Ozaki, Y., Nakagawa, F., Sudo, S., Tsuruta, H., & Yoshida, N. (2006). Hydrogen and carbon isotopic measurements of methane from agricultural combustion: Implications for isotopic signatures of global biomass burning sources. *Journal of Geophysical Research: Atmospheres*, *111*(D16). https://doi.org/10.1029/2005JD006750

Yeung, L. Y. (2016). Combinatorial effects on clumped isotopes and their significance in biogeochemistry. *Geochimica Et Cosmochimica Acta*, *172*, 22-38. https://doi.org/10.1016/j.gca.2015.09.020

Yeung, L. Y., Murray, L. T., Martinerie, P., Witrant, E., Hu, H., Banerjee, A., Orsi, A. J., & Chappellaz, J. A. (2019). *Diffusivity measurements for the LOCK-IN site* (PANGAEA. https://doi.org/10.1594/PANGAEA.901223

Yeung, L. Y., Young, E. D., & Schauble, E. A. (2012). Measurements of 18O18O and 17O18O in the atmosphere and the role of isotope-exchange reactions. *Journal of Geophysical Research: Atmospheres*, *117*(D18). https://doi.org/10.1029/2012JD017992

Yoshinaga, M. Y., Holler, T., Goldhammer, T., Wegener, G., Pohlman, J. W., Brunner, B., Kuypers, M. M. M., Hinrichs, K.-U., & Elvert, M. (2014). Carbon isotope equilibration during sulphate-limited anaerobic oxidation of methane. *Nature Geoscience*, *7*(3), 190-194. https://doi.org/10.1038/ngeo2069

Yoshioka, H., Sakata, S., & Kamagata, Y. (2008). Hydrogen isotope fractionation by Methanothermobacter thermoautotrophicus in coculture and pure culture conditions. *Geochimica Et Cosmochimica Acta*, *72*(11), 2687-2694. https://doi.org/10.1016/j.gca.2008.03.015

Young, E. D. (2019). A Two-Dimensional Perspective on CH4 Isotope Clumping: Distinguishing Process from Source. In I. D. BN Orcutt, R Dasgupta (Ed.), *Deep Carbon: Past to Present* (pp. 388-414). Cambridge Univ. Press. https://doi.org/10.1017/9781108677950.013

Young, E. D., Kohl, I. E., Lollar, B. S., Etiope, G., Rumble, D., Li, S., Haghnegahdar, M. A., Schauble, E. A., McCain, K. A., Foustoukos, D. I., Sutclife, C., Warr, O., Ballentine, C. J., Onstott, T. C., Hosgormez, H., Neubeck, A., Marques, J. M., Pérez-Rodríguez, I., Rowe, A. R.,…Bryndzia, L. T. (2017). The relative abundances of resolved l2CH2D2 and 13CH3D and mechanisms controlling isotopic bond ordering in abiotic and biotic methane gases. *Geochimica Et Cosmochimica Acta*, *203*, 235-264. https://doi.org/10.1016/j.gca.2016.12.041

Young, E. D., Kohl, I. E., Sherwood Lollar, B., Etiope, G., Rumble, D., Li, S., Haghnegahdar;, M. A., Schauble;, E. A., McCain;, K. A., Foustoukos;, D. I., Sutclife;, C., Warr;, O., Ballentine;, C. J., Onstott;, T. C., Hosgormez;, H., Neubeck;, A., Marques;, J. M., Pérez-Rodríguez;, I., Rowe;, A. R.,…Bryndzia, L. T. (2017). The relative abundances of resolved l2CH2D2 and 13CH3D and mechanisms controlling isotopic bond ordering in abiotic and biotic methane gases. *Geochimica Et Cosmochimica Acta*, *203*, 235-264. https://doi.org/10.1016/j.gca.2016.12.041

Young, E. D., Rumble, D., Freedman, P., & Mills, M. (2016). A large-radius high-mass-resolution multiple-collector isotope ratio mass spectrometer for analysis of rare isotopologues of O2, N2, CH4 and other gases. *International Journal of Mass Spectrometry*, *401*, 1-10. https://doi.org/10.1016/j.ijms.2016.01.006

Yu, X., Millet, D. B., Henze, D. K., Turner, A. J., Delgado, A. L., Bloom, A. A., & Sheng, J. (2023). A high-resolution satellite-based map of global methane emissions reveals missing wetland, fossil fuel, and monsoon sources. *Atmos. Chem. Phys.*, *23*(5), 3325-3346. https://doi.org/10.5194/acp-23-3325-2023

Yver Kwok, C., Laurent, O., Guemri, A., Philippon, C., Wastine, B., Rella, C. W., Vuillemin, C., Truong, F., Delmotte, M., Kazan, V., Darding, M., Lebègue, B., Kaiser, C., Xueref-Rémy, I., & Ramonet, M. (2015). Comprehensive laboratory and field testing of cavity ring-down spectroscopy analyzers measuring H₂O, CO₂, CH₄ and CO. *Atmos. Meas. Tech.*, *8*(9), 3867-3892. https://doi.org/10.5194/amt-8-3867-2015

Zavala-Araiza, D., Lyon, D., Alvarez, R. A., Palacios, V., Harriss, R., Lan, X., Talbot, R., & Hamburg, S. P. (2015). Toward a functional definition of methane super-emitters: Application to natural gas production sites. *Environmental Science & Technology*, *49*(13), 8167-8174. https://doi.org/10.1021/acs.est.5b00133

Zhang, L., Tian, H., Shi, H., Pan, S., Chang, J., Dangal, S. R. S., Qin, X., Wang, S., Tubiello, F. N., Canadell, J. G., & Jackson, R. B. (2022). A 130-year global inventory of methane emissions from livestock: Trends, patterns, and drivers. *Global Change Biology*, *28*(17), 5142-5158. https://doi.org/10.1111/gcb.16280

Zhang, N., Prokhorov, I., Kueter, N., Li, G., Tuzson, B., Magyar, P. M., Ebert, V., Sivan, M., Nakagawa, M., Gilbert, A., Ueno, Y., Yoshida, N., Röckmann, T., Bernasconi, S. M., Emmenegger, L., & Mohn, J. (2025). Rapid High-Sensitivity Analysis of Methane Clumped Isotopes (Δ13CH3D and Δ12CH2D2) Using Mid-Infrared Laser Spectroscopy. *Analytical Chemistry*, *97*(2), 1291-1299. https://doi.org/10.1021/acs.analchem.4c05406

Zhang, N., Snyder, G. T., Lin, M., Nakagawa, M., Gilbert, A., Yoshida, N., Matsumoto, R., & Sekine, Y. (2021). Doubly substituted isotopologues of methane hydrate (13CH3D and 12CH2D2): Implications for methane clumped isotope effects, source apportionments and global hydrate reservoirs. *Geochimica Et Cosmochimica Acta*, *315*, 127-151.

Zhang, Q., Sun, L., Wei, N., Wu, L., & Mao, H. (2021). The characteristics and source analysis of VOCs emissions at roadside: Assess the impact of ethanol-gasoline implementation. *Atmospheric Environment*, *263*, 118670. https://doi.org/10.1016/j.atmosenv.2021.118670

Zhang, T., & Krooss, B. M. (2001). Experimental investigation on the carbon isotope fractionation of methane during gas migration by diffusion through sedimentary rocks at elevated temperature and pressure. *Geochimica Et Cosmochimica Acta*, *65*(16), 2723-2742. https://doi.org/10.1016/S0016-7037(01)00601-9

Zhang, Z., Poulter, B., Feldman, A. F., Ying, Q., Ciais, P., Peng, S., & Li, X. (2023). Recent intensification of wetland methane feedback. *Nature Climate Change*, *13*(5), 430-433. https://doi.org/10.1038/s41558-023-01629-0

Zhang, Z., Poulter, B., Knox, S., Stavert, A., McNicol, G., Fluet-Chouinard, E., Feinberg, A., Zhao, Y., Bousquet, P., Canadell, J. G., Ganesan, A., Hugelius, G., Hurtt, G., Jackson, R. B., Patra, P. K., Saunois, M., Höglund-Isaksson, L., Huang, C., Chatterjee, A., & Li, X. (2022). Anthropogenic emission is the main contributor to the rise of atmospheric methane during 1993–2017. *National Science Review*, *9*(5), nwab200. https://doi.org/10.1093/nsr/nwab200

Zhang, Z., Zimmermann, N. E., Stenke, A., Li, X., Hodson, E. L., Zhu, G., Huang, C., & Poulter, B. (2017). Emerging role of wetland methane emissions in driving 21st century climate change. *Proceedings of the National Academy of Sciences*, *114*(36), 9647-9652. https://doi.org/10.1073/pnas.1618765114

Zhao, J., Ciais, P., Chevallier, F., Canadell, J. G., van der Velde, I. R., Chuvieco, E., Chen, Y., Zhang, Q., He, K., & Zheng, B. (2025). Enhanced CH4 emissions from global wildfires likely due to undetected small fires. *Nature Communications*, *16*(1), 804. https://doi.org/10.1038/s41467-025-56218-w

Zhao, Y., Saunois, M., Bousquet, P., Lin, X., Berchet, A., Hegglin, M. I., Canadell, J. G., Jackson, R. B., Hauglustaine, D. A., Szopa, S., Stavert, A. R., Abraham, N. L., Archibald, A. T., Bekki, S., Deushi, M., Jöckel, P., Josse, B., Kinnison, D., Kirner, O.,…Zheng, B. (2019). Inter-model comparison of global hydroxyl radical (OH) distributions and their

impact on atmospheric methane over the 2000–2016 period. *Atmos. Chem. Phys.*, *19*(21), 13701-13723. https://doi.org/10.5194/acp-19-13701-2019

Zhao, Y., Saunois, M., Bousquet, P., Lin, X., Hegglin, M. I., Canadell, J. G., Jackson, R. B., & Zheng, B. (2023). Reconciling the bottom-up and top-down estimates of the methane chemical sink using multiple observations. *Atmos. Chem. Phys.*, *23*(1), 789-807. https://doi.org/10.5194/acp-23-789-2023